MEASUREMENT 2025

15th International Conference on Measurement

June 2–4, 2025
Smolenice Castle, Slovakia

Institute of Measurement Science
Slovak Academy of Sciences

MEASUREMENT 2025

The 15th International Conference on Measurement

ORGANIZERS OF THE CONFERENCE

Organizer

Institute of Measurement Science, Slovak Academy of Sciences, Bratislava

Technical sponsorship

IEEE Czechoslovakia Section

Slovak Metrological Society

Slovak Society of Biomedical Engineering and Medical Informatics

MEASUREMENT 2025

Proceedings of the
15th International Conference on Measurement

Congress Center of the Slovak Academy of Sciences
Smolenice Castle, Slovakia
June 2-4, 2025

MEASUREMENT 2025

Editors: Andrej Dvurečenskij, Ján Maňka, Jana Švehlíková, Viktor Witkovský,
Cover Design: Igor Holländer
Publisher: Institute of Measurement Science
Slovak Academy of Sciences
Dúbravská cesta 9
841 04 Bratislava Slovakia

ISBN 978-80-69159-00-6

COMMITTEES

Conference Chairman

J. Maňka, Slovakia

International Program Committee

J. Švehlíková, Slovakia, Chairman
B. Antić, Serbia
I. Bajla, Slovakia
M. Bittera, Slovakia
V. Boháč, Slovakia
E. Bruneel, Belgium
E. Cocherová, Slovakia
O. Dössel, Germany
R. Harťanský, Slovakia
L. Janoušek, Slovakia
P. Jurák, Czech Republic
B. Kessel, Sweden
O. Kochan, Ukraine
R. Köning, Germany
I.C. Lira, Chile
J. Markovič, Slovakia
K. Meigas, Estonia
V. Mlynarik, Austria
V. Novickij, Lithuania
M. Paluš, Czech Republic
K. Roubík, Czech Republic
Y. Serinagaoglu, Turkey
M. Soleimani, United Kingdom
Z. Starčuk, Czech Republic
M. Štork, Czech Republic
S. Takayama, Japan
P. Tino, United Kingdom
D. Tyler, United Kingdom
M. Tyšler, Slovakia
J. Volaufova, USA
G. Wimmer, Slovakia
V. Witkovský, Slovakia
A. Woźniak, Poland

Young Investigator Award Jury

Boris Antić, Serbia
Vladimír Juráš, Slovakia
Orest Kochan, Ukraine
Jan Mikulka, Czech Republic
Przemysław Otomanski, Poland
Teodor Toth, Slovakia
Viktor Witkovský, Slovakia

Local Organizing Committee

A. Dvurečenskij, Chairman
E. Gurišová
D. Gogola
I. Holländer
A. Krafčík
Z. Rošťáková
M. Škrátek
M. Teplan
L. Zelieska

Reviewers

The submitted papers were evaluated by 67 reviewers, members of the International Program Committee and experts in the fields of measurement science and technology. Each paper was scored by two or three reviewers.

Preface

When you can measure what you are speaking about,
and express it in numbers, you know something about it.
Lord Kelvin (1824 - 1907)

The **MEASUREMENT 2025 conference is** marking the **15th edition** of our conference series. The inaugural conference was held nearly **30 years ago**, and since then, all editions—except for the **2021 online event**—have taken place in the scenic surroundings of **Smolenice Castle**.

This year's conference continues to explore our traditional general topics:

- **Theoretical problems of measurement**
- **Measurement of physical quantities**
- **Measurement in biomedicine**

In addition to the keynote lectures, continue our tradition of **special sessions**, which this year highlight three topical areas:

- **AI in Medicine**
- **Quantitative MRI**
- **Modeling and Simulation of Biological Signals**

Selected speakers have been invited to contribute to these sessions, offering valuable insights into these dynamic fields.

The authors contributing to this year's Proceedings come from **nine different countries**. We are particularly grateful and inspired by the participation of our **Ukrainian colleagues**, who join us despite the challenging situation in their country.

We hope that the contributions presented at MEASUREMENT 2025 will prove insightful, foster new collaborations, and support the ongoing development of measurement science research.

Ján Maňka, Jana Švehlíková, Andrej Dvurečenskij, Viktor Witkovský

Contents

AI in Medicine

ISBN 978-80-69159-00-6

Measurement Image Reconstruction in Electrical Impedance Tomography through 1D-UNet

Serge Ayme Kouakouo Nomvussi, Jan Mikulka

Department of Theoretical and Experimental Electrical Engineering Brno,
Brno, Czech Republic
Email: 244245@vut.cz

Abstract. *This paper presents a deep learning approach for image reconstruction in Electrical Impedance Tomography using a one-dimensional U-Net model. The model's performance is evaluated against traditional methods such as the Total Variation and Gauss-Newton algorithms. Experimental results demonstrate that 1D-UNet consistently achieves superior reconstruction accuracy, particularly in noisy environments. In noise-free conditions, the model attains higher correlation coefficients and structural similarity values than conventional approaches, preserving fine details effectively. Under noisy conditions (30 dB and 60 dB), 1D-UNet maintains a significantly higher correlation and structural similarity, demonstrating its robustness. The strong generalization and adaptability of the proposed method underscore its potential for enhancing tomographic imaging applications in biomedical diagnostics, industrial process monitoring.*

Keywords: Electrical Impedance Tomography, U-Net, Deep Learning, Image Reconstruction, Neural Networks

1. Introduction

Electrical Impedance Tomography (EIT) is widely applied in various domains, including biomedical imaging, geophysics, and industrial process monitoring [1]. It reconstructs an object's internal conductivity distribution using electrical measurements taken at its periphery. Due to the inverse nature of the problem [2], conventional reconstruction methods such as the Gauss-Newton and Total Variation algorithms [3] often face limitations, especially when handling noisy data.

Deep learning, particularly Convolutional Neural Networks (CNNs) [4], has revolutionized image processing by providing data-driven solutions that improve reconstruction accuracy. This study proposes a U-Net-based framework tailored for one-dimensional EIT voltage measurements. Unlike traditional CNNs, U-Net employs an encoder-decoder structure with skip connections, allowing the model to preserve essential spatial features and enhance the fidelity of the reconstructed conductivity distribution.

2. Methodology

A synthetic dataset was generated using the EIDORS framework, a MATLAB-based tool for EIT simulations. The dataset contains boundary voltage measurements and conductivity distributions representing various target shapes and conductivity levels (0.01 S/m to 0.12 S/m) in a water-filled medium (0.04 S/m). Measurements were collected from 16 boundary electrodes positioned around the domain.

The dataset is structured as follows:

- **Training Set:** 208 × 10647 matrix of voltage inputs and 1024 × 10647 matrix of conductivity outputs.

ISBN 978-80-69159-00-6

- **Validation & Test Sets:** Each consists of 3549 samples with the same format.

This structured dataset enables the model to learn the mapping between boundary voltages and corresponding conductivity distributions, facilitating more accurate EIT reconstructions.

The 1D U-Net architecture shown in Fig. 1 is used for EIT image reconstruction in this study. It follows an encoder-decoder framework with skip connections that enhance feature propagation by allowing the network to retain essential spatial details throughout the reconstruction process. The input layer takes a 1 x 208 voltage measurement vector, which serves as the starting point for feature extraction. The encoder path (down sampling) consists of three 1D convolutional layers with increasing filter sizes (64, 128, and 256 filters) to extract hierarchical spatial features. Each convolutional layer is followed by batch normalization, which stabilizes training and improves convergence, and a ReLU activation function, introducing non-linearity to capture complex patterns. The bottleneck layer, positioned at the deepest part of the network, employs a 256-filter convolutional layer to learn high-level representations of the input data.

In the decoder path (up sampling), 1D transposed convolution layers gradually reconstruct the image by reversing the down sampling process. These transposed convolutions progressively reduce the number of filters from 256 → 128 → 64, aligning with the encoder layers. Skip connections allow information from earlier encoding layers to be directly transferred to corresponding decoding layers, preserving fine-grained spatial details lost during down sampling. The final reconstruction is completed by a fully connected output layer, which reshapes the decoded feature maps into a 1 x 1024 conductivity vector. A regression output layer ensures that the model generates continuous-valued conductivity predictions, making it suitable for EIT applications.

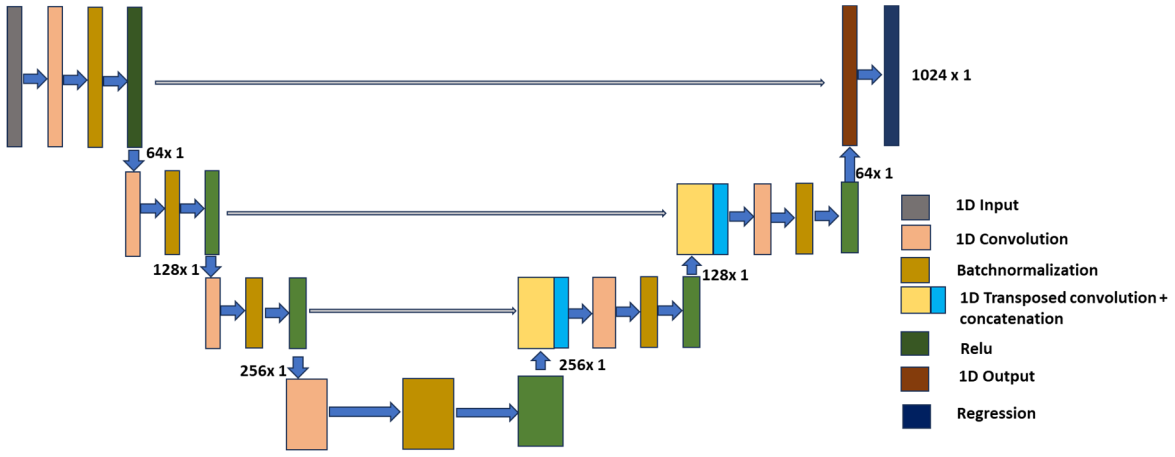

Fig. 1. 1D U-Net Architecture

Performance evaluation [5] is based on the following metrics:

- **Mean Squared Error (MSE):** Measures reconstruction accuracy between the predicted and reconstructed images.
- **Correlation Coefficient (CC):** Quantifies the relationship between reconstructed and original images.
- **Structural Similarity Index (SSIM):** Evaluates the preservation of structural details.

ISBN 978-80-69159-00-6

3. Results

The training process was conducted using a single GPU, with a piecewise learning rate schedule. The training ran for 2500 iterations, with validation performed every 15 iterations. The Mean Squared Error (MSE) improved from 48.96 at the first iteration to 6.93 at iteration 1080, indicating successful convergence as shown in Fig 2.

The reduction in training and validation loss over time highlights the network's capacity to learn meaningful representations and generalize well. Initially, the loss drops rapidly, reflecting the model's ability to capture key features early in training. As training progresses, the loss reduction stabilizes, indicating fine-tuning of network weights to optimize reconstruction accuracy.

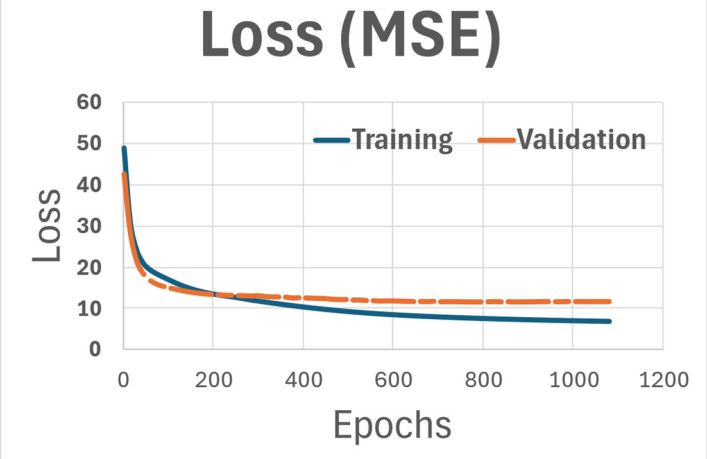

Fig. 2. Loss of 1D-UNet

Table 1. Comparison between 1D-Unet and the traditional methods (Total Variation and Gauss-Newton)

Position / Noise	Model	Reconstructed image Total Variation algorithm	Reconstructed image Gauss-Newton algorithm	Reconstructed image with 1D-UNet
1/No		 CC = 0.597 SSIM = 0.607	 CC = 0.644 SSIM = 0.605	 CC = 0.710 SSIM = 0.610
2/No		 CC = 0.776 SSIM = 0.619	 CC = 0.457 SSIM = 0.617	 CC = 0.821 SSIM = 0.623
3/No		 CC = 0.782 SSIM = 0.605	 CC = 0.831 SSIM = 0.598	 CC= 0.843 SSIM = 0.618
4/Yes 30 dB		 CC = 0.081 SSIM = 0.552	 CC = 0.171 SSIM = 0.574	 CC = 0.499 ssim = 0.605
5/Yes 60 dB		 CC = -0.146 SSIM = 0.387	 CC = 0.252 SSIM = 0.561	 CC = 0.723 SSIM = 0.611

ISBN 978-80-69159-00-6

The 1D-UNet model consistently outperforms the Total Variation (TV) and Gauss-Newton algorithms, particularly under noisy conditions. The correlation coefficient (CC) and structural similarity index (SSIM) were used to evaluate reconstruction accuracy across different scenarios.

The results in Table 1 show that in noise-free conditions (Positions 1–3), the 1D-UNet achieves the highest correlation and SSIM values, ensuring better reconstruction accuracy compared to TV and Gauss-Newton. Under noisy conditions (30 dB and 60 dB, Positions 4–5), TV and Gauss-Newton methods experience significant performance degradation, with correlation values as low as -0.146 and 0.252, while 1D-UNet maintains a much higher correlation of 0.499 and 0.723. The SSIM scores of 1D-UNet also remain superior, confirming its robustness in challenging conditions.

These findings highlight the advantage of 1D-UNet in preserving structural details and achieving more reliable reconstructions, making it highly suitable for industrial applications.

4. Discussion and Conclusion

This study confirms that 1D-UNet significantly outperforms TV and Gauss-Newton across all tested conditions. While traditional methods struggle with noise, leading to poor correlation and SSIM values, 1D-UNet maintains high performance even in challenging environments.

Its superior performance is due to deep feature extraction, efficient up sampling, and skip connections that preserve fine details. These results emphasize its potential for real-time medical imaging, industrial process monitoring, and geophysical exploration.

Future work will focus on optimizing architecture, incorporating attention mechanisms, and hybrid models to enhance robustness and efficiency, paving the way for more accurate EIT reconstruction applications.

Acknowledgements

The results of the work were published with the support of a specific research project of the Department of Theoretical and Experimental Electrical Engineering of BUT.

References

[1] Harikumar, R., Prabu, R., & Raghavan, S. (2013). Electrical impedance tomography (EIT) and its medical applications: a review. *International Journal of Soft Computing and Engineering*, 3(4), 193-198.

[2] Zhang, T., et al. (2022). Advances of deep learning in electrical impedance tomography image reconstruction. *Frontiers in Bioengineering and Biotechnology*, 10, 1019531.

[3] Farha, M. (2017). Combined algorithm of total variation and Gauss-Newton for image reconstruction in two-dimensional Electrical Impedance Tomography (EIT). In *Proceedings of the 2017 International Seminar on Sensors, Instrumentation, Measurement and Metrology (ISSIMM)*. IEEE.

[4] Li, X., et al. (2020). One-dimensional convolutional neural network (1D-CNN) image reconstruction for electrical impedance tomography. *Review of Scientific Instruments*, 91(12).

[5] Nomvussi, S. A. K., & Mikulka, J. (2024). Enhanced image reconstruction in electrical impedance tomography using radial basis function neural networks. *Measurement Science Review*, 24(6), 200-210.

Application of Deep Learning Algorithms for Automated MRI Knee Joint Image Segmentation

[1,2]Iveta Pajanova, [2]Andrej Krafcik

[1]Faculty of Electrical Engineering and Information Technology, Slovak University of Technology, Bratislava, Slovakia

[2]Institute of Measurement Science, Slovak Academy of Sciences, Bratislava, Slovakia
Email: iveta.pajanova@savba.sk

Abstract. *Manual segmentation of knee joint structures in 3D Magnetic Resonance Imaging (MRI) scans is a labor-intensive process, often requiring several hours per scan for detailed segmentations. This paper presents a deep learning approach utilizing a modified 3D U-Net architecture for automated segmentation of knee MRI images from the Osteoarthritis Initiative (OAI) dataset. Trained on 507 subjects, the model achieves minimum Dice similarity coefficients of 98.5% for femoral and tibial bone, 85.0% for femoral cartilage, and 70.8% for tibial cartilage. The average inference time per one subject was under 30 seconds, demonstrating a reduction in processing time compared to manual annotation. These results suggest that CNN-based segmentation offers a reliable and efficient alternative to manual segmentation, enhancing diagnostic workflows in osteoarthritis monitoring.*

Keywords: Artificial Neural Network, Automated MRI Image Segmentation, Convolutional Neural Network, Deep Learning, Knee Joint, Osteoarthritis

1. Introduction

Magnetic Resonance Imaging (MRI) is an essential tool for diagnosing musculoskeletal conditions, particularly in evaluating knee joint health. However, manual segmentation of MRI scans is time-intensive and requires specialized expertise. Segmenting cartilage manually in a 3D knee MRI may take as long as 6 hours per knee.[1] To address this challenge, deep learning techniques, particularly Convolutional Neural Networks (CNNs), offer a promising solution for automating MRI image segmentation. This study explores the application of a modified 3D U-Net architecture for knee joint MRI segmentation. By leveraging a dataset of 507 subjects from the Osteoarthritis Initiative (OAI), the model aims to reduce segmentation time while maintaining high segmentation performance.

2. Subject and Methods

Dataset

A dataset of 507 human subjects from the Osteoarthritis Initiative (OAI) was provided by the Zuse Institute Berlin (ZIB). The dataset (Table 1) consists of manually segmented, high-resolution 3D double echo steady-state (DESS) MRI scans of knee joints, acquired using a Siemens 3T Trio system. It includes subjects with varying degrees of osteoarthritis pathology. As of December 1, 2022, the data is publicly available online (`https://pubdata.zib.de`). Experts at the Zuse Institute Berlin manually segmented the MRI data for each patient in the OAI-ZIB dataset. The segmentations identified five distinct categories, including four anatomical-morphological classes: femoral bone (FB), femoral cartilage (FC), tibial bone (TB), tibial cartilage (TC), and background. The composition of the training and validation datasets, including the acquisition protocol (baseline and/or 12-month follow-up), is detailed in Reference [2]. The manually segmented 3D MRI data was downsampled to a resolution of

$128 \times 128 \times 80$. The dataset was divided into training, validation, and testing subsets in a $6:2:2$ ratio.

Table 1: Summary of the OAI-ZIB dataset [2].

Parameter	Value
MRI scanner	Siemens 3T Trio
MRI sequence	DESS
Acquisition plane	sagittal
Resolution	$0.36 \times 0.36 \times 0.7$ mm^3
Size	$384 \times 384 \times 160$ voxels
Segmentation	bones, cartilage
Subjects	507
Sex (M/F)	262 / 245
Age (years)	61.87 ± 9.33
BMI (kg/m^2)	29.27 ± 4.52
OA grade (0-4)	(60, 77, 61, 151, 158)
Timepoints	baseline

Convolutional Neural Network (CNN) Architecture: 3D U-Net

The proposed segmentation model (Fig. 1) is a 3D U-Net architecture, inspired by the work of Ronneberger et al. [6] and Cicek et al. [3]. It follows an encoder-decoder structure, making it well-suited for volumetric medical image segmentation The encoder has multiple convolutional blocks, each with two 3D convolutional layers using ReLU activation, followed by max-pooling for downsampling. The bridge serves as a bottleneck, capturing deep feature representations before the decoder phase. The decoder symmetrically upsamples the feature maps using transposed convolutions, with skip connections from the corresponding encoder layers to preserve spatial information. Dropout is applied to improve generalization and prevent overfitting. The final output layer uses a 3D convolution with a softmax activation function, allowing for multi-class segmentation.

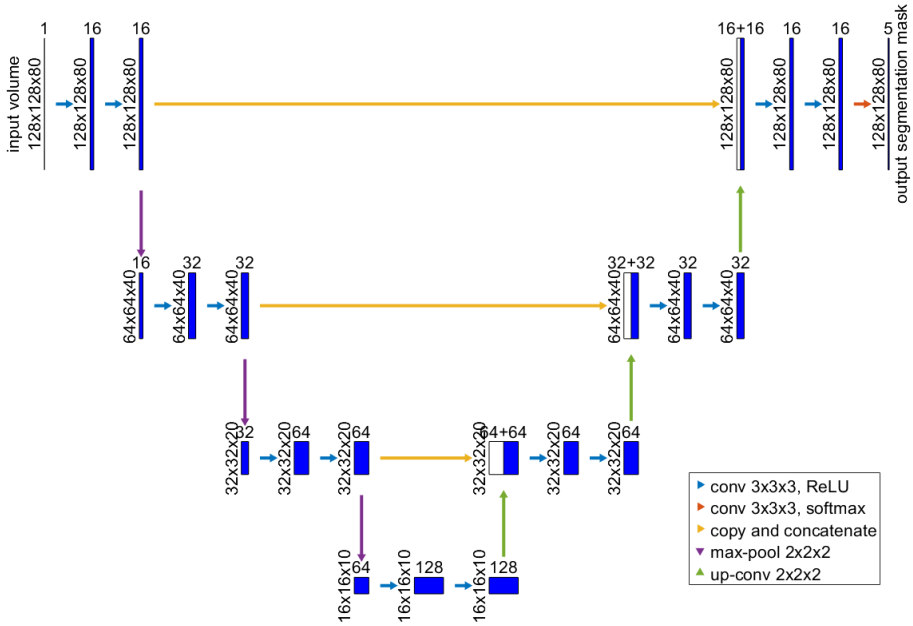

Fig. 1: The implemented 3D U-Net architecture. Blue boxes represent feature maps at different stages of the network. White boxes indicate skip connections, where feature maps from the encoder path are concatenated with those in the decoder path to retain spatial information. The number of filters at each layer is specified above the corresponding feature maps.

ISBN 978-80-69159-00-6

Training and Validation

The 3D U-Net model was implemented using TENSORFLOW and KERAS in PYTHON, ensuring efficient deep learning-based segmentation. The training process was structured with 150 epochs, using the Sparse Categorical Crossentropy loss function for multi-class segmentation and the RMSprop optimizer with a learning rate of 0.0001. The model was trained in a supervised learning mode, utilizing a custom training loop with a gradient tape for automatic differentiation. The training pipeline used batch-wise gradient updates and a dropout regularization (dropout rate = 0.3) to reduce overfitting. The Sparse Categorical Accuracy metric was used to evaluate segmentation performance during training and validation phases. A custom training function was implemented to iterate over 150 epochs, with performance tracking at each epoch. Both training and validation losses and accuracies were logged, and the model checkpoints were saved based on the best validation loss and best validation accuracy. Implemented [4] in TENSORFLOW 2.12.0 (available online: `https://www.tensorflow.org`, accessed on 19 March 2025) module in PYTHON 3.9.18 (Python Software Foundation, 2023, `https://www.python.org`) environment on a PC with an 11th Gen Intel(R) Core(TM) i7-11700F @ 2.50GHz processor, 32GB RAM, and an NVIDIA GeForce RTX 3070 GPU.

Performance quantification

The Dice coefficient [5] is a key parameter in image segmentation as it assesses how well a segmented region matches the ground truth. It quantifies the overlap between the predicted segmentation and the actual region of interest. Higher DC values indicate better segmentation performance. Mathematically, the Dice coefficient is a statistical measure used to quantify the similarity between two sets of data. It is computed as twice the number of shared elements (e.g. voxels) divided by the total number of elements in both sets. The result ranges from 0 (no overlap) to 1 (complete overlap). A Dice coefficient of 0.7 or higher is generally considered a good segmentation result, while a Dice coefficient below 0.3 is regarded as poor. In this work, we measure the spatial overlap between manual and automated segmentation masks.

3. Results

The training time for the deep learning model was 6071.03 seconds (101.18 minutes), demonstrating the computational demands of training and validating the modified 3D U-Net architecture for knee joint MRI segmentation. Table 2 presents the Dice coefficient for each worst class of individual patients, providing insight into segmentation performance across different anatomical structures. Additionally, Fig. 2 presents the training and validation process, depicting the loss and accuracy curves over the training epochs.

Table 2: Minimum Dice Coefficients per Class Across Individual Patients.

Class:	Femoral bone	Fem. Cartilage	Tibial bone	Tib. Cartilage	Overall
Patient ID	$DC_1[\%]$	$DC_2[\%]$	$DC_3[\%]$	$DC_4[\%]$	$DC[\%]$
9646958	**95.61**	87.41	**94.51**	78.03	94.55
9627716	98.43	**79.61**	98.55	83.63	97.58
9646958	98.53	85.00	98.47	**70.75**	97.50

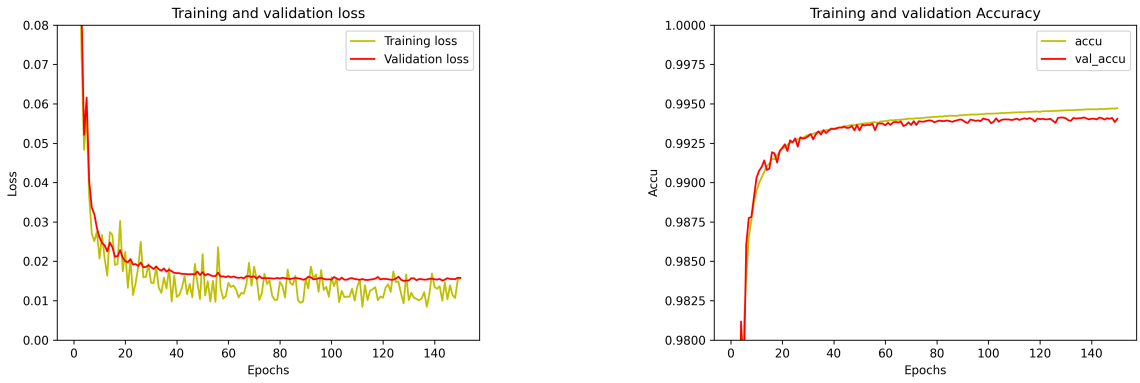

(a) (b)

Fig. 2: Training and Validation Loss (a) and Accuracy (b)

4. Discussion

The study demonstrates the effectiveness of deep learning in medical image analysis, particularly in knee MRI segmentation. The proposed 3D U-Net model, trained on downsampled 3D MRI knee data, achieves reliable segmentation results, as indicated by Dice coefficient values. The findings suggest that CNN-based segmentation can significantly reduce manual workload and increase consistency in diagnosing knee-related conditions such as osteoarthritis. Future research could explore model optimization, domain adaptation techniques, and real-world clinical applications to further enhance automated knee MRI analysis.

Acknowledgements

This research was funded by the EU NextGenerationEU through the Recovery and Resilience Plan for Slovakia under the project No. 09I03-03-V02-00016.

References

[1] Almajalid R., Shan J., Zhang M. , Stonis G. and Zhang M., "Knee Bone Segmentation on Three-Dimensional MRI," *2019 18th IEEE International Conference On Machine Learning And Applications (ICMLA*), Boca Raton, FL, USA, 2019, pp. 1725-1730,

[2] Ambellan F, et al. (2019). Automated segmentation of knee bone and cartilage combining statistical shape knowledge and CNNs: Data from the OAI. *Med Image Anal.*,52,109-118.

[3] Cicek, O., et al. (2016). *Lect. Notes Comput. Sci.*, 9901 LNCS, 424-432.

[4] Chollet, F. (2021). *Deep Learning with Python, 2nd Edition.* Manning, Shelter Island, NY.

[5] Dice L. R. (1945). Measures of the amount of ecologic association between species Ecology 26 297–302.

[6] Ronneberger, O., Fischer, P., Brox, T. (2015). U-Net: Convolutional Networks for Biomedical Image Segmentation. In: *International Conference on Medical Image Computing and Computer-Assisted Intervention* Springer, Cham, 234-241.

Non-Invasive Approaches for Premature Ventricular Contractions Localization

[1]Beata Ondrusova, [2]Canberk Almus, [3]Jana Svehlikova, [2]Yesim S. Dogrusoz

[1]Johannes Kepler University, Linz, Austria
[2]Electrical and Electronics Eng Dept, METU, Ankara, Turkey
[3]Institute of Measurement Science, SAS, Bratislava, Slovakia
Email: beata.ondrusova@jku.at

Abstract. *Electrocardiographic Imaging (ECGI) has some limitations due to inaccuracies in some patients. Here, we explore 3 methods for the localization of premature ventricular contractions (PVCs): Tikhonov Regularization (TR), Bayesian Maximum A Posteriori Estimation (BMAP), and Multivariate Adaptive Regression Splines (MARS). A cohort of 5 patients with frequent PVCs was used, and the computations assumed both homogeneous and inhomogeneous torso models. Additionally, BMAP and MARS were computed using simulated prior knowledge of PVC endoepicardial potentials, originating either from the entire myocardium or a physiologically relevant area. The localization error (LE) was assessed as the Euclidean distance between the ECGI solution and the ground truth. BMAP method showed the lowest median LE with physiologically relevant prior knowledge for both torso models, outperforming TR. In contrast, the MARS method underperformed when applied to these pre-selected datasets. Overall, the results indicate that certain methods may improve accuracy under specific conditions, but further research is needed to explore their full potential and limitations in ECGI.*

Keywords: Electrocardiographic Imaging, Tikhonov Regularization, Bayesian Estimation, Multivariate Adaptive Regression Splines

1. Introduction

Electrocardiographic Imaging (ECGI) is a non-invasive method that identifies abnormal cardiac activity, such as premature ventricular contractions (PVCs), using body surface potentials (BSPs) recorded on the torso. ECGI can guide radiofrequency catheter ablation (RFA). Regrettably, the inverse problem is ill-posed, making its solution challenging, and various methods have been developed to improve the accuracy of the solution.

Tikhonov regularization (TR) is a widely used method that adds a regularization term to the least-squares formulation of the problem [1]. Despite its simplicity, choosing the right regularization parameter might be challenging. With advances in computational power, different approaches are gaining more attention. In this work, we focus on TR and two less commonly used methods - one based on a statistical approach and the other on spline fitting. Bayesian Maximum A Posteriori Estimate (BMAP) is a statistical approach that uses prior knowledge derived from known physiological properties or in-silico simulations, and it provides valuable statistical measures, like Bayesian error covariance, which improve the interpretability of the results [2]. The Multivariate Adaptive Regression Splines (MARS) method uses piecewise splines to model complex, nonlinear relationships in the data. Spline-based methods allow efficient parameterization with fewer unknowns and thus can improve robustness and accuracy [3]. However, both methods, BMAP and MARS, have their own challenges, such as modeling prior information and determining the optimal number of splines.

Unfortunately, no method is universally optimal; one may outperform another in specific tasks. In this work, we apply the methods mentioned above with an aim to evaluate their accuracy to identify the origin of PVCs using clinical data.

ISBN 978-80-69159-00-6

2. Data and Methods

This study uses a subset of 5 patients from the Bratislava dataset. The data used were BSPs recorded with the ProCardio8 measuring system equipped with 128 electrodes and patient-specific geometric models created from CT scans. Each patient underwent a successful RFA, and the known origin of PVCs was used for validation. We tested 2 torso models, homogeneous (HT) and inhomogeneous (HBLT), which included lungs and blood pools. The pipeline of this study is shown in Fig. 1, panel A. Due to space constraints, we refer the reader to study [4] for further details about data and to studies [2], [3], [4] for more information about methods used.

Tikhonov regularization (TR): We applied zero-order TR and optimized the solution using the median λ_t values obtained from the L-curve method [4].

Bayesian Maximum A Posteriori (BMAP): BMAP treats the endoepicardial potentials and noise as random variables, aiming to maximize the posterior probability density function (pdf) based on the likelihood of the measurements and prior information. In this study, the endoepicardial potentials and BSPMs were assumed to be jointly Gaussian, with Gaussian noise that is uncorrelated with the potentials [2]. The prior knowledge was derived from PVC simulations described below.

Multivariate Adaptive Regression Splines (MARS): MARS models the relationship between BSPs and endoepicardial potentials by constructing a non-parametric regression model. The method uses a set of spline basis functions to map BSPs to endoepicardial potentials. Given the endoepicardial potentials and corresponding BSPs computed through the forward solutions, MARS automatically builds an initial model and reduces complexity during the pruning step to obtain the best functional representation [3]. To evaluate the accuracy in comparison with BMAP, the same training sets of endoepicardial potentials were used as described below.

Prior Information: Patient-specific PVC simulations using CT-derived models were computed with the cellular automaton to model activation propagation. Activation was initiated from 211-306 predefined locations across the entire myocardial volume. Endoepicardial and torso potentials were subsequently computed using the Boundary Element Method. Each simulation duration was matched to the patient's PVC duration extracted from recorded signals. The training datasets included concatenated cardiac potentials, and we tested three cases, shown in Fig. 1, panel B:

- FSD (Full Simulation Dataset): All PVC simulations, covering the entire myocardium.
- PST10 (Patient-Specific Top 10% Dataset): Top 10% of PVC simulations with the highest correlation between measured and computed BSPs (21–31 per patient).
- CPT10 (Cross-Patient Top 10% Dataset): PVC simulations from 23 points with the highest correlation between measured and computed BSPs.

Validation: The PVC origin was identified as the earliest activated node in the activation sequence that was computed using spatiotemporal smoothing. The estimated PVC origin was then compared to the RFA-derived origin, and the localization error (LE) was calculated as the Euclidean distance between them [4].

3. Results

The LEs for both torso models, as well as all patients and methods, are shown in Fig. 1, panel C. The statistical distribution of LEs for each method is shown in panel D. Due to space constraints, values are shown within the graphs in panels C and D, with only median values presented in panel D.

ISBN 978-80-69159-00-6

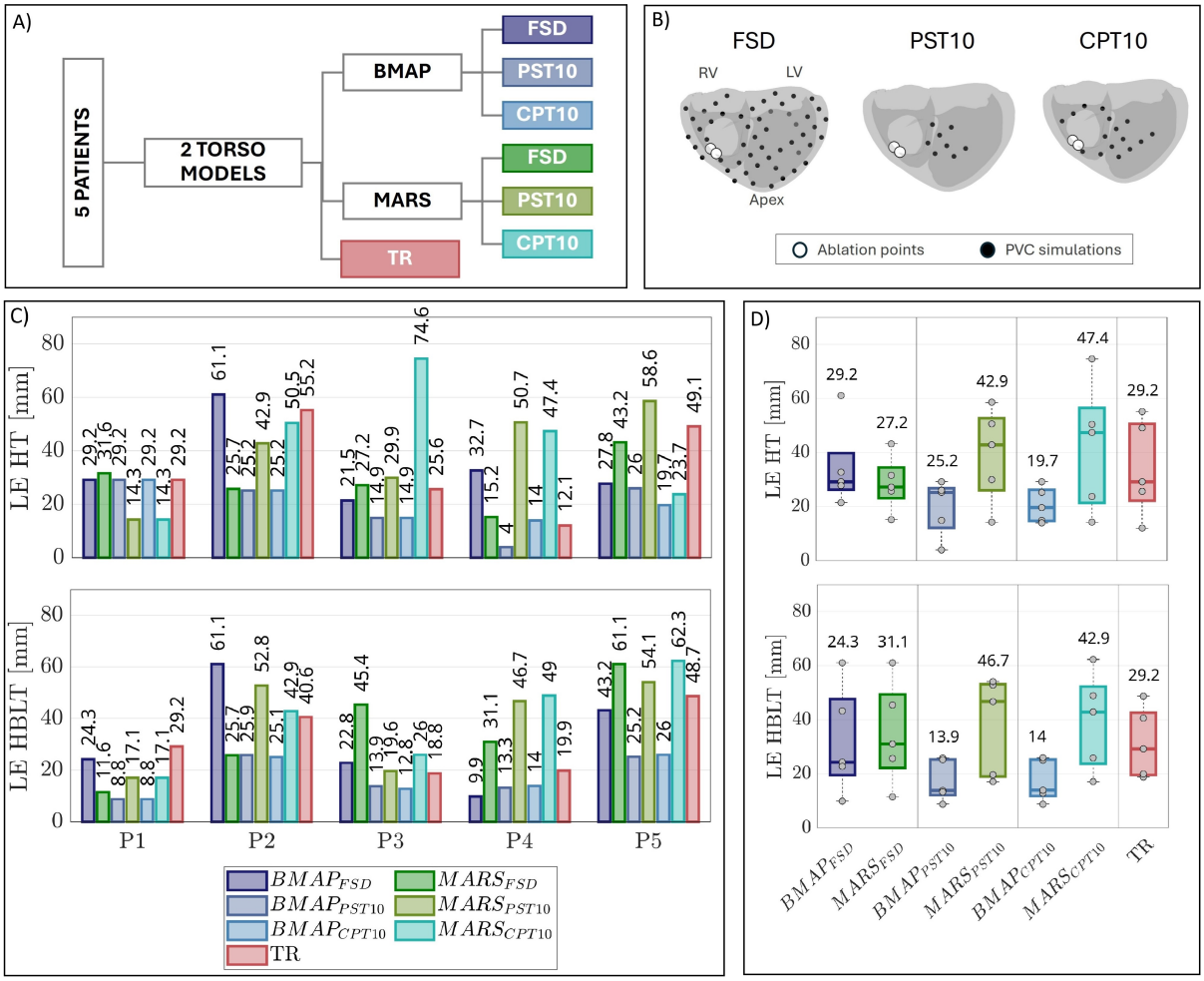

Fig. 1: A) Pipeline. B) Training sets depicted for P1. C) LE for each patient and method. D) Statistical distribution of LEs for each method with median LE presented above each box. The grey dots represent LE values obtained for all patients. Panels C and D: HT (top) and HBLT (bottom).

4. Discussion

In this study, we investigated the accuracy of different methods for localizing PVCs, including the commonly used TR and lesser-used methods that have been only minimally tested on clinical data. First, we discuss the results at the patient-specific level as shown in Fig. 1, panel C. The lowest LE was observed in patient P4 with BMAP using the PST10 training set and HT model, and in patient P1 with BMAP using the PST10 and CPT10 training sets and the HBLT model. In both cases, LE was below 10 mm. In contrast, the highest LE of 75 mm was observed in patient P3 using MARS with the CPT10 training set. This result needs further investigation, as other methods performed significantly better for this patient, and applying an HBLT model reduced the LE to 26 mm. From our cohort, all methods performed well in patient P1, with the highest LE of 32 mm. Like some other patients, P2 and P5 were showing high LEs across multiple methods. Several factors may contribute to this, including underlying comorbidities that ECGI may not be able to accurately capture, as well as inaccuracies in geometrical modeling and signal processing errors. These findings highlight the need for further investigation into these results.

Fig. 1, panel D, illustrates the statistical distribution of localization LEs for each method. Given the limited cohort size of only 5 patients, drawing conclusions is challenging, as a larger sample size would be necessary for robust statistical analysis. Nevertheless, the results offer

ISBN 978-80-69159-00-6

some interesting insights when comparing methods and torso models. When comparing methods, the BMAP method demonstrated superior performance in identifying PVCs particularly when trained with smaller datasets as evidenced by its lower median LE values and tighter interquartile range (IQR), outperforming TR. These findings suggest that BMAP could be used for PVC identification, especially when using smaller, physiologically relevant training datasets. In contrast, the MARS method exhibited poorer performance, as indicated by higher LE values across most cases. However, an interesting exception occurred with the HT torso model for the MARS method using FSD training sets, which included all PVC simulations. In this case, the method showed its best performance. This observation suggests that the MARS method may achieve good results without the additional step of selecting a specific training dataset, potentially saving time and reducing the risk of introducing errors associated with dataset selection. When comparing torso models, the BMAP method performed better with the HBLT model for all training sets in terms of median LE.

This study has several limitations, including a small cohort of 5 patients, thus requiring validation on a larger dataset. PVC localization relied on expert mapping, which may have introduced alignment inaccuracies, potentially affecting LE. Both BMAP and MARS showed poor performance in some cases, highlighting the need to identify potential sources of error. Additionally, these models were trained on simulated data, which may not fully capture real cardiac activity, and model errors should be considered when interpreting the results. Despite their less common use in ECGI, our findings suggest that BMAP and MARS can, in certain cases, achieve accuracy comparable to TR or even outperform it. However, the results should be interpreted with caution, and further research is required to assess their accuracy.

5. Conclusions

In conclusion, BMAP and MARS offer potential alternatives to TR for PVC localization, with BMAP showing better performance on smaller training datasets. However, further investigation is needed to address inconsistencies observed in some cases and validate the methods on larger datasets.

Acknowledgements

This work received support from the joint project between TUBITAK (grant no: 120N200) and the SAS (grant no: 536057), by the VEGA Grant Agency (grant no: 2/0109/22) and the Research and Development Agency in Slovakia (grant no: APVV-19-0531).

References

[1] Tikhonov AN, et al. (1995). Numerical methods for the approximate solution of ill-posed problems on compact sets. *Springer Science+Business Media Dordrecht*.

[2] Serinagaoglu, Y., Brooks, D. H., MacLeod, R. S. (2006). Improved performance of Bayesian solutions for inverse electrocardiography using multiple information sources. *IEEE transactions on bio-medical engineering*, 53(10), 2024–2034.

[3] Onak, Ö. N., Erenler, T., Dogrusoz, Y. S. (2022). A Novel Data-Adaptive Regression Framework Based on Multivariate Adaptive Regression Splines for Electrocardiographic Imaging. *IEEE Transactions on Biomedical Engineering*, 69(2), 963-974.

[4] Dogrusoz, Y. S., et al. (2023). Comparison of dipole-based and potential-based ECGI methods for premature ventricular contraction beat localization with clinical data. *Frontiers in physiology*, 14, 1197778.

Halfway Between CP and Tucker Model: PARALIND Analysis of Human Electroencephalogram

Zuzana Rošťáková, Roman Rosipal, Nina Evetović

Institute of Measurement Science, Slovak Academy of Sciences, Bratislava, Slovakia
Email: zuzana.rostakova@savba.sk

Abstract. *Subject-specific narrowband oscillatory rhythms in human electroencephalogram (EEG) can be detected using tensor decomposition. In our previous studies, we explored the CANDECOMP/PARAFAC (CP) decomposition together with the more flexible Tucker model. However, we found that CP decomposition sometimes required a high number of latent components to represent the data latent structure accurately. On the other hand, the Tucker model appeared too generalized, leading to very sparse solutions. Therefore, in this study, we focus on the PARALIND model, which combines the more straightforward interpretability of CP decomposition with the flexibility of the Tucker model. We demonstrate its performance on EEG recordings from a patient following an ischemic stroke, comparing it to the previous two models.*

Keywords: Electroencephalogram, Tensor, CP Decomposition, Tucker Model, PARALIND

1. Introduction

The effectiveness of tensor decomposition methods to successfully reveal the latent structure of EEG signal has been proved in our previous study [1], which focused on the CANDECOMP/PARAFAC (CP) decomposition and Tucker model [2, p. 43 and 59]. However, we discovered that CP decomposition needed a considerably higher number of components to effectively represent the latent structure of the data when the EEG signal was recorded using a limited number of electrodes focused on specific brain regions, such as the central sensorimotor cortex [1]. The Tucker model, on the other hand, produced a very sparse decomposition, indicating it is too flexible for the analyzed data. In this study, we, therefore, focus on an alternative model called PARALIND - the parallel profiles with linear dependencies [3] - combining the flexibility of the Tucker model with the intuitive interpretability of the CP decomposition and discuss its performance when detecting narrowband brain oscillatory rhythms.

2. PARALIND and its relationship with other tensor decomposition models

The PARALIND model [3] with (M,N,O) signatures and $F \geq \max\{M,N,O\}$ common components can be described using two equivalent formulas

$$\underline{X} = \underline{\Lambda} \times_1 \underbrace{(AH_A)}_{A^\star} \times_2 \underbrace{(BH_B)}_{B^\star} \times_3 \underbrace{(CH_C)}_{C^\star} + \underline{E} = \sum_{f=1}^{F} \lambda_{fff} \underbrace{(AH_A)_f}_{\mathbf{a}_f^\star} \circ \underbrace{(BH_B)_f}_{\mathbf{b}_f^\star} \circ \underbrace{(CH_C)_f}_{\mathbf{c}_f^\star} + \underline{E}, \tag{1}$$

$$\underline{X} = \underbrace{(\underline{\Lambda} \times_1 H_A \times_2 H_B \times_3 H_C)}_{\underline{G}^\star} \times_1 A \times_2 B \times_3 C + \underline{E} = \sum_{m=1}^{M} \sum_{n=1}^{N} \sum_{o=1}^{O} \underbrace{\left(\sum_{f=1}^{F} \lambda_{fff} \mathbf{h}_{mf}^A \mathbf{h}_{nf}^B \mathbf{h}_{of}^C \right)}_{g_{mno}^\star} \mathbf{a}_m \circ \mathbf{b}_n \circ \mathbf{c}_o + \underline{E}, \tag{2}$$

where $\underline{X} \in \mathbb{R}^{I \times J \times K}$ denotes a data tensor and $\underline{E} \in \mathbb{R}^{I \times J \times K}$ represents model error. The component matrices $A = [\mathbf{a}_1, \mathbf{a}_2, \ldots, \mathbf{a}_M] \in \mathbb{R}^{I \times M}, B = [\mathbf{b}_1, \mathbf{b}_2, \ldots, \mathbf{b}_N] \in \mathbb{R}^{J \times N}, C = [\mathbf{c}_1, \mathbf{c}_2, \ldots, \mathbf{c}_O] \in \mathbb{R}^{K \times O}$ represent the temporal (TS), spatial (SpS) and frequency signatures (FS) of the latent components. The relationships between signatures in different modes are captured by the dependency matrices $H_A \in \mathbb{R}^{M \times F}, H_B \in \mathbb{R}^{N \times F}, H_C \in \mathbb{R}^{O \times F}$. Unlike in [3], where the dependency

matrices were assumed to be known and fixed, we have chosen to estimate them simultaneously along with the component matrices using the alternating least squares algorithm [2].

The core tensor $\underline{\Lambda} \in \mathbb{R}^{F\times F\times F}$ is super-diagonal with $\lambda_{mno} \neq 0$ only if $m = n = o$. The f^{th} column of the matrix product $AH_A = A^\star$ is denoted by $(AH_A)_f = \mathbf{a}_f^\star$. Finally, $\underline{X} \times_n Y$ represents the tensor-matrix product in the n^{th} mode and $\mathbf{a} \circ \mathbf{b}$ is an outer product of two vectors [2].

Considering Eq. (1), PARALIND is a CP model with F components and component matrices $A^\star, B^\star, C^\star$. Due to the superdiagonality of $\underline{\Lambda}$, the f^{th} column of $A^\star$ is related only with the the f^{th} columns of $B^\star$ and $C^\star$. Additionally, PARALIND can also be interpreted as an (M,N,O)-Tucker model with the core tensor $\underline{G}^\star$ following a CP structure, as described in Eq. (2) [3].

3. Data

In this study, we focused on the multichannel EEG signal from 13 recordings of an 84-year-old man with post-stroke right-sided hemiplegia [4]. The EEG signals were recorded at a sampling frequency of 250 Hz, using 10 electrodes positioned over the sensorimotor area[1] and referenced to linked ears. Following [1], we inspected and corrected potential artefacts semi-automatically using the BrainVision Analyser 2 software.

For each recording day, the EEG signal was divided into overlapping two-second time windows. For each time window, we computed the oscillatory part of the amplitude spectrum, and the $\log_{10}$-transformed values were concatenated into a tensor $\underline{X} \in \mathbb{R}^{I\times J\times K}$, where I, J, and K represent the number of time windows, the number of electrodes, and the number of frequencies, respectively. Before tensor decomposition, the tensor $\underline{X}$ was centered in the first mode.

To be consistent with [1], we applied the nonnegativity constraints for TS and SpS, as well as unimodality constraints for FS in the CP decomposition, Tucker model, and PARALIND. Based on our earlier findings [1], we expected the lateralization of latent components - a different temporal activation of the same brain oscillation in the left and right hemisphere. Therefore, we selected the number of signatures in the various models as follows:

- CP with F components (F signatures in all three modes),
- Tucker model with either $(F,2,F)$ or $\left(F,2,\frac{F}{2}\right)$ signatures (denoted as T1 and T2),
- PARALIND with F common components and $(F,2,F)$ or $\left(F,2,\frac{F}{2}\right)$ signatures (PL1, PL2).

Here, F is an even number ranging from four to 20, which leads to nine CP, PL1, PL2, T1, and T2 models for each training day.

4. Results

The suitability of the PARALIND application was validated by two main observations: first, the presence of duplicate components in the CP decomposition, which indicated the same oscillation occurring with different temporal activities in both hemispheres; second, the trilinear and sparse structure of the core tensors $\underline{G}$ in both Tucker models, where the percentage of nonzero elements ranged from 5% to 25%. The trilinear structure of $\underline{G} \in \mathbb{R}^{F\times 2\times \frac{F}{2}}$ in T2 was confirmed by the core consistency diagnostics (CCD) [2, p. 78], which was close to or equal to 100% for all days assessed. The ratio of the T1 core tensors with CCD values exceeding the 90% threshold (indicating pure trilinearity) varied from 0.44 on Day 10 to 1 on Days 2 and 9, with a mode of 0.89 observed over five days.

In the next step, we compared the mean squared error (MSE) across models with the same number of common components F. As depicted in Fig. 1, the CP, T1, and PL1 models achieved

[1] Electrode placement followed the 10-20 system, with electrodes positioned at FC3, C1, C3, C5, CP3, and FC4, C2, C4, C6, CP4.

ISBN 978-80-69159-00-6

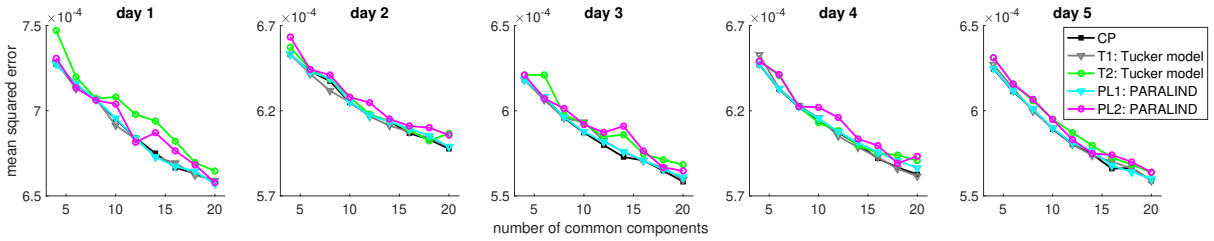

Fig. 1: The mean squared error of CP and two versions of both the Tucker model and PARALIND with the number of common components $F \in \{4,6,\ldots,20\}$ when applied to the first five recording days.

similar MSE values. The slightly higher MSE observed in T2 and PL2 (Fig. 1, green and magenta) was expected, as these models used half the number of FS compared to the corresponding CP, PL1, and T1. Another reason could be that the T2 and PL2 structure is more restricted to laterality. Nonetheless, from a quantitative point of view, we can conclude that both versions of PARALIND modeled the data latent structure comparably to the CP and Tucker model.

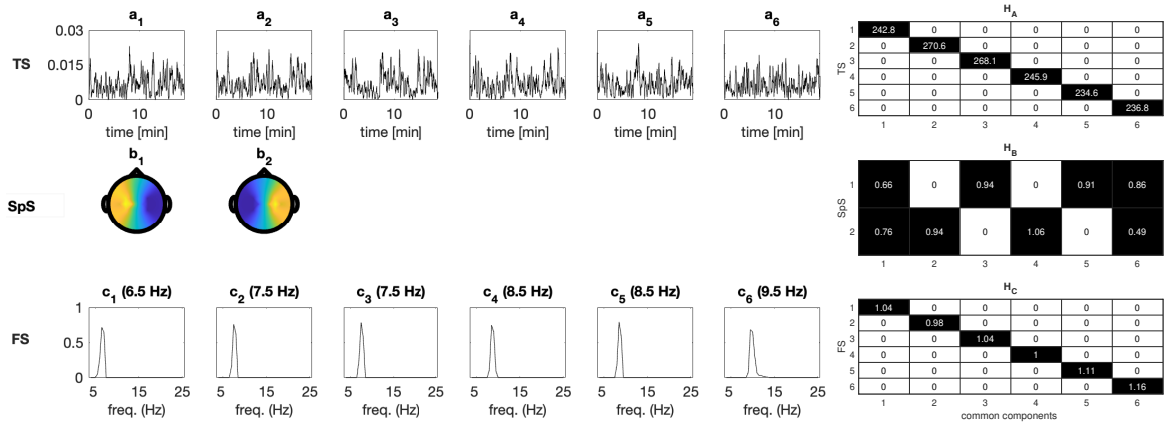

Fig. 2: Day 12 - PARALIND model PL1 with (6,2,6) signatures and six common components. The component signatures are depicted on the left, and the dependency matrices H_A, H_B, H_C are on the right.

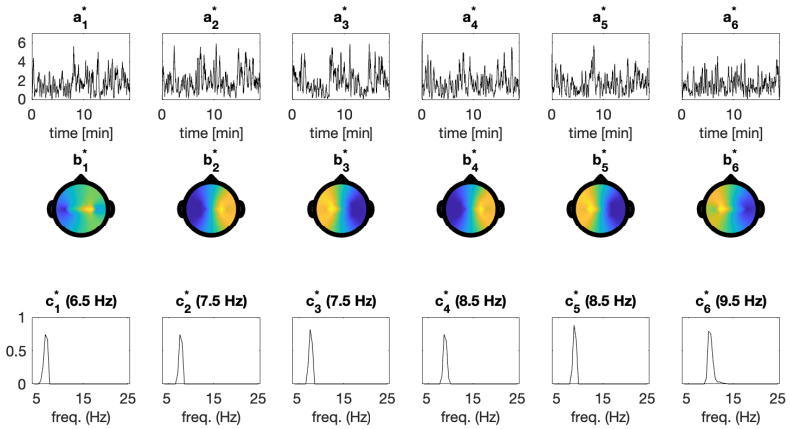

Fig. 3: Day 12 - Common component signatures from the PARALIND model PL1 depicted in Fig. 2.

The interpretability of the PARALIND decomposition is also essential. Let us examine the outcome of the PL1 model with (6, 2, 6) signatures and $F = 6$, applied to data from Day 12 (Fig. 2). Two SpS represent oscillatory activity in the left and right hemisphere (Fig. 2, left, middle row). Observing six FS, we notice some duplicates, such as two instances of 8.5 Hz and 7.5 Hz, a phenomenon also found in CP decomposition. By examining the nonzero elements in the first columns of dependency matrices (Fig. 2, right), we found that the first latent component oscillates at 6.5 Hz (FS c_1), with its time score corresponding to a_1 and spatial representation

given by the linear combination of two SpS: $b_1^\star = 0.66b_1 + 0.76b_2$. Additionally, an analysis of the second and third, or fourth and fifth columns of the dependency matrices shows that these latent components represent a lateralized version of the 7.5 Hz and 8.5 Hz rhythms. Moreover, PL1 can be easily represented in a CP-like structure (Fig. 3).

The dependency matrices of the PL2 model with (6, 2, 3) signatures and $F = 6$ revealed a sparse structure that effectively highlights the lateralization of three oscillatory rhythms on 7, 8.5, and 9.5 Hz (Fig. 4). For example, the first two latent components represent 9.5 Hz rhythm (FS c_1), observed both in the left (SpS b_1, TS a_2) and in the right hemisphere (SpS b_2, TS a_4).

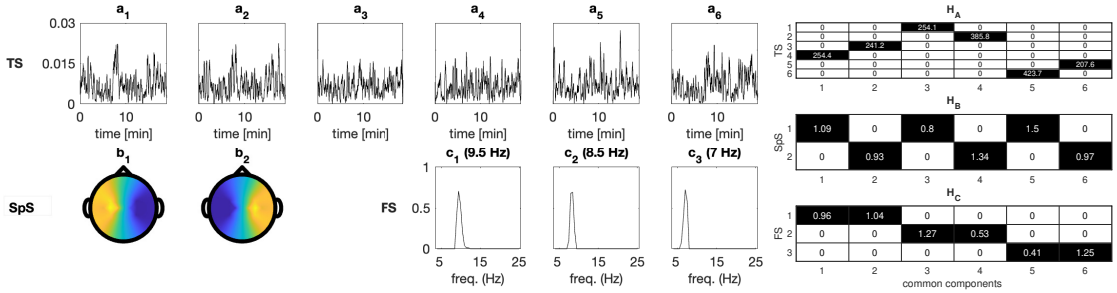

Fig. 4: Day 12 - PARALIND model PL2 with (6,2,3) signatures and six common components. The component signatures are depicted on the left, and the dependency matrices H_A, H_B, H_C are on the right.

5. Conclusion

This study explored the potential use of the PARALIND model for detecting narrowband brain oscillatory rhythms in EEG signal. The validity of PARALIND was supported by duplicate components estimated through CP decomposition, the trilinear structure of the core tensor in Tucker models, and comparable MSE across all models when applied to the same data. An important advantage of PARALIND is its straightforward representation in a CP-like structure, where each latent component is defined by its TS, SpS, and FS. Additionally, its dependency matrices provide a more intuitive interpretation compared to the core tensor in the Tucker model. A limitation of PARALIND are numerical instabilities when estimating dependency matrices and challenging selection of the appropriate number of signatures, highlighting the need for future research in this area.

Acknowledgements

Funded by the EU NextGenerationEU through the Recovery and Resilience Plan for Slovakia under the project No. 09I03-03-V04-00205 (Z.R.) and project No. 09I03-03-V04-00443 (R.R.). N.E. received funding from the HORIZON-MSCA-2022-DN, 101118964-DONUT project.

References

[1] Rošťáková, Z., Rosipal, R., Seifpour, S., Trejo, L. J. (2020). A comparison of non-negative Tucker decomposition and parallel factor analysis for identification and measurement of human EEG rhythms. *Measurement Science Review* 20(3), 126 – 138.

[2] Cichocki, A., Zdunek, R., Phan, A. H., Amari, S. (2009). *Nonnegative matrix and tensor factorizations: applications to exploratory multi-way data analysis and blind source separation*. United Kingdom: John Wiley & Sons.

[3] Bro, R., Harshman, R. A., Sidiropoulos, N. D., Lundy, M. E. (2009). Modeling multi-way data with linearly dependent loadings. *Journal of Chemometrics: A Journal of the Chemometrics Society* 23(7-8), 324–340.

[4] Polyanskaya, A., Rosipal, R., Sobolová, G., Rošťáková, Z., Porubcová, N. (2024). A small step towards the detection of mental fatigue induced by BCI-HMD training. In: *Proceedings of the 9th Graz Brain-Computer Interface Conference 2024*. pp. 109–114.

Measurement in Biology and Medicine

ISBN 978-80-69159-00-6

Growth of Saccharomyces Cerevisiae in a 50 Hz Magnetic Field

[1]Michal Teplan, [1]Hoang Vu Viet, [2]Lubomír Kremnický, [3]Martin Bereta

[1]Institute of Measurement Science, Slovak Academy of Sciences, Bratislava, Slovakia,
[2]Institute of Chemistry, Slovak Academy of Sciences, Bratislava, Slovakia,
[3]Faculty of Health Sciences, Catholic University in Ruzomberok, Slovakia
Email: michal.teplan@savba.sk

Abstract. *The influence of low-frequency magnetic fields (LF-MFs) on biological systems remains a subject of debate due to conflicting findings. This study investigates the impact of a 50 Hz, 3.5 mT magnetic field on the growth of Saccharomyces cerevisiae CCY 21-4-99. Yeast culture was incubated under controlled conditions with and without LF-MF exposure, and growth was assessed turbidimetrically. Our results showed no statistically significant difference between the exposed and control groups, suggesting that LF-MF exposure under these conditions does not affect yeast growth. Given the inconsistencies in previous research, our study highlights the need for rigorous methodology and replication efforts in LF-MF studies.*

Keywords: Low-Frequency Magnetic Fields, Biological Effects, Saccharomyces Cerevisiae

1. Introduction

The effects of low-frequency magnetic fields (LF-MFs) at 50 Hz and 60 Hz on biological systems have drawn significant scientific interest, yielding diverse findings. Yeast *S. cerevisiae* showed inhibited growth following LF-MF exposure [1], while human dermal fibroblasts exhibited reduced proliferation without viability loss [2]. Conversely, human epidermal stem cells displayed increased proliferation under LF-MFs [3].

LF-MFs reduced viability in breast cancer cells while sparing non-cancerous lines and protected HMO6 cells from oxygen-glucose deprivation-induced death [5]. *Aspergillus niger* showed increased acidic protease production under LF-MFs [6], and enhanced proliferation in HeLa and IMR-90 cells was linked to lower ROS levels [7]. Research on MCF10A and MCF7 cells showed reduced number, viability, and DNA synthesis, without affecting cell death [8]. These varied responses highlight the need for further research on LF-MF effects.

2. Methods

Experimental platform

The experimental setup included cultivation chambers, an MF generation system, and a temperature regulation system (Fig. 1). The MF system supplied a 50 Hz, 3.5 mT field to each chamber using Helmholtz coils (50 turns of 2.2 mm copper wire, 110 mm diameter) with 95% homogeneity. A signal generator produced alternating currents, which were amplified and regulated to maintain impedance. Customized thermal boxes, equipped with heating foils and a PID regulator, ensured a stable 35 °C environment. A microcontroller with DS18B20 digital sensors monitored temperature every 10 seconds.

ISBN 978-80-69159-00-6

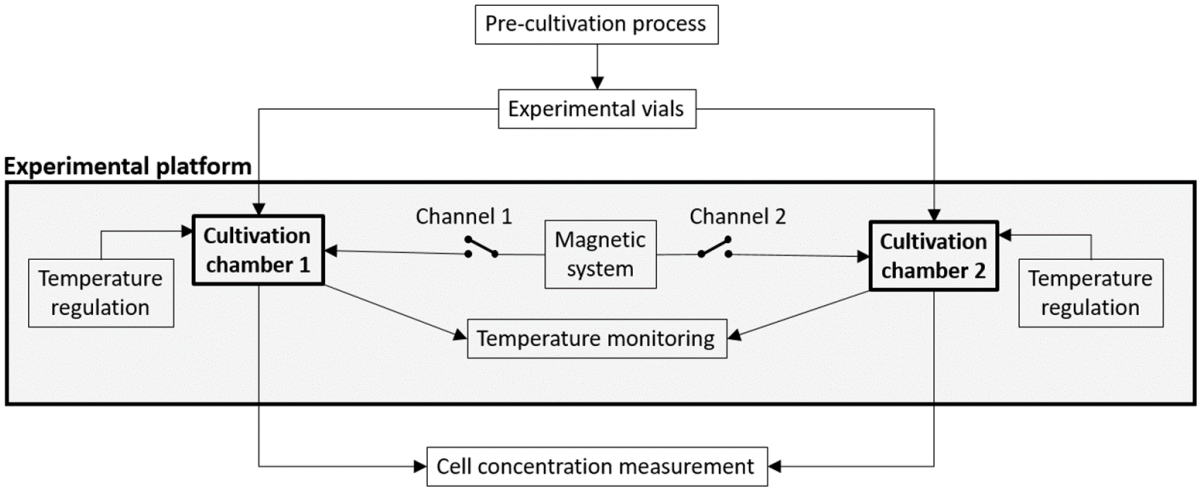

Fig. 1. Workflow scheme illustrating the experimental platform incorporating the paired experimental design.

Microbial Strain and Culture Conditions

Saccharomyces cerevisiae CCY 21-4-99 was cultivated in YPD medium (1% yeast extract, 2% peptone, and 2% glucose) at 35 °C. A 24-hour-old liquid pre-culture was stored at 7 °C for up to 10 days before use as an inoculum (viability: 98.5–99.0%).

To establish a growth curve, a diluted yeast pre-culture in YPD medium was divided into two sets of 42 flat-bottom vials, each containing 13 ml of culture, and incubated simultaneously in water baths within two separate thermostatic chambers to maintain temperature stability. At each measurement point, three vials per chamber were removed and analyzed turbidimetrically for cell growth.

For testing growth under MF exposure, the pre-culture, appropriately diluted in YPD medium, was distributed into 10 flat-bottom vials, each containing 13 ml of culture. Sets of five vials were placed in water baths within separate cultivation chambers inside Helmholtz coils. The cultures were incubated simultaneously for 18 hours, either with or without MF exposure, depending on the experimental conditions.

3. Results and Discussion

Before evaluating the impact of MF, we first examined the biological system under controlled conditions. Yeast cultures were cultivated in parallel in two identical incubators, starting at approximately 300 cells/ml, and biomass growth was monitored over time. Yeast cell concentration was measured turbidimetrically between the 12th and 36th hours. Figure 2a presents the mean values from both incubators, with the fitted growth curve interpolated using a sixth-order polynomial, including an extrapolation to a single point at 36 hours.

The cell growth curve demonstrated that biomass levels remained below half of the fully developed biomass observed at 37 hours until the 19th hour. In particular, data show that the exponential growth phase extended up to the 19th hour, with biomass levels staying below 50% of the stationary phase maximum (Fig. 2a). The terminal part of the exponential growth phase is a time period the most sensitive to growth disturbances. This was the reason why 18 hours were chosen for the duration of the experiment with MF.

ISBN 978-80-69159-00-6

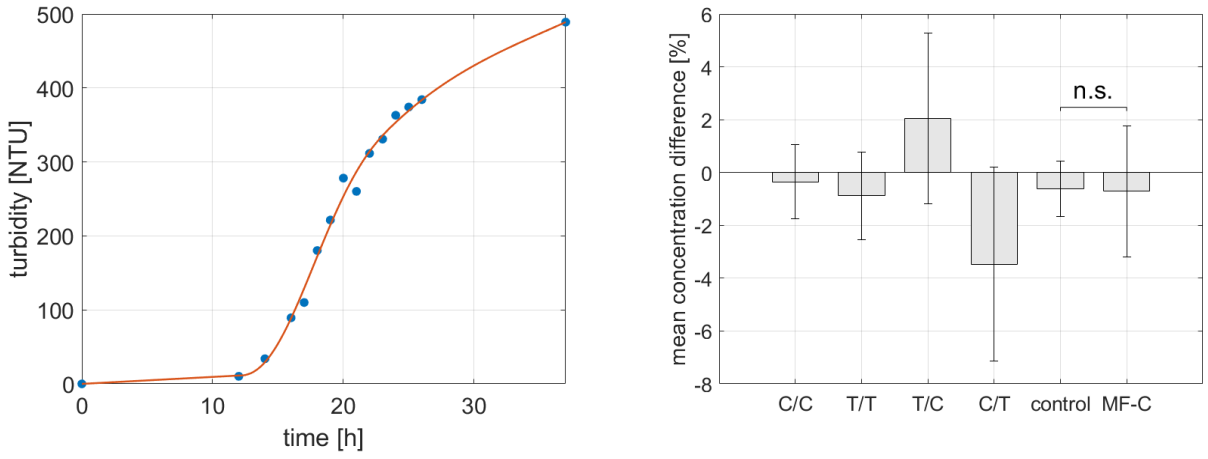

(a) (b)

Fig. 2: (a) Growth curve illustrating the increase in cell concentration of *S. cerevisiae* CCY 21-4-99 in temperature conditions of 35 °C. (b) Mean cell concentration differences between the two incubators of the paired experiment. All error bars are equal to ±SD. C/C - both chambers without MF (N = 6), T/T - both chambers with MF (N = 6), T/C - MF on in chamber 1 while off in chamber 2 (N = 6), C/T - MF off in chamber 1 while on in chamber 2 (N = 6), control - unification of C/C and T/T data sets (N = 12), MF-C - unification of T/C and C/T data (N = 12).

From each experimental run, environmental conditions were evaluated using three parameters: the mean temperature in chamber 1, the mean temperature in chamber 2, and the mean temperature difference between the two chambers. Only experimental runs that met the following three temperature criteria were included in further analysis: the mean temperature in chamber 1 and in chamber 2 had to remain within 35±0.3 °C, and the mean temperature difference between the chambers had to be within ±0.3 °C.

Figure 2b presents the mean cell concentration differences between cultures in the two chambers of a paired experimental setup across six data sets: both chambers in control mode (MF off), both chambers in test mode (MF on), MF on in chamber 1 while off in chamber 2, MF off in chamber 1 while on in chamber 2, a combined control group (from the first 2 data sets), and a combined MF-C group (from the 2 data sets, calculated as MF output minus control output). The first four data sets contained six outcomes each, leading to a 12 vs. 12 statistical comparisons in the final two sets.

The mean value from the test settings (-0.71%) closely matched that of the combined control group (-0.62%). A one-sample t-test showed no significant difference between the test and control datasets ($p = 0.97$), indicating that the observed variation was negligible. Therefore, in this study, exposure to a 50 Hz, 3.5 mT LF-MF had no measurable impact on yeast cell growth.

We found no effect, whereas previous studies report both positive and absent effects. While the majority of published research suggests some influence of ELF magnetic fields, the reported effects are highly variable and sometimes contradictory, making it difficult to establish clear patterns. Moreover, many findings lack independent verification, with replication efforts often yielding conflicting results, highlighting the challenge of reproducing subtle biological effects.

It is well-documented that positive findings are more likely to be published than negative ones (i.e., absence of effects) [9]. Additionally, researchers may be prone to various biases, collectively suggesting that the true proportion of null results is likely significantly underreported. Our study contributes to this debate by emphasizing methodological rigor, stable environmental conditions, and careful experimental design. Based on our firsthand experience with the challenges of ensuring reproducibility and controlling environmental factors that could

ISBN 978-80-69159-00-6

introduce false effects, we suspect that many reported effects may be artifacts rather than genuine biological responses.

4. Conclusions

This study found no measurable effect of a 50 Hz, 3.5 mT LF-MF on the growth of *S. cerevisiae* CCY 21-4-99. While numerous studies have reported diverse and sometimes contradictory effects of LF-MFs on biological systems, many results lack independent verification. Our findings underscore the importance of methodological rigor, stable environmental conditions, and replication to avoid false effects. Given the challenges of achieving reproducibility and minimizing external influences, we question whether some previously reported effects could stem from experimental artifacts rather than true biological responses.

Acknowledgements

The research was supported by the research grant 2/0160/25 from the VEGA Grant Agency.

References

[1] Novak, J. et al.: Effects of low-frequency magnetic fields on the viability of yeast Saccharomyces cerevisiae. *Bioelectrochemistry,* vol. 70, p. 115-121, 2007.
[2] Pasi, F. et al. (2016). Effects of extremely low-frequency magnetotherapy on proliferation of human dermal fibroblasts. *Electromagnetic Biology and Medicine*, 35, 343-352.
[3] Zhang, M. et al. (2013). Effects of low frequency electromagnetic field on proliferation of human epidermal stem cells: An in vitro study. *Bioelectromagnetics*, 34, 74-80.
[4] Xu, A. et al. (2020). Low-Frequency Magnetic Fields (LF-MFs) Inhibit Proliferation by Triggering Apoptosis and Altering Cell Cycle Distribution in Breast Cancer Cells. *International Journal of Molecular Sciences*, 21(8), 2952.
[5] Duong, C. N., Kim, J. Y. (2016). Exposure to electromagnetic field attenuates oxygen-glucose deprivation-induced microglial cell death by reducing intracellular Ca2+ and ROS. *International Journal of Radiation Biology*, 92, 195-201.
[6] Liu, J. et al. (2024). Low frequency magnetic field assisted production of acidic protease by Aspergillus niger. *Archives of Microbiology*, 206, 273.
[7] Song, K. et al. (2018). A 60 Hz uniform electromagnetic field promotes human cell proliferation by decreasing intracellular reactive oxygen species levels. *PLoS ONE* 13(7).
[8] Lee, H. Ch. et al. (2015). Effect of extremely low frequency magnetic fields on cell proliferation and gene expression. *Bioelectromagnetics*, 36, 506-516.
[9] Mlinarić, A. et al. (2017). Dealing with the positive publication bias: Why you should really publish your negative results. *Biochemia Medica*, 27(3), 447-452.

Adjustment Algorithm for Multi-Lead QRS Detection

Antónia Kováčová, Ondrej Kováč, Ján Šaliga
Technical University of Kosice, Letna 9, 04200 Kosice, Slovakia
Email: antonia.kovacova@tuke.sk

Abstract. *This paper examines a multi-lead adjustment algorithm for multi-lead ECG (electrocardiogram) signals based on single-lead QRS complex detections. The algorithm uses the Pan-Tompkins detector (PTD) and considers statistical parameters like the mode of detections and the average and median lengths of heart-depolarization intervals. The proposed algorithm is evaluated on two EKG databases: Lobachevsky University and Physikalisch-Technische Bundesanstalt diagnostic cardiography databases. The results demonstrate that reducing the acceptable interval for QRS complex timestamp differences during the decision phase increases error rates. Compared to manual QRS timestamps, the adjusted detection shows less than 2% error within chosen intervals considered acceptable for accurate detection.*

Keywords: ECG, Multi-Lead, Pan-Tomkins, QRS Complex Detection

1. Introduction

The QRS detection of heart depolarizations in ECG (electrocardiography) signals is fundamental for diagnosing cardiovascular diseases [1], [2]. Accurate QRS detection is an essential and valuable tool for various ECG signal processing applications. In work [3] a QRS detector was used to divide the ECG signal into frames with one heart-depolarization for parametric dictionary learning for compressed sensing applications. An ECG compressed sensing method proposed in [4] incorporates a QRS detector for frame division, enabling high compression of ECG signals with minimal error. The detection of QRS complexes is also essential for ECG delineation algorithms such as [1] or [5].

The multi-lead adjustment algorithm for the QRS detector evaluated in this work was proposed in [6] to divide the frames for the correlation analysis. As the one-lead QRS detector, the well-known Pan-Tomkin's algorithm (PTD) was used [7]. The adjustment algorithm was based on the statistical parameters of QRS detection in multiple leads. There are several similar approaches to multi-lead QRS detection based on single-lead detection, such as works [8] and [9] using multi-lead fusion to repair false detections. In this paper, the adjustment algorithm proposed in [6] for correlation analysis is refined to reduce the error rate and evaluated on two databases, one containing manually determined QRS complexes by medical professionals.

2. Proposed multi-lead adjustment algorithm

The first step of the proposed method is the one-lead QRS detection. Many QRS detectors examine the slope of the R wave and its peak to detect the location of the QRS complexes without explicitly estimating Q and S points [2], [7]. The PTD algorithm is used for one lead detection with the same setting as in [6]. In each record r and its lead l, where $l \in \{1, 2, \dots 12\}$, several QRS complexes $d_{r,l}$ are detected. The number of detections in $d_{r,l}$ may vary between leads of the same recording. To set a uniform detection number, the mode value of detections m_D for record r is computed:

$$m_D = mode(D_r) \tag{1}$$

where D_r is a set of QRS detection vectors $\{d_{r,1}, d_{r,2}, \dots d_{r,12}\}$ for record r. Number m_D sets the desired number of detections for each lead of the examined records. The leads that do not satisfy m_D are considered signals with redundant or missing detections:

ISBN 978-80-69159-00-6

$$D_r = \begin{cases} d_{r,l} \in R_T & if\ card(d_{r,l}) = m_D \\ d_{r,l} \in R_F & other \end{cases} \quad (2)$$

where r is an index of the record, R_T is a set of QRS detections that satisfy m_D and R_F is a set that does not satisfy m_D.The second step involves examining the time interval between two consecutive detections. Although the number of detections meets the m_D threshold, there may still be delayed detections occurring outside the QRS complex. Since the time intervals between consecutive heart depolarizations in simultaneous recordings tend to be similar, the uniformity of these intervals can be calculated using their average and median values [6]. For this purpose, the set M_T is introduced to evaluate time intervals between R-peak detections. First, using the q-th detection and its next $q+1$ in the set R_T, the average interval between two QRS detections is calculated. This average serves as a threshold to determine which values contribute to the median computation and which are not considered. If there are more intervals with lengths below the average, $M_T[q]$ is computed based on those intervals, and vice versa:

$$M_T[q] = median(\{t_{q,1}, t_{q,2}, \dots t_{q,l_{trh}}\}) \quad (3)$$

where $t_{q,k}$ is the q-th interval $q \in \langle 1, 2, \dots m_D \rangle$ between two adjacent detections of leads and l_{trh} represents the total number of leads considered. Checking the intervals between two adjacent detections is the next step of the proposed method. The acceptable interval was derived from the average length of QRS complexes from the results of the work [10]. The average length of 400 adult patients' QRS complexes was 0.0971 seconds. Based on this value, the acceptable intervals were set to $\langle M_T[q] - c_s f_s\ ;\ M_T[q] + c_s f_s \rangle$ seconds, where $c_s = \{0.045,\ 0.0225\}$ which represents acceptable samples difference derived from half and fourth of the average QRS complex length. If there is one interval in the signal outside the acceptable interval, the signal is removed from the set R_T. Then it is considered as a false one and is added to the set R_F. The false detections are subjected to QRS timestamps adjustment based on the average values $\mu[q]$ where $q \in \langle 1, 2, \dots m_D \rangle$ of set R_T signals marked as accurate. According to the $\mu[q]$, a timestamp of detections from set R_F with a minimal difference n_{VAL} and its index n_{IDX} is chosen:

$$d_{r,l_{ADJ}}[q] = n_{VAL} + \mu[q] - \mu[n_{IDX}] \quad (4)$$

where $d_{r,l_{ADJ}}$ is a vector for lead l with adjusted timestamps of QRS detection. It follows from the equation that the new adjusted values are computed based on a single detection from the whole signal and the mean timestamp values $\mu[q]$ across $q \in \langle 1, 2, \dots m_D \rangle$. The improved detections $d_{r,l_{ADJ}}$ are merged with the rest of the signals.

3. Results

The two databases were used to evaluate the proposed detection of QRS complexes. First, the Lobachevsky University cardiography database [11] consists of 200 records of 12-lead EKG rhythm with a 10-second length sampled at the rate of 500 Hz and acquired from healthy volunteers and patients with cardiovascular diseases. This database also contains data files with manually determined ECG wave information. Physikalisch-Technische Bundesanstalt (PTB) diagnostic ECG database [12] is the second multi-lead ECG database used for evaluation. This database comprises 549 records from 294 patients acquired with high-resolution at a 1000 Hz sampling frequency. Each record consists of 12 standard leads and 3 Frank XYZ leads (only standard leads were used for experiments).

ISBN 978-80-69159-00-6

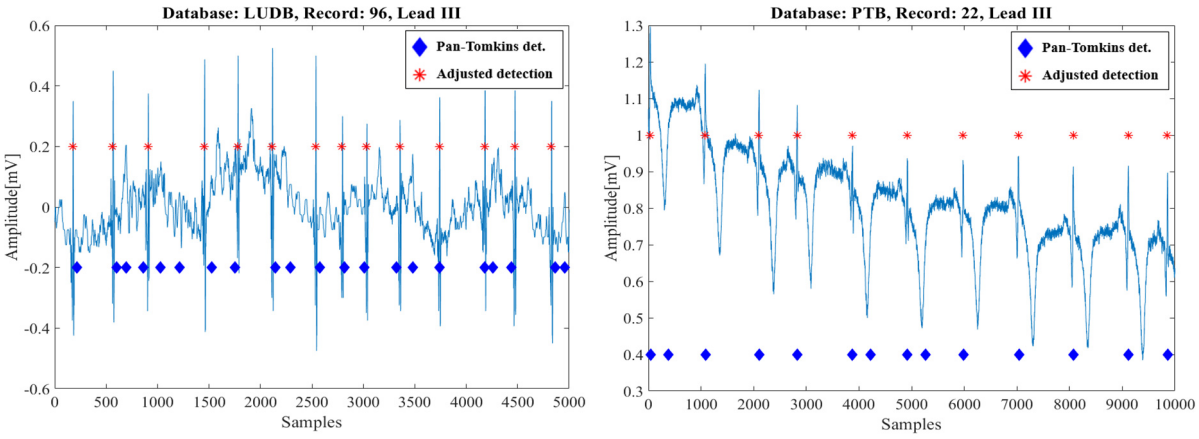

a) b)

Fig. 1 QRS detection comparison for PTD with and without adjustment: (a) for LUDB signal, (b) for PTB signal.

The one lead PTD was used, as in work [6]. Since there are two different databases with different sampling frequencies, the detector was adjusted to 1 kHz for PTB records and 500 Hz for LUDB records. The examples of single-lead adjustments for two different signals are depicted in Fig. 1a and Fig. 1b.

Table 1. Results of the adjustment algorithm of QRS detections for the LUDB and PTB databases.

Database	Number of signals	Sampling freq.[Hz]	Diff. c_s $[s]$	Missing QRS det.	False QRS det.	Not in Interval	Only M_T
LUDB	200 × 12	500	0.045	54	107	397	1
		500	0.0225	54	107	753	1
PTB	549 ×12	1000	0.045	165	303	1623	11
		1000	0.0225	165	303	2557	18

The results of the adjustment process across the full length of signals for both databases are presented in Table 1. The 'Missing QRS detections' column represents signals where the PTD method failed to detect some of the actual QRS complexes. Column 'False QRS detections' refers to cases where the PTD method identifies more QRS complexes than are present in the signal. A column 'Only $\boldsymbol{M_T}$' column represents the number of 12-lead recordings where no suitable signals, fitting the median values, were found, so detections are based solely on the $\boldsymbol{M_T}$ values. As expected, a lower acceptable difference interval results in the number of false detections rising, and more detections need to be adjusted.

Table 2. Error Rate evaluation of the proposed algorithm based on manually annotated QRS-peak complexes

Database	Total number of QRSs	Diff. c_s $[s]$	Acc. delay $c_{tst}[s]$	Beats out of acc. diff.	Error rate for QRS det. [%]
LUDB	21924 (1827 × 12)	0.0225	0.045	141	0.64
			0.0225	426	1.94
		0.045	0.045	135	0.62
			0.0225	411	1.87

As was mentioned, the LUDB consists of datasets with timestamps for P wave, QRS complex, and T-wave boundaries manually annotated by cardiologists. Those annotated QRS peaks were used to evaluate the error rate of the proposed algorithm for detection improvement. The results for the two acceptable samples' difference c_s are summarized in Table 2. The error rate was evaluated for two acceptable delays c_{tst} between manual determination and proposed detection.

ISBN 978-80-69159-00-6

4. Conclusion

This paper presents a refined multi-lead adjustment algorithm for ECG signal processing based on single-lead QRS detections using PTD. The proposed method incorporates statistical parameters to improve the detection accuracy of single-lead detectors. The performance was evaluated on two databases with a total number of 749 records of 12-lead EKG signals. The records were adjusted based on two acceptable differences from the median values: half and fourth of the mean length of the QRS complex, to be sure that the detection timestamp will lie within the QRS complex. The results show that more interval adjustments were made for narrower acceptable intervals of ± 0.0225 s. The comparison for LUDB with the control QRS values shows a lower error ratio for wider intervals (± 0.045 s). The accuracy under the stated condition was within the range of 98.06% - 99.38%, which can be suitable for signal processing applications such as dictionary learning or compression.

Acknowledgements

The work is a part of the project supported by the Science Grant Agency of the Slovak Republic (No. 1/0413/22).

References

[1] C. Chauhan, M. Agrawal, and P. Sabherwal, “A Multi-Lead Fusion Method for the Accurate Delineation of QRS Complex Location in 12 Lead ECG Signal,” 2021, doi: 10.48550/ARXIV.2107.05469.

[2] P. Dolinsky, I. Andras, J. Saliga, and L. Michaeli, “High sensitivity experimental QRS detector,” in *2018 28th International Conference Radioelektronika (RADIOELEKTRONIKA)*, Prague: IEEE, Apr. 2018, pp. 1–4. doi: 10.1109/RADIOELEK.2018.8376373.

[3] L. De Vito, E. Picariello, F. Picariello, S. Rapuano, and I. Tudosa, “A Dictionary Optimization Method for Reconstruction of ECG Signals after Compressed Sensing,” *Sensors*, vol. 21, no. 16, p. 5282, Aug. 2021, doi: 10.3390/s21165282.

[4] J. Šaliga, I. Andráš, P. Dolinský, L. Michaeli, O. Kováč, and J. Kromka, “ECG compressed sensing method with high compression ratio and dynamic model reconstruction,” *Measurement*, vol. 183, p. 109803, Oct. 2021, doi: 10.1016/j.measurement.2021.109803.

[5] J. P. Martinez, R. Almeida, S. Olmos, A. P. Rocha, and P. Laguna, “A Wavelet-Based ECG Delineator: Evaluation on Standard Databases,” *IEEE Trans. Biomed. Eng.*, vol. 51, no. 4, pp. 570–581, Apr. 2004, doi: 10.1109/TBME.2003.821031.

[6] A. Juskova, O. Kovac, J. Kromka, and J. Saliga, “A 12-Lead ECG signal correlation analysis in multiple domains,” *Measurement: Sensors*, p. 101417, Dec. 2024, doi: 10.1016/j.measen.2024.101417.

[7] J. Pan and W. J. Tompkins, “A Real-Time QRS Detection Algorithm,” *IEEE Trans. Biomed. Eng.*, vol. BME-32, no. 3, pp. 230–236, Mar. 1985, doi: 10.1109/TBME.1985.325532.

[8] C. Chauhan, M. Agrawal, and P. Sabherwal, “Accurate QRS complex detection in 12-lead ECG signals using multi-lead fusion,” *Measurement*, vol. 223, p. 113776, Dec. 2023, doi: 10.1016/j.measurement.2023.113776.

[9] W. Zhao *et al.*, “A Multilead QRS Complex Detection Method on 12-Lead Electrocardiogram Signals,” presented at the 2018 Computing in Cardiology Conference, Dec. 2018. doi: 10.22489/CinC.2018.082.

[10] S. McGinn and P. D. White, “The duration of the QRS complex in the normal and in the abnormal electrocardiogram,” *American Heart Journal*, vol. 9, no. 5, pp. 642–654, Jun. 1934, doi: 10.1016/S0002-8703(34)90444-0.

[11] A. Kalyakulina *et al.*, “Lobachevsky University Electrocardiography Database.” doi: 10.13026/EEGM-H675.

[12] R. Bousseljot, D. Kreiseler, and A. Schnabel, “Nutzung der EKG-Signaldatenbank CARDIODAT der PTB über das Internet,” *Biomedizinische Technik/Biomedical Engineering*, pp. 317–318, Jul. 2009, doi: 10.1515/bmte.1995.40.s1.317.

Measurement of Haemoglobin Iron Content in the Blood of Laboratory Animals with the SQUID Magnetometer.

[1]Martin Škrátek, [1]Ján Maňka, [2]Michal Kluknavský, [2]Iveta Bernátová

[1]Institute of Measurement Science, Slovak Academy of Sciences, Bratislava, Slovakia,
[2]Institute of Normal and Pathological Physiology, Centre of Experimental Medicine, Slovak Academy of Sciences, Bratislava, Slovakia
Email: martin.skratek@savba.sk

Abstract. *Magnetic properties of haemoglobin in different concentrations were studied, and from these measurements, the dependence of the saturation magnetisation on the haemoglobin concentration was obtained. This enabled the determination of the content of haemoglobin in the blood of laboratory animals (BHR male rats) based on magnetization measurements using a SQUID magnetometer.*

Keywords: SQUID Magnetometry, Endogenous Iron, Haemoglobin

1. Introduction

Iron is one of the most important elements found in living organisms; it participates in many metabolic processes. As a part of haemoglobin (Hb), it participates in the transport of oxygen and carbon dioxide through the blood. Determining the amount of iron in the blood and organs is essential for monitoring its metabolism. This could be done using colorimetric, spectrophotometric, and histochemical methods or by atomic absorption spectrometry [1]. However, these methods do not allow for the distinction between its individual endogenous forms that coexist in the body. From a magnetometric perspective, we encounter three different magnetic contributions in the body: *1.* haemoglobin, myoglobin, hemin or hematin exhibit paramagnetism, which originates from the single ion magnetism of Fe^{2+} or Fe^{3+} incorporated in their molecules; *2.* Ferritin, as the iron storage protein, contains Fe atoms mineralised in the form of oxyhydroxide nanoparticles, whose behaviour is superparamagnetic [2]; *3.* organic tissue matrix (lipids, proteins, sugars, DNA, etc.) exhibits diamagnetism. Considering this, SQUID magnetometry is an accurate tool for the detection and quantification of different endogenous iron forms with high sensitivity [3]. This work focuses on the magnetic properties of haemoglobin, their relationship to its concentration, and also shows a simple procedure for determining its quantity in blood samples of laboratory animals.

2. Subject and Methods

Animals

In this study, a group of 7 male borderline hypertensive rats (BHR) at the age of 15-16 weeks were used. Rats were born in the certified animal facility of the Institute of Normal and Pathological Physiology, Centre of Experimental Medicine, Slovak Academy of Sciences. Rats were fed with pelleted chow Altromin 1324 (Altromin Spezialfutter, Lage, Germany). The pellet food and water were available ad libitum. Rats were housed under standard conditions at 22–24 °C, 45–65% humidity, and with a 12 h light/dark cycle. Rats were exposed to isoflurane anaesthesia (3.5 %), and blood was collected from the right heart ventricle under anaesthesia. Then the rats were immediately decapitated. Blood samples were immediately frozen in liquid nitrogen and kept at - 80 °C until magnetometric measurements were performed. All of the

ISBN 978-80-69159-00-6

procedures used were approved by the State Veterinary and Food Administration of the Slovak Republic in accordance with the European Union Directive 2010/63/EU.

Sample preparation

Samples of blood (b1 – b7) were defrosted and shortly stirred in ultrasonic bath. 33 µl of blood was pipetted on a pre-weighted 18 cm long and 6 mm wide strip of standard office paper (80 g/m^2), which was bent over the long side to the shape of V, which prevented the sample in the form of a drop from spreading to the sides of the paper. Then the samples were dried in air for 24 h at room temperature. After drying the actual dry weight of the sample was obtained. The strip of paper is diamagnetic and long enough to have a negligible output signal to the sample's magnetic moment. To gain information about the magnetic properties of different amounts of Hb in a sample, a concentration model was prepared. This model is represented as a set of solutions (1 – 6) of Hb (H7379, lyophilised powder, Merck, Slovakia) with deionised water. Each solution was pipetted (33 µl) to a small piece of cotton fitted to 18 cm long copper wire and was then dried for 24 h at room temperature, dry weight of these model Hb samples is in Table 1.

SQUID magnetometry

Magnetic properties of prepared samples were measured by the Quantum Design MPMS XL-7 AC SQUID magnetometer. The DC magnetisation $M(H)$ was measured at 2 and 300 K up to 7 T field. The data were normalized to the dry weight of the samples.

3. Results

Figure 1a and 1b show $M(H)$ curves for Hb concentration model samples measured at 300 K and 2 K respectively. At 300 K the dependences are linear with negative magnetic susceptibility, showing the diamagnetic behaviour. The diamagnetic contribution of the sample matrix was determined for each curve. Fig 1b shows the low-temperature $M(H)$ dependences after subtracting the diamagnetic contributions. The curves showed weak ferromagnetic behaviour, which came to the foreground with decreased temperature and changed for each of the samples. Three main parameters were determined from the measured $M(H)$ dependences – the saturation magnetisation (M_S), remanent magnetisation (M_R) and coercivity (H_C), and are presented in Table 1. As can be seen from the table, the values of M_R and H_C behave unpredictably with increasing haemoglobin content; only the value of M_S shows an increasing trend. Therefore, the M_S was chosen as the parameter that best describes the change in magnetism of the samples [3,4]. A concentration dependence (Figure 1c) was made as a linear regression of M_S values and the dry mass of Hb contained in the samples.

Table 1. Dry weight of Hb, saturation magnetisation M_S, remanent magnetisation M_R and coercivity H_C measured at 2 K of Hb samples.

Hb sample	Hb weight [mg]	M_S [10^{-3}Am^2/kg]	M_R [10^{-6}Am^2/kg]	H_C [10^3A/m]
1	0.39	49.3	175	5.29
2	0.83	96.7	133	2.11
3	1.27	107.5	209	3.04
4	1.64	133.9	200	2.22
5	1.98	150.5	75	0.67
6	2.13	182.9	136	1.26

ISBN 978-80-69159-00-6

The blood samples obtained from BHR were measured similarly. Figure 1d shows measured $M(H)$ dependences at the temperature of 2 K after subtraction of diamagnetic contributions, which were determined from curves measured at 300 K (not presented). $M(H)$ dependences show clearly very similar weak-ferromagnetic behavior to the Hb samples.

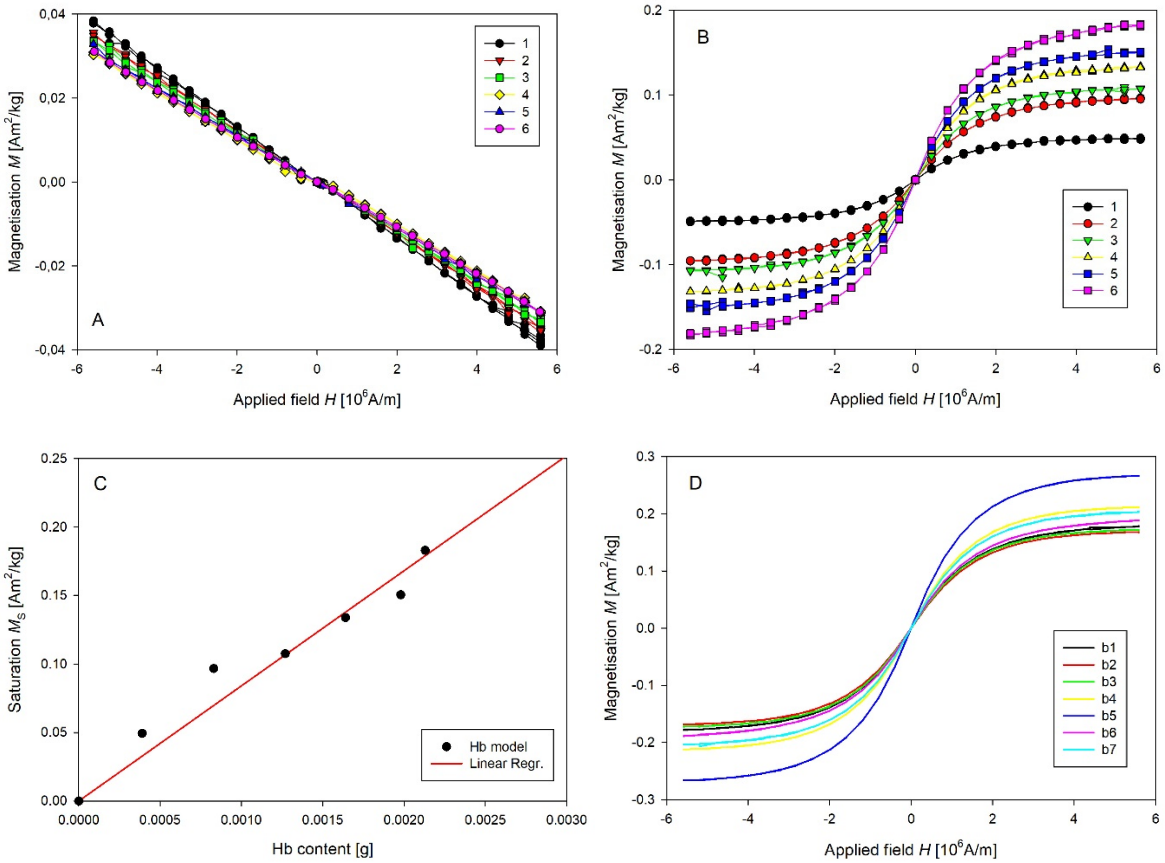

Fig. 1. A) $M(H)$ curves measured at 300 K for the Hb concentration models; B) 2 K $M(H)$ dependences after subtraction of the diamagnetic contributions; C) concentration dependence for Hb models (correlation coefficient r=0.981); D) $M(H)$ curves measured at 2 K in the blood of BHR.

Table 2. Hb content (dry weight), saturation magnetisation M_S, remanent magnetisation MR, and coercivity H_C measured at 2 K in the blood of BHR.

Solution	Hb weight [mg]	M_S [10^{-3}Am^2/kg]	M_R [10^{-6}Am^2/kg]	H_C [10^3A/m]
b2	1.99	167.3	316	3.35
b3	2.04	171.7	321	2.82
b1	2.11	177.9	280	2.58
b6	2.23	188.2	190	1.67
b7	2.41	203.1	279	2.33
b4	2.51	211.6	292	2.08
b5	3.17	266.4	511	3.07

ISBN 978-80-69159-00-6

All parameters (M_S, M_R, H_C) were also determined and are summarised in Table 2. Using the previously determined concentration dependence, the corresponding Hb content in the blood samples was determined from the obtained M_S values.

4. Discussion

The present work deals with the determination of the amount of endogenous iron in the form of haemoglobin in the rat blood. Of course, such a measurement can be performed using other standardised analytical methods, but our method allows the differentiation of different endogenous forms of iron. For example, distinguishing between iron in the form of haemoglobin and ferritin in the liver tissue is interesting for monitoring of iron metabolism. To increase the accuracy of the method, it will be necessary to measure several samples for one concentration of Hb and in a larger range, because the current concentration model does not reach the Hb level as measured for blood samples. It will also be necessary to modify the preparation of the concentration model, since the use of cotton wool turns out to be a complication with regard to its unforeseen magnetic properties - a weak temperature-dependent ferromagnetism.

In conclusion, the Hb content in the blood samples has a defined effect on M_S, and it is therefore possible to determine it using this parameter. The presented method is functional and sufficiently sensitive for the given task. Further work is needed to improve the range and accuracy of the method.

Acknowledgements

This work has been funded by the EU NextGenerationEU through the Recovery and Resilience Plan for Slovakia under the project No. 09I03-03-V04-00528.

References

[1] Miranda, J.L.A., Mesquita, R.B.R., Leite, A., Silva, A.M.N., Rangel, M., Rangel, A.O.S.S. (2023). Non-transferrin-bound iron determination in blood serum using microsequential injection solid phase spectrometry–proof of concept. *Talanta*, 257, 124345.

[2] Fernández-Afonso, Y., Asín, L., Beola, L., Moros, M., de la Fuente, J. M., Fratila, R. M., Grazú, V., Gutiérrez (2022). Iron Speciation in Animal Tissues Using AC Magnetic Susceptibility Measurements: Quantification of Magnetic Nanoparticles, Ferritin, and Other Iron-Containing Species. *ACS Applied Bio Materials, 5* (5), 1879-1889

[3] Škrátek, M., Dvurečenskij, A., Kluknavský, M., Barta, A., Bališ, P., Mičurová, A., Cigáň, A., Eckstein-Andicsová, A., Maňka, J., Bernátová, I. (2020). Sensitive SQUID Bio-Magnetometry for Determination and Differentiation of Biogenic Iron and Iron Oxide Nanoparticles in the Biological Samples. *Nanomaterials*, *10*, 1993.

[4] Zysler, R. D., Lima, E. Jr., Vasquez Mansilla, M., Troiani, H. E., Mojica Pisciotti, M. L., Gurman, P., Lamagna, A., Colombo, L.(2013). A new quantitative method to determine the uptake of SPIONs in animal tissue and its application to determine the quantity of nanoparticles in the liver and lung of Balb-c mice exposed to the SPIONs. *J Biomed Nanotechnol*, 9 (1), 142-5.

Theoretical Problems of Measurement I

ISBN 978-80-69159-00-6

Comparative Analysis of Approaches to Uncertainty Evaluation of Indirect Correlated Measurements

Igor Zakharov, Olesia Botsiura

Kharkiv National University of Radio Electronics, Kharkiv, Ukraine,
Email: newzip@ukr.net

Abstract. *Two approaches to uncertainty evaluation of indirect correlated measurements are considered: the approach described in the GUM and the approach based on the reduction method. The main expressions for evaluation of the numerical value of the measurand, its standard and expanded uncertainty are given. The advantages of the reduction method are shown. An example of uncertainty evaluation of electrical resistance measuring using the ammeter-voltmeter method is considered.*

Keywords: Indirect Measurements, Measurement Uncertainty, Correlation, Reduction Method

1. Introduction

Correlated indirect measurements are often encountered in metrological practice [1-3]. The cause of the correlation may be the simultaneous measurements of several input quantities in a measurement model, the variability of which is affected by a common factor; the use of the same measuring instrument with a significant systematic error when measuring several input quantities in a measurement model; an implicit relationship between several input quantities, etc.

Processing of indirect correlated measurements according to the GUM approach [2] requires preliminary linearization of the measurement model, calculation of the correlation coefficient between dependent input quantities, and subsequent consideration of its value at calculating the combined and expanded uncertainties of the measurand. This complicates the measurement processing and makes its result inaccurate, since expansion in a first-order Taylor series causes a bias in the estimate of the measurand and its uncertainty with a nonlinear measurement model [4,5]. In addition, expanded uncertainty evaluation is difficult because the Welch–Satterthwaite equation given in the GUM does not take correlation into account when calculating the effective degrees of freedom.

An alternative to the GUM procedure for processing indirect correlated measurements is the reduction method [1], which, using all the information obtained during the measurement, allows one to obtain an unbiased estimate of the numerical value and uncertainty of the measurand, eliminates the correlation coefficient when calculating the uncertainty of the measurement, gives an accurate estimate of degrees of freedom and allows one to accurately calculate the expanded uncertainty.

However, the reduction method is not generally accepted in regulatory documents on measurement uncertainty [2], therefore, the corresponding procedures based on it have not been developed in metrological practice.

The purpose of the manuscript is a comparative analysis of both approaches to uncertainty evaluation of indirect correlated measurements.

2. Basic Regulations

Table 1 presents the main relationships for implementing the GUM approach and the reduction method for processing indirect measurements in the presence of an observed correlation between the measurement results of two input quantities.

ISBN 978-80-69159-00-6

Table 1. Basic expressions of two approaches to processing indirect measurements with observed correlation

GUM approach	**Reduction method**
Mathematical model of the measurement	
$Y = f(X_1, X_2, ..., X_N)$ (1)	
Estimates of input quantities	
$x_1, x_2, ..., x_N$	
Standard uncertainties of input quantities	
$u_A(x_i)$, $u_B(x_i)$, $i = 1, 2, ..., N$ $u(x_i) = \sqrt{u_A^2(x_i) + u_B^2(x_i)}$ (2) $\nu_i = \dfrac{u^4(x_i)}{\dfrac{u_A^4(x_i)}{(n_i - 1)} + \dfrac{u_B^4(x_i)}{\nu_{Bi}}}$ (3)	
Contributions to the standard uncertainty of measurand	
$u_{Ai}(y) = c_i u_A(x_i)$, $u_{Bi}(y) = c_i u_B(x_i)$, $u_i(y) = c_i u(x_i)$, $c_i = \partial y / \partial x_i$ (4)	
Estimate of a measurand	
$y = f(x_1, x_2, ..., x_N)$ (5)	$y = \bar{y} = \dfrac{1}{n}\sum_{q=1}^{n} y_q$, (9) $y_q = f(x_1, x_2, ..., x_{lq}, x_{mq}, ..., x_N)$, (10) $q = 1, 2, ..., n$
Standard uncertainty of a measurand	
$u(y) = \sqrt{\sum_{i=1}^{N} u_i^2(y) + 2 r_{l,m} u_{Al}(y) u_{Am}(y)}$, (6) $r_{l,m} = \dfrac{\sum_{q=1}^{n} (x_{lq} - \bar{x}_l)(x_{mq} - \bar{x}_m)}{\sqrt{\sum_{q=1}^{n} (x_{lq} - \bar{x}_l)^2 \sum_{q=1}^{n} (x_{mq} - \bar{x}_m)^2}}$ (7)	$u(y) = \sqrt{u_r^2(y) + \sum_{i=1, i \neq l, m}^{N} u_{Ai}^2(y) + \sum_{i=1}^{N} u_{Bi}^2(y)}$, (11) where $u_r(\bar{y}) = \sqrt{\dfrac{1}{n(n-1)} \sum_{q=1}^{n} (y_i - \bar{y})^2}$ (12)
Effective degrees of freedom	
$\nu_{eff} = u^4(y) \Big/ \left\{ \sum_{i=1, i \neq l, m}^{N} \dfrac{u_{Ai}^4(y)}{n_i - 1} + \sum_{i=1}^{N} \dfrac{u_{Bi}^4(y)}{\nu_{Bi}} + \dfrac{[u_{Al}^2(y) + u_{Am}^2(y) + 2 r_{lm} u_{Al}(y) u_{Am}(y)]^2}{n - 1} \right\}$ (8)	$\nu_{eff} = \dfrac{u^4(y)}{\dfrac{u_r^4(\bar{y})}{n-1} + \sum_{i=1, i \neq l, m}^{N} \dfrac{u_{Ai}^4(y)}{n_i - 1} + \sum_{i=1}^{N} \dfrac{u_{Bi}^4(y)}{\nu_{Bi}}}$ (13)
Expanded uncertainty	
$U(y) = t_{p;\nu_{eff}} u(y)$ (14)	
Result of the measurement	
$Y = y \pm U(y), \; p = 0{,}95$ (15)	

The measurement model (1) is real, explicit, one-dimensional, linear or linearizable. In it, Y is the measurand; $X_1, X_2, ..., X_N$ are the input quantities. Among the input quantities, there are quantities X_l, X_m whose results of *n*-fold measurements $x_{l1}, x_{l2}, ..., x_{ln}$, $x_{m1}, x_{m2}, ..., x_{mn}$ are dependent, which leads to the occurrence of a correlation between them.

Estimates of input quantities X_i are obtained by single measurements, multiple measurements with number of observations n_i, or taken from external sources.

ISBN 978-80-69159-00-6

Each estimate of the input quantity x_i ($i = 1,2,...,N$) is assigned standard uncertainties of type *A* with the degrees of freedom $\nu_{Ai} = n_i - 1$ and type *B* with the degrees of freedom ν_{Bi}, which, according to the variance sum law, are united into a combined standard uncertainty $u(x_i)$ (2) with the number of degrees of freedom ν_i (3).

All standard uncertainties of input quantities $u_i(y)$ form proportional contributions to the uncertainty of the measurand in accordance with expressions (4), in which c_i are sensitivity coefficient calculated as partial derivatives of the measurand with respect to the corresponding input quantity.

3. GUM Approach

Having estimates of the input quantities $x_1, x_2, ..., x_N$, we can substitute them into the measurement model (1) to obtain an estimate of the measurand *y* (5).

Having the contributions of the uncertainty of the input quantities to the uncertainty of the measurand $u_i(y)$ (4), we can, taking into account the observed correlation coefficient r_{lm} (7), estimate the standard uncertainty of the measurand $u(y)$ (6) and calculate the effective degrees of freedom ν_{eff} using formula (8), obtained by the authors in [6].

4. Reduction Method

The numerical value of the measurand *y* is found by the reduction method as the arithmetic mean $\overline{y}$ (9) of the numerical values of measurand repeated observations $y_q = f(x_1, x_2, ..., x_{lq}, x_{mq}, ..., x_{Nq})$, $q = 1,2,...,n$ (10).

The standard uncertainty of the measurand $u(y)$ is found by formula (11) in which $u_r(y)$ is its standard uncertainty of repeatability (12), estimated as the standard deviation of the arithmetic mean $\overline{y}$.

The standard uncertainty of repeatability is assigned the degrees of freedom $\nu_r = (n-1)$, taking into account which the effective degrees of freedom ν_{eff} is estimated by formula (13).

5. Measurement Result

Formula (14) allows us to estimate the expanded uncertainty $U(y)$ as the product of the standard uncertainty of the measurand $u(y)$ and the *t*-factor $t_{p;\nu_{eff}}$ for a given level of confidence *p* and the effective degrees of freedom ν_{eff}. Taking this into account, the measurement result for *p* approximately equal to 0.95 will be written in the form (15).

6. Example: Uncertainty Evaluation of Electrical Resistance Measuring Using the Ammeter-Voltmeter Method

The practice for uncertainty evaluation of electrical resistance measuring by simultaneously measuring electric voltage and current five times using the GUM procedure and the reduction method is considered (Table 2). The correlation coefficient between the results of repeated observations was 0.77. The results of the measurements uncertainty evaluation obtained by both methods are presented in Table 2.

ISBN 978-80-69159-00-6

Table 2 Results obtained using the GUM procedure and the reduction method

Method	Measurand Value, Ohm	Measurand standard uncertainty, Ohm	Effective degrees of freedom	Coverage factor	Expanded uncertainty, Ohm
GUM	0,970	0,0214	2,6	3,63	0,078
GUM [6]	0,970	0,0214	13	2,21	0,047
Reduction	0,972	0,0215	13	2,21	0,048

7. Conclusions

1. The Welch-Satterthwaite equation given in the GUM does not take into account the correlation when calculating the effective degrees of freedom, which leads to incorrect estimates of the expanded uncertainty of indirect correlated measurements.

2. For the correct calculation of the effective degrees of freedom, a modified expression for the Welch-Satterthwaite formula (8) is proposed.

3. An alternative to the GUM procedure for processing indirect correlated measurements is the reduction method, which, using all the information obtained during the measurement, allows one to obtain an unbiased estimate of the numerical value and uncertainty of the measurand, eliminates the correlation coefficient at measurement uncertainty calculating, provides an accurate estimate of the degrees of freedom and allows one to correctly calculate the expanded uncertainty.

4. The considered example showed that the results obtained by the modified GUM method and reduction method are close to each other, however, processing the measurement results by the reduction method made it possible to take into account the bias in the numerical value of the measurand and its standard and expanded uncertainty.

Acknowledgements

The authors thank the organizers of the Measurement 2025 conference for their assistance and support.

References

[1] Rabinovich, S.G. (2010). *Evaluating Measurement Accuracy. A Practical Approach*. Springer.

[2] JCGM 100:2008 (GUM 1995 with minor corrections). (2008). *Evaluation of measurement data – Guide to the expression of uncertainty in measurement*. JCGM.

[3] Zakharov, I.P. (2007). Estimating measurement uncertainty on the basis of observed and logical correlation. *Measurement Techniques*, 50 (8), 808-816.

[4] Botsiura, O., Zakharov, I., Neyezhmakov, P. (2018). Reduction of the measurand estimate bias for nonlinear model equation. *Journal of Physics: Conference Series*, 1065 (21), 212002.

[5] Zakharov, I.P., Neyezhmakov, P.I., Botsiura, O.A. (2019). Reduction of the bias of measurement uncertainty estimates with significant non-linearity of a model equation. *Journal of Physics: Conference Series*, 1379 (1), 012013.

[6] Zakharov, I.P., Botsiura, O.A., Neyezhmakov, P.I. (2021). Expanded uncertainty evaluation taking into account the correlation between estimates of input quantities. *Ukrainian Metrological Journal*, (1), 4-8.

Parameter Selection for Prediction-Based Denoising of Measured Deterministic Time Series

Hana Krakovská, Anna Krakovská

Institute of Measurement Science, Slovak Academy of Sciences, Bratislava, Slovakia
Email: hana.krakovska@savba.sk

Abstract. *This study focuses on a numerical algorithm for noise reduction in discretely sampled observables from deterministic dynamical systems. The method utilises forecasting within the space formed by time-delay reconstruction, effectively leveraging the system's inherent dynamics to distinguish signal from noise. A key challenge is the optimal selection of denoising parameters without access to clean data. To address this, we propose a selection strategy that utilises the sample entropy of the filtered signal, reflecting the expectation of reduced randomness and increased determinism in the denoised data. The effectiveness of this approach is tested on complex chaotic observables contaminated with Gaussian white noise.*

Keywords: Predictive Noise Reduction, Parameter Optimization, Sample Entropy

1. Introduction

In the early 1980s, Packard, Takens, et al. [1], [2] introduced the idea that a single observable $x(t)$ from a dynamical system could provide a faithful multidimensional state-space representation of the whole dynamics via time-delay embedding

$$[x(t), x(t-\tau), x(t-2\tau), \ldots, x(t-(m-1)\tau)],$$

where m is the embedding dimension and τ is the time lag between consecutive components.

Under the assumption of a noise-free measurement of unlimited length, the reconstructed and original trajectories are diffeomorphic for almost any choice of τ and for a dimension m greater than twice the box-counting dimension of the original attractor [3]. As a result, they share essential dynamical properties, allowing valuable insights into the original system to be extracted from the reconstructed state portrait. Given these benefits, the simple time-delay reconstruction is now routinely used as a starting point for nonlinear analysis methods, such as attractor complexity estimation and, crucially for our study, system prediction [4].

In the following section, we explain how predictions made in reconstructed spaces can help reduce noise in data. This method builds upon and refines the idea put forth by Farmer and Sidorowich in the 1980s [5]. Next, we propose a strategy that leverages sample entropy for parameter selection in the predictive filtering method. Finally, we present the results from the test data and conclude with a discussion of the findings.

2. Subject and Methods

Data

In order to challenge the noise-reduction method to its limits, we used several demanding chaotic processes as our test data. In this work, we adopt the Rössler system as a case study:

$$\begin{aligned} \dot{x} &= -1.015y - z, \\ \dot{y} &= 1.015x + 0.15y, \\ \dot{z} &= 0.2 + z(x - 10), \end{aligned}$$

with the coordinates of the initial point randomly selected from the interval (0, 1). The x-variable was used as a test observable. Gaussian noise with a zero mean and variance proportional to the variance of the clean data (10%, 25%, and 50%) was then added to the observable.

ISBN 978-80-69159-00-6

Predictive noise reduction method

We consider a fairly common real-world scenario in which a single recorded time series, x, serves as a representative manifestation of an underlying deterministic dynamical system, X. When faced with such a case, one effective noise-reduction approach is utilising the fact that there are predictable deterministic patterns in data, which can help distinguish deterministic behaviour from random noise. The actual prediction process involves locating earlier situations that closely match the current state (historical neighbours) and extrapolating future outcomes based on their immediate consequences. The idea of forecasting based on analogous past situations can be traced back to Lorenz's pioneering work in 1969 [6].

The next step—using predictions to suppress noise—is not a new idea either. As early as 1988, Farmer and Sidorovich suggested that the ability to forecast enables transporting different points to the same point in time and merging them for noise reduction purposes [5]. To examine this idea, we implemented an algorithm that integrates both forward and backward predictions to reduce noise [7]. By including backward predictions, offline filtering can leverage information not only from earlier but also from later observations to adjust time series points.

The algorithm proceeds as follows:

- The time series x is embedded in a state space using delayed coordinates.
- To reduce noise at $x(t)$, we assume $x(t-1)$ is the last known value, identify its historical neighbours, generate one-step predictions, and replace $x(t)$ with their average. This local prediction approach, using nearest neighbours and zero-order approximations, is the simplest and widely preferred choice [8]. One-step predictions can be followed by using neighbours of $x(t-2)$ for two-step predictions and analogously for longer forecasting horizons.
- The same procedure is applied to the time-reversed series, producing one-step and multi-step backward predictions.
- Each $x(t)$ value is ultimately replaced by the average of all corresponding forward and/or backward predictions. This adjustment is applied iteratively to the entire time series until the noise level no longer decreases.

By focusing on short-term predictions, the method remains effective even in chaotic processes, where long-term forecasting is typically unreliable, yet short-term forecasts are still feasible.

Mean Absolute Error

This study focuses on optimising denoising parameters for effective noise removal. Obviously, in real-world applications, parameter tuning must be performed without access to clean data. However, while developing optimization strategies, we validated our approach using noisy datasets with available clean counterparts. To evaluate the differences between clean, noisy, and filtered observables, we used a traditional mean absolute error (MAE):

$$E_{nc} = \frac{1}{n}\sum_{i=1}^{n} |x_{noisy_i} - x_{clean_i}|, \qquad E_{fc} = \frac{1}{n}\sum_{i=1}^{n} |\hat{x}_i - x_{clean_i}|,$$

where

- n is the number of data points,
- x_{noisy_i} is the noisy value for the i-th data point,
- x_{clean_i} is the noise-free value for the i-th data point,
- $\hat{x}_i$ is the filtered value for the i-th data point.

E_{nc} is the MAE between the noisy and the clean data, and E_{fc} is the MAE between the filtered and clean data.

ISBN 978-80-69159-00-6

Parameter selection for the predictive noise reduction based on sample entropy

The predictive noise reduction method outlined above requires five parameters to be set:

- embedding dimension m,
- time delay τ,
- number of prediction steps (prediction horizon),
- number of nearest neighbours,
- number of iterations.

We also need to determine whether noise suppression should rely solely on forward predictions, solely on backward predictions, or a combination of both.

Optimising parameters often involves scanning the parameter space while tracking an invariant reflecting the method's purpose. Here, we use the data's measure of determinism as the invariant evaluated by a simple entropic measure called sample entropy (SE). Specifically, we use SE $(m = 3)$, which measures time series complexity by estimating the probability that close patterns of three consecutive points remain close when extended by one more point [9]. We used the closeness threshold of 20% of the signal's variance (while this is not a standard choice, it proved effective in our context.). We compute SE for signals filtered using various parameters to find the setting that minimises SE. Lower SE values indicate more regular, deterministic behaviour, expected after noise reduction.

3. Results and Discussion

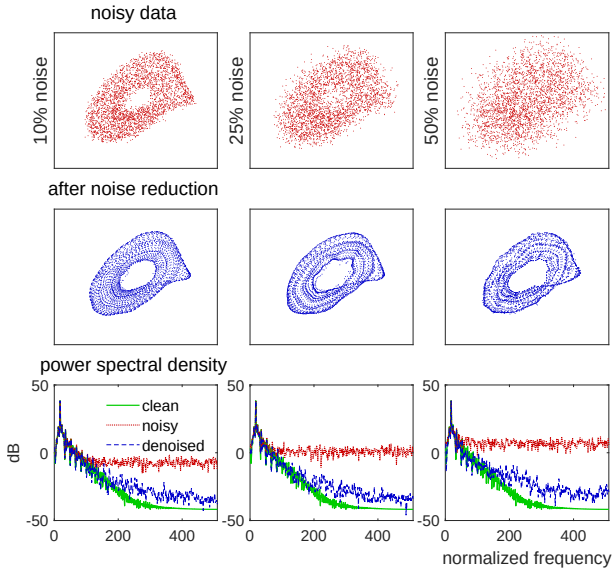

noise level		10%	25%	50%
embedding dimension m		14 24	24 64	64 64
time delay τ		5 1	3 1	1 1
no. of prediction steps		11 11	21 11	11 11
no. of nearest neighbours		22 22	12 22	12 22
no. of iterations		1 1	2 2	3 2
MAE	E_{nc}	0.640	1.653	3.288
	E_{fc} best	0.208	0.396	0.661
	E_{fc} SE-based	0.245	0.413	0.676

Fig. 1: Predictive filtering of 3000 points of noisy x-variable of the Rössler system. Reconstruction plots before and after noise reduction, along with power spectral densities. On the right: optimal parameters and below them those suggested by SE, followed by the MAE of noisy and denoised data.

The results are presented in Fig. 1 and Fig. 2. We found that when the error E_{fc} (between the filtered and clean data) is minimised for the optimum parameter settings, the sample entropy of the denoised signal also reaches or approaches its minimum under the same settings, as demonstrated in Fig. 2. This alignment indicates SE's ability to identify near-optimal filtering parameters without any knowledge of the clean data, highlighting its potential and practical applicability as a method that, with extensive testing, could become a reliable solution.

The (near)-optimal parameters presented in Fig. 1 follow well-established principles in reconstructed state-space analysis. For example, when dealing with sparsely sampled observables or iterative maps, a delay time of 1 is typically the best choice. Larger delays are useful only in

ISBN 978-80-69159-00-6

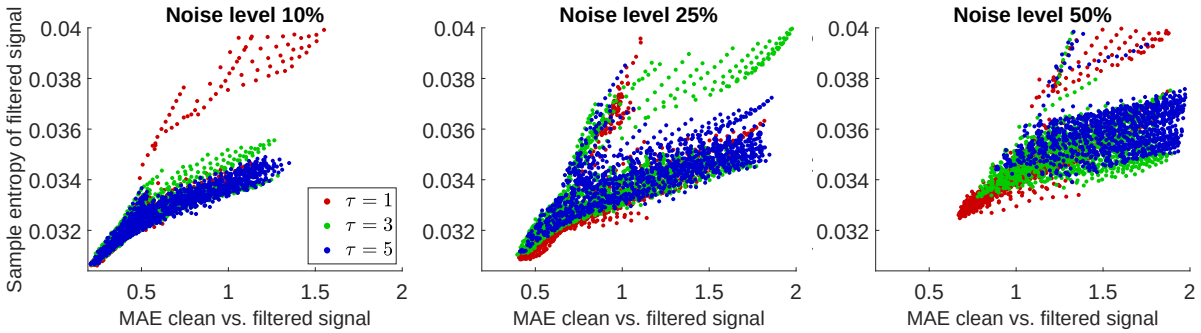

Fig. 2: E_{fc} vs. SE after noise reduction of 3000 points of the Rössler observable with noise levels of $10\%, 25\%$, and 50%. Each point corresponds to a unique setting of denoising parameters. Results are shown for one algorithm iteration for 10% noise, and two iterations for 25% and 50% added noise, using both forward and backward predictions, with $\tau = \{1, 3, 5\}$.

oversampled data—such as in our Rössler system test case—where they can capture a substantial fraction of the trajectory without the need to work in prohibitively high-dimensional spaces. Regarding the embedding dimension, it should exceed the system's intrinsic dimensionality, with substantial over-embedding proving beneficial in cases of high noise and dense sampling.

We demonstrated that selecting the parameters for the predictive noise reduction algorithm is very well manageable, even when no prior information about the underlying dynamics is available beyond the noisy data themselves.

The MATLAB implementation of the predictive filter with automatic parameter selection will be publicly available at *MathWorks File Exchange*.

Acknowledgements

Supported by the Slovak Grant Agency for Science (VEGA 2/0023/22), the Slovak Research and Development Agency (APVV-21-0216 and SK-CZ-RD-21-0109) and Recovery and Resilience Plan - Project DigiDent (09I05-03-V02-00080).

References

[1] Packard, N. H. et al. (1980). Geometry from a time series. *Physical Review Letters*, 45 (9), 712.

[2] Takens, F. (1980). Detecting strange attractors in turbulence. *Dynamical Systems and Turbulence*, Springer, 366-381.

[3] Sauer, T. et al. (1991). Embedology. *Journal of Statistical Physics*, 65 (3-4), 579-616.

[4] Kantz, H., Schreiber, T. (2004). *Nonlinear Time Series Analysis*. Cambridge University Press.

[5] Farmer, J. D., Sidorowich, J. J. (1988). Exploiting chaos to predict the future and reduce noise. *Evolution, Learning and Cognition*, 277-330.

[6] Lorenz, E. N. (1969). Atmospheric predictability as revealed by naturally occurring analogues. *Journal of the Atmospheric Sciences*, 26 (4), 636-646.

[7] Krakovská, A., Jakubík, J. (2025). Noise reduction strategies in nonlinear time series. *Submitted manuscript*.

[8] Farmer, J. D., Sidorowich, J. J. (1987). Predicting chaotic time series. *Physical Review Letters*, 59 (8), 845.

[9] Richman, J. S., Moorman, J. R. (2000). Physiological time-series analysis using approximate entropy and sample entropy. *American Journal of Physiology-Heart and Circulatory Physiology*, 278 (6), H2039-H2049.

Noise Measurement of High-Ohm Metal-Oxide Resistors

Lukáš Zdražil, Zdeněk Roubal

Department of Theoretical and Experimental Electrical Engineering, FEEC, BUT,
Technická 3082/12, 616 00 Brno, Czech Republic,
Email: Lukas.Zdrazil1@vutbr.cz

Abstract. *This paper deals with the comparison of low-frequency noise of high-ohm metal-oxide resistors and resistors made by thick-layer technology. For measuring very small currents in the order of 10^{-10} A to 10^{-15} A, a feedback ammeter is very often used, where high-ohm resistors must be connected to the feedback of a precision operational amplifier. Feedback resistors can reach resistance of several hundred GΩ. As the resistance increases, the level of Johnson´s thermal noise also increases. Most high-ohm resistors are manufactured by thick-layer technology that generates also low-frequency flicker noise with a frequency dependence of 1/f. Resistors based on metal-oxide technology should not generate low-frequency flicker noise, but their price is several times higher than the price of resistors made using thick-layer technology.*

Keywords: Metal-Oxide Resistors, High-Ohm Resistors, Flicker Noise, Thermal Noise

1. Introduction

When measuring DC currents in the order of 10^{-10} A to 10^{-15} A, it is very important to achieve the lowest possible level of low-frequency noise. In electronic circuits, two types of noise are generated, which are distinguished by their frequency dependence. White noise is characterized by a uniform distribution of frequency components in the spectrum. The second type of noise is colored noise, which is characterized by a non-uniform spectral distribution.

The most important of the white noises for us is Johnson's thermal noise. It occurs in conductors and semiconductors and is generated by both active and passive components. It is generated by the movement of electrons at temperatures above 0 K. Its spectral power level can be considered constant up to a frequency of 100 THz, at higher frequencies other types of noise start to appear and the spectral power density takes an increasing trend. The approximate effective value of the noise voltage on a resistor due to Johnson´s thermal noise is given by [1]:

$$U_{N\_T} = \sqrt{4 \cdot k_B \cdot T \cdot R \cdot B_N} \qquad [\mathrm{V; JK^{-1}, K, \Omega, Hz}], \tag{1}$$

where k_B is the Boltzmann constant ($k_B = 1.380 \cdot 10^{-23}$ J·K^{-1}), T is the absolute temperature of the resistor in Kelvin, R is the resistance of the resistor and B_N is the considered noise bandwidth. The Eq. 1 shows that the square of the noise voltage increases with the resistance of the resistor.

Another type of noise that needs to be considered when measuring very small DC currents is 1/*f* flicker noise. Resistors made using thick-layer technology generate flicker noise at a level significantly higher than resistors made using thin-layer technology. The spectral density of the flicker noise voltage can be expressed as a function of the voltage drop across the resistor [2]. As the voltage drop increases, the spectral density of the flicker noise voltage also increases.

In paper [3], authors describe that flicker noise is generated in semiconductors due to defects in the crystal lattice at the interface Si-SiO_2. Charge carriers alternate between two states only if the energies of the two states are equal. In the first state, the carriers are caught in a trap

(defect) and do not contribute to current flow. In the second state, they are free and contribute to current flow. In the steady state, when the voltage between gate and source is constant, the trap occupancy function is a function of the trap energy and the Fermi level of the traps. Traps whose energy is nearly equal to the Fermi level of free carriers in silicon are responsible for the noise.

In paper [4] it is experimentally tested whether flicker noise is generated more on the surface of semiconductor materials or inside. In multilayer graphene structures, for the number of atomic layers n ≤ 7, the 1/*f* noise is generated predominantly on the surface. With a larger number of atomic layers, noise generation inside the graphene structure prevails.

2. Measurement Setup

Resistor flicker noise can be measured using two identical resistors according to the circuit diagram in Fig. 1 from Thesis [5]. The principle of the circuit is two symmetrical voltage sources, which must supply exactly the same voltage level to the circuit. The two voltage sources were replaced by one voltage source and two OPA211 low-noise operational amplifiers, one for each channel. One amplifier in inverting configuration and the other in non-inverting configuration. Their gain must be equal to one. Resistors R_F and capacitors C_F represent a low-pass filter. Resistors R_D are two identical measured resistors on which can be any voltage drop, because at their common node the voltage against ground will always correspond only to their noise voltage and the background noise of the measuring system. The limitation is due to the thermal noise of the resistors and the input noise voltage of the operational amplifiers used.

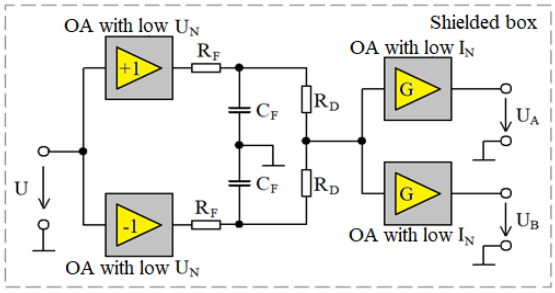

Fig. 1 Circuit diagram for measuring resistor flicker noise with two identical resistors and two channels of spectrum analyzer [5]

The circuit uses the properties of the uncorrelated noise of the measured resistors and the background noise of the measurement system according to paper [6]. This approach uses two low-noise operational amplifiers with a gain of 40 dB connected after the measured resistors. Operational amplifiers with very low input noise current LMC6001A were used. Subsequently, a discrete Fourier transform is performed in both channels of the spectrum analyzer and mathematical operations are used to obtain the correlation of the spectra of the signals at the output of both operational amplifiers. The noise generated in the circuit by the operational amplifiers is largely eliminated in this way because it is uncorrelated, unlike the noise of the measured resistors. The outputs U_A and U_B are connected to the inputs of the spectrum analyzer.

3. Measured Results

According to the diagram in Fig. 1, measurements were made with two identical resistors. Metal-oxide resistors of 1 GΩ were measured, as well as resistors made with thick-layer

ISBN 978-80-69159-00-6

technology of the Slim-Mox series for comparison. The resistance accuracy of all resistors was ±1 %. The resistors are placed on Teflon spacers and the connections are made in air to limit the influence of leakage currents. In addition, the sensitive part is enclosed in a small shielding box, which is shielded by means of a buffer [1], [5]. Voltage applied to the resistors was 4.9 V in both cases. The power supply was from batteries. A photography of the measuring equipment in the shielding box is shown in Fig. 2.

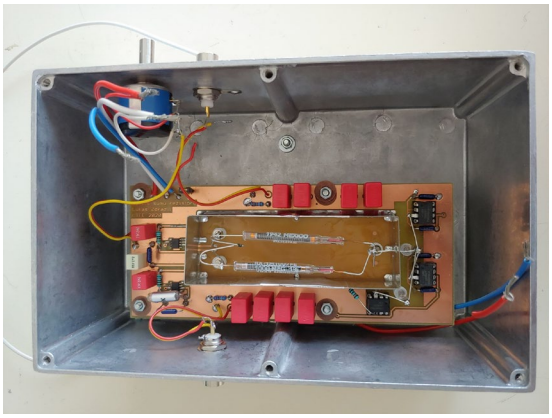

Fig. 2 Photography of the measuring equipment in the shielding box

Fig. 3 shows the spectral density dependence of the noise voltage for both metal-oxide resistors and resistors made by thick-layer technology. The spectral density of the noise voltage was measured in two frequency bands for both resistors. The lower frequency band was from 0.3 Hz to 20 Hz and the higher frequency band was from 10 Hz to 100 Hz. In both frequency bands, averaging from 100 measurements was performed. For a thick-layer resistors, a high increase in spectral density at low frequencies due to 1/*f* flicker noise is visible. The noise of the metal-oxide resistors can be considered constant over both measured bands. At the lowest measured frequency of 0.3 Hz, the noise of the thick-layer resistors is twice as high as the noise of the metal-oxide resistors, even though they are very high quality thick-layer resistors. In the figure, the theoretical level of Johnson´s thermal white noise for a 1 GΩ resistor is also plotted, which is calculated using the Eq. 1.

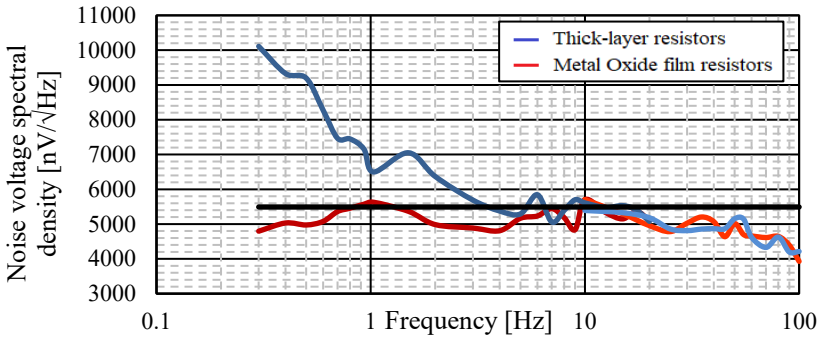

Fig. 3 Measured noise spectral density of the resistors

The resistance dependence on the applied voltage was also measured for both resistors. The measurements were performed using a 6517A electrometer from Keithley Instruments. Using a built-in high voltage source, the applied voltage was adjusted and the current through the resistors was measured. The resistance dependence was then calculated from the measured

ISBN 978-80-69159-00-6

current (Fig. 4). It can be observed from the figure that the metal-oxide resistor is more accurate and also more stable in terms of the applied voltage.

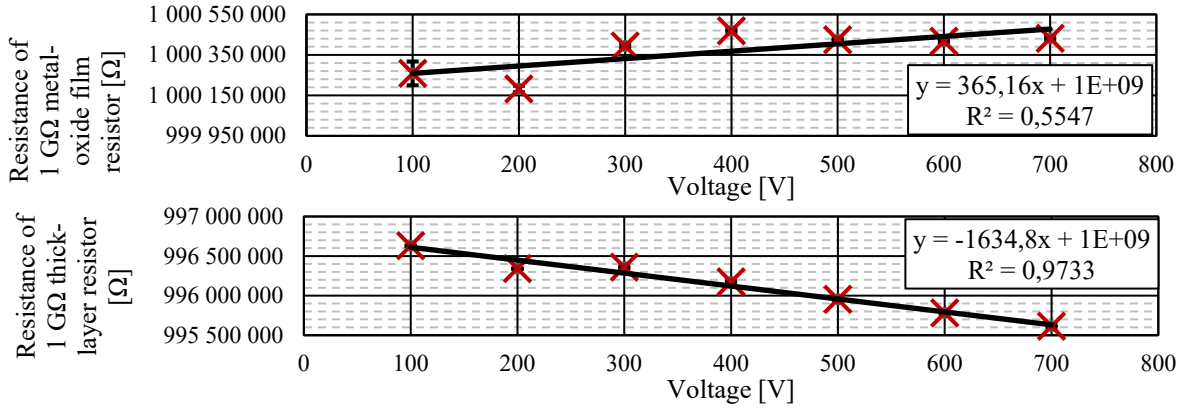

Fig. 4 Resistance dependence on the applied voltage for 1 GΩ metal-oxide resistor and 1 GΩ thick-layer resistor

4. Conclusions

A new equipment was designed to measure the noise spectral density of high-ohm resistors. This equipment measures the noise spectral density using only two identical resistors. Only one voltage source is needed because a precise symmetrical source is created using low-noise operational amplifiers. Using the two outputs of the equipment, correlation of the spectra of the output signals can be performed. Noise caused by the operational amplifiers is thus largely suppressed. The measuring equipment therefore achieves very accurate measurement results. For the measured high-ohm metal-oxide resistor, the theory was confirmed that it does not generate low-frequency 1/*f* noise and its noise spectral density over the entire measured range corresponds to the calculated value of Johnson's thermal noise. The measured resistance dependence on applied voltage shows that the metal-oxide resistors are very precise.

Acknowledgements

The research was completed under support from the project No. FEKT-S-23-8425, which was supervised by the BUT internal grant office.

References

[1] Keithley Instruments, Inc. (2002). *Low Level Measurements Handbook: Precision DC Currents, Voltage, and Resistance Measurements*. Ohio, USA.

[2] Seifert, F. (2009). *Resistor Current Noise Measurements* [online].

[3] Dubey, D., Gupta, A. (2015). A low power low noise amplifier for biomedical applications. In *2015 IEEE International Conference on Electrical, Computer and Communication Technologies (ICECCT)*. IEEE, 1-6. ISBN 978-1-4799-6084-2.

[4] Liu, G., Rumyantsev, S., Shur, M.S., Balandin, A.A. (2013). Origin of 1/*f* noise in graphene multilayers: Surface vs. volume. In *Applied Physics Letters*. 102(9). ISSN 0003-6951.

[5] Zdražil, L. (2020). *Design and Optimization of Special Low-Level Amplifier for Measurement of Air Ions*. Master´s thesis. Brno University of Technology.

[6] Ciofi, C., Crupi, F., Pace, C. (2002). A new method for high-sensitivity noise measurements. In *Transactions on Instrumentation and Measurement*. IEEE, 51(4), 656-659.

A Python Application for Generating Digital Calibration Certificate

George Sammarah, Martin Halaj
Slovak University of Technology in Bratislava, Faculty of Mechanical Engineering, Institute of Automation, Measurement and Applied Informatics, Mýtna 36, 811 07 Bratislava, Slovakia
Email: george.sammarah@stuba.sk

Abstract: *The paper deals with the possibility of creating an application tool to make the digital calibration certificate, especially in terms of converting human-readable text to machine-readable format and securing it. It initially defines a tool that generates a digital calibration certificate. It describes the main structure of the digital calibration certificate and the procedure for creating a digital calibration certificate. It also presents the authors' analysis concerning individual aspects of digitalization in terms of additional information used to improve digital certificates.*

Keywords: Digital Calibration Certificate, .Exe Application, XML, JSON, Python

1. Introduction – What Is a Calibration Certificate

a. A calibration certificate is an official document verifying a measuring system's accuracy. As instruments change over time, regular calibration ensures precision. The certificate records calibration results, confirming the system's reliability and performance. [2]

b. A calibration certificate includes key details such as customer and provider info, device identification, the calibration method, measurement data, and uncertainty analysis. It is usually signed by certified personnel and shows traceability to national or international standards. These certificates ensure measurement accuracy and compliance, and are widely used in industries like manufacturing, healthcare, and research.

   The international standard ISO/IEC 17025:2017 establishes rules and principles for how testing and calibration laboratories should conduct their business, including matters related to certificates and reporting. ISO/IEC 17025 does point out the need for calibration certificates and reports to meet specific criteria regardless of their format. [1]

   Whether using paper or digital certificates, laboratories must ensure both meet required standards and any additional regulations from accrediting bodies or industry guidelines. Acceptance of digital certificates can also depend on the specific sector or regulatory environment.

c. Digitizing calibration certificates improves efficiency, accuracy, and accessibility. It reduces errors, enables secure storage, quick retrieval, remote access, system integration, and supports data analysis - saving time and costs.

ISBN 978-80-69159-00-6

Table 1. SWOT analysis – what does a digital calibration certificate bring better to the table compared to a classic certificate using the application [4]

Strengths	Weaknesses
- Increased work efficiency thanks to the elimination of manual administrative activity - Reduced data error rate thanks to automated systems - Effective securing of certificates and easier follow-up to other standards - Possibility to modify information - Possibility of simple search in archived data thanks to machine reading - Mutual compatibility of the information presented in the mandatory parts of the certificate	- Initial investment costs for both hardware and software - Necessary training of personnel to work with digital tools - Possibility of data loss due to incorrect handling (archiving) - Necessary adoption of additional measures to prevent unauthorized handling
Opportunities	**Threats**
- Support of progressive trends - Industry 4.0, Internet of Things (IoT) - The possibility of direct and indirect application of calibration results to meter corrections or calculation of measurement uncertainty - The possibility of simulating the operation of the meter in a digital copy of the measuring process - Simplified possibility of inspection of mandatorily calibrated gauges by inspection bodies	- Security risks associated with unauthorized handling of data (its authenticity, integrity and confidentiality) - The need to strictly adhere to the prescribed format of mandatory data - Incorrect implementation of data from the customer's digital certificate

2. Why to Use Python Application for DCC

A Python-based application for generating digital calibration certificates modernizes the traditional, paper-based process. It creates electronic certificates for various measuring instruments, making calibration records more efficient, secure, and accessible.
With encryption and access controls, digital certificates prevent unauthorized changes. They also allow instant access to data, reducing downtime and improving productivity.
Automation and structured data management streamline the calibration process, saving time and resources. Records are digitally stored, organized, and easy to retrieve.
This application marks a significant step forward in metrology and quality assurance, enhancing accuracy, efficiency, and data integrity.

A software application designed to create calibration certificates is a solution that simplifies the process of documenting calibrations.
Here's an overview of what such an application might include:

- User Interface,
- Data Input,
- Data Storage,
- Digital Signatures,
- Certificate Generation,
- Export Formats,
- Reporting and Analytics,
- Security Measures,
- Integration,
- Compliance and Standards.

ISBN 978-80-69159-00-6

Creating such an application requires knowledge of software development, cryptography, user experience design, and system integration. Python is a popular choice due to its universality and ease of use. Features will vary depending on the user's or organization's specific needs.

3. The DCC in Principle

The digital calibration certificate (widely assigned as DCC) serves as a counterpart, to a calibration certificate. It enables the automated generation, insertion, and processing of calibration results in a format. The simplest way to digitize this certificate is by saving a paper version as a document (like PDF) or an image file (such, as JPG) without making any modifications. This approach is particularly convenient when certificates are initially created digitally and then printed out. It can be applied extensively in different scenarios for the electronic storage, archiving, and sharing of certificates.

The structure of the digital calibration certificate must contain necessary information about the calibration process and the results obtained for a specific measuring instrument or device. However, the format may differ based on the organization and measuring region. In general, depending on the viewpoint, the content of a calibration certificate can be classified in numerous ways. We split the contents of a digital calibration certificate into four categories for the purposes of this document [3]:

1. Administrative information (regulated area),
2. Calibration results (regulated area),
3. Comments (unregulated area),
4. Additional information (unregulated area)

A well-structured digital calibration certificate requires a specific information that provides a clear and concise overview of the calibration process and its results while ensuring transparency, traceability, and compliance with industry standards and regulations.

The following list is essential and common information that is usually included in a digital calibration certificate [1, 3]:

-Certificate Identification,
-Instrument Details,
-Calibration Laboratory Information,
-Calibration Procedure,
-Calibration Environment,
-Reference Standards,
-Measurement Data,
-Uncertainty Analysis,
-Calibration Results,
-Comments and Notes,
-Digital Signatures,
-Attachments,
-Validity Period,
-Contact Information.

It's vital to remember that legislation, guidelines, and quality standards particular to the industry may have an impact on the content and appearance of a digital calibration certificate. Therefore, maintaining a uniform and organized certificate format would improve its use, traceability, and regulatory compliance.

4. The Application for Creating a DCC principle

A sort of computer software that includes instructions in machine code format is a ".exe" (executable) application. It is made to be immediately run by an operating system on a computer. The operating system loads the program into memory and begins running its instructions when you launch a ".exe" file, enabling you to interact with the software. The most prevalent form of executable files in this context is a ".exe" file, which is used frequently with Windows operating systems. They can include a wide variety of software programs, from simple utilities to sophisticated ones like games, office programs, and more. ".exe" files might

ISBN 978-80-69159-00-6

possibly carry security hazards since they can execute code that could be harmful due to their executable nature. As a result, it's crucial to only execute ".exe" files from reliable sources and to safeguard your computer using security tools like antivirus software.

In order to provide a digital calibration certificate, the tool is designed as a four-stage application. Python is used throughout every stage of development in the "PyCharm CE" environment. We must complete these steps in order to obtain the final secured document for the digital calibration certificate:

1. Filling form for the essential information that DCC should contain
2. Converting human readable text to machine readable format
3. Converting MR format to human readable text
4. Securing the file format (XML, JSON and PDF) with hash number

5. Conclusion

In conclusion the main goal for digital calibration certifications are generally consistent with its overall aim to advance precise measurement, guarantee accuracy, and promote trustworthy metrological practices.

Furthermore, the creation of an executable (".exe") application written in Python is a strong solution for producing digital calibration certificates. The user-friendly, human-readable input form provided by this tool ensures both usability and accuracy. Convenience and strong security are combined with the option to convert this data into a machine-readable format and create a secure PDF document that is hash-protected. This method is a useful tool for businesses in need of trustworthy digital calibration certifications because it not only modernizes the calibration procedure but also improves data integrity and accessibility.

Acknowledgment

This paper was created under the support of the following grants: APVV-21-0216 „ Advanced mathematical and statistical methods for measurement and metrology “.

References

[1] ISO/IEC 17025: 2017 *General requirements for the competence of testing and calibration laboratories.*

[2] Halaj, Martin. *Digitálny kalibračný certifikát (1)*. In ATP Journal. Roč. 26, č. 6 (2019), s. 34-35. ISSN 1335-2237. Dostupné online na https://www.atpjournal.sk/rubriky/prehladove-clanky/digitalny-kalibracny-certifikat-1.html?page_id=29044

[3] Halaj, Martin. *Digitálny kalibračný certifikát (2)*. In ATP Journal. Roč. 26, č. 7 (2019), s. 42-44. ISSN 1335-2237. Dostupné online na https://www.atpjournal.sk/rubriky/prehladove-clanky/digitalny-kalibracny-certifikat-2.html?page_id=29230

[4] Halaj, Martin; Sammarah, George. 2021, *Digitalizácia v priemyselnej metrológii - úvod.* In Metrológia a skúšobníctvo. Roč. XXVI, č. 1 (2021), s. 2-7. ISSN 1335-2768. Dostupné online na https://www.normoff.gov.sk/files/docs/e-mas-3-2021-format-pdf-61f7ceea19a24.pdf?csrt=15088672491119315344

Poster Session I

ISBN 978-80-69159-00-6

Tests for Integer-valued Time Series Based on the Probability Generating Function

Aneta Kostárová

Department of Probability and Mathematical Statistics, Charles University in Prague, Faculty of Mathematics and Physics, Sokolovská 83, CZ-18675 Praha 8, Czech Republic,
Email: kostarova@karlin.mff.cuni.cz

Abstract. *This paper addresses models for time series of integer-valued variables. Such series arise in various applications, often as increment series for counts of interest. A model with a GARCH-type structure with the Skellam conditional distribution is considered. We propose a novel testing procedure to assess the null hypothesis that a set of integer-valued observations follows such model. The proposed test statistic incorporates the empirical probability generating function computed from the data.*

Keywords: Incremental Time Series, Skellam Distribution, INGARCH Model, Goodness–of–fit Test, Empirical Probability Generating Function

1. Introduction

In many cases, we observe time series of discrete random variables with non-negative values, such as the number of customers or the number of insurance claims. The corresponding series of the first differences then consists of variables with values in $\mathbb{Z}$ that can be dependent. Such time series, known as incremental time series, for instance, capture the changes in the number of customers over specified time intervals. Incremental time series can be encountered in various industries such as finance (intraday stock prices), biostatistics (differences in the number of epileptic seizures or tumors observed before and after treatment), or betting (the difference in the number of goals scored in a match). Fig. 1, provides an example of such time series, namely the goal differences for the Florida Panthers ice hockey team for matches in the 2023–24 season.

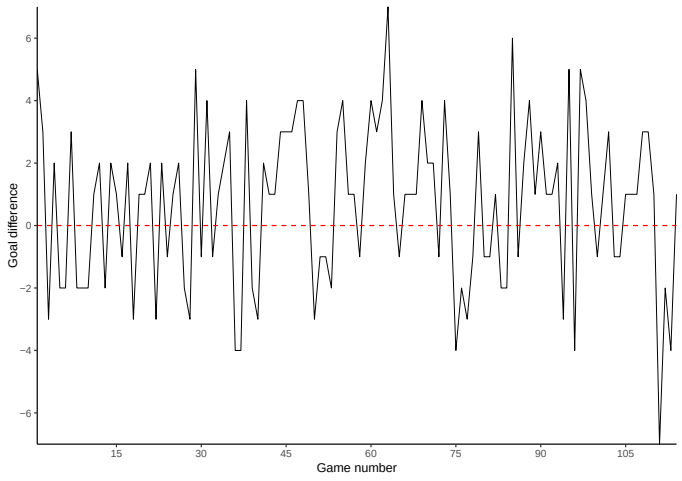

Fig. 1: The time series of the goal differences for the Florida Panthers ice hockey team during the 2023–24 season.

Let $\{Z_t, t \in \mathbb{Z}\}$ represent an integer-valued time series of interest. In some applications, it is desirable to forecast not only the future mean but also the entire future distribution. If the data discreteness is substantial, as, e.g., in Fig. 1, then the traditional time series models such as ARMA-GARCH (see, e.g., [2] and [3]) are not suitable for modeling, because they are primarily

ISBN 978-80-69159-00-6

designed for continuous data. The goal, therefore, is to model the conditional distribution of Z_t given the past using a suitable discrete distribution on $\mathbb{Z}$.

The most well-known distribution for integers is the Skellam distribution (see [7]). Based on the symmetric Skellam distribution, Alomani et al. [1] introduced the first model for analyzing $\mathbb{Z}$-valued time series, known as the symmetric Skellam INGARCH(1,1) model. Within the INGARCH framework, alternative integer distributions may be considered, or the models can be constructed from different perspectives. More INGARCH models are discussed in the review article by Li et al. [6].

Our aim is to construct a goodness–of–fit (GOF) tests for distributional assumptions regarding Skellam INGARCH models. In deriving these tests, we follow a procedure similar to that of Hudecová et al. [5], who proposed GOF tests for count time series models. Hence, the main tool for constructing the test statistic is the probability generating function (PGF), which for an arbitrary integer-valued random variable Z, is defined as $g_Z(s) = \mathbb{E}[s^Z],\ s \in [-1,1]$. Based on the data, the PGF can be estimated either entirely non-parametrically or, by exploiting the structure and properties of the model in constructing the estimate, semiparametrically. In this way, we obtain two estimates of the same quantity, which should be close if the model holds. Conversely, if these two estimates differ significantly, it indicates that the considered model is not valid.

This paper is organized as follows. The Skellam distribution is introduced in Section 2. Section 3 specifies the considered model, and the GOF test statistic is constructed in Section 4.

2. Skellam distribution

A Skellam random variable Z can be expressed as the difference between two independent Poisson random variables, X and Y, with parameters λ_1 and λ_2, respectively. The probability mass function of $Z = X - Y$ is given by

$$P(Z=z) = e^{-\lambda_1-\lambda_2}\left(\frac{\lambda_1}{\lambda_2}\right)^{z/2} I_{|z|}(2\sqrt{\lambda_1\lambda_2}), \quad z \in \mathbb{Z}, \tag{1}$$

where

$$I_r(x) = \left(\frac{x}{2}\right)^r \sum_{k=0}^{\infty} \frac{(x^2/4)^k}{k!(r+k)!} \tag{2}$$

is the modified Bessel function of order r.

The first two moments of Z are $\mathbb{E}(Z) = \mu_Z = \lambda_1 - \lambda_2$ and $\mathsf{Var}(Z) = \sigma_Z^2 = \lambda_1 + \lambda_2$. Consequently, $\lambda_1 = (\sigma_Z^2 + \mu_Z)/2$ and $\lambda_2 = (\sigma_Z^2 - \mu_Z)/2$. When $\mu_Z = 0$, we have $\lambda_1 = \lambda_2$ and Z follows a symmetric Skellam distribution, denoted as $Z \sim SS(\lambda_1)$. If $\lambda_1 \neq \lambda_2$, Z follows an asymmetric Skellam distribution, denoted as $Z \sim AS(\lambda_1, \lambda_2)$.

The probability generating function (PGF) of the symmetric Skellam distribution $SS(\lambda_1)$ is expressed for $s \in [-1,1]$ as follows

$$\begin{aligned} g_Z(s) &= \mathbb{E}[s^Z] = \mathbb{E}[s^{X-Y}] = \mathbb{E}[s^X]\,\mathbb{E}[s^{-Y}] = g_X(s)\,g_Y(1/s) \\ &= e^{\lambda_1(s-1)}\,e^{\lambda_1\left(\frac{1}{s}-1\right)} = e^{\lambda_1\left(s+\frac{1}{s}-2\right)}, \end{aligned} \tag{3}$$

where we used the fact that the PGF of the Poisson distribution with mean λ is given by $e^{\lambda(s-1)}$.

3. Integer-valued INGARCH models

Let $\mathscr{F}_t$ denote the information set available at time t, defined as the σ-field $\mathscr{F}_t = \sigma\{Z_s, s \le t\}$ generated by the past values of the time series $\{Z_t, t \in \mathbb{Z}\}$ up to time t. Alomani et al. [1]

ISBN 978-80-69159-00-6

proposed the symmetric Skellam INGARCH(1,1) model satisfying

$$Z_t|\mathscr{F}_{t-1} \sim SS\left(\frac{\lambda_t}{2}\right), \quad \lambda_t = \omega + \alpha Z_{t-1}^2 + \beta\lambda_{t-1}, \quad t \geq 2, \tag{4}$$

where $\omega, \alpha, \beta > 0$ are model parameters, and λ_t is the conditional variance $\mathsf{var}[Z_t|\mathscr{F}_{t-1}]$ taking the form of a typical GARCH(1,1) model. If $\alpha + \beta < 1$, then there exists a unique strictly stationary and absolutely regular solution to Eq. 4, see Doukhan et al. [4].

The unknown parameters of the model can be estimated using the conditional maximum likelihood method or the conditional least squares method, as shown by Alomani et al. [1]. Both methods give strongly consistent and asymptotically normal estimates, Li et al. [6].

4. Test statistics

Assume that $Z_t, t = 1, \ldots, n$, are data coming from a strictly stationary process $\{Z_t, t \in \mathbb{Z}\}$. The objective is to test the null hypothesis

$$\mathscr{H}_0 : \{Z_t, t \in \mathbb{Z}\} \text{ follows model in Eq. 4 for some } \theta = (\omega, \alpha, \beta)^\top \in \Theta,$$

where $\Theta = \{(\omega, \alpha, \beta)^\top; \omega, \alpha, \beta > 0, \alpha + \beta < 1\} \subset \mathbb{R}^3$, against a general alternative that $\mathscr{H}_0$ does not hold.

We propose testing the null hypothesis $\mathscr{H}_0$ using a Cramér–von Mises type test statistic

$$S_{n,w} = \int_\varepsilon^1 \left(\hat{g}_n(s) - \tilde{g}_n(s)\right)^2 w(s)\mathrm{d}s, \tag{5}$$

where $\varepsilon > 0$ and $w(s)$ is a non-negative integrable weight function. The test statistic $S_{n,w}$ is defined as a weighted L2-type distance between the empirical probability generating function

$$\hat{g}_n(s) = \frac{1}{n}\sum_{t=1}^{n} s^{Z_t}, \tag{6}$$

which is a non-parametric estimate of the marginal PGF of Z_t, and a semiparametric estimate $\tilde{g}_n(s)$ of the same PGF imposed by the model. Under $\mathscr{H}_0$, the marginal population PGF of Z_t satisfies

$$\begin{aligned} g_{Z_t}(s) = \mathbb{E}[s^{Z_t}] = \mathbb{E}\left[\mathbb{E}[s^{Z_t}|\mathscr{F}_{t-1}]\right] = \mathbb{E}\left[e^{\frac{\lambda_t}{2}\left(s+\frac{1}{s}-2\right)}\right] = \\ = \mathbb{E}\left[e^{(\omega+\alpha Z_{t-1}^2+\beta\lambda_{t-1})\left(\frac{s}{2}+\frac{1}{2s}-1\right)}\right]. \end{aligned} \tag{7}$$

By substituting the parameter vector $(\omega, \alpha, \beta)^\top$ in Eq. 7 with its estimate $(\hat{\omega}_n, \hat{\alpha}_n, \hat{\beta}_n)^\top$ and replacing the expectation by the sample mean, we obtain a semiparametric estimate of the marginal PGF,

$$\tilde{g}_n(s) = \frac{1}{n}\sum_{t=2}^{n}\left[e^{(\hat{\omega}_n+\hat{\alpha}_n Z_{t-1}^2+\hat{\beta}_n\hat{\lambda}_{t-1})\left(\frac{s}{2}+\frac{1}{2s}-1\right)}\right], \tag{8}$$

where $\hat{\lambda}_t = \hat{\omega}_n + \hat{\alpha}_n Z_{t-1}^2 + \hat{\beta}_n\hat{\lambda}_{t-1}$ is calculated recursively from the initial values $\hat{\lambda}_0 = Z_1$ and $Z_0 = Z_1$.

Hudecová et al. [5] considered a similar Cramér–von Mises type test statistic for count time series models and showed that the asymptotic distribution of $\sqrt{n}S_{n,w}$ is quite complex as it can be expressed as an infinite weighted sum of independent χ^2 variables, where the weights

depend on the unknown parameters in a complicated way. It can be assumed that the limiting distribution of $\sqrt{n}S_{n,w}$ exhibits similar properties also for Skellam INGARCH process, and, therefore, we propose a parametric bootstrap procedure for evaluating the significance of $S_{n,w}$

Consider the data $Z_t, t = 1, \ldots, n$, and the estimate $\hat{\theta}_n = (\hat{\omega}_n, \hat{\alpha}_n, \hat{\beta}_n)^\top$ to calculate the value of the test statistic $S_{n,w} := S_{n,w}(Z_1, \ldots, Z_n; \hat{\theta}_n)$. Let B be a specified number of bootstrap samples. For $b = 1, \ldots, B$:

1. Generate a time series $\{Z_t^{(b)}\}_{t=1}^n$ from the model in Eq. 4 with θ replaced by $\hat{\theta}_n$.
2. Fit the model in Eq. 4 with the bootstrap data $\{Z_t^{(b)}\}_{t=1}^n$ and compute the estimate $\hat{\theta}_n^{(b)} = (\hat{\omega}_n^{(b)}, \hat{\alpha}_n^{(b)}, \hat{\beta}_n^{(b)})^\top$.
3. Calculate the test statistic $S_{n,w}^{(b)} = S_{n,w}(Z_1^{(b)}, \ldots, Z_n^{(b)}; \hat{\theta}_n^{(b)})$.

The empirical distribution of $S_{n,w}^{(1)}, \ldots, S_{n,w}^{(B)}$ simulates the distribution of the test statistic $S_{n,w}$ under $\mathscr{H}_0$. The null hypothesis $\mathscr{H}_0$ is rejected at significance level $\alpha \in (0,1)$ if the value of $S_{n,w}$ exceeds $(1-\alpha)\%$-empirical quantile calculated from $S_{n,w}^{(1)}, \ldots, S_{n,w}^{(B)}$. Alternatively, the p-value is given as $p = \frac{1}{B}\sum_{b=1}^{B} \mathbb{I}[S_{n,w}^{(b)} > S_{n,w}]$.

5. Conclusions

We propose a procedure for testing the null hypothesis that a given integer-valued time series follows a symmetric Skellam INGARCH(1,1) model. A simulation study and an application to real data, demonstrating the practical use of this procedure, are currently in progress.

Acknowledgements

The research was supported by the Czech Science Foundation project GAČR No. 25-15844S.

References

[1] Alomani, G. A., Alzaid, A. A., Omair, M. A. (2018). A Skellam GARCH model. *Brazilian Journal of Probability and Statistics*, 32 (1), 200–214.

[2] Bollerslev, T. (1986). Generalized autoregressive conditional heteroskedasticity. *Journal of Econometrics*, 31 (3), 307–327.

[3] Box, G. E. P., Jenkins, G. M., Reinsel, G. (1994). *Time Series Analysis. Forecasting and Control*. Prentice-Hall.

[4] Doukhan, P., Mamode Khan, N., Neumann, M. H. (2021). Mixing properties of integer-valued GARCH processes. *Latin American Journal of Probability and Mathematical Statistics*, 18 (1), 401–420.

[5] Hudecová, Š., Hušková, M., Meintanis, S. G. (2015). Tests for time series of counts based on the probability-generating function. *Statistics*, 49 (2), 316–337.

[6] Li, Q., Chen, H., Zhu, F. (2023). Z-valued time series: Models, properties and comparison. *Journal of Statistical Planning and Inference*, 230.

[7] Skellam, J. G. (1946). The frequency distribution of the difference between two Poisson variates belonging to different populations. *Journal of the Royal Statistical Society*, 109 (3), 296.

Introducing SPECTER 2.0 - an Enhanced Version of the Tensor Based Eye Blink Removal Algorithm

Zuzana Rošťáková, Roman Rosipal

Institute of Measurement Science, Slovak Academy of Sciences, Bratislava, Slovakia
Email: zuzana.rostakova@savba.sk

Abstract. *SPECTER (the Signal sPECtrum Tensor decomposition and Eye blink Removal) is a novel algorithm designed to detect and elimininate eye blink-related artifacts from electroencephalogram (EEG) recordings. Our previous study [1] demonstrated its superior performance compared to established regression-based methods or independent component analysis, especially in situations where these approaches failed to accurately detect eye blinks or introduced spurious oscillations into the signal. In this study, we introduce SPECTER 2.0, an improved version that addresses the limitations of the original algorithm, and we demonstrate its improved performance on a real EEG dataset affected by eye blinks.*

Keywords: Eye Blink Removal, Electroencephalogram (EEG), Tensor Decomposition

1. Introduction

Human electroencephalogram (EEG) provides valuable insights into brain activity. However, raw EEG signals can be contaminated by various artifacts, which may arise from factors such as eye blinks, muscle movements, electrical resistance between the skin and electrodes, and nearby electronic devices. These non-EEG sources can significantly impact data analysis. Therefore, the removal of these artifacts is a crucial preprocessing step for EEG data.

In our previous study [1], we introduced a tensor-based eye-blink removal algorithm called SPECTER. A key advantage of SPECTER is that it does not require information from an electrooculogram, unlike regression-based eye-blink removal methods. Moreover, SPECTER avoids the problem of spectrum overestimation, a known limitation of artifact correction using independent component analysis [2].

Despite its strengths, the preliminary version of SPECTER had several drawbacks, primarily related to a slight time shift and the opposite sign problem. This study aims to address these issues with SPECTER 2.0, an improved version of the original algorithm, and demonstrate its performance on the same set of real EEG data used in [1].

2. A brief overview of the original SPECTER algorithm

The SPECTER algorithm is described in detail in [1], so we provide only a brief overview. First, consider an EEG signal recorded by J electrodes at a sampling rate of S_f Hz. The initial step involves dividing the EEG signal from each electrode into overlapping time windows of length W. Within each time window, the EEG signal is convolved with the Hanning window, and the Fast Fourier Transform is applied to compute its amplitude spectrum. Then, the $\log_{10}$-transformed spectral values are concatenated into a three-dimensional tensor $\underline{X} \in \mathbb{R}^{I \times J \times K}$, where I represents the number of time windows, J is the number of electrodes, and K denotes the number of considered frequencies.

In the second step, tensor $\underline{X}$ is decomposed using the CANDECOMP/PARAFAC (CP) method [3]. Artifact-related components are identified through an automatic selection criterion, followed by manual inspection if necessary, and are subtracted from $\underline{X}$ [1]. The cleaned tensor

ISBN 978-80-69159-00-6

is then transformed into a nonnegative form using the element-wise $10^{\frac{X}{}}$ function. Finally, the clean EEG signal is reconstructed by the spectrum-to-signal transformation [4].

3. SPECTER 2.0

Due to the effects of windowing and convolution with the Hanning window, the original SPECTER version struggled to accurately reconstruct the first and last $\frac{S_f}{2}W$ time points of the EEG signal. Additionally, the reconstructed signal sometimes exhibited slight time shifts either to the left or right compared to the original EEG signal (Fig. 1, red). To mitigate these timing discrepancies, we applied the dynamic time warping (DTW) algorithm [5] between the original and reconstructed EEG signals in [1]. However, DTW can be time-consuming, and the length of the input time series limits its effectiveness.

The second issue arises from missing information regarding the phase spectrum of the cleaned EEG, which causes discrepancies in the signs of the values between the original and reconstructed signal. In [1], we proposed a heuristic based on the Spearman correlation coefficient ρ between the original and reconstructed signals over short, non-overlapping time intervals. If $\rho < 0$ or other criteria were met, the reconstructed signal in that interval was multiplied by -1.

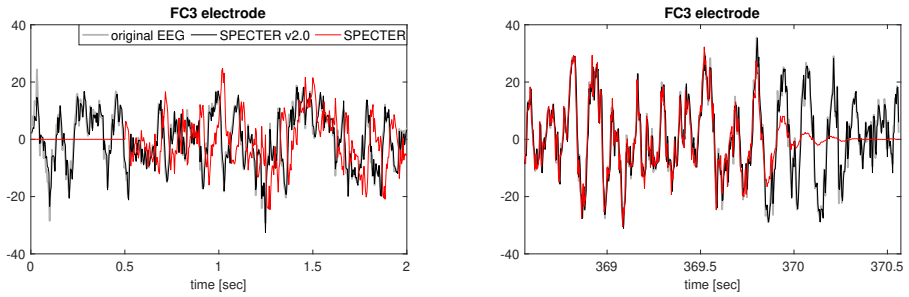

Fig. 1: An example of the EEG signal (grey) from the FC3 electrode, showing the first (left) and last two seconds (right), along with its versions reconstructed by SPECTER (red) and SPECTER 2.0 (black).

To address both issues, we propose the following modifications in SPECTER 2.0:

- Before applying SPECTER 2.0, we extend the EEG signal by adding constant segments of length $\frac{S_f}{2}W$ to both the beginning and the end of the original signal for each electrode. These segments are equal to the initial and final values of the EEG, respectively. After reconstructing the signal, we trimmed the added segments to ensure that the cleaned EEG signal matched the length of the original one. Nevertheless, the option to apply DTW remains available in SPECTER 2.0.

- In the spectrum-to-signal transformation step, the unknown phase spectrum of the cleaned EEG was replaced by the phase spectrum of the original EEG. We hypothesize that, during non-artifact intervals, the phase spectra of both the original and reconstructed signals should overlap. As will be described in Section 5, this adjustment significantly improved the issue of opposite signs. The heuristic introduced in [1] can still be applied to correct any remaining intervals with opposite sign values.

4. Data

To demonstrate the advantages of SPECTER 2.0 over the original version, we focused on the same eye-blink corrupted OSF dataset used in [1]. This dataset includes EEG signal from 19 electrodes[1] collected from 40 subjects divided into four groups (studies). Additionally, the EEG

[1]Fp1 (or AF3), F3, F7, C3, T7, P3, P7, O1, Pz, Fp2 (or AF4), Fz, F4, F8, Cz, C4, T8, P4, P8, and O2

ISBN 978-80-69159-00-6

signal for each subject consists of eight-second segments labeled as either “eye blink” or “non-blink.” The sampling frequency was 100 Hz (for study 04) or 200 Hz (for studies 01-03). In both versions of SPECTER, we applied 0.5-second time windows with 400 ms of overlap.

5. Results

In the initial step, the reconstructed EEG signal was divided into 100 ms time intervals. We examined the ratio of these intervals that exhibited the opposite sign problem for each electrode separately. For the EEG signal reconstructed using the original version of SPECTER, approximately half of the time intervals for each subject and electrode required a sign change (see Fig. 2, red). In contrast, with SPECTER 2.0, the average ratio of time intervals needing a sign change decreased to between 0.10 and 0.19 for all electrodes (see Fig. 2, black).

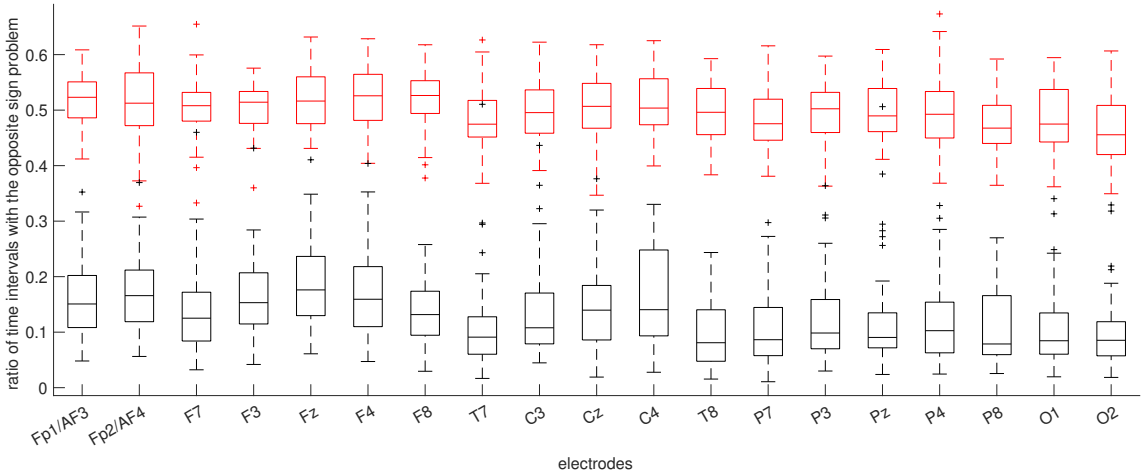

Fig. 2: The ratio of time intervals with the opposite sign problem after signal reconstruction with SPECTER (red) and SPECTER 2.0 (black) in 40 subjects from the OSF dataset.

In the second step, we focused on the slight time shift problem. The reconstructed and original EEG signal were time-aligned by DTW for each non-blink time segment. Then, the Euclidean distance D_{dtw} between the warping and the real time was computed. Given the modifications made, we anticipated that the warping time would be closer to the actual time in SPECTER 2.0 compared to the original version of the method. To test this expectation, we applied the non-parametric Wilcoxon signed-rank test to assess the following hypothesis:

$$H_0 : D_{dtw}^{SPECTER} \leq D_{dtw}^{SPECTER\_2.0} \qquad \text{vs.} \qquad H_1 : D_{dtw}^{SPECTER} > D_{dtw}^{SPECTER\_2.0}$$

The test was conducted for each electrode individually. We rejected the null hypothesis for all 19 electrodes, as the p-values were approximately $\approx 10^{-17}$, which were well below the Bonferroni-corrected threshold of $\frac{0.05}{19} = 0.0026$.

Furthermore, we computed the Spearman correlation coefficient between the original EEG signal and its reconstructed version over non-blink intervals. Similarly to the findings in [1], we hypothesized that the signals would overlap on these intervals. The results for 19 subjects are illustrated in Fig. 3. Without the DTW correction for slight time shifts, SPECTER 2.0 achieved higher correlations than the original SPECTER (Fig. 3, dotted lines). Moreover, SPECTER 2.0 without DTW produced results comparable to SPECTER with DTW for several subjects, including Subjects 2 and 3 from study 01 and Subject 5 from study 02 (Gig. 3). is consistent with the significantly lower distance between the original and warping time in SPECTER 2.0.

When applying the DTW correction, SPECTER 2.0 generated a reconstructed EEG signal that was more similar to the original signal. This conclusion was supported by higher or comparable correlation values relative to the previous version of SPECTER (Fig. 3, solid lines).

ISBN 978-80-69159-00-6

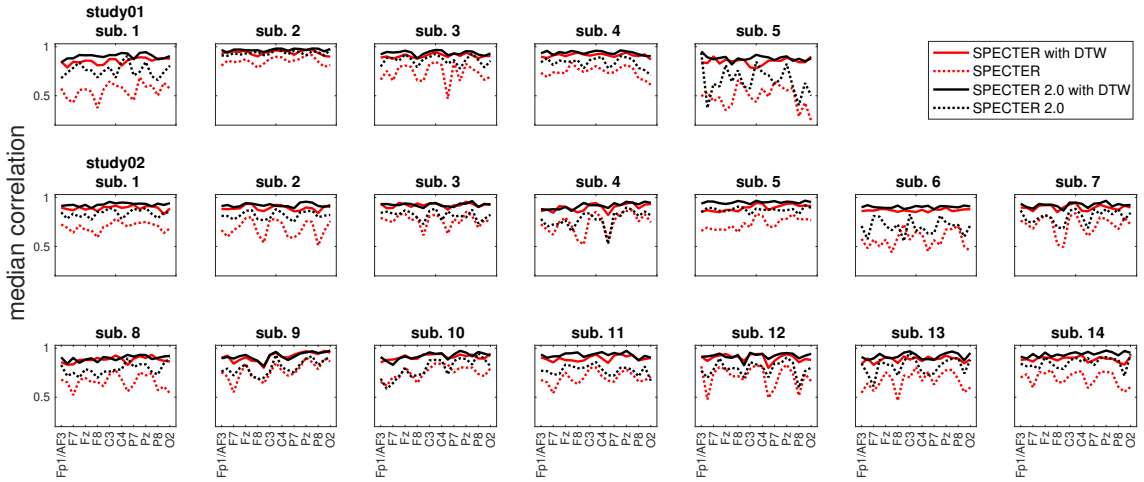

Fig. 3: The median Spearman correlation coefficient between the original EEG signal and its versions reconstructed by SPECTER (red) and SPECTER 2.0 (black) over the non-blink epochs. In both cases, correlations were computed without (dotted line) or with (solid line) the DTW correction for the slight time shift problem. Only labels for each second electrode are depicted on the x-axis.

6. Conclusion

In this study, we introduced an enhanced version of the eye-blink removal algorithm known as SPECTER. The modifications we made significantly reduced the proportion of time intervals containing opposite sign values. Additionally, SPECTER 2.0 produced EEG signals with a lower incidence of slight time shifts. This improvement was evident in two ways: the warping time was closer to the real time compared to the original SPECTER version, and there were comparable correlations between the original EEG signal and the reconstructed signals from both SPECTER 2.0 without DTW and the original SPECTER followed by DTW. This held true across multiple subjects. Nevertheless, in the future, we plan to evaluate the performance of SPECTER 2.0 on EEG signals affected by other types of artifacts, in addition to eye blinks.

Acknowledgements

Funded by the EU NextGenerationEU through the Recovery and Resilience Plan for Slovakia under the project No. 09I03-03-V04-00205 (Z.R.) and project No. 09I03-03-V04-00443 (R.R.).

References

[1] Rošťáková, Z., Rosipal, R., Trejo, L. J. (2025). SPECTER - The Signal sPECtrum Tensor decomposition and Eye blink Removal algorithm. *Biomedical Signal Processing and Control* 99, 106889.

[2] Wallstrom, G. L., Kass, R. E., Miller, A., Cohn, J. F., Fox, N. A. (2004). Automatic correction of ocular artifacts in the EEG: a comparison of regression-based and component-based methods. *International Journal of Psychophysiology* 53(2), 105–119.

[3] Yu, H., Larsen, K. G., Christiansen, O. (2025). Optimization methods for tensor decomposition: A comparison of new algorithms for fitting the CP(CANDECOMP/PARAFAC) model. *Chemometrics and Intelligent Laboratory Systems* 257, 105290.

[4] Masuyama, Y., Yatabe, K., Oikawa, Y. (2018). Griffin-Lim like phase recovery via alternating direction method of multipliers. *IEEE Signal Processing Letters* 26(1), 184–188.

[5] Müller, M. (2007). Dynamic time warping. *Information retrieval for music and motion* pp. 69–84.

Common Problems With Real-World GSM Antenna Usage

Michal Dzuris, Jakub Krchnak, Anatolii Kliuchka, Rene Hartansky

Institute of Electrical Engineering, Faculty of Electrical Engineering and Information Technology, Slovak University of Technology, Ilkovicova 3, 812 19 Bratislava, Slovakia, Email: michal.dzuris@stuba.sk

Abstract. *This article deals with the problem of transmitting and receiving data in GSM networks in cases of inappropriate placement of the radiator – antenna. The gain and directivity of an ideally placed antenna are analyzed and compared with those of an antenna placed in a metal casing – a tube. Such a topology often occurs in communication between a base station and a mobile vehicle, such as a car, motorbike, or bicycle, where communication is part of tracking or vehicle safety.*

Keywords: Electromagnetic Field, Antenna Gain, Radiation Pattern, Tracking Sensors

1. Introduction

The GSM network, which was primarily developed for data transmission [2], has since been used for many technical, telemetry, and security applications [7], [8]. In the context of mobile vehicle tracking, the GSM network is often used to transmit position, speed, and vehicle status data. In almost all cases, vehicles are made of various composites or metal alloys that affect such transmissions. The most significant influence occurs at the level of altering the properties of the antenna used for transmission. This problem is even more pronounced in small vehicles, where antenna placement is critical not only for information transmission but also due to limited usable space on the vehicle and, last but not least, the need for safe antenna placement (to prevent the unauthorized removal of the antenna and, subsequently, the entire vehicle). In such cases, antennas are placed in concealed or hard-to-reach locations. The result is a device with an antenna that is protected from unauthorized removal but, in many cases, also non-functional. [5]. Therefore, the objective of this paper is not only to analyze such a device but also to propose a solution that ensures reliable transmission in a GSM network and enables secure data transmission and reception.

2. Subject and Methods

In this chapter, we will discuss the characteristics of a commercially available GSM-band antenna that is commonly used to transmit telemetry data between a wheeled vehicle and a receiving station.

GSM antenna in a circuit recommended by the manufacturer

The GSM band used in Slovakia for the transmission of telemetry data operates in the 800 to 900 MHz frequency range [2]. A commercially available antenna has been developed for this band and is mounted on a ceramic substrate, where radiation is achieved through a suitable arrangement of conductive surfaces on the active side of the substrate. Fig. 1a shows a digital model of this antenna, which is placed on a circular printed circuit board (PCB). The PCB represents a realistic finite environment for the application of such antennas in various devices and applications. The next figure, Fig. 1b, illustrates its radiation characteristics. As seen in the figure, the antenna exhibits a quasi-omnidirectional radiation pattern with a maximum gain of approximately -3.5 dBi. For an antenna only a few centimeters in size, this characteristic

ISBN 978-80-69159-00-6

is highly beneficial, especially in small electronic devices where space optimization is crucial without compromising functionality or reliability of IoT devices. Although the gain of the modeled antenna is relatively low compared to a half-wave dipole, it is more than sufficient for data transmission between a vehicle and a base station over distances ranging from a few kilometers to several tens of kilometers.

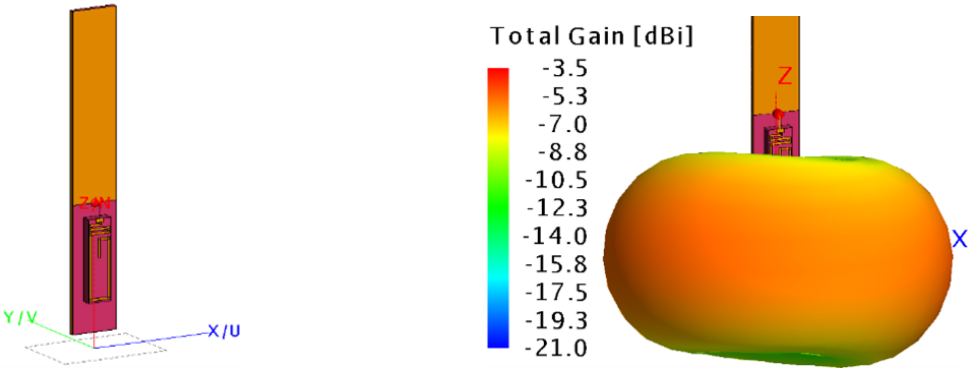

(a) GSM antenna (b) Radiation pattern

Fig. 1: Simulation model of the GSM antenna mounted on a PCB and its radiation pattern with gain indication.

GSM antenna in a critical circuit configuration

As already mentioned, when placing the antenna on small single-track vehicles, problems with the metal parts of the vehicle and the lack of space will arise. The worst-case scenario can occur if the antenna is placed in a housing, such as an open metal tube. In many cases, such placement is recommended to the designers themselves. In such a "housing," the characteristics of the antenna will be significantly degraded, reducing its ability to receive or transmit signals at the operating frequencies. Fig. 2a shows a model of a ceramic antenna placed in an open metal tube, with the lower edge of the antenna facing the end of the tube. Fig.2b shows the

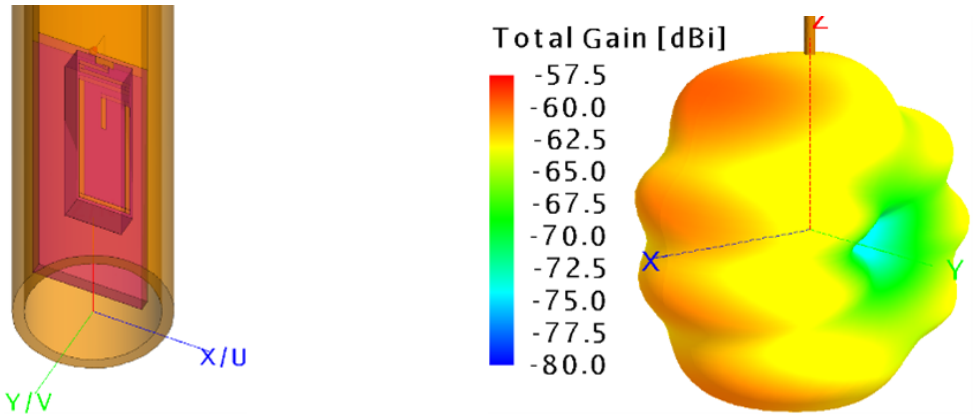

(a) GSM antenna (b) Radiation pattern

Fig. 2: Simulation model of the GSM antenna placed in the housing and its radiation pattern with gain indication.

radiation pattern of the antenna placed in this way. The approximate maximum gain in this case is around -57.5 *dBi*, which represents a 54 *dB* drop, compared to the conditions without partial shielding (no conducting tube). Such a drop in gain poses a serious problem for the transmission of signals between the vehicle and the base station [4]. The amplitudes of the signals transmitted

ISBN 978-80-69159-00-6

by such a positioned antenna are already very close to the electromagnetic background of the environment and in many cases well below the noise floor. A significant reduction in antenna gain means a severe reduction in data rate, outages, or a complete shutdown of service. To compensate for such gain reduction, amplifiers in different topologies would have to be used, which would disrupt the low-power nature of the vehicle telemetry transmission.

A new design for a GSM antenna

Taking into account the results obtained from previous analyses and simulations [3], [6], different types of simple antennas have been proposed that could be more suitable for such a highly electrically shielded environment. Fig. 3a shows a model of a monopole antenna with a capacitive extender implemented on a section of a printed circuit board for the 800 MHz - 900 MHz band, embedded in a conducting pipe. We report this antenna as the most suitable among the simulated, designed, and measured antennas. As shown in Fig. 3b, the directional characteristic is admittedly not quasi-all-directional (nor does it have the shape of an anuloid), as was the case in Fig. 1a for the commercially used antenna. However, if we consider that the antenna in Fig. 1 was placed in free space and the antenna in Fig. 3 is placed in a metal tube, the change in the radiation pattern does not appear to be that significant. The gain of the monopole antenna

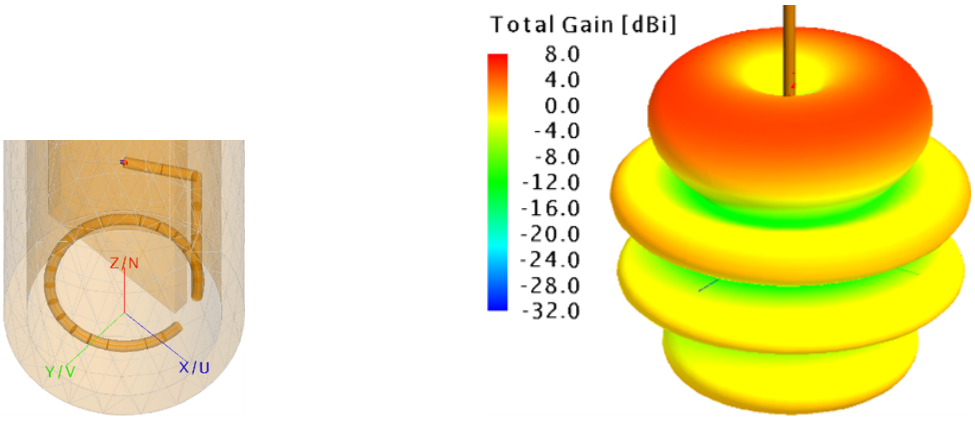

(a) GSM antenna (b) Radiation pattern

Fig. 3: Simulation model of the GSM antenna placed in the housing and its radiation pattern with gain indication.

with the capacitive attachment, which is placed in a metal tube (Fig. 3a), is excellent, reaching up to 8 dBi at maximum. This performance was not achieved even by a commercial antenna in free space (see Fig. 1a). It should be noted that the maximum gain is only in the part of the space facing outward from the metal tube (in the circle that forms the base of the cone, with the top of the cone in the plane of the tube). In other directions, the monopole antenna in the tube also performs well, with a minimum of -32 dBi and average gain values between -15 dBi and 0 dBi. Such a result is excellent for the applications mentioned at the beginning of the article, as even with such a simple antenna, more than a 40 dB improvement over the commercial product was achieved.

3. Conclusion

Based on both simulations and later measurements at a vehicle tracking company, it was evaluated that commercial ceramic antennas are not suitable for use in indoor or hidden vehicle compartments. The reliability of data transmission using such antennas is questionable. And

ISBN 978-80-69159-00-6

when it comes to securing the vehicle against unauthorized removal or tracking, these antennas are almost worthless. On the contrary, the antenna-monopole with capacitive attachment, developed on the basis of [3], [6], meets the requirements for both reliable data transmission and possible placement in confined and electromagnetically unsuitable spaces. This has been confirmed, for example, by ANDIS [1].

Acknowledgements

This work was supported by the project APVV 20-0042 *Microelectromechanical sensors with radio frequency data transmission*, VEGA 1/0045/21 *Electromagnetic compatibility of wireless IoT devices*, ENEFS 09I05-03-V02-00041 *Novel electrically enhanced wireless method for sensing of mechanical quantities*.

References

[1] *Andis*. Online. `www.andis.sk`. [cit. 2025-03-06]

[2] The international engineering consortium. (1983) *Global System for Mobile Communication (GSM)*. IEC, 19.

[3] Balanis, C.A. (2015) *Antenna Theory. Analysis and Design*. John Wiley & Sons

[4] Gabrisak, M., Hallon,J., Bittera, M., Kovac, K. (2023) . Variability of electromagnetic field homogeneity during immunity test according to EN 61000-4-3. In *Measurement 2023: 14th International conference on Measurement*. Slovak Academy of Sciences, 159–162.

[5] Dzuris, M., Hartansky, R., Krchnak, J. (2023). Measuring the radiation pattern of large FM antenna system. In *Measurement 2023: 14th International conference on Measurement*. Slovak Academy of Sciences, 135–138.

[6] Hartansky, R., Hallon, J. (2016) *Sensors for electromagnetic field measurement*. STU

[7] *VSU Truck*. Online. `www.vsutruck.sk`. [cit. 2025-03-06]

[8] *LiveViewGPS*. Online. `www.liveviewgps.com`. [cit. 2025-03-06]

Analysis of the Influence of 3D Printing Factors on the Geometric Accuracy of the Product

Teodor Toth, Miroslav Kohan, Miroslav Dovica

Department of Biomedical Engineering and Measurement,
Faculty of Mechanical Engineering, Technical University of Košice, Košice, Slovakia
Email: teodor.toth@tuke.com

Abstract. *The aim of this study was to determine geometric accuracy based on the positioning of objects during the manufacturing process. The manufactured objects were manufactured using FFF technology on the DeltiQ 2 device (Trilab, Czech Republic). The scanning of the manufactured objects was performed on an industrial computed tomography Metrotom 1500 Gen 1 (Carl Zeiss, Germany). The results showed the smallest geometric deviations on the object at position A (0.074 mm). The remaining objects show a geometric deviation of 0.174 mm (at position B) and 0.157 mm (at position C). In terms of time, the fastest manufactured object was in position A (4 hours and 14 minutes). Objects in positions B and C were manufactured in approximately the same time (4 hours and 40 minutes).*

Keywords: Geometric Accuracy, Scanning, FFF Technology

1. Introduction

Additive technology, also known as 3D printing, is currently widely used in various fields [1,2,3]. However, in this context, many questions arise regarding the accuracy of the final product. Geometric accuracy can be defined as the comparison of the final product with the design of the digital model. To achieve geometric accuracy in 3D printing, several factors need to be considered. The basic factors that influence the geometric accuracy of the final product are the type of technology used, the material, the 3D printing parameters, as well as post-processing. There are many research studies comparing the accuracy of individual additive technologies [4,5]. One of them is the study by Al-Ahmari et al. [6], which evaluates different types of additive technologies and their geometric accuracy. When comparing FFF and SLA technologies, the authors of the study concluded that the geometric accuracy of surfaces was better in SLA than in FFF technology. The difference may be due to a different principle of fixing individual layers to each other, as well as the fact that the given devices operate with different accuracy. A similar study by Butt et al. [7] compared the geometric accuracy at different settings of FFF technology. The authors found that different widths of the deposited layer have a significant impact on the dimensional accuracy and surface roughness of the manufactured objects. With a higher value of the extruded layer, the roughness of the manufactured objects also increased. The same result was also recorded in the dimensional analysis of the x,y,z axes, where a layer width of 0.2 mm showed more accurate dimensions compared to larger width settings of the layer extrusion (0.4 mm ; 0.6 mm). Other parameters that have an impact on the dimensional accuracy of manufactured objects in connection with FFF technology are printing speed, extruder and platform temperature, cooling and "extrusion multiplier". Another important factor in the accuracy of FFF technology is the material. Thermoplastic materials have specific properties such as viscosity, melting point, shrinkage, which contribute to the accuracy of the 3D printing process [8].

The aim of the study was to compare the geometric deviations of manufactured objects at different orientations during production.

ISBN 978-80-69159-00-6

2. Subject and Methods

Object and material characteristics

Based on the analysis of geometric accuracy, an object defined by a limit curve in a sinusoidal profile was created. A mathematical function was created to precisely define this curve (see Eq. 1). CATIA V5 software (Dassault Systemes, France) was used to create a 3D model of a precisely defined curve in the shape of a sinusoid. In the initial phase of modeling, a mathematical function was used in the "Law Editor" software function where the desired curve was created. The next step was to create a surface based on the defined curve and then the "extrude" function itself to create a 3D object. The material chosen for the creation of geometric shapes was the thermoplastic polymer Polyethylene Terephthalate Glycol (PETG) from Devil Design (Poland).

$$z = 15 + 10 * \sin\frac{2\pi x}{100} \tag{1}$$

Methodology of production

The geometric shapes were produced using FFF technology on a DeliQ 2 device (Trilab, Czech Republic). A DQ2 Volcano print head (Trilab, Czech Republic) with a brass nozzle with a diameter of 0.4 mm was used to extrude the PETG material. Positioning and 3D printing settings were performed in the Slicesoftware Simplify 3D (Simplify 3D, USA). Table 1 shows the production settings on the 3D printer.

Table 1. 3D printing parameters

Temperature settings [°C]		**Dimensional settings** [mm]		**Speed settings** [mm/s]	
Platform	90	Layer height	0.2	Default	50
Extruder	240	Layer width	0.4	Outline	30
Cooling	60% intensity of fun	Infill	Rectilinear (45°; -45°)	Infill	40

The total number of manufactured objects was n = 3. Each object was manufactured at a different position relative to the base platform of the 3D printer. The location and position of the individual objects are shown in Figure 1. The diameter of the base platform of the 3D printer is defined as Ø 250 mm, with the zero point (the starting point of the coordinate system) given in the center.

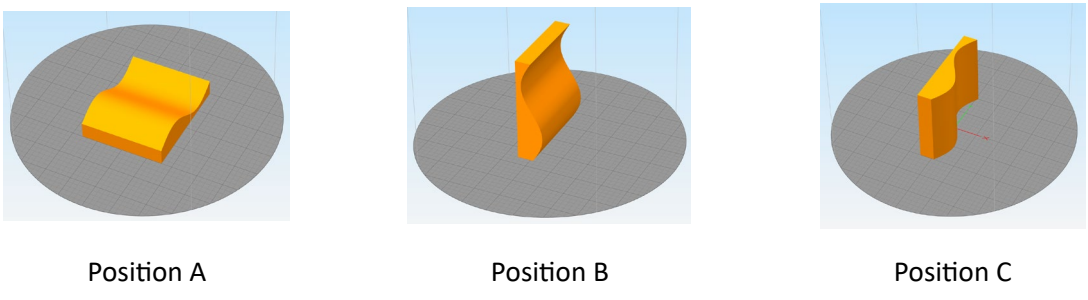

Fig. 1 Object positioning the 3D printing process

Methodology of scanning

The scanning of the manufactured objects was performed on an industrial computed tomography scanner Metrotom 1500 Gen 1 (Carl Zeiss, Germany).

ISBN 978-80-69159-00-6

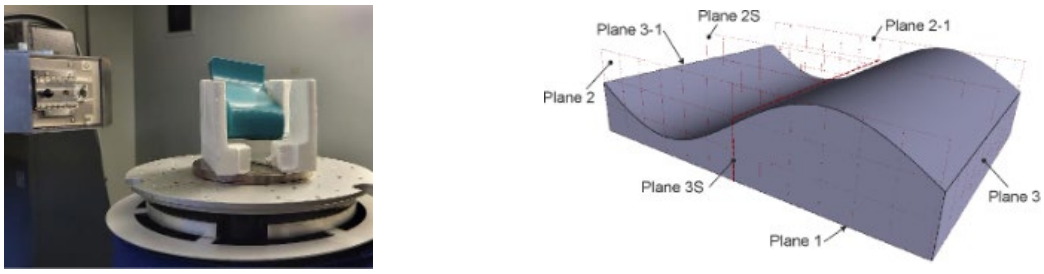

Fig. 2 Position of the object during scanning (left) and description of individual planes (right)

The objects were placed in a polystyrene holder (Fig. 2 - left) and scanned in the same position and settings. The voxel size is 119.81 µm for all samples. The scans were processed in VGStudioMAX software (Volume Graphics, Germany). The coordinate system (Fig. 2 - right) was created on the CAD model with features Plane 1, Plane 2S (midplane Plane 2, Plane 2-1) and Plane 3S (midplane Plane 3, Plane 3-1).

3. Results

Each object was aligned in the same coordinate system and the deviation was evaluated over the entire surface of the sample, not just on the sinusoidal surface. The maximum deviation for the scan match with the CAD model at the level of 90% and 95% as well as the surface match for a deviation of 0.1 mm and 0.2 mm were evaluated (see Table 2). Figure 3 shows the deviations on the sinusoidal surface of the sample, places outside the tolerance of ±0.2 mm are shown in purple (+) and burgundy (-) color.

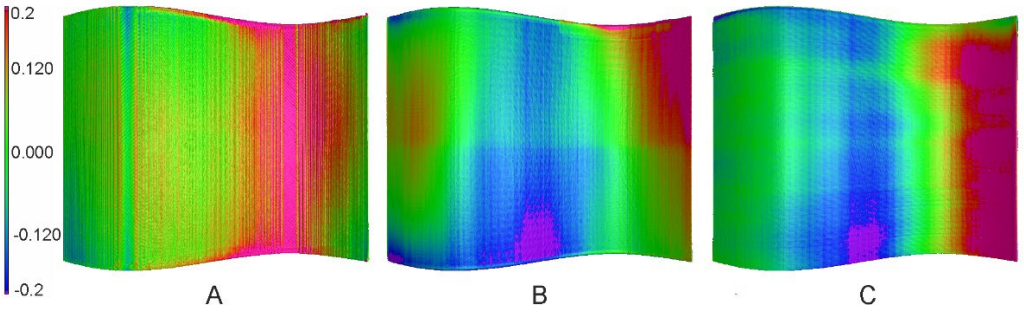

Fig. 3 Map of deviations between the 3D model and manufactured objects

Table 2. Evaluation of deviations for each position of the manufactured objects

	90% [mm]	95% [mm]	0,1 mm [%]	0,2 mm [%]
Position A	0.255	0.376	51.1	85.2
Position B	0.184	0.283	64.4	92.0
Position C	0.230	0.261	60.2	82.9

In addition to surface deviations, selected geometric tolerances such as flatness of reference planes and perpendicularity and parallelism of planes to the platform were also evaluated.

4. Conclusions

The smallest geometric deviations are shown by sample A. This is due to the printing position, where the sample is placed on the printing plate with its largest area and has the smallest height in the Z-axis direction. The average deviation is 0.074 mm. The manufactured object in position B has an average deviation of 0.174 mm, which is mainly influenced by the perpendicularity of Plane 1 to the base plate. The manufactured object in position C has a deviation of 0.157 mm

ISBN 978-80-69159-00-6

where the deviations are more evenly distributed, but the deviation of the straightness of Plane 1 is more than 2 times the deviation of the objects manufactured in positions A and B.

For the observed deviations, the object manufactured in position B has the largest match. The deviations for the manufactured objects in positions A and C are relatively symmetrically distributed. For the manufactured object in position B, the deviation at the farthest part from the build plate is asymmetric.

From a production perspective, no support structures were used for object creation. The reason for not using support structures was to avoid damaging the surface of the manufactured objects, which would ultimately affect the scanning results. From a production time perspective, the manufactured object in position A was manufactured in 4 hours and 14 minutes, while the objects in positions B and C took approximately the same amount of time (Position B: 4 hours and 40 minutes; Position C: 4 hours and 41 minutes).

Acknowledgements

The results achieved were created with the investigation of project no. VEGA 1/0191/24 (Development, optimization, and application of coordinate measurement strategies of geometric parameters and structure of additive products), project no. 025TUKE-4/2025 (Implementation of measurement systems of human physiological parameters in the educational process in the biomedical engineering program) and project APVV SK-CZ-RD-21-0056 (Bioresorbable materials for additive manufacturing of vessel substituents and their biomechanical characterization).

References

[1] Salmi, M., (2021). Additive manufacturing processes in medical applications. *Materials*, 14(1), p.191.

[2] Camacho, D.D., Clayton, P., O'Brien, W.J., Seepersad, C., Juenger, M., Ferron, R. and Salamone, S., (2018). Applications of additive manufacturing in the construction industry–A forward-looking review. *Automation in construction*, 89, pp.110-119.

[3] Najmon, J.C., Raeisi, S. and Tovar, A., (2019). Review of additive manufacturing technologies and applications in the aerospace industry. *Additive manufacturing for the aerospace industry*, pp.7-31.

[4] Gibson, I., Rosen, D., Stucker, B., Khorasani, M., Rosen, D., Stucker, B. and Khorasani, M., (2021). Additive manufacturing technologies (Vol. 17, pp. 160-186). Cham, Switzerland: Springer.

[5] Wong, K.V. and Hernandez, A., 2012. A review of additive manufacturing. International scholarly research notices, 2012(1), p.208760.

[6] Al-Ahmari, A., Ashfaq, M., Mian, S.H. and Ameen, W., 2019. Evaluation of additive manufacturing technologies for dimensional and geometric accuracy. International Journal of Materials and Product Technology, 58(2-3), pp.129-154.

[7] Butt, J., Bhaskar, R. and Mohaghegh, V., 2022. Analysing the effects of layer heights and line widths on FFF-printed thermoplastics. The International Journal of Advanced Manufacturing Technology, 121(11), pp.7383-7411.

[8] Kechagias, J. and Zaoutsos, S., 2024. Effects of 3D-printing processing parameters on FFF parts' porosity: Outlook and trends. Materials and Manufacturing Processes, 39(6), pp.804-814.

Usability Evaluation and Characterization of Active Electrodes in Electrical Impedance Tomography

Roman Vaněk, Jan Mikulka

Department of Theoretical and Experimental Electrical Engineering, Brno University of Technology, Technicka 3082/12, 616 00 Brno, Czech Republic,
Email: 240707@vut.cz

Abstract. *This paper proposes an active electrode design for electrical impedance tomography with enhanced noise robustness and dynamic range to measure voltages from* 48 V *to* 26 mV *from* DC *to* 40 kHz *with posibility to extended its frequency range up to* 100 kHz. *The design incorporates a combination of a programmable-gain amplifier and a programmable voltage divider to achieve its voltage range. The paper also provides a description of evaluation methods used to measure the frequency response performance of the proposed design. The active electrode aims to provide a versatile laboratory solution to diverse electrical impedance tomography applications.*

Keywords: Electrical Impedance Tomography, Active Electrode, Programmable Gain Amplifier

1. Introduction

Electrical Impedance Tomography (EIT) is a relatively new imaging method for the reconstruction of the admittivity distribution. A typical EIT system uses a set of conducting electrodes attached to the surface of the material under investigation. One can apply a current through the electrodes and measure the resulting voltage and phase on other electrodes, from which the admittivity distribution can be reconstructed. One of the challenges in EIT is that the inverse problem is highly ill-posed, meaning that small errors in the measurement can lead to large errors in the reconstructed admittivity distribution. The contact impedance between the electrode and the material tends to be relatively high, which means that all interference sources have a large effect; these include common-mode gain error, thermal noise, and electromagnetic interference (EMI) and cross-talk between cables [1]. These factors make it challenging for passive systems to achieve high accuracy.

This paper proposes an active electrode design for EIT systems that addresses these issues, amplifying the signal directly on the electrode. Furthermore, the active electrode can adaptively adjust its gain, using a programmable-gain amplifier (PGA) to amplify small signal at adjacent electrodes placed further from current injection and programmable voltage divider to lower the voltage and prevent PGAs saturation, to obtain full analog-to-digital convertor (ADC) quantization range utilization.

The use of active electrodes is motivated by the work of Mikulka et al., who proposed a laboratory system with a scalable design [2, 3], and the work of Gaggero et al. and Wang et al., who demonstrated the feasibility of active electrodes for human thoracic and in other medical applications [1, 4]. Rather than focusing on specific field or material type, this design aims to provide a versatile laboratory solution that can be adapted to various applications, i.e., admittivity imaging of water dams and other geophysical applications [5].

2. Active electrode design

The schematic of the active electrode is shown in Fig 1. To measure voltages from millivolts up to ±48 V, which is the maximum voltage that can be multiplexed using commonly avail-

ISBN 978-80-69159-00-6

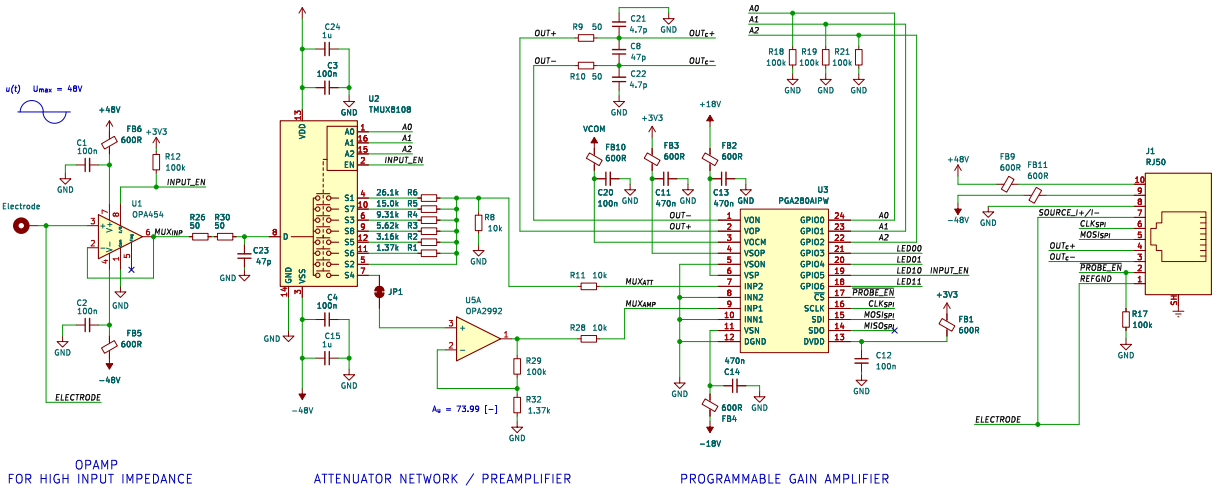

Fig. 1: Schematic diagram of proposed active electrode

able components [6], the PGA280 was selected as the most suitable PGA for the application. The PGA280, with its built-in general-purpose input/output (GPIO) pins controls, the voltage divider, a high-voltage switch TMUX8108 with resistor dividers at its output. All active electrodes are connected to the central system via the serial peripheral interface (SPI), where switching, communication and data acquisition are managed.

Selectable voltage gains

The resistor values are chosen to form a sequence of voltage attenuation in an arithmetic series, ranging from 1 V/V to 0.28 V/V. The maximum attenuation of 0.28 V/V reduces the input voltage from ±48 V to 13.44 V, allowing the PGA to process the signal without saturation. The common gain difference ΔG_{att} evaluated from the arithmetic sequence is approximately 0.120 833 V/V. The voltage attenuation values can be expressed as

$$G_{\text{att}_n} = 1 + (n-1) \cdot \Delta G_{\text{att}}, \tag{1}$$

$$n \in \{1, 2, \ldots, \text{N}\}, \tag{2}$$

where N stands for the number of switchable ranges (in this case, N = 7). By combining both the voltage attenuation G_{att} and the gain of the PGA, G_{pga}, multiple equally distributed voltage gain combinations are achieved: $G = G_{\text{att}} \cdot G_{\text{pga}}$, ranging from 0.275 V/V to 128 V/V respectively corresponding to input voltages from 48 V to 26 mV, which are converted to 1.65 V output that is suitable for an ADC. The second input of the PGA280 is used in combination with OPA2992 operational amplifier (Op Amp) with fixed gain to additional gain for voltages below 25.8 mV, expanding the scope of measurable material types.

3. Automation of data acquisition

A MATLAB application was developed to interface with firmware through an application programming interface (API). The application allows user to read measured voltages at the electrode input and configure various parameters, including the voltage amplification, sampling frequency, and electrode operating mode. Multiple voltage gains were sequentially selected via the API to measure the frequency and phase response. Figure 2 shows the frequency and phase response of selected voltage gains differentiated by their indices.

The data points of frequency response, which are plotted in frequencies above 1 MHz, are outside the working range of the measurement evaluation methods. The same applies to the

ISBN 978-80-69159-00-6

phase response plot for frequencies greater than 200 kHz, where the signal was substantially attenuated for the amplitude, phase and frequency measurement algorithm to be accurate.

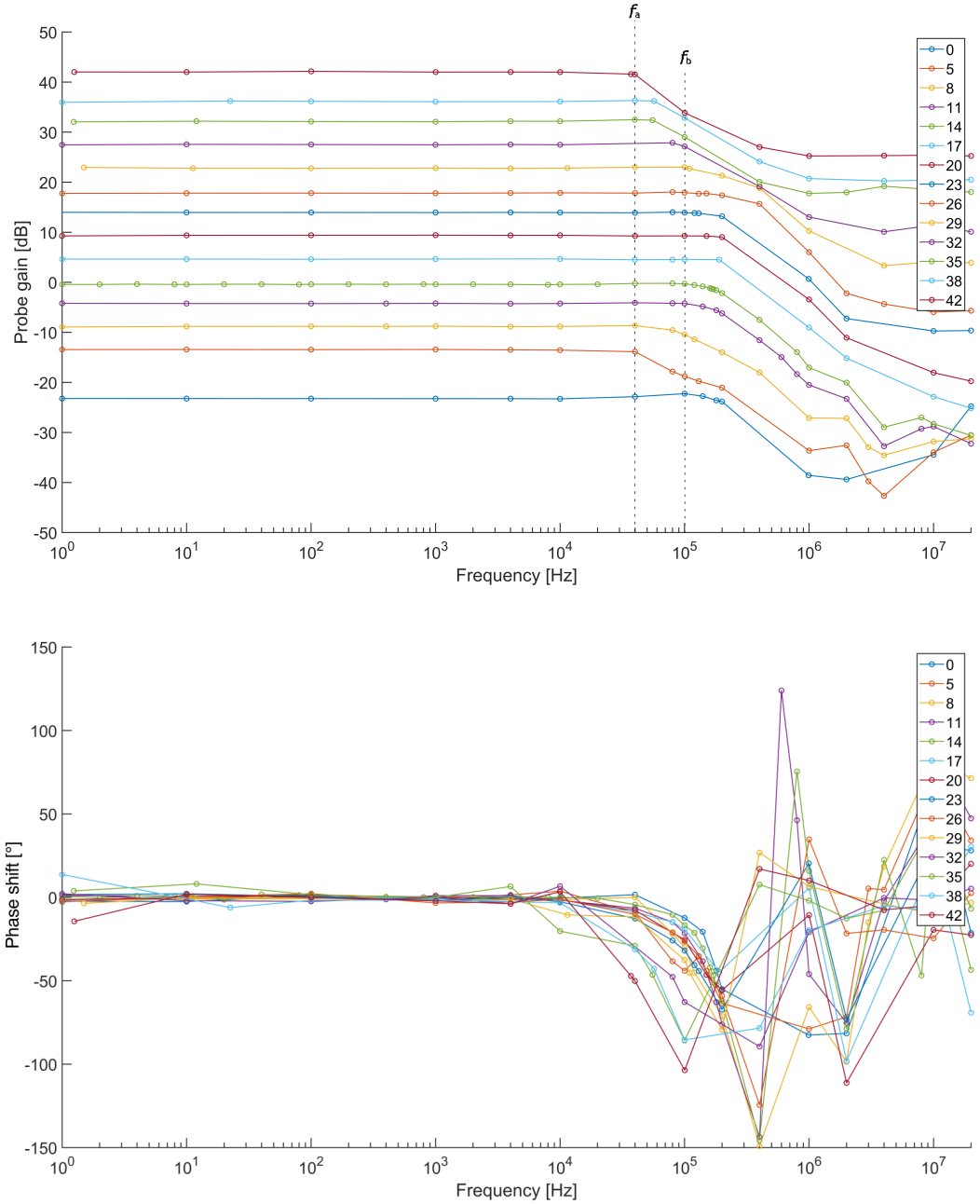

Fig. 2: Frequency and phase response of proposed active electrode for multiple voltage gains. The frequency ranges f_a and f_b are evaluated for input voltages from 26 mV to 48 V and from 136 mV to 5.176 V, respectively.

ISBN 978-80-69159-00-6

Algorithm overview

A linear interpolation is used to estimate N zero-crossing locations from sampled data. Using the differences between consecutive zero-crossing indices, $\Delta Z_i = Z_{i+1} - Z_i$, the fundamental frequency is determined as

$$f = \frac{f_\mathrm{s}}{\frac{1}{N-1}\sum_{i=1}^{N-1} |\Delta Z_i|}, \tag{3}$$

where f_s is the sampling frequency.

In the phase shift determination algorithm, the differences of corresponding zero-crossing indices $\Delta K_i = Z_{2,i} - Z_{1,i}$ in two signals are calculated. Then, for a phase shift, we can write

$$\phi = 360 \times \frac{\frac{1}{f_\mathrm{s} \times (N-1)}\sum_{i=1}^{N-1} |\Delta K_i|}{T}. \tag{4}$$

The values are then normalized to the range $[-180^\circ, 180^\circ]$.

4. Results

The measurements resulted in verification of constant voltage transfer from DC to 100 kHz for amplification from 0.6375 V/V to 24.2666 V/V, in which we are able to measure voltage from 136 mV to 5.176 V with full ADC quantization range utilization. For voltages above 5.176 V and below 136 mV, the maximum frequency of constant voltage transfer is 40 kHz. That means we can measure voltage from 26 mV to 48 V within DC to 40 kHz frequency range.

5. Discussion

The phase response shows that undesirable phase shift increases as electrode amplification value rises at frequencies near 100 kHz. Minor phase shift errors, which are observed for amplification with index 29 and higher, will be partially compensated using the same circuitry in the current sensing part. The phase shift measurement error remains near zero from DC to 40 kHz for gain indexes below 29. However, for gain indexes above 29, the near-zero phase shift is measured only to 6 kHz. The accuracy of the phase and voltage acquisition algorithm shall be further investigated.

References

[1] Gaggero, P. O., Adler, A., Brunner, J., Seitz, P. (2012). Electrical impedance tomography system based on active electrodes. *Physiological Measurement* 33(5), 831.

[2] Mikulka, J., Dušek, J., Dědková, J., Pařilková, J., Műnsterová, Z. (2019). A Fast and Low-cost Measuring System for Electrical Impedance Tomography. In: *2019 PhotonIcs Electromagnetics Research Symposium - Spring (PIERS-Spring)*. pp. 3751–3755.

[3] Mikulka, J., Zimniok, D., Dušek, J. (2023). Laboratory System of Electrical Impedance Tomography. In: *2023 14th International Conference on Measurement*. pp. 71–74.

[4] Wang, C., Lu, W., Huang, J., Guo, Q., Zhou, T., Zhao, J., Li, Y. (2024). Flexi-EIT: A Flexible and Reconfigurable Active Electrode Electrical Impedance Tomography System. *IEEE Transactions on Biomedical Circuits and Systems* 18(1), 89–99.

[5] Boyle, A. (2016). Geophysical Applications of Electrical Impedance Tomography. Doctor of Philosophy, Carleton University, Ottawa, Ontario.

[6] Vaněk, R., Mikulka, J. (2024). Modular system for electrical impedance tomography. In: *Proceedings II of the 30st Conference STUDENT EEICT 2024: Selected Papers*. Brno, Czech republic, pp. 40–43.

Weighted Estimation and Uncertainty Propagation in Nonlinear Errors-in-Variables Regression for Metrological Applications

Viktor Witkovský

Institute of Measurement Science, Slovak Academy of Sciences, Bratislava, Slovak Republic
Email: witkovsky@savba.sk

Abstract. *This paper explores weighted estimation strategies for nonlinear errors-in-variables (EIV) regression, with applications in metrology where accurate uncertainty propagation is critical. The OEFPIL (Optimal Estimating Equations for Parameters by Iterated Linearization) method enables full use of the structured uncertainty matrix, incorporating both Type A and Type B components, including correlations. Although theoretically optimal under the Gauss–Markov framework, using the full matrix may yield fitted models that appear biased or inconsistent with experimental intuition. As an alternative, we propose a locally weighted least squares (LWLS) method that improves interpretability at the cost of some statistical efficiency. We present the mathematical formulation and illustrate the trade-offs between statistical rigor and empirical consistency, relevant to practitioners in measurement science and uncertainty analysis.*

Keywords: Measurement Uncertainty, EIV Regression, Locally Weighted Least Squares, OEFPIL

1. Introduction

Regression techniques are fundamental in modern measurement science and metrology, supporting tasks such as curve fitting, calibration, inverse modeling, and uncertainty evaluation. In many experimental scenarios, both input (stimulus) and output (response) quantities are affected by significant—and often correlated—measurement errors, resulting in a structured uncertainty matrix. Moreover, the relationship between true input and output values is frequently nonlinear and often only implicitly defined. In such cases, the assumptions of standard ordinary least squares (OLS) regression—particularly the assumption of error-free inputs—are violated. This motivates the use of more advanced statistical approaches, such as *errors-in-variables* (EIV) models. In metrological applications, this leads naturally to the explicit treatment of uncertainties in all measured quantities using the full *uncertainty matrix*—a structured covariance matrix that enables rigorous uncertainty propagation through the model [1, 2, 3].

The metrological uncertainty matrix accounts for both Type A (statistical) and Type B (systematic) contributions, combining data from repeated observations with expert judgment and model-based evaluations. Unlike sample covariance matrices estimated empirically, the metrological uncertainty matrix is structured and supports comprehensive uncertainty evaluation in accordance with the GUM framework [4, 5, 6, 7].

A central challenge in EIV regression is the selection of an appropriate weighting matrix. According to the Gauss–Markov theorem, optimal weights are inversely proportional to the joint covariance matrix of input and output variables—which is typically unknown in practice. Generalized least squares (GLS) provides a practical alternative by using the inverse of the residual covariance matrix. In metrological EIV settings, however, the full uncertainty matrix is often available and directly used for weighting. Yet, strong off-diagonal correlations or dominant Type B components may distort the regression, yielding results that appear biased or physically implausible compared to the observed data. This has been observed, for instance, in the calibration of the tip area function in instrumented indentation testing [8], where using

ISBN 978-80-69159-00-6

only the diagonal (i.e., uncorrelated) part of the uncertainty matrix often produces results more consistent with experimental expectations—though at the cost of statistical efficiency.

To address this trade-off, we revisit the *Optimal Estimating Equations for Function Parameters by Iterated Linearization* (OEFPIL) method—see, e.g., [9]—a robust framework for nonlinear EIV regression in metrology. OEFPIL iteratively linearizes the constraint equations and applies the Gauss–Markov theorem to compute best linear unbiased estimators (BLUE). While theoretically sound and supporting full uncertainty propagation, OEFPIL may yield regression results that are visually inconsistent when the full uncertainty matrix is applied.

As a practical alternative, we propose a *Locally Weighted Least Squares* (LWLS) method using a pre-specified positive definite weighting matrix, typically based on the diagonal or Type A components of the uncertainty matrix. While this approach sacrifices Gauss–Markov optimality, it can produce more physically interpretable results that better reflect empirical behavior.

2. Subject and Methods

We consider a general class of measurement models for nonlinear errors-in-variables (EIV) regression, particularly suited to metrological applications involving structured uncertainty. The model combines a stochastic observation equation with deterministic functional constraints on the unknown parameters:

$$\mathbf{X} = \boldsymbol{\mu} + \boldsymbol{\varepsilon}, \quad \text{subject to} \quad \mathbf{f}(\boldsymbol{\mu}, \boldsymbol{\beta}) = \mathbf{0}, \tag{1}$$

where $\mathbf{X} \in \mathbb{R}^N$ denotes the vector of observed (measured) quantities, including both input and output variables. The vector $\boldsymbol{\mu} \in \mathbb{R}^N$ represents the unknown true values of the measured quantities, and $\boldsymbol{\varepsilon}$ is a zero-mean random error vector with known covariance matrix $\mathbf{U}$, typically identified as the *uncertainty matrix* in metrology. The function $\mathbf{f}(\boldsymbol{\mu}, \boldsymbol{\beta}) = \mathbf{0}$ defines a system of q nonlinear constraint equations involving both the true values $\boldsymbol{\mu}$ and the model parameters $\boldsymbol{\beta} \in \mathbb{R}^p$, which typically represent the measurands of interest; see, e.g., [10] for further details.

Standard OEFPIL Method

The OEFPIL method addresses this estimation problem by iteratively linearizing the constraint function and solving a constrained optimization problem. The estimation is formulated as the minimization of a weighted residual norm using the known uncertainty matrix $\mathbf{U}$:

$$\min_{\boldsymbol{\mu}, \boldsymbol{\beta}} (\mathbf{X} - \boldsymbol{\mu})^\top \mathbf{U}^{-1} (\mathbf{X} - \boldsymbol{\mu}) \quad \text{subject to} \quad \mathbf{f}(\boldsymbol{\mu}, \boldsymbol{\beta}) = \mathbf{0}. \tag{2}$$

At each iteration, the constraint is approximated by a first-order Taylor expansion around current estimates $(\boldsymbol{\mu}^{(k)}, \boldsymbol{\beta}^{(k)})$:

$$\mathbf{f}(\boldsymbol{\mu}, \boldsymbol{\beta}) \approx \mathbf{f}^{(k)} + \mathbf{B}_1^{(k)} (\boldsymbol{\mu} - \boldsymbol{\mu}^{(k)}) + \mathbf{B}_2^{(k)} (\boldsymbol{\beta} - \boldsymbol{\beta}^{(k)}),$$

where $\mathbf{f}^{(k)} = \mathbf{f}(\boldsymbol{\mu}^{(k)}, \boldsymbol{\beta}^{(k)})$, and $\mathbf{B}_1^{(k)}$, $\mathbf{B}_2^{(k)}$ are the Jacobians of $\mathbf{f}$ with respect to $\boldsymbol{\mu}$ and $\boldsymbol{\beta}$, respectively. For brevity, we write $\mathbf{B}_1 = \mathbf{B}_1^{(k)}$ and $\mathbf{B}_2 = \mathbf{B}_2^{(k)}$. The linearized constraint then becomes $\mathbf{B}_1 \boldsymbol{\mu} + \mathbf{B}_2 \boldsymbol{\beta} + \mathbf{b} = \mathbf{0}$, with $\mathbf{b} = \mathbf{f}^{(k)} - \mathbf{B}_1 \boldsymbol{\mu}^{(k)} - \mathbf{B}_2 \boldsymbol{\beta}^{(k)}$.

Locally Weighted Least Squares Method

As a sub-optimal yet practically useful alternative to OEFPIL, we consider a *Locally Weighted Least Squares* (LWLS) approach. In this method, the model parameters $\boldsymbol{\mu}$ and $\boldsymbol{\beta}$ are estimated

ISBN 978-80-69159-00-6

by minimizing a weighted quadratic loss using a user-defined positive definite weighting matrix $\mathbf{W}$, which may differ from the optimal weighting matrix $\mathbf{W}_{\text{opt}} = \mathbf{U}^{-1}$:

$$\min_{\boldsymbol{\mu},\boldsymbol{\beta}} (\mathbf{X}-\boldsymbol{\mu})^{\top}\mathbf{W}(\mathbf{X}-\boldsymbol{\mu}) \quad \text{subject to} \quad \mathbf{f}(\boldsymbol{\mu},\boldsymbol{\beta}) = \mathbf{0}, \tag{3}$$

where $\mathbf{W}$ is a user-defined positive definite weighting matrix. While the optimal choice is $\mathbf{W}_{\text{opt}} = \mathbf{U}^{-1}$, alternatives such as the inverse of the diagonal or the Type A component of $\mathbf{U}$ may improve robustness and interpretability in practice.

3. Results

For solving (3), in each iteration step we consider the following Lagrangian function:

$$\mathcal{L} = (\mathbf{X}-\boldsymbol{\mu})^{\top}\mathbf{W}(\mathbf{X}-\boldsymbol{\mu}) - 2\boldsymbol{\lambda}^{\top}(\mathbf{B}_1\boldsymbol{\mu} + \mathbf{B}_2\boldsymbol{\beta} + \mathbf{b}). \tag{4}$$

Taking derivatives with respect to $\boldsymbol{\mu}$, $\boldsymbol{\beta}$, and $\boldsymbol{\lambda}$ and solving the resulting system gives:

$$\hat{\boldsymbol{\mu}} = \mathbf{X} + \mathbf{W}^{-1}\mathbf{B}_1^{\top}\hat{\boldsymbol{\lambda}}, \tag{5}$$

$$\mathbf{B}_2^{\top}\hat{\boldsymbol{\lambda}} = 0, \tag{6}$$

$$\mathbf{B}_1\hat{\boldsymbol{\mu}} + \mathbf{B}_2\hat{\boldsymbol{\beta}} + \mathbf{b} = 0. \tag{7}$$

Substituting (5) into (7) and simplifying leads to the linear system:

$$\begin{pmatrix} \mathbf{B}_1\mathbf{W}^{-1}\mathbf{B}_1^{\top} & \mathbf{B}_2 \\ \mathbf{B}_2^{\top} & \mathbf{0} \end{pmatrix} \begin{pmatrix} \hat{\boldsymbol{\lambda}} \\ \hat{\boldsymbol{\beta}} \end{pmatrix} = \begin{pmatrix} -\mathbf{B}_1\mathbf{X} - \mathbf{b} \\ \mathbf{0} \end{pmatrix}. \tag{8}$$

Let us define the matrix $\mathbf{Q}$ as:

$$\mathbf{Q} = \begin{pmatrix} \mathbf{Q}_{11} & \mathbf{Q}_{12} \\ \mathbf{Q}_{21} & \mathbf{Q}_{22} \end{pmatrix} = \begin{pmatrix} \mathbf{B}_1\mathbf{W}^{-1}\mathbf{B}_1^{\top} & \mathbf{B}_2 \\ \mathbf{B}_2^{\top} & \mathbf{0} \end{pmatrix}^{-1}. \tag{9}$$

Then, the solution for the Lagrange multiplier $\hat{\boldsymbol{\lambda}}$ and the parameter vector $\hat{\boldsymbol{\beta}}$ is given by:

$$\begin{pmatrix} \boldsymbol{\lambda} \\ \hat{\boldsymbol{\beta}} \end{pmatrix} = \mathbf{Q}\begin{pmatrix} -\mathbf{B}_1\mathbf{X} - \mathbf{b} \\ \mathbf{0} \end{pmatrix} = \begin{pmatrix} -\mathbf{Q}_{11}(\mathbf{B}_1\mathbf{X} + \mathbf{b}) \\ -\mathbf{Q}_{21}(\mathbf{B}_1\mathbf{X} + \mathbf{b}) \end{pmatrix}. \tag{10}$$

Thus, the estimators for $\boldsymbol{\mu}$ and $\boldsymbol{\beta}$ become:

$$\begin{pmatrix} \hat{\boldsymbol{\mu}} \\ \hat{\boldsymbol{\beta}} \end{pmatrix} = \begin{pmatrix} \mathbf{I} - \mathbf{W}^{-1}\mathbf{B}_1^{\top}\mathbf{Q}_{11}\mathbf{B}_1 \\ -\mathbf{Q}_{21}\mathbf{B}_1 \end{pmatrix}\mathbf{X} + \begin{pmatrix} -\mathbf{W}^{-1}\mathbf{B}_1^{\top}\mathbf{Q}_{11} \\ -\mathbf{Q}_{21} \end{pmatrix}\mathbf{b} \tag{11}$$

Consequently, the proper joint uncertainty matrix associated with the estimated model parameters $\boldsymbol{\mu}$ and $\boldsymbol{\beta}$, derived based on uncertainty propagation according to the GUM uncertainty framework, is given as:

$$\mathbf{U}_{\hat{\boldsymbol{\mu}},\hat{\boldsymbol{\beta}}}^{LWLS} = \begin{pmatrix} (\mathbf{I} - \mathbf{W}^{-1}\mathbf{B}_1^{\top}\mathbf{Q}_{11}\mathbf{B}_1)\mathbf{U}(\mathbf{I} - \mathbf{B}_1^{\top}\mathbf{Q}_{11}\mathbf{B}_1\mathbf{W}^{-1}) & -(\mathbf{I} - \mathbf{W}^{-1}\mathbf{B}_1^{\top}\mathbf{Q}_{11}\mathbf{B}_1)\mathbf{U}\mathbf{B}_1^{\top}\mathbf{Q}_{21}^{\top} \\ -\mathbf{Q}_{21}\mathbf{B}_1\mathbf{U}(\mathbf{I} - \mathbf{B}_1^{\top}\mathbf{Q}_{11}\mathbf{B}_1\mathbf{W}^{-1}) & \mathbf{Q}_{21}\mathbf{B}_1\mathbf{U}\mathbf{B}_1^{\top}\mathbf{Q}_{21}^{\top} \end{pmatrix}. \tag{12}$$

If $\mathbf{W} = \mathbf{U}^{-1}$ (the optimal choice of the weighted matrix), the result is consistent with OEFPIL:

$$\mathbf{U}_{\hat{\boldsymbol{\mu}},\hat{\boldsymbol{\beta}}}^{OEFPIL} = \begin{pmatrix} \mathbf{U} - \mathbf{U}\mathbf{B}_1^{\top}\mathbf{Q}_{11}\mathbf{B}_1\mathbf{U} & -\mathbf{U}\mathbf{B}_1^{\top}\mathbf{Q}_{12} \\ -\mathbf{Q}_{21}\mathbf{B}_1\mathbf{U} & -\mathbf{Q}_{22} \end{pmatrix}. \tag{13}$$

ISBN 978-80-69159-00-6

4. Conclusions

The OEFPIL method provides locally optimal estimates when the full uncertainty matrix **U** is used as the weighting matrix. However, in practical metrological applications, this can result in fitted models that appear biased or inconsistent with experimental intuition. A modified approach using an alternative weighting matrix **W**—such as one based on the diagonal of **U**—may reduce statistical efficiency but often yields estimates that better reflect observed data, align with physical expectations, and are more acceptable to practitioners.

Acknowledgements

This work was supported by the Slovak Research and Development Agency under projects APVV-22-0328, APVV-21-0216 and SK-CZ-RD-21-0109, as well as by the Scientific Grant Agency of the Ministry of Education of the Slovak Republic and the Slovak Academy of Sciences under projects VEGA 2/0023/22 and VEGA 2/0120/24.

References

[1] Forbes, A. B. (2006). Algorithms for structured gauss-markov regression. *Numerical Algorithms* 41(1), 47–56.

[2] Malengo, A., Pennecchi, F. (2013). A weighted total least-squares algorithm for any fitting model with correlated variables. *Metrologia* 50(6), 654–662.

[3] ISO (2010). The determination and use of straight-line calibration functions. Technical Report ISO/TS 28037:2010.

[4] BIPM, IEC, IFCC, ILAC, ISO, IUPAC, IUPAP, and OIML (2008)a. Evaluation of measurement data — guide to the expression of uncertainty in measurement. Technical Report JCGM 100:2008, Joint Committee for Guides in Metrology (JCGM). GUM:1995 with minor corrections.

[5] BIPM, IEC, IFCC, ILAC, ISO, IUPAC, IUPAP, and OIML (2008)b. Evaluation of measurement data — supplement 1 to the "guide to the expression of uncertainty in measurement" — propagation of distributions using a monte carlo method. Technical Report JCGM 101:2008, Joint Committee for Guides in Metrology (JCGM).

[6] BIPM, IEC, IFCC, ILAC, ISO, IUPAC, IUPAP, and OIML (2011). Evaluation of measurement data — supplement 2 to the "guide to the expression of uncertainty in measurement" — extension to any number of output quantities. Technical Report JCGM 102:2011, Joint Committee for Guides in Metrology (JCGM).

[7] BIPM, IEC, IFCC, ILAC, ISO, IUPAC, IUPAP, and OIML (2020). Guide to the expression of uncertainty in measurement — part 6: Developing and using measurement models. Technical Report JCGM GUM-6:2020, Joint Committee for Guides in Metrology (JCGM).

[8] Campbell, A. C., Šlesinger, R., Witkovský, V., Wimmer, G., Buršíková, V. (2025). Applications of iterated linearization for non-linear errors-in-variable regression to metrological data. *Measurement: Sensors* p. 101729.

[9] Campbell, A. C., Geršlová, Z., Šindlář, V., Šlesinger, R., Wimmer, G. (2024). New framework for nanoindentation curve fitting and measurement uncertainty estimation. *Precision Engineering* 85, 166–173.

[10] Witkovský, V., Wimmer, G., Campbell, A. C., Klapetek, P., Šlesinger, R. (2025). Estimation of function parameters through iterated linearization for nonlinear errors-in-variable regression with correlated variables. *Measurement: Sensors* p. 101728.

Evaluation of the Numerical Value and Type A Standard Uncertainty of Repeated Observations from Their Extreme Values

Igor Zakharov, Olesia Botsiura

Kharkiv National University of Radio Electronics, Kharkiv, Ukraine,
Email: newzip@ukr.net

Abstract. *Situations are listed when, during repeated measurements, it is impractical or impossible to record all the results of observations, but only their minimum and maximum values. The possibility of determining an estimate of the numerical value and standard uncertainty of type A from the range of repeated observation results, taking into account their number and distribution law, is considered. An example of evaluation type A measurement uncertainty at hygrometer calibration is considered.*

Keywords: Repeated Measurements, Extreme Values of a Sample, Range, Midrange, Estimate of the Measurand, Measurement Uncertainties of Type A

1. Introduction

There are a number of situations where it is impossible or impractical to record all results of repeated observations, and one has to limit oneself to extreme values only. Such circumstances include: limitations on memory capacity and data processing speed at high-frequency observations; long-term experiments spanning large periods of time, when storing all intermediate data is difficult; rare catastrophic events (earthquakes, floods, accidents) where the focus is on extreme values characterizing the scale of the disaster; research into the limits of possibilities in sports, engineering, when extremes allow to assess the boundaries of capabilities and optimize parameters; limitations related to visual, rapidly changing observations, etc.

It is important to note that analyzing only extreme values can lead to a loss of information about the process dynamics and its intermediate states. Moreover, extreme values are sensitive to outliers, so their use can introduce significant errors into the measurement result. Therefore, the feasibility of this approach must be carefully assessed in each specific case.

The report discusses the specifics of finding the numerical value of the measurand and type A uncertainty through the extreme values of a sample of known size.

2. Key Points

When conducting repeated measurements, there is a need to increase their productivity by improving their processing methods. One possible solution to this issue is to use the range characteristics of the sample obtained from repeated measurements as estimates of the measurand and its uncertainty. This is particularly useful in situations where it is not possible to record all the results of the sample obtained from repeated observations, but only its extreme values.

Evaluation of the measurand

To evaluate the results of repeated measurements, various estimates of the mathematical expectation presented in Table 1 [1] can be used. They have different efficiency for different probability density functions (PDF) of observation results.

In practice, the PDF is unknown, therefore the efficiency of the different estimators must be investigated for different possible PDF of measurement results.

ISBN 978-80-69159-00-6

Table 1 Expressions for various estimates of the measurand

Estimators	Midrange – –	Arithmetic mean —	Median – · –
Formulas	$y = \frac{y_{\max} + y_{\min}}{2}$	$y = \frac{1}{n}\sum_{q=1}^{n} y_q$	$y = \begin{cases} y_{(n+1)/2}, & n - \text{odd} \\ \frac{y_{n/2} + y_{n/2+1}}{2}, & n - \text{even} \end{cases}$

The Monte Carlo method was used to investigate the dependences of the efficiency of different estimators of the mathematical expectation for different PDF of the observed dispersion of indicating measuring instruments (IMIs) readings.

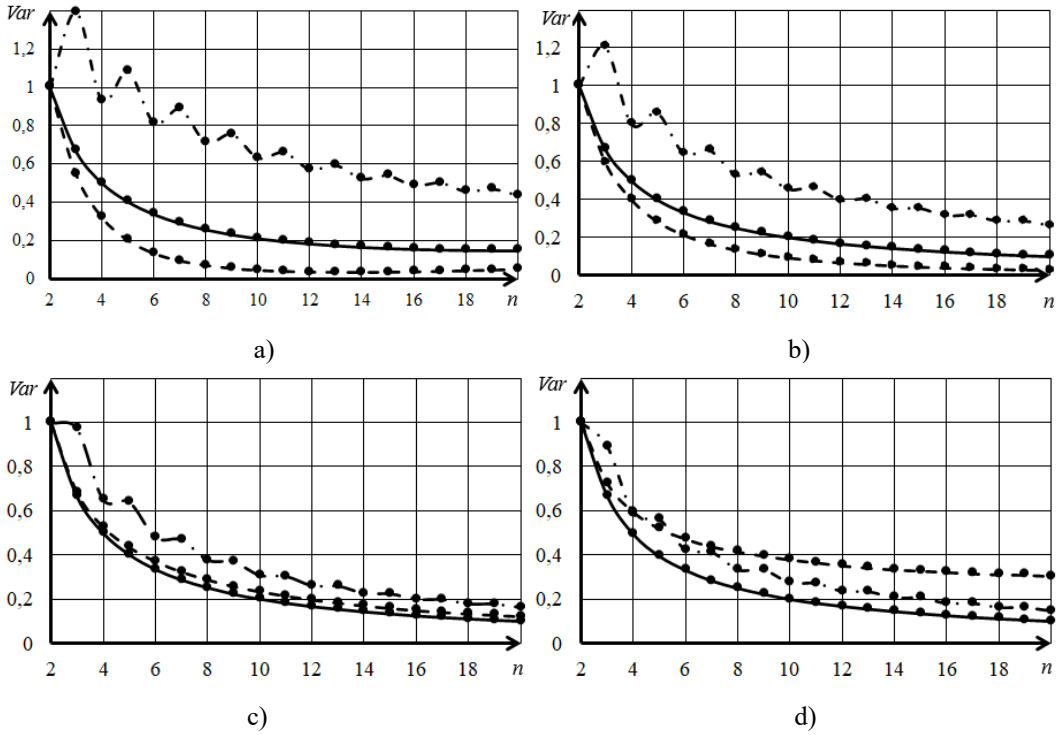

Fig. 1. Dependencies of the efficiency *Var* of various estimators of mathematical expectation for different PDFs of the observed dispersion of IMIs readings: a) arcsine; b) uniform; c) triangular; d) normal.

The efficient estimate has minimal variation compared to other estimates. From Fig. 1 it is clear that the arithmetic mean is the efficient estimate for normal and triangular PDFs, and the midrange is the efficient estimate for arcsine and uniform PDFs [2,3]. It should be noted that the arcsine PDF of the IMIs readings corresponds to the real situation of the presence of pulsations and interference from the AC power supply network in the measuring circuits of the IMIs, and the uniform law is usually adopted for an unknown distribution law of the input value specified by the boundaries [4].

Evaluation the type A uncertainty of a measurand

To evaluate the standard uncertainty of type A by range, it is necessary to evaluate the standard deviation of these measurements s, and then divide it by the square root of the given number of observations n. To determine the standard deviation, it is necessary to know the PDF of the observation results.

In the work [5] it is shown that the estimate of the standard uncertainty of the observed variability of the IMIs readings can be obtained through its range $R = y_{\max} - y_{\min}$:

ISBN 978-80-69159-00-6

$$s = \frac{y_{\max} - y_{\min}}{\alpha},$$

where the coefficient α depends both on the PDF of the observed dispersion of readings and on the number n of measurements taken.

We calculated the dependence of the coefficient $\alpha = (y_{\max} - y_{\min})/s$ on the sample size n for different PDFs using the Monte Carlo method (Fig. 2) [6].

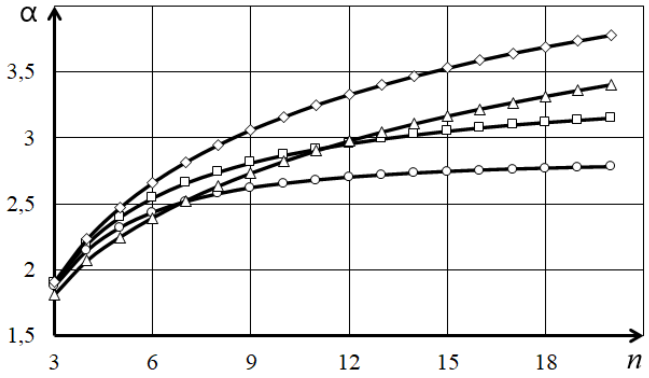

Fig. 2. Dependences of the coefficient α on n for different distribution laws: o – arcsine; ◊ – normal; □ – uniform; Δ – real.

It should be noted that since the real law of distribution of IMIs readings, derived from empirical data, may differ from those listed, the dependence of α on n may also not coincide with those shown in Fig. 2.

3. Example: Evaluation of the Numerical Value and Type a Uncertainty of a Standard Hygrometer

Based on repeated humidity measurements carried out using a standard hygrometer, the dependences of the arithmetic mean and the midrange were obtained depending on the sample size n (Fig. 3).

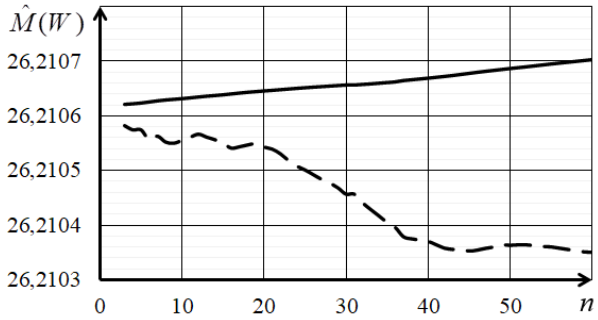

Fig. 3. Experimental dependence of arithmetic mean (—) and midrange (– –) of the hygrometer readings for different sample sizes n.

The figure shows that with increasing sample size, the arithmetic mean of the sample increases, while the midrange decreases. For n=60, the difference in estimates can be 0.0035%RH. This difference can be neglected if the resolution of the reference hygrometer is more than 0.01%RH.

Fig. 2 shows the dependence of the coefficient on the sample size n for the real law of distribution of hygrometer readings. The real distribution was derived from empirical data. It is evident from the figure that the real dependence is not approximated by any of the theoretical

ones. Therefore, for the real dependence, an approximation was found in the form:

$$\alpha = 0{,}8508 \cdot \ln(n) + 0{,}862 .$$

Using this approximation, we will calculate $u_A(\hat{W}_s)$ for the data obtained as a result of the experiment. The maximum humidity value was 26.14 %RH, the minimum 26.10 %RH. Therefore, the standard uncertainty of type A, estimated through the range, for 10 measurements was:

$$u_A(\hat{W}_s) = \frac{26{,}14 - 26{,}10}{[0{,}8508 \cdot \ln(10) + 0{,}862]\sqrt{10}} = 0{,}00449 \text{ %RH}.$$

The value of type A uncertainty calculated as the standard deviation of the arithmetic mean [3] of the hygrometer readings is equal to 0.00471% RH, i.e. the error in determining the standard uncertainty of type A through the sample range was no more than 5%.

4. Conclusions

1. Situations are listed when, during repeated measurements, it is impractical or impossible to record all the results of observations, but only their minimum and maximum values.
2. Dependencies of the efficiency *Var* of various estimators of mathematical expectation (arithmetic mean, midrange, median) for different PDFs of the observed dispersion of IMIs readings (arcsine; uniform; triangular; normal) were calculated.
3. The possibility of using the characteristics of the range of an observations sample to estimate the numerical value of a measurand and its standard uncertainty of type A is substantiated.
4. An example of evaluation the humidity value and its standard uncertainty of type A using a standard hygrometer is considered. The admissibility of using sample range parameters for this purpose is shown.

Acknowledgements

The authors thank the organizers of the Measurement 2025 conference for their assistance and support.

References

[1] ISO 3534-1:2006 Statistics – Vocabulary and symbols. Part 1: General statistical terms and terms used in probability.

[2] Zakharov, I.P., Shtefan, N.V. (2005) Algorithms for reliable and effective estimation of type A uncertainty. Measurement Techniques, 2005, 48(5), pp. 427–437 DOI: 10.1007/s11018-005-0160-7.

[3] Dorozhovets, M., Popovych, I., Warsza, Z. L. (2016) Method of evaluation the measurement uncertainty of the minimal value of observations and its application in testing of plastic products. In monograph: R. Jabłoński, T. Brezina (Eds)' Advanced Mechatronics Solutions' vol. 393, series Advances in Intelligent Systems & Computing. Springer, pp. p.421-430, DOI: 10.1007/978-3 319-23923-1_62

[4] JCGM 100:2008 (GUM 1995 with minor corrections). (2008). Evaluation of measurement data – Guide to the expression of uncertainty in measurement.

[5] Tippett, L. H. C. (1925) On the extreme individuals and the range of samples taken from a normal population. Biometrika, Volume 17, Issue 3-4, December 1925, pp. 364–387.

[6] https://uncertainty.nist.gov/

Remote-Controlled Measurement System for Sample Signal Generation with Measurement of Selected Parameters of This Signal

Zbigniew Krawiecki, Przemysław Otomański

Poznan University of Technology, Institute of Electrical Engineering and Electronics,
Piotrowo street 3A, 60-965 Poznań, Poland
Email: zbigniew.krawiecki@put.poznan.pl

Abstract. *The paper describes a computer-controlled teaching station for generating waveforms from samples with measurement of selected parameters of the generated waveform. The control software was written in the LabVIEW environment. It allows you to generate a waveform in this program, visualize the waveform, transfer samples to the digital generator's memory, configure the generator, and remotely measure the rms value with a digital multimeter with a TrueRMS converter. Using a digital oscilloscope, the waveform obtained at the output of the generator is visualized. The made measuring station is used during laboratory classes on the subject of computer measurement systems.*

Keywords: Signal Generation, Remote Measurement of Signal Parameters, LabVIEW

1. Introduction

Digital arbitrary generators are used to generate electrical waveforms of various shapes. Such generators are equipped with a memory into which data can be written. The data entered into memory is then processed and a continuous signal is generated using a digital-to-analog converter. Generation involves converting samples from digital form to an analog signal in the form of a voltage. In this conversion, it is required to take into account the amplitude of the signal and its frequency. An important parameter at the waveform generation stage is the number of samples used to represent the signal envelope. The number of samples can significantly affect the shape of the envelope of the generated signal. Too few points, which form the envelope of the signal, translates into a pronounced deformation of the signal that is obtained at the output of the generator. This feature was the reason for creating a teaching station with waveform generation and measurement of the rms value of the voltage. Too few points, which form the envelope of the signal, translates into a pronounced deformation of the signal that is obtained at the output of the generator. This feature was the reason for creating a teaching station with waveform generation and measurement of the rms value of the voltage. The rms value of the voltage is determined in the program using an appropriate algorithm and measured using a digital multimeter with a TrueRMS converter. The purpose of this work was to implement teaching issues using a computer-controlled teaching station to generate a waveform as a function of the number of samples and evaluate the result of measuring the rms value of voltage with a digital multimeter for such a waveform [1, 2].

2. Subject and Methods

The stand was built in the concept of a virtual instrument. Such an instrument was composed of a software part and a hardware part [3]. The program controls the hardware part, it also performs tasks, i.e. data formatting, waveform visualization, voltage rms determination. The program was written in the LabVIEW environment with implemented VISA I/O libraries and SCPI programming messages for the generator, multimeter and oscilloscope [4, 5]. A digital arbitrary generator from Agilent 33120A was used as the signal source [6]. LabVIEW libraries were used to operate the generator remotely. The generator control program performs

ISBN 978-80-69159-00-6

instrument initialization and configuration. Setup includes preparing the generator to receive samples and write them to internal memory. Along with the samples, the value of the frequency and amplitude of the waveform is sent. The data is transferred to the instrument using VISA Write. The program also implements waveform restoration from samples that have been saved in a text file. One period of the waveform should be stored in the file, along with the value of frequency and voltage. A sinusoidal waveform is generated by software. One period of the waveform is assumed to be generated from points 10 to 100. The frequency of such a waveform is assumed to be 50 Hz with an amplitude of 1.5 V. The program runs in a loop and it is possible to automatically perform measurements with a 1-sample incremental change in the number of samples per run period. The software-generated waveform is sent to a block where the rms value of the voltage is determined. This value is then compared with the rms value measured with a multimeter. The multimeter measurement is performed remotely. In the control program, it is checked whether the waveform generation procedure has been completed, and only then is the voltage measured with a multimeter and the shape recorded with an oscilloscope. An Agilent 34401A instrument was used to measure the rms value of the AC voltage [7]. Communication with the generator and multimeter was implemented using the NI GPIB-USB-HS controller. Single-byte addressing was used.

3. Results

Using the executed bench, two waveforms are compared, one obtained by software and the other obtained by measuring with an instrument. The software-generated waveform is visualized using the Waveform Graph display. The second is the waveform acquired from the generator output using a digital oscilloscope. Figure 1 shows example images for 11 and 100 signal samples, and Table 1 shows the rms values of the voltage from multimeter and software measurements.

a)

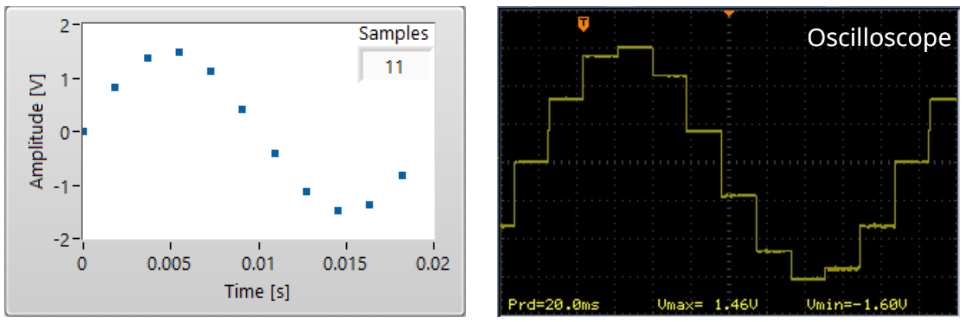

b)

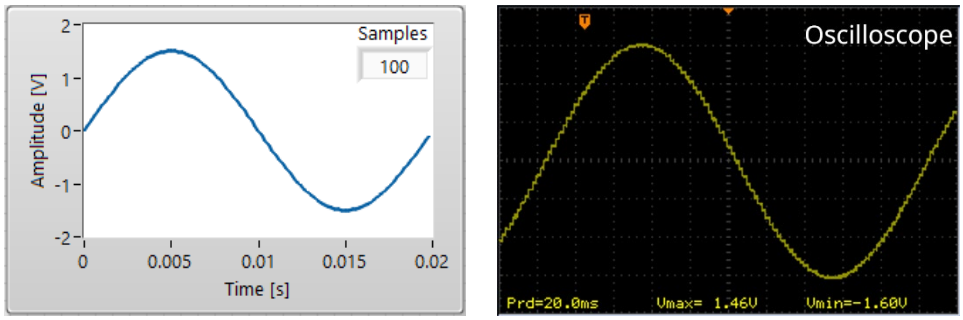

Fig. 1. Example waveforms generated programmatically in LabVIEW and waveforms generated with an arbitrary generator and recorded with a digital oscilloscope: (a) N=11, (b) N=100.

ISBN 978-80-69159-00-6

Table 1. Example results of measuring voltage U_{zm} with a multimeter with TrueRMS converter and voltage determined by U_{prog} software in LabVIEW.

N samples	U_{zm} [V]	U_{prog} [V]	N samples	U_{zm} [V]	U_{prog} [V]
10	1,129	1,061	40	1,073	1,061
12	1,074	1,061	50	1,076	1,061
14	1,101	1,061	60	1,074	1,061
16	1,073	1,061	70	1,075	1,061
18	1,090	1,061	80	1,074	1,061
20	1,073	1,061	90	1,075	1,061
30	1,080	1,061	100	1,074	1,061

The rms values of the voltage were determined for these waveforms. However, for the waveform from the output of the arbitrary generator, the rms value of the voltage is obtained by remote measurement with a multimeter with a TrueRMS converter. The results obtained are compared. An important step in this comparison is the correlation of the results with the number of samples, which forms the waveform envelope. With a small number of samples, the waveform is largely distorted. In the generated waveform, which is imaged on the oscilloscope screen, significant changes in the voltage level caused by the operation of the DAC in the generator are noticeable. It is possible to observe and compare the hardware-generated waveform with the software-generated waveform.

4. Discussion

Measurement of the rms value of the generated waveforms is realized by software and hardware. The result from the program is obtained from the generally known relation in which the signal samples are converted. In contrast, the hardware measurement was made with an Agilent 34401A multimeter. This result is subject to error, which is due to the specifications of the instrument and additional error from the waveform. In this paper, the difference of the two readings was determined and designated as ΔU. The difference between the value measured with a multimeter and the value determined in the software as a function of the number of samples (from 10 to 100 samples) that form the envelope of the signal is illustrated in the form of characteristics in Figure 2.

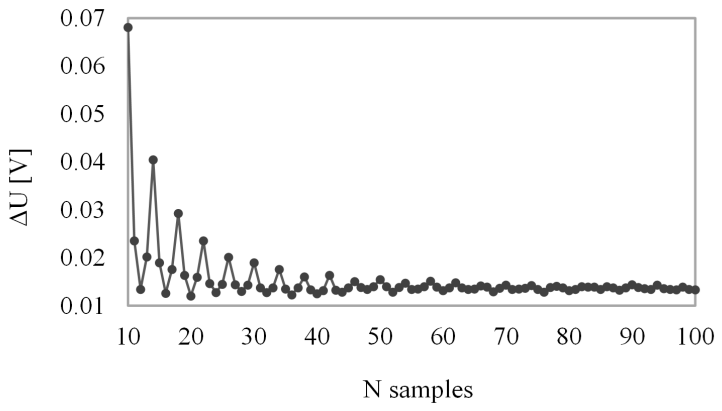

Fig. 2. Difference between the multimeter indication voltage and the value determined in the program as a function of the number of samples forming the waveform envelope.

ISBN 978-80-69159-00-6

The results obtained illustrate a significant difference in readings for the relatively small number of samples from which the waveform envelope is constructed. Significant deformation of the waveform caused by the DAC operation translates into the result of multimeter measurement. As can be seen from Figure 2, an increase in the number of samples above 60 does not result in a significant reduction in the value of the difference in ΔU readings between the multimeter measurement and the values determined in the LabVIEW application.

5. Conclusions

This paper presents a measuring station with remote operation of measuring instruments. It is intended for teaching purposes. During the class, selected aspects of digital signal generation are discussed. The shape of the obtained waveform is considered in conjunction with the determination of the rms value of the voltage. A program in the LabVIEW environment was written to control the station. The program controls the instruments and allows the generation of a waveform as a function of the number of samples, with presentation of its shape and measurement of the rms value of the voltage. The results presented are those determined in the program and measured with measuring instruments

References

[1] Otomański P., Krawiecki Z. (2023). Using LabVIEW to record and measure the RMS voltage of a distorted waveform. In *14th International Conference on Measurement*, Institute of Measurement Science Slovak Academy of Sciences, 171-174.

[2] Szlachta A., Pawłowski E., Otomański P., Krawiecki Z. (2022). LabVIEW jako element nauki zdalnej. In *Metrologia: badania i zastosowania*. Wydawnictwo Politechniki Świętokrzyskiej, 257-267.

[3] Świsulski D. (2005). *Komputerowa Technika Pomiarowa, Oprogramowanie wirtualnych przyrządów pomiarowych w LabView*, Agenda wydawnicza PAK, Warszawa.

[4] Otomański P., Krawiecki Z., Odon A. (2010). The application of the LabVIEW environment to evaluate the accuracy of alternating voltage measurements, *Journal of Physics: Conference Series*, vol. 238.

[5] Nawrocki W. (2007). *Komputerowe systemy pomiarowe*, WKŁ.

[6] Agilent 33120A 15 MHz Function Arbitrary/Waveform Generator, User's Guide, (2002).

[7] Agilent 34401A 6½ Digit Multimete, User's Guide, Agilent Technologies, (2007).

ISBN 978-80-69159-00-6

Design of Non-Contact Measurement Methods and Evaluation of the Impact of Surface Layers on the Mechanical Properties of Functional Implant Components

Miroslav Matuš, Jaromír Markovič, Mário Drbúl, Michal Šajgalík, Peter Špuro, Jozef Mrázik,

Faculty of Mechanical Engineering, University of Zilina, Zilina, Slovakia
Email: Miroslav.matus@fstroj.uniza.sk

Abstract. *The surface morphology of titanium implants critically affects their biological integration and functionality. This study used non-contact methods to assess how different surface treatments influence roughness and biomechanical properties. Ti6Al4V samples were treated by sandblasting, etching, and anodization, and analyzed using a confocal microscope to measure Rt, Rz, and Rsm. Results showed that combining sandblasting and anodization significantly increased roughness, potentially enhancing osseointegration.*

Keywords: Dental implants, Roughness, Titanium Alloy, Non-contact measurement

1. Introduction

The roughness of titanium implants plays a crucial role in the biological processes associated with osseointegration, which is essential for the stability and longevity of the implant. Research has shown that increased surface roughness enhances bone-to-implant contact (BIC), thereby improving mechanical stability and supporting bone tissue regeneration [1-3]. This effect is attributed to the greater surface area and improved cell adhesion. Micro-rough surfaces, created through techniques such as sandblasting and etching, exhibit superior osteoconductive properties compared to smooth surfaces [4, 5]. Additionally, these surfaces promote hydrophilicity, which facilitates protein adsorption and initiates healing processes [6, 7]. Surface topography also influences bacterial presence. Studies by Bormann and Kim indicate that properly modified surfaces can reduce bacterial colonization, thus lowering the risk of peri-implantitis [8, 9]. Brüm et al. further demonstrated that biofilm formation varies depending on surface roughness, which may impact the long-term success of implants [10]. Other studies have focused on advanced surface modifications, such as the application of TiO_2 coatings, which improve biocompatibility, wear resistance, and mechanical stability of implants under long-term loading conditions [11, 12]. Overall, the appropriate level and quality of surface roughness in titanium implants are critical for effective osseointegration, infection prevention, and long-term functionality. The aim of this study is to design and apply non-contact measurement methods to evaluate the surface morphology of titanium implants and analyze how different types of surface treatments affect roughness parameters, which directly influence biological integration and mechanical properties. The results are expected to contribute to the optimization of implant component design, with an emphasis on long-term stability and biocompatibility.

ISBN 978-80-69159-00-6

2. Material and Methods

For the purposes of this study, the titanium alloy Ti6Al4V was selected as the base material to produce dental implants. This material was chosen due to its biocompatibility, high corrosion resistance, excellent mechanical properties, and extensive clinical validation in the field of implantology. The samples were subsequently subjected to various surface treatment methods to evaluate the effect of these treatments on surface morphology. The chemical composition of the titanium alloy is presented in Table 1.

Table 1 Chemical Composition of the Titanium Alloy Ti6Al4V

C [%]	V [%]	Al [%]	N [%]	H [%]	O2 [%]	Fe [%]
0.0143	3.9400	6.0200	0.0045	0.0015	0.1100	0.0540

Surface Topography Measurement

The surface morphology of the samples was analyzed using a confocal optical microscope, Alicona Infinite Focus G5 (Alicona Imaging GmbH, Austria), under stable laboratory conditions. Measurements were performed with a 100× objective lens, suitable for detailed analysis of microstructures after implant surface treatment. Each sample was measured in four quadrants around its circumference to capture possible surface variations. To assess the influence of different surface treatments on roughness parameters, the measured values were statistically analyzed. Surface topography was evaluated based on the primary profile, focusing on *Rt*, *Rz*, and *Rsm* parameters.

3. Results

The probability distribution of the surface roughness parameter *Rt* for different surface treatments is shown in Fig. 1. The graph shows that surface treatment significantly influences *Rt* values, with the highest values in sandblasted and etched (P+L) samples and the lowest in turned (S) surfaces. Intermediate *Rt* values were observed in sandblasted (P), polished (L), and anodized (A) samples. The *Rt* value of the base material (Z) is indicated by a dashed line. These differences reflect distinct surface topographies, which may affect cell interactions and osseointegration in implantology.

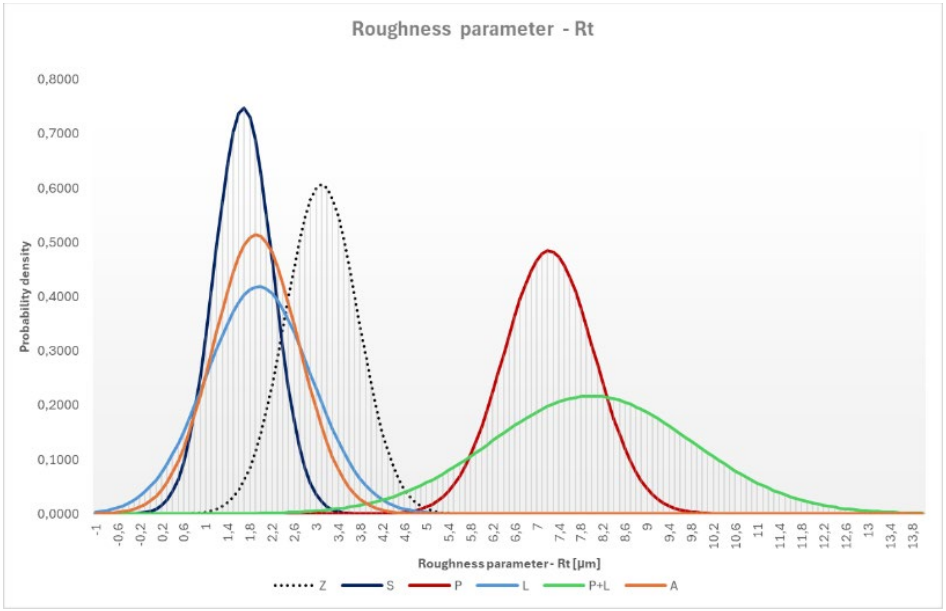

Fig. 1. Comparison of the distribution of roughness parameter *Rt* for different surface treatments of the samples

ISBN 978-80-69159-00-6

The probability distribution of the *Rz* parameter, which is one of the most used parameters for quantitative surface roughness evaluation, is shown in Fig. 2. The graph clearly demonstrates that surface treatment has a significant effect on the height and variability of surface irregularities. While polishing results in lower profile heights, sandblasting increases roughness and leads to the formation of more pronounced topography. These differences may influence the biological behavior of the surface, such as cell adhesion and osseointegration.

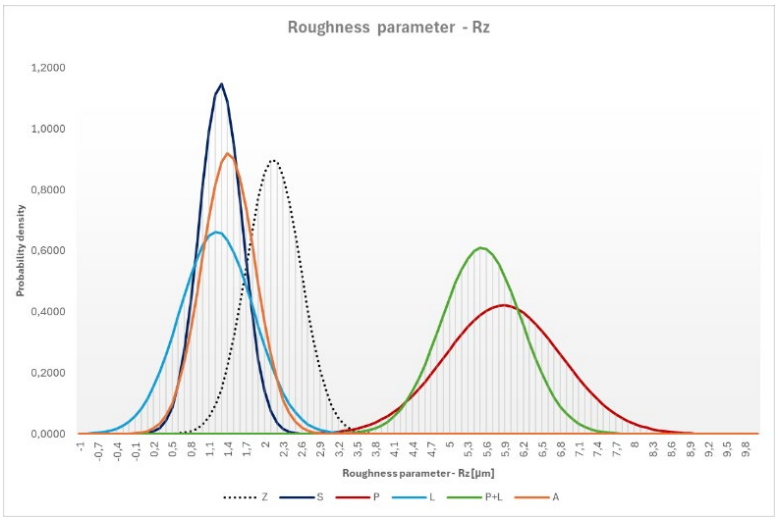

Fig. 2. Distribution of *Rz* values for different surface treatments

The graph shows that the highest *Rt* values (>7.5 µm) were found in samples treated with sandblasting and etching (P+L), while individually sandblasted samples (P) had slightly lower but still elevated values. The lowest *Rt* values (1.5–2.5 µm) were observed in turned (S), anodized (A), and polished (L) surfaces. Reference samples (Z) showed intermediate values around 3.5 µm. These results confirm that surface treatments significantly influence *Rt*, with combined methods producing much higher roughness than individual treatments.

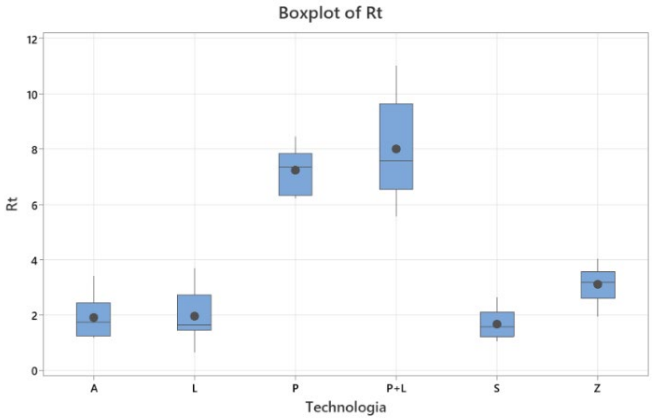

Fig. 3. Statistical comparison of surface roughness *Rt* between treated and reference samples.

4. Discussion and Conclusion

This study confirmed that surface treatment significantly affects the roughness of titanium implants. Sandblasting combined with etching produced the highest *Rt* and *Rz* values, creating a structured topography favorable for cell adhesion and osseointegration. Turned, anodized, and polished surfaces showed lower roughness, potentially reducing tissue interaction. Confocal microscopy proved to be a reliable non-contact method for assessing microtexture. Statistical

ISBN 978-80-69159-00-6

analysis of surface deviations improved the objectivity of the results. Interestingly, anodization reduced roughness instead of increasing it. Overall, optimizing surface morphology through targeted treatments can enhance implant performance, and the applied measurement methods are effective for developing biocompatible devices.

Acknowledgements

This research was funded by the University of Žilina project APVV-22-0328: "Design of a methodology and its verification for measuring selected parameters of Ti implants in the manufacturing process.", VEGA 1/0722/25 "Research on additive technologies with a focus on their application in the design and construction of cutting tools", and 09I05-03-V02-00080 -DigiDent "Research on the Digitalization of Dental Implant Components for the Creation of Personalized 3D Models for the Manufacturing Process"

References

[1] Gahlert, M. – Röhling, S. – Wieland, M. – Eichhorn, S. – Küchenhoff, H. – Kniha, H. A comparison study of the osseointegration of zirconia and titanium dental implants: A biomechanical evaluation in the maxilla of pigs. *Clinical Implant Dentistry and Related Research*, 2010, 12(4), 297–305. https://doi.org/10.1111/j.1708-8208.2009.00168.x

[2] Ruiz, M. – Perez-Martinez, C. – Martin-del-Llano, J. – Cardá, C. – Labaig-Rueda, C. In vitro preliminary study of osteoblast response to surface roughness of titanium discs and topical application of melatonin. *Medicina Oral, Patología Oral y Cirugía Bucal*, 2015, 20(1), e88–e93. https://doi.org/10.4317/medoral.19953

[3] Cheng, A. – Humayun, A. – Cohen, D. – Boyan, B. – Schwartz, Z. Additively manufactured 3D porous Ti-6Al-4V constructs mimic trabecular bone structure and regulate osteoblast proliferation, differentiation and local factor production in a porosity and surface roughness dependent manner. *Biofabrication*, 2014, 6(4), 045007. https://doi.org/10.1088/1758-5082/6/4/045007

[4] Fernandes, D. Influence of temperature and time of acid etching on the surface morphology of titanium for dental implants. *Research & Development in Material Science*, 2018, 4(5). https://doi.org/10.31031/rdms.2018.04.000596

[5] Lorenzetti, M. – Luxbacher, T. – Kobe, S. – Novak, S. Electrokinetic behaviour of porous TiO_2-coated implants. *Journal of Materials Science: Materials in Medicine*, 2015, 26(6). https://doi.org/10.1007/s10856-015-5521-4

[6] Lee, J. – Nam, J. – Nam, K. – Kim, H. – Yoo, J. Pre-treatment of titanium alloy with platelet-rich plasma enhances human osteoblast responses. *Tissue Engineering and Regenerative Medicine*, 2016, 13(4), 335–342. https://doi.org/10.1007/s13770-016-9079-0

[7] Kim, K. – Eo, M. – Nguyen, T. – Kim, S. General review of titanium toxicity. *International Journal of Implant Dentistry*, 2019, 5(1). https://doi.org/10.1186/s40729-019-0162-x

[8] Brum, R. – Apaza-Bedoya, K. – Labes, L. – Volpato, C. – Pimenta, A. – Benfatti, C. Early biofilm formation on rough and smooth titanium specimens: A systematic review of clinical studies. *Journal of Oral and Maxillofacial Research*, 2021, 12(4). https://doi.org/10.5037/jomr.2021.12401

[9] Shafik, A. – Kamal, R. – Hassin, M. – Badr, A. Surface roughness of implant-retained mandibular acrylic overdenture treated with titanium dioxide nanoparticles: An in vitro comparative study. *Egyptian Dental Journal*, 2023, 69(4), 2909–2915. https://doi.org/10.21608/edj.2023.223281.2639

[10] Qosim, N. – Supriadi, S. – Saragih, A. – Whulanza, Y. Surface treatments of Ti-alloy based bone implant manufactured by electrical discharge machining. *Ingeniería y Universidad*, 2018, 22(2). https://doi.org/10.11144/javeriana.iyu22-2.sttb

[11] Tavakoli, M. – Yaghini, J. – Izadi, M. – Molavi, H. – Sabet, N. Effects of titanium curette, air polishing and titanium brush on implant surface roughness using scanning probe microscopy. *Avicenna Journal of Dental Research*, 2019, 11(1), 21–25. https://doi.org/10.34172/ajdr.2019.04

[12] Unursaikhan, O. – Lee, J. – Cha, J. – Park, J. – Jung, U. – Kim, C. – Choi, S. Comparative evaluation of roughness of titanium surfaces treated by different hygiene instruments. *Journal of Periodontal & Implant Science*, 2012, 42(3), 88–94. https://doi.org/10.5051/jpis.2012.42.3.88

Optimizing Measuring Artifact Design for Accuracy Assessment of Additive Manufacturing Devices

Richard Joch, Mário Drbúl, Jaromír Markovič, Miroslav Cedzo, Jozef Mrázik, Jozef Holubják

Department of Machining and Production Technology, Faculty of Mechanical Engineering, University of Žilina, Univerzitná 1, 010 26 Žilina, Slovakia
Email: richard.joch@fstroj.uniza.sk

Abstract. *The accuracy of additive manufacturing is crucial for its use in technical and industrial applications. Measurement artifacts are commonly used to analyze geometric and dimensional deviations in 3D prints. In this study, two artifacts were evaluated - one standardized according to ISO/ASTM 52902 and a custom design adapted for efficient coordinate measuring machine measurement. Both samples were fabricated using the same FDM 3D printing process and tested under the same conditions. The measurement results along the X, Y, and Z axes revealed no statistically significant differences between the artifacts. This suggests that the custom artifact can serve as a viable alternative to the standardized solution, while offering advantages in terms of material and time savings. The findings support the use of customized measurement benchmarks for applications that do not require strictly standardized accuracy verification.*

Keywords: Additive Manufacturing, Artifact, Dimensional Accuracy

1. Introduction

Additive manufacturing holds immense promise for revolutionizing various industries, but the accuracy of the fabrication process remains a critical concern. Achieving precise dimensional and geometric accuracy is essential for functional parts, particularly in demanding applications like aerospace and medical devices[1, 2]. Benchmark artifacts play a vital role in evaluating and ensuring this accuracy [3]. These meticulously designed objects incorporate various geometric features that challenge the capabilities of AM machines, allowing for a comprehensive assessment of their performance [4].

The design of the measurement artifact is a critical aspect of the assessment process. It should incorporate a range of geometric features that are representative of the types of parts that will be manufactured using the additive manufacturing equipment [3, 5]. These features may include planes, cylinders, spheres, cones, and freeform surfaces, each carefully selected to challenge the capabilities of the additive manufacturing process and the CMM measurement system [6]. Furthermore, the artifact should be designed with consideration for the specific additive manufacturing process being used [7]. For instance, the orientation of the artifact during printing can significantly impact the accuracy of certain features, particularly those with overhangs or complex geometries[8, 9].

The importance of metrology in artifact design is highlighted by the design-for-metrology approach, as advocated by Santos et al. [10]. This approach emphasizes the need to consider the measurement process during the artifact design phase, optimizing features for accurate and efficient measurement with specific tools like CMMs. The work of Vorkapić et al. [11] further exemplifies this by presenting a novel benchmark artifact coupled with a dedicated deviation measurement method. Rebaioli and Fassi [12] emphasize the need for standardized evaluation procedures and a focus on true process repeatability rather than just spatial repeatability.

ISBN 978-80-69159-00-6

For measuring machine accuracy, standardized measurement artifacts, such as the ISO/ASTM 52902, are commonly used to evaluate 3D printer capabilities across various axes and geometric features. This study aims to compare measurement results of the standardized ISO artifact and a newly designed custom complex artifact, both manufactured using the same FDM 3D printer. Coordinate measuring machine measurements evaluated deviations in the X, Y, and Z axes. Statistical analysis determines if the custom artifact design can serve as an alternative to the standardized solution, considering advantages in manufacturing, simplicity, and flexibility.

2. Methodology

The methodology for assessing the geometric and dimensional accuracy of additive manufacturing equipment using CMM measurements of measurement artifacts involves a systematic approach encompassing artifact design, manufacturing, measurement, and data analysis. The design of the measurement artifact is a critical step, requiring careful consideration of the geometric features that are most relevant to the intended application of the additive manufacturing equipment. The artifact should be manufactured using the additive manufacturing equipment being evaluated, ensuring that the part reflects the actual performance of the machine under typical operating conditions.

Once the artifact is manufactured, it is then measured using a Zeiss Eclipse coordinate measuring machine, which precisely captures the coordinates of points on the artifact's surface. A 3mm diameter ruby probe was used for the measurement. The surface scan speed was 3mm/s. Planes were measured using a raster and cylindrical surfaces in three sections. These measurements are then compared to the nominal values defined in the artifact's CAD model, and the deviations are quantified and analyzed.

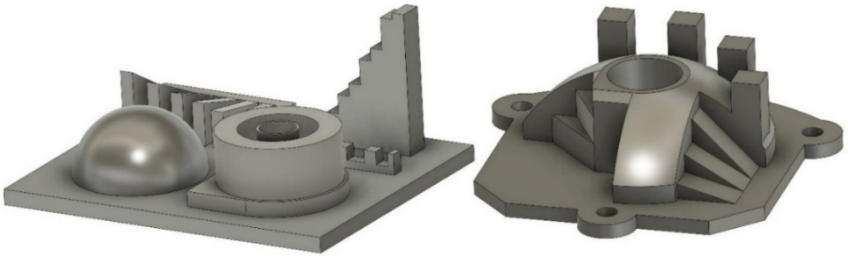

a) b)

Fig. 1. 3D models of the measurement artifacts a) standard artifact based on ISO/ASTM 52902, b) designed complex artifact

The methodology used a standardized measurement artifact designed in accordance with ISO/ASTM 52902 (Fig. 1a). The artifact includes several geometric features enabling a comprehensive assessment of 3D printing accuracy. A linear feature was used to measure distance for the assessment of accuracy in the X and Y planes, and a circular feature was used to assess the circularity and accuracy of the diameter of the cylindrical shape. Angular accuracy was verified using resolution slotted angle features. Since one of the goals was to also assess printing accuracy in the Z axis direction, the artifact also included a vertically oriented linear feature and a hemispherical feature, which is used to evaluate shape accuracy in space.

The proposed complex artifact (Fig. 1b) is designed to meet the basic geometric requirements for testing the accuracy and repeatability of additive manufacturing equipment. In addition to a spherical model, the artifact should incorporate typical geometric features observed in the additive manufacturing process. The artifact should be easily measurable using a coordinate measuring machine. Cylindrical elements assess shape accuracy in the XY plane, while steps allow evaluation of parallelism in the upper surfaces and Z-axis accuracy. Inclined surfaces test the angular accuracy of the device. The sphere and concentric hole are included as positive and

ISBN 978-80-69159-00-6

negative features, which can indicate shape accuracy and surface quality related to layer thickness in the 3D printing process. The complex designed artifact offers advantages such as a 35% reduction in material usage and a 40% decrease in production time. However, this design requires the development of a more intricate coordinate measuring machine program, which may necessitate additional time. Nevertheless, this drawback is offset by the shorter measurement duration enabled by the artifact's complexity.

3. Results

The dimensional deviations measured on both artifacts—one designed in accordance with ISO 52902 and the other custom-designed—were statistically evaluated to assess the dimensional and geometric accuracy of the FDM 3D printing process using PLA material. All samples were manufactured under identical printing parameters and the measured data are shown in Fig 2.

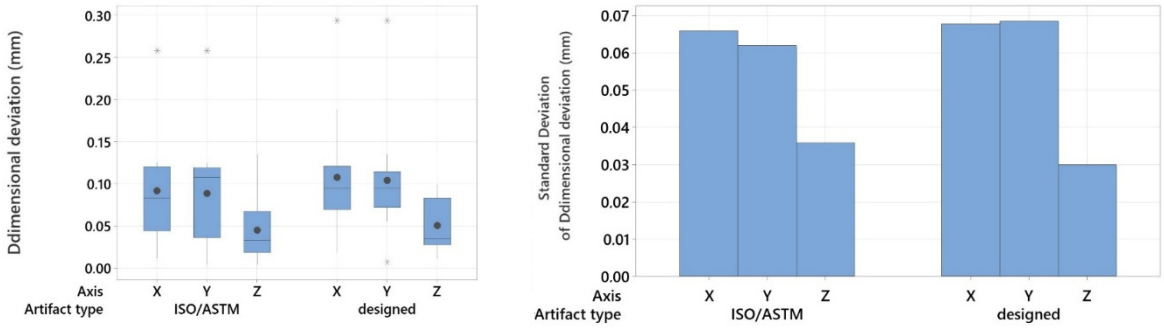

a) b)

Fig. 2. Comparison of measured data in the XYZ axes; a) dimensional deviations b) standard deviations

A one-way ANOVA test was conducted to compare absolute dimensional deviations in the X, Y, and Z directions between the two artifacts. The analysis yielded a p-value of 0.215, indicating that there is no statistically significant difference between the deviations measured on the two artifacts at the 95% confidence level.

Furthermore, the ISO-based artifact allowed for evaluation of standardized features, such as linear distances, circularity, and angular accuracy through resolution slotted angle features. The custom artifact offered more flexibility in the design and enabled measurement of features positioned more densely in space. However, both artifacts demonstrated comparable results in terms of deviation trends and overall dimensional fidelity.

The largest deviations were observed in the X and Y directions, with peak values exceeding ±0.2 mm, consistent with known limitations of the FDM process. The Z-axis showed lower variability, confirming the layered nature of deposition as more stable in vertical resolution (Fig. 2).

Overall, the results support the use of both artifacts for evaluating the performance of additive manufacturing devices, with the ISO artifact providing standard comparability and the custom artifact offering adaptability to specific needs.

4. Discussion and conclusions

The study findings indicated that the standardized artifact conforming to ISO/ASTM 52902 and the customized design both provided comparable data regarding the dimensional accuracy of FDM 3D printing utilizing PLA material. Despite the lack of statistically significant differences in the measured deviations between the two artifacts, their designs offered distinct advantages.

ISBN 978-80-69159-00-6

The ISO-based artifact enable standardized and reproducible assessments across different laboratories, while the custom artifact provided enhanced flexibility and the capacity to adapt to specific measurement requirements or device limitations. In both cases, the well-known limitations of FDM technology were corroborated – higher variability along the X and Y axes compared to the more consistent Z axis, which can be attributed to layering and thermal effects during the printing process. The comparative analysis thus demonstrated that the custom artifact, optimized for CMM-based measurement, can serve as an effective and material-efficient alternative for routine or application-specific accuracy verification. Future research could focus on automating the CMM measurement of complex artifacts and exploring methods to optimize the measurement program to reduce time without compromising accuracy, as well as examining a broader spectrum of additive manufacturing technologies and materials.

Acknowledgements

This research was funded by the University of Žilina project: APVV-23-0366: Research of reference standards and measurement methods ensuring determination of the relationship of geometric specifications and qualitative indicators of 3D objects created by additive technologies; VEGA 1/0722/25 Research on additive technologies with a focus on their application in the design and construction of cutting tools; 09I05-03-V02-00080 DigiDent (Research on the Digitalization of Dental Implant Components for the Creation of Personalized 3D Models for the Manufacturing Process)

References

[1] Wong, K.V., Hernandez, A. (2012). A review of additive manufacturing. ISRN Mechanical Engineering, 2012, 1–10. https://doi.org/10.5402/2012/208760

[2] Ngo, T.D., Kashani, A., Imbalzano, G., et al. (2018). Additive manufacturing (3D printing): A review of materials, methods, applications and challenges. Composites Part B: Engineering, 143, 172–196. https://doi.org/10.1016/J.COMPOSITESB.2018.02.012

[3] Subbaian Kaliamoorthy, P., Subbiah, R., Bensingh, J., et al. (2020). Benchmarking the complex geometric profiles, dimensional accuracy and surface analysis of printed parts. Rapid Prototyping Journal, 26. https://doi.org/10.1108/RPJ-01-2019-0024

[4] de Pastre, M.A., Toguem Tagne, S.C., Anwer, N. (2020). Test artefacts for additive manufacturing: A design methodology review. CIRP Journal of Manufacturing Science and Technology, 31, 14–24.

[5] Minetola, P., Calignano, F., Galati, M. (2020). Comparing geometric tolerance capabilities of additive manufacturing systems for polymers. Additive Manufacturing, 32, 101103. https://doi.org/10.1016/j.addma.2020.101103 Minetola, P., Iuliano, L., Marchiandi, G. (2016). Benchmarking of FDM machines through part quality using IT grades. In Procedia CIRP. Elsevier B.V., 1027–1032.

[6] Beniak, J., Holdy, M., Križan, P., Matúš, M. (2019). Research on parameters optimization for the additive manufacturing process. Transportation Research Procedia, 40, 144–149. https://doi.org/10.1016/J.TRPRO.2019.07.024
Joch, R., Šajgalík, M., Drbúl, M., et al. (2025). Impact of powder bed fusion printing process parameters on the achieved quality of PA12 manufactured parts. Progress in Additive Manufacturing. https://doi.org/10.1007/s40964-025-01053-0

[7] Son, J., Choi, S. (2016). Orientation selection for printing 3D models. In 2015 International Conference on 3D Imaging (IC3D) - Proceedings. IEEE.

[8] Rivas Santos, V.M., Thompson, A., Sims-Waterhouse, D., et al. (2020). Design and characterisation of an additive manufacturing benchmarking artefact following a design-for-metrology approach. Additive Manufacturing, 32. https://doi.org/10.1016/j.addma.2019.100964 Vorkapic, N., Pjevic, M., Popovic, M., et al. (2020). An additive manufacturing benchmark artifact and deviation measurement method. Journal of Mechanical Science and Technology, 34. https://doi.org/10.1007/s12206-020-0633-2

[9] Rebaioli, L., Fassi, I. (2017). A review on benchmark artifacts for evaluating the geometrical performance of additive manufacturing processes. International Journal of Advanced Manufacturing Technology, 93, 2571–2598. https://doi.org/10.1007/s00170-017-0570-0

Investigation on a Dual Beam Fabry-Perot Interferometer

[1] Y. C. Wang, [2] C. P. Chang, [1] C. C. Kuo, [1] M. H. Tsai

[1] Department of Mechanical Engineering, National Yunlin University of Science and Technology, Douliou, Yunlin, Taiwan
[2] Department of Mechanical and Energy Engineering, National Chiayi University, Chiayi, Taiwan
Email: wangyc@yuntech.edu.tw

Abstract. *Laser interferometer is indispensable for precision displacement measurements and calibrations of linear actuator systems, e.g. precision machine tools, nano-positioning stages or semiconductor manufacturing equipments. Compared with Michelson interferometer with two optical paths along different axes, the significant characteristic of the common path in a Fabry-Perot interferometer enables to minimize the influence of environmental parameters.*
Due to multi-interferences, the conventional Fabry-Perot interferometer (FPI) suffers from the non-orthogonal interference signals that lead to possible interpolation errors while higher resolutions would be demanded. To improve the phenomenon, a coaxial dual-beam Fabry-Perot interferometer (FPI) has been developed to facilitate high-precision linear displacement measurements in this article.
By manipulating the polarization state and some specific optical components, the proposed interferometer can attain the goal of the coaxial path and orthogonal signals such that the above-mentioned concerns will be resolved. Theoretical simulations based on the modified innovative optical structure and preliminary experimental testing have revealed that orthogonal signals generated in the dual-beam FPI are able to overcome limitations of the conventional FPI. Interpolation simulations showed that the measurement accuracy has been enhanced by approximately 40 nm with this structure in comparison with the results from a conventional FPI.
Keywords: Fabry-Perot Interferometer, Dual Beam Interference, Polarization, Precision Displacement Measurement, Orthogonal Signal, Nonlinearity

1. Introduction

Laser interferometers are essential for length metrology in precision mechanical engineering. They are employed in precision measurements and positioning tasks, since they provide a means for attaining high metric resolution and precision, even over long measurement ranges. The versatility and broad applicability of laser interferometers are unattainable using any other metrological methods [1].

Typical Michelson interferometer or its variants serve widespreadly as measurement modules or the reference standard of calibrations in precision mechanical industries [2]. Its dual-beam structure provides a pair of sine- and cosine-form signals and the quadrature phase detection enables ideal incremental and bidirectional precision displacement measurements [3]. However, its reference and measurement beam propagate in different optical paths which can cause errors due to different environmental effects in each beam. Obviously that will deteriorate the measurement accuracy demanded in nano- or subnanometer order.

The influence of non-common path can be significantly mitigated by Fabry-Perot interferometer which possess the common optical path that will eliminate the errors induced by environmental disturbances [4, 5]. In order to solve the problems of both the non-common path of Michelson interferometer and the deteriorative orthogonal signals of the conventional

FPI, a dual-beam FPI has been developed to promote the measuring performance by regulating corresponding polarization states in this study.

2. Measurement principle and structure

The optical path sketch and theory of Michelson interferometer, conventional FPI and dual-beam FPI are briefly described as follows. Because Michelson interferometer is more well-known, here only the expressions about the interference calculation of the conventional and dual-beam FPI are demonstrated.

Michelson Interferometer

Michelson interferometer belongs to the most commonly used commercial interferometer and its basic optical arrangement is shown in Figure 1. As a dual-beam interferometer with arms in different axes, its interference signals vary sinusoidally during the linear motion of the measurement mirror. By detecting its quadrant-phase signals, the displacement measurement can be achieved by counting incremental signals (I_1 and I_2 in Fig. 1).

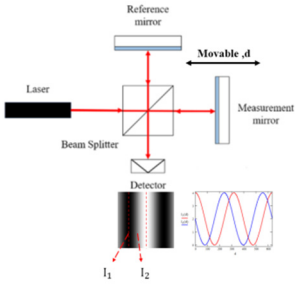

Fig. 1 Michelson interferometer

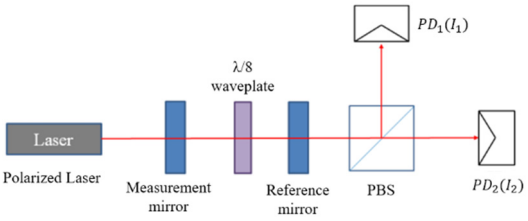

Fig. 2 Fabry-Perot interferometer

Conventional Fabry-Perot interferometer

The structure of this interferometer [6] is shown in Fig. 2. It consists of a laser source and a resonance cavity including the reference and measurement mirror. The light beam is incident in the resonance cavity with a nearly perpendicular direction ($\alpha \approx 0$) and then the transmitted beam is reflected multiple times in the cavity and the emerging beams from the cavity will be overlapped one another to form a multiple-interferences phenomenon.

The intensity of the interference beam can be derived theoretically and expressed in Eq.1, assuming that the amplitude of incident light, wavelength, the intensity of penetrating light, the reflectance of reference mirror and measuring mirror, the transmittance of reference mirror, the resultant transmittance of the optical components and the cavity length are A_0, λ, $I_{1,2}$, R_1, R_2, T, T' and d respectively.

$$I_1 = \frac{\frac{1}{2}{A_0}^2 \cdot T^2 \cdot T'}{1 + R^2 \cdot T'^2 - 2 \cdot T' \cdot R \cdot \cos(2\delta)} \tag{1}$$

$$I_2 = \frac{\frac{1}{2}{A_0}^2 \cdot T^2 \cdot T'}{1 + R^2 \cdot T'^2 - 2 \cdot T' \cdot R \cdot \cos(2\delta + \frac{\pi}{2})} \tag{2}$$

where

$$\delta = \frac{4 \cdot \pi \cdot d}{\lambda} \tag{3}$$

The phase δ varies with displacements of the measurement mirror and can be evaluated by Eq.3. In the case of R= 25%, λ = 632.8 nm, a simulation result of the interference intensity is

shown in Fig. 3 during the length *d* altered from 0 to 632.8 nm, i.e. two cycles. Evidently the interference signals are not sinusoidal and an elliptical fitting is required for the linear subdivision of the resolution in nanometer-order.

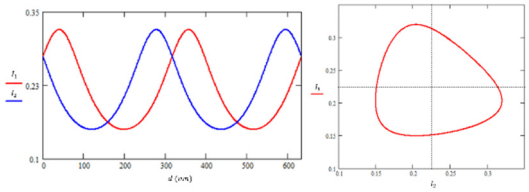

Fig. 3 Intensity distribution of a conventional FPI

Dual Beam Fabry-Perot Interferometer

The modified optical structure of conventional FPI is illustrated in Fig. 4. With this optical arrangement, the non-coaxial path of a Michelson interferometer and non-orthogonal signals of a conventional FPI can be prevented. The first reflected beam from the reference mirror and the second reflected beam from the measurement mirror overlap each other to form the interference. The third beam reflected from the reference mirror is not able to pass through the polarizer P_2 due to the polarization altered by $\frac{\lambda}{4}$ retarder in the resonance cavity as indicated in Fig. 4. In principle, it's the superposition of only two beams as usual interference model and the equations for determining the interference intensity is denoted in Eq.4 and Eq.5. An intensity distribution in Fig. 5 is the simulation result under the condition of *R*= 25%.

$$I_1 = I_0 \cdot \cos(\delta\emptyset) \qquad (4)$$

$$I_2 = I_0 \cdot cos\left(\delta\emptyset - \frac{\pi}{2}\right) = I_0 \cdot sin(\delta\emptyset) \qquad (5),\ \text{here } \delta\emptyset = \frac{4\pi d}{\lambda}$$

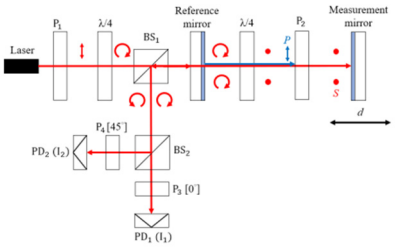

Fig. 4 Schematic diagram of a dual-beam FPI

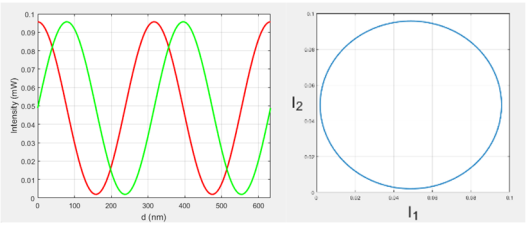

Fig. 5 Intensity distribution of a dual-beam FPI

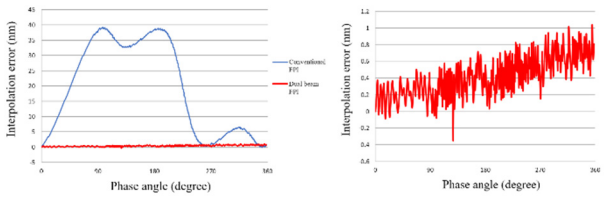

Fig. 6 Interpolation Simulation Analysis

3. *Signal simulation analysis and experiment*

The interpolation simulation analyses yielded the linearity enhancement of the orthogonal signals through the dual beam FPI, as shown in Fig. 6. To verify its orthogonality, it has been fabricated shown in Fig. 7 and the practical testing was carried out. The experimental results in Fig. 8 demonstrated that the linearity error of the dual beam FPI is ca. 0.96 nm that is evaluated by the standard deviation of acquired data. The interpolation error has been significantly eliminated.

ISBN 978-80-69159-00-6

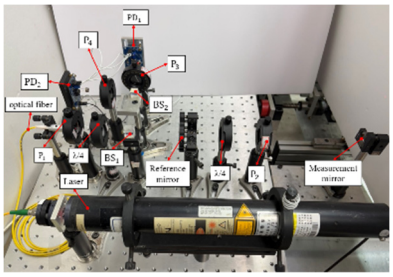

Fig. 7 Optical arrangement of dual beam FPI

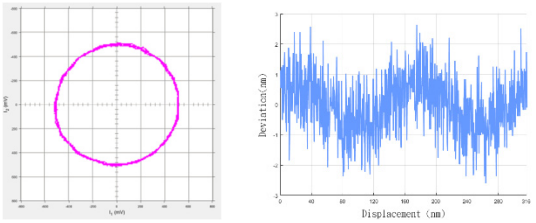

Fig. 8 Experimental signals

4. Conclusion

To deal with the non-orthogonal signals caused by multiple interferences in conventional FPI, a dual-beam modified FPI has been constructed and analysed in the article. By regulating polarization states, the modified interference of a coaxial dual beam FPI can be realized. By theoretical simulations and experimental verification, its practical validity and the concerning measurement performance have been verified. Simulation analyses and experimental results demonstrated that orthogonal signals can be acquired from this novel interferometer such that the complicated signal processing for the conventional FPI will be excluded. That would be beneficial for the simplification of signal processing modules and the elimination of interpolation errors in the conventional FPI where simulation analysis revealed that its maximum error could be around 40 nm that could be eliminated by utilizing the dual-beam FPI with which the linear error has been reduced to ca. 1 nm. Furthermore, the measurement mirror should be altered with a retroreflector e.g. corner cube prism in order to enlarge its measuring ranges when the dynamic tilt angles escalate during the linear motion.

Acknowledgements、Funding

This investigation was funded by National Science and Technology Council (NSTC), Taiwan, under Grant No. NSTC-113-2221-E-224-057. Authors would like to express our gratitude to NSTC for the financial support

References

[1] G. Jaeger, "Limitations of precision length measurements based on Interferometer", Measurement, Vol. 43, Issue 5, pp. 652-658, 2010

[2] G. Jaeger, "Three-Dimensional Nanopositioning and Nanomeasuring Machine with a Resolution of 0.1 nm", Optoelectronics, Instrumentation and Data Processing, Vol. 46, No. 4, pp. 318-323, 2010.

[3] Peter Gregorčič, Tomaž Požar and Janez Možina, "Quadrature phase-shift error analysis using a homodyne laser interferometer", Vol. 17, Issue 18, Optics Express, pp. 16322-16331, August 2009

[4] J. R. Lawall, "Fabry-Perot metrology for displacements up to 50 mm", Journal of the Optical Society of America A, Vol. 22, No. 12, pp. 2786- 2798, 2005.

[5] K. N. Joo, J. D Ellis, J. W Spronck and R. H M. Schmidt, "Design of a Folded, Multi-pass Fabry-Perot Cavity for Displacement Metrology", Measurement Science and Technology, vol. 20, No.10, pp. 107001(5), 2009.

[6] Syuan-Cheng Chang, Chung-Ping Chang, Yung-Cheng Wang, " Linear Displacement and Straightness Measurement by Fabry-Perot Interferometer Integrated with an Optoelectronic Module ", Technical Journal, Vol. 16, No. 3, pp. 420-425, 2022.

Design and Construction of Novel Instrumentation to Measure the Anisotropy of Commonly used Neutron Sources

[1]Daniel Gogola, [2]Pavol Blahušiak, [1]Dušan Mašek, [1]Rudolf Tanglmajer

[1]Institute of Measurement Science, Slovak Academy of Sciences, Bratislava, Slovakia
[2]Department of Ionizing Radiation, Slovak Institute of Metrology, Bratislava, Slovakia
Email: daniel.gogola@savba.sk

Abstract. *Precise measurements and description of properties are an integral parts of metrological standardization. The standardization of neutron sources means the measurement and description of their spatial anisotropy. For this purpose, hardware and software have been developed to automate the measurement of the anisotropy of neutron sources and especially for measurement of neutron detectors response as a function of the angle or angular distribution and thus make the work more comfortable and reliable.*

Keywords: Anisotropy, Neutron Sources, Automatization, Ionizing Radiation, Standardization

1. Introduction

Neutron sources as reference standards are necessary elements in neutron metrology. Real neutron radiation sources are generally not ideally spherical in shape, and neither the active matter in them is uniformly distributed. Therefore, for metrological standardization, it is necessary to know the anisotropy $F(\theta)$ in addition to other parameters such as the emission rate B Eq. 1.

$$B = \frac{\Phi}{4\pi r^2} \tag{1}$$

Where Φ is a neutron fluence rate in $cm^{-2}s^{-1}$ at distance r in cm. The anisotropy is a dimensionless quantity expressing the dependence of the angular orientation between the source, in this case, the neutron source and the detector. The anisotropy $F(\theta)$ can be determined by the equation [1], [2]:

$$F(\theta_i) = \frac{2C(\theta_i)}{\sum_{j=1}^{19} C(\theta_j)\left[\cos\left((\theta_{j-1}+\theta_j)/2\right)-\cos\left((\theta_j+\theta_{j+1})/2\right)\right]} \tag{2}$$

Where C [cps] is the count rate from the detector with respect to the angle of the orientation of the emitter. To obtain the ideal emission rate Eq.3, the Eq. 2 can simply be inserted into Eq. 1. For the purpose of neutron-source anisotropy measurement and last but not least for measurement of neutron detectors response as a function of the angle or angular distribution (for the spatial dose equivalent - H*10), dedicated electromechanical rotating devices are being developed. The main purpose of such devices is to allow measurements of this type to be automated.

Fig. 1 shows a measurement of the anisotropy of a ^{239}Am-Be neutron source (AMERSHAM X14 capsule) that was placed in a prism in the laying position during the measurement. The prism was sequentially rotated with a step of 1.8° during the measurement [2]. The comparison of the measurements, as carried out in the study [2], with the theoretically determined values, reveals the deviations in certain areas.

$$B(\theta_i) = \frac{\Phi}{4\pi r^2} F(\theta_i) \tag{3}$$

ISBN 978-80-69159-00-6

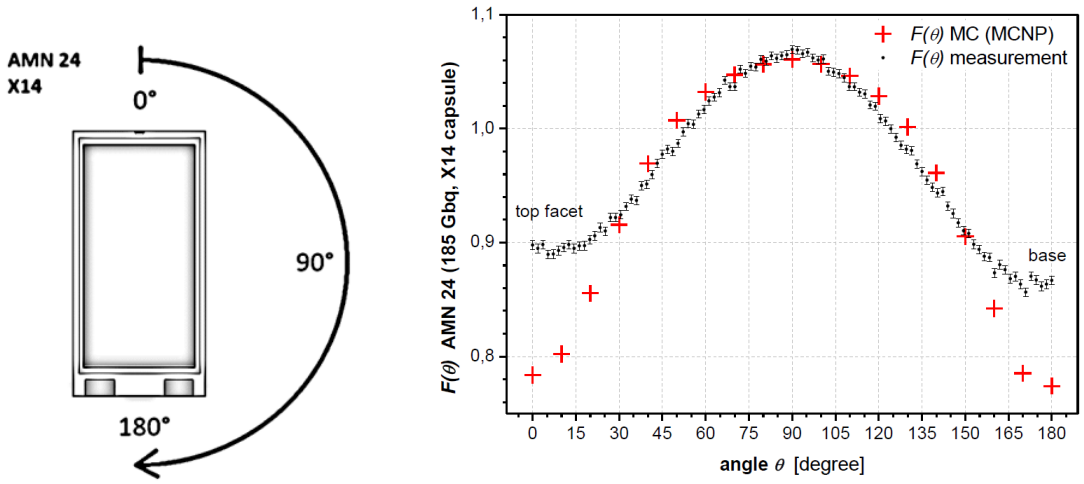

a) b)

Fig. 1. Demonstration of the measurement of the source ^{239}Am-Be anisotropy $F(\theta)$ and its comparison with the Monte Carlo simulation. a) schematic of experimental set-up, b) comparison of measured and simulated values.[2]

2. Subject and Methods

For the purpose of supporting neutron metrology laboratories and for the standardization of neutron emitters, an automated turntable Fig. 2 and associated software was developed.

Hardware

The mechanism of the proposed turntable has a height of 227 mm. The maximum load capacity is 50 kg. The diameter of the turntable is 350 mm. The rotation of the platter is provided by a 12 Nm stepper motor of NEMA 34 series (34HS59-6004D-E1000) with built-in optical incremental encoder. This type of stepper motor together with the Hybrid Servo Drive HSS86 provide a capability of 40000 steps per turn which represents a rotation step of 0.009 degrees. The driver and stepper motor are powered by a MEAN WELL NDR-240-24 switching power supply with a maximum output of 240 W. The driver enables motor control via RS-232 serial link and MODBUS communication protocol. The driver also allows control by General-Purpose Input/Output (GPIO) via pulse, direction and enable signal. The driver also provides status indication such as “In position signal” and “Alarm signal” [3], [4].

Software

A desktop application has been developed for the purpose of controlling the driver. C# was chosen as the programming language. It is a modern, object-oriented programming language developed by Microsoft as a part of the .NET platform. It has been designed to be simple, powerful and secure. C# is widely used in various types of applications, from desktop applications to web and mobile applications. An equally important reason for choosing C# is that it is a very popular programming language with a large community of developers.

3. Results

A drawing of the overall assembly of the proposed device is shown in Fig. 2. The whole structure is made of duralumin material. The stepper motor itself is placed inside the duralumin cylinder which also forms the supporting structure of the device. Two axial bearings were used to define the longitudinal forces. The stepper motor is connected to the rest of the electronics (driver and power supply) by the 4 m long cables, which allows to place this complex electronics outside of the main radiation zone.

ISBN 978-80-69159-00-6

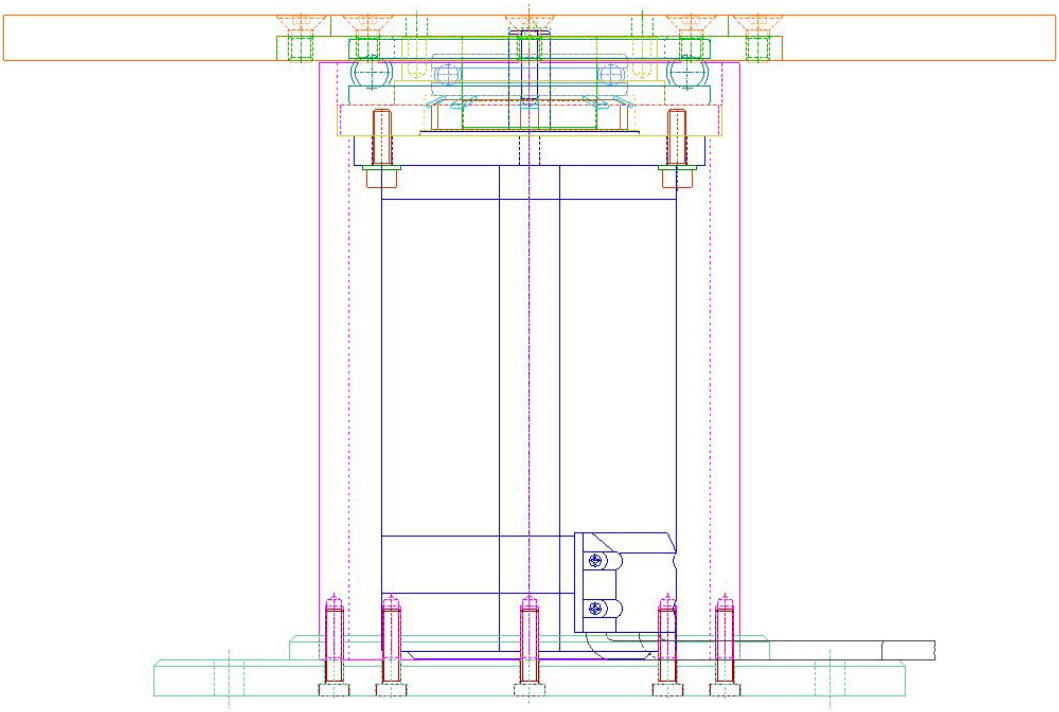

Fig. 2. A drawing of the overall assembly of the proposed device.

The designed application has two language localizations, Slovak and English, which can be switched while the application is running. After start, the application automatically searches for the serial port to which the device is connected. The application allows to start the rotary motion in two modes, namely position control (controlled in the “Step” section) and speed control (controlled in the “Continuous motion” section). For both modes, the rotation speed can be set in the angle per second. The application allows to set the current position of the rotation mechanism as a reference position (position representing zero rotation angle), by pressing the “Starting position” button in the monitor section. The built-in pipeline server functionality allows the application to be controlled by scripts, allowing fully automated measurements. Pipeline is supported in scripting languages such as C# script, PowerShell or Python.

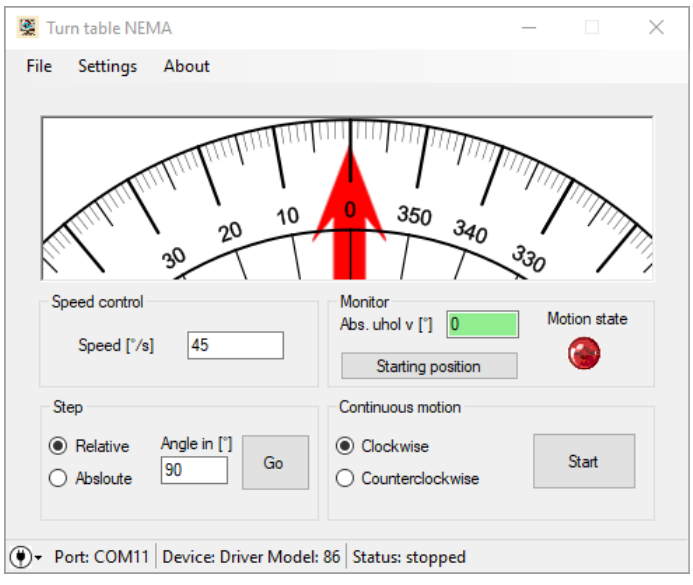

Fig. 3. Program to control the designed turntable.

ISBN 978-80-69159-00-6

4. Discussion and Conclusions

For the purpose of standardization of neutron emitters as well as other measurements in laboratories dealing with neutron metrology, a turntable and software for its operation were developed. The developed application can be easily extended with additional functionalities using scripts such as PowerShell (preferred). Such a script can provide turning of the measured emitter, reading of the measured data, for example from a detection system (BSS 7") and recording it in a file. This approach makes it possible to fully automate the measurement and thus make the overall work more comfortable.

Acknowledgements

This work was supported by Slovak Scientific Grant Agency, project VEGA 2/0004/23. Funded by the EU NextGenerationEU through the Recovery and Resilience Plan for Slovakia under the project No. 09I03-03-V04-00544. This work was supported by the Slovak Research and Development Agency under the contract No. APVV-21-0170.

References

[1] Roberts, N.J., Moiseev, N.N., Králik, M. (2011). Radionuclide neutron source characterization techniques. *Metrologia*, 48 (6), S239. http://dx.doi.org/10.1088/0026-1394/48/6/S02

[2] Blahušiak, P., Javorník, A., Lüley, J., Krivošík, M., Vrban, B., Čerba, Š., Filová, V., Slučiak, J., Šurínová, P., Bonková, I. (2022). Development of device for determination of the neutron source emission rate based on the manganese bath technique in the Slovak Institute of Metrology. *The European Physical Journal Special Topics.*

[3] JB CNC & Linear Components AB, Gislaved, Sweden. (2021). *HSS86 2-phase hybrid stepper servo driver*. https://www.jbcnc.se/images/datasheets/HSS86.pdf

[4] Just Motion Control, Shenzhen. China. *2HSS86H-KH-XX hybrid stepper servo drive*. https://www.jmc-motor.com/uploads/20240730/f1b87e742c12b01fa7436514eceedb95.pdf

Shortening of T_2 Relaxation Time in MRI Due to Presence of Physiological and Pathological Ferritin: Simulations Preliminary Results

[1]Andrej Krafcik,[2]Oliver Strbak

[1]Institute of Measurement Science, Slovak Academy of Sciences, Bratislava, Slovakia,
[2]Jessenius Faculty of Medicine in Martin, Comenius University in Bratislava, Martin, Slovakia
Email: andrej.krafcik@savba.sk

Abstract. *Shown classical description of Néel and Brownian rotation of biogenic iron single domain magnetic nanoparticles (MNPs). They can accumulate in basal ganglia as ferritin in the physiological and pathological form, i.e. native ferritine (NF) and magnetoferritine (MF), respectively. MNPs cause shortening of T_2 relaxivity of water ^{1}H-nuclei (protons) in MRI of human brain. Different magnetic properties of ferritine forms affect protons' relaxation rates. This behavior is modeled as Monte Carlo simulations via protons random-walk around MNPs clusters in B_0 field. Behavior of modeled free induction decay (FID) signal, as the response on a single radio-frequency (RF) excitation pulse on water samples with ferritin content of various form, cluster size, volume fraction, and B_0 is presented. These models could be used for non-invasive monitoring of neurodegenerative diseases progress or their therapy in a future.*

Keywords: Ferritin, Magnetic Resonance Imaging, Monte Carlo Simulations, Stochastic Landau-Lifshitz-Gilbert Equations, Transversal Spin-spin Relaxivity

1. Introduction

The corrupted iron metabolism or its accumulation in non-physiological forms in human body can imply several pathological conditions, such as increased concentrations of biogenic MNPs in human brain's functional and anatomical structures such as basal ganglia. Description of physiological and pathological conditions accompanied with accumulation of this MNPs in brain (FYI it is still not known, if it is cause or effect) on physical level, can elucidate as well as utilize this knowledge for early detection of potential neuro-pathological condition, or to monitoring of its progress using techniques, which are sensitive to magnetic properties of investigated samples and are noninvasive, as e.g., MRI, or magnetic particle imaging (MPI).

2. Subject and Methods

Ferritin magnetic nanoparticles as biogenic iron, its physiological and pathological form, was modeled as spherical magnetic iron-oxide cores in the cavity of NF and MF, respectively, forming MNPs of core and shell diameters of ≈ 8 and 12 nm, respectively. Its physical properties, not only magnetic, was described previously [1, 2, 3, 4]. Ferromagnetic MNPs of such size are single-domain, which in the case of room temperature in the water as ambient fluid imply super-paramagnetic behavior and can be described with stochastic Landau-Lifshitz-Gilbert equations (sLLG) [5]:

$$\frac{\partial \vec{m}}{\partial t} = \vec{\omega} \times \vec{m} - \frac{\gamma_e}{1+\alpha^2} \left\{ \vec{m} \times \left(\vec{B}_{\text{eff}} - \frac{\vec{\omega}}{\gamma_e} \right) + \alpha \vec{m} \times \left[\vec{m} \times \left(\vec{B}_{\text{eff}} - \frac{\vec{\omega}}{\gamma_e} \right) \right] \right\}, \tag{1}$$

$$\vec{I}_{\text{p}} \cdot \frac{\partial \vec{\omega}}{\partial t} + \kappa \vec{\omega} = \frac{\mu_{\text{s}}}{\gamma_{\text{e}}} \frac{\partial \vec{m}}{\partial t} + \mu_{\text{s}} \vec{m} \times \left(\vec{B}_0 + \vec{B}_{\text{th}} \right) + \vec{N}_{\text{th}}, \tag{2}$$

$$\frac{\partial \vec{n}}{\partial t} = \vec{\omega} \times \vec{n}, \tag{3}$$

ISBN 978-80-69159-00-6

where $\vec{B}_{\text{eff}} = \vec{B}_0 + \vec{B}_{\text{an}} + \vec{B}_{\text{th}}$, $\vec{B}_0$, and $\vec{B}_{\text{an}} = 2\frac{K_{\text{m}}}{M_{\text{s}}}(\vec{m}\cdot\vec{n})\vec{n}$, $\vec{B}_{\text{th}}$ are an effective, an external homogeneous magnetic (e.g. in MRI), a magnetic anisotropy flux density field, and a thermally fluctuating magnetic flux density field, respectively. The $\vec{B}_{\text{th}}$ has zero mean and variance defined as $\left\langle B_{\text{th},i}(t)B_{\text{th},j}(t')\right\rangle = 2\alpha\frac{k_{\text{B}}T}{\gamma_e\mu_{\text{s}}}\delta_{ij}\delta(t-t')$, where δ_{ij} is Kronecker delta with indices for Cartesian components, and $\delta(t-t')$ is Dirac delta function. In equation (2) is presented additional stochastic term as thermally fluctuation torque $\vec{N}_{\text{th}}$ with zero mean and variance of magnitude $\left\langle N_{\text{th},i}(t)N_{\text{th},j}(t')\right\rangle = 2\kappa k_{\text{B}}T\delta_{ij}\delta(t-t')$ due to thermal motion of water molecules surrounding MNPs. The symbols $\vec{n}$, $\vec{m}$ and $\vec{\omega}$, $\vec{I}_{\text{p}}$, K_{m}, μ_{s}, γ_{e}, α, κ, T, k_{B}, $M_{\text{s}} \equiv \frac{\mu_{\text{s}}}{V_{\text{m}}}$, and V_{m} used in above equations define unit vector of easy magnetization axis, magnetization axis and angular velocity vectors, particle inertia tensor, magnetic anisotropy constant, magnetic moment of MNP, electron gyro-magnetic constant, damping parameter, Stokes friction coefficient, temperature, and Boltzmann constant, saturation magnetization, and volume of magnetic core, respectively.

Solution of the sLLGs, as 6-dimensional stochastic differential equations (SDEs) system with 6-independent Wiener processes, was obtained using Runge-Kutta-type method for solution of SDEs with small noise [6]. The N MNP ensembles whit their averaged longitudinal magnetization of ferritin MNPs for each B_0 and T over N ensembles give dependence $\langle m_z\rangle_N(B_0)$.

The Monte Carlo simulations: Obtained averaged magnetization of MNPs in B_0 field was an input for further Monte Carlo simulations [7] of diffusion of water molecule with ^{1}H nuclei around such MNP cluster (see Fig. 1b) with volume fraction f in B_0 field, for time evolution of macroscopic sample over N_{s} spins' ensemble average of transverse magnetization of accumulated phases of spins $\hat{m}_{xy}(t_k) \equiv \frac{1}{N_{\text{s}}}\sum_{j=1}^{N_{\text{s}}}\exp\left[i\phi_j(t_k)\right]$. In diffusion model of water molecule with ^{1}H nuclei spins we simulate their random walk around MNPs clusters. Each cluster consists of N_{p} ferritin MNPs and is handled as compact structure with its random initial relative rotation and position to the $\vec{B}_0$ field, and random initial relative position of N_{s} ^{1}H nuclei. Discrete jumps of water molecule with magnitude jump $\equiv\sqrt{6D\Delta t}$ are defined with the self-diffusion coefficient of water D at temperature T and time-step size Δt for spin in radial distance r_i and angle θ_i between magnetization vector $\vec{M}$ with origin in the i-th MNP center in the cluster. Clusters are randomly orientated in space relatively to the $\vec{B}_0$. Each spin feels $B_z \equiv \sum_{i=1}^{N_{\text{p}}}\sqrt{\frac{5}{4}}\frac{\Delta\omega_r r_{\text{m}}^3}{\gamma_{\text{p}}}\frac{\left(3\cos^2\theta_i-1\right)}{r_i^3}$. The $\Delta\omega_r = \frac{8\pi}{3\sqrt{5}}\gamma_{\text{p}}M\mu_0$ is a root-mean-square angular frequency shift at the MNP's magnetic core surface in rad/s, with r_{m}, γ_{p}, and μ_0 as the MNP's magnetic core radius, proton gyromagnetic ratio, and vacuum permeability, respectively. The j-th spin in $(k+1)$-th time step $t_{k+1} = t_k + \Delta t$ change phase according $\phi_j(t_{k+1}) = \phi_j(t_k) + \Delta\phi_j$, where $\Delta\phi_j = \gamma_{\text{p}}B_z\Delta t$.

The T_2^* relaxation time, i.e. the transverse spin-spin relaxation time, is further obtained from the time exponential decay of transverse magnetization signal $m_{xy}(t)$ of N_{s} ^{1}H nuclei spins ensemble in macroscopic sample of water and MNPs with volume fraction f of clusters formed with N_{p} MNPs to the $\exp(-1)$ fraction from its maximum value at the beginning of the simulation. These dependencies can be experimentally observed during capturing of FID signal in MRI receiver coil in specimen of spins excited by $\frac{\pi}{2}$-RF-pulse to the transverse plane. In addition to the single-pulse excitation sequence, CPMG (i.e. Carr-Purcell-Meiboom-Gill mechanism) sequence was also simulated. The CPMG sequence contains phase π-flipping pulses every half of a specified echo time TE with result in reduction of local inhomogeneities in the external static magnetic field. Its characteristic time for exponential decay is known as spin-spin T_2 relaxation time.

ISBN 978-80-69159-00-6

3. Results

After sufficiently long simulation time of a sufficiently large ensemble of MNPs for both forms of ferritin, the sLLGs system reached steady state for each B_0 field with dependence of averaged longitudinal magnetization over N MNPs on B_0 field, $\langle m_z \rangle_N (B_0)$, shown in Fig. 1a. This dependencies can be fitted with Langevin function for classical paramagnetism.

Averaged steady MNPs' longitudinal magnetization $\vec{M} \equiv \vec{e}_z \, V_\mathrm{m} \langle m_z \rangle_N (B_0)$ enters algorithm for Monte Carlo simulation of T_2/T_2^* relaxation times. Their reciprocal values define R_2/R_2^* relaxation rates. The relaxation rate obtained from the simulations with specific N_p of MNPs in cluster, their f, and particular B_0 field and TE are shown for NF and MF in Fig. 2.

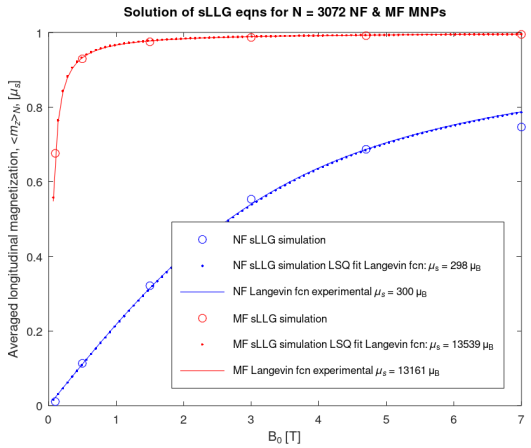

(a) Averaged longitudinal magnetization over N ferritin MNPs ($\langle m_z \rangle_N$) from simulation. Shown LSQ fit as Langevin function of simulation points for NF and MF MNPs with particle saturation magnetic moment (μ_s); and Langevin function for experimental saturation magnetic moment.

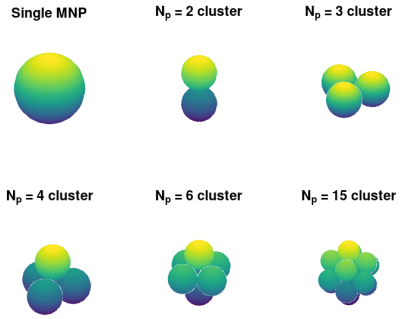

(b) Considered configurations of MNPs into the clusters.

Fig. 1: (Color online.) Magneto-ferritin (MF) and native ferritin (NF) magnetic nanoparticles (MNPs) in external B_0 fields and water with temperature $T = 300\,\mathrm{K}$ simulated by the solution of the stochastic Landau-Lifshitz-Gilbert equations. A Bohr magneton is denoted as μ_B.

4. Discussion

Presence of ferritin MNPs in native physiological, as well as pathological form strongly affect water ^{1}H nuclei spin-spin transverse relaxation rates increasing with raising of MNPs volume fraction f in specimen. The effect is magnified for pathological form of biogenic iron in magnetoferritin, which is in accordance with the knowledge that accumulated iron in neural structures like basal ganglia for neuro-pathological conditions shortens the transverse spin-spin T_2 and T_2^* relaxation times with amplified negative contrast in T_2 weighted MRIs of this structures.

Acknowledgements

This work was supported by the Slovak Research and Development Agency (APVV-22-0122), the Slovak Scientific Grant Agency (VEGA 2/0004/23), and the Ministry of Health of the Slovak Republic (2018/11-UKMT-7).

References

[1] Papaefthymiou, G. (2010). The Mössbauer and magnetic properties of ferritin cores. *Biochimica et Biophysica Acta - General Subjects* 1800(8), 886–897.

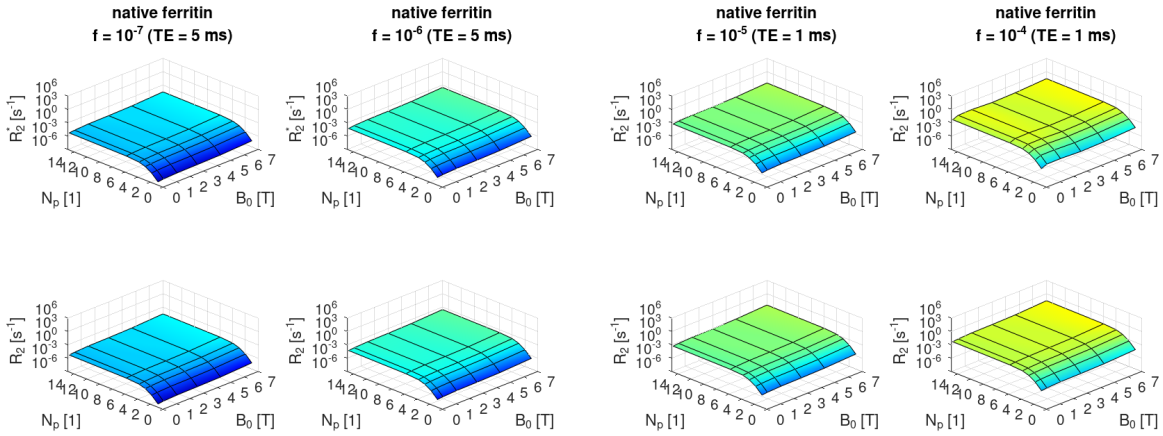

(a) R_2 relaxivity for NF, TE = 5 ms.

(b) R_2 relaxivity for NF, TE = 1 ms.

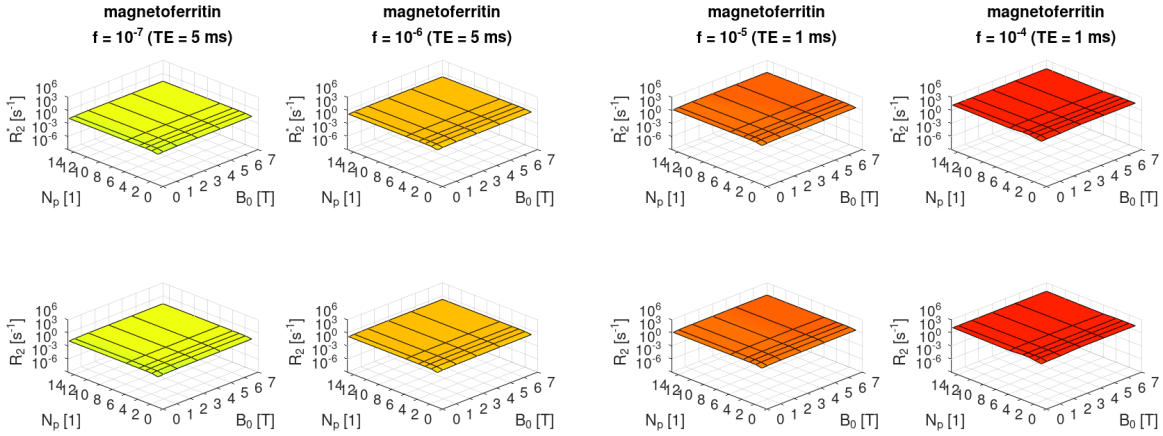

(c) R_2 relaxivity for MF, TE = 5 ms.

(d) R_2 relaxivity for MF, TE = 1 ms.

Fig. 2: (Color online.) The R_2^* and R_2 relaxation rates of water ^{1}H nuclei affected with the presence of clusters of N_p ferritin magnetic nanoparticles in water as fluid ambient with specified volume fraction f and MRI magnets with defined B_0 magnetic flux density field obtained with Monte Carlo simulations of $N_\mathrm{s} = 16\,000$ spins per grid point in each surface plot.

[2] Moro, F., De Miguel, R., Jenkins, M., et al. (2014). Magnetic anisotropy of polycrystalline magnetoferritin investigated by SQUID and electron magnetic resonance. *Journal of Magnetism and Magnetic Materials* 361, 188–196.

[3] Chasteen, N., Harrison, P. (1999). Mineralization in ferritin: An efficient means of iron storage. *Journal of Structural Biology* 126(3), 182–194.

[4] Bulte, J., Douglas, T., Mann, S., et al. (1994). Magnetoferritin: Characterization of a novel superparamagnetic MR contrast agent. *Journal of Magnetic Resonance Imaging* 4(3), 497–505.

[5] Usadel, K., Usadel, C. (2015). Dynamics of magnetic single domain particles embedded in a viscous liquid. *Journal of Applied Physics* 118(23).

[6] Milstein, G., Tretyakov, M. (2021). *Stochastic Numerics for Mathematical Physics*. Springer Nature Switzerland AG 2021: Springer Cham, second edition.

[7] Matsumoto, Y., Jasanoff, A. (2008). T2 relaxation induced by clusters of superparamagnetic nanoparticles: Monte Carlo simulations. *Magnetic Resonance Imaging* 26(7), 994–998.

ISBN 978-80-69159-00-6

Measurement of Resistance/Force Conversion Characteristics of FSR Elements for Evaluation of Contact Skin Pressure by PPG Sensors

Jiří Přibil, Anna Přibilová, Tomáš Dermek

Institute of Measurement Science, SAS, Bratislava, Slovak Republic.
Email: Jiri.Pribil@savba.sk

Abstract. *This paper describes realization of a simple measuring tool for easy, but precise investigation of resistance/force conversion characteristics of force-sensitive resistors (FSR) by comparative measurements with the help of calibration weights. Due to proposed further use of FSRs in measurement experiments with human subjects, only a lower part of the force range (up to 250 grams) was investigated. Then, a linearization of depicted FSR's conversion characteristics based on the linear regression was performed. This is important for practical implementation into the control program of the currently proposed prototype of a wearable multi-sensor working on a photoplethysmography principle.*

Keywords: Force-Sensitive Resistor, Contact Skin Pressure, Photoplethysmography Signal

1. Introduction

Optical sensors based on photoplethysmography (PPG) have been successfully used for a long time in clinical practice for non-invasive investigation of the human cardiovascular system [1]. At present, PPG sensors are increasingly applied for continual monitoring of cardiorespiratory parameters during some fitness or sporting activities [2]. The quality of sensed PPG waves depends on the actual state of a skin surface and on the applied contact pressure force at the site of sensor placement. This is most important in the case of wearable multi-channel PPG sensors [3] and smart devices used for monitoring of different vital parameters. A lot of studies confirmed the effect of degradation of the sensed PPG signal due to too low or too high contact pressure applied on the skin of the finger (wrist) [4]. The localized physical pressure can be measured using force-sensitive resistors (FSR) [5].

We are focused on mapping of physiological and mental effects of scanning in the magnetic resonance imaging (MRI) tomograph on the examined person based on real-time sensed multi-channel PPG signals. For this purpose, we realized several prototypes of wearable PPG sensors [6]. In the last period, we tried to develop a PPG sensor enabling contact pressure force (CPF) and skin temperature measurement where the CPF intensity is measured by an FSR component. Before its practical use within the wearable PPG sensor, the resistance/force conversion characteristics must be verified by comparative measurements.

This paper describes the realization of a simple measuring tool and its use for investigation of the resistance/force conversion characteristics of two types of FSR components by comparative measurements with the help of calibration weights. The developed measuring tool can work in the manual mode when the measurement is controlled by an integrated touch panel on the output graphical display, or in the semi-automatic mode when the measurement process is controlled by an external control device (notebook, tablet, etc.) via wireless BT connection. Due to the use of FSRs in measuring experiments with human subjects, only a lower part of the force range (up to 250 grams) was investigated. Finally, a linearization of depicted conversion characteristics based on the linear regression approach was proposed for easier implementation into the PPG sensors' control program.

ISBN 978-80-69159-00-6

2. Methods and Subject

2.1. CPF calculation of the FSR elements

FSR elements are based on the polymer thick film which exhibits a decrease in resistance with an increase in the force applied to the active surface. As documented by an example in Fig. 1, there exists a non-linear dependence between the resistance in kΩ (or conductance in mS) of the FSR and the force in grams. For measurement of the applied pressure force based on the FSR, the voltage divider using a pull-down resistor $R1$ is usually applied. The actual resistance of the FSR is given as $R_{FSR} = R1 \times (V_{CC} / V_{OUT} - 1)$ [kΩ], where V_{CC} is applied power supply voltage, and V_{OUT} is an output voltage of the voltage divider. To express the force in grams the conductance of the FSR is calculated as $G_{FSR} = 1/R_{FSR}$ [mS]. The resistance of the used $R1$ has influence on the output range of V_{OUT} and G_{FSR} values. Hence, the parameter G_{RANGE} defined as difference between G_{FSR} values for maximum (Fg_{MAX}) and minimum (Fg_{MIN}) applied force $G_{RANGE} = G_{FSR}(Fg_{MAX}) - G_{FSR}(Fg_{MIN})$ was used to describe the final sensitivity of the FSR element. The conductance curve (G_{FSR}) can be linearized by one or more-line parts, using a linear regression based on mean square method (MSE). To evaluate linearization accuracy, the difference ΔFg between really applied force by weights (F_W) and determined from the linearized G_{FSR} curve (F_{LIN}) is $\Delta Fg = F_W - F_{LIN}$ [gram]. These values are analyzed to obtain basic statistical parameters: minimum, maximum (ΔFg_{MAX}), mean (ΔFg_{MEAN}), and standard deviation – std (ΔFg_{STD}) for further comparison.

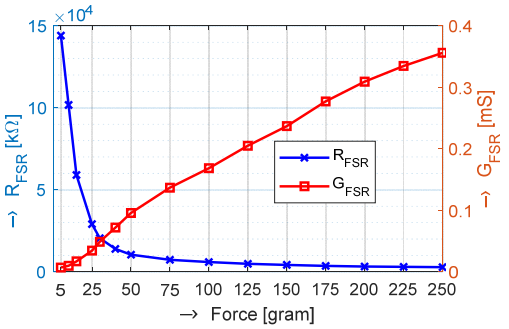

Fig. 1. Example of resistance/conductance vs. force conversion characteristics for an FSR element.

2.2. Description of the measuring tool for FSR elements

The developed prototype of the measuring tool consists of: (1) the Arduino micro-controller board Nano v. 3.3 based on the processor ATmega328P with integrated eight 10-bit A/D converters, working at 16 MHz[1], (2) the BT BLE communication module MLT-BT05, working at 2.4 GHz in BT 4.1 standard, (3) the programmable touch control panel EA KIT160-6 LEDTP[2], (4) the measuring plate for testing of different types of FSRs. All parts are supplied via a USB port by a 5 V power bank. For these calibration measurements, a set of 8 calibration weights 10g-500g in the accuracy class M2[3] was used. The measuring plate enables testing of FSR®400 with 4 mm diameter active sensing area and FSR®402 ones with 13 mm circle area. If no pressure is applied to the FSR, its resistance is more than 1 MΩ, with full pressure applied the resistance is typically about 2.5 kΩ[4]. The symbolic switch of pull-down resistors $R1$a-e in the wiring diagram in Fig. 2 was realized as a connection to pins of a parallel digital port of the ATmega328P. The capacitor $C1$ connected in parallel suppresses possible peaks and performs partial integration of the analog signal V_{OUT} connected to the processor's A/D converter.

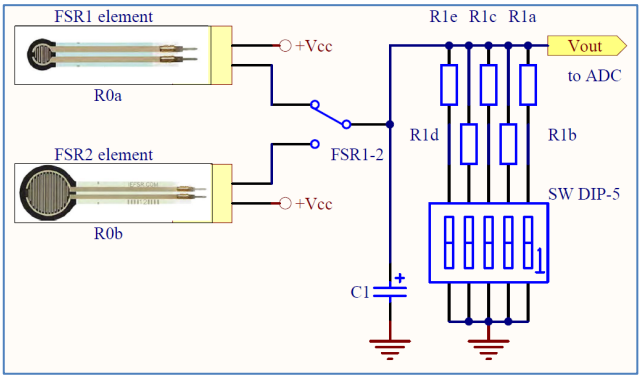

Fig. 2. Principal wiring diagram of the measuring plate for FSR®400/402 components.

[1] http://arduino.cc/en/Main/ArduinoBoardNano
[2] https://www.lcd-module.de/lcd-module/produkte/touch.html
[3] https://www.kern-sohn.com/shop/en/products/test-weights/oiml-m2/354-04/
[4] https://www.sparkfun.com/datasheets/Sensors/Pressure/fsrguide.pdf

ISBN 978-80-69159-00-6

The whole measuring tool can work in manual or semi-automatic modes. In the manual mode the measurement is controlled via the 160x80 dots display with an integrated touch panel connected to the Arduino micro-controller and communicates via the RS-232 interface. The measuring parameters (power supply voltage V_{CC}, type of FSR, and $R1$ value) are set with the help of a virtual key on the touch panel. Obtained discrete V_{OUT} and calculated R_{FSR}, G_{FSR}, and F_{MEAS} values are immediately shown on the display, without any storing or other processing. When the semi-automatic mode is chosen, the Arduino board creates a wireless BT connection with an external control device (PC, notebook, etc.) and next works as a "slave" device – waiting for commands from a "master" control device and subsequently performing requested operations. Setting of measuring parameters and real-time transmission of a digitalized analogue signal V_{OUT} is operated wirelessly from the control device. The received data blocks can be stored to an external file in the MS Wave form (with 16-bit quantization, mono, PCM coding) for further analysis in the Matlab environment.

3. Experiments and Results

While both tested FSR types can measure forces to 1 kg, we investigated only the lower part of the force range up to 250 grams due to planned mapping of the CPF effect caused by an optical part of a wearable PPG sensor. The truncation of the force range originates from real conditions of experiments with human subjects, where the CPF applied on fingers is practically limited by possible pain or other negative impacts. Therefore, measurements with applied 15 force values by weights of Fg = {5, 10, 15, 25, 30, 40, 50, 75, 100, 125, 150, 175, 200, 225, and 250 grams} were performed only. First, for each applied force the corresponding V_{OUT} value is measured manually. Then, in semi-automatic mode, 4-k sample data records of V_{OUT} signal sampled at f_S = 125 Hz were received and stored. Next, $R_{FSR}(Fg)$ relations and G_{FSR} conversion characteristics were calculated with finally denoted linearization by the MSE method. This set of measurements was repeated for five values of the push-down resistor – $R1$ = {2.2, 3.3, 4.7, 6.8, and 8.2 kΩ} and two tested FSR types. In this way, we finally collect a small database consisting of 2×5×15=150 data records in total. Visualization of the influence of the used resistor $R1$ value on G_{FSR} for FSR®402 type is shown in Fig. 3, detailed numerical comparison is shown in Table 1. Partial results of the applied linearization of G_{FSR} conversion characteristics are visualized in Fig. 4. Summary numerical results of determined features of both tested FSRs are presented in Table 2.

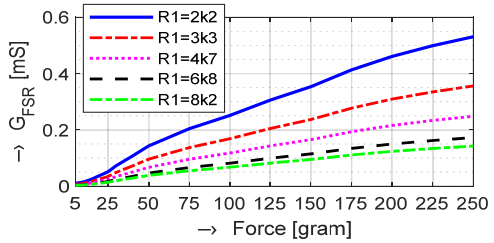

Fig. 3. Influence of a push-down resistor $R1$ on G_{FSR} for FSR®402; V_{CC}=4.98V.

Table 1. Numerical comparison for using different $R1$ values for FSR®402 element type; V_{CC} = 4.98 V.

FSR®402	R1a	R1b	R1c	R1d	R1e
$R1$ [kΩ]	2.2	3.3	4.7	6.8	8.2
V_{OUT} [V] A)	2.78	2.30	1.60	1.11	0.75
G_{RANGE} [mS] B)	0.531	0.356	0.248	0.173	0.142

A) for Fg = 50 grams. B) Fg_{MAX} = 250, Fg_{MIN} = 5 grams.

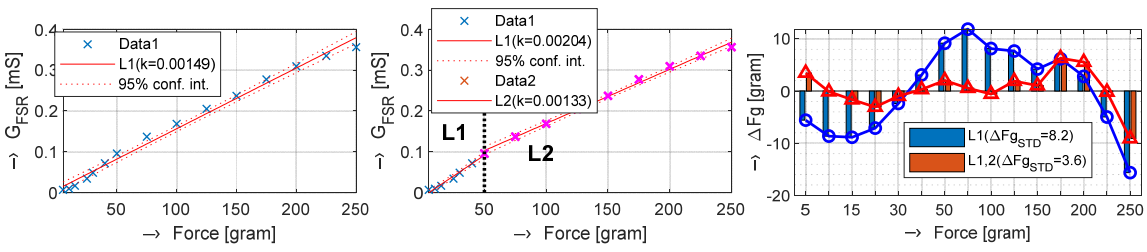

Fig. 4. G_{FSR} linearization: a) one line for whole range Fg_{L11}=<5÷250>, b) two-line parts: Fg_{L21}=<5÷50), Fg_{L22} = (50÷250> with denoted 95% confidence intervals, c) resulting ΔFg, ΔFg_{STD} values; FSR®402, $R1$=3.3kΩ.

Table 2. Summary numerical comparison of determined FSR features for $R1$=3.3 kΩ.

FSR type	Sens. area [mm^2]	G_{RANGE} [mS]	Directions k_{L11}; k_{L21}/k_{L22} [$\times 10^{-4}$]	ΔFg_{MAX} L1/L1,2 [gram]	ΔFg_{MEAN} L1/L1,2 [gram]	ΔFg_{STD} L1/L1,2 [gram]
FSR®400	12.57	0.301	7.7; 11/7.1	-12.8/5	1.4e-14/-0.36	7.8/2.9
FSR®402	122.72	0.356	15; 20/13	-15.6/-9.1	1.4e-12/0.37	8.2/3.6

4. Discusion and Conclusion

The developed measuring tool was successfully used in comparative measurements of FSR®400/402 components with the help of calibration weights in the range from 5 to 250 grams and their conversion characteristics were subsequently linearized. The performed measurements confirm that the resistance/force characteristics have markedly hyperbolic character. Hence, the conductance curve (G_{FSR}) which can be linearized by one or more-line parts, was finally used for contact force calculation in the Arduino micro-controller and/or in the Windows control application. The preliminary analysis of the influence of the used push-down resistor $R1$ on measured G_{FSR} characteristics shows that higher $R1$ decreases the G_{FSR} nonlinearity, but also dynamic range (sensitivity). Therefore, as a compromise choice, setting of $R1$ = 3.3 kΩ was finally used in the main investigation experiment. Both types of measured FSRs are constructed with the same technology but differ in the effective size of sensing area. For the same reason, they also differ in sensitivity, dynamic range of G_{FSR} and finally, different linearization parameters (direction coefficient $k_{11}/k_{21,22}$) must be applied. The two-part linearization always produces lower $\Delta Fg_{MAX, MEAN}$ and ΔFg_{STD} values as documented in Table 2. In this case, Fg=50 gram as a border value was used to switch the linearization parameters – see Fig. 4a,b, where just about this point the G_{FSR} curve changes its slope.

In the next research step, both FSR types will be assembled to optical parts of a multi-channel PPG sensor which is typically worn on finger(s) and a wrist [6]. When it is necessary to sense the PPG wave in a vein or an artery, the size of the used PPG sensor part is greater than the finger's one, so the FSR element with larger sensing area may be applied. Therefore, we will map the conversion characteristics of other FSR components – e.g. the FSR®404 type (20 mm Donut with 5.5 mm hole) in the near future.

Acknowledgements

This work was funded by the project VEGA 2/0004/23.

References

[1] Bonomi A.G. et al. (2018). Atrial fibrillation detection using a novel cardiac ambulatory monitor based on photo-plethysmography at the wrist, *J. Am. Heart Assoc.,* 7, e009351.

[2] Charlton, P.H., Marozas, V. (2022). Wearable photoplethysmography devices. In P.A. Kyriacou, and J. Allen (Eds.) *Photoplethysmography: Technology, Signal Analysis, and Applications*, pp. 401–438, Elsevier: London, UK.

[3] Kuduz, H., Kacar, F. (2024). Biomechanical sensor signal analysis based on machine learning for human gait classification. *Journal of Electrical Engineering*, 75 (6), 513-521.

[4] L. D'Acquisto, et al. (2019). A preliminary investigation of the effect of contact pressure on the accuracy of heart rate monitoring by wearable PPG wrist band. In Proceedings of the *II Workshop on Metrology for Industry 4.0 and IoT* (MetroInd4.0&IoT), Naples, Italy, 2019, pp. 334-338.

[5] Dontha B. et al. (2022). Wearable sensors based on force-sensitive resistors for touch-based collaborative digital gaming. *Sensors*, 22, 342.

[6] Přibil, J., Přibilová, A., Frollo, I. (2022). Comparison of Three Prototypes of PPG Sensors for Continual Real-Time Measurement in Weak Magnetic Field. *Sensors*, 22, 3769.

Flexible Remote Teaching Workplace Configured for DMM Frequency Error Measurement

Miroslav Kamenský, Imrich Szolik, Martin Gabrišák, Ján Halgoš

Slovak University of Technology in Bratislava, Faculty of Electrical Engineering and Information Technology, Institute of Electrical Engineering, Bratislava, Slovakia, Email: miroslav.kamensky@stuba.sk

Abstract. *Our institute is gradually building the modular system of remote access workplaces. It simplifies the design of a new didactic workplace. The principles of the system and the process of adding a new module are explained in the paper. The software part of the recently designed module is oriented towards configurable SCPI communication, where the teacher, as a local user, determines the sequence of commands sent to the device. In the hardware part, we used a digital multimeter (DMM) with this configurability and an arbitrary function generator. This pare of devices allows several measurement configurations. During classes it was employed for additional frequency error measurement of a DMM. We received feedback from 40 students who appreciated the remote tool as a supporting aid.*

Keywords: Remote Access, LabVIEW, E-learning, Frequency Error of DMM, SCPI

1. Introduction

The teacher tries to impart the highest possible level of knowledge to his students. However, there are several limitations to the teaching process. Typically, it is the time designated for the given taught subject, the recent level of knowledge of the students and their abilities, but also abilities of the teacher. In technical disciplines, another aspect is the availability of technological resources, while the preparation of didactic equipment is also the task of teachers. It is often useful to design own software to work with the devices, which increases pedagogical efficiency.

At our Institute of Electrical Engineering, we have been using various software tools. One can just extend MS Excel with macros to collect data from a data acquisition (DAQ) device or create a Matlab script when advanced data processing is required. As our team belongs to the department of measurement, we have often controlled programmable T&M hardware from National Instruments (NI) environments LabWindows and LabVIEW. In more specialized cases, like for image recognition or for automated measurement systems, one might prefer standard programming languages like C++ or C#. Whatever the tool is, adding a remote control to the workplace was a general trend [1] and might bring advantage of reducing some pedagogical limitations. Therefore, we gradually expanded our software designs to include remote access.

E-learning represents a modern approach to distance education and a way to enable effective studies for people who cannot be present daily. Its importance has grown significantly during the COVID-19 pandemic. Specialized Learning Management Systems (LMS) were designed years ago, while modern platforms like Zoom or MS Teams supporting remote meetings became popular recently due to added interactivity [2]. Learning platforms and team collaboration applications are powerful environments for e-learning practices. However, one still needs to find a way of establishing remote access to hardware resources relevant to the subject matter.

ISBN 978-80-69159-00-6

In the paper, we present our actual approach and state of development of the system for remote access. The system can be employed as a supporting tool for traditional education or also as an aid for establishing effective laboratory exercises in the case of distance learning.

2. Subject and Methods

LabVIEW has become standard equipment at technical universities. It is based on easy to learn graphical programming language G. Still, it is a real programming environment which makes programming more convenient for non-IT oriented technicians. It is also rich in libraries oriented in measurement and DAQ. For our department of measurement, it was a natural choice to build didactic software using LabVIEW. There are more common languages like C++, C#, Visual Basic, Java etc. some of them used at our workplace too. So, we would desire to build a modular software system where modules designed in different environments might co-exist.

LabVIEW offers tools and libraries that accelerate design of modern measurement workplace. For establishing a remote access there are several strategies [1]:

a) Remote Panel has been the most traditional approach available for years. In addition to configuring the LabVIEW Web Server, it can be activated in the Block Diagram window of a standard application via an easy-to-use Web Publishing Tool.

b) Web Service – supported from LabVIEW version 8.6 also uses built-in Web Server. Web Service can be established within the LabVIEW project. It is a more challenging approach as HTML with JavaScript parts are needed to form the project front-end.

c) Third party tools – request extra means (e.g. LabVNC) and experiences but the tool might be multiplatform and principally simplifies the task.

d) G Web Development Software – is a modern and quite recent module that came to LabView as a follow-up to the LabVIEW NXG editions.

Remote Panel is the easiest way for the designer and was our original preference, however, it requires LabVIEW Runtime Engine to be installed on client computers. Later, we wanted to allow remote access from smartphones, too. Therefore, we started building our own front-end in the Web Service project [3]. We decided to create a modular system where a target DoModule controls the didactic workplace, and a publishing module called GoProject is responsible for data and control distribution (Fig.1). This simplifies migration from one technology to another.

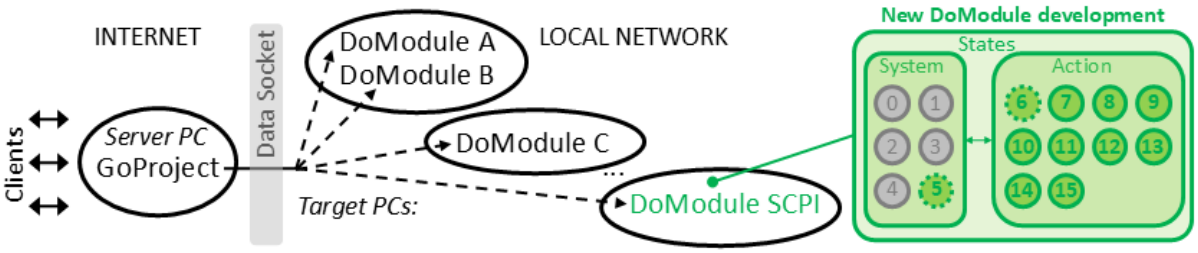

Fig. 1. Simplified structure of remote access system: GoProject is located on a server computer accessible via the internet, and DoModules are running on local computers. The green part describes actions needed for the development of the new SCPI DoModule.

Target and publishing modules cooperate in our software system via DataSocket variables, which is a network technology available within LabVIEW. GoProject residing on a separate server computer can stay immutable when adding a new workplace. This approach simplifies designs of a new workplaces and offers software security for target computers. The activities needed in the process of development of a new DoModule are shown in green in Fig.1. If we

ISBN 978-80-69159-00-6

use a standard older module (market generally as A, B, C in Fig.1) working as a state machine, most of the system states 1-5 [3] responsible for communication with GoProject do not change, only state 5 requires modification in decisions about which state to follow. Within action states the control of hardware is realized and a total of 10 of these states were used in the new SCPI DoModule. Some action states might be partially inherited like state 6 initializing user buttons.

3. SCPI workplace of additional error measurement

There are a number of dedicated university workstations [4] designed for remote access, and in the past, we have also developed quite unique modules that run under our modular software system. Our recent effort should have been aimed at creating a more flexible workplace using common programmable measuring instruments controlled via SCPI (Standard Commands for Programmable Instruments) commands. This should make it possible to cover several topics by one set-up. The workplace we arranged consisted of two programmable instruments controlled from the same PC: single channel arbitrary function generator (AFG) Tektronix AFG2021 and digital multimeter (DMM) Agilent 34405A. The way we let a user access both devices was different. For AFG the user might set parameters via a Parameter edit line of UI (Fig.2) confirmed by AFGout button. Such parameter can be frequency only, or also space-separated Low and High voltage levels. The corresponding sequence of SCPI commands is chosen automatically by the software. In the case of DMM, there is a submenu behind the Setup DMM (1) button. Then it is possible to edit sequence of SCPI commands. In order to evaluate the amplitude characteristic, only one command MEAS:VOLT:AC? to measure AC voltage is necessary. The system was configured by teacher such that the frequency set on AFG and last reply from DMM will be used as data for graph. A point is added to the plot every time the Meas button is pressed or the graph data are cleared via the Clear Graph button.

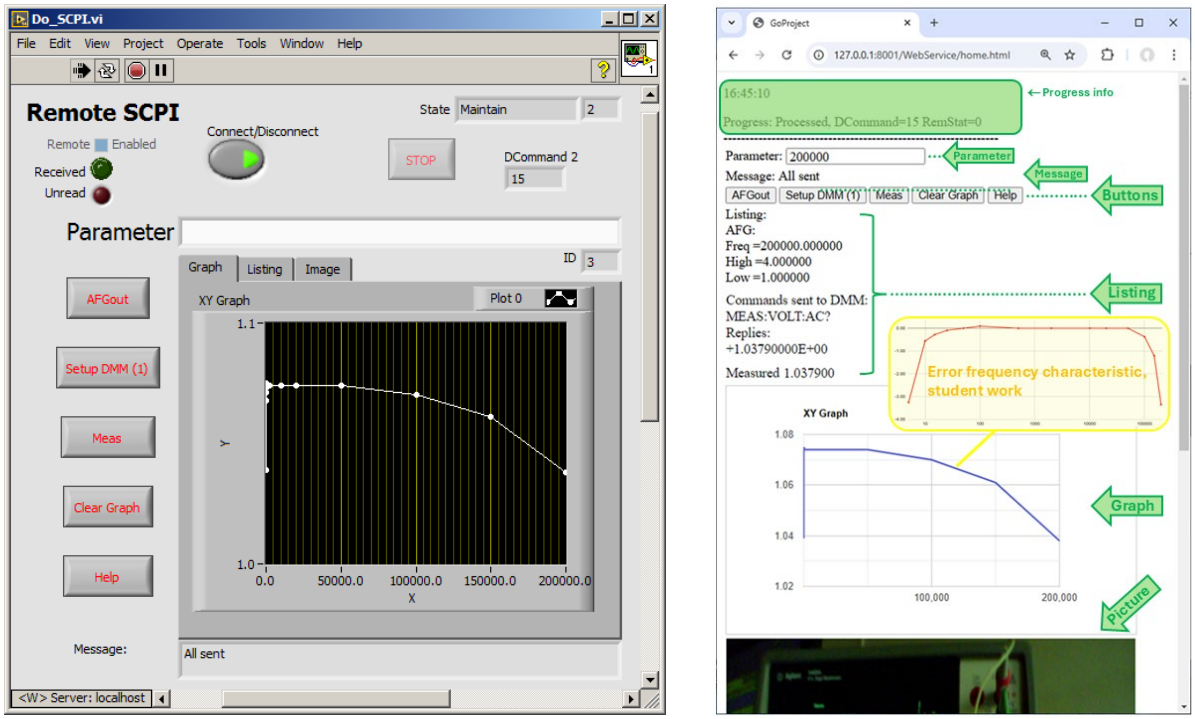

a) b)

Fig. 2. UI of the designed pair of applications: a) DoModule allowing local operation; b) GoProject intended for mediating remote connections: in green, comments are added explaining the parts corresponding to DoModule controls, and the yellow frame shows the characteristic after processing in MS Excel.

ISBN 978-80-69159-00-6

4. Results and Discussion

The SCPI workplace was used in subject Measurement technique 1 of the second year of bachelor's studies. The teacher configured a workplace for measuring the additional frequency error of DMM. A remote student was guided by Help how to modify frequency and measure amplitude. Points were automatically collected by the software and plotted in a linear scale. Students were obliged to take notes of measured data and process them into percentual frequency error characteristics of DMM considering amplitude measured at 50 Hz for accurate reference. Example of such an error characteristic is shown inside yellow frame in Fig.2b.

A total of 40 students completed the exercise in the proposed remote form. We let them to fill out a questionnaire summarized in Table 1. Students formulated a positive attitude towards the use of the remote tool as a study support – questions 1 and 2. Opinions differ more when it comes to the deployment of distance learning, either for common or unique topics. Correlation coefficient R_L was evaluated between replies on the first 3 questions vs the last one. One can see that the majority of students with a positive attitude to the use of remote tools for a unique topic would accept even common laboratories to be taught remotely. On the other hand, there is no clear correlation between the last question and the answers that address the tool as a support aid. Hypothetically, the cause can be in various motivations with unclear overlapping, e.g. one to better understand the subject and the other to save time and travel costs.

Table 1. Statistical results of a questionnaire filled out by students after the remote exercise.

Question: How do you like:	*Replies*	*Score*	*STD*	R_L
1. if the teacher uses such a remote tool?	39	7.21	2.46	0.11
2. remote access to a workplace for self-study?	39	7.95	2.11	-0.13
3. complete unique topic taught only remotely?	38	5.47	2.92	0.85
4. complete common laboratories taught only remotely?	38	5.01	3.07	-----

5. Conclusion

A new configurable SCPI module was created in LabVIEW to run under our remote access software system. It was used during practical exercises for evaluation of DMM additional frequency error. From the collected opinions of the students, it emerged that they prefer using such a tool as a support aid, while their attitude to exercises performed remotely is not profiled. A correlation analyses suggested that there might be different tendencies in student motivations.

Acknowledgements

This work was supported by the Slovak Research and Development Agency grant APVV-20-0042.

References

[1] Mokhtar, A., Mikhail, G. R., Seong-Joo, Ch. (2014). A Survey on Remote Laboratories for E-Learning and Remote Experimentation. *Contemporary Engineering Sciences*, 7 (29), 1617 – 1624.

[2] Khoruzha, L., Hrynevych, L., Bodnenko D., Vakulova, I., Proshkin, V. (2022). Online Education at a Modern University: Tools for Interactive Learning. In *E-learning in the Transformation of Education in Digital Society*. Studio Noa for University of Silesia, 163-177.

[3] Kamenský, M., Hilko, K., Bittera, M., Králiková, E. (2023). Employing LabVIEW Web service in design of application twins with remote access. In *14th International Conference on Measurement (Measurement 2023)*. IEEE, 199-202.

[4] Otomański, P., Pawlowski, E., Szlachta, A. (2021). The Evaluation of Expanded Uncertainty of DC Voltages in the Presence of Electromagnetic Interferences using the LabVIEW Environment. *Measurement Science Review*, 21(5), 136-141.

Slovak National Standards and Czech State Standards of Ionizing Radiation

[1]Jozef Leja, [2]Jana Sochorová, [1]Jan Rybář, [1]Stanislav Ďuriš, [1]Peter Onderčo, [1]Andrej Smetánka, [2]Jana Gerneschová

[1]Faculty of Mechanical Engineering, Slovak University of Technology, Bratislava, Slovakia
[2]Czech Metrology Institute, Prague, Czech Republic
Email: jozef.leja@stuba.sk

Abstract. *The paper deals with the comparison of Slovak national standards and Czech state standards in the field of ionizing radiation. In this area, the Slovak Institute of Metrology maintains 4 national standards and the Czech Metrology Institute maintains 6 state standards. The set of quantities, their ranges of values and their combined standard uncertainties reproduced by these standards are compared.*

Keywords: Ionizing Radiation, Dosimetry, National Standard

1. Introduction

Metrology of ionising radiation is extremely important because it ensures accurate measurement and control of radiation levels, which is essential for various applications in medicine, industry, research and environmental protection. National standards play the most important role in the national metrology system. National standards are measurement standards recognised by a national authority to serve as a basis for assigning the values of quantities to other measurement standards in a given country.

2. Slovak national standards of ionizing radiation

In the Slovak Republic, the Slovak Institute of Metrology (SMÚ) is responsible for the creation, development and maintenance of national standards. Currently, SMÚ maintains 28 national standards and 5 measurement standards are in the process of being declared national standards. In the field of ionising radiation, SMÚ maintains 4 national standards: 1. National standard of radionuclide activity, 2. National standard of dosimetric quantities of gamma radiation, 3. National standard of dosimetric quantities of X-ray radiation, 4. National standard of dosimetric quantities of neutron radiation. The quantities, ranges of values and combined standard uncertainties reproduced by Slovak national standards are listed in Tables 1 – 4.

3. Czech state standards of ionizing radiation

In the Czech Republic, the Czech Metrology Institute (ČMI) is responsible for the creation, development and maintenance of state standards. Currently, ČMI maintains 63 state standards and 1 measurement standard is in the process of being declared a state standard. In the field of ionising radiation, ČMI maintains 6 state standards: 1. State standard of radionuclide activity unit, 2. State standard of absorbed dose to water and absorbed dose to water rate of photon radiation, 3. State standard of exposure, exposure rate, air kerma and air kerma rate of photon radiation, 4. State standard of neutron emission from radionuclide sources, 5. State standard of fluence rate and spectral fluence rate of neutrons, 6. State standard of fluence rate of thermal neutrons. The quantities, ranges of values and combined standard uncertainties reproduced by Czech state standards are listed in Tables 5 – 10.

ISBN 978-80-69159-00-6

Table 1: National standard of radionuclide activity [1].

Quantity	Range	Uncertainty (k=2)
Radionuclide activity (A)	$(1 – 1.10^{11})$ Bq	(0,7 – 10) %

Table 2: National standard of dosimetric quantities of gamma radiation [2].

Quantity	Range	Uncertainty (k=2)
Air kerma (K_a)	$(1.10^{-9} – 50)$ Gy	(0,45 – 3,5) %
Air kerma rate ($\dot{K}_a$)	$(3.10^{-8} – 50)$ Gy.h^{-1}	(0,45 – 3,5) %
Ambient dose equivalent (H^*)	$(1.10^{-9} – 50)$ Sv	(1,3 – 3,6) %
Ambient dose equivalent rate ($\dot{H}^*$)	$(3.10^{-8} – 50)$ Sv.h^{-1}	(1,3 – 3,6) %
Personal dose equivalent (H_p)	$(1.10^{-8} – 10)$ Sv	(1,5 – 2,0) %
Personal dose equivalent rate ($\dot{H}_p$)	$(1.10^{-7} – 1)$ Sv.h^{-1}	(1,5 – 2,0) %
Absorbed dose to water (D_w)	(0,1 – 50) Gy	0,65 %
Absorbed dose to water rate ($\dot{D}_w$)	(18 – 50) Gy.h^{-1}	0,65 %

Table 3: National standard of dosimetric quantities of X-ray radiation [3].

Quantity	Range	Uncertainty (k=2)
Air kerma (K_a)	$(8.10^{-7} – 2.10^{-2})$ Gy	1,4 %
Air kerma rate ($\dot{K}_a$)	$(5.10^{-5} – 2.10^{-2})$ Gy.h^{-1}	1,4 %
Ambient dose equivalent (H^*)	$(1.10^{-6} – 4.10^{-2})$ Sv	2,5 %
Ambient dose equivalent rate ($\dot{H}^*$)	$(9.10^{-5} – 4.10^{-2})$ Sv.h^{-1}	2,5 %

Table 4: National standard of dosimetric quantities of neutron radiation [4].

Quantity	Range	Uncertainty (k=2)
Ambient dose equivalent (H^*)	$(1.10^{-7} – 10)$ Sv	2,1 %
Ambient dose equivalent rate ($\dot{H}^*$)	$(1.10^{-7} – 1.10^{-1})$ Sv.h^{-1}	2,1 %
Personal dose equivalent (H_p)	$(1.10^{-7} – 10)$ Sv	2,2 %
Personal dose equivalent rate ($\dot{H}_p$)	$(1.10^{-7} – 1.10^{-1})$ Sv.h^{-1}	2,2 %

ISBN 978-80-69159-00-6

Table 5: State standard of radionuclide activity unit [5].

Quantity	Range	Uncertainty (k=2)
Radionuclide activity (A)	$(1.10^2 – 1.10^5)$ Bq	(0,2 – 5) %

Table 6: State standard of absorbed dose to water and absorbed dose to water rate of photon radiation [5].

Quantity	Range	Uncertainty (k=2)
Absorbed dose to water (D_w)	Unspecified[1]	(0,6 – 2) %
Absorbed dose to water rate ($\dot{D}_w$)	(15 – 50) Gy.h^{-1}	(0,6 – 2) %

Table 7: State standard of exposure, exposure rate, air kerma and air kerma rate of photon radiation [5].

Quantity	Range	Uncertainty (k=2)
Exposure (X)	Unspecified[1]	(0,6 – 4,3) %
Exposure rate ($\dot{X}$)	$(6.10^{-13} – 7.10^{-4})$ A.kg^{-1}	(0,6 – 4,3) %
Air kerma (K_a)	Unspecified[1]	(0,6 – 4,3) %
Air kerma rate ($\dot{K}_a$)	$(7.10^{-8} – 90)$ Gy.h^{-1}	(0,6 – 4,3) %

Table 8: State standard of neutron emission from radionuclide sources [5].

Quantity	Range	Uncertainty (k=1)
Neutron emission (B)	$(3.10^4 – 1.10^9)$ s^{-1}	0,7 %

Table 9: State standard of fluence rate and spectral fluence rate of neutrons [5].

Quantity	Range	Uncertainty (k=2)
Neutron fluence rate ($\dot{F}$)	Unspecified[2]	(2 – 6) %
Spectral neutron fluence rate ($\dot{F}_E$)	(2 – 6) %	

Table 10: State standard of fluence rate of thermal neutrons [5].

Quantity	Range	Uncertainty (k=2)
Neutron fluence rate ($\dot{F}$)	$(1{,}0.10^3 – 2{,}9.10^4)$ cm^{-2}s^{-1}	3,6 %

ISBN 978-80-69159-00-6

Note.
[1] Depends on the exposure time.
[2] The upper limit is determined by the emission and the minimum acceptable distance.

4. Discussion

A comparison of measurement standards of radionuclide activity shows that Slovak national standard provides a wider range of values, while Czech state standard has a smaller uncertainty interval. Measurement standards for photon radiation are organized differently. While Slovak national standards are divided according to the type of ionizing radiation, Czech state standards are divided according to the quantities they reproduce. A comparison of quantities shows that Czech state standards reproduce exposure and exposure rate that Slovak national standards do not reproduce. On the other hand, Slovak national standards reproduce ambient and personal dose equivalents and their rates that Czech state standards do not reproduce. For absorbed dose in water rate, the range of values is approximately the same, but Slovak state standard has a smaller uncertainty. For air kerma rate, Czech state standard provides a wider range of values as well as a smaller uncertainty. For neutron radiation, SMÚ maintains one national standard and ČMI maintains three state standards. The quantities reproduced by the measurement standards are different. While Slovak national standard reproduces the ambient and personal dose equivalents and their rates, Czech state standards reproduce neutron emission, neutron fluence and neutron fluence rate. An important property of measurement standards is their metrological traceability. A comparison of the metrological traceability of individual measurement standards requires a separate study. In general it can be said [6] that most Slovak national standards of ionizing radiation are not primary standards but are linked to the measurement standards of ČMI, the German National Metrology Institute (PTB) and the Austrian Federal Office of Metrology and Surveying (BEV).

Acknowledgements

This work was supported by the projects KEGA 024STU-4/2023 (Building a laboratory of medical metrology), APVV-21-0195 (Research the possibility of digital transformation of continuous transport systems) and APVV-21-0216 (Advanced mathematical and statistical methods for measurement and metrology). The authors are also grateful for the support of the Slovak University of Technology and the Czech Metrology Institute.

References

[1] Halaj, M., Švec, A. (2012). Certificate of national standard No. 017/12.SMÚ.
[2] Halaj, M., Dobrovodský, J. (2011). Certificate of national standard No. 028/11. SMÚ.
[3] Halaj, M., Compel, J. (2011). Certificate of national standard No. 015/11. SMÚ.
[4] Halaj, M., Valent, J. (2012). Certificate of national standard No. 006/12. SMÚ.
[5] Ionizing radiation. (2025, January 28). *Czech metrology institute website.* https://cmi.gov.cz/ionizujici zareni.
[6] Leja, J., Ďuriš, S., Rybář, J., Miadik, R. (2024). National measurement standards of ionizing radiation. In *27th Conference of Slovak Physicists*. Slovak Physical Society, 69–70.

Influence of Wire Misalignment in Current Injection Probe on the Bulk Current Injection (BCI) Test

Martin Gabrišák, Jozef Hallon, Mikuláš Bittera, Michal Dzuriš

Slovak University of Technology in Bratislava, Faculty of Electrical Engineering and Information Technology, Institute of Electrical Engineering, Slovakia
Email: martin.gabrisak@stuba.sk

Abstract. *In this paper, the wire misalignment inside the current injection probe during BCI testing is analyzed. It is critically examined whether a wire misalignment has a significant impact on the total measurement uncertainty and the reproducibility of the BCI test. For this analysis, a special fixation for a cable wire inside the current injection probe was developed to evaluate different positions of wire misalignment. After measuring the 13 different misalignment positions of the wire, the measured data are compared and evaluated. The main purpose of this analysis is then to decide if the misalignment has a significant impact on the BCI test.*

Keywords: Bulk Current Injection, Wire Misalignment, Injected Current Deviation

1. Introduction

In view of the high number of electronic components in modern vehicles (especially in electric vehicles), electromagnetic compatibility (EMC) testing of new electronic devices becomes very important in the process of introducing new vehicles on the market. Due to the high electrification of modern vehicles (for example, sensors monitoring the environment or headlamp adjustment), cable wires are mounted inside the whole vehicle. During the standard operation of the vehicle, it may happen that interference currents will be induced into these wires by other devices, which can cause functional upset or damage to the device connected to these wires.

To assess, if such interference currents affect the proper operation of electronic devices, a conducted susceptibility test, also called Bulk Current Injection (BCI) test, must be performed as a part of the EMC testing process. The standard ISO 11452-4 prescribes the injection of current into the wiring harness of the equipment under test (EUT) via a current injection probe in a frequency range from 0.1 MHz to 400 MHz with different current levels applied on the test harness [1].

Due to different limitations (e. g. size of the EUT or stiffness of the wiring harness), the test setup must often be modified. These modifications can have a considerable influence on the total measurement uncertainty of the BCI test and on the reproducibility of the BCI test within the same or by other EMC test laboratories. One of the possible modifications is the misalignment of the wiring harness inside the current injection probe. In [2] it was shown that above 100 MHz a shift in position of the wire can have an influence on the level of injected current in the wire. Therefore, we decided to verify how a position shift of a wiring harness inside the BCI current injection probe influences the test result.

2. Test setup and measurement

The experiment was set up on a ground plane inside a semi anechoic chamber according to test setup in standard ISO 11452-4. The wire used for this measurement was an isolated copper lead terminated with a 50 Ω load at one end. At the opposite end of the wire, the EUT was simulated by an EMI test receiver used to measure the injected current. The plates (see Fig. 1 right), where

ISBN 978-80-69159-00-6

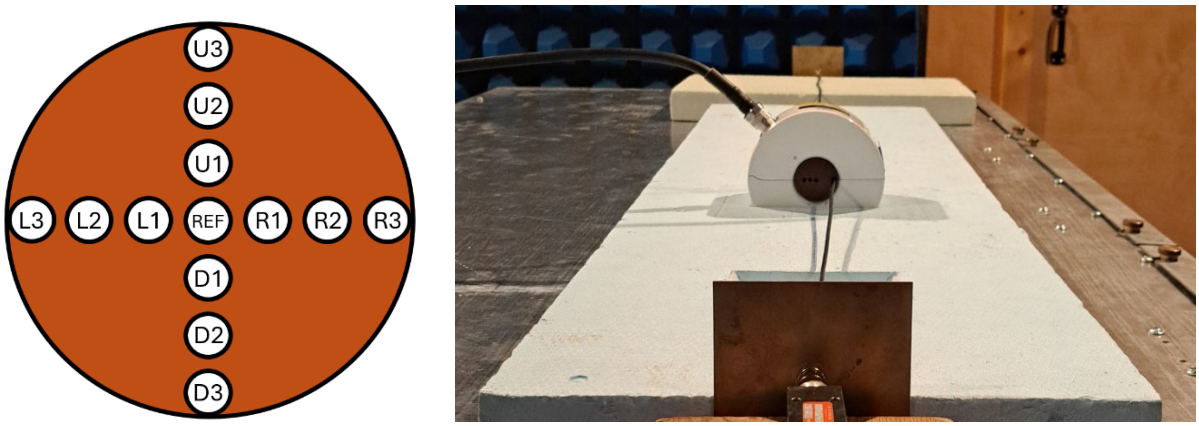

Fig. 1. Tested misalignment positions (left) and test setup (right)

the wire was terminated, were used for RF grounding of the 50 Ω termination impedances. To verify whether wire misalignment inside the injection probe had an influence on the BCI test, a special nonconductive measurement fixation had been created. This fixation also guaranteed that the wire was at the required position during the whole test and the distances between the measured positions were still the same. Because the misalignment effects occurred at higher frequencies, the frequency range, in which these effects were analyzed, had been set from 10 MHz to 400 MHz. To analyze in detail the impact of misalignment in the chosen frequency range a 1% frequency step was set and a 100 mA injected current was applied on the cable wire.

During testing, the substitution method was applied to investigate all deviations caused by wire misalignment inside the injection probe. The substitution method is a testing process during which the current is injected into three different positions of the wire. This should ensure that the EUT is tested to the demanded current level in the whole frequency range. Following the requirements of standard ISO 11452-4, the injection probe was located in three different positions: P1 = 150 mm, P2 = 450 mm and P3 = 750 mm from the EUT resp. in our case the EMI test receiver during the measuring process. The applied forward power into the injection probe was the forward power obtained during the calibration. This guaranteed that during the misalignment verification at each position, the same forward power was applied on the current injection probe.

13 misalignment positions inside the injection probe had been measured at each of the three probe positions. This means that a total of 39 measurement runs were performed to analyze the misalignment effect on the BCI test. The radius of the nonconductive filling was 20 mm and the radial distance between each position was 6 mm. First measured position was the reference position in the center of the injection probe (see Fig. 1 left). In this position, the coupling of the injected current into the wire should be the most effective because the wire is located in the axis of the magnetic circuit of the probe, which is generated inside the probe. Therefore, the measured values from other wire positions were compared with the obtained data from the reference position.

The next step in the measurement process was the misalignment of the wire. Because the characteristic impedance of the wire depends on the height of the wire above the ground plane, different measurement results were expected when comparing data between positions U3 and D3 [3].

ISBN 978-80-69159-00-6

3. Results

The data obtained from the measurement of the misalignment positions were saved and then compared with data from the reference position. The injected current deviation of the misaligned position from the reference position for the measured frequency range was then

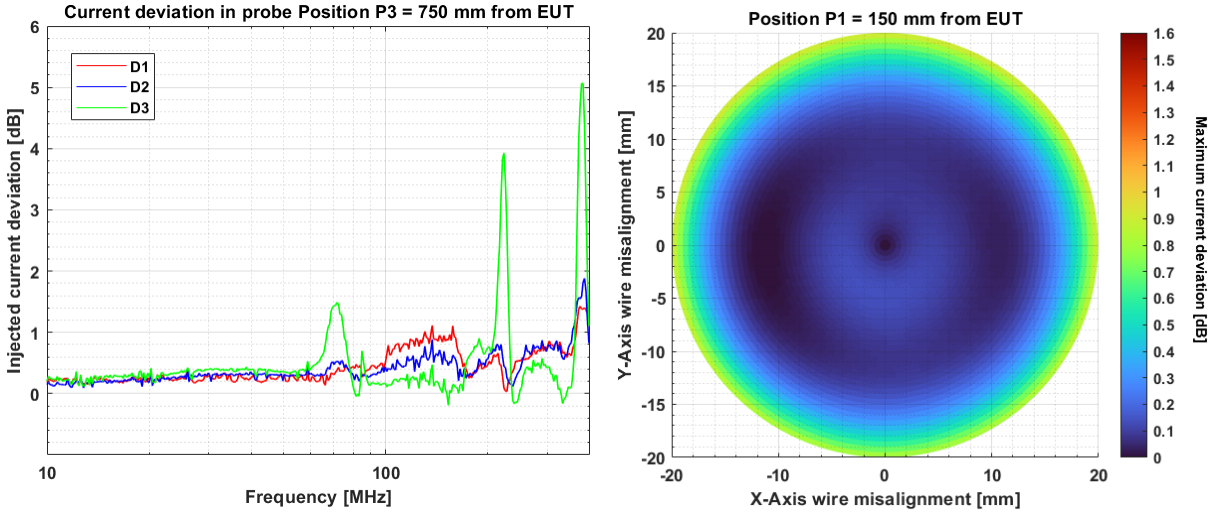

Fig. 2. Current deviations in probe position P3 for wire positions D1, D2 and D3 (left) and variance current deviation in position P1

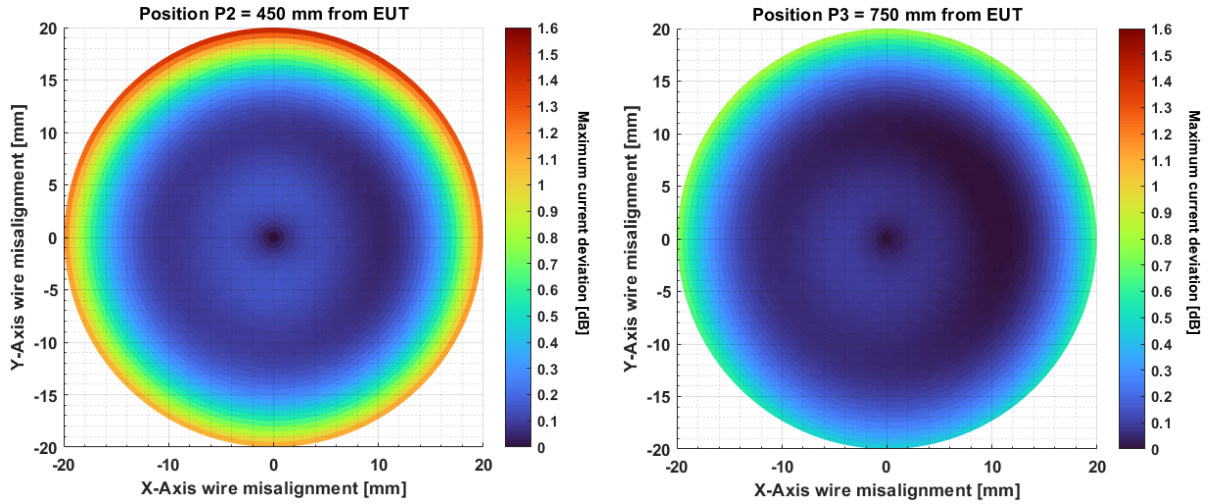

Fig. 3. Variance current deviation in probe position P2 (left) and P3 (right)

in dB. After calculating the injected current deviation for all positions, the deviations were then compared with each other. The results of the comparison indicated that there had not been stable values of the current deviation above 100 MHz (See Fig. 2 left). So, it was decided, to calculate a variance from all deviations in the frequency range from 10 MHz to 400 MHz. This variance represents the expected value of the squared deviation from the mean in dB, which was obtained during the misalignment testing in the whole frequency range at each wire position and at each current probe position. These values were then used to analyze, at which configuration is the highest injected current deviation.

By interpolating the variance data, a simulation model had been created, where the impact of the location of the wire inside the probe on the injected current deviation was shown. (See Fig. 2. right and Fig. 3.). This model shows the misalignment effect on the injected current for all three probe positions. The highest deviances are at the inner walls of the injection probe,

ISBN 978-80-69159-00-6

especially at position U3. If the wire is misaligned to position D3, then the deviance is lower than the deviance at U3. This is because the wire at position D3 is closer to the ground plane which results in a lower characteristic impedance. Because there is a mismatch between the 50 Ω termination impedance and the wire (normally, the characteristic impedance for a wire of radius 2 mm located 50 mm above the ground plane is 322.5 Ω), each lowering of wire height reduces the mismatch, which means that the deviation will not be as high as during the misalignment in position from U1 to U3 [4].

With a closer look at these results in Fig. 2. right and Fig. 3., it could be observed, that the deviations are higher in the probe position P2 (450 mm from the EUT). Whereas the maximum injected current deviations at position P1 and P3 are below 1 dB, the maximum deviation at P2 is 1.6 dB, although in real life application the wire will not be so close to the inner wall of the probe. This increase in deviation can be caused by the change of the characteristic impedance of the wire and standing waves on the wire at this probe position.

4. Conclusion

In this paper, the effect of the misalignment of a wire on the injected current was analyzed. Although there is no significant impact on the testing process, it still affects the test results, because when misaligned, the induced current is almost always lower than when the wire is centered. This means that wire misalignment may not have a high impact on the testing process when the closed loop method [1] (a testing method, where the forward power applied to the current injection probe is regulated to reach the demanded test level) is used. However, misalignment may affect the testing process when the substitution method is used.

It also can have an impact on total measurement uncertainty calculations. Misalignment of the cable inside the injection probe is a common problem, because most of the tested cables are very stiff and sometimes, they cannot be aligned according to standard. For a misalignment error in positions R1, L1, U1 and D1, which normally occurs during measurement, the maximum deviation is 0.3 dB. At extreme conditions, with a maximum deviation of 1.6 dB, misalignment can increase the total uncertainty value of the testing process. This means that the misalignment effect should be also considered to be included in the uncertainty calculation process.

Acknowledgment

This work was supported by the project APVV 20-0042 "Microelectromechanical sensors with radio frequency data transmission" and by the Slovak University of Technology via the Young Investigator Grant EMCA2024 “Increasing the validity of EMC tests for the automotive industry”.

References

[1] ISO. International Standard ISO 11452-4, Road vehicles - Component test methods for electrical disturbances from narrowband radiated electromagnetic energy – Part 4:Harness excitation methods. ISO. 2020-04. Fifth edition. 44 pages.

[2] DeRoy, P., Toscani, N., Grassi, F., Schulz, W., Rostamazadeh, C., (2018). Sensitivity Analysis of RF Current Injection Techniques for Immunity Testing of Automotive Ethernet. In *2018 IEEE Symposium on Electromagnetic Compatibility, Signal Integrity and Power Integrity (EMC, SI & PI)*. Long Beach, CA, USA, IEEE, ISBN 978-1-5386-6621-0

[3] Gabrišák, M., Hallon, J., Bittera, M., (2024). Critical Analysis of Bulk Current Injection (BCI) Test Methods. In *Applied Electronics 2024*. Pilsen. Czech Republic, ISBN 979-8-3503-5073-9

[4] Harťanský R., Smieško V., Maršálka L., (2013). Numerical Analysis of Isotropy Electromagnetic Sensor Measurement Error. In *MEASUREMENT SCIENCE REVIEW, Volume 13, No. 6, 2013*. p.311-314. Walter de Gruyter GmbH. ISSN 1335-8771

Magnetic Properties of Nanocolloids Based on Titanium and Ionic Liquid BMIM PF6

[1]Andrej Dvurečenskij, [1]Alexander Cigáň, [2]György Radnóczi, [1]Martin Škrátek, [1]Melinda Majerová, [3]Zuzana Hájovská, [4]Eva Kováčová, [1]Ján Maňka

[1]Institute of Measurement Science, Slovak Academy of Sciences, Bratislava, Slovakia
[2]Institute of Technical Physics and Materials Science, Centre of Energy Research, Budapest, Hungary
[3]Institute of Materials and Machine Mechanics, Slovak Academy of Sciences, Bratislava, Slovakia
[4]Institute of Electrical Engineering, Slovak Academy of Sciences, Bratislava, Slovakia
Email: andrej.dvurecenskij@savba.sk

Abstract. *Two nanocolloids with different titanium contents were prepared by magnetron sputtering onto the ionic liquid [BMIM][PF₆]. Their magnetic properties were measured using a SQUID magnetometer, and their structure was characterized by transmission electron microscopy (TEM). The magnetic behavior at 300 K is dominated by a paramagnetic contribution. In the low-field magnetic susceptibility measurements, a temperature-independent contribution was observed in both nanocolloids above ~100 K. TEM analysis revealed that increasing the titanium content results in a morphological change of the titanium particles from small nanoparticles to larger, rectangular-faceted aggregates.*

Keywords: Titanium, Nanocolloids, Magnetron Sputtering, SQUID Magnetometer, Ionic Liquids [BMIM].[PF6], Magnetic Susceptibility

1. Introduction

Titanium (Ti), titanium-based alloys and their nanostructures have been among the most interesting materials for their applications and research for several decades. Titanium itself and its alloys have a ratio of yield and tensile strength to mass higher than traditional structural steel materials. Therefore, they found use in the automotive, aerospace and farming industries and naval ships, [1]. Ti and its alloys exhibit excellent biocompatibility, [2]. During the last decades, the importance of ionic liquids (ILs) in materials research has grown significantly. ILs open new routes for environmentally friendly production processes and a future generation of functionalized materials and nanostructures, [3, 4].

Although titanium metal-based materials are among the most studied materials, there is still a lack of information about their properties, namely, at various novel structural and composition conditions. Thus, our papers show the preparation of nanocolloids (NCs) based on Ti and hydrophobic IL [BMIM].[PF6] and the results of a detailed study of their magnetic and structural properties.

2. Subject and Methods

Two Ti nanocolloids, NC Ti-L and NC Ti-H, were prepared by magnetron sputtering of high-purity Ti targets in a vacuum onto the surface of the IL [BMIM].[PF6]. The IL in a glass Petri dish was degassed in the load-lock system under vacuum. Before sputtering Ti, the background pressure was usually 2×10^{-7} mbar. The deposition was performed at stabilized magnetron power of 2×250 W and deposition time 250 s and 2000 s for NC Ti-L and NC Ti-H, respectively. We estimated the Ti content in the colloids based on experimental experience with thin films. It was 382 μg/ml for NC Ti-L and 755 μg/ml for NC Ti-H.

Microstructural investigations were performed by transmission electron microscopy (TEM) using a JEOL 1200FX microscope operating at 80 kV. NC samples for TEM were prepared by

ISBN 978-80-69159-00-6

placing 2 µl of NC into the center of an ultrathin holey carbon support grid (Ted Pella). Excessive IL was washed away by ~6 ml of a 50:50 mixture of acetone and acetonitrile.

Magnetic properties were measured by the Quantum Design MPMS XL-7 SQUID magnetometer. Temperature dependences of the magnetic moment of pure IL and NC samples were measured in the zero field cooling (ZFC) and field cooling (FC) modes. DC magnetization, $M(H)$, was measured at 300 K and 2 K up to 5.6 MA/m. Every magnetization curve includes small (±0.16 MA/m) and noncomplete high (±5.6 MA/m) magnetization loops. The measured magnetic characteristics for NC samples were corrected for contributions from the sample holder and the pure IL. Samples for magnetic measurements were prepared so that typically 70 µl of the pure IL or the NCs were injected into a cylindrical plastic capsule and fixed in a plastic straw provided by Quantum Design.

3. Results

Fig. 1 shows photos of the two nanocolloids, NC Ti-L and NC Ti-H, immediately after deposition. The visible color difference between the samples reflects the varying Ti content. Both NCs exhibit good homogeneity in the distribution of Ti nanoparticles (NPs).

Fig. 1. Petri dishes containing NC Ti-L (left) and NC Ti-H (right) with ionic liquid [BMIM].[PF6] after Ti deposition by magnetron sputtering

TEM images of Ti NPs prepared in the IL [BMIM][PF6] are shown in Fig. 2. The left image shows a sample with NC Ti-L, displaying individual NPs with an approximate mean size of 3–5 nm. The right image shows the NC Ti-H sample, with NPs the mean size of 5–8 nm, where the NPs form aggregates.

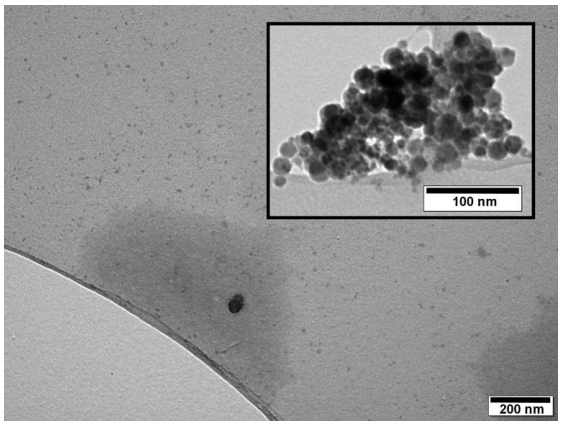

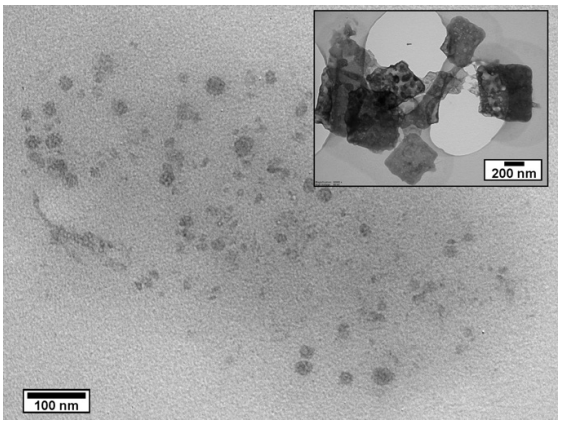

Fig. 2. TEM images of Ti nanoparticles in [BMIM].[PF6]. Left: NC Ti-L. Right: NC Ti-H with larger nanoparticles forming aggregates. Inserts show larger rectangular-faceted Ti nanoparticle aggregates.

In Fig. 3, the corrected mass magnetization M_c (corrected to the sample holder and IL) of the NC Ti-L and NC Ti-H samples is shown at temperature (T) of 2 K and 300 K at the applied magnetic field (H) of ~ $\pm 6 \times 10^6$ Am^{-1}. The dominant influence of the paramagnetic component can be observed (linear part curves) for all samples, but for NC Ti-L at 2 K, only at higher magnetic fields ($H_a > 3 \times 10^6$ Am^{-1}). Additionally, when the temperature changes from 300 K to 2 K, only a slight increase in magnetization is observed in both samples, with a smaller increase for NC Ti-H. The insert shows the dependences at low H ($\pm 1 \times 10^5$ Am^{-1}). At T = 2 K,

ISBN 978-80-69159-00-6

a slide magnetization hysteresis can be observed at higher values of H for both NCs. We ascribe its origin to the interference of Ti NPs with IL, [5].

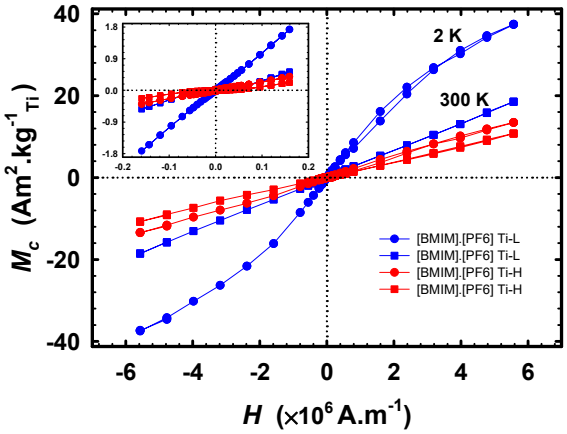

Fig. 3. Corrected mass magnetization M_c of NC Ti-L (blue) and NC Ti-H (red) samples of Ti NPs prepared in [BMIM].[PF6] IL, as a function of applied magnetic field H at 300 K (squares) and 2 K (circles). The insert shows the dependences at low H.

The corrected (to the sample holder and IL) ZFC and FC molar magnetic susceptibility χ_c (per mol of Ti) of the samples vs. temperature T measured at 4 kA.m^{-1} is in Fig. 4. Temperature dependence of molar magnetic susceptibility of pure IL is also shown. The insert shows the measured magnetic moments data (before the corrections) of M vs. T. All samples could be characterized by linear temperature-independent components (TICs) of magnetic susceptibility χ_{TIC} in the range of (150–300) K. Deviations from the linear dependence of the ZFC characteristics in the range of (220–280) K can be attributed to the interaction between the IL and Ti NPs during the glass transition of the IL. Thus, the χ_{TIC} values of NCs were determined only from data in the ranges of (100–200) K to depress the effect of IL glass transition, [6]. Positive values of χ_{TIC} were obtained for the NCs contrary to IL, which shows diamagnetic behavior in a larger temperature range with a negative value of $\chi_{TIC_{IL}} = -1.8 \times 10^{-9}$ m^3.mol^{-1}.

The corresponding corrected (IL, TIC) magnetic characteristics are in Fig. 5, together with the estimated value of χ_{TIC} for the NCs. NC Ti-L shows negative decreasing values with a decrease of T for both ZFC and FC characteristics of $\chi_{c\text{-}TIC}$ at low temperatures. Note that metal titanium is a superconductor with critical temperature (0.25–0.50) K under atmospheric conditions, [7]. Moreover, for single crystal Ti samples, an antiferromagnetic decrease of magnetic susceptibility has been reported at decreasing temperatures below room temperature, [8].

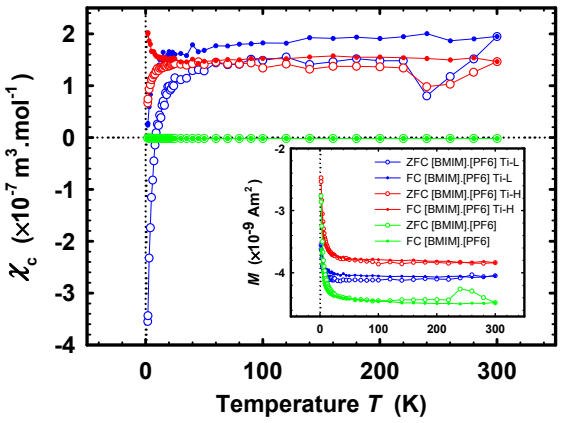

Fig. 4. Corrected ZFC, FC molar magnetic susceptibility χ_c (per mol of Ti) of NC Ti-L (blue), NC Ti-H (red), and pure IL [BMIM].[PF6] (green) samples, versus T measured at the field of 4 kA.m^{-1}. The insert shows the measured magnetic moments data of M vs. T before correction.

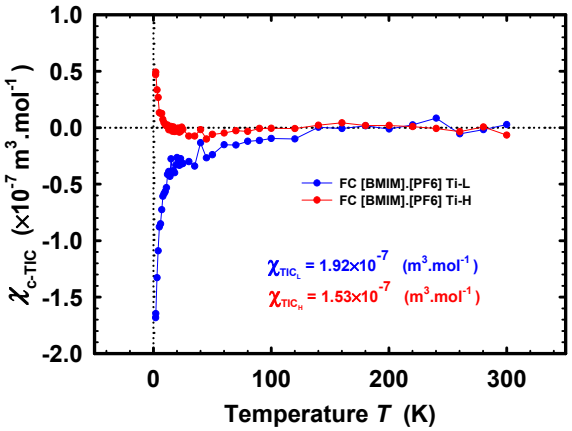

Fig. 5. FC corrected (to the sample holder, IL, and TIC) molar magnetic susceptibility $\chi_{c\text{-}TIC}$ versus T of NC Ti-L (blue), and NC Ti-H (red), measured at 4 kA.m^{-1}.

ISBN 978-80-69159-00-6

We assume that a lower value of χ_{TIC} for NC Ti-H signalizes lower degrees of charge delocalization in the (100–200) K temperature range. However, at lower temperatures, the temperature dependence of the FC characteristic for NC Ti-H suggests core electron localization.

4. Conclusions

Two nanocolloids (NC Ti-L/H) with different contents of sputtered Ti were prepared by magnetron sputtering onto ionic liquid [BMIM].[PF6]. TEM microscopy shows that a twofold higher content of Ti of NC Ti-H sample leads to a change in the morphology of Ti particles from small to larger rectangle-faceted nanoparticle aggregates, and results in larger aggregate sizes. Their magnetic properties were measured by a SQUID magnetometer. The magnetic properties are predominantly influenced by the paramagnetic contribution, mainly at 300 K. At the change of the temperature from 300 K to 2 K, the magnetization changes only slightly more for the NC Ti-L. The temperature-independent contribution of χ_{TIC} for both NCs dominates over ~100 K, being (1.92×10^{-7} and 1.53×10^{-7}) $m^3.mol^{-1}$ for NC Ti-L and NC Ti-H, respectively. The twofold higher content of Ti of NC Ti-H results in a temperature-dependent behavior of the FC magnetic susceptibility (Curie-Weiss) below 20 K.

Acknowledgements

This work was supported by the following projects: VEGA 2/0104/25, APVV-22-0328, APVV-21-0299, APVV-23-0366 and 09I05-03-V02-00080.

References

[1] Najafizadeh, M., Hosseinzadeh, M., Yazdi, S., Bozorg, M., Zarrabian, M., Ghasempour-Mouziraji, M., Cavaliere, P. (2024). Classification and applications of titanium and its alloys: A review. *Journal of Alloys and Compounds Communications, 3*, 100019.

[2] Sagadevan, S., Imteyaz, S., Murugan, B., Lett, J. A., Sridewi, N., Weldegebrieal, G. K., Fatimah, I., Oh, W.-Ch. (2022). A comprehensive review on green synthesis of titanium dioxide nanoparticles and their diverse biomedical applications. *Green Processing and Synthesis, 11*, 44–63.

[3] Verma, Ch., Ebenso, E. E., Quraishi, M. A. (2019). Transition metal nanoparticles in ionic liquids: Synthesis and stabilization. *Journal of Molecular Liquids, 276*, 826–849.

[4] Zhang, Y., Liu, W., Chen, S., Gao, Q., Li, Q., & Zhu, X. (2020). Ionic liquids for the controllable preparation of functional TiO_2 nanostructures: a review. *Ionics, 26*(12), 5853–5877.

[5] Dvurečenskij, A., Cigáň, A., Lobotka, P., Radnóczi, G., Škrátek, M., Benyó, J., Kováčová, E., Majerová, M., Maňka, J. (2022). Colloids of HEA nanoparticles in an imidazolium-based ionic liquid prepared by magnetron sputtering: Structural and magnetic properties. *Journal of Alloys and Compounds*, 896, 163089.

[6] Endo, T., Murata, H., Imanari, M., Mizushima, N., Seki, H., Nishikawa, K. (2012). NMR study of cation dynamics in three crystalline states of 1-butyl-3-methylimidazolium hexafluorophosphate exhibiting crystal polymorphism. *Journal of Physical Chemistry B*, 116(12), 3780–3788.

[7] Bashkin, I. O., Tissen, V. G., Nefedova, M. V., Ponyatovsky, E. G. (2007). Superconducting temperature of the ω-phase in Ti, Zr, and Hf metals at high pressures. *Physica C*, 453, 12–14.

[8] Editor: H. P. J. Wijn. (1991). Magnetic Properties of Metals: d-Elements, Alloys and Compounds (Data in Science and Technology), Sringer-Verlag Berlin Heidelberg, p.68-69.

Selection and Preliminary Measurements of Optical Absorbance Liquid Filters as Reference Materials

[1,2]Liudmyla Petrushchenko, [1]Michal Mariassy, [3]Farshid Manoocheri, [4]Natalia Parkhomenko, [5]Yelizaveta Tarasenko, [3]Yasaman Rezazadeh, [1]Peter Pavlasek

[1]Slovak Institute of Metrology (SMU), Bratislava, Slovakia,
[2] Slovak University of Technology in Bratislava (STU), Bratislava, Slovakia,
[3]Aalto University, Espoo, Finland,
[4]Physikalisch-Technische Bundesanstalt (PTB), Braunschweig, Germany,
[5]State Enterprise "All-Ukrainian State Research and Production Center for Standardization, Metrology, Certification and Consumers Rights Protection" (UMTS), Kyiv, Ukraine
Email: petrushchenko@smu.gov.sk

Abstract. *Optical absorbance liquid filters (OALFs) have been considered as standard reference materials (SRMs) for calibrating spectrophotometers used in clinical chemistry laboratories, often called in vitro diagnostic medical devices (IVD MDs), which mainly use optical absorbance as the basic quantity. Based on an analysis of technical characteristics (working wavelength, photometric range, etc.) of IVD MDs, the main criteria for OALFs were established. Three new types of OALFs that demonstrate good suitability for use as absorbance SRMs for IVD MDs calibration were formulated; they cover 15 of the important wavelengths. Preliminary measurements of the chosen OALFs showed some differences between the institutes´ results; agreement of the results is inferior for institutes with less experience. Factors affecting the accuracy and reproducibility will be investigated and taken into account in the next stages of the project.*

Keywords: IVD MDs, Traceability, Reference Material, Optical Absorbance Liquid Filters

1. Introduction

Many measuring systems used in clinical in vitro diagnostics (e.g., ultraviolet-visible (UV-VIS) spectrophotometers, biochemical analyzers, and immunological analyzers) measure optical absorbance in microvolumes of liquid biospecimens as a basic measurement quantity to determine the concentration of analyte. Since indirect measurements are mostly used in IVD MDs to determine the measurand from other quantities by a measurement model (often a formula), each of the input quantity values should itself be metrologically traceable [1-4]. Existing standards for medical laboratories [4-7] deal with metrological requirements for reference materials, but no requirements are specified for measuring systems or measuring instruments. Only recommendation [8] specifies general characteristics of spectrophotometers and methods of testing and verifying them, as well as requirements for reference material for absorbance. However, this reference no longer meets the current state of the art, and it does not provide procedures that can be fully adopted for IVD MDs, where solid glass standards cannot be used.

Metrological traceability is one of the main conditions for the reliability of measurement results in laboratory medicine. NMIs need to provide optical absorbance measurement results traceable to SI units to accredited calibration laboratories, inspection bodies, and IVD MD manufacturers. OALFs can be used to achieve this, but further work is needed. To resolve the issue described above, a European Partnership on Metrology (EPM) project, "Establishing European traceability for medical measuring devices through optical absorbance liquid filters" (23RPT02

ISBN 978-80-69159-00-6

ETraceAbs), was started, which aims to develop and study OALFs suitable to provide metrological traceability of IVD MDs.

2. Subject and Methods

Based on a wide review of modern spectrophotometric analyzers and systems used in laboratory medicine, the most important optical wavelengths used for biological material testing were defined: 236; 259; 302; 340; 376; 405; 450; 480; 492; 505; 546; 570; 578; 580; 600; 620; 630; 660; 670; 700 and 800 nm. An absorbance range declared by IVD MDs manufacturer is within limits from 0.001 up to 3.0 (corresponding to an internal transmittance of 99.77 % and 0.1 %).

Analysis of the literature and existing SRMs shows that inorganic water solutions of metal ions could be appropriate for the absorbance scale calibration of IVD MDs [9], [10]. However, already known SRMs are not characterized for the required wide photometric range and do not cover all wavelengths. The main criteria OALFs should meet are: the presence of flat absorbance regions (or flat maxima that coincide with the wavelengths at which IVD MDs operate) in the range from 220 to 800 nm and high solubility of the components in order to prepare solutions with absorbance up to 3. Other criteria were also considered, which related to availability, cost, safety issues, stability and chemical properties of raw materials.

Based on the spectra of individual metal ions, a simulator was prepared in Excel to model the spectral characteristics of aqueous solutions containing various components in different concentrations. Using this simulator, numerous spectra of solutions with different metal ions in different concentrations were modeled. It was concluded that a flat absorbance curve covering the entire range from 220 to 800 nm cannot be obtained from the common metal ions. However, three solutions with overlapping spectral ranges were chosen as promising for further research. Source chemicals used for the preparation of solutions are nickel(II) nitrate hexahydrate, chromium(III) nitrate, cobalt(II) nitrate, copper nitrate, nitric acid, nickel(II) sulfate, potassium dichromate, and sulfuric acid. OALFs were prepared by dissolution of the source chemicals (reagent grade) in ultrapure water with the addition of acid (see Table 1). Test measurements of the spectral characteristics of the prepared solutions, performed at SMU, confirmed good agreement between the simulator output and spectra of the prepared solutions.

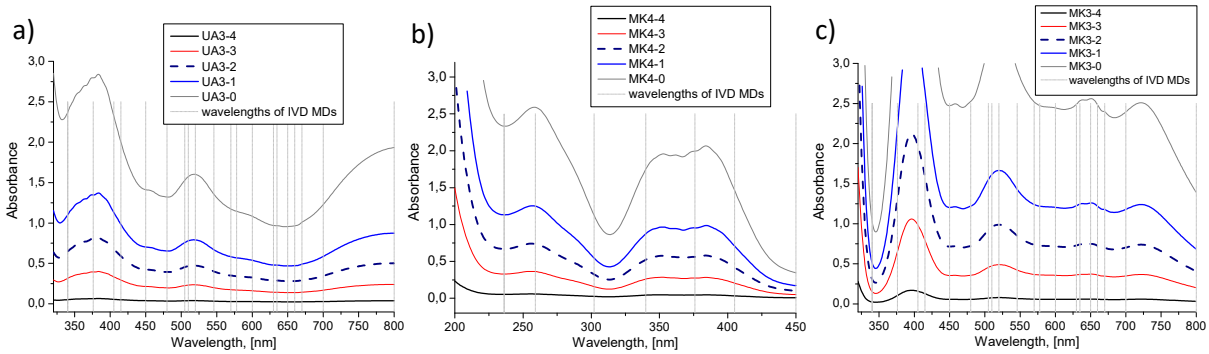

Fig. 1. Spectral characteristics of three types of OALF of 5 concentrations (MK3-0, MK4-0 and UA3-0 have the highest concentration; MK3-4, MK4-4 and UA3-4 have the lowest).

For the purpose of preliminary measurements, the three solutions mentioned above with 5 different concentrations were prepared by SMU, packaged into plastic bottles, and delivered to SMU, UMTS, PTB and Aalto. The main aims of these preliminary measurements were to develop skills and procedures for the handling of OALFs and to test the measurement capabilities of the mentioned NMIs for OALFs. The estimation of uncertainty for these measurements will be established later when a thorough study of the solutions is finished. Each

ISBN 978-80-69159-00-6

NMI performed measurements on its double-beam high-performance spectrophotometer (see Table 2) with a thermostabilizing system under agreed conditions: spectral bandwidth 1 nm, sample temperature 20ºC, integration time 1 s, scanning step 1 nm. Spectral characteristics of solutions MK3, MK4, and UA3 measured by SMU are shown in Fig. 1

Table 1. Concentrations of other ions relative to nickel concentration for the proposed OALFs.

	Ni^{2+}		Cr^{3+}	Cu^{2+}	$Cr_2O_7^{2-}$
MK3	1	0.479	0.133	0.0328	-
MK4	1	-	-	-	0.00229
UA3	1	1.998	0.519	0.952	0.00485

Table 2. Spectrophotometers used for preliminary measurement.

NMI	SMU	PTB	UMTS	Aalto
Instrument model	Cary 4E	Cary 5000	SHIMADZU 3600i Plus	Cary 7000

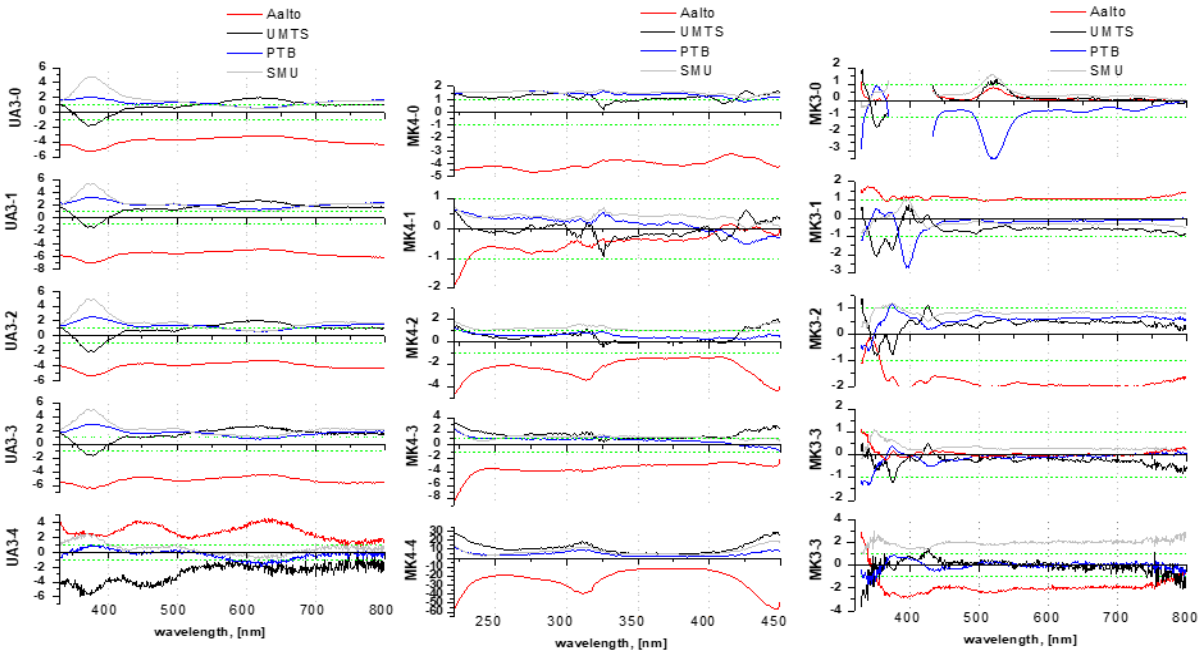

Fig. 2. Relative absorbance difference [%] for 5 concentrations of three types of OALFs related to the mean value (the green dotted lines are used only to indicate the deviation of 1%).

3. Results

Results of preliminary measurements were estimated for all three solutions with 5 concentrations in the entire spectral region by the relative difference of each NMI's values related to the mean value of four NMIs (Fig. 2).

From the 21 wavelengths of interest, proposed OALFs cover 15 wavelengths, which exceeds the project target of 10 wavelengths covered.

4. Discussion and Conclusions

Figure 1 shows that the selected solutions do not behave exactly like a neutral filter, which is due to the properties of the metal ions used. As a result, at those wavelengths that fall on the steep slope of the spectral absorbance of the solution, it is not possible to establish the absorbance values very accurately.

The analysis of the data presented in Fig. 2 shows the better consistency of the data of the three institutes (SMU, PTB, and UMTS), which already have extensive experience in measuring

ISBN 978-80-69159-00-6

OALFs. However, the reason for the differences is still unknown at this stage of the study. Possible influencing factors are potential extreme temperatures of the solutions during transport, storage conditions, the correct measurement of the baseline for measurements (this has a significant impact especially, for low concentrations), the stability of the spectrophotometer and the temperature of the solution during the entire measurement time, the operating procedure, the human factor, the NMI experience with OALFs measurements, etc. This will be addressed in the following stages of the project, involving a very thorough analysis and investigation of all factors that may affect the measurement accuracy of the absorbance for OALFs, as well as the development of a detailed guide for the technical assessment of the measuring system, a description of the preparation and measurement process, measurement conditions, etc.

Overall, the three selected solutions demonstrate good suitability for use as absorbance SRMs for IVD MDs calibration, although with certain limitations that should be clearly specified and explained in the OALFs instructions for use. For the absorbance values uncertainty budget estimation, all contributing components should be established and studied, as well as temperature and spectral bandwidth dependence, short- and long-term stability, etc.

Preliminary measurements have revealed a number of factors affecting the accuracy and reproducibility, the influence of which will be investigated and taken into account in the next stages of the project. The discrepancies in the measurement of very high and low absorbance values of OALFs were expected. Each of the participants involved in preliminary measurements confirmed their capabilities in measuring this type of sample.

Acknowledgements

The research presented has been part of the European project (23RPT02 ETraceAbs), which has received funding from the European Partnership on Metrology, co-financed by the European Union's Horizon Europe Research and Innovation Program and by the Participating States.

References

[1] JCGM GUM-6:2020 Guide to the expression of uncertainty in measurement — Part 6: Developing and using measurement models.

[2] JCGM 200:2012 International vocabulary of metrology – Basic and general concepts and associated terms (VIM). 3rd edition.

[3] Onderčo, P., Rybář, J., Leja, J., Smetánka, A., Gerneschová, J. (2024) Physical quantities and units - correct, uniform and practical. In *27th Conference of Slovak Physicists: Proceedings.* 1st ed. Košice: Slovak Physical Society, 59-60.

[4] ISO/TS 20914:2019 Medical laboratories — Practical guidance for the estimation of measurement uncertainty.

[5] REGULATION (EU) 2017/746 on in vitro diagnostic medical devices.

[6] ISO 15189:2022 Medical laboratories — Requirements for quality and competence.

[7] ISO 17511:2020 In vitro diagnostic medical devices — Requirements for establishing metrological traceability of values assigned to calibrators, trueness control materials and human samples.

[8] OIML R 135 (2004). Spectrophotometers for medical laboratories.

[9] Burke, R.W., Mavrodineanu, R. (1977). Standard Reference Materials: Certification and use of acidic potassium dichromate solutions as an ultraviolet absorbance standard – SRM 935. NBS Special publication 260-54. 157.

[10] Burke, R.W., Deardorff, E.R., Menis, O. (1972). Liquid Absorbance Standards. In *Journal of Research of the National Bureau of Standards.* Vol. 76A. № 5 September-October. 469-482.

Modeling the Physical Mechanisms of Recombination-Based Sensors for the Detection of Biological Markers in Living Systems

[1]B. Sus, [2]K. Przystupa, [1]O. Kozynets, [2]J. Caban, [1]S. Lytvynenko, [1]O. Tsymbalyuk, [1]O. Bauzha, [3]V. Yeromenko, [4]A. Ivanyshyn, [4]R. Kochan

[1]Taras Shevchenko National University of Kyiv, Kyiv, Ukraine,
[2]Lublin University of Technology, Lublin, Poland,
[3]West Ukrainian National University, Ternopil, Ukraine,
[4]Lviv Polytechnic National University, Lviv, Ukraine
Email: roman.v.kochan@lpnu.ua

Abstract*. A model describing the operation of semiconductor recombination sensor structures is proposed. The relationship between the illumination intensity of the sensor and the photocurrent changes is established. This approach enables the correlation of photocurrent, effective adsorbed charge, surface band bending, illumination intensity in specific zones, and recombination parameters at the interface. Additionally, a method for obtaining supplementary experimental information about the analyte from photocurrent measurements under varying illumination intensities is proposed.*

Keywords: Recombination Sensor, Interfacial Charge, Analytes, Photoresponse, Surface Recombination.

1. Introduction

The development of modern sensor systems is associated with the search for efficient sensing elements characterized by high sensitivity, selectivity, and compatibility with existing technological solutions [1]. If a sensor operates based on a novel transducer principle and employs an interaction mechanism that has not been previously used for the detection of specific substances, it can enhance the sensitivity and selectivity of detection and provide additional information beyond that obtained from existing sensors. The operating principle of recombination-type sensor structures is based on controlled and reproducible changes in the recombination properties of the semiconductor surface interface induced by adsorption. The measured parameter is the photocurrent of a silicon wafer with a deep barrier under illumination with a high absorption coefficient [2]. The photocurrent is determined by the physicochemical state of the interface and can vary by 2–3 orders of magnitude due to adsorption. Owing to their unique properties, recombination-type sensors hold significant potential for human health monitoring, particularly for detecting enzyme activity in biological fluids. Moreover, they are capable of distinguishing carbon nanotube modifications and can be integrated into complex sensor systems, such as "electronic nose" devices, for analyzing a broad range of compounds. Direct detection of enzymes using such structures is a promising approach; however, its implementation is complicated by the lack of fragments with a pronounced dipole moment in biomolecules. Instead, enzyme activity can be determined indirectly by analyzing reactions in which enzymes act as catalysts [3]. In a given environment (e.g., at a constant pH), if reagents change their effective charge, conditions for their detection may arise. The specificity of detecting certain biomarkers is related to the fact that intermediate reaction products contain fragments with dipole moments and exhibit activity in modifying the band bending near the surface, as well as influencing the recombination center parameters at the interface. Considering the multistep nature of the chemical processes accompanying enzymatic reactions, it is necessary to increase the volume of information obtained about the analyte. For this purpose, a combined use of modulated and constant illumination or a constant voltage may be applied. Portable versions of such sensors can be integrated into automated systems for monitoring human health and controlling environmental parameters using ad hoc measurements [4].

ISBN 978-80-69159-00-6

2. Physical Principles of Operation of the Recombination Sensor

Let's consider the modeling approaches that describe the operation of a silicon sensor Fig. 1. Assume that the initial band bending is zero in the absence of contact with the analyte ($Y_{s0} = 0$) and that adsorption induces an effective charge ($Qef > 0$) near the *SiOx/Si* interface. This results in a change in electronic band structure bending (Ys) and the photocurrent through the sensor. An increase in charge ($Qef > 0$) (and the corresponding increase in Ys) initially leads to hole depletion, followed by a transition to intrinsic conductivity and accumulation in the near-surface region of the sensor. Let the intensity of the probing illumination define the injection level of nonequilibrium carriers ($\Delta p = \Delta n$) at the plane corresponding $x=L$ (edge of space charge region). From the first integral of the electro-neutrality equation and Gauss's theorem [6], it follows that

$$\frac{Q_{ef}}{\sqrt{2\varepsilon_{s[}\varepsilon_0 kT}} \pm \left[(n_0+\Delta n)(e^{\frac{Y_s}{kT}}-1) + (p_0+\Delta p)(e^{\frac{-Y_s}{kT}}-1) + Y_s(p_0-n_0) \right]^{\frac{1}{2}} = 0, \quad (1)$$

where n_o and p_o equilibrium concentrations of carriers in p-Si .

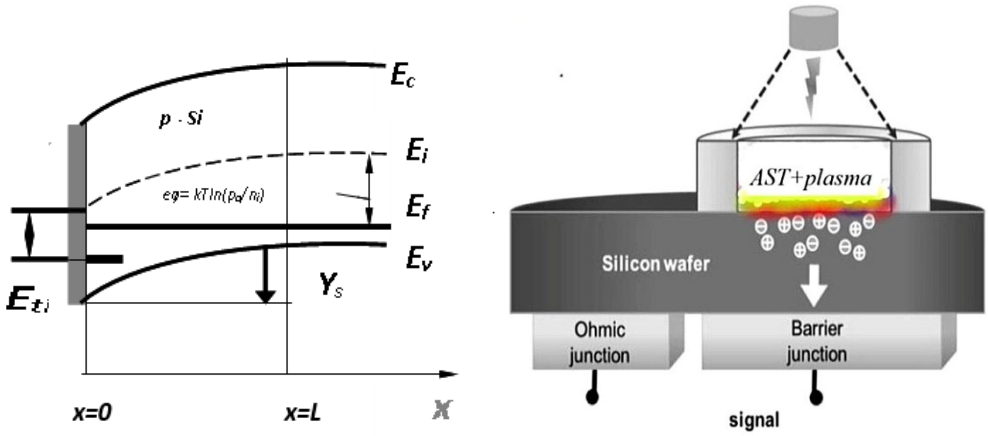

Fig. 1. Energy diagram of the near-surface region of a recombination sensor based on p-Si

In the case of a single energy level at the interface, the effective recombination rate Ssurf according to Stevenson- Keyes theory [5], is

$$S(Y_s) = \frac{c_p c_n N_t (p_0+n_0+\Delta p)}{c_n(n_s(Y_s)+n_i \exp(\frac{Eti}{kT}))+c_{,p}(p_s(Y_s)+n_i \exp\left(-\frac{Eti}{kT}\right))}, \quad (2)$$

where $\Delta p = \Delta n$ is the injection level, c_n c_p are electron and hole capture cross-sections, nt is intrinsic carrier concentration of silicon, N_t is the concentration of recombination centers, Et is the energy level of the recombination center, $n_s=n_o exp(Ys/kT)$ and $p_s=p_o exp(-Ys/kT)$ are relations between surface and bulk carrier concentrations. Equation (2) enables the analysis of injection regimes over a wide range. The photocurrent generated in the p-type base, which serves as the sensor signal, is expressed as [2].

$$i \cong \frac{1+\frac{s(Ys)}{\alpha(\lambda)D}}{s(Ys)\frac{l}{D}sh\left(\frac{d}{l}\right)+ch\left(\frac{d}{l}\right)}, \quad (3)$$

where $\alpha(\lambda)$ is the absorption coefficient in silicon, l-diffusion length of minority carriers, d - thickness of the base region (silicon wafer), D-diffusion coefficient, λ-wavelength. A self-consistent solution of (1)–(3) enables a simplified mathematical model describing the operation of the recombination sensor. The variation of the photocurrent must be expressed in terms of the effective charge near the surface $\Delta i(Qef)=i(Y_s)-i(Y_{s0})$.

ISBN 978-80-69159-00-6

3. Analysis of Results

Using (1)–(3), we calculate the dependence of the photocurrent on the adsorbed charge at different illumination intensities and analyze its characteristic features.

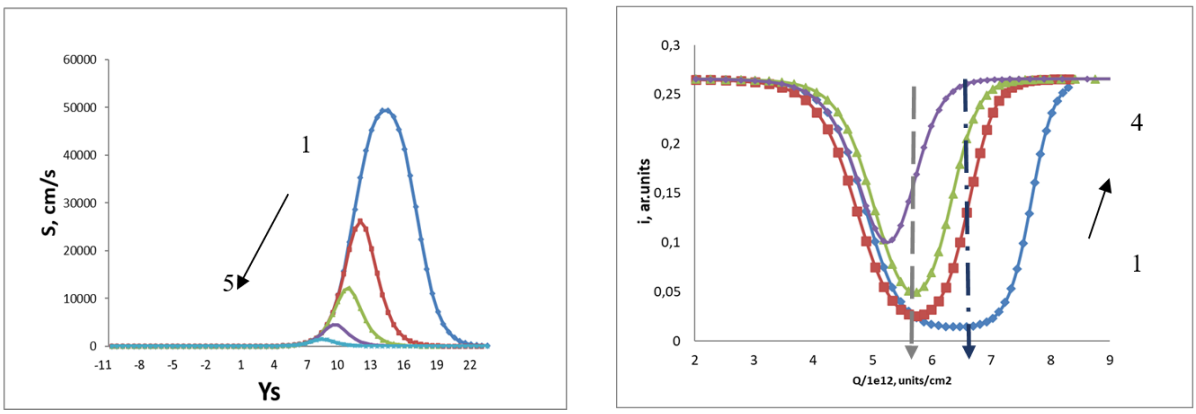

a) **b)**

Fig. 2. a) Dependences of the surface recombination rate on the injection level (illumination intensity used for scanning): 1) 1e2 1/cm³, 2) 1e4 1/cm³, 3) 1e7 1/cm³, 4) 1e8 1/cm³, 5) 1e9 1/cm³; b) Dependences of the photocurrent of the buried barrier structure on the effective positive charge Q_{ef} adsorbed on the sensor surface for different injection levels $\Delta p = \Delta n$ (illumination intensity parameter): 1) 10^2 cm^{-3}, 2) 10^4 cm^{-3}, 3) 10^7 cm^{-3}, 4) 10^8 cm^{-3}; parameters of the silicon sensor: c_n=c_p = 10^{-12}cm², N_t = 10^{11} 1/cm², Et = 0.05 eV, p_0=10^{15} cm^{-3}, $d \approx l$ = 200 μm, λ = 532 nm (α(λ) ≈ 10000 1/cm).

As follows from Fig. 2a, with increasing injection level, the recombination rate S_{surf} drops, and the shape of the curves changes significantly. The condition for the maximum S_{surf} when n_s and p_s are equal, is now satisfied at larger energy band bending. The reduction in recombination within the depletion region (7–13 kT) is associated with an electron depletion, while in the inversion region (15–22 kT) it is caused by a hole deficit. Fig. 2b shows the variation of the photocurrent (for a fixed Qef, the band bending and injection level are uniquely related by (1)). Thus two different analytes with Q_{ef1} and Q_{ef2} (horizontal arrows in panel b) will correspond to distinct sets of photocurrent values. To experimentally determine these values, it is necessary to measure the photocurrent amplitudes under multiple surface scanning conditions using light with varying injection levels $\Delta p = \Delta n$. This provides more information about the analyte and enhances detection probability. Since a substantial increase in illumination intensity may reduce the sensor's efficiency, employing a set of measurements is preferable. In practice, the optimal injection level range can be easily selected by adjusting the radiation source power (LED or laser) within 10 to 50 mW.

Let's consider the experimental results of enzymatic reaction studies using two probing intensities. Fig. 3 demonstrates the effect of illumination intensity on the spatial distribution of the sensor signal. A comparison of these distributions experimentally confirms the theoretical assumptions. Thus, the proposed analysis enables a more effective detection methodology. This approach represents a universal method for evaluating the performance of recombination-based sensors and allows estimating the sensor signal for a given substrate conductivity type, doping level, and recombination center parameters at the interface.

ISBN 978-80-69159-00-6

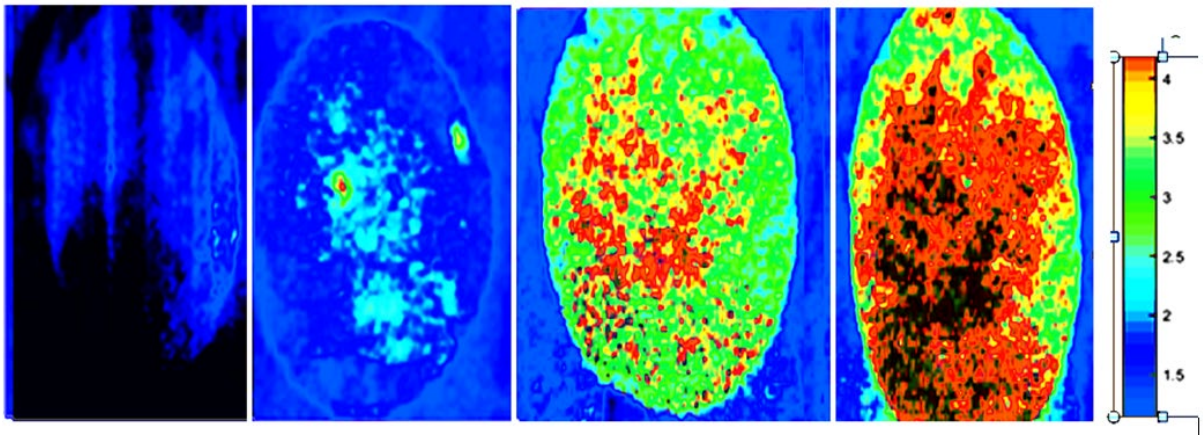

a) b) c) d)

Fig. 3. Photocurrent distribution maps illustrating the reaction catalyzed by the enzyme alanine aminotransferase (transaminase) under variable illumination intensity: a), b) — before mixing the reagents; c), d) — after mixing; λ = 532 nm; b), d) — 10 mW, and a), c) — 50 mW.

4. Conclusions

A mathematical model was developed to describe the operation of a silicon-based recombination sensor under various injection levels corresponding to different illumination intensities. It takes into account the interplay between surface recombination processes, band bending, and the influence of adsorbed charge, enabling a comprehensive analysis of the sensor's photocurrent response. Based on this model, an experimental methodology is proposed to acquire additional information about the analyte by measuring the photocurrent under variable illumination conditions. This approach enhances the sensor's analytical capabilities, improving both sensitivity and selectivity through controlled modulation of carrier injection levels**.**

References

[1] Jun, S., et al. (2015). Methods of reducing the effect of the acquired thermoelectric inhomogeneity of thermocouples on temperature measurement error. Meas. Tech. 58(3), 327–331.

[2] Khan, A. et al. (2020). The biochemical and clinical perspectives of lactate dehydrogenase: an enzyme of active metabolism. Endocrine Endocr. Metab. Immune. Disord. Drug Targets 20(6), 855-868.

[3] Kozinetz, A. et al. (2017). Physical properties of silicon sensor structures with photoelectric transformation on the basis of deep p–n-junction. Ukr. J. Phys. 62,(4), 318-325.

[4] Kozinetz, A., et al. (2024). Photovoltaic recombination sensor as system for real-time determination of lactate dehydrogenase activity. Sens. Bio-Sens. Res., 43, 100620.

[5] Sze S.M. (1982), Physics of Semiconductor Devices, Wiley, New York, 1982.

[6] Stevenson, D. T., Keyes, R. J. (1954). Measurements of the recombination velocity at germanium surfaces. Physica, 20(7-12), 1041-1046.

ISBN 978-80-69159-00-6

Research on the Influence of Irradiation Angle on Temperature Measurement Results for Raman Thermometry

[1]Tetiana Bubela, [2]Jacek Majewski, [1]Oleh Seheda, [2]Krzysztof Przystupa, [1]Orest Kochan, [1]Pylyp Scoropad, [3]Anna Szlachta, [1]Ivan Pytel, [1]Ihor Mykytyn, [1]Serhii Artemuk, [4]Valerii Yeromenko

[1]Lviv Polytechnic National University, Lviv, Ukraine,
[2] Lublin University of Technology, Lublin, Poland,
[3]Politechnika Rzeszowska im. Ignacego Łukasiewicza, Rzeszow, Poland,
[4] West Ukrainian National University, Ternopil, Ukraine
Email: orest.k.kochan@lpnu.ua

Abstract. *The work presents experimentally measured surface temperature of a solid body using the Raman effect. In particular, the study experimentally determines the influence of the irradiation angle on the measurement results, which helps address existing concerns regarding the prospects of the method and its potential for metrological certification.*

Keywords: Raman Effect, Temperature Transducer, Uncertainty

1. Introduction

Modern contact thermometry achieved considerable progress in the measurement accuracy [1-3]. However, this progress is related to large objects. Modern thermometry is investigating the methods of measuring temperature in the realm of microworld. All countries that have embraced nanotechnology recognize the necessity of advancing metrology to keep pace with this rapidly evolving field. The application of laser-based optical temperature measurement methods [4] allows reducing the thermometering zone size to tens of micrometers.

In the field of optical metrology, the key challenge is the development and implementation of new measurement methods and the identification of conditions necessary to meet the demands of next-generation advanced manufacturing. For instance, by applying a method based on light combination scattering, we can study temperature distribution in microelectronic components with micron-scale resolution.

However, the metrological aspects of this method remain insufficiently explored due to its novelty and uniqueness. In particular, the impact of the irradiation angle on temperature measurements has not been thoroughly investigated.

The goal of this work is determining the maximum permissible angle between the laser beam and the object under test for Raman thermometry.

2. Subject and Methods

The ability to detect a signal associated with temperature changes in the studied sample, as well as the result interpretation, depends on the applied measurement methods and the knowledge of the sample's geometric parameters.

Within Raman method the temperature measuring can be conducted by the ratio of intensities of Stokes (*Is*) and anti-Stokes (*Ias*) components in spectrum. There is distinct temperature (*T*) dependence of ratio of intensities of Stokes (*Is*) and anti-Stokes (*Ias*) components of dispersion light which is determined through appropriate currents of the photo transducer – i_s, i_{as} [4-6]:

ISBN 978-80-69159-00-6

$$T = \frac{hcv_0}{k\ln\frac{i_s}{i_{as}} - 3k\ln\frac{v_i - v_0}{v_i + v_0}}, \quad (1)$$

where, c is speed of light, h is Plank's constant, k is Boltzmann's constant, ν_i is wave number of incident photons, cm^{-1}; v_0 is Raman shift frequency, cm^{-1}.

Experimental researches were conducted on a calibrated optical bench. The reflected spectrum from the sample was recorded by HS 102H camera in vertical binning mode and stored digitally using the PCI-Line program. SL03/1 laser with the wavelength of 632 nm was used as the source of light. All data processing was done in Python.

The temperature determination formula does not account for influencing factors such as the shape, surface irregularities of the sample, or the angle of incidence and reflection of radiation. Additionally, it is impossible to position the equipment perfectly perpendicular to the object under test. Plates (particularly thin semiconductor single crystals) typically exhibit certain deviations from the ideal plane-parallel form due to the specifics of cutting, grinding, and polishing processes, as well as the challenges in controlling geometric parameters during the technological process. Post-process inspection only records the presence and degree of non-ideality, but reprocessing the plates to eliminate these imperfections is almost never performed. Therefore, the interpretation of result of laser probing depends on knowledge of the geometric properties of the investigated object. Neglecting geometric features sometimes leads to the detection of fictitious micro- and macro-objects in single crystals (e.g., regions of "anomalous" light absorption, "wave-like" impurity distribution, etc.) [4, 5].

Various deviations from the ideal shape affect the interaction of light differently. For example, when a laser beam interacts with a thin semiconductor single-crystal plate, light interference occurs. However, its manifestation in the reflected beam can correspond to any of the possible scenarios constrained by boundary conditions—ranging from interference in an ideal plate to a degenerate regime with multiple internal reflections of laser rays without interference. Within a single crystal with the diameter of 75–150 mm, the full spectrum of these possibilities may sometimes be observed. We will experimentally examine certain typical features of the influence of the geometric shape of plates and the angle of the installed equipment, which introduce significant impact onto the measurement results. Wedge-shaped deviation (non-parallelism of surfaces) implies a variation in plate thickness along an arbitrary direction and is characterized by the angle φ between the surfaces. For small angles ($\leq 10^{-3}$ degrees), it can be approximated as $tg\varphi \approx \varphi \approx dh/dx$. The thickness variation can be either monotonic (non-random) or non-monotonic (random). In former, the entire plate exhibits a wedge shape, whereas the latter requires measuring local wedge deviations across the entire surface (or at multiple points) and determining the root mean square value to describe the plate's shape. The magnitude dh/dx, which characterizes the random wedge deviation of plates (with two polished surfaces) made of monocrystalline silicon and other semiconductors, is relatively small, ranging from 10^{-6} to 10^{-4}. For Raman scattering spectra, the influence of the wedge-shaped sample on the measurement results is minimized by simultaneously reading the Stokes and anti-Stokes bands and comparing them for thermometry purposes. Therefore, for the Raman method, this deviation does not pose a significant issue.

3. Results

To assess the impact of sample wedge deviation on measurement results, an experimental temperature determination was conducted using the Raman scattering method for a silicon plate

ISBN 978-80-69159-00-6

with the thickness of 2 mm and the wedge deviation of $dh/dx = 10^{-5}$, as well as for a silicon plate of the same thickness with the wedge deviation of $dh/dx = 10^{-3}$ (≤1 degree).

The obtained Raman spectra were used for the experimental determination of the measurement error of temperature due to the wedge-shaped deviation of the investigated sample.

The calculated temperature value for both samples was determined using (1) with the reference temperature of 23°C. It showed that the influence of the plate's wedge-shaped deviation on the Raman spectra does not exceed 0.01% compared to the plane-parallel sample.

In measurement praxis this error can be considered negligibly small. Other components of the measurement error are more significant. However, the angle of incidence and reflection is not determined solely by the wedge-shaped plate. It is more often associated with the equipment.

The geometric dimensions of the laser and the mounting components of the spectrophotometer make it impossible to use an optical fiber to transmit laser radiation and read the reflected optical signal through a fiber optic channel. That problem, related to determining the optimum angle between the laser beam and the optical fiber head. This problem was solved experimentally.

To assess the numerical value of the temperature measurement error, a series of spectral measurements were performed for three different materials (synthetic diamond, silicon crystal, and carbon nanotubes) and for two different temperatures see Fig. 1.

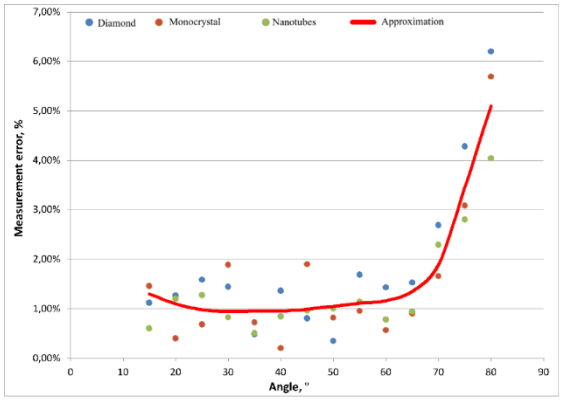

A) T=20°C

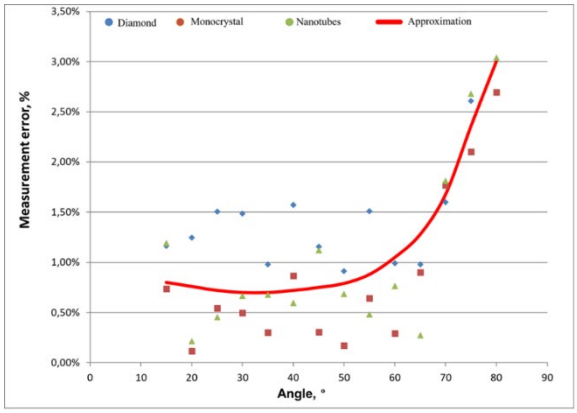

B) T=70°C

Fig. 1. Dependence of temperature measurement error on the angle between the laser and the investigated object (A - temperature 20°C; B - temperature 70°C).

4. Discussion

From the obtained experimental data, it is not possible to determine a single optimal angle between the laser beam and the investigated object with absolute certainty. However, a clear

ISBN 978-80-69159-00-6

trend is observed in both graphs, indicating that the measurement error remains relatively low and stable for angles up to approximately 50-55°. Beyond this range, a sharp increase in measurement error is evident, particularly for angles greater than 60-65°. This suggests that while minor variations in the angle within the lower range do not significantly affect the measurement error, deviations beyond 60° introduce substantial error.

The analysis of different materials – diamond, monocrystal, and nanotubes – reveals that despite some variations in individual data points, all three materials exhibit a consistent pattern of error increase at higher angles. The approximation curve further supports this observation, demonstrating a gradual rise in error up to 50-55°, followed by an exponential increase beyond 60°. The underlying cause of this behavior may be attributed to changes in the interaction dynamics between the laser beam and the material surface, including increased scattering effects and possible misalignment of the reflection path at steeper angles.

5. Conclusions

The geometric dimensions of the samples have a significant impact on the interaction results. Even minor deviations from an ideal flat surface may lead to irregularities in beam reflection, particularly at larger angles, increasing measurement error. This is especially critical for laser-based temperature measurement techniques, where precise alignment is essential for minimizing errors. These findings emphasize the importance of maintaining the laser-object angle within an optimal range, ideally below 60°, to ensure reliable and accurate data acquisition. Future studies can explore the effects of surface roughness, material absorption properties, and alternative optical configurations to further refine the optimal angle range for such measurements.

Acknowledgements

The authors are grateful to the Armed Forces of Ukraine for the opportunity to work safely. The authors are also grateful to Staff of the Information-Measuring Department for assistance in preparing the materials for publication.

References

[1] Jun, S., & Kochan, O. (2015). Common mode noise rejection in measuring channels. *Instruments and Experimental Techniques*, 58, 86-89.

[2] Zhengbing, H., Jotsov, V., Jun, S., Kochan, O., Mykyichuk, M., Kochan, R., & Sasiuk, T. (2016). Data science applications to improve accuracy of thermocouples. *In IEEE 8th International Conference on Intelligent Systems (IS)*, 180-188.

[3] Krayovskyy, V., Haraniuk, P., Horpeniuk, A., Romaka, V. (2024). Simulation of characteristics of sensitive elements of temperature converters based on TiCo1-xCrxSb. *Measuring Equipment and Metrology,* 85(4), 30-36.

[4] Stadnyk, B., Yatsyshyn, S., Seheda, O. (2010). Metrology of temperature transducer based on Raman effect. *Sensors & Transducers*, ISSN 1726-5479.

[5] Shedd, T., Anderson, B. (2005). An automated non-contact wall temperature measurement using thermoreflectance. *Measurement Science and Technology*, 16(9), 2483-2488.

[6] Kaminskii, A. (1996). *Laser Crystals: Their Physics and Properties*. Springer.

Measurement of Physical Quantities I

ISBN 978-80-69159-00-6

Comparison of Train Speed Estimates Determined Using Different Fusion Methods

Józef Wiora

Department of Measurements and Control Systems,
Silesian University of Technology, ul. Akademicka 16, 44-100 Gliwice, Poland
jozef.wiora@polsl.pl

Abstract. *Train on-board system calculates its speed based on values provided by several sensors. This work deals with a hypothetical case where the speed is estimated throughout 60 seconds during braking. Information from five sensors characterized by different error models is fused in three ways: mean, median, and the weighted method. Although the weighted method is the most complex, it exhibits the best fit to the reference value.*

Keywords: Train Speed Estimation, Weighted Data Fusion, Measurement Uncertainty

1. Introduction

The train speed estimation is crucial for safe driving. Currently, the broadly launched European Train Control System (ETCS) uses several speed sensors simultaneously to obtain the most reliable estimate. None of these is perfect. Wheel sensors are sensitive to slips and slides. The estimates rely on wheel diameters, which decrease with distance. The Doppler radar suffers in winter, when snow disturbs its correct working. Accelerometers exhibit drifts. Satellite systems like GPS do not work correctly in canyons and tunnels. Other methods can also be used, but they have their inherent weaknesses, too [1, 2].

This work aims to compare fusion methods used for estimating train speed. It is based on synthetic data illustrating working in nominal conditions, where no sensor provides a value significantly different to the reference one.

2. Subject and Methods

A hypothetical train movement is considered. Let the train pass over a balise at a speed of 100 km/h. Then the driver starts braking with deceleration shown in Fig. 1 as the green curve. The speed of the trains decreases as it is seen in the blue curve. This speed is treated as the reference during further analysis. It is also assumed that speed offsets of sensors are zeroed while passing over the balise. This assumption is not totally in line with real situations where only distance offsets are zeroed.

The train is equipped with five sensors: an accelerometer, two wheel sensors (WS1 and WS2), Doppler radar, and GPS. The accuracy of the sensors is modeled in Table 1. Values used during simulations are typical for railway applications. The maximum permissible errors are after the technical notes, while the values used for speed estimations are about 70 – 80% of the maximum errors.

The measurements are taken every 100 ms. For each sample and each sensor, the speed is calculated. Additionally, the random and systematic errors are estimated. If needed, the random errors are joined using the root of the sum of squares, while the systematic errors are the sum of absolutes. Finally, the standard uncertainty (u) is calculated as [3]

$$u = \sqrt{\sigma^2 + \Delta_{\max}^2/3}, \tag{1}$$

ISBN 978-80-69159-00-6

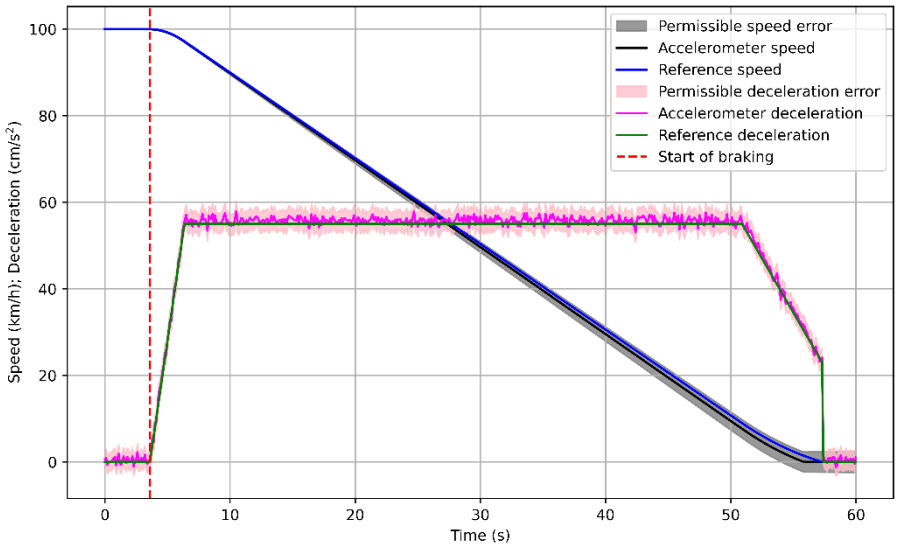

Fig. 1. Deceleration and speed profile used during simulations as the reference values and values provided by the accelerometer with their permissible errors.

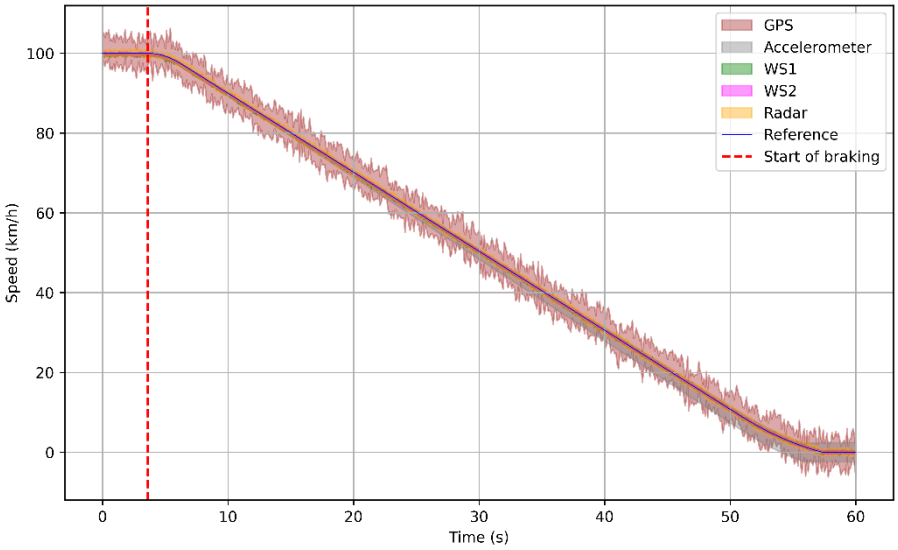

Fig. 2. Speed of sensors with permissible errors and reference values.

Table 1. Models used to simulate errors of sensors. The symbols used: a – deceleration; v – speed; $N(\sigma^2;\bar{x})$ – random variable having the normal distribution with the variance of σ^2 and the expectation of $\bar{x}$; G – gain error; x_0 – offset.

Sensor	Error model
Accelerometer	$a = a_{ref}(1 + G_{\text{acc}}) + N(\sigma^2_{\text{acc}}; a_{0\text{acc}})$
WS1	$v = v_{ref}(1 + G_{\text{WS1}}) + N(\sigma^2_{\text{WS1}}; 0)$
WS2	$v = v_{ref}(1 + G_{\text{WS2}}) + N(\sigma^2_{\text{WS2}}; 0)$
Radar	$v = v_{ref} + v_{0\text{Radar}} + N(\sigma^2_{\text{Radar}}; 0)$
GPS	$v = v_{ref} + v_{0\text{GPS}} + N(\sigma^2_{\text{GPS}}; 0)$

ISBN 978-80-69159-00-6

where σ is the assessed standard deviation of the random error (which is a bit greater than the standard deviation of the noise added in simulations), and Δ_{max} is the systematic error.

The fusion of sensor outputs can be realized using a different manner. The most common is calculating the mean values. Such an estimate is good if there are many sources with normally distributed errors. If only a few sensors are available, medians provide better estimates. Another approach is the estimation of the results based on the uncertainties of the quantities taken into account. The weighted method estimates the fused value y based on values x_i and their uncertainties u_i as [4]

$$y = \frac{\frac{1}{u_1^2}x_1 + \frac{1}{u_2^2}x_2 + \frac{1}{u_3^2}x_3 + \cdots}{\frac{1}{u_1^2} + \frac{1}{u_2^2} + \frac{1}{u_3^2} + \cdots} \tag{2}$$

3. Results and Discussion

Using the above-described reasoning, Fig. 1 presents the outputs of the accelerometer. The permissible errors are double standard uncertainties. Similar calculations were performed for other sensors. Fig. 2 presents these values. The declared accuracies of the sensors are different, so the variabilities of the curves with the permissible errors are also various.

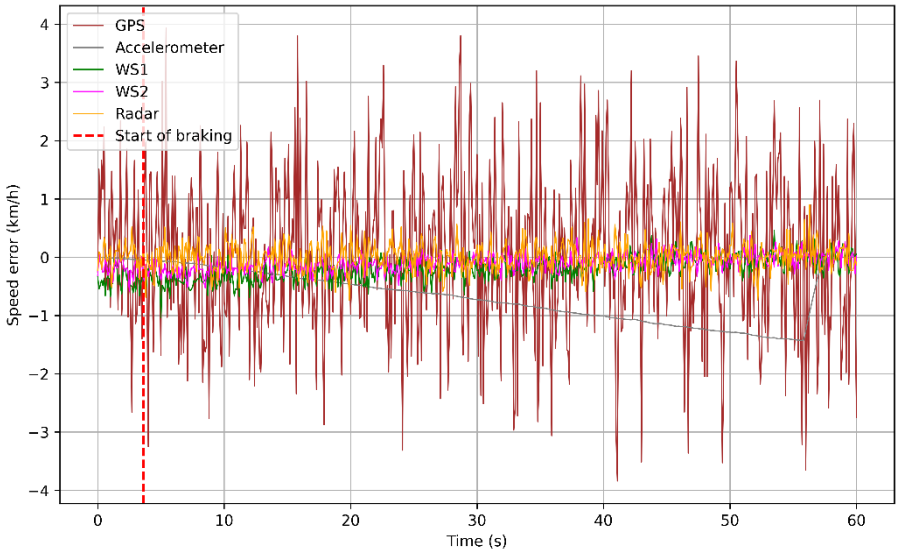

Fig. 3. Speed of sensors with permissible errors and reference values.

Comparing the sensor speed outputs with the reference speed leads to the speed errors shown in Fig. 3. The different nature of the plots is clearly visible. The GPS provides a noisy signal, while the accelerometer can introduce drifts. In nominal conditions, the accelerometer and wheel sensors provide the most accurate values.

Applying the approaches of the speed fusions, Fig. 4 is obtained. It can be observed that the estimates calculated using the weighted method are the closest to zero. Standard deviations of the speed errors are 0.29, 0.14, and 0.11 km/h for the means, medians, and weighted ones, respectively. The values change after each simulation due to randomization, but the weighted estimate is always more accurate.

The weighted fusion method may also be applied without further modification in case of sensor malfunctions. The only need is the estimation of speed uncertainty. GPS modules typically

ISBN 978-80-69159-00-6

provide such assessments. Other sensors need to add software detectors to identify this state. Usually, such detectors are present on the vehicle board.

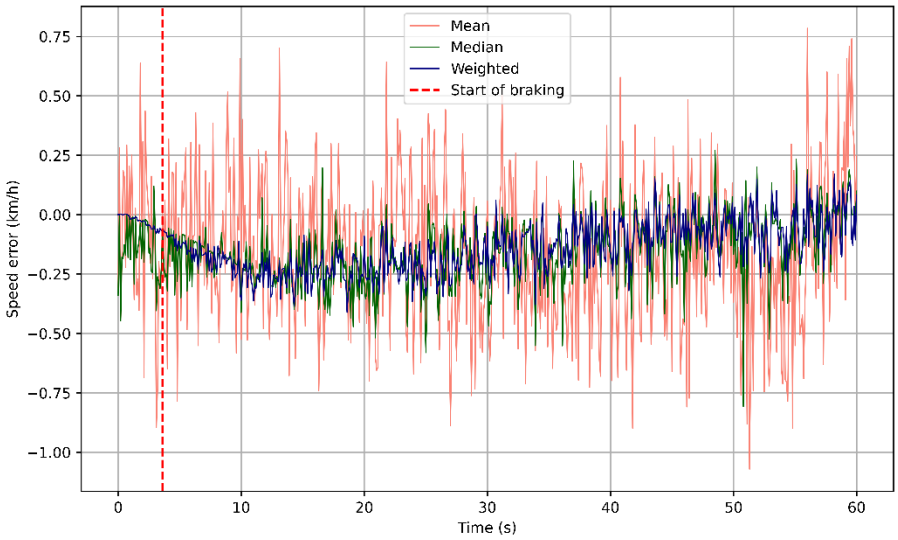

Fig. 4. Fused speed error based on means, medians and weights.

4. Conclusions

The simulated train speed estimates during deceleration are analyzed in this work. The obtained results allow us to conclude as follows. Calculation of means is the most commonly used data fusion method. The estimates are, however, weak. Better estimates are from medians. The best ones can be obtained by calculating a weighted sum with the weights inversely proportional to assessed squares of uncertainties. The uncertainties have to be appropriately modeled. The error propagation should be treated separately for systematic and random effects. These make the most accurate weighted method the most complicated.

Acknowledgements

Funded by the Polish Ministry of Science and Higher Education (02/050/BK-25/0047).

References

[1] Liudvinavičius, L., Sładkowski, A. (2017). Train Protection Systems in Different Railway Gauges. In: Sładkowski, A. (eds) Rail Transport—Systems Approach. Studies in Systems, Decision and Control, vol 87. Springer, Cham. https://doi.org/10.1007/978-3-319-51502-1_7

[2] Chen, W., Yang, G., Tu, Y. (2024). A Digital Track Map-Assisted SINS/OD Fusion Algorithm for Onboard Train Localization. *Applied Sciences*, 14 (1), 247.

[3] BIPM (2008). Evaluation of measurement data-Guide to the expression of uncertainty in measurement (GUM:1995 with minor corrections). *Bureau International des Poids et Mesures.* JCGM.

[4] Wiora, J., Kozyra, A., Wiora, A. (2016). A weighted method for reducing measurement uncertainty below that which results from maximum permissible error. *Measurement Science and Technology*, 27 (3), 035007

Measurement of Atomic and Ionized (Pb I and Pb II) Spectra of Lead, Using Unique Technique - Hybrid Plasma System

[1]Arnolds Ubelis, [1]Zane Metra, [1]Aleksandrs Kolesniks, [2]Janis Rupkus

[1]NSP FOTONIKA-LV, University of Latvia, Riga, Latvia,
[2]Riga Photonics Centre, Riga, Latvia
Email: metrazane@gmail.com

Abstract. *The report is highlighting the first results of application of hybrid plasma system: hollow cathode discharge combined with low pressure inductively coupled radiofrequency plasma (HC & RF-ICP) in studies of spectroscopy of atomic lead. The experimental measurements and analysis resulted in increasing substantially the knowledge base on the spectroscopic properties of atomic Pb I and eventually for ion Pb II. Current advances in atomic physics envisage that the data on atomic spectroscopy of Pb I and Pb II need to be substantially enriched, to open new opportunities for the studies of basic properties of atoms and ions of lead. The limiting factor for that, until now, were insufficiently intensive sources of emission needed for such research in case of lead, having low volatility. The presentation and extended abstract of the conference will report the first promising results of pilot research.*

1. Introduction

Currently, substantial progress in theoretical atomic physics and growing needs of astrophysics envisage that experimental data on atomic spectroscopy of atomic *(Pb I)* and ionic *(Pb II and more)* lead need to be substantially enriched to open new opportunities for the studies of basic properties of atoms and ions of lead and theoretical calculations. The limiting factor for that, until now, absence of intensive enough sources of emission.

Additionally, there is growing need to improve sensitivity, and to make more user-friendly methods, used in detection of traces of lead containing pollutants in the environment. Possible breakthrough – application of resonance fluorescence, which could be effectively used in case of presence of intensive sources of basic resonance lines. The best evidence of that, is the case of mercury, for which sophisticated resonance florescence techniques where developed, and standardized during the last decades increasing the sensitivity substantially [1]. Our research aims to move toward similar results in the case of lead.

2. Subject and Methods

To address these demands, our team worked towards the development of hybrid plasma source, being among the first in coupling hollow cathode and radiofrequency *(54MHz)* inductively coupled low pressure plasma discharge in the hybrid system (*HC & RF-ICP), (see Fig. 1).*

Fig 1a **the conceptual drawing of the geometry of hybrid plasma system.**2 – hollow cathode; 3- Anod: 4 – ICP-RF inductor; 5-ultrasil window; 6 – Vacuum pumping and gas supply: 7 – diffusion of sputtered by HC discharge atoms into the area of ICP-RF plasma.

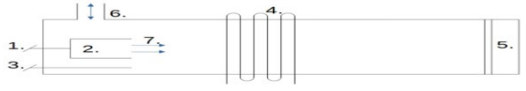

Fig. 1b. ICP-RF inductor positioned on industrial **small power lead** HC lamp (1): 2-hollow cathode; 3 – ICPRF Inductor

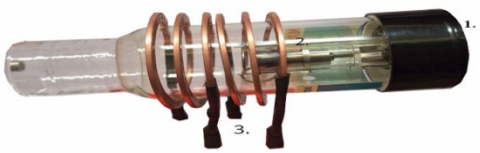

The spectrum of light coming from such device is dominated by the group of intensive resonance spectra lines of Pb I and main resonance lines of Pb II located in near VUV *(0.000-*

ISBN 978-80-69159-00-6

69 739.603 eV: 143.396 nm*;0.000-66 124.53 eV:151.242* nm*; and 0.000 - 57 910.48: 172.675* nm*)*. Modified industrial hollow cathode lamp of lead was used to build hybrid plasma system. Hollow cathode of lead powered with DC voltage up to 500V ensured current of hollow cathode discharge within the range of 10-20 mA, slightly about nominal of used industry lamp. The lead HC lamp was linked to glass vacuum stand adapted for calibrated supply of Ar gas into the lamp. The pressure of Ar, used during the studies, was in the range of 1-2 Torr. The inductor of ICP generator was positioned in the lamp in front of hollow cathode, *(see Fig. 1b).* Atomic Spectroscopy of lead was performed on Princeton Instruments SpectraPro 2300 monochromator with 1200 lines grating.

The following procedure was employed for the study. Firstly, the intensities of spectra lines from hollow cathode discharge were recorded *(column 2 in the table below)*, followed by recording lines of spectra from hybrid system: HC & RF-ICP*(column 2 in the table below)*.Then, the lead atoms and ions produced at cathode*(filled with lead)* by HC plasma discharge diffused into the region covered by ICP plasma, *(see Fig. 1a),* and the spectrum of Pb I and ionic spectra of Pb II were initiated under influence of skin effect of ICP H *(magnetic)* component of plasma discharge, where temperature of electrons reach around 10 000K. It is well known, that in optimized conditions, ICP plasma produces spectra of atoms with intensities up to 100 times higher than HC discharge [2], but the usage of ICP is limited by ability to vaporize *(atomise)* the used element. So far, the primary research efforts performed in different labs are focussed on the development and use of hollow cathodes with sophisticated geometry to make progress in the studies of atomic and ion spectra of hardly volatile elements, see in [3] the article published in 2024, only one year ago.

To study Pb I and in the search for Pb II spectra lines we used Princeton Instruments: SpectraPro 2300 monochromator having the grating with 1200 lines. **Hβ** – Balmer beta from H_2spectra – always appearing in ICP plasma source due to transparency of heated silica, or glass, and can be used as an excellent wavelength standard for the calibration of spectrometers recordings.

3. Results

During this pilot study of spectroscopy of atomized lead, using hybrid plasma source, we recorded very rich spectrum of Pb I and several lines of Pb II as well. Tab.1 below represents the list of more intensive lines and illustrates the increase of intensities when hybrid plasma is in operation.

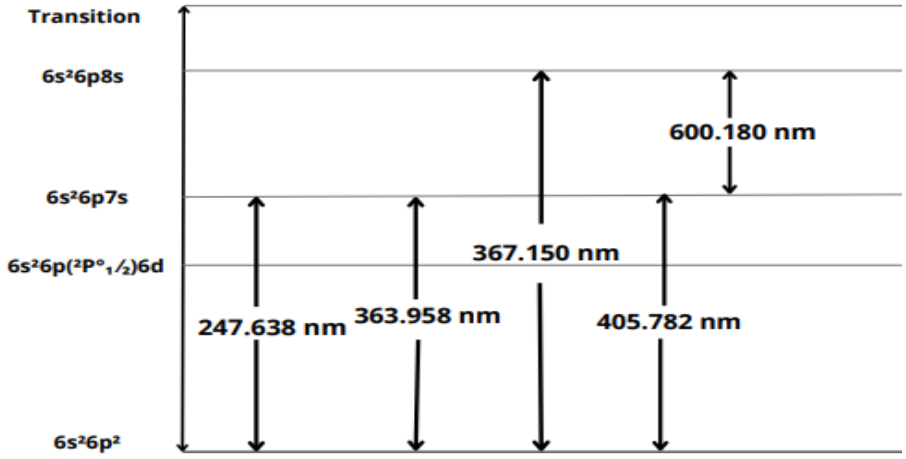

Fig. 2. An abbreviated Pb-atom energy-level diagram showing the origins of the lines of this study

ISBN 978-80-69159-00-6

Tab.1. The list of measured spectral lines of Pb I and Pb II emitted from the hybrid (*HC& RF-ICP)* plasma sources. Column 2: I_1 intensities of lines camming from hollow cathode discharge. Column 3: I_2 intensities of lines coming from hybrid *(HC& RF-ICP)* plasma. Column 4: amplification coefficient I_2/I_1. Column 5. I_3 intensities of lines coming from hybrid *(HC& RF-ICP)* plasma when splash of Argon brought more of Pb into area of ICP plasma. Transition between energetic levels. Column 6. Transition between energetic levels,

λ (nm)	I_1*(arb. units)*	I_2*(arb. units)*	I_2/I_1	I_3 *(arb.units)*	Transition levels (eV), [4]
Pb I 240.195	600	2530	4.22	not measur.	7 819.2626- 49 439.6165
Pb I 247.638	not observ.	3050		not measur.	7 819.2626 - 48 188.6296
Pb I 261.365 Pb I 261.418	1050	1720	1.64	not measur.	7 819.2626 - 46 068.4385
Pb I 266.317	610	2110	3.48	4140	10 650.3271 - 48 188.6296
Pb I 280.200	930	1750	1.88	not measur.	10 650.3271- 46 328.6668
Pb I 282.319	1050	6110	5.79	not measur.	10 650.3271 -46 060.8364
Pb I 283.307	1330	6070	4.55	21470	0,000 - 35 287.2244
Pb I 357.273	1060	2020	1.90	1740	21 457.7982 - 49 439.6165
Pb I 363.958	1570	2290	1.46	not measur.	7 819.2626 - 35 287.2244
Pb I 368.347	1860	2830	1.52	4100	7 819.2626 - 34 959.9084
Pb I 405.782	6820	9400	1.37	12700	10 650.3271 - 35 287.2244
Pb II 415.29	1360	3120	2.27	5390	-
Pb I 416.805	1870	4250	2.27	7620	21 457.7982 - 45 443.1710
Pb I 434.64	1620	3570	2.20	4870	29 466.8303 - 52 499.6391
Pb II 435.27	1900	3730	1.93	4230	-
Pb II 457.905 Pb II 458.23	1430	3300	2.26	3410	-
Pb I 589.59	760	3320	4.37	3070	34 959.9084 - 51 916.9408
Pb I 600.18	not observed	3230	-	not measur.	51 916.9408 - 51 944.1059
Hβ$_{656.281}$	4110	17870	4.34	14650	2s - 3p
Pb I 722.911	1590	2460	1.54	not measur.	51 944.1059 - 35 287.2244

Note: there are few P I lines observed only in emmision from Hybrid plasma.

4. Discussion

Tab.1 convincingly shows the increase of intensities of spectral lines on Pb I as well as few recorded lines of Pb II when hybrid plasma is in operation. The increase differs for different lines and that will be subject for further studies. Increase of intensities *(especially for the main resonance lines see Tab.1 Fig 2 above)* under influence of splash of Ar is very promising, indicating eventual improvements in such experiments. Evidently, the application of weak flow of argon through hybrid plasma will result in the increase of intensities substantially, because more atoms and ions from the hollow cathode will be excited by ICP plasma. Evidently, another advancement in the follow-up studies, will be to run hollow cathode discharge at much higher power supply to produce more atoms and ions for ICP plasma. We will apply our competence, developed, and tested for years technique for the design and production of glass, silica glass tubes, and glass vacuum stands incorporating Ar gas supply system, to design and produce wholly silica glass tube for hybrid plasma systems in geometry similar to industry produced. Practically zero thermal expansion of silica glass and melting temperatures above 1200 ºC will

ISBN 978-80-69159-00-6

make possible much higher currents for hollow cathode without danger of damage and resulting in higher ion concertation in plasma.

Results of this pilot experiment indicate very promising outcomes for follow up research and future applications of such hybrid source of resonance lines of atomic and ionic lead:

- ✓ The possibility to produce intensive source of resonance lines of lead with profiles of lines without reabsorption which means ideal case for both version *(absorption and resonance fluorescence)* of analytical spectroscopy.
- ✓ The presence of large number of spectral lines in the spectrum will allow branching ratio studies for many groups of spectral lines like our studies in case of Se I [6]., Te I [7]., and As I [8].
- ✓ The presence of spectral lines of Pb II in the spectra from hybrid plasma indicates on broad opportunities to study ion spectra of lead for the first time, using ICP plasma, and evidence on such opportunity for many other ions of different elements.

The research team is looking forward to performing pioneering research for atoms, and ions of many hardly volatile elements, to contribute to knowledge base having strongly growing demand, emerging in nearest decade provoked by results of observations of spectra by foreseen fleet of space-based telescopes, [9], and steady demand from atomic physics and astrophysics [10].

References

[1] Telliard, W. A., and M. Andersson. (2005). Method 245.7 Mercury in Water by Cold Vapor Atomic Fluorescence Spectrometry. *US EPA Office of Science and Technology, 1-33.*

[2] S. A. Kazantsev, V. I. Khutorshchikov, G. H. Guthohrlein. L. Windholz, Practical Spectroscopy of High-Frequency Discharges, *Plenum Press, New York, and London, 1998, 2013, 337 pp.*

[3] Sen Sarma, P. R., Belmonte, M. T., & Mar, S. (2024). Characterisation of a hollow-cathode lamp to measure accurate branching fractions of rare-earth elements. *The European Physical Journal D*, *78*(6), 76. 1-9

[4] Kramida, A., Ralchenko, Yu., Reader, J., and NIST ASD Team (2024). *NIST Atomic Spectra Database (ver. 5.12)*, [Online]. Available: https://physics.nist.gov/asd, 2025, March [5] National Institute of Standards and Technology, Gaithersburg, MD. DOI: https://doi.org/10.18434/T4W30F

[5] Ubelis, A. P., Berzinsh, U. V. (1986). Transition probability measurements of Se I spectral lines by emission method. *Physica Scripta, 1986, 34 (6B), S. 805-806..*

[6] Ubelis, A. P., & Berzinsh, U. V. (1983). Transition probability measurements of Te I spectral lines by methods of emission and absorption of radiation. *Physica Scripta*, *28*(2), 171-178.

[7] Berzins, U., Ubelis, A., & Bziskjans, A. (2021). Branching fraction measurements of arsenic 4p25s-4p3 transitions. *Journal of Quant. Spectr. and Radiative Transfer*, *276*, 107943.

[8] PLAnetary Transits and Oscillations of stars *(PLATO)* is a *space telescope* under development by the ESA for launch in 2026

[9] Advances in Atomic Physics: An Overview, by Nobel Prise Laureate Claude Cohen-Tannoudji, and David Guery-Odelin. *2011 by World Sci.Illustr. Kindle Edition, 794 pages.*

Application of Resonance Atomic Spectra Lines of Se I and Te I in Measurement Transmittance of optical Fibers in far UV

Aleksandrs Kolesniks, Arnolds Ubelis, Austris Pumpurs

NSP FOTONIKA-LV, University of Latvia, Riga, Latvia,
Email: *AleksandrsKolesniks45@gmail.com*

Abstract. *The report will present and discuss the potential and advantage of the application of resonance atomic spectra lines of Se I and Te I in the measurement transmittance of optical fibers in far ultraviolet spectra region up to 160 nm, in response to the demand for such fibers in experimental spectroscopy research, industry applications, and health treatment.*

Keywords: Atomic Spectra Lines, Transmittance Measurement, Far UV

1. Introduction

Our research team used its early collected experience of development and application of combined Se & Te low pressure inductively coupled radio frequency (54 MHz)plasma source producing intensive and rich with lines resonance spectra of atoms of both elements to measure basic properties of Se I and Te, [1], [2]. About 133 Pa of Ar gas was used to ignite the discharge into the vapour phase of Se and Te filled into the bulb in the proportion 4 : 1.

It's well known that high quality silica glass has transparency up to 160 nm, [3], and the challenge for the industry is to move as far as possible with the transparency of optical fibers and bundles of optical fibers towards 160 nm (the limit set by the transparency of Ultrasil type silica glass) as far as possible.

2. Subject and Methods

There are a lot of situations in experimental research where the information about curves of transparency of industry-produced optical fibers in UV and far UV regions needs to be precisely tested. Currently used sources of spectra having a continuum in UV and far UV are not handy enough and therefore time consuming. Particularly, frequently used deuterium arc lamps spectrum has limits around 200 nm, *(see e.g. [4])*. Industry produced arc lamps of Xe and Kr have the same problem and demand energy sources based on high-power electronics.

In this report we are sharing our experience and results of the exploration of industry produced high-quality fiber bundle (5 m long) on its transparency in far UV. We used Prinston Instruments SpectraPro 2300 monochromator with 1200 lines grating for our studies with the detection system able to detect spectra up to 180 nm. In order to avoid absorption of oxygen O2 in the air, we used the flow of nitrogen *(N2 molecule has no absorption bands up to far UV)*. The weak flow of nitrogen passed via the monochromator *(substituting air there)*, and escaping through the entrance slit was directed into the tube forming an optical pass to the spectra source. In this case, powered by an inductively coupled plasma RF generator combined electrodeless discharge lamp of Se & Te *(see Fig. 1, Fig. 2, Fig. 3 and Fig. 4.)*. Highest quality synthetic silica glass was used for the bulbs of lamps to ensure transparency up to 160 nm. Resonance spectra of Se I and Te are positioned in the UV spectral range from 250 nm to 160 nm and are rich with intensive lines.

ISBN 978-80-69159-00-6

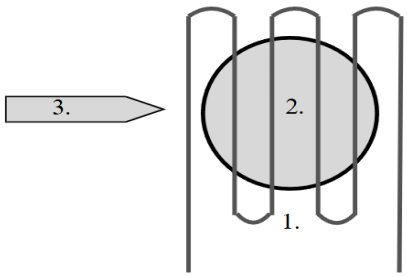

Fig. 1 The conceptual drawing of the geometry for optical fiber testing. 1 - ICP-RF inductor. 2 - Low-pressure Se Te lamp. 3 - optical fiber connected to spectrometer.

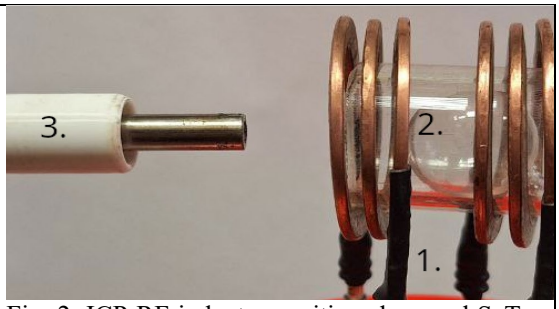

Fig. 2. ICP-RF inductor positioned around SeTe. 1- ICP-RF inductor. 2 - SeTe lamp; 3 – optical fiber.

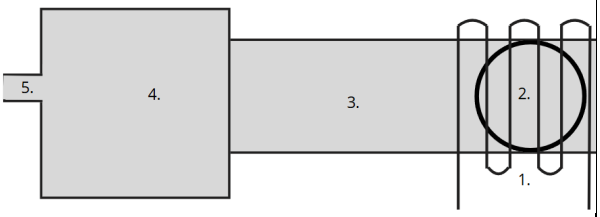

Fig. 3. The conceptual drawing of the geometry for testing without optical fiber.1 - ICP-RF inductor. 2 - Low-pressure Se Te lamp. 3. Quartz tube connected to a spectrometer. 4 - Spectrometer. 5 - Nitrogen gas input.

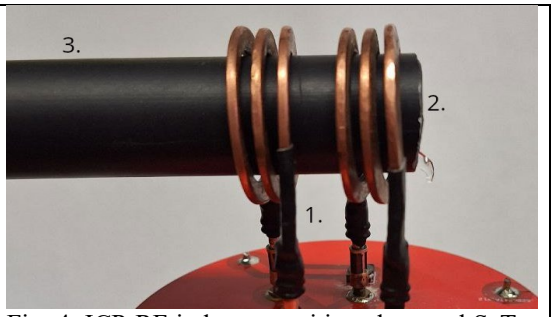

Fig. 4. ICP-RF inductor positioned around SeTe. 1- ICP-RF inductor. 2 - SeTe lamp; 3 – Quartztube.

3. Results

The outcomes of our studies are presented in the pictures below *(see Figs. 5, 6, and 7).*

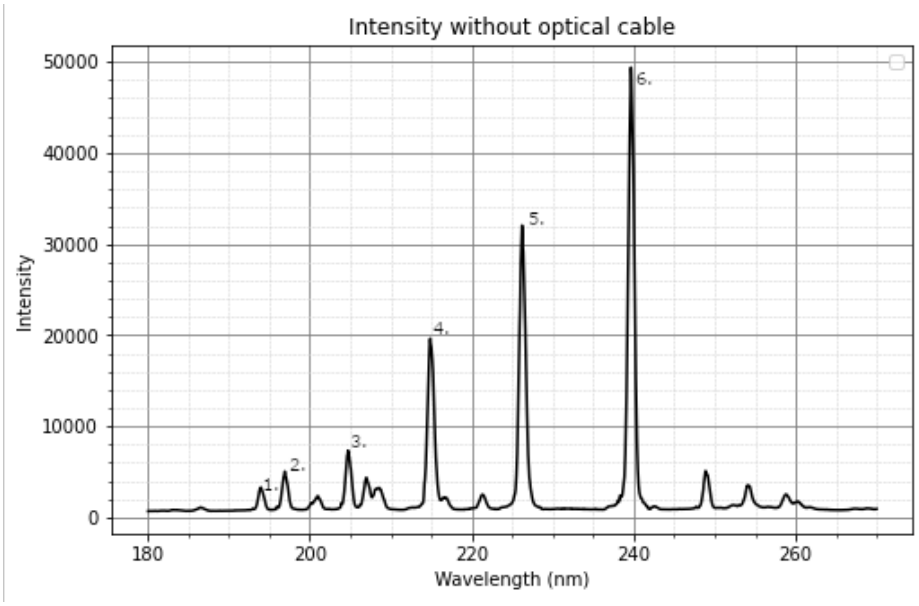

Fig. 5. Intensity of Se and Te spectral lines without an optical cable in far UV. Labelled spectral lines are: 1. – C I 193.09 nm, 2. – Se I 196.09 nm, 3. - Se I 203.98 nm, 4. - Te I 214.72 nm, 5. - Te I 226.55 nm, 6. – Te I 238.32 nm.

ISBN 978-80-69159-00-6

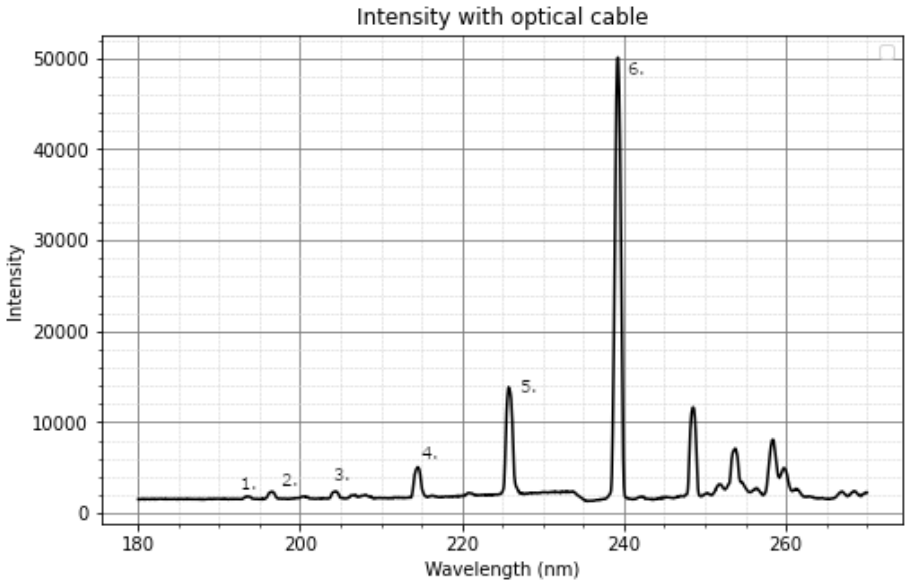

Fig. 6. Intensity of Se and Te spectrum using an optical cable in far UV. Labelled spectral lines are: 1. – C I 193.09 nm, 2. – Se I 196.09 nm, 3. - Se I 203.98 nm, 4. - Te I 214.72 nm, 5. - Te I 226.55 nm, 6. – Te I 238.32 nm.

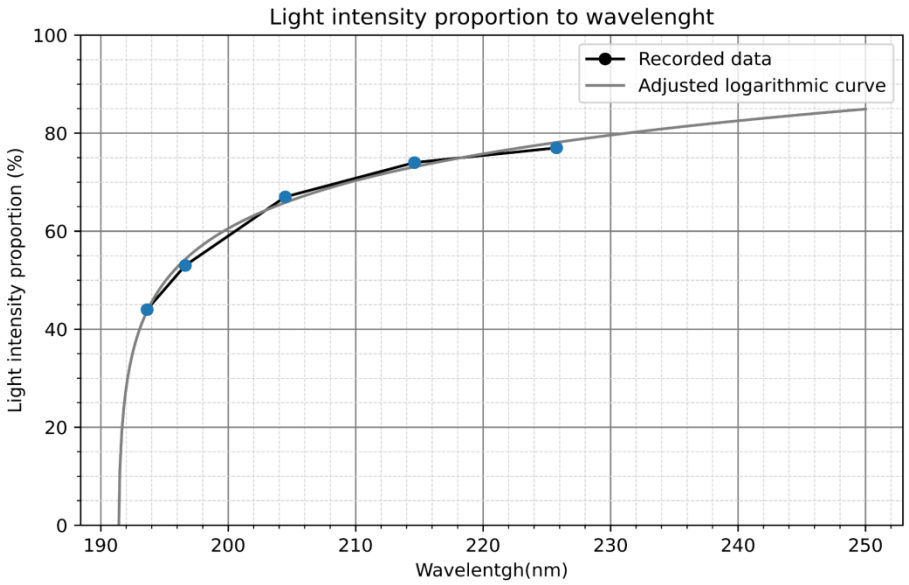

Fig. 7. Light transmittance depending on wavelength, with a logarithmic curve to predict transmittance in different wavelengths.

A comparison of the graphs *(Fig. 5 and Fig. 6)* shows that placing the optical fiber in the optical path reduces the intensity of the far UV spectrum, with a significant drop in spectral line intensity below 200 nm. Although the setup allowed spectral line detection down to 180 nm, Fig. 7. illustrates that the light transmittance curve, fitted with a logarithmic trend, was reliable only down to approximately 190 nm.

ISBN 978-80-69159-00-6

4. Discussion and Conclusions

The obtained results demonstrate the effectiveness and practicality of using atomic resonance spectra sources for studying and measuring the transparency limits of industrially produced optical fibers. Based on our experience in dealing with resonance spectra sources of various elements, we foresee that, alongside the combined ICP electrodeless discharge lamps of Se and Te, lamps based on As, Sb, S, and I could also be used [5]. Our method offers a simple and cost efficient alternative suitable for the transmittance analysis of optical fibers from 250 nm to 180 nm range or even shorter if a VUV spectrometer is used, in comparison to traditional sources like deuterium or xenon arc lamps [6], which are limited below 200 nm and require complex systems,

Currently, producers of optical fibers are making efforts to produce optical fibers with transparency below 190 nm, particularly because there is emerging demand for using ArF laser radiation (193 nm) in photolithography, laser processing [7], etc.

References

[1] Ubelis, A. P., Berzinsh, U. V. (1986). Transition probability measurements of Se I spectral lines by emission method. Physica Scripta, 1986, 34 (6B), S. 805-806.

[2] Ubelis, A. P., & Berzinsh, U. V. (1983). Transition probability measurements of Te I spectral lines by methods of emission and absorption of radiation. Physica Scripta, 28(2), 171-178.

[3] Fanderlik, I. (Ed.). (2013). Silica glass and its application. Elsevier, 303 pp.

[4] Soltani, Abolfazl. (2021). Solar System Wave Function and its Achievements. 10.33774/coe-2021-n3vv9-v7.

[5] Smalins, E., Gross, U., Jansons, J., & Ubelis, A. (2005). Atomic spectra from RF electrodeless discharge sources for UV and VUV spectrometry and analytical measurements. Meas. Sci. Rev, 5(3), 94-97.

[6] Presciutti, Andrea & Asdrubali, Francesco & Marrocchi, Assunta & Broggi, Alessandra & Pizzoli, Giuliano & Damiani, Alessio. (2014). Sun Simulators: Development of an Innovative Low Cost Film Filter. Sustainability. 6. 6830-6846. 10.3390/su6106830.

[7] Obenschain S. P., Schmitt A. J., Bates J. W., Wolford M. F., Myers M. C., McGeoch M. W., Karasik M. and Weaver J. L. (2020).Direct drive with the argon fluoride laser as a path to high fusion gain with sub-megajoule laser energyPhil. Trans. R. Soc. A.37820200031.

ISBN 978-80-69159-00-6

Identification of a Faulty Antenna in Large FM Antenna System Using Hybrid Dataset

Jakub Krchnak, Michal Dzuris, Rene Hartansky, Michal Stibrany

Faculty of Electrical Engineering and Information Technology, Slovak University of Technology, Ilkovicova 3, 812 19 Bratislava, Slovakia
Email: jakub.krchnak@stuba.sk

Abstract. *Faulty antenna identification by direct comparison between calculated and measured radiation patterns is already an efficient method, however, the real environment and parameters of the real antenna system complicate any following analysis. The goal of this study is to improve the resemblance between measured radiation patterns and patterns predicted by numberical calculations in numerical software by substracting a difference function from the measured pattern. The difference function is based on the calculated and measured datasets. Implementation of this method may lead to a more robust method of identifying the faulty antenna in an antenna system.*

Keywords: Large Antenna System, Faulty Antenna Identification, Radiation Pattern Measurement, Numerical Calculation

1. Introduction

Terrestrial broadcasting of FM and DVB-T signals is facilitated by large antenna systems (AS) often mounted on antenna masts, or antenna towers in significant height above the ground. Moreover, these antenna structures are situated at elevated places such as hilltops in order to achieve the desired coverage and radiation pattern. Such placement exposes individual antennas to severe meteorological conditions, which can, over time, lead to failures or the antenna can be physically damaged by e.g. by falling chunks of ice. In the best case scenario, the faulty/non-radiating antenna causes minor reduction of signal coverage at certain region - usually the region of the faulty antenna main lobe direction. In other cases, the fault caused by the physical damage (such as a broken connector) can lead to rise of the Voltage Standing Wave Ration (VSWR) at the transmitter input and subsequently (as a sefety precaution) to limiting the power distributed to the AS. This results in significant reduction of signal coverage in all directions.

Currently, there are two main methodologies of faulty antenna identification. One employs a repeated measurement of VSWR. During this procedure, a team of technicians has to be present directly at the AS and the AS and any other AS present at the antenna tower cannot radiate. The alternative to this procedure is the faulty antenna identification by radiation pattern measurement. This methodology was initially proposed based on a mathematical analysis of radiation patterns for linear and planar antenna arrays [1]. Based on the changes in the shape of the radiation pattern resulting from the faulty/non-radiating element (antenna) the faulty antenna could be identified. This process was improved by the use of various adaptive algorithms such as deep neural networks [2] or mathematical/statistical analyses [3]. Method of faulty antenna identification from radiation pattern data analysis was later employed for large antenna systems using numerical calculations in FEKO in [4] and subsequently, this method was tested in the field utilizing quadcopter and specialized measurement device [5].

By comparing the calculated and measured data, it was possible to localize the non-radiating antenna, however, there was noticeable difference between measured and calculated patterns caused by the real environment and real AS parameters. This fact could be problematic for antenna systems with large amount of antennas where faulty antenna causes only minor deviations

ISBN 978-80-69159-00-6

or if different faulty antennas cause very similar pattern change. This study aims to improve the faulty antenna identification using radiation pattern analysis by combining the calculated data for fully functional AS and for the AS with faulty antenna with the data from radiation pattern measurement of fully functional AS. The goal of this procedure is to create the corrected radiation pattern data for further failure analysis, based on the proposed difference function.

2. Subject and Methods

In order to perform the faulty antenna identification by radiation pattern measurements, it is necesary to possess a calculated radiation pattern (an ideal case) that measurements can be compared to. This ideal case can be obtained by numerical calculations for example in a computational software such as FEKO. The exact numerical replica of the AS has to be created with individual elements (antennas) distributed in space and amplitudes and phases of their input signals being adjusted according to the technical documentation. The exact process of creating the numerical representation of the AS is closely described in [5]. Antennas in antenna systems are often designated by a letter and a number, where number defines the level at which the antenna is placed and letter defines the azimuth to which antenna is rotated. For example the antenna "A1" is placed in the lowest level (compared to the other antennas of the AS) and the antenna "B1" is also placed in the first level but rotated in different azimuth. This designation will be used throughout the entire article. Obtaining the deformed radiation pattern can be achieved by setting the input signal at specific antenna to zero - simulation of a complete failure (antenna does not radiate).

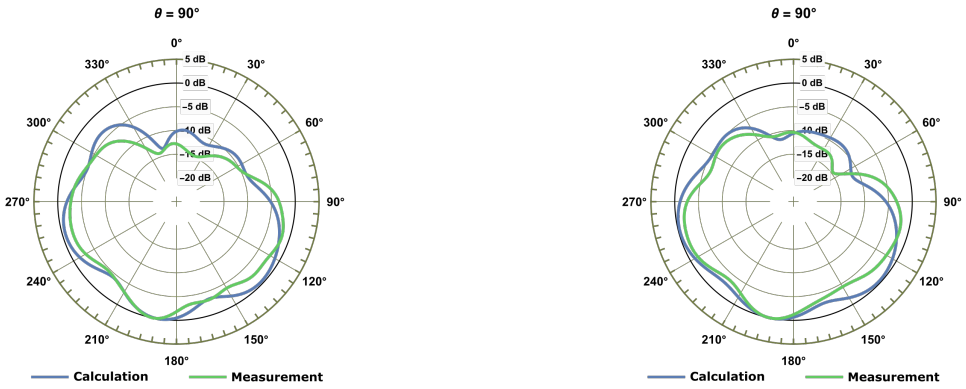

Fig. 1: A comparison between calculated and measured radiation pattern for the case of AS with faulty antenna: Faulty antenna A1 (a), faulty antenna A2 (b)

Calculated radiation patterns in horizontal plane for the AS with faulty antenna are displayed in polar diagrams in Fig. 1 (the blue curves). The examples are given for the case when antenna "A1" did not radiate in Fig. 1a and in Fig. 1b the antenna "A2" did not radiate. These patterns are also directly compared with the measured radiation patterns of the same AS with same faulty antennas. The radiation patterns were measured by the quadcopter with specialized measurement device for EM field intensity measurement, where the quadcopter performed circular horizontal flight around the AS with flight radius 150 m and the measurement device measured the tangential component of the EM field at frequency 105.8 MHz. The measurement setup and methodology are closely described in [6].

Already at first glance, the calculated and measured radiation patterns show similar features, such as the maximum radiation being located at the azimuth approximately 190°, significant sidelobes at regions $\sim 75° - 165°$ and $\sim 215° - 290°$ and the attenuation of ~ 10 dB accross

ISBN 978-80-69159-00-6

the backlobe region caused by the faulty antenna in azimuth "A". While the patterns exhibit considerable similarity, also noticeable are non-negligible differences. These deviations are caused by the real AS parameters e.g. real antenna materials, real feeding lines and power dividers as well as presence of real environment effects. In the case when two different faulty antennas cause very similar changes to the radiation pattern, as is shown in Fig. 1 with blue patterns, these effects could lead to misidentifying the faulty antenna.

The deformed radiation pattern estimation

In order to circumvent the issue of distinct differences, an approach of combining the calculation and measurement data can be taken. Achievment of this goal requires two steps, with first involving only calculations. The first calculation is for fully functional AS which yields the pattern at full operation and the second for the AS with one faulty antenna. By subtracting the deformed pattern from a fully functional one the difference function, which defines the changes to the radiation pattern caused by the non-radiating antenna, can be obtained. This function can then be substracted from the in-situ measured radiation pattern of the fully functional AS - creating the hybrid dataset. The resulting pattern retains the features of the real environment pattern and also is affected by the estimated difference caused by the faulty antenna. This process is illustrated in Fig. 2

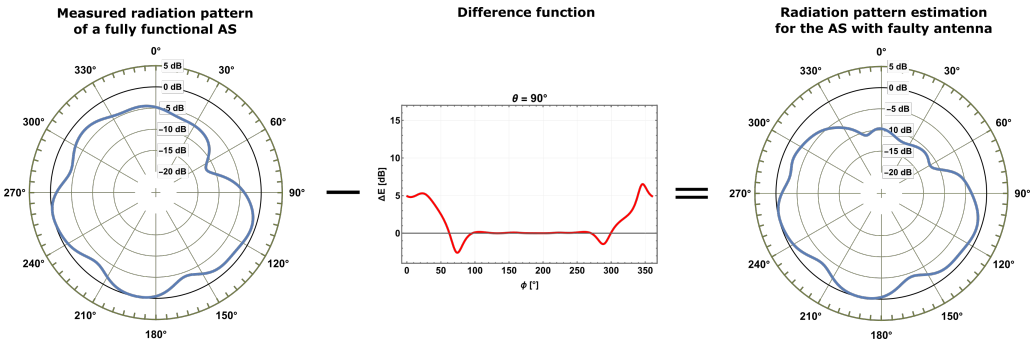

Fig. 2: The illustration of creating the corrected radiation pattern using the difference function

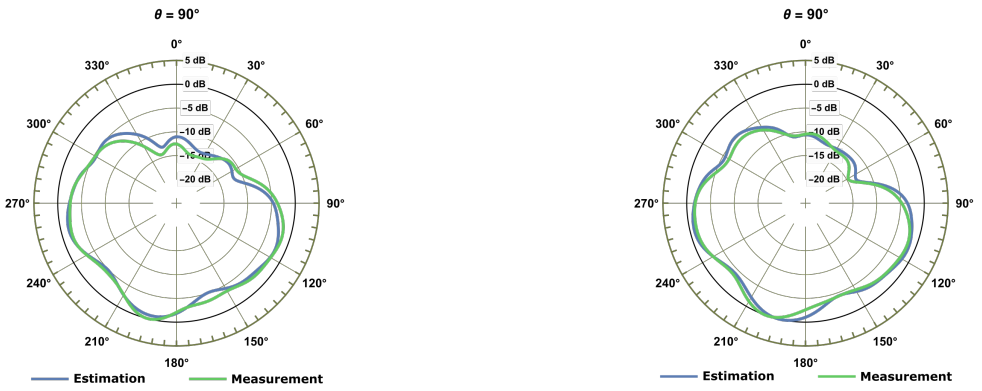

(a) (b)

Fig. 3: A comparison between the created estimation and measured radiation pattern for the case of AS with faulty antenna: Faulty antenna A1 (a), faulty antenna A2 (b)

Utilizing this procedure, the deformed radiation patterns were created for the cases presented in Fig. 1 and are displayed in Fig. 3 as the blue pattern. These patterns are again compared with the measured patterns from the Fig. 1. The "corrected" patterns resemble the measured patterns even more faithfully than in the case of pure simulations. These observations were

ISBN 978-80-69159-00-6

further validated by the calculation of Pearson's correlation coeficient - similar procedure as in [5]. Further measurements involved radiation patterns measured at two distances (flight radii - *r*) and at two frequencies[1] for the cases of two different faulty antennas respectively. In each case, by using the presented method it was possible to enhance the similarity of the estimation and measurements (larger values of correlation coefficient) and succesfully identify the faulty antenna.

3. Conclusions

This study explored a method of obtaining and estimation of radiation pattern shape of the real AS containing a faulty antenna. The estimation was established as a combination calculated and measured radiation pattern data. The advantage lies especially in combining the flexibility of calculation (regarding simulating many different iterations of faulty antenna) and the characteristics of real AS radiation pattern introduced by real conditions. This study demonstrated a notable enhancement of the similarity between the predicted shape of the radiation pattern and in-situ measurement. The results aid in preparation of a basis for a more robust similarity/feature analysis based on deep learning methods that can be employed in the future. One downside of this method is the requirement for the possession of the fully functional AS radiation pattern measurement data.

Acknowledgements

This work was supported by the project APVV 20-0042 "Microelectromechanical sensors with radio frequency data transmission", ENEFS 09I05-03-V02-00041 "Novel electrically enhanced wireless method for sensing of mechanical quantities".

References

[1] Rodriguez-Gonzalez, J. A., Ares-Pena, F., Fernandez-Delgado, M., Iglesias, R., Barro, S. (2009). Rapid method for finding faulty elements in antenna arrays using far field pattern samples. *IEEE Transactions on Antennas and Propagation*, 57(6): pp. 1679-1683.

[2] Nielsen, M. H., Zhang, Y., Xue, C., Ren, J., Yin, Y., Shen, M. (2022). Robust and Efficient Fault Diagnosis of mm-Wave Active Phased Arrays Using Baseband Signal. *IEEE Transactions on Antennas and Propagation*, 70(7): pp. 5044-5053.

[3] Shenone, V., Fedeli, A., Estatico, C., Pastorino, M., Randazzo, M. (2022). Detection of failures in antenna arrays through a Lebesgue-space approach. *IEEE Open Journal of Antennas and Propagation*: pp. 1-1.

[4] Krchnak, J., Hartansky, R., Grilli, N. (2021). UHF DTV antenna system diagnostics by radiation pattern measuring. In *Measurement 2021:* 13^{th} *International Conference on Measurement*. Slovak Academy of Sciences, pp. 232–235.

[5] Krchnak, J., Hartansky, R., Dzuris, M., Halgos, J., Grilli, N., Stibrany, M. (2023). Identification of faulty antenna in large FM antenna system using quadcopter measurements. *International Journal on Communications Antenna and Propagation*, 13(5): pp. 238-248.

[6] Dzuris, M., Hartansky, R., Krchnak, J. (2023). Measuring the radiation pattern of large FM antenna system. In *Measurement 2023:* 14^{th} *International Conference on Measurement*. Slovak Academy of Sciences, pp .135–138.

[1] The EM field intensity was measured at both frequencies simultaneously.

Measurement of Physical Quantities II

ISBN 978-80-69159-00-6

Colpitts Oscillator for a Mechanical Quantity Sensor

Tibor Rózsár, Vladimír Jančárik, Michal Dzuriš, Ján Halgoš

Slovak University of Technology, Faculty of Electrical Engineering and Information Technology, Institute of Electrical Engineering,
Ilkovičova 3, 841 04 Bratislava, Slovakia
Email: tibor.rozsar@stuba.sk

Abstract. *This paper presents the development of a low-power Colpitts oscillator for use in stand-alone sensors measuring mechanical quantities, such as force. The Colpitts oscillator, known for its ease of tuning, was designed to function as a fundamental component of a force measurement system utilizing capacitance-to-frequency conversion. By utilizing a parallel LC resonant circuit with variable capacitance, the oscillator efficiently converts mechanical deformations into frequency shifts, enabling accurate force detection. The number of circuit components was minimized to 7, significantly reducing the power consumption to less than 0.5 mA without compromising stability. Experimental results confirm that the designed oscillator provides a tunable frequency source, making it a strong candidate for further miniaturization and integration into wireless sensor applications.*

Keywords: Colpitts, Oscillator, Sensor, Radio frequency

1. Introduction

In the realm of modern sensor technology, the Colpitts oscillator can be one of the useful components in developing radio frequency (RF) devices, particularly in applications that require precise measurement of mechanical quantities. Notably, wireless sensors utilizing these oscillators have demonstrated remarkable potential in various fields, from environmental monitoring to medical diagnostics, as highlighted by advancements in microelectromechanical systems. Recent studies have underscored the importance of integrating advanced resonator designs, which can dramatically improve the quality (Q) factor of sensors, enabling more accurate readings and measurements [1].

2. Subjects and Methods

a. Overview of Oscillators and Their Importance in Sensor Technology

Oscillators play one of a key role in sensor technology by creating steady, repetitive signals that help measure and track different physical quantities. How accurately these oscillators function can have effect on the performance and dependability of sensor systems. For instance, the Colpitts oscillator, known for its stability and ease of tuning, can provide a good solution for applications requiring high-frequency oscillations. This is particularly evident in wireless sensor networks, where minimal power consumption is crucial [2]. Moreover, the integration of advanced oscillator designs allows for more accurate readings in humidity sensors, positively correlating moisture levels to frequency changes, thereby enhancing environmental monitoring capabilities etc. [3] In our case, we will design and use an oscillator for mechanical quantity sensor - to measure force.

b. Colpitts Oscillator

The Colpitts oscillator incorporates a tank circuit composed of a parallel resonant configuration of capacitors and an inductor, which helps the oscillator to achieve the requisite frequency

ISBN 978-80-69159-00-6

stability and amplitude control. Its design employs a combination of capacitors in series, which significantly influences the oscillators frequency stability and performance.

Measurement of force with the use of passive transducers is usually accomplished by an *LC* resonant circuit with a variable capacitance. The variable capacitance is achieved by creating a compliant mechanical body that slightly changes its shape when subjected to force, as demonstrated in Figure 1b. The compact compliant mechanical body (CCMB) design allows the creation of capacitor plates in the middle of the compliant body, while the threads of an inductor are embedded in the exterior portion of the compliant body, creating a parallel resonant circuit (PRC) as can be seen in Figure 1a [4].

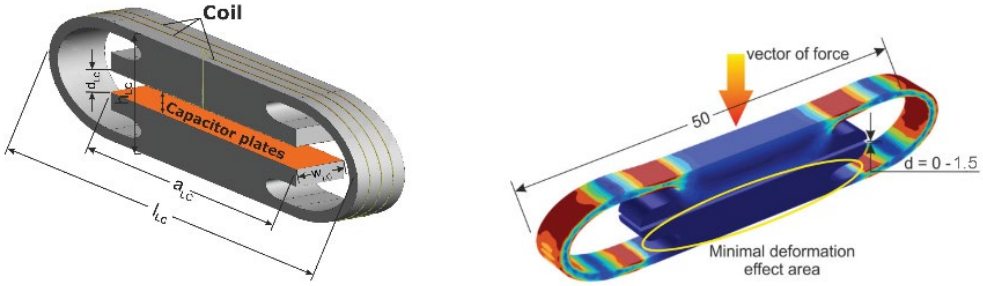

Fig. 1. Visualization of the experimental transducer (compact compliant mechanical body with inductor and capacitor in parallel). (a) 3D model with dimensions. (b) Deformation of the elastic element [4].

c. Oscillation frequency

Oscillation frequency, which is the parallel *LC* tank resonant frequency f_r can be calculated as

$$f_r = \frac{1}{2\pi\sqrt{L_T C_T}}, \tag{1}$$

where L_T (C_T) represents the total inductance of inductors (capacitance of capacitors).

For the series connection of inductors and capacitors of the Colpitts (and also Hartley) oscillator, the following applies:

$$L_T = L_1 + L_2, \tag{2}$$

$$\frac{1}{C_T} = \frac{1}{C_1} + \frac{1}{C_2} \quad \text{or} \quad C_T = \frac{C_1 C_2}{C_1 + C_2}. \tag{3}$$

By changing the sensor capacitance (*LC* tank) in the range of ±100 pF (L =30 nH, C_1 = 68 pF, C_2 = 68 pF to 680 pF), we can induce a frequency change in the range of 157.59 MHz to 116.87 MHz. In the case of changing the components (coil L with a different inductance value or capacitor C_1 with a different capacitance value), we can achieve different frequencies with the same change in C_2. This means that we can also change the ranges of the

capacitance-frequency conversion.

d. Minimizing the number of components

The topology of the Colpitts oscillator is nothing new and unknown. Currently, we can find various designs in various literature, for example with a common emitter, etc. These designs are proven and stable, but in our case, when it is necessary to miniaturize the circuits, it would be appropriate to reduce the number of components to a minimum so that the stability of the oscillator is maintained. Figure 3 shows one of the more widespread and well-known Figure 2. circuit diagram. It was this circuit that we tried to simplify.

ISBN 978-80-69159-00-6

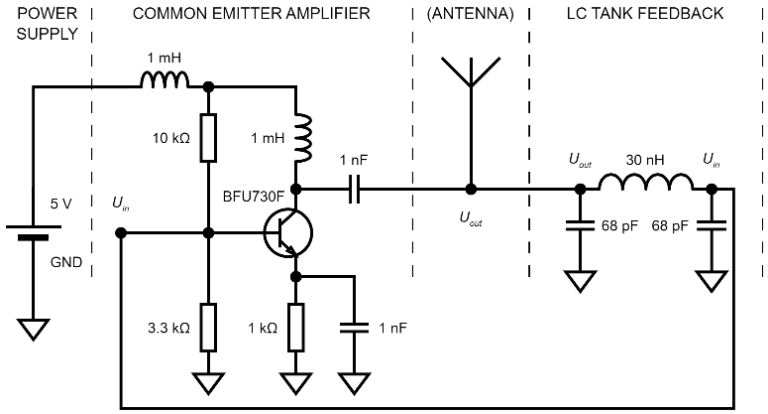

Fig. 2. Circuit diagram of Colpitts oscillator with a common emitter.

We removed all the "unnecessary" components and modified the remaining ones so that the stability of the oscillator is maintained. In this way, we managed to develop an oscillator with almost the same result from the original 11 components, but it is made up of only 7 components and also with lower power consumption (before was 1.68 mA, now less than 0.5 mA).

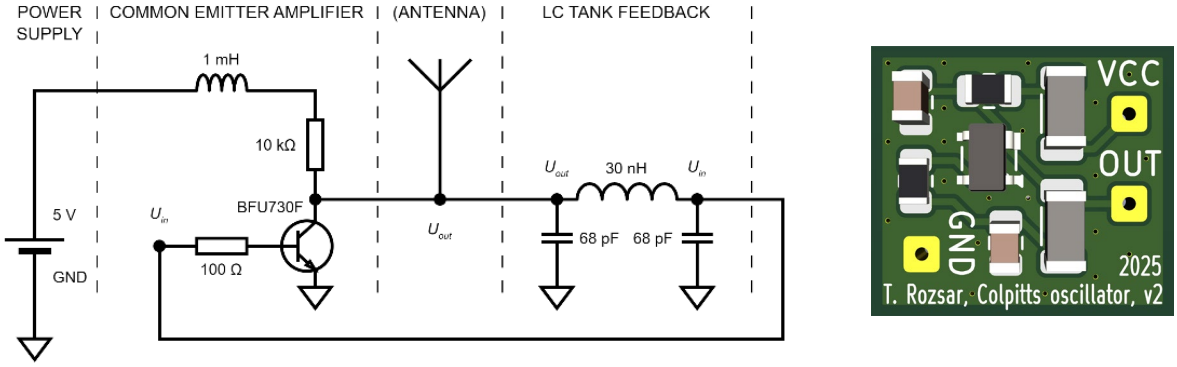

Fig. 3. Simplified Colpitts oscillator circuit diagram (left), printed circuit board design (right).

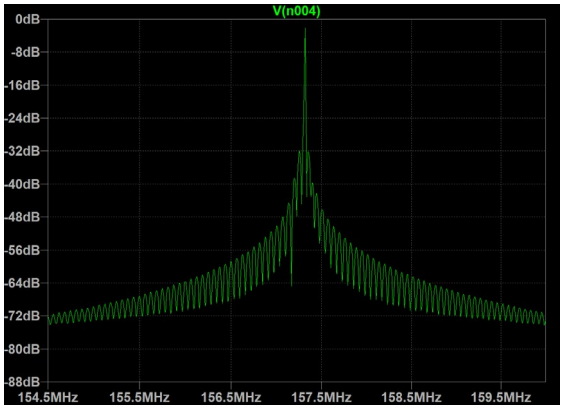

Fig. 4. Frequency spectrum of the simulated circuit of original Colpitts oscillator with a common emitter.

ISBN 978-80-69159-00-6

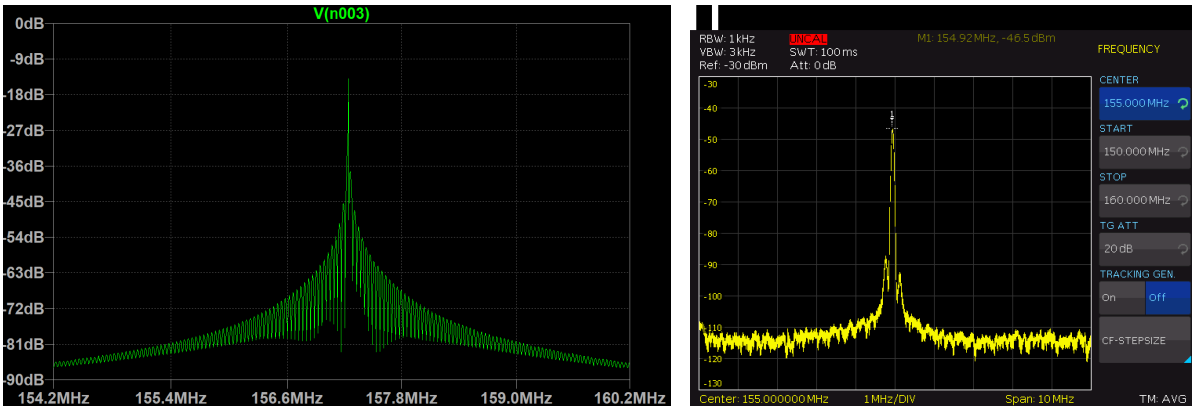

Fig. 5. Frequency spectrum of the simulated circuit (left) and the real oscillator (right).

3. Conclusion

In conclusion, a low-power Collpits oscillator with a current consumption of 430 µA has been designed for use in standalone sensors of mechanical quantities, which has a good frequency spectrum and tunability with low power consumption. In the case of modifying the oscillator to a voltage-controlled oscillator (VCO), we will be able - unlike monolithic integrated circuits (Colpitts VCOs) - to observe artifacts on the tuning voltage. Its low-frequency spectrum will contain information about reaching the resonant frequency of the *LC* element inserted into the electromagnetic field generated by the VCO. The designed oscillator represents a good basis for miniaturization, as it contains a minimal number of electronic elements for stable operation.

Acknowledgements

This work was supported by the project APVV 20-0042 "Microelectromechanical sensors with radio frequency data transmission", ENEFS 09I05-03-V02-00041 "Novel electrically enhanced wireless method for sensing of mechanical quantities" and project SMVRFP24 “Mechanical quantity sensor based on radio frequency principle”.

References

[1] Chen, P.-Y., Sakhdari, M., Hajizadegan, M., Cui, Q., Cheng, M.,

[2] El-Ganainy, R., Alù, A. (2018). *Generalized Parity-Time Symmetry Condition for Enhanced Sensor Telemetry.* [Online]. Available: http://arxiv.org/abs/1812.08296 [Accessed: 2025-03-01]

[3] Walia, A.S. (2009). *Novel Current-Mode Sensor Interfacing and Radio Blocks for Cell Culture Monitoring*. Bioengineering, Imperial College London. [Accessed: 2025-03-01]

[4] Malan, F.S. (2002). *Study of moisture in concrete utilizing the effect on the electromagnetic fields at UHF frequency on an embedded transmission line.* University of Bedfordshire. [Online]. Available: https://core.ac.uk/download/80683815.pdf [Accessed: 2025-03-01]

[5] Hartansky, R., Mierka, M., Jancarik, V., Bittera, M., Halgos, J., Dzuris, M., Krchnak, J., Hricko, J., Andok, R. (2023). *Towards a MEMS Force Sensor via the Electromagnetic Principle.* Sensors 23, no. 3: 1241. [Online]. Available: https://doi.org/10.3390/s23031241 [Accessed: 2025-03-18]

Study of Thermal Properties of Ca2Al2SiO7 Glasses by a Combination of Differential Scanning Calorimetry and High Temperature X-Ray Diffraction

[1]Melinda Majerová, [2]Anna Prnová, [3]Beata Pecušová, [3]Jozef Kraxner, [2,3]Dušan Galusek

[1]Institute of Measurement Science, Slovak Academy of Sciences, Bratislava, Slovakia
[2]Vitrum Laugaricio – Joint Glass Center of the IIC SAS, TnU AD and FChPT STU, Trenčín, Slovakia
[3]Centre for Functional and Surface Functionalized Glass, Alexander Dubček University of Trenčín, Trenčín Slovakia
Email: melinda.majerova@savba.sk

Abstract. *$Ca_2Al_2SiO_7$ (gehlenite) glasses doped with Bi (0.5, 1.0 and 3.0 mol. % Bi_2O_3) were prepared by flame synthesis. The prepared glass microspheres were X-ray amorphous. The thermal properties of prepared glasses were studied by differential scanning calorimetry (DSC) and high temperature X-ray diffraction. The results showed a significant influence of bismuth on the thermal properties. With increasing Bi content, the crystallization pattern of gehlenite changes from a single step to a two-step one.*

Keywords: $Ca_2Al_2SiO_7$ Glasses, Flame Synthesis, DSC Analysis, HT-XRD

1. Introduction

X-ray diffraction (XRD) combined with "in-situ" high-temperature experiments is a powerful tool in characterizing the structural parameters of materials. Thermal "in-situ" observations using high temperature X-ray (HT-XRD) equipment provide unique information such as temperature-dependent phase transformations, thermal changes in structural parameters, etc. for a variety of materials such as ceramic, ferroelectric, pyroelectric, magnetic, and superconducting. Another advantage is that by using HT XRD equipment, relevant changes in physical properties can be simulated, similarly to the changes that occur during the industrial production of materials [1]. When studying the properties of materials, the results of HT-XRD analysis are usually supplemented or combined with the results of other methods, such as thermal or optical methods [2, 3]. A combination of differential thermal analysis (DTA) and HT-XRD was used in the work of Dias et al. to develop glass ceramics for biomedical applications in a calcium phosphate-based system. The studies showed that by varying the heat treatment cycle, it is possible to produce glass-ceramics with different contents of bioactive and biocompatible phases in the system [3].
Gehlenite ($Ca_2Al_2SiO_7$) is a mineral belonging to the calcium aluminosilicates and has been extensively studied over the last few decades because it is a suitable host for optically active ions [4]. Studies have mostly focused on the crystalline form of gehlenite, but Bernardo et al. have pointed out that in the case of amorphous materials, there is a more homogeneous distribution of optically active ions, and the amorphous matrix is also able to bind a higher content of optically active ions. Both facts lead to an increase in the optical efficiency of the developed materials [5]. However, the preparation of gehlenite glasses is challenging due to their high melting temperatures and high tendency to crystallization. One option for the preparation of these glasses is their preparation by flame synthesis in the form of microspheres and subsequent sintering of the prepared systems [6]. For the successful preparation of lumped glasses, information on the thermal properties of glass microspheres is essential.

ISBN 978-80-69159-00-6

The main objective of this work is to investigate the thermal properties of Bi doped gehlenite glasses prepared by flame synthesis in a methane-oxygen flame. Precursors powders for the flame synthesis were prepared by solid-state reaction. The prepared glass microspheres were analyzed by XRD analysis. The thermal behavior of the prepared microspheres was monitored by HT-XRD and DSC analysis.

2. Subject and Methods

Flame synthesis was used to prepare gehlenite glass microspheres doped with different Bi contents. Precursor powders for flame synthesis were prepared from high purity powders: SiO_2 (p.a., Polske odczynniki chemiczne, Gliwice), Al_2O_3 (p.a., Centralchem, Bratislava), Bi_2O_3 (99.9 %, Strem Chemicals, USA), and CaCO3 (p.a., Strem Chemicals, USA), Strem Chemicals, USA), Centralchem, Bratislava) by solid-state reaction. A detailed description of the preparation procedure is given in [7]. X-ray powder diffraction analysis was used to determine the phase composition of prepared microspheres after flame synthesis. A Panalytical Empyrean diffractometer with a Cu cathode with an X-ray wavelength of $\lambda = 1.5405$ Å in the range of 2θ angles of 10-80° was used to record the X-ray patterns. The measured diffraction data sets were evaluated using HighScore Plus version 3.0 software with the COD2024 database. In the first step, the thermal properties of the prepared microspheres were studied by DSC. The measurements were carried out using a Netzsch STA 449 F1 Jupiter TG/DTA/DSC simultaneous thermal analyzer. The individual measurements were carried out in the temperature range 30-1200 °C using an N_2 atmosphere and a heating rate of 2, 4, 6, 8 and 10 °C/min. The measured DSC records were evaluated using Netzsch Proteus Thermal Analysis version 6.0.0. HT-XRD was used to determine the phase transformations in the temperature range 25-1100 °C. For the HT-XRD analysis, the same diffractometer was used as for the laboratory temperature measurements, but the measurements were carried out in a high temperature cell (Anton Paar, HTK16). Measurements were made in the 2θ interval 20-55°. The temperature regime during HT-XRD measurement was as follows: At the beginning of the experiment, the sample was heated from laboratory temperature to 600 °C at a heating rate of 10 °C/min. From 600 °C to 1100 °C the sample was heated at a rate of 5 °C/min and diffraction patterns were recorded every 10 °C under isothermal conditions. In addition, two long X-ray diffraction patterns were recorded at 25°C in the 2θ interval 10-80° for each sample. The first record was measured at the beginning of the analysis, after the sample had been deposited on the Pt heating strip, and the last record was measured after the sample had been cooled at the end of the analysis (from 1100°C to 25°C). The sets of measured diffraction data sets were evaluated using High Score software.

3. Results

XRD diffraction analysis confirmed the X-ray amorphous nature of all prepared systems. The measured records contained only a broad amorphous shoulder in the 2θ range of 24°- 36° and did not contain any diffraction traces indicating the presence of crystalline phases. DSC records of the prepared glasses measured at different heating rates are summarized in Figure 1. Only one exothermic effect was present in the DSC records of sample GBi0.5. In the case of the GBi1.0 sample, two significant exothermic effects were observed at lower heating rates (2 and 4 °C/min), which begin to overlap at higher heating rates. The exothermic effect at ~916°C in the DSC record measured at a heating rate of 8°C/min is observed as a so-called “shoulder” of the significant effect at 973°C (Fig. 1b). An even more complicated situation occurs when comparing the DSC records of the GBi3.0 sample with the highest Bi content. In all DSC records, the presence of two exothermic effects was observed. In addition, in the DSC curves

ISBN 978-80-69159-00-6

recorded at the heating rates of 4 and 6 °C/min, a hint of a third exothermic effect with maxima at 894 °C and 909 °C was observed (Fig. 1c).

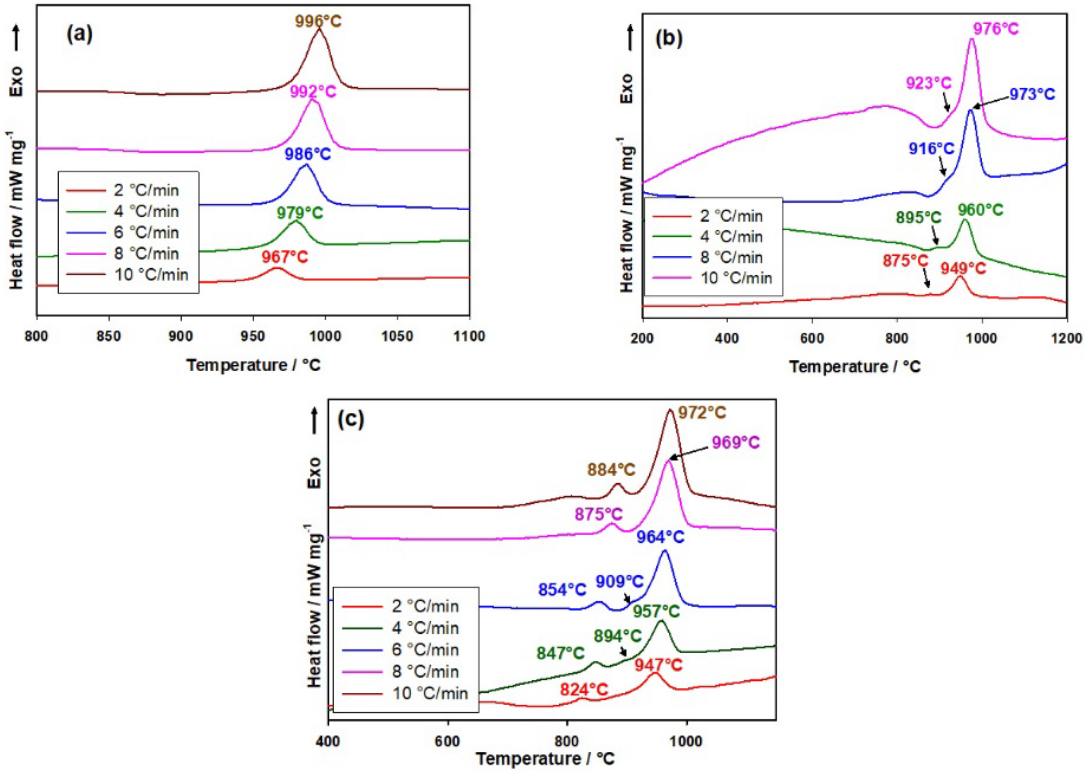

Fig. 1: DSC records at different heating rates (a) GBi0.5; (b) GBi1.0; GBi3.0.

To determine the events belonging to each exothermic peak in the DSC records, HT-XRD records were measured. In all glass microspheres the crystallization of the gehlenite phase occurred. In the sample with the lowest Bi content, crystallization of another phase, namely calcium-aluminum oxide ($CaAl_2O_4$), was observed (Fig. 2). The onset of crystallization of this phase was observed at 940°C. No significant crystallization peak was observed at this temperature in the measured DSC recordings. In terms of thermal analysis, this indicates a very slow crystallization process of this phase or a very low content of this phase with negligible crystallization heat. Diffraction records show a gradual decrease in the crystallization temperature of the gehlenite, with increasing Bi content. The temperatures decreased in the following order: GBi0.5 → 930 °C, GBi1.0 → 880 °C, GBi3.0 → 800 °C. Since the predominant process in the thermal behavior of glasses in the studied temperature interval is the crystallization of gehlenite, the temperature intervals with the highest increase in the proportion of this crystalline phase were constructed.

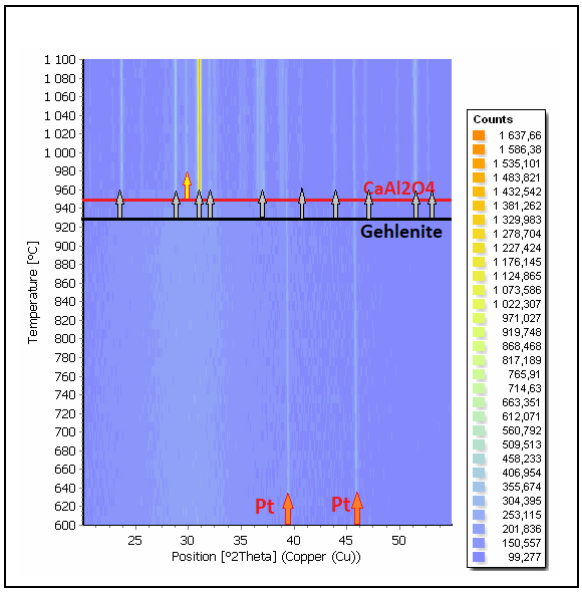

Fig. 2 Heatmap (temperature (°C) vs. position (°2θ) and he intensity is shown in colour) of The HT_XRD data for GBi0.5

ISBN 978-80-69159-00-6

From these dependences we determined the temperature intervals of interest (Table 1). In the case of the GBi0.5 sample, this curve is steep. Samples with higher Bi content show a more gradual, moderate increase in the crystalline phase content with temperature. In the sample with the highest Bi content, the presence of two temperature intervals with the highest increase in the content of the gehlenite phase can be observed, which indicates the crystallization of this phase in two steps. The dependences also show a shift in the onset of crystallization of the gehlenite phase with increasing content of Bi.

Table 1: Summarization of temperature interval with the most significant increase in the relative intensity (IR) of the most significant diffraction maximum of the gehlenite (2θ = 31.394°; d = 2.84720 Å; (hkl = 211)).

Sample	Temperature interval with the most significant increase in I_R [°C]
GBi0.5	940 – 950
GBi1.0	960 - 970
GBi3.0	800 – 820 930 -940

4. Conclusions

HT-XRD diffraction analysis in combination with DSC analysis was used to study the thermal behavior of Bi doped gehlenite glass microspheres. Based on the comparison of the results of HT-XRD diffraction and DSC analysis, we can conclude that in the investigated temperature interval 25-1200°C, gehlenite crystallization occurs as the predominant process. Also, with increasing addition of Bi, the onset of crystallization of the investigated systems shifts to lower temperatures. A more detailed study of HT-XRD diffraction records showed that in the case of GBi0.5 sample gehlenite phase crystallization occurs in one step. In systems with higher Bi content (sample GBi1.0 and GBi3.0), a more moderate increase in the proportion of gehlenite phase was observed, and in sample GBi3.0 with the highest content if Bi, gehlenite crystallization occurs most slowly and in two steps, which is consistent with the results of DSC analysis, that shows 2 exothermic peaks. The results of the investigation will be used in the preparation of glass-ceramic materials by controlled crystallization.

Acknowledgements

The financial support of this work by the projects VEGA 2/0077/24, VEGA 2/0104/25 is gratefully acknowledged.

References

[1] Hu, Ch-X., Liu, P., Liu, Y. (2011). High temperature X-ray diffraction studies of the sample heating units. *Procedia Engineering*, 24, 404-411.

[2] McClane, D.L. et al. (2019). Nepheline crystallization behavior in simulated high-level waste glasses. *Journal of Non-Crystalline Solids*, 505, 215-224.

[3] Dias, A.G. et al. (2005). In situ thermal and structural characterization of bioactive calcium phosphate glass ceramics containing TiO_2 and MgO oxides: High temperature – XRD studies. *Journal of Non-Crystalline Solids*, 351, 810-817.

[4] Shih, S.J. et al. (2016). Preparation and characterization of Eu-doped gehlenite glassy particles using spray pyrolysis. *Ceramics International*, 42, 11324–11329

[5] Bernardo, E., Fiocco, L., Prnová, A., Klement, R., Galusek, D. (2014). Gehlenite:Eu^{3+} phosphors from a silicone resin and nano-sized fillers. *Optical Materials*, 36,1243-1249.

[6] Rosenflanz, A. et al. (2004). Bulk glasses and ultrahard nanoceramics based on alumina and rare-earth oxides. *Nature Publishing Group*, 430, 761-764.

[7] Majerová, M. et al. (2022). Structure and magnetic properties of Bi-doped calcium aluminosilicate glass microspheres. *Pure and Applied Chemistry*, 94(2), 197-213.

Preparation and Characterization of Magnetic HEO with the Composition $(Al_{0.2}Co_{0.2}Cr_{0.2}Ni_{0.2}Fe_{0.2}X_{0.2})_3O_4$; X= Mg, Zn

[1]T. Sabadková, [1,2]J. Valúchová, [3]M. Majerová, [1]P. Švančárek, [1]M. Švančárková, [3]M. Škrátek, [3]A. Dvurečenskij, [4,5] D. Drdlík, [1,2]A. Prnová, [1,2]D. Galusek

[1] FunGlass, A. Dubček University of Trenčín, Trenčín, Slovakia,
[2] Join Glass Centre of the IIC SAS, TnUAD, FChPT STU, Trenčín, Slovakia,
[3] Department of Magnetometry, Institute of Measurement Science, Slovak Academy of Sciences, Bratislava, Slovakia,
[4] CEITEC BUT, Brno University of Technology, Brno, Czech Republic
[5]Institute of Materials Science and Engineering, University of Technology, Brno, Czech Republic
Email: terezia.sabadkova@tnuni.sk

Abstract. *A ceramic material consisting of two distinct compositions, $(Al_{0.2}Co_{0.2}Cr_{0.2}Ni_{0.2}Fe_{0.2}Zn_{0.2})_3O_4$ and $(Al_{0.2}Co_{0.2}Cr_{0.2}Ni_{0.2}Fe_{0.2}Mg_{0.2})_3O_4$, was synthesized using solid-state synthesis of the powder, followed by cold pressing and cold isostatic pressing. Pressed green bodies were sintered at two different temperatures (1223 K and 1423 K). The study examined the effects of composition and sintering temperature on the structural and magnetic properties of the materials, utilizing X-ray diffraction (XRD) analysis and SQUID magnetometry. High-entropy oxide samples with a single-phase spinel structure (space group Fd-3m) were prepared. Analysis of the magnetic properties revealed that the samples exhibited soft magnetic characteristics, indicating potential applications in the development of reversible magneto-active composites, such as magnetorheological elastomers.*

Keywords: High-Entropy Oxide, Magnetic Properties, Sintering

1. Introduction

The continuing interest in high entropy oxide (HEO) is mainly related to their excellent physicochemical, optical, thermal, and magnetic properties [1 - 3]. HEO find applications in various fields such as catalysts, lithium-ion batteries, dielectric and electromagnetic materials, and in the fabrication of corrosion-resistant batteries and coatings [4, 5]. Ferrites with cubic spinel structures (Fd-3m) are known for their optical, magnetic, dielectric, and photocatalytic properties that are useful in a variety of potential applications [6, 7]. HEO with such spinel structure and the composition $(Co_{0.2}Cr_{0.2}Fe_{0.2}Mn_{0.2}Ni_{0.2})_3O_4$ was prepared by Dabrowa et al. using high-energy ball milling, followed by sintering at 1323 K [8]. Mao et al. prepared a HEO with the same composition by solution combustion synthesis (SCS) [9]. They investigated the structure and magnetic properties of $(Cr_{0.2}Mn_{0.2}Fe_{0.2}Co_{0.2}Ni_{0.2})_3O_4$ HEO in cases where the magnetic Co^{2+} or Ni^{2+} ions were replaced by non-magnetic Zn^{2+} ions. The results showed a decrease in magnetization [10]. Zhu et al. synthesized a six-component $(Al_{1/6}Co_{1/6}Cr_{1/6}Mn_{1/6}Ni_{1/6}Fe_{1/6})_3O_4$ using the SCS method and investigated the effect of annealing temperature and the substitution of Al^{3+} with magnetic Co^{2+}, Mn^{3+}, and Ni^{2+}. It was found that replacing Al^{3+} with Mn^{3+} and Ni^{2+} led to an increase in magnetization while substituting Al^{3+} with Co^{2+} did not result in any change in magnetization [11]. According to the literature, the addition of Al^{3+} cations to ferrites enables control over their functional properties, and magnetic properties in particular [12].

Based on the available literature, precursor materials with two compositions $(Al_{0.2}Co_{0.2}Cr_{0.2}Ni_{0.2}Fe_{0.2}Zn_{0.2})_3O_4$ a $(Al_{0.2}Co_{0.2}Cr_{0.2}Ni_{0.2}Fe_{0.2}Mg_{0.2})_3O_4$ were prepared by solid-state synthesis

from high-purity oxides. The samples were axially pressed at laboratory temperature using cold-pressing (CP) and cold isostatic press (CIP) methods. To investigate the effect of sintering temperature on magnetic properties, the prepared green compacts were sintered in the air at 1223 K and at 1423 K for 6 hours. Phase composition and magnetic properties have been investigated by XRD and SQUID methods.

2. Subject and Methods

Oxide powders: Al_2O_3 (99.6%, Laboratórne chemikálie Milan Adamík), CoO (99.6%, Sigma-Aldrich), Cr_2O_3 (98%, Alfa Aesar), NiO (p.a. Lachema), Fe_2O_3 (99%, Slavus), ZnO (99.6%, Centralchem), MgO (98%, Centralchem) were used for preparation of two precursor powders with $(Al_{0.2}Co_{0.2}Cr_{0.2}Ni_{0.2}Fe_{0.2}Zn_{0.2})_3O_4$ and $(Al_{0.2}Co_{0.2}Cr_{0.2}Ni_{0.2}Fe_{0.2}Mg_{0.2})_3O_4$ compositions. The weighed oxides (the final mass of each mixture was 10g) were quantitatively transferred into a PE bottle with ZrO_2 grinding bodies (Ø= 2mm; powder/grinding body ratio was 1/8) and with the addition of 20 mL of isopropyl alcohol (p.a., Mikrochem, Slovakia). The final slurry was ball milled for 24 hours, and subsequently dried on a magnetic stirrer at a temperature of 403 K and the rotation speed of 300 rpm for 4 hours. A hydraulic press (Trystom Olomouc H-62, operated at a force of 22 kN for 1 min) was used for axial pressing: whereby about 1.3 g of each powder was weighed to prepare a cylindrical pellet with the diameter of 12.2 mm diameter and 3.8 mm thick. CIP (HIP 300 E, P/O/Weber GmbH, Germany, pressure of 700 MPa with a holding time of 5 min) was used for the final pressing to maximise compaction of prepared samples. All pressed green bodies were sintered first at 1223 K for 6 hours and in the next step 2 of them were sintered at 1423 K for 6 hours in the air. In both sintering experiments, a heating rate of 5 $K \cdot min^{-1}$ and a cooling rate of 20 $K \cdot min^{-1}$ were applied. Table 1 summarizes the details of the synthesis process of the samples.

XRD analysis was used to study the phase composition of the sintered samples, using a Panalytical Empyrean DY1098 X-ray diffractometer operating at 45 kV accelerating voltage and CuKα radiation with $\lambda = 1.5405$ Å. Reflection-transmission spinner was used as sample holder. The dates were recorded in the 2θ-range 10-80°. Diffraction data were evaluated with the HighScore Plus software (v.3.0.4, PAN Analytical, The Netherlands) using the Crystallographic Open Database (COD 2024). The magnetic properties of the samples were determined by Quantum Design MPMS XL-7AC SQUID magnetometer. Measurement of the magnetization as a function of field was carried out at the temperature of 300 K.

Table 1. Compositions and the conditions of milling and heat treatment in the sample synthesis process.

Sample	Composition	Milling		Heat treatment		Single Phase
		Speed (r/min)	Time (h)	First	Second	
SZn1	$(Al_{0.2}Co_{0.2}Cr_{0.2}Ni_{0.2}Fe_{0.2}Zn_{0.2})_3O_4$	150	24	1223K/6h	---	Yes
SZn2	$(Al_{0.2}Co_{0.2}Cr_{0.2}Ni_{0.2}Fe_{0.2}Zn_{0.2})_3O_4$	150	24	1223K/6h	1423K/6h	Yes
SMg1	$(Al_{0.2}Co_{0.2}Cr_{0.2}Ni_{0.2}Fe_{0.2}Mg_{0.2})_3O_4$	150	24	1223K/6h	---	Yes
SMg2	$(Al_{0.2}Co_{0.2}Cr_{0.2}Ni_{0.2}Fe_{0.2}Mg_{0.2})_3O_4$	150	24	1223K/6h	1423K/6h	Yes

3. Results

Figure 1 compares the XRD patterns of all prepared samples with that of $MgFe_2O_4$. The XRD records demonstrate that all samples display consistent diffraction patterns. The positions of diffraction maxima align closely with the diffraction lines of the $MgFe_2O_4$ standard as documented in the literature [13]. The diffraction maxima are consistent with the crystallographic planes (111), (220), (311), (222), (400), (422), (511), (440), (620), (533) of $MgFe_2O_4$. This supports the conclusion that all samples share the same structure, which is identified as a single spinel structure belonging to the space group Fd-3m. [14].

ISBN 978-80-69159-00-6

To investigate the effect of the addition of ZnO and MgO and the synthesis temperature on the magnetic properties of the synthesized $(Al_{0.2}Co_{0.2}Cr_{0.2}Ni_{0.2}Fe_{0.2}X_{0.2})_3O_4$; X= Mg, Zn samples, magnetic hysteresis loops were measured at room temperature up to a magnetic field of 10 kOe. All samples display of either ferrimagnetic or ferromagnetic behavior, and each curve shows a typical magnetic hysteresis loop. The presence of hysteresis can be attributed to the sample containing equilibrated magnetic moments or the projection of magnetic moments at room temperature. It was also noted that the hysteresis loop did not reach saturation even at the maximum applied magnetic field of 10 kOe. Similar results were observed by Mao et al. who studied the magnetic properties of $(CoCrFeMnNi)_3O_4$ high-entropy oxide nanocrystalline powder [9]. Moreover, magnetic properties such as magnetization (M), remanent magnetization (M_r) and coercivity (H_c) have been determined from the measured hysteresis loops and the results are summarized in Table 2.

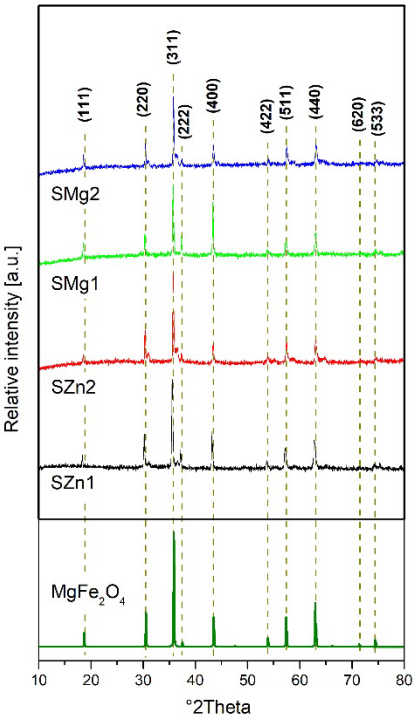

Fig. 1. XRD patterns of the prepared samples compared to $MgFe_2O_4$

The sample containing magnesium (Mg) after single-step sintering at 1223 K displayed the most favorable magnetic properties. Following a second heat treatment, the impact of additional sintering became evident: the values M, M_r and H_c experienced a marked decline, irrespective of whether the sample contained Mg or zinc (Zn). Heat treatment clearly led to narrower hysteresis loops, which are more indicative of ferrimagnetic behavior.

The magnetic characteristics of high-entropy oxides (HEOs) can be affected by various factors, including their phase structure, synthesis methods, chemical composition, and local structural and chemical disturbances within the HEO framework. In a related study, Mao et al. investigated the magnetic properties of (CoCuMgNiZn)O HEO nanocrystalline powder, which displayed a distinct long-range antiferromagnetic behavior. [15]. Adding non-magnetic ions such as Mg^{2+} or Zn^{2+} can suppress antiferromagnetism, which can be attributed to the presence of Ni^{2+} or Co^{2+} (NiO and ZnO are antiferromagnets). In another work, Mao et al. reported that the nanocrystalline powder with the composition $(CoCrFeMnNi)_3O_4$ had ferromagnetic properties [9]. For better understanding of the measured magnetic properties, further studies of magnetic as well as structural properties are necessary to explain the obtained results.

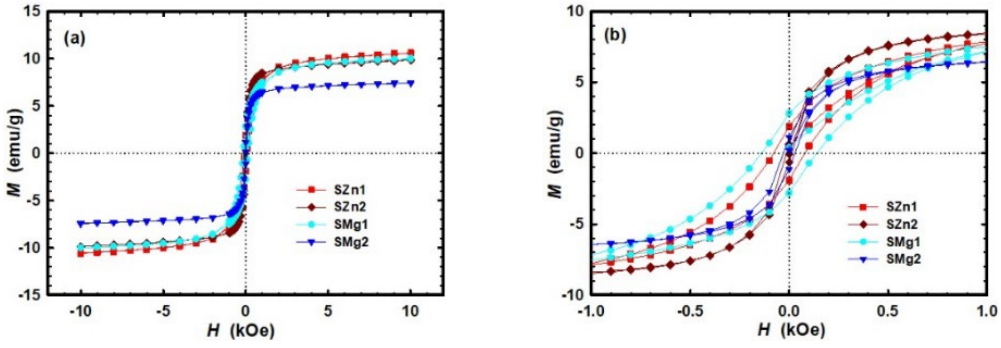

Fig. 2. Magnetic hysteresis loops for prepared samples measured at 300 K (a), enlarged view of the hysteresis loops within the range of ± 1kOe (b)

ISBN 978-80-69159-00-6

Table 2. Magnetic properties of $(Al_{0.2}Co_{0.2}Cr_{0.2}Ni_{0.2}Fe_{0.2}X_{0.2})_3O_4$; X= Mg, Zn samples (magnetization (M), remanent magnetization (M_r) and coercivity (H_c))

Sample	M (emu/g)	M_r (emu/g)	H_c (Oe)
SZn1	10.62	1.91	77.91
SZn2	9.89	0.65	14.19
SMg1	10.04	2.82	139.08
SMg2	7.46	1.15	30.28

4. Conclusions

Two high-entropy oxide samples $(Al_{0.2}Co_{0.2}Cr_{0.2}Ni_{0.2}Fe_{0.2}X_{0.2})_3O_4$; X= Mg, Zn were prepared by one- or two-step pressureless sintering. The prepared samples had a single-phase spinel structure. M-H curves of all samples indicated that all samples exhibited ferromagnetic or ferrimagnetic behavior. The measured values of M, M_r and H_c of the prepared soft magnetic materials were mainly influenced by the heat treatment conditions; the influence of composition was less pronounced. Further analysis of both magnetic and structural properties is required to better understand the influence of heat treatment as well as the influence of Zn and Mg addition.

Acknowledgements: The financial support of this work by the projects VEGA 2/0104/25, APVV 23-0424 and APVV 23-0352 is gratefully acknowledged.

References

[1] Xiang, H. et al. (2021). High-entropy ceramics: Present status, challenges, and a look forward. *Journal of Advanced Ceramics*, 10 (3), 385-441.
[2] Sarkar, A. et al. (2019). High-Entropy Oxides: Fundamental Aspects and Electrochemical Properties. *Advanced Materials*, 1806236.
[3] Sarkar, A., Kruk, R., Hahn, H. (2021). Magnetic properties of high entropy oxides. *Dalton Transactions*, 50, 1973-1982.
[4] Xiao, M. *et al.* (2025). High-entropy materials for solid oxide cells: Synthesis, applications, and prospects. *Journal of Energy Chemistry*, 104, 268–296.
[5] Oses, C., Toher, C., Curtarolo, S. (2020). High-entropy ceramics. *Nature Reviews Materials*, 5, 295–309.
[6] Mallesh, S. et al. (2022). Effect of Ni substitution and annealing temperature on structural and magnetic properties of MnZn-Ferrites: Cytotoxicity study of ZnO and SiO_2 coated core shell structures. *Applied Surface Science*, 605, 154648.
[7] Somvanshi, S. et al. (2020). Hyperthermic evaluation of oleic acid coated nano-spinel magnesium ferrite: Enhancement via hydrophobic-to-hydrophilic surface transformation. *Journal of Alloys and Compounds*, 835, 155422.
[8] Dąbrowa, J. et al. (2018). Synthesis and microstructure of the $(Co,Cr,Fe,Mn,Ni)_3O_4$ high entropy oxide characterized by spinel structure", *Materials Letters*, roč. 216, s. 32–36, apr. 2018, doi: 10.1016/j.matlet.2017.12.148.
[9] Mao, A. et al. (2019). Facile synthesis and ferrimagnetic property of spinel $(CoCrFeMnNi)_3O_4$ high-entropy oxide nanocrystalline powder. *Journal of Molecular Structure*, 1194, 11-18.
[10] Mao, A. et al. (2020). A new class of spinel high-entropy oxides with controllable magnetic properties. *Journal of Magnetism and Magnetic Materials*, 497, 165884.
[11] Zhu, H. et al. (2021). Structure and magnetic properties of a class of spinel high-entropy oxides. *Journal of Magnetism and Magnetic Materials*, 535, 168063.
[12] Kanagesan, S. et al. (2012). Structural and magnetic properties of conventional and microwave treated Ni–Zr doped barium strontium hexaferrite. *Materials Research Bulletin*, 47, 188–192.
[13] Chen, C. et al. (2023) Micro-structural and magnetic analysis of spinel high entropy oxides synthesized by two-step pressureless sintering provides insight into high entropy ceramics. *Materials Today Communications*, 35, 106122.
[14] Mao, A. et al. (2020). A novel six-component spinel-structure high-entropy oxide with ferrimagnetic property. *Journal of Magnetism and Magnetic Materials*, 503, 166594.
[15] Mao, A. et al. (2019). Solution combustion synthesis and magnetic property of rock-salt $(Co_{0.2}Cu_{0.2}Mg_{0.2}Ni_{0.2}Zn_{0.2})O$ high-entropy oxide nanocrystalline powder. *Journal of Magnetism and Magnetic Materials*, 484, 245-252.

Measurement and Preparation of Reference Tubes for the Primary Standard Piston Flowmeter

[1]Jan Rybář, [2]Matej Hruška, [1]Frederik Ujhelyi, [2]Miroslav Chytil

[1] Faculty of Mechanical Engineering, Slovak University of Technology, Bratislava, Slovakia
[2]Slovak Institute of Metrology, Bratislava, Slovakia
Email: jan.rybar@stuba.sk

Abstract.

This paper deals with the measurement, evaluation and visualization of reference tubes for a primary reference piston flowmeter. The aim is to accurately analyze the geometrical properties of the tubes that will be used in the primary standard piston flowmeter at the Slovak Institute of Metrology. The work discusses and compares two methods of evaluating radius of one of the tubes. One based on geometric measurement and the other based on weighing.

Keywords: Flowmeter, Weighing, Geometrical Measurement, Tube

1. Introduction

The Slovak Institute of Metrology (SMU) has always tried to implement metrological standards in-house. This has many advantages: the development of the device will be fully under the control of the SMU and the members of the implementation team will gain incomparable experience working on the finished device. The need for Primary Standard Piston Flowmeter began when the existing old flowmeter manufactured by external company started to fall apart. After close investigation it was clear that repairment would be harder than making a new one. The new solution will be completely designed in SMU while new parts or unified components will be bought in respective companies suited for such needs.

This paper mainly deals with the tubes that will be part of Primary Standard Piston Flowmeter. Luckily, we can make use of existing tubes that were used in old device. However, we need to measure the exact volume of such tubes [6]. There are two ways to measure volume. By geometrical measurement of tubes or by gravimetric determination of volume.

2. Subject and Methods

The main principle of Primary Standard Piston Flowmeter is based on constant speed of piston. The exact knowledge of volumes of the tubes is necessary for correctly determining flow values. The piston will be pushing air (or other gas) in tube and with knowledge of speed and volume we can calculate the volume of air that was pushed. This standard is intended for the calibration of lower-order meters, such as venturi nozzles, gas meters and flowmeters.

In this paper we will compare diameter results of two different methods only for one of the tubes.

Method for calculating radius using geometrical parameters

The data used were measured on 3D measuring machine Zeiss Prismo Ultra. The tube was adjusted into a y-axis of a measuring machine on two prismatic bases Fig. 1. The circularity measurement was carried out on the internal surface at the end of the tube. We carried circularity

ISBN 978-80-69159-00-6

measurements in 10 places, that were distanced 45 mm respectively. The straightness measurement was carried out in 8 places also on the internal surface around the perimeter [4].

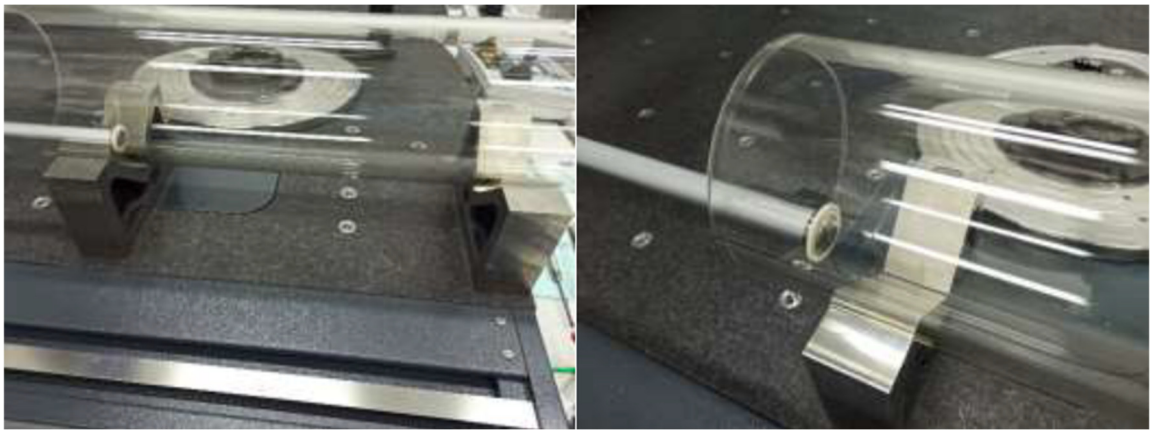

Fig. 1. Placement of the sensor in tube [2].

The obtained data were converted into polar coordinates [1]. Only circularity measurement was used to determine radius using least square circles method [3]. Because of the length of the tube, we needed to measure from both sides. Radius of one cross-section circle was average value of roughly 520 measurements across whole circumference. For final value of radius, we used an average of all 10 radiuses of respective cross-section circles. Straightness measurement was mainly used to determine whether the tube has large irregularities of shape for which it could not be used for its purpose [2].

Weighing method for evaluating the internal surface

The second method is based on gravimetric weighing of the tube. The point is to compare the tube before and after filling with a known liquid [6]. Using the weight difference, we can calculate the internal surface and acquire the diameter using Eq. 1. However, for this we need the exact value of liquid density. Determining the density requires accurate values of temperature, pressure and humidity of the environment, as well as the temperature of the liquid. We will use distilled water, which was degassed by pumping to remove air bubbles, thereby reducing weighing errors.

$$d = 2\sqrt{\frac{S}{\pi}} \tag{1}$$

Where S is the internal surface and d is diameter of the tube.

Weighing was done on mass comparator Mettler Toledo XP5003S with range up to 5100 g and resolution 1 mg. During weighing we were monitoring temperature of distilled water on 4 points and averaged this value. Using temperature we calculated exact density. Lastly, we needed the total length of tube, which was measured here in SMU on Renishaw XL-80 laser interferometer.

ISBN 978-80-69159-00-6

3. Results

In Fig. 2 on the left we show circularity of various values of radiuses with respect to angle in different cross-section cuts on first side [1, 3]. On the right we can see same thing but on the second side of the tube.

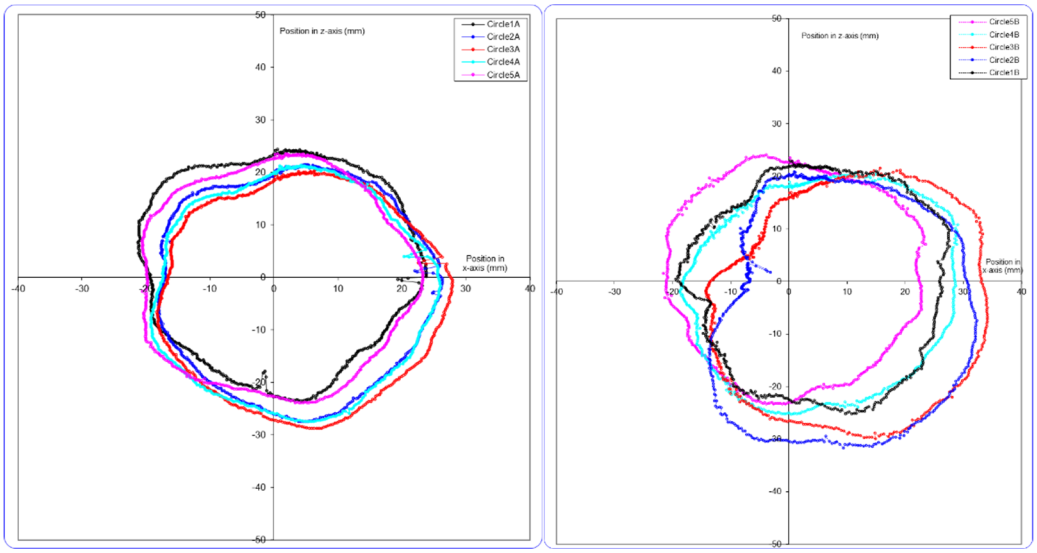

Fig. 2. Circularity of cross-section cuts. Source: own.

Table 1 presents final values of radius evaluated using the first method based on geometrical measurements. It includes all measured circles, or rather, specific locations on the tube, where *r* represents the radius of the respective circle, *ur* is the uncertainty of this radius.

Table 1 - Averages of radiuses for all circles

Circle	1a	2a	3a	4a	5a	5b	4b	3b	2b	1b	Average
r (mm)	22.2216	22.2212	22.2217	22.2207	22.2220	22.2242	22.2255	22.2319	22.2256	22.2240	22.2238
ur (%)	0.018	0.038	0.027	0.028	0.010	0.011	0.042	0.083	0.083	0.037	0.0377

Uncertainty of geometrical method

We have evaluated uncertainty of type A with formula 2, where *r* is radius and *n* is number of measurements. The type B uncertainty includes the deviation from cylindricity, as well as the machine's accuracy and resolution [5].

$$u_A = \sqrt{\frac{\sum_{i=1}^{n}(r_i - \bar{r})^2}{n\,(n-1)}} \tag{2}$$

Uncertainty of the weighting method

Since it was very difficult to repeat measurements of tube filled with water because keeping the tightness of the bottom turned out to be problematic. Because it was a mass comparative method, we use the accuracy of the weights which was 0.5 mg and the readability of the mass comparator 1 mg. Additionally, we included the highest contributor of error from leakage which was estimated to be 500 mg [5].

Results

Diameter calculated using geometrical measurement is as follows

$$d = (44.448\ \pm 0.033)\ \text{mm}, (k = 2) \tag{3}$$

ISBN 978-80-69159-00-6

And diameter calculated using weighing method

$$d = (44.463\ \pm 0.016)\ \text{mm}, (k = 2) \quad (4)$$

4. Discussion

This paper discussed differences in measured values of tube. As we can see from Eq. 3 and 4 there are some differences but both methods largely confirm each other. We do not believe that changing the methodology in the future is necessary. Given the lower uncertainty, we assumed that the weighing method probably makes more sense for this particular tube.

5. Conclusions

We have concluded that for larger tubes the method using geometry will be better but for this particular tube it seems that the geometric parameters such as straightness and circularity will primally serve as confirmation that the tube resembles a cylinder. We will use this knowledge to measure other tubes. These results will be very useful for the development of flow standards in metrology of Slovakia.

Acknowledgements

The authors would like thank the Slovak University of Technology in Bratislava (Faculty of Mechanical Engineering), Slovak Metrology Institute, the grant agency KEGA project number 024STU-4/2023 (Building a laboratory of medical metrology), the grant agency APVV project number APVV-21-0216 (Advanced mathematical and statistical methods for measurement and metrology) for their support and the grand agency APVV project number APVV-21-0195 Research the possibility of digital transformation of continuous transport system.

References

[1] Kesemen, O., Tiryaki, B., Tezel, Ö., Pak, A., (2020). Some Statistics in Polar Coordinate System with Uniform Angles. *Gazi University Journal of Science*. 33 p. 1-1. 10.35378/gujs.610086.

[2] Gorog, A., (2024). *Analýza makrogeometrie veľkej sklenenej trubice.* Výskumná správa - Slovenský metrologický ústav/*Analysis of the Macrogeometry of a large glass tube.* Research Report - Slovak Institute of Metrology. 7 p.

[3] Sui, W., Zhang, D. Four Methods for Roundness Evaluation. (2012) *Physics Procedia*, 24 p. 2159-2164. ISSN 1875-3892.

[4] Segura, Á., García-Alonso, A. (2019). Steel Tube Cross Section Geometry Measurement by 3D Scanning. In: Graña, M., *et al.* International Joint Conference SOCO'18-CISIS'18-ICEUTE'18. SOCO'18-CISIS'18-ICEUTE'18 2018. *Advances in Intelligent Systems and Computing,* vol 771. Springer, Cham. https://doi.org/10.1007/978-3-319-94120-2_6

[5] Palenčár R., Wimmer G., Palenčár J., Witkovský V. (2021). *Navrhovanie a vyhodnocovanie meraní/ Designing and Evaluating of Measurements,* 160 p. ISBN 978-80-227-5080-6.

[6] Enrera, R. (2022) *Volume in Science | Measurement, Calculation & Examples*. Study.com. https://study.com/academy/lesson/volume-scientific-overview-examples-chemistry.html

Quantitative MRI

ISBN 978-80-69159-00-6

Quality Control Pipeline for Skeletal Muscle Energy Metabolism Assessed by ^{31}P MRS in Patients with Muscle Weakness

[1,2,3,4]Radka Klepochová, [5]Dita Pajuelo, [5]Monika Dezortová, [5]Peter Kordač, [5]Martin Burian, [5]Milan Hájek, [1,2]Ivica Just, [5]Petr Šedivý, [1,4]Pavol Szomolányi, [1,2]Martin Krššák

[1] High-Field MR Center, Department of Biomedical Imaging and Image-Guided Therapy, Medical University of Vienna, Austria,
[2] Division of Endocrinology and Metabolism, Department of Internal Medicine III High Field MR Centre, Department of Biomedical Imaging and Image Guided Therapy, Medical University of Vienna, Vienna, Austria
[3] Institute of Experimental Endocrinology, Biomedical Research Center, Slovak Academy of Sciences, Bratislava, Slovakia
[4] Institute of Measurement Science, Slovak Academy of Sciences, Bratislava, Slovakia
[5] MR-Unit, Department of Diagnostic and Interventional Radiology, Institute for Clinical and Experimental Medicine, Prague, Czech Republic
Email: umerklep@savba.sk

Abstract: *Phosphorus magnetic resonance spectroscopy (^{31}P MRS) is a valuable noninvasive tool for assessing muscle metabolism. However, ensuring data quality remains a challenge due to variations in patient characteristics and experimental setups. This study assesses the applicability and transferability of the quality control score (QCS) developed by Naegel et al., using our dataset collected at the High-Field MR Center (HFMRC) in Vienna. A total of 124 datasets were included, comprising healthy controls, obese volunteers, and patient groups with muscle-related conditions. Dynamic ^{31}P MRS spectra were acquired using ^{31}P MRS each site, and metabolic parameters such as mitochondrial capacity (Qmax) and phosphocreatine (PCr) recovery time constants (τ) were analyzed. The original QCS-REF criteria based on Naegel et. al. proved inadequate, leading to the development of modified quality control thresholds (QCS1 and QCS2). These adjustments improved data classification, ensuring a more reliable assessment of muscle metabolism. The study highlights the need for adaptable QC parameters in ^{31}P MRS research, particularly when applied across diverse patient populations and experimental settings. The modified QC thresholds enhance the robustness of muscle metabolism assessments, supporting their use in clinical diagnostics and research applications.*

Keywords: Quality Control, Skeletal Muscle Metabolism, ^{31}P MRS

1. Introduction

Phosphorus magnetic resonance spectroscopy (^{31}P MRS) is a noninvasive technique of choice for dynamically assessing the concentration of phosphorylated metabolites, which are directly related to the respiratory capacity of mitochondria [1,2]. However, processing and evaluating dynamic data can be challenging, as large discrepancies in results may arise due to the quality of the data, which is often influenced by patient characteristics and the experimental setup. A recently presented advanced data quality control (QC) pipeline [3] aims to ensure unbiased and accurate results when large patient datasets are used in clinical settings. Based on expert consensus [1], the QC pipeline introduced six key parameters to assess the quality of ^{31}P MRS measurements, such as phosphocreatine (PCr) depletion, the coefficient of determination (R^2) for kinetic fits, and recovery time constants (τ) of PCr and inorganic phosphate (Pi).

ISBN 978-80-69159-00-6

This study aims to evaluate the applicability and transferability of the QC score (QCS) developed by Naegel et al. [3, 4] using a dataset from 124 patients at the High-Field MR Center of the Medical University of Vienna. Additionally, it seeks to determine the sensitivity and limitations of in vivo ^{31}P MRS in assessing muscle metabolism and diagnosing conditions associated with reduced muscle strength, such as sarcopenia and myopathies, within this patient group.

2. Subjects and methods

The study included six groups: healthy young controls (HCY), elderly healthy controls (HCE), obese volunteers (OV), patients with Parkinson's Disease (PD), Alzheimer's Disease (AD), and Mild Cognitive Impairment (MCI).

Table 1: Characteristics of patient groups

Patient group	ALL	PD	AD	MCI	OV	HCE	HCY
Number	124	17 (6f+11m)	19 (13f+6m)	35 (33f+2m)	18 (13f+5m)	22 (19f +3m)	13 (9f+4m)
Age (yrs)	59 ± 18	68 ± 8	76 ± 8	70 ± 7	38 ± 7	69 ± 8	34 ± 5
BMI	26 ± 4	25 ± 3	25 ± 7	26 ± 5	34 ± 4	26 ± 5	21 ± 5

Measurements were performed in the morning after overnight fasting in a single exercise-recovery session. Volunteers were positioned supine with the right calf placed on the RF coil, which was installed on a non-magnetic ergometer, inside the scanner. Dynamic ^{31}P MR spectra were obtained using the DRESS sequence (TR/TE* = 2000/0.4 ms, NA = 1, vector size of 1024; 420 measurements) with the VOI placed to the gastrocnemius medialis muscle. The examination protocol included a two-minute rest, a 6-minute exercise (plantar flexion, 2s), and a 6-minute recovery period. An MR-compatible ergometer with pneumatic pedal resistance and exercise triggering via sound feedback was used. Resistance was set at 25-30% of maximal voluntary force (MVF).

^{31}P MR spectra were analyzed using the AMARES fitting routine in jMRUI v5.0 and MATLAB script to produce consistent and comparable results.

Metabolic parameters such as mitochondrial capacity (Qmax) and recovery time constants (τ) of PCr and Pi were calculated. T. Naegel et al. [3] proposed a set of criteria (QCS-REF) to assess data quality, including parameters like PCr depletion, R^2 values for recovery and exercise fits, and stability of PCr + Pi sum.

3. Results

The quality control limits (QCS-REF) from the earlier publication [3] were found to be inadequate for our patient groups. Specifically, only 32% of all patient data from all the data met the QCS-REF criteria. Additionally, fewer data points from these groups met the QCS-REF standards during the exercise (on-kinetics) phase.

This discrepancy prompted the development of two new quality control sets, QCS1 and QCS2, which were designed to better accommodate the specific characteristics of the patient populations. The newly introduced quality control limits proved to be more effective in classifying the ^{31}P MRS data as high-quality, offering reliable insights into muscle energy metabolism during exercise.

ISBN 978-80-69159-00-6

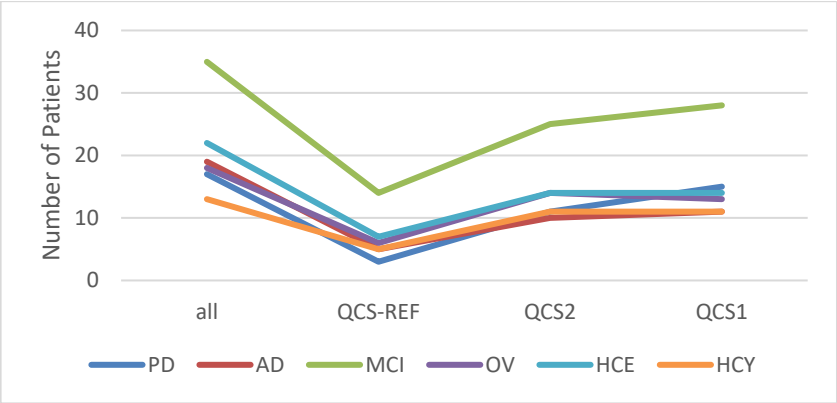

Fig. 1. **Data acceptable for further evaluation:** The number of patients across different groups (PD, AD, MCI, OV, HCE, HCY) is shown for all data, followed by classification based on the Quality Control Score from Naëgel et al. (2023) (QCS-REF). The number of patients increased when applying our modified QCS1 and QCS2, indicating a broader inclusion of data under these criteria.

The evaluation process focused on several key parameters, as outlined by the original study [3], which included the R^2 determination coefficient for the exponential fit of the kinetics of PCr and inorganic phosphate (Pi), the decrease in PCr during the recovery phase, the coefficient of variation (CV) for PCr at the end of both the exercise and recovery phases, and the pH change during the exercise phase. To evaluate data quality, three quality control schemes were applied: the original reference-based scheme (QCS_REF), and two modified variants (QCS1 and QCS2), which are described below.

QCS-REF: **The original set of quality control limits from the reference study [3, 4].**

1. **PCr depletion < 20%:** less than 20% - the interpretation of τPCr recovery is not valid
2. **R^2 $\tau PCr_{rec}/\tau Pi_{rec}$ < 0.7:** coefficient of determination less than 70% reflects poor data quality
3. **R^2 $\tau PCr_{exercise}/\tau Pi_{exercise}$ < 0.7:** coefficient of determination less than 70% reflects poor data quality
4. **$PCr + Pi_{rest} = PCr + Pi_{exercise}$:** large variation in PCr + Pi reflects corrupted data
5. **$\tau PCr_{exercise}/\tau Pi_{exercise}$ > 100 s:** reflects a linear behavior unlikely to represent mitochondrial function
6. **Coefficient of variation of $\tau PCr_{recovery}/\tau Pi_{recovery}$ > 10%:** excluded
7. **SNR**

QCS1 omitted the original criteria 2 and 3, which excluded data based on R^2 values for τPi during recovery (R^2 τPi-Rec < 0.7) and exercise (R^2 τPi-Ex < 0.7), while leaving the remaining criteria unchanged. In contrast, **QCS2** retained the conceptual basis of QCS_REF but replaced the separate evaluation of PCr and Pi fits (criteria 2 and 3: R^2 τPCr < 0.7 and R^2 τPi < 0.7) with a combined exclusion threshold of (R^2 τPCr + R^2 τPi) < 1.4 for both exercise and recovery phases.

Since no significant differences in recovery (τREC) or exercise time constants (τEx) were found between the patient groups when applying our modified QCS limits, we determined that these limits remain applicable. These parameters are essential for the long-term monitoring of muscle health.

ISBN 978-80-69159-00-6

Table 3: Time Constants τPCr for Recovery Different Patient Groups

	Time constant τ_{PCr} for recovery period					
	PD	**AD**	**MCI**	**OV**	**HCE**	**HCY**
QCS-REF	46 ± 18	96 ± 41	48 ± 27	39 ± 23	55 ± 25	68 ± 26
QCS1	62 ± 27	111 ± 66	48 ± 29	60 ± 47	47 ± 24	60 ± 33
QCS2	89 ± 62	100 ± 71	54 ± 38	63 ± 49	48 ± 24	61 ± 34

4. Conclusions

This project successfully achieved its objectives by developing a joint methodology for evaluating the quality of dynamic ^{31}P MR spectra. The findings are expected to enhance diagnostic practices and advance clinical research in muscle metabolism.

The study confirmed that parameters such as PCr depletion, R^2 values for τPCr and τPi, and the coefficient of variation (CV) of τPCr are effective for objectively assessing the quality of 31P MRS measurements. The transferability of the original QCS-REF pipeline was found to be highly dependent on patient groups and the repetition time (TR) used. Shorter TRs resulted in lower signal-to-noise ratios (SNR) for Pi, which made it challenging to meet some of the QCS criteria. Nevertheless, the modified QCS1 and QCS2 thresholds provided a reliable approach for ensuring data quality.

In conclusion, this study highlights the importance of adjusting quality control parameters according to patient characteristics and experimental conditions to ensure reliable, comparable data in clinical applications of 31P MRS. The revised quality control limits (QCS1 and QCS2) were more suitable for our patient's dataset, improving the classification of high-quality data and offering more reliable insights into muscle energy metabolism during exercise. For future manuscripts, we will include data from a comparable group of volunteers with muscle weakness from the Institute of Clinical and Experimental Medicine in Prague, where different experimental setups and ergometer types are used, to assess whether the modification of QCS thresholds is also suitable for their cohorts.

Acknowledgements

This study was supported by OEAD (CZ 14/2023 to R.Klep), FWF (#KLI 904 to MKrss), (APVV 21/0299 to P.Szom)

References

[1] Meyerspeer M, Boesch C, Cameron D, Dezortová M, Forbes SC, Heerschap A, et al. 31P magnetic resonance spectroscopy in skeletal muscle: Experts' consensus recommendations. NMR Biomed. 2021 May 1;34(5):e4246.

[2] Kemp G, Meyerspeer M, Moser E. Absolute Quantification of Phosphorus Metabolite Concentrations in Human Muscle in Vivo by 31P MRS: A Quantitative Review. NMR Biomed. 2007;20(6).

[3] Naëgel A, Ratiney H, Karkouri J, Kennouche D, Royer N, Slade JM, et al. Alteration of skeletal muscle energy metabolism assessed by phosphorus-31 magnetic resonance spectroscopy in clinical routine, part 1: Advanced quality control pipeline. NMR Biomed. 2023 Dec 1;36(12).

[4] Naëgel A, Ratiney H, Karkouri J, Kennouche D, Royer N, Slade JM, et al. Alteration of skeletal muscle energy metabolism assessed by 31 P MRS in clinical routine: Part 2. Clinical application. NMR Biomed. 2023 Dec 1;36(12).

Knee Positioning Influences Cartilage Thickness but Not Volume in MRI Segmentation

[1,3]Veronika Janacova, [1,2]Pavol Szomolanyi, [1]Diana Sitarcikova, [1,3,4,5]Siegfried Trattnig, [1]Vladimir Juras

[1]High Field MR Centre, Department of Biomedical Imaging and Image-guided Therapy, Medical University of Vienna, Vienna, Austria
[2]Institute of Measurement Science, Slovak Academy of Sciences, Bratislava, Slovakia
[3]CD Laboratory for MR Imaging Biomarkers (BIOMAK), Vienna, Austria
[4]Austrian Cluster for Tissue Regeneration, Ludwig Boltzmann Institute for Experimental and Clinical Traumatology, Vienna, Austria
[5]Institute for Clinical Molecular MRI in the Musculoskeletal System, Karl Landsteiner Society, Vienna, Austria
Email: veronika.janacova@meduniwien.ac.at

Abstract. *The aim of this study was to assess the impact of knee positioning on the volume and thickness of nine femoral cartilage segments, as variations in knee alignment can affect measurements. Eight volunteers underwent a test-retest scan using a 3D DESS sequence in five knee positions. Knee position angles were measured in axial view and correlated to cartilage volume and thickness in the femoral region. We found that knee positioning during measurement has minimal impact on femoral cartilage volume. However, the thickness of the lateral anterior and central trochlear femur cartilage is affected.*

Keywords: MRI, Cartilage, Segmentation, Volume, Thickness

1. Introduction

The cartilage thickness and volume measurement from MRI images has become a vital part of clinical trials and longitudinal OA studies. Due to the availability of automatic segmentation tools, assessment of cartilage volume becomes quick and accessible [1, 2]. As volume is measured from hundreds to thousands of voxels per ROI, it is relatively robust [3]. The case cartilage thickness is much more complicated, as in a plane, the cartilage tissue spans across 2-10 voxels, and inclusion or exclusion of voxels at the boundary can make a large difference. Furthermore, the measured thickness of cartilage can vary with the slice positioning. Many parts of a protocol, such as MR sequence parameters, MR hardware, or time between follow-ups, are fixed to ensure that the observed change in cartilage volume and thickness is caused by degenerative/regenerative processes and not by other confounders. Consistent patient positioning during follow-up visits improves the overall precision; however, due to various reasons, such as pain, the same positioning might not be possible. The objective of this experiment was to assess the effect of knee positioning on cartilage volume and thickness in healthy young volunteers.

2. Subject and Methods

The left knees of eight healthy volunteers (4 male, 4 female, mean age: 35.5 ± 10.2 years) were scanned on 3T Siemens PrismaFit (Siemens Healthineers AG, Forchheim, Germany). The 3D DESS (TE=5ms, TR=14.1ms, 160 slices, 0.6x0.6x0.6mm^3, flip angle=25°, acquisition=5:58min) was used. Each volunteer's patella center was marked with a black line,

ISBN 978-80-69159-00-6

and two additional lines spaced 1cm apart were drawn on each side (Fig. 1). A dedicated 15-channel knee coil was positioned to align these lines with the scanner laser, producing five distinct knee positions: neutral, two medial rotations, and two lateral rotations. Knee Position Angles were measured using RadiAnt DICOM Viewer (Medixant, Poznań, Poland) (Fig. 2).

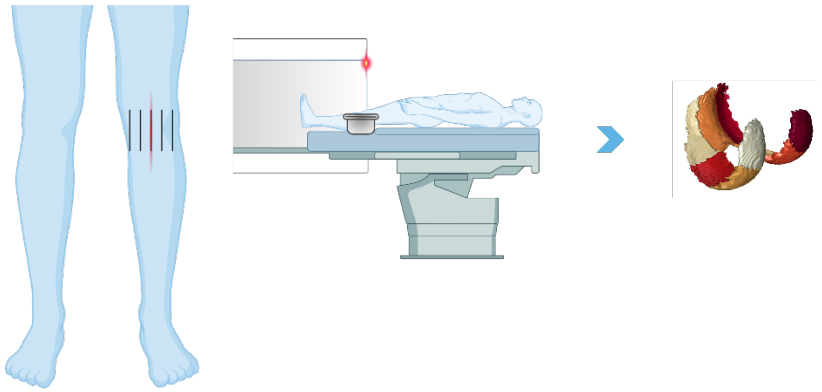

Fig. 1. Knee positioning and segmentation of the 9 femoral cartilage segments: medial (anterior/central/posterior), trochlear (lateral/central/medial), and lateral (anterior/central/posterior).

Images were automatically segmented using MR ChondralHealth version 3.1 (Siemens Healthineers AG, Forchheim, Germany), with manual corrections applied when necessary. Nine femoral cartilage regions were assessed: medial (anterior/central/posterior), trochlear (lateral/central/medial), and lateral (anterior/central/posterior).

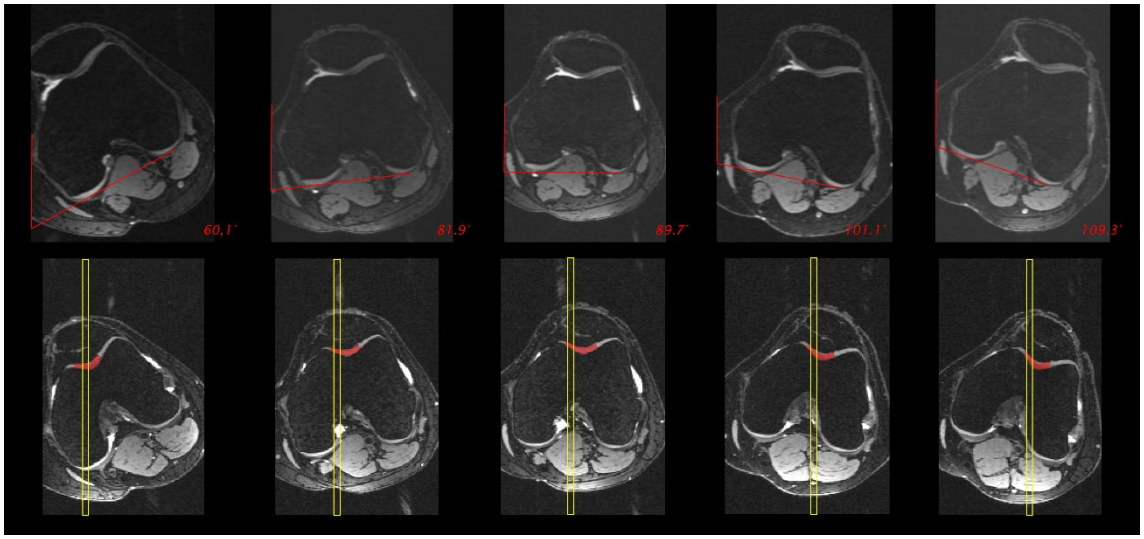

Fig. 2. Knee Position Angle measurements (top row) and visualization of the medial region of Central Trochlea (red) positioned in a sagittal slice (yellow) (bottom row).

Cartilage volume was calculated by multiplying voxel volume by the number of cartilage voxels. Cartilage thickness was computed using a custom Python script. Cartilage voxels adjacent to the bone (proximal surface) (Fig. 3) were identified, and the real-world coordinates of voxel vertices shared between bone and cartilage at the bone-cartilage interface were calculated using the affine matrix. The distal surface voxel vertices were identified as vertices shared with the background (value 0) neighboring voxels. For each voxel along the distal surface, the nearest voxel along the proximal surface was found using a KDTree nearest-neighbor search (SciPy library [4]). Cartilage thickness was calculated as the mean of Euclidean distances between each distal surface voxel and its corresponding nearest neighbor on the proximal surface, performed separately for each slice. The average thickness for each cartilage

ISBN 978-80-69159-00-6

segment was then obtained by averaging the thickness values across all slices within that segment. Slices with large discrepancies between the number of proximal and distal surface vertices may result in overestimated cartilage thickness. Therefore, measurements exceeding 3 mm were excluded. A 2D approach was chosen to reflect the manual slice-wise measurement method, which relies on drawing multiple lines between the proximal and distal surfaces based on anatomical landmarks. Finally, correlations between knee rotation angles, cartilage volume, and thickness were evaluated using Spearman's correlation coefficient (ρ).

3. Results

The observed correlations are listed in Table 1. The only significant correlations were observed in the lateral anterior central trochlear cartilage.

Table 1 Spearman's correlation coefficients between Knee Position Angle and Cartilage Volume and Cartilage thickness. Significant correlations are marked in bold.

Femoral cartilage segment	Correlation between Angle and Volume	p-value	Correlation between Angle and Thickness	p-value
Lateral anterior	0.146	0.370	**0.414**	**0.008**
Lateral central	-0.130	0.424	-0.134	0.408
Lateral posterior	-0.196	0.225	-0.209	0.196
Medial anterior	-0.048	0.770	0.208	0.197
Medial central	-0.156	0.335	0.113	0.487
Medial posterior	-0.300	0.060	-0.017	0.916
Trochlea central	0.041	0.800	**0.326**	**0.040**
Trochlea lateral	0.076	0.640	0.093	0.567
Trochlea medial	0.014	0.932	0.078	0.630

4. Discussion

While there are weak correlations between knee rotation angle and femoral cartilage volume in healthy individuals, these correlations are not statistically significant and vary across different cartilage regions. There are, however, significant correlations between lateral femoral cartilage ($\rho_{\text{Lateral Anterior}} = 0.414$, $p = 0.008$) and trochlear cartilage ($\rho_{\text{Trochlea central}} = 0.326$, $p = 0.040$). As seen in the case of central trochlea, the relative position in the image position resulting in cross-sections with varying thickness (Fig.2). In longitudinal studies, these variations might lead to apparent changes in cartilage thickness that are due to positioning inconsistencies, not disease progression.

5. Conclusions

Knee positioning in terms of rotation during measurement has minimal impact on femoral cartilage volume in 3D assessments. The consistent positioning of the patient should be secured for each follow-up in longitudinal studies.

ISBN 978-80-69159-00-6

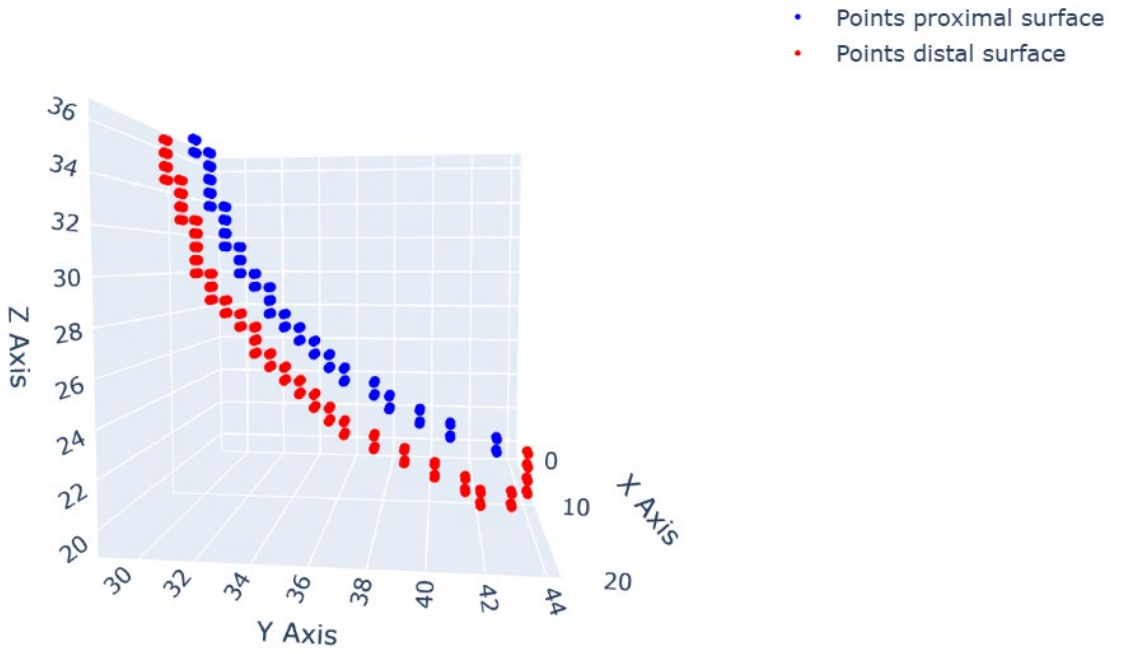

Fig. 3. Example of extracted voxel vertices. Blue - proximal cartilage surface; Red – distal cartilage surface

References

[1] Juras V, Janáčová V, Szomolanyi P, Schreiner M, Laurent D, Scotti C, et al. Fully automated pipeline for quantitative MRI evaluation of knee articular cartilage for longitudinal OA trials. *Osteoarthritis and Cartilage* 2021;29:S321–2. https://doi.org/10.1016/j.joca.2021.02.423.

[2] Hou W, Zhao J, He R, Li J, Ou Y, Du M, et al. Quantitative measurement of cartilage volume with automatic cartilage segmentation in knee osteoarthritis. *Clin Rheumatol* 2021;40:1997–2006. https://doi.org/10.1007/s10067-020-05388-7.

[3] Eckstein F, Schnier M, Haubner M, Priebsch J, Glaser C, Englmeier K-H, et al. Accuracy of Cartilage Volume and Thickness Measurements With Magnetic Resonance Imaging. *Clinical Orthopaedics and Related Research®* 1998;352:137.

[4] Virtanen P, Gommers R, Oliphant TE, Haberland M, Reddy T, Cournapeau D, et al. SciPy 1.0: fundamental algorithms for scientific computing in Python. *Nat Methods* 2020;17:261–72. https://doi.org/10.1038/s41592-019-0686-2.

Quantitative MRI Imaging Methods for Osteoarthritis Clinical Trials

[1,2]Vladimir Juras, [1,2]Veronika Janacova, [1,3]Pavol Szomolanyi, [1]Diana Sitarcikova, [1,2,4,5]Siegfried Trattnig

[1]High-Field MR Center, Department of Imaging Methods and Image-Guided Therapy, Medical University of Vienna, Vienna, Austria
[2]CD laboratory for Clinical Molecular MR Imaging, Vienna, Austria
[3]Institute of Measurement Science, Slovak Academy of Sciences, Bratislava, Slovakia
[4]Austrian Cluster for Tissue Regeneration, Ludwig Boltzmann Institute for Experimental and Clinical Traumatology, Vienna, Austria
[5]Institute for Clinical Molecular MRI in the Musculoskeletal System, Karl Landsteiner Society, Vienna, Austria
Email: vladimir.juras@meduniwien.ac.at

Abstract. *Magnetic Resonance Imaging (MRI) has emerged as a pivotal tool in clinical trials for osteoarthritis (OA) due to its superior ability to visualize joint structures and quantify disease progression. Advanced MRI techniques, including T2 and T2* mapping, ultrashort echo time (UTE) imaging, sodium imaging, and also volumetric analysis, enable detailed assessment of cartilage integrity, subchondral bone changes, and synovial inflammation. Semi-quantitative scoring systems facilitate standardized evaluation, while automated image analysis enhances reproducibility. Integration of MRI biomarkers with clinical outcomes improves the sensitivity of detecting therapeutic effects, making MRI indispensable for modern OA research. In this work, the accuracy, reproducibility, and sensitivity of fully automated methods are elaborated upon.*

Keywords: Osteoarthritis, MRI, Quantitative

1. Introduction

Osteoarthritis (OA) is a prevalent degenerative joint disease characterized by the progressive degradation of articular cartilage, subchondral bone remodeling, and synovial inflammation. Accurate and sensitive assessment of these structural changes is essential for evaluating disease progression and the efficacy of therapeutic interventions in clinical trials. Magnetic Resonance Imaging (MRI) has become a cornerstone in OA research due to its non-invasive nature and superior capability to visualize and quantify joint structures [1]. Recent advancements in MRI techniques have significantly enhanced the ability to assess cartilage integrity, subchondral bone alterations, and synovial inflammation with greater precision. Techniques such as T2 and T2* mapping provide valuable insights into cartilage composition and hydration status [2]. Sodium imaging offers a unique approach to evaluating cartilage glycosaminoglycan content, a key biomarker of cartilage health [3]. Additionally, volumetric analysis facilitates comprehensive quantification of cartilage volume and thickness, providing critical data for monitoring disease progression [4].

2. Volumetric analysis of cartilage

Volumetric analysis of cartilage is an essential component of osteoarthritis (OA) research and clinical trials, providing comprehensive quantitative data on cartilage volume, thickness, and morphology. Unlike conventional two-dimensional imaging techniques, volumetric analysis

ISBN 978-80-69159-00-6

utilizes three-dimensional (3D) MRI acquisitions to generate detailed reconstructions of joint cartilage, enabling precise measurement of cartilage loss and structural changes over time.

High-resolution MRI sequences, such as double echo steady-state (DESS), 3D spoiled gradient-echo (SPGR), and fast low-angle shot (FLASH), are commonly used for volumetric cartilage assessment. These techniques produce isotropic voxel data, allowing accurate segmentation and volume calculation in multiple planes without the need for interpolation. Automated and semi-automated segmentation algorithms are increasingly employed to delineate cartilage boundaries efficiently, reducing observer variability and improving reproducibility (Figure 1).

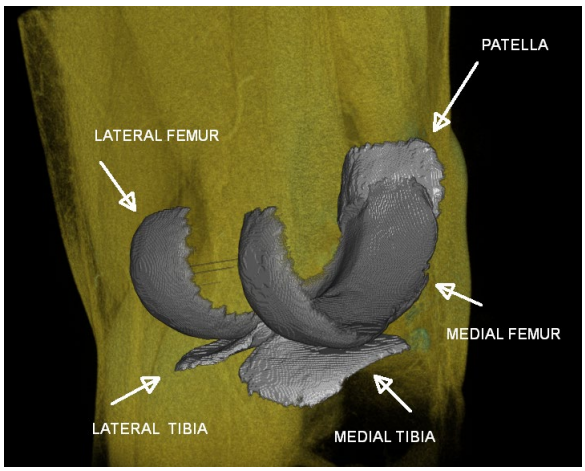

Fig. 1. Example of the automated cartilage segmentation

Ground truth is critically important in the training of the automated cartilage segmentation as it serves as the reference standard for training, validation, and evaluation of segmentation algorithms. Typically generated through manual or semi-automated expert annotation of MR images, ground truth data represent the most accurate depiction of cartilage boundaries and morphology. High-quality ground truth is essential for supervised machine learning approaches, such as convolutional neural networks (CNNs), which learn to mimic expert-level segmentation. There are a few publicly available datasets of manual cartilage segmentation, such as ZIB (https://www.zib.de/research/pubdata) and SK-10 (https://ski10.grand-challenge.org/). Before using the ground truth from public repositories, it needs to be carefully reviewed (Figure 2).

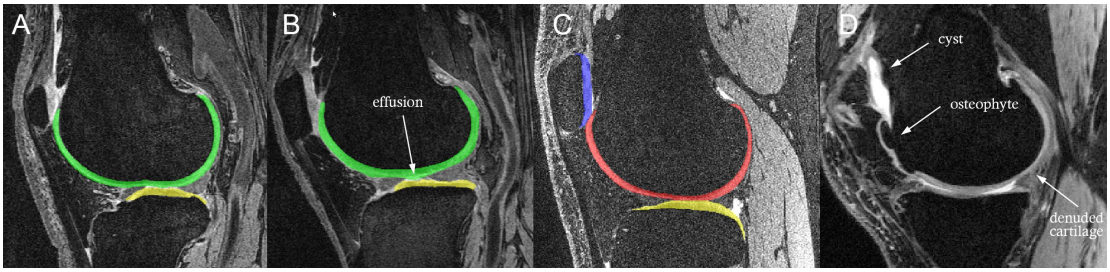

Fig. 2. The pitfalls of the ground truth generation for automated cartilage segmentation: A: an example of accurate manual segmentation from ZIB; B: an example of inaccurate manual segmentation from ZIB (segmentation leaks to effusion); C: in-house created ground truth (Medical University of Vienna, Austria); D: the most common challenges in late OA patients segmentation (osteophytes, cysts, effusion, cartilage thinning).

Cartilage thickness measurement from MR images is another quantitative assessment in osteoarthritis (OA) research, as it provides an insight into cartilage degeneration and disease progression. Thickness measurements are typically obtained by calculating the shortest distance between the cartilage surface and the bone interface at each voxel location.

ISBN 978-80-69159-00-6

T2 and T2 mapping*
T2 and T2* mapping are advanced MRI techniques widely used to assess cartilage integrity in osteoarthritis. T2 mapping measures the transverse relaxation time, reflecting water content and collagen network integrity within the cartilage matrix. Increased T2 values typically indicate cartilage degeneration, including collagen disruption and increased water content. T2* mapping, on the other hand, is sensitive to magnetic field inhomogeneities and provides information about tissue composition, including calcification and iron deposition.

Sodium imaging
Sodium MRI is an advanced imaging technique used to assess cartilage health in osteoarthritis by directly measuring sodium ion concentration, which correlates with glycosaminoglycan (GAG) content. GAGs are essential components of cartilage that contribute to its compressive strength and hydration. Reduced sodium signal intensity indicates a loss of GAGs, reflecting cartilage degeneration and early signs of OA. Sodium nuclei (^{23}Na) have a low natural abundance and low gyromagnetic ratio, resulting in a significantly weaker signal compared to conventional proton MRI. Achieving adequate SNR often requires long acquisition times or ultra-high-field MRI (≥7T), which may not be readily available. To improve SNR, sodium MRI typically uses larger voxel sizes, compromising spatial resolution. This makes it challenging to accurately assess thin cartilage layers, especially in small joints or early-stage osteoarthritis. Sodium MRI requires specialized coils and ultra-high-field MRI systems, which are costly and not widely available in clinical settings. Additionally, sequence optimization and advanced reconstruction algorithms are needed to enhance image quality.

3. Automated pipeline for OA evaluation

Volumetric analysis provides valuable insights into the spatial distribution of cartilage loss, which is crucial for detecting focal cartilage defects and subtle changes that may indicate disease progression or therapeutic response. Additionally, combining volumetric data with compositional MRI techniques, such as T2 and T2* mapping or sodium imaging, enhances the ability to assess not only cartilage quantity but also quality. Our research group has developed an automated pipeline for quantitative cartilage parameter extraction, including fully automated knee cartilage segmentation, T2 mapping, sodium concentration mapping as well as texture analysis [5]. The proposed automated technique for evaluating knee cartilage using morphological images delivers highly reproducible results while significantly reducing the effort needed for cartilage segmentation in longitudinal, large-cohort studies. The analysis of 21 cartilage subregions enables a comprehensive assessment of the entire joint, allowing for a more targeted evaluation of cartilage degeneration or treatment monitoring. Furthermore, the automated detection of these precisely defined cartilage subregions represents a novel approach, making it particularly valuable for studies involving patients with knee osteoarthritis, where cartilage deterioration may occur in multiple areas. Additionally, the ability to extract information from T2 maps regarding early changes in cartilage texture within these regions paves the way for developing qualitative biomarkers that can enhance differentiation between treatment options.

4. Conclusions

T2 and T2* mapping offer quantitative, non-invasive biomarkers for detecting early cartilage degeneration before morphological changes become apparent. Both are valuable for monitoring disease progression and evaluating therapeutic interventions, providing critical insights into cartilage health and structural integrity in OA clinical trials. Sodium MRI provides a non-invasive, quantitative biomarker for evaluating cartilage composition, offering unique insights

ISBN 978-80-69159-00-6

that complement conventional MRI techniques like T2 mapping. By providing precise and reproducible quantification of cartilage volume and morphology, volumetric analysis plays a pivotal role in evaluating the efficacy of novel therapeutic interventions and enhancing the sensitivity of OA clinical trials.

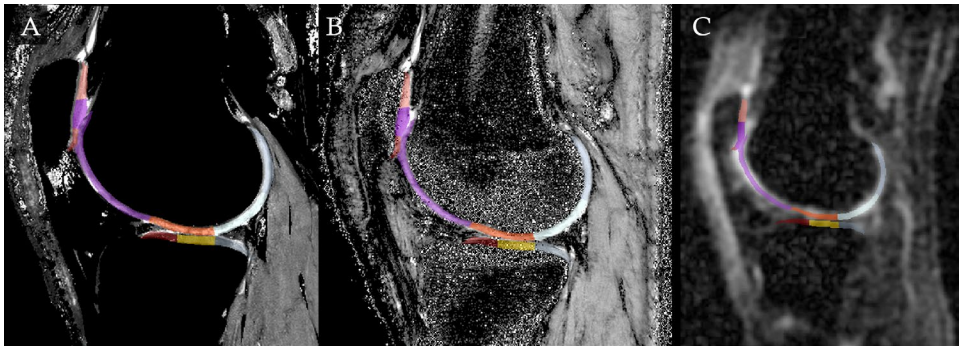

Fig. 3. The output of the automated OA evaluation pipeline from MR images: A: T2 map overlaid with the segmentation acquired from DESS images; B: T2* map; and C: sodium MR image. Quantitative biomarkers are automatically extracted from the registered 3D datasets.

Acknowledgements

This research was funded in whole or in part by the Austrian Science Fund (FWF) 10.55776/PIN5555423 and grant number APVV-21-0299 of the Slovak Research and Development Agency.

References

[1] Sneag, D.B., F. Abel, H.G. Potter, J. Fritz, M.F. Koff, C.B. Chung, V. Pedoia, and E.T. Tan, MRI Advancements in Musculoskeletal Clinical and Research Practice. *Radiology*, 2023. 308(2): p. e230531.

[2] Banjar, M., S. Horiuchi, D.N. Gedeon, and H. Yoshioka, Review of Quantitative Knee Articular Cartilage MR Imaging. *Magn Reson Med Sci,* 2022. 21(1): p. 29-40.

[3] Zbyn, S., V. Mlynarik, V. Juras, P. Szomolanyi, and S. Trattnig, Evaluation of cartilage repair and osteoarthritis with sodium MRI. *NMR Biomed*, 2016. 29(2): p. 206-15.

[4] Ebrahimkhani, S., M.H. Jaward, F.M. Cicuttini, A. Dharmaratne, Y. Wang, and A.G.S. de Herrera, A review on segmentation of knee articular cartilage: from conventional methods towards deep learning. *Artif Intell Med*, 2020. 106: p. 101851.

[5] Juras, V., V. Janacova, P. Szomolanyi, M. Schreiner, D. Laurent, C. Scotti, E. Raithel, and S. Trattnig, Fully Automated Pipeline for Quantitative Mri Evaluation of Knee Articular Cartilage for Longitudinal Oa Trials. *Osteoarthritis and Cartilage*, 2021. 29: p. S321-S322.

Fast 3D ^{31}P B_1^+ Mapping Using Concentric Ring Trajectory MRSI at 7 T

[1,2]Ladislav Valkovič, [2]Ferenc E. Mózes, [2]Yuanyuan Lyu, [3]Jabrane Karkouri, [3]Christopher T. Rodgers, [4]Fabian Niess, [4]Wolfgang Bogner, [1]Pavol Szomolányi

[1]Department of Imaging Methods, Institute of Measurement Science, Slovak Academy of Sciences, Bratislava, Slovakia
[2]Oxford Centre for Clinical MR Research (OCMR), RDM Cardiovascular Medicine, University of Oxford, Oxford, UK
[3]Wolfson Brain Imaging Centre, Department of Clinical Neurosciences, University of Cambridge, Cambridge, UK
[4]High-field MR Centre, Department of Biomedical Imaging and Image-guided Therapy, Medical University of Vienna, Vienna, Austria
Email: ladislav.valkovic@savba.sk

Abstract. *^{31}P protocols, even at 7 T, are long, severely limiting the time available to collect flip angle maps needed for metabolite quantification across the heart. Here we aimed to evaluate the feasibility of accelerating ^{31}P B_1^+ mapping in the myocardium at 7 T. Using the Bloch-Siegert B_1 mapping technique, flip angle maps were estimated using Cartesian 2D-MRSI (FA_{CSI}) and concentric ring trajectory-based 3D-MRSI (FA_{CRT}) and compared in the thigh of 4 participants. FA_{CRT} was also estimated in the myocardium of 3 participants. We have found a non-identity linear relationship between FA_{CSI} and FA_{CRT}, raising the need for a correction. This correction yielded homogeneous flip angle values in the myocardium. Our 3D B_1^+ mapping approach, using half the acquisition time of a 2D Cartesian CSI-MRSI can significantly shorten the length of ^{31}P protocols at 7 T while allowing absolute quantification of myocardial energetics.*

Keywords: MRSI, B1 Mapping, Bloch-Siegert, 7 T, Concentric Ring

1. Introduction

Phosphorus magnetic resonance spectroscopy (^{31}P-MRS) can probe the energy metabolism of the human heart in vivo by measuring the phosphocreatine to adenosine triphosphate concentration ratio (PCr/ATP), an indicator of heart failure [1], or the chemical kinetics of the oxidative phosphorylation system. Absolute quantification of metabolite concentrations is needed where stable ATP levels cannot be guaranteed or when fluxes are to be quantified.

Quantification of metabolite concentrations often requires the precise measurement of the transmit B_1 field (B_1^+), particularly at 7 T where single-transmit coils are associated with large inhomogeneity of the B_1^+ field. B_1^+ measurements are also necessary for the assessment of ATP production rate constants using the four-angle saturation transfer [2] method. Bloch-Siegert B_1^+ mapping has been described as a reliable method [3] at 7 T.

However, the standard Cartesian sampling strategy employed for this B_1^+ mapping method still requires long acquisition times, e.g., ~40mins [4]), if the whole heart is to be covered. Thus, the aim of this work was to compare B_1^+ maps collected using the standard Cartesian trajectory and using an accelerated concentric ring trajectory (CRT) [5] in the thigh muscle; and demonstrating the feasibility of accelerated 3D- B_1^+ mapping in the heart at 7 T.

ISBN 978-80-69159-00-6

2. Subject and Methods

The thigh of the dominant leg of four healthy volunteers (2 females, age 32 years, weight 64kg), and the hearts of three healthy male volunteers (age 31 years, weight 77kg) were scanned supine in a Siemens Magnetom 7 T scanner (Siemens Healthineers, Germany) equipped with a whole-body birdcage transmit and 16-channel receive array coil (Rapid Biomedical, Germany) (4).

Standard 2D Cartesian chemical shift imaging (CSI)-based and a 3D CRT-based Bloch-Siegert sequence were used with the following parameters: Fermi pulse with Tp=8ms, t_0=4ms, a=0.1ms, and ±1000Hz offsets; TR=2s (CSI) and 1.5s (CRT), TE=2.3ms (CSI) and 2.0ms (CRT), matrix of 16×16×1 (CSI), 10×10×10 (CRT leg) and 12×12×12 (CRT heart), bandwidth 8000Hz (CSI) and 2778Hz (CRT), FOV 400×250×30mm^3 (CSI) and 400×250×170mm^3 (CRT), spectral samples 2048 (CSI) and 756 (CRT), number of averages 2 (CSI), number of circles 11 (CRT). Only the CRT-based BS sequence was run during cardiac acquisitions. The total length of CSI-BS acquisition was 12:40 minutes, while CRT-BS took 5:16 minutes.

CSI data were reconstructed online and CRT data were reconstructed offline using the non-uniform FFT (NUFFT) toolbox with min-max Kaiser-Bessel kernel interpolation and twofold oversampling in MATLAB (MathWorks, Natick, MA, USA). No density compensation was required. Individual coil data was combined using the WSVD algorithm [6]. All spectra were fitted using the OXSA toolbox [7] and the phase difference of the PCr signal was used to quantify the B_1^+ field. B_1^+ values expressed in μT were transformed into flip angles relative to the Bloch-simulated flip angle of a sinc pulse.

3. Results

Figure 1 shows a representative example of flip angle maps of the right thigh acquired using both the CSI and CRT acquisition methods. A linear regression between flip angles determined using CSI (FA_{CSI}) and CRT (FA_{CRT}) revealed a slope of 0.39 (95% CI: 0.19-0.58) and an intercept of 21.12° (95% CI: 13.43°-28.80°) for the dependence of FA_{CRT} on FA_{CSI} (for both $p < 0.001$). Given the relationship between the two flip angles, FA_{CRT} was corrected back to FA_{CSI}.

FA_{CSI} maps were not available in the myocardium, therefore, the same correction formula was assumed. As a result, Figure 2 shows a flip angle map of the heart before and after applying the correction described above, the correction resulting in a more homogeneous flip angle distribution over the myocardium.

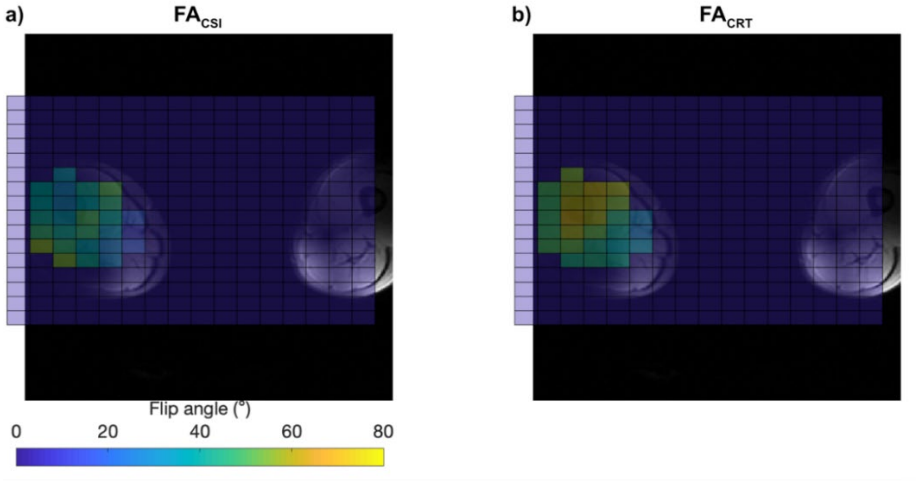

Fig 1. Example of flip angle maps acquired using a standard Cartesian CSI-MRSI (a) and an accelerated concentric ring trajectory MRSI (b) readout.

ISBN 978-80-69159-00-6

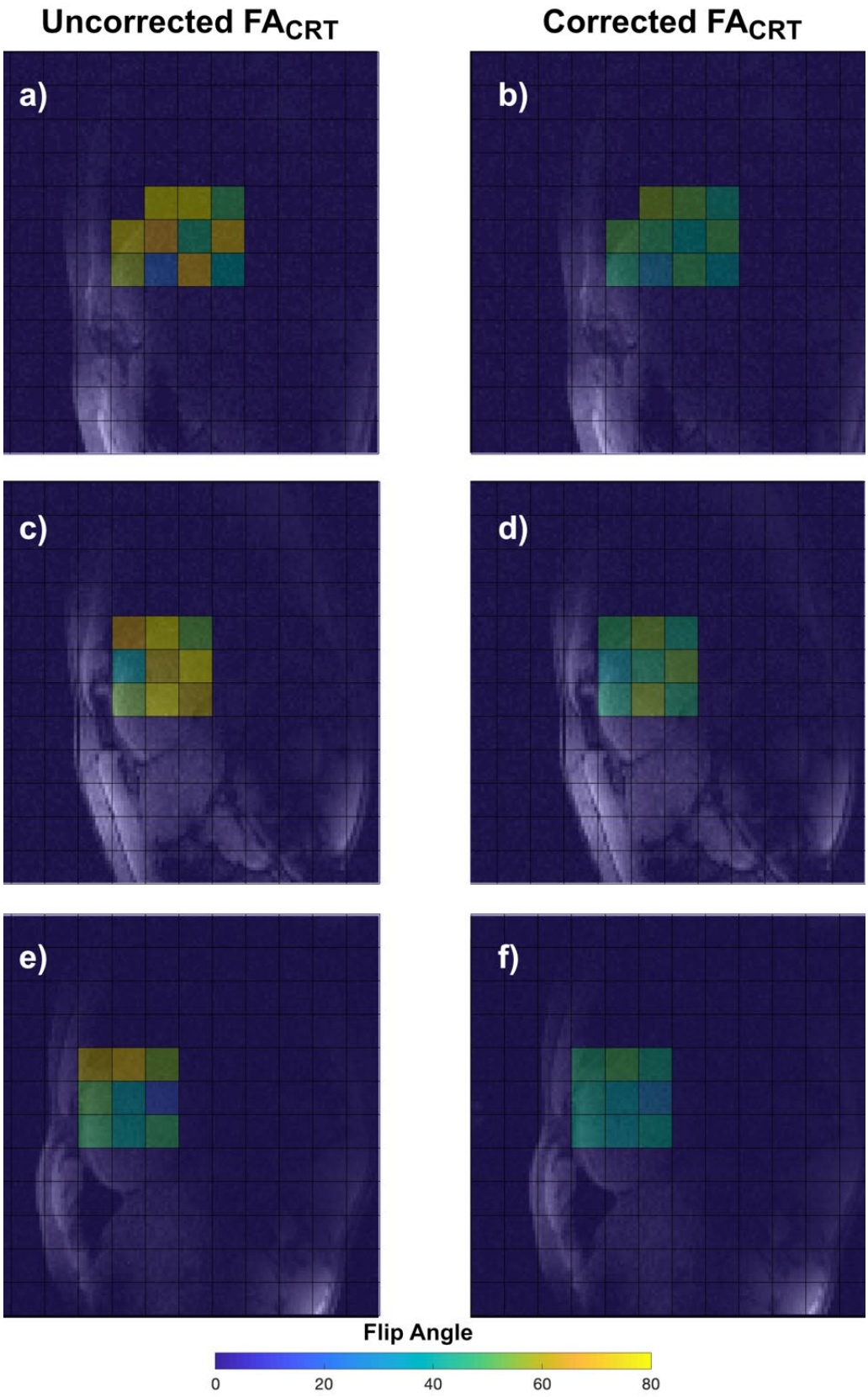

Fig 2. Flip angle maps of the myocardium of the 3 volunteers before (a, c, e) and after (b, d, f) correcting for the difference observed between FACSI and FACRT in thighs. The increased homogeneity of flip angles across the myocardium should be noted after the correction was applied.

ISBN 978-80-69159-00-6

4. Discussion

We have shown that the acquisition of a 3D B_1^+ map using an accelerated, concentric ring k-space trajectory is possible in less than half the time necessary for a 2D B_1^+ map acquired with the standard Cartesian CSI readout.

There were differences between the flip angle values from the two acquisition types, necessitating the derivation of a correction formula to transform FA_{CRT} into FA_{CSI}. These differences might be explained by phase differences accrued during the circular sampling of the free induction decay curves during the CRT acquisition.

5. Conclusions

A fast, 3D B_1^+ mapping acquisition serves not only the acceleration of ^{31}P acquisition protocols thus increasing participant comfort at 7 T, but ultimately also enables the collection of spatially more extensive ^{31}P saturation transfer measurements.

Acknowledgements

LV and FEM are supported by a Sir Henry Dale Fellowship of the Welcome Trust and the Royal Society [221805/Z/20/Z]. LV also acknowledges the support of the Slovak Grant Agencies VEGA [2/0004/23] and APVV [21–0299]. The authors thank the UK BBSRC (grant number BB/W019582/1) for support. JK was supported by Innovate UK (10032205) under the Guarantee Scheme relating to the EU Horizon Europe project MITI (101058229). This research was supported by the NIHR Cambridge Biomedical Research Centre (BRC-1215-20014). The views expressed are those of the author(s) and not necessarily those of the NIHR or the Department of Health and Social Care.

References

[1] Neubauer S. (2007). The Failing Heart — An Engine Out of Fuel. *New England Journal of Medicine*, 356 (11), 1140–1151

[2] Bottomley PA, Ouwerkerk R, Lee RF, Weiss RG. Four-angle saturation transfer (FAST) method for measuring creatine kinase reaction rates in vivo. *Magn Reson Med* 2002;47(5):850-863.

[3] Clarke WT, Robson MD, Rodgers CT. Bloch-Siegert B1+-mapping for human cardiac (31) P-MRS at 7 Tesla. *Magn Reson Med* 2016;76(4):1047-1058.

[4] Clarke WT, Robson MD, Neubauer S, Rodgers CT. Creatine kinase rate constant in the human heart measured with 3D-localization at 7 Tesla. *Magn Reson Med* 2017;78(1):20-32.

[5] Clarke WT, Hingerl L, Strasser B, Bogner W, Valkovič L, Rodgers CT. Three-dimensional, 2.5-minute, 7 T phosphorus magnetic resonance spectroscopic imaging of the human heart using concentric rings. *NMR Biomed* 2023;36(1):e4813.

[6] Rodgers CT, Robson MD. Receive array magnetic resonance spectroscopy: Whitened singular value decomposition (WSVD) gives optimal Bayesian solution. *Magn Reson Med* 2010;63(4):881-891.

[7] Purvis LAB, Clarke WT, Biasiolli L, Valkovič L, Robson MD, Rodgers CT. OXSA: An open-source magnetic resonance spectroscopy analysis toolbox in MATLAB. *PLoS One* 2017;12(9):e0185356.

Poster Session II

ISBN 978-80-69159-00-6

Modal Analysis of Functionally Oriented Fabric Laminate with 10 mm Wide Carbon Strips and a 20 mm Circular Notch

Radek Zbončák

VÚTS, a. s., Liberec, Czechia
Email: radek.zboncak@vuts.cz

Abstract. *Functionally oriented fabric (FOF) is a woven textile featuring irregularly but not randomly integrated functional material strips in both warp and weft directions, designed to locally improve the mechanical properties of laminates. Low-cost material such as glass fiber is combined with high mechanical properties material such as carbon fiber. The subject of this work is to analyze the effect of two FOF laminate layups on natural frequencies of the laminate with a notch using finite element method and experimental evaluation. The layups of analyzed laminate panels are [0/45]s and [0/30/60]s. The width of the strips is 10 mm, the span of the strips is 20 mm and there is a 20 mm circular notch in the center of the panel right among the strips. The FEA is focused on a comparison of pure glass laminate and FOF laminate with the same plies' orientation. The results show approximately 20% increase of FOF laminate natural frequencies for [0/45]s layup and about 5 % increase in twisting modes and 13 % increase of natural frequencies in bending modes for [0/30/60]s layup. The experiments focus on verifying the actual values of frequencies and subsequent comparison with numerical values determined by simulation. Experimental results show 1-10 % deviation for [0/45]s layup and 10-16 % deviation for [0/30/60]s layup. These enhancements help to prevent resonance in standard operating frequencies of mechanisms and machines, thus extending their operational lifespan. Additionally, the strategic placement of functional material strips around structural openings provides increased stiffness without the need for extra layers, effectively reducing the laminate's overall mass. This study highlights the potential of FOF to improve the dynamic performance and lifespan of laminated composite structures used in various engineering applications.*

Keywords: Functionally Oriented Fabrics, Composite Material, Modal Analysis, Natural Frequency, FEA

1. Introduction

Woven fabrics are generally sorted into two groups based on the roving material. In the first case, warp and weft roving is made of the same material. The second type of fabric is so called 'hybrid fabric', where roving in warp direction consists of different fibers than roving in weft direction, typically carbon-aramid combination [1]. Such a regular alternation of materials in the hybrid fabric leads to homogenization of the properties of the laminate layer. In contrast to these common types of fabrics, the functionally oriented fabric structure (FOFS) has irregularly distributed fibers of different materials in the warp and weft (Fig. 1). The base material (BM) predominates in the fabric. Such material is usually cheaper and has worse mechanical properties than the functional one. Functional material (FM) has a minority in the fabric and has better mechanical properties and therefore it is in principle more expensive than the base material. The base material in the fabric is E-glass EC13 272 Z20 T63C roving and functional material is carbon Tenax E HTA 40 E13 6K roving. The advantage of a FOF is the efficient use of expensive material with high mechanical performance quality.

The production of a functionally oriented structure (FOS) allows lamination without cutting the continuous fibers in the layer and so having better mechanical properties at the same time. FOF is intended for use in the layup to locally improve mechanical properties to increase strength or

ISBN 978-80-69159-00-6

stiffness in required area. The suitable applications are laminates with holes for fasteners, or with openings such as windows or mounting openings providing access to machine parts under the laminate part. Another application is a large format laminate in which the strip of functional material weaved in the fabric acts like a ‘shell rib’.

Fig. 1. Example of functionally oriented fabric (FOF).

2. Subject and Methods

Vibration performance is enhanced by stiffness properties, which is a product of the fiber and ply orientation. The good damping characteristics are attributed to the polymeric matrix. Frequency response in case of rectangular plate, where thickness is much smaller than in-plane dimensions, is an out-of-plane behavior dependent on three factors: plate aspect ratio, density given by fiber volume ratio and plate flexural stiffness given by fiber orientation [2]. Key factors are flexural rigidity and position of the contributing plies.

The damping of composite structures is more complex in analysis but is fundamentally a function of the matrix (resin), fiber-volume ratio, and ply orientation. The damping characteristic of materials is typically given as a loss factor, which is a function of the applied frequency. The loss factor is a ratio of the loss modulus to the storage modulus, both functions of frequency. The storage and loss moduli are derived from the relationship between the individual fiber and resin moduli, and the fiber-volume ratio. The loss factor of a unidirectional ply is typically dominated by the stiff fiber, but for matrix-dominated directions (45–90°) the loss factor increases significantly and is dominated by the viscoelastic matrix material. Therefore, when attempting to design a highly damped structure, a good proportion of ±45° plies is important [2].

The first method used to analyze dynamic properties of FOS is finite element method (FEM or FEA). Using ply-based modeling, 3D mesh for every layer is extruded from 2D mesh (CQUAD4 elements). The woven fabric lamina is defined by software as three layers of unidirectional fibers (UD). Two outer layers of UD (warp) and one intermediate layer of UD rotated by 90° (weft). Solution type SOL 103 and Lanczos method is used in structural analysis in SW Siemens NX. RoM model is used for predicting laminate material data [3]. The dimensions of the laminate are 200×100×thickness given by the layup.

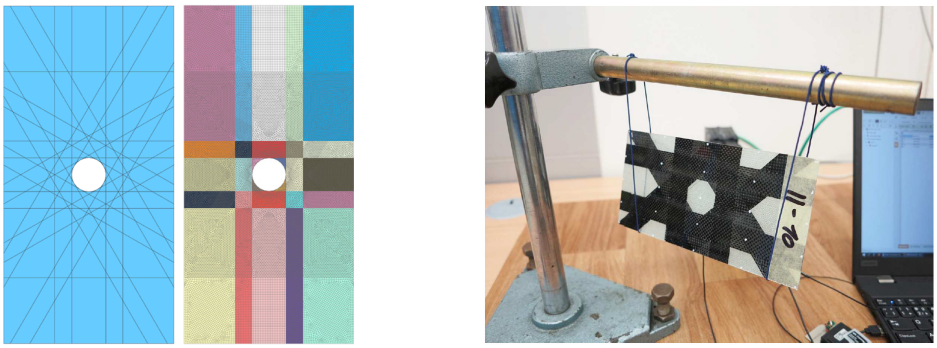

Fig. 2. Numerical models (left – CAD and FEM) and experiment setting (right).

ISBN 978-80-69159-00-6

Experimental modal analysis was performed on plates freely suspended on an elastic suspension. The system was replaced by a measurement model with 25 measurement points. The reference acceleration sensor was fixed with wax. Natural oscillations were induced using an impact hammer in the direction normal to the plate surface. Five impacts (measurements) were performed repeatedly at each location, from which the average transfer function was calculated. The modal parameters of the system were determined by regression calculation.

3. Results

Fig. 3 shows shapes of the first three modes, where the first and third mode is twisting and second and fourth (not included in the figure) is bending.

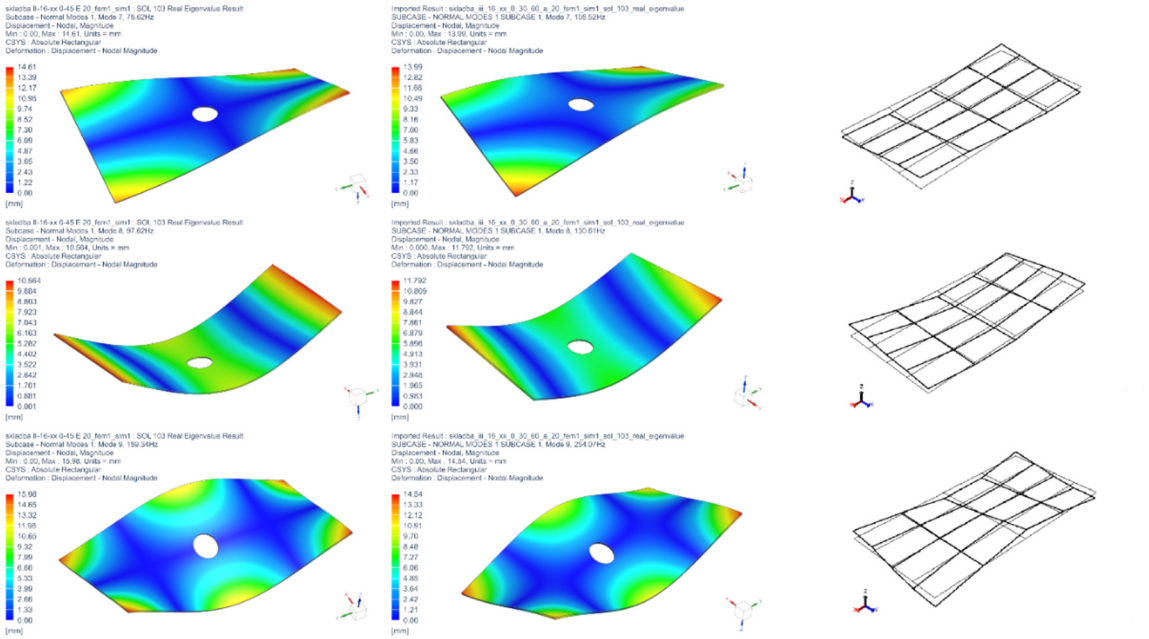

Fig. 3. Shapes of first three modes by numerical model (left – 0/45 and middle – 0/30/60) and by experiment (right).

Absolute values are summarized in the following two tables (Table 1 and Table 2). Δ1 is the deviation of natural frequencies for glass only and FOF laminates. Δ2 is the deviation of numerical and experimental values of natural frequencies for FOF laminates.

Table 1. Values of natural frequencies determined numerically and by experiment.

Layup	[0/45]s					[0/30/60]s				
Method	Numerical			Experimental		Numerical			Experimental	
	Glass	FOF	Δ_1	FOF	Δ_2	Glass	FOF	Δ_1	FOF	Δ_2
Modes	[Hz]	[Hz]	[%]	[Hz]	[%]	[Hz]	[Hz]	[%]	[Hz]	[%]
1st	63.0	78.6	20	73.1	-8	102.5	108.5	6	128.7	16
2nd	76.6	97.6	22	98.4	1	111.8	130.6	14	146.7	11
3rd	152.5	189.3	19	177.4	-7	241.7	254.1	5	300.8	16
4th	216.4	265.0	18	260.3	-2	315.8	355.8	11	-	-
5th	291.1	344.3	15	305.0	-13	447.6	471.5	5	-	-
6th	308.6	350.2	12	360.1	3	452.1	485.5	7	-	-

ISBN 978-80-69159-00-6

Experimentally evaluated damping of 0/45 layup varies from 1.2 % for 1st mode to 0.8 % for 4th mode. The damping of 0/30/60 layup is from 1.0 % for 1st mode to 0.5 % for 3rd mode.

4. Discussion

Lamination with FOF reduces the number of layers which leads to mass reduction. Laminate made of FOF can be symmetrical, has uniform thickness and can be made in a closed mold to get A-surface on both sides of the part.

The shapes of first and third mode show twisting. Second and fourth mode show bending deformation. The shapes of modes for glass only laminates and for FOF laminates are the same. The values of natural frequencies are summarized in Table 1. Natural frequencies of the first four modes of 0/45 layup increase about 20 % against glass only laminate values. In case of 0/30/60 layup FOF, the more significant increase about 14 % is noted for bending modes, while the increase about 5 % is noted for twisting modes. When comparing numerical and experimental results, better match of results from 1 to 10 % is shown by 0/45 layup. Higher deviation from 11 to 16 % in case of 0/30/60 layup is given by higher deviation of fiber orientation caused by wet layup manufacturing technology.

5. Conclusions

The benefit of FOF is effectively distributed material properties in the specific areas where the best material performance is needed. FOF allows to reduce the number of layers in layup as there is no need to puzzle cuts of different materials. That can help to reduce waste in mass production. The carbon fiber placement in warp and weft direction, strip width and span of strips can be modified during weaving process of FOF according to the application requirements. FOF structure helps to increase natural frequency of laminate, which prevents standard operating frequency mechanisms and machines to reach the resonance. The functional material strips within the structure and especially around a structural opening (hole) helps to stiffen the laminate and the opening edge respectively. Speaking about resonance and stiffening the opening edge, the FOF has potential to prevent the resonance of mechanical joints, which can extend the joints' lifespan.

Acknowledgements

This publication was supported by the Ministry of Industry and Trade (MPO) within the framework of institutional support for long-term strategic development of the research organization – provider MPO, recipient VÚTS, a. s.

References

[1] Omar, Sonam & Goel, Alka. (2009). Hybrid Textiles: A Review. Colourage. 56. 93-105.

[2] STRONG, A. Brent. Fundamentals of composites manufacturing: materials, methods, and applications. 2nd ed. Dearborn: Society of Manufacturing Engineers, c2008. ISBN 978-0-87263-854-9.

[3] ZBONČÁK, Radek. Elastic properties prediction models of continuous fibers composites: composite materials. Liberec: VÚTS, 2018. ISBN 978-80-87184-81-3.

Design of an Electrostatic Field Sensor for the Study of Air Ions and Thunderstorms

Zdeněk Roubal, Ivan Kirsanov

Department of Theoretical and Experimental Electrical Engineering, FEEC, BUT,
Technická 3082/12, 616 00 Brno, Czech Republic,
Email: roubalz@vut.cz

Abstract. *When measuring air ions in nature, it is useful to measure not only commonly used variables such as temperature, relative humidity, atmospheric pressure, but also less commonly monitored variables to characterize the environmental conditions that affect the concentration of light air ions. Among the most important are the concentration of airborne aerosols, the radioactivity of rocks and, last but not least, the strength of the Earth's electric field. This varies over time according to the current weather, and is strongly influenced by nearby storms. It is known from the literature that the concentration of light air ions increases significantly during a storm, and in this respect, it would be very valuable to have a simultaneous record of the concentration of light air ions and the near-surface electric field strength. The aim of this paper is to design a low power electrostatic field sensor with continuous recording and sufficient sensitivity, automatically selected according to the ambient conditions.*

Keywords: Electrostatic Field Earth, Air Ions, Electric Field Mill.

1. Introduction

Previous research work [1], [2] has focused on the measurement ion concentrations of light air. Using the Aspiration Condenser method, the polarity of light negative ions and their mobility can be determined. However, in order to fully characterize the actual ion conditions at the measurement site, it is necessary to also measure the concentration of airborne aerosols, radon and also the Earth's electric field strength. The aim of the effort was to develop a sensitive apparatus, applicable both for the case of nice sunny weather with low electric field strength and for the other extreme case, when a thunderstorm is present in the vicinity of the measurement and the Earth's electric field is affected by it.

Data from long-term measurements of the electrical characteristics of the atmosphere near the Earth's surface indicate the existence of an electric field of about 130 V/m and an electric current density of about 10^{-12} A/m^2 [3]. The Earth's surface has a negative charge and the ionosphere has a positive charge. These parameters are determined under so-called clear weather conditions, i.e. the absence of clouds, wind and snow storms in a given region of the Earth. Measuring the electric field near the Earth's surface allows an estimate of the Earth's effective charge, which is 10^5 C. Since the Earth's atmosphere has electrical conductivity, in the absence of sources of electric field in the atmosphere, it would discharge in about 10 minutes. According to the modern concept, storm clouds are the main source of the electric field in the troposphere and stratosphere. Storm clouds act as current generators. It should be noted that in areas where storm clouds exist, currents flow that charge the atmosphere and in areas without storm clouds, currents flow that discharge it. In the 20th century, Simpson, Machuli and Sverdrup discovered the so-called unitary variation of the atmospheric electric field, i.e., synchronous changes in the field strength on Earth [3]. During a thunderstorm, the electric field strength in the vicinity of the Earth can reach 20 kV/m and re-polarisation can occur locally. Apparatus ranges have been designed within this range. For the time being, it is considered to be placed on the surface of the earth in conjunction with an ions meter; in the future, it would be possible to place it on a

ISBN 978-80-69159-00-6

drone, for example. Simultaneous monitoring with earthquake and cosmic ray manifestations also seems promising.

2. Design of measuring apparatus

Among several measurement principles used, the principle of charge induction on the measuring plate (Electric Field Mill) was selected [4], [5]. In an electrostatic fluxmeter type device, the electric field strength is converted to electric current by means of a rotating electrostatic generator based on the electrostatic induction phenomenon. The flow of electrostatic induction of the measured field induces an electric charge on the measuring plate. A modulator - the shielding plate - periodically shields the measuring plate in the electric field, so that the value of the induced charge changes periodically. The charge flowing into and out of the plate creates a current which is amplified, for example, in a current/voltage converter. The amplitude of this current i is proportional to the strength of the electric field to be measured, the frequency of rotation of the modulating plate and the area of the measuring plate, the phase being determined by the direction of the electric field on the surface of the measuring plate [6].

$$i = \frac{\varepsilon_0 \cdot f \cdot n \cdot (R - r) \cdot E}{2}, \tag{1}$$

Where ε_0 is permittivity of vacuum, f frequency of rotation of the shielding plate, n number of rotor plates, R outer radius of the plate, r inner radius of the plate, E je measured electric field.

The original design [4] has been significantly revised. The design of the measuring probe was based on the paper [6]. The latter, in addition to the reported sensitivity, also addressed the optimal ratios of the outer and inner radii of the rotor and their spacing for a homogeneous distribution of the electrostatic field inside the probe. The outer radius and inner radius were designed to be 3 cm and 1 cm, respectively, and the air gap was designed to be 3 mm. When comparing with the factory products, the outer radius of R=7 cm and inner radius of r=2 cm was finally chosen in the proposed design considering the diameter of the structural tube and the location of the electronics. With n=6 and a speed of 2800 rpm, the current i=0.358 nA is obtained with an assumed electric field strength E=100 V/m.

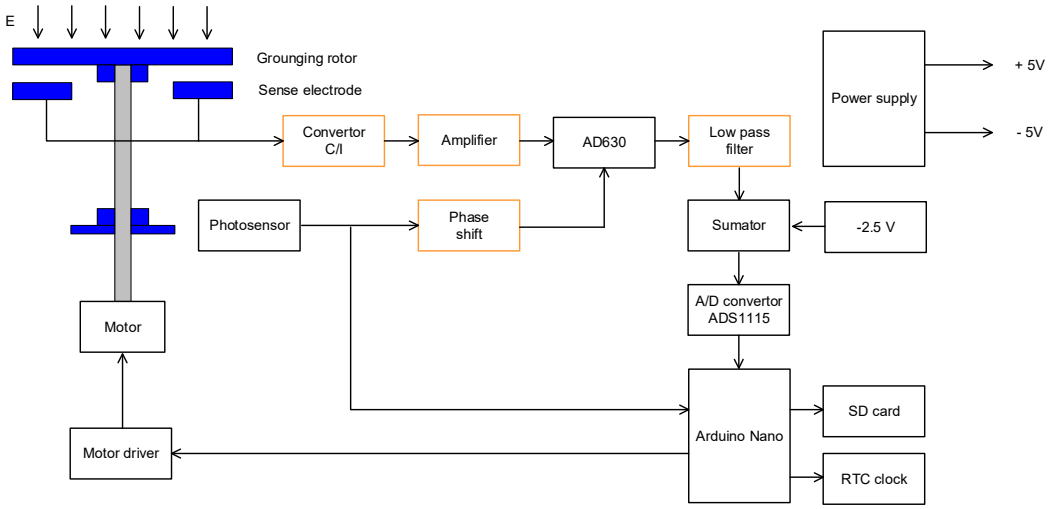

Fig. 1. Block diagram of the proposed electrostatic field sensor.

To achieve the necessary sensitivity, it is necessary to use the principles of high-impedance measurement and to place the sensing electrode on high-quality Teflon insulators. A high-quality electrometric amplifier LMC6001A with an input current of less than 20 fA was used.

ISBN 978-80-69159-00-6

In its feedback loop, two resistors 1 MΩ and 10 MΩ are switched, the time constant is short, so it is possible to measure even relatively fast changes in the electrostatic field.

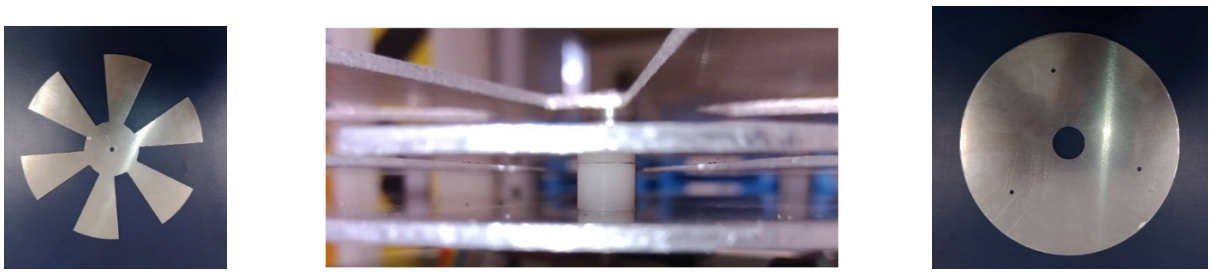

Fig. 2. Rotating part of the probe on the left, teflon insulator center and the reflection ground plane on the right

This is followed by a voltage amplifier with a gain of A_U=27, designed according to the calculated sensitivity in the frequency range 7.5 Hz to 1500 Hz. Most of the available Electric Field Mill solutions have too high-power consumption of 2.4-8 W. Neither the most commonly used stepper nor synchronous motor was used, but a low power DC motor far enough away from the sensing electrode not to cause commutator interference. Its consumption in the application is only 20 mA at 5 V supply. It is suitably EMI filtered. A synchronous detection method is used to suppress interference and noise. The motor speed is sensed through an optical sensor, a control loop is introduced to stabilize the speed through an Arduino Nano microprocessor system. The signal from the photodiode is suitably phase shifted and controlled by the AD630 circuit. At its output is an elliptic filter with switched fifth-order capacitors MAX7426 excellent for low power consumption and easy re-tuning in the range of 1 Hz to 12 kHz. The filter is followed by a summing amplifier, needed to shift the measured voltage to positive values only, so that they can be processed by the ADS1115 A/D converter. The results are periodically stored on the SD card, the time indication is obtained from the RTC circuit, which is also used to wake up the Arduino.

3. Results

The whole apparatus is placed in a metal shielding enclosure made of ferromagnetic material. The necessary structural fixings of the DC motor are made on a 3D printer. To achieve low power consumption, the principle of periodic sleeping and waking of the designed apparatus has been used. From the known waveforms of the Earth's electric field change, it seems appropriate to choose a wake-up interval of about 5 minutes, the measurement time is 1 minute. This can significantly reduce the consumption of the apparatus, achieving a consumption of 5 V/57.7 mA (288 mW) during measurement and 5 V/8 mA (40 mW) during sleeping.

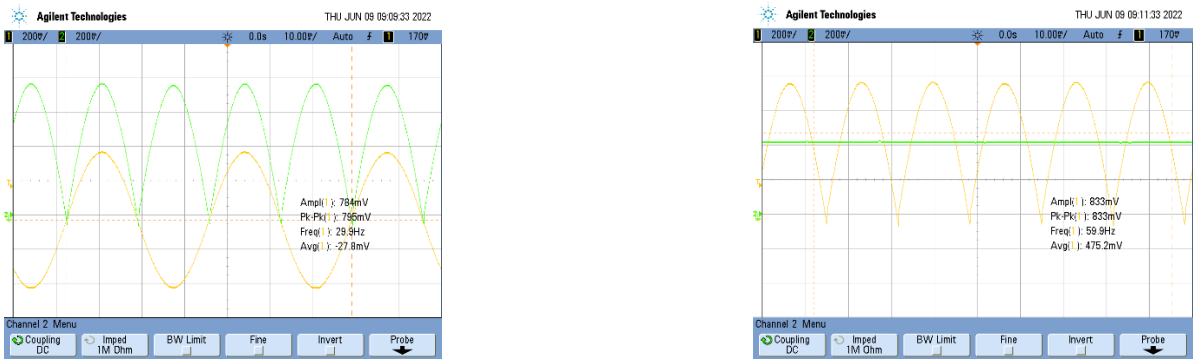

Fig. 3. Amplified signal at the amplifier output (yellow) and synchronously rectified signal at the AD630 input (green) on the left. Signal at the AD630 output (yellow) and filtered signal at the filter output (green).

ISBN 978-80-69159-00-6

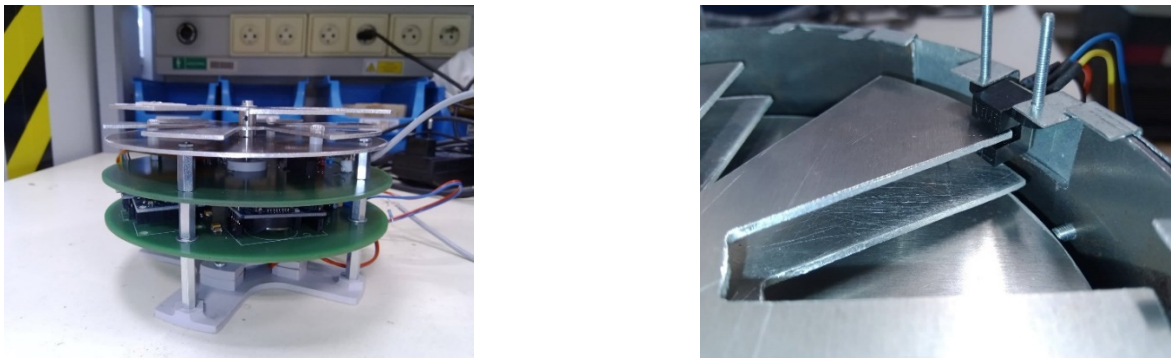

Fig. 4. Overall design of the electrostatic field structure on the left and detail of the location of the grounded rotor, sensing electrode, and referee ground plate relative to the optical speed sensor.

4. Conclusions

The proposed solution gives a high range of measured values from E=10 V/m to 50 kV/m. The sensitivity is limited mainly by the interference from the DC motor at a very low frequency of 1 Hz, which is synchronously coupled to the speed. On the other hand, the use of this low power motor gives the possibility of longer field endurance and the achieved power consumption is 10 times less than commercial solutions. A way to improve the instrument would be to place a high pass filter after the amplifier with a cutoff frequency of 20 Hz and even better DC motor suppression. The calibration will be done on a workstation with a regulated high voltage source. In particular, simultaneous measurements of electric field strength and airborne ion concentration in nature are expected. In addition to the measurements in nature, the apparatus will also be used to test building materials indoors [7].

Acknowledgements

The research was completed under support from the project No. FEKT-S-23-8425, which was supervised by the BUT internal grant office. Thanks to Ivo Fiala for solving the design of the optical speed sensor placement.

References

[1] Roubal, Z., Szabó, Z., Kadlec, R., & Zdražil, L. (2023, July). Concentration and Mobility of Air Ions in the Environment of the Cisarska Cave (moravia). In *2023 Photonics & Electromagnetics Research Symposium (PIERS)* (pp. 2193-2199). IEEE.

[2] Roubal, Z., Bartusek, K., Szabó, Z., Drexler, P., & Überhuberová, J. (2017). Measuring light air ions in a speleotherapeutic cave. *Measurement science review*, *17*(1), 27.

[3] Leblanc, F., Aplin, K., Yair, Y., Harrison, G., Lebreton, J. P., & Blanc, M. (Eds.). (2008). *Planetary atmospheric electricity* (Vol. 30). Springer Science & Business Media.

[4] Kirsanov, I. (2021) Design And Construction Of Measuring Apparatus For Lightning Research. Online. In: *Proceedings I of the 27st Conference STUDENT EEICT 2021: General papers*.

[5] Kirsanov, I. (2022). Designed and construction of measuring equipment for lighnight research. Bachelor thesis. Brno University of Technology.

[6] Cui, Y., Yuan, H., Song, X., Zhao, L., Liu, Y., & Lin, L. (2017). Model, design, and testing of field mill sensors for measuring electric fields under high-voltage direct-current power lines. *IEEE Transactions on Industrial Electronics*, *65* (1), 608-615.

[7] Zdražil, L., Roubal, Z. (2024). Electrical Properties Measurement of Building Materials. In *2024 21st International Conference on Mechatronics-Mechatronika (ME)* (pp. 1-6). IEEE.

Development of Force Sensor for Linear Guides

Jan Bělík, Pavel Klouček

VÚTS, a. s., Measurement Department, Liberec, Czech Republic
Email: jan.belik@vuts.cz

Abstract. *Task of a force measurement during technological processes in single-purpose machines was formed by their designers. No commercial solution for a simple connection to a ball screw system was found. This was an impulse for the development of a sensor designed as a replacement for the standard part. The sensor body was optimized by FEM analysis. The functional sample of the sensor was made and widely tested. Due to the force measurement from four independent strain-gauge systems, not only overall force but also non-symmetric load can be identified. It can help, for example, in control of forcing-in processes.*

Keywords: Force Sensor, Ball Screw, Linear Guide, Strain Guage

1. Introduction

The force measurement in single-purpose machines is a typical request for forcing-in processes, part insertions, or similar tasks. The force signal is used as feedback quantity and also for control of process quality. The commercial solution should be the usage of electronic pressing units, where the force measurement is implemented (produced, e.g., by Kistler), but these units are quite expensive. Usage of standard strain-gauge force sensors is demanding due to dimensions, position quite far from the acting force, non-axial load, and other problems. The monitoring of a servomotor current/torque is quite often used as a cheap and simple solution, but the accuracy of these results is quite low. Measurements done directly on ball screws or linear guides were made for diagnostics or studies of behavior (friction, pre-tightening, etc.) [1],[2],[3],[4]. A commercial solution designed for loading force measurement on the ball screw linear guides was not found. This was an impulse for the development of a sensor designed as a replacement for the standard part.

2. Sensor design

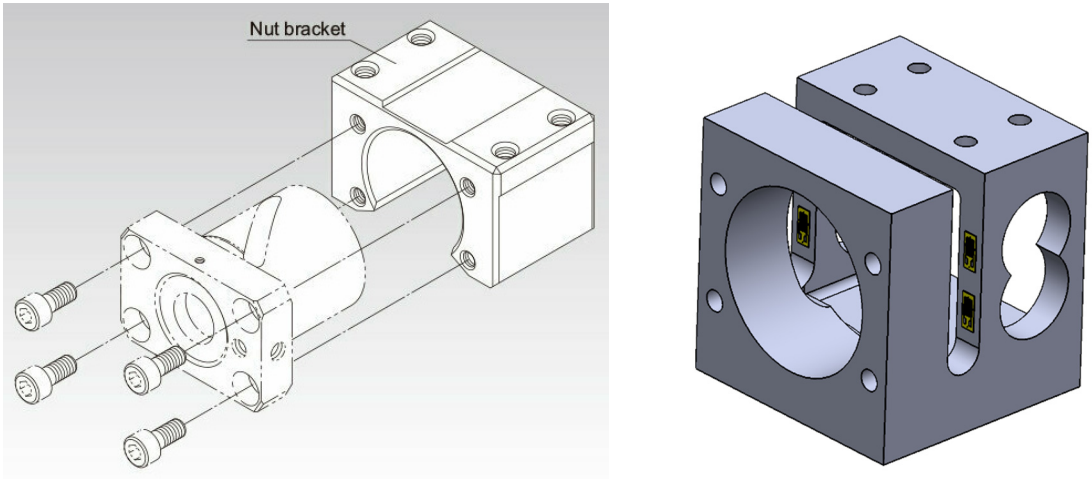

Fig. 1. Standard Nut Bracket part from THK [5] (left), the sensor body with deformation element and the same connecting points as the standard part (right)

ISBN 978-80-69159-00-6

The linear guides are typically driven by a ball screw. A ball nut is mounted to the moving table by a part called a Nut Bracket. This part was chosen as the best possibility for replacement by the force sensor.

The first idea of the sensor body shape (Fig. 1) was optimized by FEM analysis using NX 2206 software by Simens. The load force should produce deformations in the exact points of the deformation element, and both connecting surfaces can stay perpendicular. The cross-section area of the deformation zones determines the force range and sensitivity. The realized sample was designed for a maximal load of 10 kN. Fig. 2 shows the main results from the FEM analysis. It means the shape and values of the deformation in the whole sensor body. The foil strain-gauge sensors are placed in the zones with the biggest deformation. The typical level of foil stain-gauge sensors deformation is approximately 3000 µm/m for a cyclic load and 7000 – 10000 µm/m for a static load. The optimized model in Fig. 2 shows for 10 kN load the maximal deformation 4380 µm/m, so it is ideal for pseudo-static applications like forcing-in.

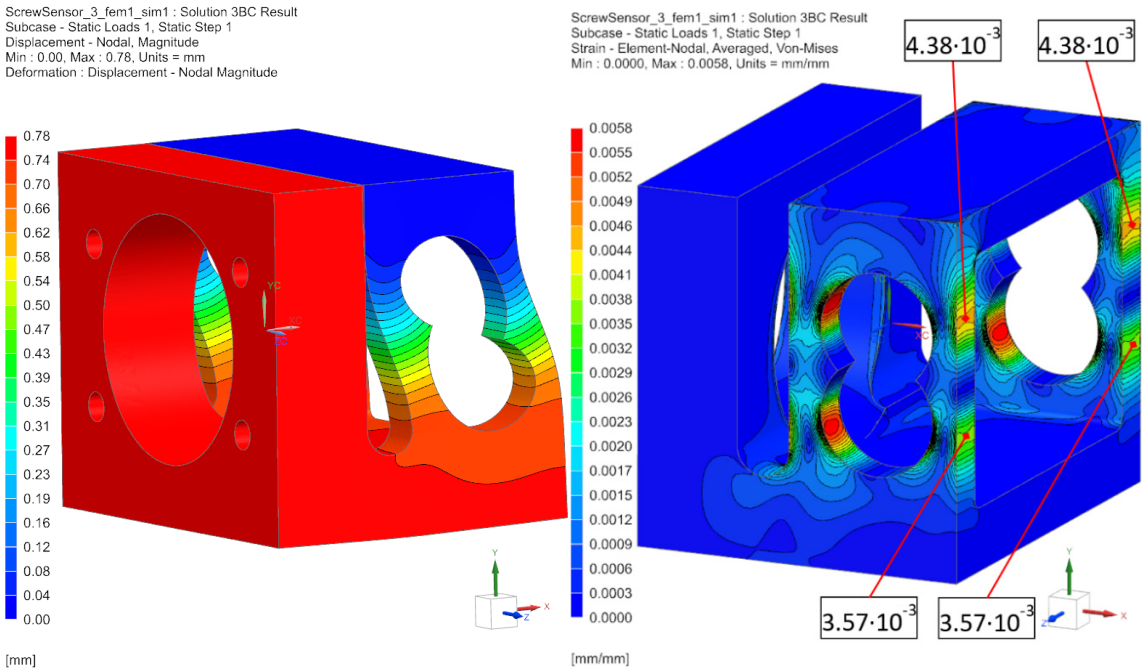

Fig. 2. FEM analysis results – shape of deformation (left) and relative deformation in mm/mm (right)

Strain-gauges EA 13 250BG 120 from Micro Measurements were chosen for the sensor. This strain gauge is made for universal usage; the grid length is 6.35 mm, and the overall length is 9.53 mm; it can measure in the temperature range from -75° to 175°C with a nominal resistance of 120 Ω. This type is designed for application to duralumin deformation elements.

3. Sensor realization

The sensor body was made from duralumin EN AW-2024 T351 AlCu4Mg1. Internal stress is reduced in this material, so it is suitable for sensor elements. The basic concept of the deformation element supported by FEM analysis planned to use eight strain-gauges in zones with the biggest deformations (see Fig. 2). Two strain gauges are glued by cyanoacrylate glue to every edge of the deformation element. Couples of the strain gauges from each edge are connected to independent half-bridges. One strain-gauge in every half-bridge is during deformation elongated and the second one is shortened. This leads to a two-time higher sensitivity of the measuring elements and compensation for the thermal influence [6]. Strain-gauges and wires are partly protected by a layer of silicone rubber.

ISBN 978-80-69159-00-6

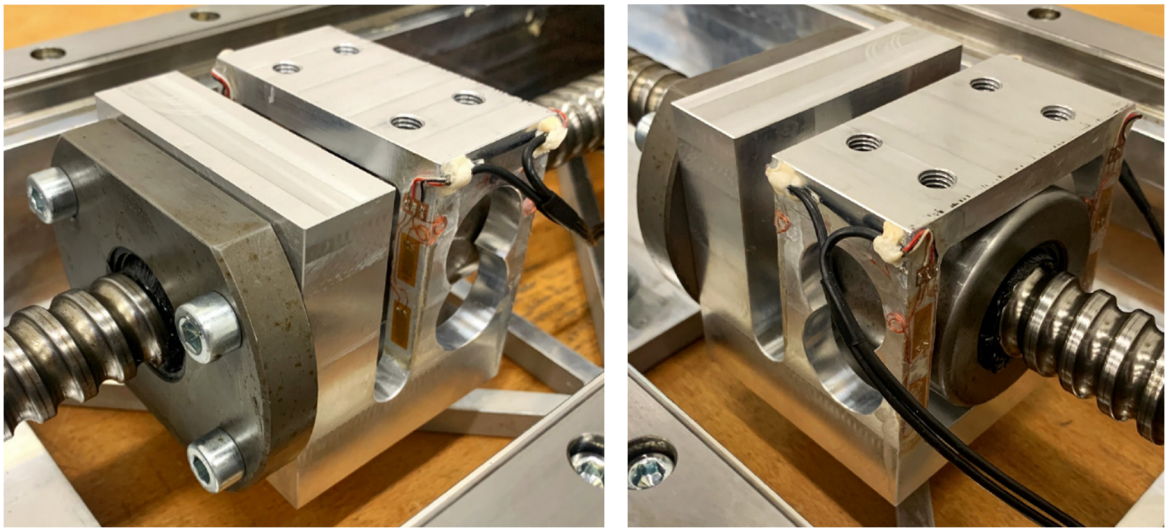

Fig. 3. The sensor before testing placed to the ball screw, the moving table is not mounted yet

4. Tests and results

The special stand with a linear guide and ball screw was made for the sensor testing. This stand can be easily modified for manual or servomotor drive, different geometry, and position of loading force. Part of the stand was a calibrated force sensor HBM U2B used as a reference value of the loading force.

The signals from the four half-bridges were recorded separately. The first test was made with an ideally symmetric load, and signals from the strain gauges were measured in [µm/m]. All four half-bridges showed nearly identical values, so it was possible to divide the load force to four equal parts. It was possible to calculate calibration constants (signal is linear) for each half-bridge; the results are: 1st half-bridge 596.26 N/mV/V, 2nd half-bridge 594.19 N/mV/V, 3rd half-bridge -581.65 N/mV/V and 4th half-bridge -586.68 N/mV/V.

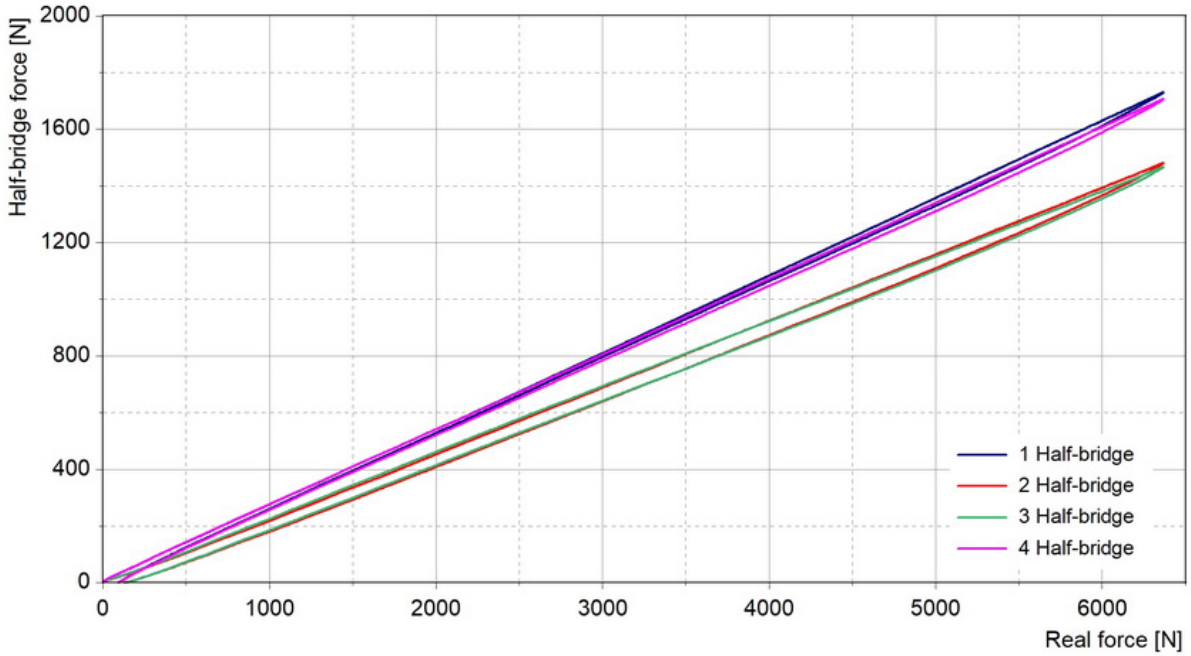

Fig. 4. Signals from four half-bridges for test with non-symmetric loading force

ISBN 978-80-69159-00-6

The sensor behavior during non-symmetric load was tested by moving the load force outside of the ball screw axis and also by the asymmetric position of rails in a linear guide. Asymmetric rails' influence is very small, but non-symmetric load force leads to unbalance between half-bridges signals (Fig. 4). Two of them have a signal higher than one-quarter of the force, and the second couple has a signal lower. The sum of all four signals represents the loading force correctly; difference between signals corresponds to the level of non-symmetricity. It can be used, for example, for control of forcing-in processes if the parts are pressed in the correct position.

The sensor signal, compared to the real loading force, is influenced by friction and passive forces in linear guides. It can be compensated by calibration in the active direction of the movement or by measurement of these parasitic forces and their adding/subtraction from the sensor signal.

5. Conclusions

The force sensor for linear guides with a ball screw was designed, produced, and tested according to single-purpose machine designers' requirements. The sensor can be easily modified for different sizes of linear guides and different force ranges.

The functional sample of the sensor for THK BTK2510V linear guide was widely tested on a special stand. Due to four independent strain gauge measuring systems, the sensor is able to detect not only the loading force but also its non-symmetricity. The sum of the signals corresponds to the overall loading force, the difference between the signals corresponds to the level of non-symmetricity. The sensor was also tested by a cyclic load for verification of long-term stability.

Acknowledgements

This result was created within the project TN02000018 "National Centre of Competence ENGINEERING," which is co-financed from the state budget by the Technology Agency of the Czech Republic under the National Centres of Competence Programme. This result was financed within the National Recovery Plan from the European Recovery and Resilience Facility.

References

[1] Kasprzak, M., & Pyzalski, M. (2021). Testing of Force Sensors for the Active Measurement and Limitation of Axial Loads in Heavy Turning. *Journal of Machine Engineering*, *21*(4), 106-117. https://doi.org/10.36897/jme/144597

[2] Liu, C., Zhao, C., Liu, Z., & Wang, S. (2021). Dynamic Analysis of Ball Screw Feed System with the Effects of Excitation Amplitude and Design Parameters. *Applied Sciences*, *11*(15). https://doi.org/10.3390/app11157070

[3] Wang, Q., & Lin, M. (2016). Electromechanical coupling measurement of a new giant magnetostrictive structure for double-nut ball screw pre-tightening. *Measurement Science and Technology*, *27*(12). https://doi.org/10.1088/0957-0233/27/12/125906

[4] Force sensing linear rolling guides based on modified metal strain gauges. (2023). *International Conference Proceedings*, *23rd*, 4.

[5] Ball Screw Peripheral Nut Bracket. Online. Available at: https://www.thk.com/sg/en/products/ball_screw/nut_bracket/. [cit. 2025-01-16].

[6] *Strain gage based transducers*. 1988. Raleigh, North Carolina, 27611, USA: Measurements Group, 1988. ISBN 0-9619057-0-0.

Refining EBIC Analysis of GaN p-n Junctions Through Numerical Simulations

[1]Juraj Priesol, [1,2]Alexander Šatka

[1]Institute of Electronics and Photonics, Faculty of Electrical Engineering and Information Technology, Slovak University of Technology in Bratislava, Slovakia
[2]Institute of Measurement Science, Slovak Academy of Sciences, Bratislava, Slovakia
Email: juraj.priesol@stuba.sk

Abstract. *Spatial distribution of electron beam induced current (EBIC) across p-GaN/n-GaN junctions is studied by 3D numerical simulations using the Monte Carlo (MC) method. The influence of beam and sample specific parameters on EBIC line profiles is examined to provide insights into the charge carrier generation, diffusion, and collection at the p-n junction. Among various parameters influencing the EBIC signal, in this paper we focus on the effect of the space charge region (SCR) on both the intensity and spatial distribution of the EBIC signal. Wider SCRs lead to flat-topped maxima shifted toward the lower doped region and problematic estimation of physical p-n junction position, whilst narrower SCRs result in a reduced signal intensity due to decreased collection efficiency.*

Keywords: Monte Carlo method, Numerical Simulation, EBIC, GaN, Diffusion Length

1. Introduction

EBIC is a powerful technique for the characterization of semiconductor p-n junctions, providing insights into carrier transport, recombination, and electric field distributions at the nanoscale [1]. In gallium nitride (GaN) devices, EBIC plays a crucial role in the evaluation of the electrical properties of p-n junctions, which are fundamental to power electronics and optoelectronic applications. However, the interpretation of EBIC measurements is often a complicated process, a situation largely due to the influence of carrier diffusion, drift, and recombination mechanisms. MC simulations provide a robust approach to modeling the spatial distribution of the EBIC signal across p-n junctions by tracking the trajectories of charge carriers in a stochastic manner [2], [3]. These simulations facilitate a deeper understanding of how material parameters, device geometry, and external conditions affect EBIC signals. In this study, we present MC simulations of the EBIC line profiles across the p-n junctions in GaN. The objective of this study is to investigate the impact of key factors such as the energy of primary electrons E_{PE}, the angle of electron beam (e-beam) incidence relative to the sample surface, the diffusion length of minority charge carriers, and the SCR width on the EBIC signal. By analyzing simulated EBIC profiles, we aim to refine the interpretation of EBIC measurements in GaN and improve the accuracy of p-n junction characterization. The insights gained from this research are relevant to the optimization of GaN-based devices for high-efficiency power conversion and advanced optoelectronic applications.

2. Subject and Methods

The process of primary electron scattering by atoms in solids is commonly described in the literature through the application of two established theoretical concepts. The first is the scattering geometry previously described by Reimer [1] and Joy [2], and the second is the slowdown approximation utilizing a modified Bethe formula. This approach has been widely accepted and was proposed by Joy and Luo; see [3] and the references therein. The energy dissipated during individual scattering events is used to estimate the number of locally

ISBN 978-80-69159-00-6

generated electron-hole pairs from the experimentally determined dependence $N_{gen} \approx \Delta E_n/(3E_g)$, where ΔE_n is the energy loss of a primary electron at the n-th scattering point and E_g is the local band-gap energy of the semiconductor [4]. Diffusion of generated charge carriers is derived from the random walk algorithm. The random walk proces terminates when the diffusing carriers reach the p-n junction SCR and those carriers are considered to contribute to the induced current. If the carriers do not reach the SCR before the end of their lifetime, they are considered to be annihilated during the radiative or non-radiative recombination.

The input parameters for the MC simulations reviewed in Tab. 1 were carefully chosen based on the physical properties of the semiconductor material and the e-beam conditions. These parameters include the e-beam energy and the incidence angle, as well as sample specific properties such as SCR width, the atomic number and the atomic weight of GaN and its specific mass, the diffusion length of minority charge carriers, and the bandgap energy.

Table 1. Material properties of GaN used in Monte Carlo numerical simulations; Diffusion lengths of minority electrons L_n and minority holes L_p are specified for various conditions including concentration of Mg-dopants [Mg] and Si-dopants [Si], concentration of acceptors N_A and donors N_D, dislocation density (DD), or their combination. Z is the atomic number, and A is the mass number of an element.

Property	**Value**	**Conditions**	**Refs.**
Mean at. number of GaN	19	$Z_{Ga} = 31$, $Z_N = 7$	[5]
Mean at. mass of GaN (g/mol)	41.865	$A_{Ga} = 69.723$, $A_N = 14.007$	[5]
Specific mass of GaN (g/cm^3)	6.09 - 6.15	-	[6-9]
Diffusion length of minority electrons L_n (nm) in p-type GaN at room temperature	26 ± 3	[Mg] = 3.5×10^{19} cm^{-3}	[10]
	93 ± 7	[Mg] ~10^{19} cm^{-3}, $N_A = 4\times10^{17}$ cm^{-3}	[11]
	200 ± 50	$N_A = 1\text{-}4\times10^{17}$ cm^{-3}	[12]
	220-950	[Mg] = 4×10^{18} to 3×10^{19} cm^{-3} and $DD < 10^8$ cm^{-2}	[13]
Diffusion length of minority holes L_p (nm) in n-type GaN at room temperature	50	$N_D = 5\times10^{16}$ cm^{-3}, DD ~ 10^8-10^9 cm^{-2}	[14]
	70-400	-	[15]
	< 250	[Si] = 4×10^{17} and 4×10^{18} cm^{-3} and $DD < 2\times10^9$ cm^{-2}	[13]
	280	N_D ~ 10^{17} cm^{-3}, DD = $2\text{-}5\times10^9$ cm^{-2}	[16]
	432 ± 30	N_D ~ 10^{17} cm^{-3}	[11]
Band-gap energy (eV)	3.4	Room temperature	[9], [17,18]

One can clearly see that the diffusion length of minority charge carriers depends significantly on the doping level and the dislocation density. Additionally, different methods used for its estimation may also introduce a certain degree of uncertainity. Therefore, instead of selecting precise diffusion length values, we used them as indicative parameters to provide a general orientation on their possible range.

ISBN 978-80-69159-00-6

3. Results and Discussion

In this paper, we focus solely on the effect of SCR on the EBIC line profiles to provide a thorough visual analysis of this parameter. The influence of other parameters, such as e-beam energy, incidence angle, and diffusion length of minority charge carriers will be discussed onsite to offer a broader perspective on their impact. Understanding these effects is essential for analyzing real EBIC measurements of complex structures such as semi-vertical GaN power diodes [19], Schottky barrier diodes [20], high electron mobility transistors (HEMTs) with p-GaN gate [21], or core-shell nanorod GaN LEDs [22]. Fig. 1 shows the MC simulation of EBIC line profiles at the asymmetrical p-GaN/n-GaN junction with various SCR widths. Here, SCR in n-type GaN is set constant to x_n = 100 nm, and SCR in p-type GaN is set to x_p = 50, 100, 200, 300 and 400 nm. The red curve in Fig. 1 is used as a reference representing the EBIC line profile across the symmetrical p-n junction. The diffusion length of minority electrons L_n in p-GaN is deliberately set equal to the diffusion length of minority holes L_p in n-GaN. In this way, the effect of diffusion lengths on EBIC line profiles is identical on both sides of the junction, and the differences we observe are attributed exclusively to the SCR width.

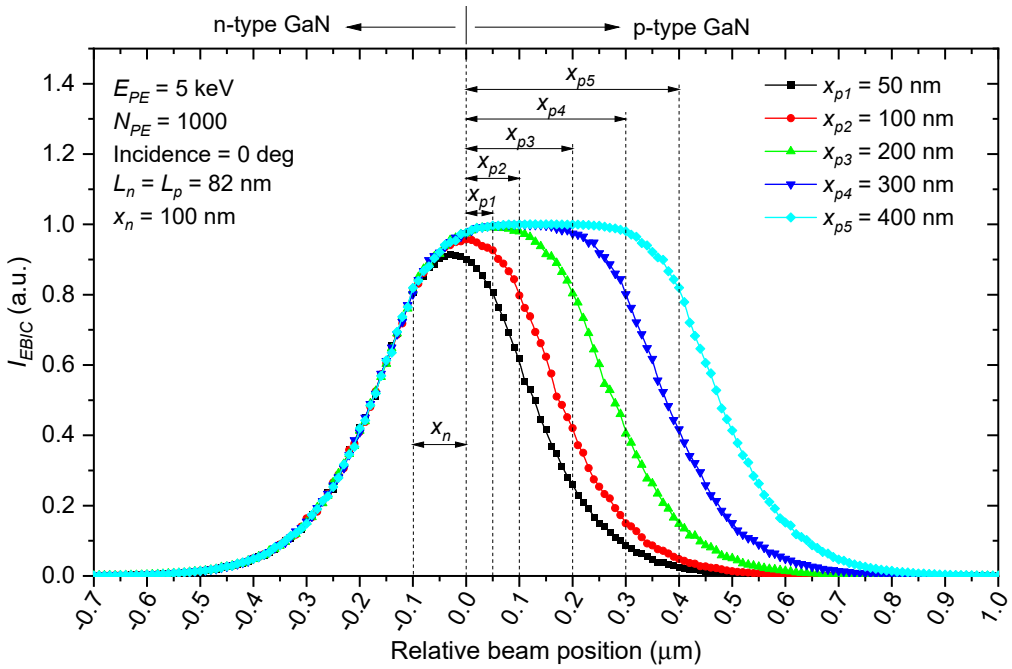

Fig. 1. Monte Carlo simulations of EBIC line profiles across a p-GaN/n-GaN junction with varying space charge region in p-type GaN x_p = 50, 100, 200, 300 and 400 nm, whilst x_n = 100 nm.

As demonstrated by the simulated EBIC line profiles, the widening of the SCR toward the p-GaN results in a flattened EBIC maximum, which makes the estimation of the exact position of the p-n interface challenging under real experimental conditions. It is also noteworthy that, in cases of particularly narrow SCR (in this case for $x_p \leq 100$ nm) the maximum intensity of the EBIC signal drops due to reduced collection efficiency within the SCR. Furthermore, in cases when $x_p < x_n$, the EBIC maximum shifts towards the n-type GaN, which may lead to inaccurate estimation of the physical p-n junction position. MC simulations allow for corrections and improved analysis of the EBIC line profiles using measured L_n and L_p, which would not be possible without numerical modeling. They are also essential for analyzing the SCR behavior under reverse bias, where the SCR extension can be quantitatively extracted from a series of normalized 1D EBIC profiles (or 2D images). Simulations help to determine an appropriate threshold level to localize the SCR edge, which should be set below 0.75 and well above the experimental noise floor of 0.1. The results highlight the importance of

ISBN 978-80-69159-00-6

accounting for SCR width when interpreting EBIC measurements of GaN-based devices, contributing to the optimization of their electrical performance in power electronics and optoelectronic applications.

4. Conclusions

The influence of SCR width on EBIC line profiles across asymmetrical p-GaN/n-GaN junctions was investigated using 3D MC simulations. The findings demonstrate that both the shape and intensity of the EBIC signal are significantly affected by the SCR width and doping profile, with wider SCRs leading to flattened maxima and narrower SCRs resulting in lower signal intensity. The applied MC simulations provide essential insights allowing quantitative EBIC data interpretation and enhance the reliability of p-n junction position estimation. The combined effects of additional parameters, such as e-beam energy, incidence angle, and minority carrier diffusion lengths were also analyzed as part of the comprehensive analysis.

Acknowledgements

This publication was supported by the EU NextGenerationEU through the Recovery and Resilience Plan for Slovakia under the project No. 09I03-03-V04-00266. The SGA of the MERDY of the Slovak Republic under the contract VEGA 1/0711/23 is also acknowledged.

References

[1] L. Reimer, Scanning Electron Microscopy, Berlin, Heidelberg: Springer-Verlag, 1985.
[2] D.C. Joy, Monte Carlo Modelling for Electron Microscopy and Microanalysis, New York: Oxford University Press, 1995.
[3] D.C. Joy, Scanning Microscopy **5**, 329 (1991).
[4] R.C. Alig and S. Bloom, Phys. Rev. Lett. **35**, 1522 (1975).
[5] *Nist.gov*, https://www.nist.gov/pml/periodic-table-elements, viewed 20 Dec. 2024.
[6] *Knovel.com*, https://app.knovel.com/hotlink/itble/rcid:kpERFMEV04/id:kt00XRDIY4/encyclopedia-rf-microwave/target-tra-table-2-physical, viewed 20 Dec. 2024.
[7] *Knovel.com*, https://app.knovel.com/hotlink/itble/rcid:kpMWCMDS06/id:kt012ULQRO/matweb-ceramics-material/table-2-material-properties, viewed 20 Dec. 2024.
[8] *Ioffe.ru*, https://www.ioffe.ru/SVA/NSM/Semicond/GaN/basic.html, viewed 20 Dec. 2024.
[9] H. Shibata, Y. Waseda, H. Ohta, et al., Mater. Trans. **48**, 2782 (2007).
[10] W.Y. Ho, Y.C. Chow, S. Nakamura, et al., Appl. Phys. Lett. **122**, 212103 (2023).
[11] S. Hafiz, F. Zhang, M. Monavarian, et al., J. Appl. Phys. **117**, 013106 (2015).
[12] Z.Z. Bandić, P.M. Bridger, E.C. Piquette, et al., Appl. Phys. Lett. **73**, 3276 (1998).
[13] K. Kumakura, T. Makimoto, N. Kobayashi, et al., Appl. Phys. Lett. **86**, 052105 (2005).
[14] T. Sugahara, H. Sato, M. Hao, et al., Jpn. J. Appl. Phys. **37**, L398 (1998).
[15] E.B. Yakimov, J. Alloys Compd. **627**, 344 (2015).
[16] Z.Z. Bandić, P.M. Bridger, E.C. Piquette, et al., Appl. Phys. Lett. **72**, 3166 (1998).
[17] S.J. Pearton, J. Yang, P.H. Cary IV, et al., Appl. Phys. Rev. **5**, 011301 (2018).
[18] R. Sharma, M.E. Law, F. Ren, et al., J. Vac. Sci. Technol. A **39**, 060801 (2021).
[19] J. Priesol, A. Šatka, M. Borga, et al., in *14th International Conference on Advanced Semiconductor Devices and Microsystems (ASDAM)*, IEEE, Smolenice, Slovakia, 23.10.-26.10. 2022, pp. 83-87 (2022).
[20] J. Priesol, A. Šatka, A. Chvála, et al., IEEE Trans. Electron Devices **68**, 216–221 (2021).
[21] S. Stoffels, N. Posthuma, S. Decoutere, et al., in *2019 IEEE International Reliability Physics Symposium (IRPS)*, Monterey, CA, USA, pp. 1-10 (2019).
[22] I. Gîrgel, A. Šatka, J. Priesol, et al., J. Phys. D: Appl. Phys **51**, 155103 (2018).

Investigation of Temperature Coefficients of New Impedance Standards

[1]Krzysztof Musioł, [1]Marian Kampik, [2]Ryszard Rybski, [2]Janusz Kaczmarek, [2]Mirosław Kozioł, [3]Maciej Koszarny, [3]Jolanta Jursza, [3]Adam Ziółek

[1]Silesian University of Technology (SUT), Gliwice, Poland
[2]University of Zielona Góra (UZG), Zielona Góra, Poland
[3]Central Office of Measures (GUM), Warsaw, Poland
Email: krzysztof.musiol@polsl.pl

Abstract. *The paper addresses issues related to the temperature stability of new impedance standards used at National Measurement Institutes. A brief description of the new infrastructure for impedance metrology recently developed in Poland is provided. Additionally, the paper presents the results of measurements of temperature coefficients for four-port resistance standards. It also includes a brief report on the stability test results of a set of temperature-controlled (ovenized) standard capacitors. The findings indicate very good temperature stability of the impedance of the standards and serve as an important source of information for selecting environmental conditions during comparisons at the highest metrological level.*

Keywords: Impedance Standards, Temperature Coefficient, Thermostat, Temperature Stability

1. Introduction

In the measurement of many physical quantities, temperature is one of the most important factors influencing the results. The effects of temperature are particularly significant in measurements requiring the highest accuracy, such as those associated with the implementation of national standards. Commercially available primary standards of basic electrical quantities used to maintain units of measurement are characterized by relative sensitivity to temperature changes from 10^{-7} 1/°C (DC voltage standards Fluke 732B) to about $3 \cdot 10^{-5}$ 1/°C (inductance standards GenRad type 1482). To eliminate or significantly reduce the uncertainty associated with temperature changes, laboratories use standards and measuring equipment with the lowest possible temperature coefficients. They also strive to stabilize environmental conditions—especially the ambient temperature in the laboratory—at a level where the effect of temperature on the comparison results can be neglected. Furthermore, many National Metrology Institutes (NMIs), due to the unsatisfactory performance of commercially available impedance standards, are designing new standards featuring an advanced temperature stabilization system.

Currently, precise measurements of impedance components commonly employ methods that involve direct comparison of the tested object with a reference standard that has known parameters (e.g., from international comparisons) [1-5]. In recent years, many National Metrology Institutes (NMIs) have implemented digital impedance comparator bridges based on quantum [4, 5] or non-quantum [2, 3] sources of AC voltage. These circuits are designed to compare impedances of the same nature (like impedances) or different nature (unlike impedances). Regardless of the digital source used, the impedance ratio is determined directly based on the known complex voltage ratio. For some types of comparison, e.g. *L-L* comparison using the comparator described in [1], the influence of temperature on the comparison results is compensated to a large extent. However, this is only possible if the compared standards have similar values for their temperature coefficients, which,

ISBN 978-80-69159-00-6

unfortunately, is not always the case. In the aforementioned digital impedance bridges, which are very popular today, the influence of temperature depends on the types of impedances being compared. Here, subtraction (for similar impedances and *R*-*L* and *R*-*C* comparisons) or summation (for *L*-*C* comparisons) of temperature coefficients can occur. However, due to the significant differences in the temperature coefficients of resistance, capacitance, and inductance standards, the influence of temperature on the comparison results in the ratio comparator bridge must be carefully analyzed.

Due to the aforementioned issues, knowledge of the temperature coefficients of standards is extremely important. This understanding allows for the design of an appropriate laboratory room temperature stabilization system or a suitable thermostatic chamber, ensuring that the uncertainty component associated with temperature changes is negligibly small.

2. New impedance standards developed in Poland

Capacitance standards

In 2025 a set of ovenized capacitance standards were manufactured at GUM (Fig. 1A). The set consists of five capacitance standards with nominal values: 1 nF, 10 nF, 100 nF, 1 μF and 10 μF. All standards use SMD 1206 GMR31 series C0G capacitors from Murata, Japan selected from a large package containing several hundred pieces. Nominal value of the temperature coefficient of the Murata capacitor is 0±30 ppm/°C. The standards were constructed as four-terminal pair (4TP) [6] and are equipped with MUSA Metrology Grade silver-plated connectors manufactured by Canford, UK. The set labeled Z42-2/2025 is ovenized using a dedicated temperature control system. Details about the stages of building the set and the materials used are presented in [7].

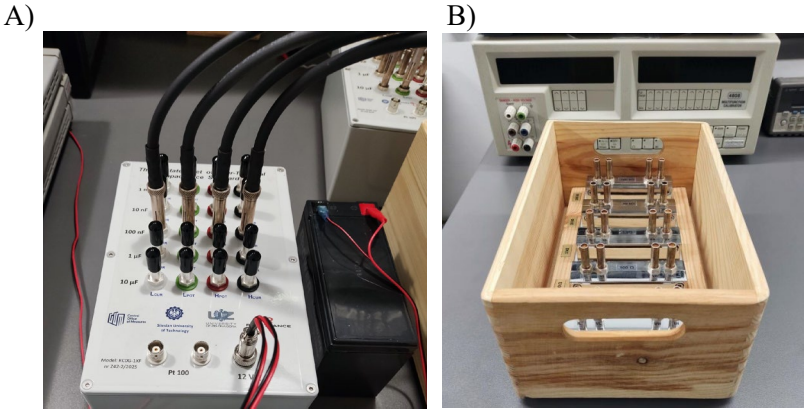

Fig. 1. Pictures of the new impedance standards developed in Poland: A) C-box Z42-2/2025, B) 4TP resistance standards.

Resistance standards

Moreover, a set of five 4TP resistance standards was manufactured at SUT (Fig. 1B). The standards have nominal values of 10 Ω, 100 Ω, 1 kΩ, 10 kΩ, and 100 kΩ. Ultra-high precision 4-terminal resistors made by Ohm-Labs were used to fabricate these standards. The Ohm-Labs resistors were mounted in chrome-plated brass housings. Since the declared temperature coefficient of resistance (*TCR*) is within ±1 ppm/°C there was no need to place them in a thermostatic chamber. For comparison, the HZ foil Vishay resistors used so far in the standard were characterized by a maximum *TCR* of ±2 ppm/°C.

ISBN 978-80-69159-00-6

3. Thermostatic chamber

Commercially available thermostatic chambers demonstrate stability of no better than ±0.1°C and uniformity of no better than ±0.5°C. These parameters may be insufficient, particularly in cases involving the comparison of inductance standards. Therefore, our team of researchers set out to build an air thermostatic chamber with stability exceeding that of commercially available options. The measurement results obtained indicate that the temperature in the thermostatic chamber is stable within ±30 mK over a twelve-hour observation period, and its homogeneity is maintained at ±0.1°C. Considering that during comparisons all impedance standards are typically placed at the same level (usually at the bottom of the chamber), temperature inhomogeneity has no impact on the temperature errors of the standards. This chamber operates at temperatures ranging from 15°C to 80°C, making it suitable for studying the temperature coefficients of standards, electronic components, and measuring instruments.

4. Results

Using the air thermostatic chamber described in Section 3 and the precision multimeter Agilent 3458A, temperature tests on the resistance standards outlined in Section 2 were conducted. For this purpose, appropriate software was developed in the LabVIEW environment, enabling the acquisition and visualization of measurement data from the aforementioned instruments at 5-second intervals. Temperature coefficient tests were performed within the temperature range of 18°C to 27°C, which corresponds to the possible temperature settings in laboratories during the calibration of standards. The temperature jump $\Delta\vartheta$ was set at time t=0 by changing the setting on the air thermostatic chamber controller and resistance changes ΔR were registered as presented in Fig.2.

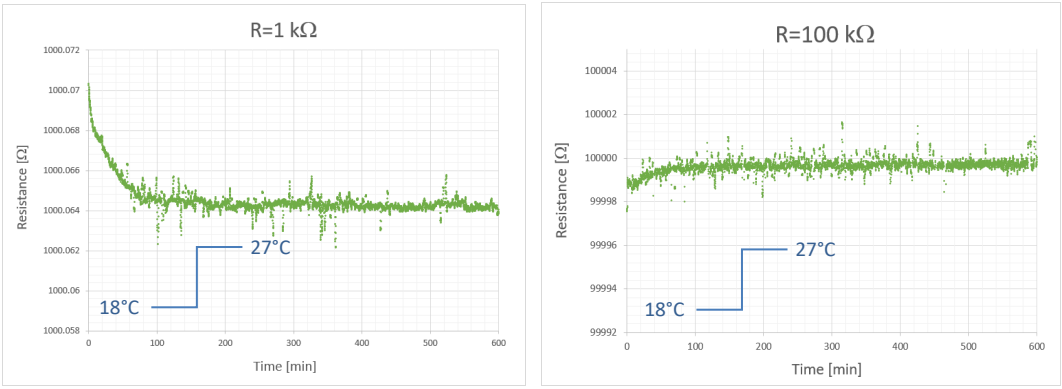

Fig. 2. Results of temperature test for two 4TP resistance standards. The given type of temperature jump $\Delta\vartheta$ is shown in each of the figures.

By analysing the measurement results presented in Fig. 2 and other graphs not presented in this paper the temperature coefficients $TCR=\Delta R/R\cdot 1/\Delta\vartheta\cdot 10^6$ of subsequent standards were determined, which are: for R=10 Ω: TCR = -11 ppm/°C, for R=100 Ω: TCR = -0.6 ppm/°C, for R=1 kΩ: TCR = -0.7 ppm/°C, for R=10 kΩ: TCR = -0.3 ppm/°C, for R=100 kΩ: TCR = +1.1 ppm/°C. Uncertainties of the measured temperature coefficients estimated based on the resolution of the temperature controller and the accuracy of the Agilent multimeter did not exceed 0.1 ppm/°C. Quite big scattering of the TCR values may indicates some differences in the construction of Ohm-Labs resistors. It is also worth noting that, due to the high inertia of the resistor housings (thick brass walls), the dynamics of resistance changes is not very high.

ISBN 978-80-69159-00-6

This positively affects measurement accuracy because the typical time for impedance standard comparison is several minutes. Additionally, tests on the heating and stability of the set of ovenized capacitance standards Z42-2/2025 were performed. The C-box was at ambient temperature, and at time t=0, the thermoregulation was activated. Temperature was measured using a Pt100 sensor built into the capacitance set. A high-precision multimeter, the Agilent 3458A, measured the four-wire resistance of the Pt100 sensor. The obtained results demonstrate temperature stability of the standard at a level of 0.003°C. The results of the temperature stability tests explain why there is no need to analyze the temperature coefficients of the capacitors used, even though, in extremely unfavorable conditions, they can be as high as 30 ppm/°C.

5. Conclusions

The obtained values of temperature coefficients allow us to assess the impact of temperature changes on the accuracy of impedance standard comparisons. Furthermore, they enable us to decide on the potential use of an external thermostatic chamber when temperature influences are too significant and unacceptable concerning the desired measurement uncertainty. Accurate knowledge of the temperature coefficients of the impedance infrastructure, along with information on changes in ambient temperature, allows us to determine the uncertainty component of the comparison related to temperature changes. Temperature tests performed with the set of ovenized capacitors provide users with information on the necessary stabilization time required to achieve a steady temperature state. The low dynamics of the standards observed in the graphs positively impact any potential changes in their parameters during measurement. Given that the typical duration of standard comparisons using most digital bridges does not exceed several minutes, the influence of ambient temperature fluctuations during comparisons can generally be neglected.

Acknowledgements

This work was supported by Polish Ministry of Science and Higher Education - grant No. PM-II/SP/0067/2024/02, realized within the framework of programme „Polish Metrology II”.

References

[1]. Musioł K., Met A., Skubis T. (2010). *Automatic Bridge for Comparison of Inductance Standards*. Measurement, Volume 43, Issue 10, December 2010, pp. 1661 – 1667.

[2]. Mašláň S., Šíra M., Skalická T, Bergsten T. (2019). *Four-Terminal Pair Digital Sampling Impedance Bridge up to 1MHz*, in IEEE Transactions on Instrumentation and Measurement, vol. 68, no. 6, pp. 1860-1869.

[3]. Ortolano M, Palafox L., Kučera J., Callegaro L., D’Elia V., Marzano M., Overney F., and Gülmez G. (2018). *An international comparison of phase angle standards between the novel impedance bridges of CMI, INRIM and METAS.* Metrologia 55 pp. 499-512.

[4]. Pimsut Y. (2024). *Development and implementation of an automated four terminal-pair Josephson impedance bridge*. Metrologia, vol. 61, no. 2, p. 025007.

[5]. Bauer S., Behr R., Elmquist R.E., Götz M., Herick J., Kieler O., Kruskopf M., Lee J. Palafox L., Pimsut Y. (2021). *A Four-terminal-pair Josephson impedance bridge combined with a graphene-quantized Hall resistance*”, Meas. Sci. Technol. 32 065007.

[6]. Calhoun A.R. (1996). *Four terminal pair concepts*. Cal Lab, pp. 38–41, Nov./Dec. 1996.

[7]. Musioł K., Koszarny M., Kampik M., Kubiczek K., Ziółek A., Jursza J. (2022). *A new impedance metrology infrastructure at GUM*. W: , red. 25th IMEKO TC-4 International Symposium on Measurement of Electrical Quantities, September 12-14, Brescia, Italy. Proceedings. IMEKO; 2022:243–247.

Formation of LIPSS on GaAs in Water Using Vector Laser Beams

[1]Kalvis Kalnins, [1]Uldis Berzins, [2]Vyacheslav V. Kim, [2]Rashid A. Ganeev

[1]Institute of atomic physics and spectroscopy University of Latvia, Riga, Latvia,
[2]Institute of Fundamental and Applied Research TIIAME National Research University, Tashkent, Uzbekistan
Email: kalvis.kalnins.lu@lu.lv

Abstract. *We present the results of measurements of the Laser-Induced Periodic Surface Structures (LIPSS) produced on the surface of GaAs submersed in water. The linear structures were formed using the 532 nm, 30 ps laser pulses by moving the sample in the focal plane of the focused laser beam. S-waveplate was used to transform the linearly polarized Gaussian beam into radially or azimuthally polarized helical beams. The morphological measurements using scanning electron microscopy were used to define the optimal parameters of laser radiation for various LIPSS formation. These results are useful for further investigation of LIPSS formation using the vector beams possessing different polarization states. The processed GaAs surface exhibits specific functional properties beneficial for the applications in various areas.*

Keywords: LIPSS, Radial Polarization, Azimuthal Polarization, S-Waveplate, GaAs

1. Introduction

Laser-Induced Periodic Surface Structures (LIPSS), sometimes called ripples or nanoripples, can be formed on the surface of many different materials as a result of interaction with laser radiation. The morphology of LIPSS depends on the laser polarization, wavelength, pulse duration, fluence, and parameters of the used material. By controlling these parameters, one can achieve the required structures for specific applications.

LIPSS can be used to change the material properties such as colour or wettability ranging from superhydrophilic to superhydrophobic [1]. They can be used to increase the optical storage and make polarization sensitive optical elements [2, 3]. Also, there are attempts to increase the efficiency of solar cells using LIPSS [4, 5].

In the case of LIPSS produced using linearly polarized laser beam, the linear structures can be classified based on the spatial period (Δ), controlled by variation of the experiment parameters. In general, the low spatial frequency LIPSS (LSFL, $0.5\lambda < \Delta_{\mathrm{LSFL}} < \lambda$), high spatial frequency LIPSS (HSFL, $\Delta_{\mathrm{HSFL}} < 0.5\lambda$), and supra-wavelength LIPSS (SWL, $\Delta_{\mathrm{SWL}} > 2\lambda$) which are often termed as grooves, can be obtained [6, 7].

This study is a continuation of our previous research where we compared LIPSS produced on a single spot using different polarizations of laser radiation [8]. A search of the parameters for high-quality LIPSS formation on the samples immersed in water has proven to be much more difficult. In this research we demonstrate the generated structures using radially and azimuthally polarized helical beams and the morphology of the ripples.

2. Experimental setup

The experimental scheme for generating LIPSS formation is shown in Fig. 1. During these experiments we used the polished GaAs (100) wafer (99%, Sigma-Aldrich). The laser (PL2230, EKSPLA) used in fabrication of LIPSS generated linearly polarized 30 ps, 50 Hz, 532 nm pulses. Neutral density (ND) filters were used to tune the energy of the of the pulsed radiation. For transforming the polarization and wavefront shape of the beam we used the S-waveplate

ISBN 978-80-69159-00-6

(RPC-0515-15, Altechna) mounted in a rotational mount, which allowed to choose the polarization of the transformed beam – radial, azimuthal, or a mix of both – based on the angle between the laser polarization direction and the orientation of S-waveplate.

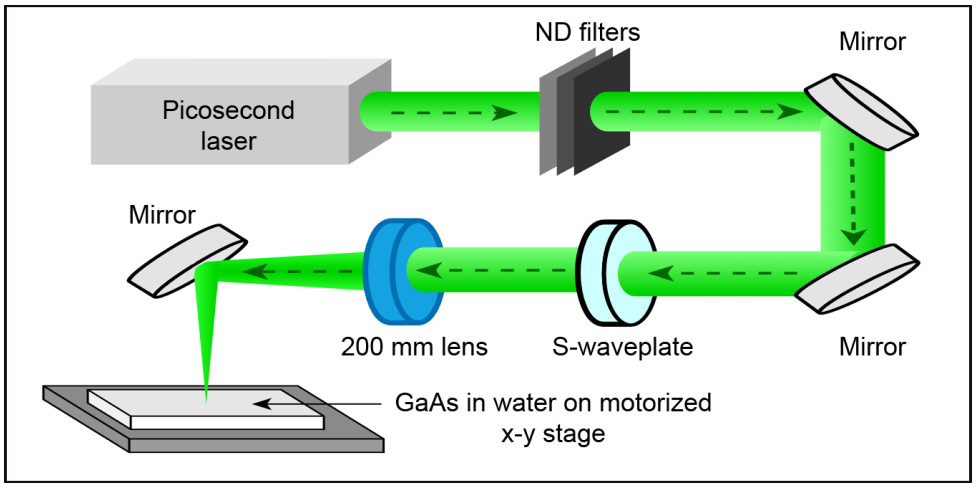

Fig. 1: Scheme of the experimental setup used to produce LIPSS on GaAs using 30 ps 532nm laser.

The motorized x-y stage was replaced with CMOS camera, to analyze images of the beam cross-section at the focal plane, which are shown in Fig. 2. The sample and the camera were placed closer to the lens where the diameter of the annular beam was 300 μm to increase the width of the LIPSS line. The sample was placed in distilled water, the water level was 5 mm above the surface of the semiconductor. It was then fixed on motorized x-y translation stage, which allowed the slow movement of the sample. This regime of LIPSS formation was mandatory for creation of the continuous linear structure due to the low repetition rate of the laser.

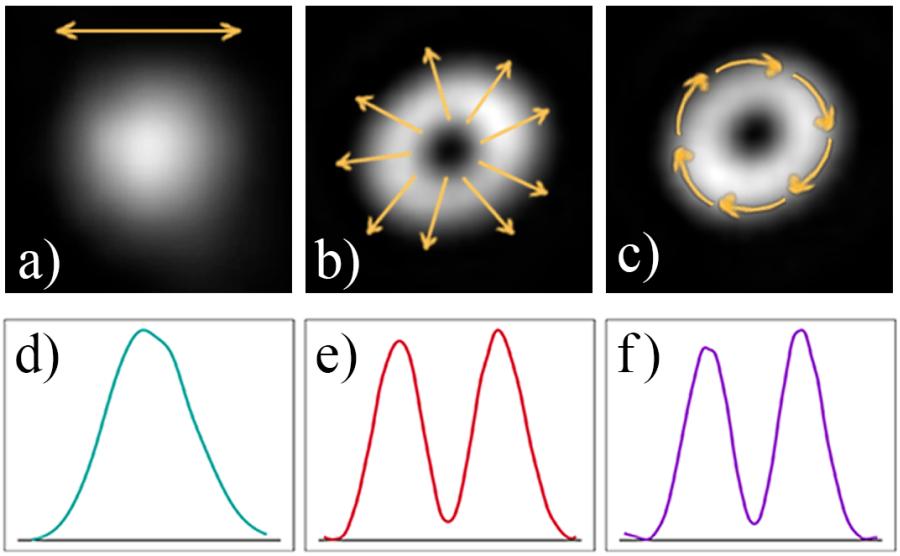

Fig. 2: Images show the shapes of the beams with **(a)** linear polarization, **(b)** radial polarization, **(c)** azimuthal polarization. The corresponding intensity distributions at the middle line are visible in **(d-f)**. The orange arrows show the polarization directions.

ISBN 978-80-69159-00-6

3. Results

To generate the best structures, various parameters could be changed. However, to simplify the experiment, we varied only the speed at which the sample is moved in the focal plane and the energy of the laser pulses, while other parameters were kept constant.

The best images with optimal parameters are shown in Fig. 3. We see a distinct difference between the parts of the formed linear structures, where the pores are observed at the central part of the scanned line, while at the edges of the line one can see the grooves, which were parallel to the polarization. The grooves were oriented vertically in the case of the radially polarized beam and horizontally for the azimuthally polarized beam. In the case of radial polarization, the spatial period was $\Delta_{\text{rad}} = 805 \pm 100\ nm$ and in the case of azimuthal polarization we measured $\Delta_{\text{az}} = 910 \pm 132\ nm$. Upon closer inspection there are also linear structures with much smaller spatial period compared with the grooves. They were aligned orthogonally to the grooves. We measured the spatial period of these fine linear structures to be $\Delta_{\text{rad}} = 419 \pm 56\ nm$ and $\Delta_{\text{az}} = 411 \pm 75\ nm$ and identified them as the ripples under the groove structures.

At the center of the scanned line, we observed the craters, which were randomly positioned. Upon closer inspection of the edges of craters, the ripples were found with small spatial period. Those ripples were oriented in different directions.

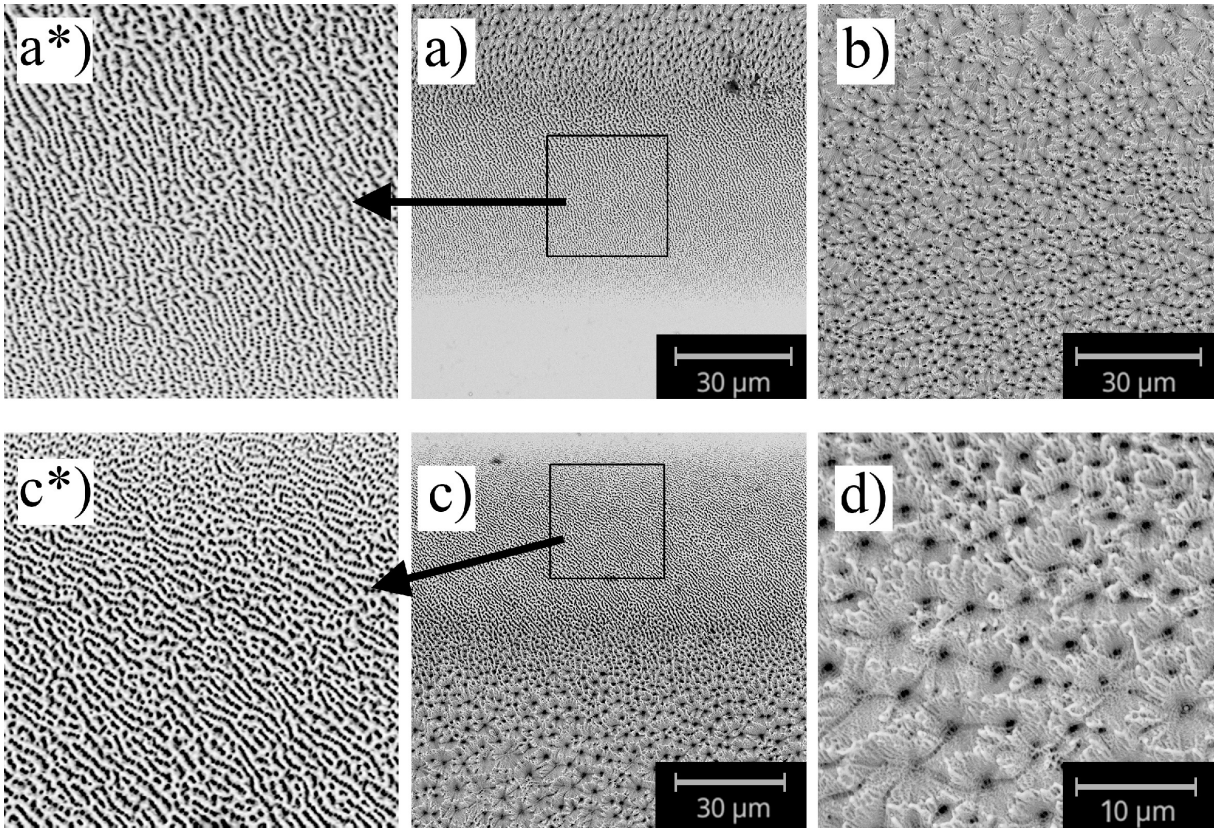

Fig. 3: LIPSS formed using the radially polarized beam **(a** and **b)**, and with azimuthally polarized beam **(c** and **d)**. The edge of the line is visible in **(a)** and **(c)**, but the middle of the line are shown in **(b)** and **(d)**. Images denoted with asterisk **(*)** are the enlarged sections of the shown area which is 30 μm wide. $E = 163 \mu J, v_{\text{scan}} = 0.02 mm/s$

4. Discussion

In presented research we demonstrated different morphology of produced LIPSS. At the edges of scanned lines, we observed the overlapping structures with spatial period larger than the

laser wavelength, alongside the spatial period slightly lower than the laser wavelength. The directions of these structures showed a strong correlation with the polarization state of the beam – the grooves are oriented parallel to the polarization, but the LSFL are oriented perpendicularly to the polarizations. At the centers of the lines, the craters decorated with the ripples, oriented randomly were formed.

This research is an important step in elaborating an experimental approach for producing the large-area laser processed surfaces on different materials. The large-area structured surfaces will allow altering various characteristics (e.g. colour and wettability) of the materials.

Acknowledgements

Work was supported by Fundamental and Applied Research Project (Nr. lzp-2023/1-0199): "The Laser Photodetachment Spectroscopy on Negative Ions".

We would like to express our sincere gratitude to K. Salmins and A. Sarakovskis for the help with acquiring the necessary equipment for experiments.

References

[1] Vorobyev, A. Y., Guo, C. (2013). Direct femtosecond laser surface nano/microstructuring and its applications. *Laser & Photonics Reviews* 7(3), 385–407.

[2] Gu, M., Li, X., Cao, Y. (2014). Optical storage arrays: A perspective for future big data storage. *Light: Science & Applications* 3, e177.

[3] Lei, Y., Wang, H., Shayeganrad, G., Kazansky, P. G. (2022). Ultrafast laser nanostructuring in transparent materials for beam shaping and data storage. *Opt. Mater. Express* 12(9), 3327–3355.

[4] Nigo, F., Hashida, M., Tsukamoto, M., Sakabe, S., Kusaba, M. (2020). Reflectance and crystallinity of silicon solar cells with lipss produced by xecl excimer laser pulses. *Applied Physics A: Materials Science and Processing* 126(2), 129.

[5] Heffner, H., Soldera, M., Lasagni, A. F. (2023). Optoelectronic performance of indium tin oxide thin films structured by sub-picosecond direct laser interference patterning. *Scientific Reports* 13(1), 9798.

[6] Zhang, Y., Jiang, Q., Long, M., Han, R., Cao, K., Zhang, S., Feng, D., Jia, T., Sun, Z., Qiu, J., Xu, H. (2022). Femtosecond laser-induced periodic structures: mechanisms, techniques, and applications. *Opto-Electronic Science* 1(6), 220–005.

[7] Sun, H., Li, J., Liu, M., Yang, D., Li, F. (2022). A review of effects of femtosecond laser parameters on metal surface properties. *Coatings* 12(10), 1596.

[8] Kalnins, K., Kim, V. V., Reddy, A. N. K., Sarakovskis, A., Ganeev, R. A. (2024). Spatially variable ripple and groove formation on gallium arsenide using linear, radial, and azimuthal polarizations of laser beam. *Photonics* 11(8), 710.

Measurements of Potential Positive Ion Sources of Gadolinium

Matīss Čakšs

Institute of Atomic Physics and Spectroscopy, University of Latvia, Riga, Latvia
Email: matiss.cakss@lu.lv

Abstract. *The work describes measurements of potential sources of gadolinium (Gd) ions. The measurement methods and preliminary results are presented. The aim of this research is to develop a positive Gd ion source for further experiments, particularly the measurements of negative ions. Two methods were used for creating Gd atom and ion emission spectral lines: laser-induced breakdown spectroscopy (LIBS) and hollow cathode (HC) discharge combined with radiofrequency inductively coupled plasma (ICP). For this research, samples of gadolinium oxide Gd2O3 and gadolinium Gd were used in HC-ICP device, and Gd2O3 samples for LIBS. The recorded plasma spectra was analyzed to identify atomic and ion emission lines.*

Keywords: Gadolinium Ions, Spectroscopy, Laser-Induced Breakdown Spectroscopy, Hollow Cathode, Indictively Coupled Plasma

1. Introduction

The research of negative ions is important to gain more information about the structure and dynamics of atoms. Negative ions of gadolinium are of particular interest, as it is not clearly known whether such ions exist. Negative ions can be created using a positive ion beam and a charge exchange cell [1]. Therefore, developing a positive ion source is an important step toward negative ion generation. Laser-induced breakdown spectroscopy (LIBS) uses pulse laser to ablate and excite the sample, producing plasma [2] that contains both atoms and positive ions of the sample. Positive ions of Gd have been observed [3] with LIBS. Another method is to use hollow cathode (HC) discharge to sputter the sample and create plasma containing atoms and ions [4]. In addition, radiofrequency (RF) inductively coupled plasma (ICP) can be used to more completely ionize and excite the sputtered sample [5]. In an earlier study, an ion source combining a modified HC lamp and an RF-ICP generator was developed in our laboratory. In this research, experimental setups of HC discharge with ICP and LIBS were used to produce positive Gd ions from Gd metal and Gd_2O_3. The spectra of produced plasma were analyzed to identify Gd ion emission lines to confirm the formation of ions.

2. Subject and Methods

Laser-Induced Breakdown Spectroscopy

Experimental setup for for LIBS is shown in Fig. 1. The laser (EKSPLA PL2230) was used to produce a 1064 nm pulse laser beam, which was split into two parts for measurement of the pulse energy and for breakdown spectroscopy of the sample. The sample was positioned on a motorized platform, and the laser beam was directed from above. A converging lens focuses the laser beam on the sample surface, where ablation of the sample and plasma formation takes place. The light emitted from the plasma plume was collected with an optical fiber positioned next to the sample. The spectra were recorded using the Flame-T-XR1-ES digital spectrometer, which recorded data with a step size of 0.25 nm.

ISBN 978-80-69159-00-6

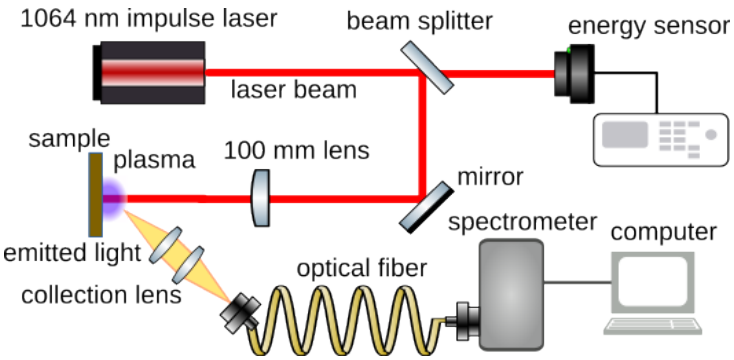

Fig. 1: LIBS experimental setup.

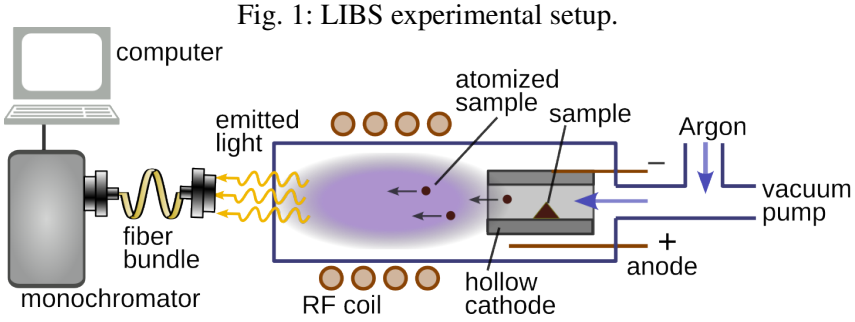

Fig. 2: Experimental setup for the HC discharge with ICP.

HC discharge combined with ICP

Experimental setup for measuring Gd spectra using HC discharge with RF-ICP generator is shown in Fig. 2. This hybrid system was developed to generate ions of other elements such as Cd, Zn, and B. The system is composed of a wide quartz glass tube. A smaller tube is attached to one end to evacuate air and supply argon. The other end of the tube is removable to allow the sample to be inserted. Within the tube, a cylindrical hollow graphete cathode is attached by a conductive electrode in front of the evacuation tube. A metal anode is placed next to the cathode. The RF coil is placed around the tube. The sample is placed inside the hollow cathode. The main advantage of this HC setup compared to commercial HC lamps is the ability to change the sample in the device.

The system has to be prepared for measurements after the new sample is inserted. After the device was closed, air was pumped out of the system. The system was held under vacuum, and the cathode was heated several times to increase air deabsorption from the cathode. For the spectra measurements, argon was supplied to the system until a pressure of 1-1.2 torr was reached. Voltage was applied to the cathode and anode and to the RF generator to start the discharge and create ICP. The emitted light is collected with a fiber bundle and analyzed with a SpectraPro 2300i spectrometer equipped with a Pixis 400 CCD camera. The spectrometer records the spectrum in segments of 64 nm, which are combined to form the full spectral range. The recorded data have 0.03 nm step size, and the specified wavelength accuracy is 0.2 nm.

The captured spectra were analyzed using LabPLot software. Visible peaks in the spectrum were compared with known gadolinium atom (Gd I) and ion (Gd II, Gd III) spectral lines from the NIST atomic line database [6]. Comparison was primarily focused on resonance and strong emission lines that are more likely to be detected in the measured spectra.

ISBN 978-80-69159-00-6

3. Results

The Gd emission spectrum was first produced from the Gd_2O_3. The Gd_2O_3 powder was pressed into pellets for the LIBS setup. The laser was operated at 1.3 mJ pulse energy and 5 Hz pulse frequency. The pulse energy, frequency, and positioning of the collecting lens influenced the clarity of spectral peaks in the spectra. The recorded spectra are shown in Fig.3. The spectra show strong continuum background, and emission lines were hard to identify. The two identified lines are shown in Fig.3.b.

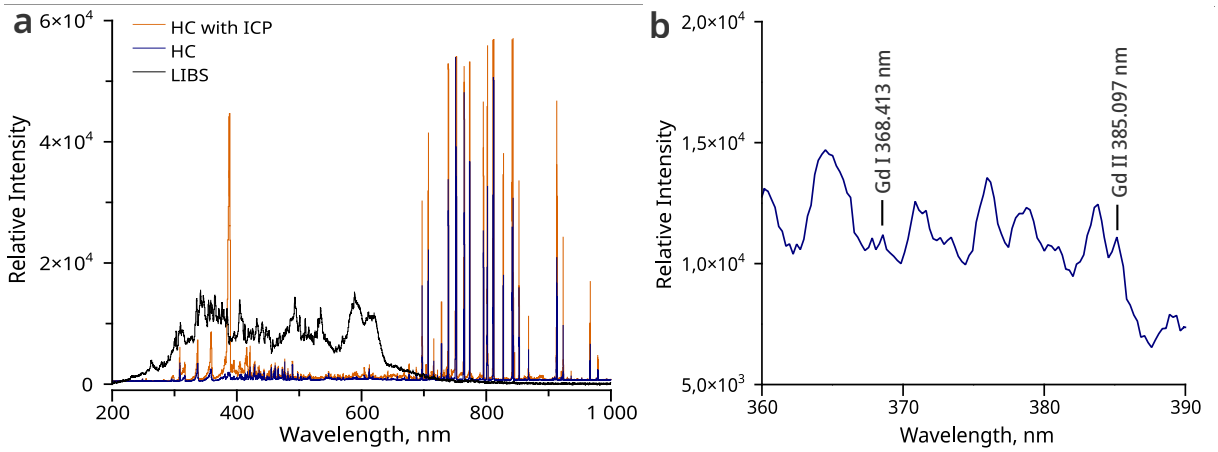

Fig. 3: (a) Emission spectra of the Gd_2O_3 sample captured using LIBS and HC with and without RF-ICP and (b) identified Gd emission lines in the LIBS spectrum. The emission lines of Gd are mostly located in the 200 nm to 700 nm region, Ar emission lines can be seen in the 700 nm to 1000 nm region.

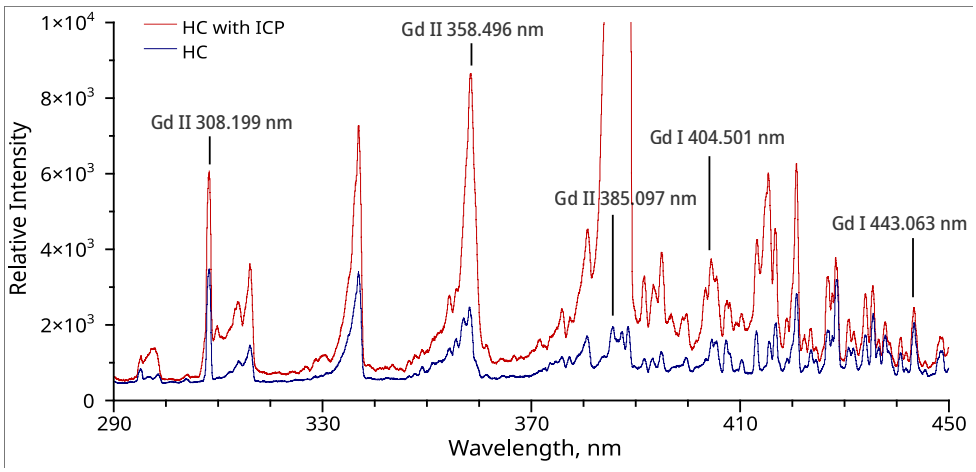

Fig. 4: Identified Gd emission lines from the Gd_2O_3 sample captured using HC with and without ICP.

Spectra measurements were performed with HC discharge combined with RF-ICP and with only HC discharge for both Gd_2O_3 and Gd samples. The voltages used for HC and RF-ICP were, respectively, 450 V and 500 V, at an Ar pressure of 1.0 torr. The full spectra from the Gd_2O_3 sample are shown in Fig.3-a. Spectra regions with identified lines are shown in Fig.4 and Fig.5.

Analysis of HC-ICP spectra showed that visible Ar spectral peaks differed from the respective known Ar lines by 0.05 to 0.5 nm. The errors change between different 64 nm sections of the spectra captured by the spectrometer. When identifying peaks in the measured Gd spectra, strong Gd lines ± 0.2 nm from the peak were considered.

ISBN 978-80-69159-00-6

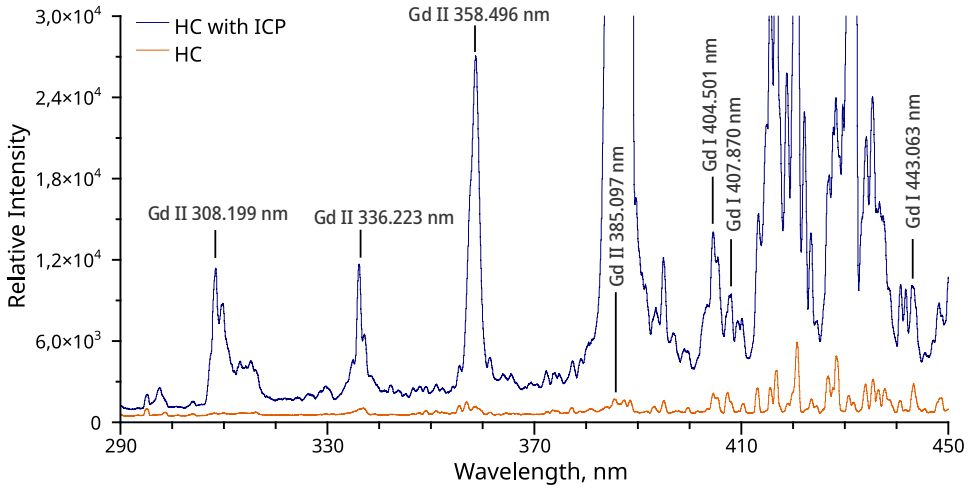

Fig. 5: Identified Gd emission lines from the Gd sample captured using HC with and without ICP.

4. Discussion

Combined HC-ICP discharge and LIBS were successfully used to record gadolinum spectra. The LIBS gadolinium spectra from Gd_2O_3 show weak Gd emission lines. Two resonance lines were identified: Gd I and Gd II. Line identification was difficult because of the strong continuum background. Different LIBS setup parameters and the use of Gd metal as the sample could produce clearer spectra. Spectra of the combined ICP-HC discharge show spectral peaks more intense than those of the HC discharge alone, indicating a higher level of sample atomatization, ionization, and excitation. Several lines of Gd I and Gd II were identified, some corresponding to strong spectral peaks, which indicate a significant number of Gd ions. The identification of emission lines was limited by the large wavelength errors of the spectrometer. A calibration of the spectrometer would improve the analysis of the recorded spectra. The research results obtained so far suggest that HC discharge combined with ICP is a viable source of positive Gd ions.

References

[1] Fortes, F. J., Moros, J., Lucena, P., Cabalín, L. M., Laserna, J. J. (2013). Laser-induced breakdown spectroscopy. *Analytical chemistry*, 85(2), 640-669.

[2] Alton, G. (2005). Negative-Ion Formation Processes and Sources. In: *Electrostatic Accelerators. Particle Acceleration and Detection.* Springer, Berlin, Heidelberg, 222-273.

[3] Khumaeni, A., Tampo, M., Katsuaki, A., Miyabe, M., Ikuo, W. (2013). Enhancement of LIBS emission using antenna-coupled microwave. *Optics Express*. 21 (24), 6–7.

[4] Mavrodineanu R. (1984). Hollow Cathode Discharges: Analytical Applications. *Journal of Research of the National Institute of Standards and Technology*. 89 (2), 143–185.

[5] Blahins, J., Ubelis, A. (2022). Towards Next-Generation Small-Size Boron Ion Implanting Apparatus. In *Proceedings of the Latvian Academy of Sciences. Section B. Natural, Exact, and Applied Sciences*. Sciendo, 198-203.

[6] Kramida, A., Ralchenko, Yu., Reader, J., and NIST ASD Team (2024). NIST Atomic Spectra Database (ver. 5.12), [Online]. Available: https://physics.nist.gov/asd [2025, March 19]. National Institute of Standards and Technology, Gaithersburg

ISBN 978-80-69159-00-6

Equivalent Model of Electrodynamic Exciter and Its Verification

Norbert Palsovics, Martin Černík, Martin Pustka

VÚTS, a. s., Measurement Department, Liberec, Czech Republic,
Email: norbert.palsovics@vuts.cz

Abstract. *The linear equivalent model of an electrodynamic exciter based on the mechanical-electrical analogy was built and experimentally verified. The measurement was performed using external excitation by means of an electrodynamic shaker. The frequency dependencies of dynamic force, exciter magnet velocity, output voltage and output current were studied for different electric shunt impedances.*

Keywords: Electrodynamic Exciter, Linear Equivalent Model, Experimental Verification

1. Introduction

The AuraSound AST-2B-4 electrodynamic exciter was used as the main vibration source for the therapeutic vibration bed with haptic feedback. To create a reliable computational model of the whole system for design purposes, it was necessary to build and experimentally verify an equivalent model of the exciter. The verification of exciter model was the basic condition for its application in calculations and equipment design.

The electrodynamic exciter converts the input electric field into acoustic vibration by means of electromagnetic field. The solenoidal coil connected to external terminals is positioned in the cylindrical cavity. Inside the coil, the magnet is mounted on a flexible suspension. AC current feeding the coil excites magnet oscillations, which subsequently generate a dynamic force on the exciter base. Alternatively, forced vibration of the exciter base generates magnet oscillations and corresponding voltage induced on the solenoidal coil. This induced voltage at the terminals can be measured to determine the relative velocity between the magnet and the coil. The exciter performance can further be affected by an electric shunt connected to the terminals (resistor or short-circuit). This facts were utilized for the exciter model verification.

2. Equivalent Model

The simplified linear electromechanical model was built in the form of an equivalent electrical circuit [1], [2]. This model is based on the mechanical-electrical analogy [3] (equivalent quantity substitution of current/voltage and force/velocity) and can estimate the influence of exciter electric load on the mechanical parameters. The model is linear and possible non-linearities (e.g. the magnet suspension compliance c_m is dependent on the magnet position) can affect the results in varying degrees. Thus, the comparison of simulation and measurement results can also indicate the influence of non-linear behavior.

The equivalent model in Fig. 1 describes the relationship between the phasors of the dynamical force $\hat{F}_k$ and the exciter base velocity $\hat{v}_S$. When the symbolic-complex method is applied, the total input mechanical impedance is given as $Z_{Min} = \hat{F}_k/\hat{v}_S$. The excitation velocity phasor $\hat{v}_S = \hat{a}_S/j\omega_k$ is calculated from the acceleration $\hat{a}_S$ for every angular frequency ω_k. The constant acceleration $\hat{a}_S = a_S \cdot \exp(j0)$, where $a_S = 0.5\ g$ and $g = 9.81\ \mathrm{ms}^{-2}$ was chosen for both calculation and experimental verification.

The model verification was carried out for the exciter fixed to the force sensor, as given in section 3. For this reason, the force sensor impedances Z_{m1} and Z_{m2} are included in the model.

ISBN 978-80-69159-00-6

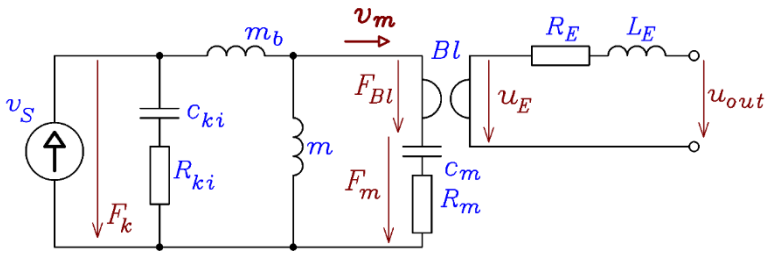

Fig. 1. Equivalent circuit of electrodynamic exciter

The input mechanical impedance Z_{Min} is given by a formula

$$Z_{Min} = Z_{m1} \parallel (Z_{m2} + Z_{m3} \parallel Z_{m4}) = \\ = \frac{Z_{m1}Z_{m2}Z_{m3} + Z_{m1}Z_{m2}Z_{m4} + Z_{m1}Z_{m3}Z_{m4}}{Z_{m1}Z_{m3} + Z_{m2}Z_{m3} + Z_{m1}Z_{m4} + Z_{m2}Z_{m4} + Z_{m3}Z_{m4}}, \quad (1)$$

where $Z_{m1} = 1/j\omega c_{ki}$ ($c_{ki} = 2.02 \cdot 10^{-9}$ m/N) is the impedance of force sensor elastic parameters, $Z_{m2} = j\omega m_b$ ($m_b = 2.0$ kg) is the impedance of force sensor mounting base, $Z_{m3} = j\omega m$ ($m = 0.4$ kg) is the impedance of exciter magnet and $Z_{m4} = 1/j\omega c_m + R_m + Bl^2/Z_E$ ($c_m = 33 \cdot 10^{-6}$ m/N, $R_m = 7.6$ Ω) is the mechanical impedance of damped flexible suspension. The electrodynamical coupling is characterized by the constant $Bl = 4.7$ Tm. If the electric terminals are open or only voltmeter is connected ($Z_E \to \infty$), we can set $Z_{m4} = 1/j\omega c_m + R_m$. If the shunt impedance Z_{sh} is connected to the electric side, it also affects the mechanical side. The total input impedance is then given as a serial connection of resistor, inductor and shunt Z_{sh} with the total impedance $Z_E = R_E + j\omega L_E + Z_{sh}$ ($R_E = 3.64$ Ω, $L_E = 416$ μH). The impedance Z_E is substituted into Z_{m4} calculation. For short-circuit $Z_{sh} = 0$ is supposed. The relation between the input velocity and the force has a form

$$\hat{F}_k = Z_{Min}\hat{v}_S . \quad (2)$$

The relative velocity $\hat{v}_m$ between exciter fixed and moving part derived from the equivalent circuit is

$$\hat{v}_m = \hat{v}_S \cdot \frac{Z_{m1}}{Z_{m1} + Z_{m2} + \frac{Z_{m3}Z_{m4}}{Z_{m3} + Z_{m4}}} \cdot \frac{Z_{m3}}{Z_{m3} + Z_{m4}} . \quad (3)$$

Using the formula for the electrodynamical coupling $\hat{F}_{Bl} = Bl \cdot \hat{\imath}$, the open circuit voltage $\hat{u}_E = \hat{v}_m/Bl$ can be determined. When the load impedance Z_{sh} is connected, the output current is equal to $\hat{\imath}_{sh} = \hat{u}_E/Z_E$ and the voltage on the load is $\hat{u}_{sh} = \hat{\imath}_{sh} \cdot Z_{sh}$. The circuit parameters necessary for the calculation were estimated by measurement or by fitting the measured frequency response functions [4].

3. Experimental Verification

The model results were verified by measurement of AuraSound AST-2B-4 tactile transducer, which was externally excited by the electrodynamic shaker Data Physics GW-V400LT, see the test setup in Fig. 2. The shaker generated sinusoidal vibrations in exciter main axis direction in the wide frequency range. The shaker table acceleration 0.5 g was constant for all excitation frequencies.

The exciter base was fixed to the multicomponent dynamometer Kistler 9129AA, which was connected to the shaker table. The dynamometer measured the dynamic force in the axis

direction. The base acceleration was sensed by the uniaxial accelerometer Kistler 8702B. The voltage was sampled directly at electric terminals, for the short circuit current measurement the clamp current probe Chauvin-Arnoux E3N was used. The data acquisition was carried out using DEWE-2600 measurement analyzer with the sampling frequency of 10 kHz.

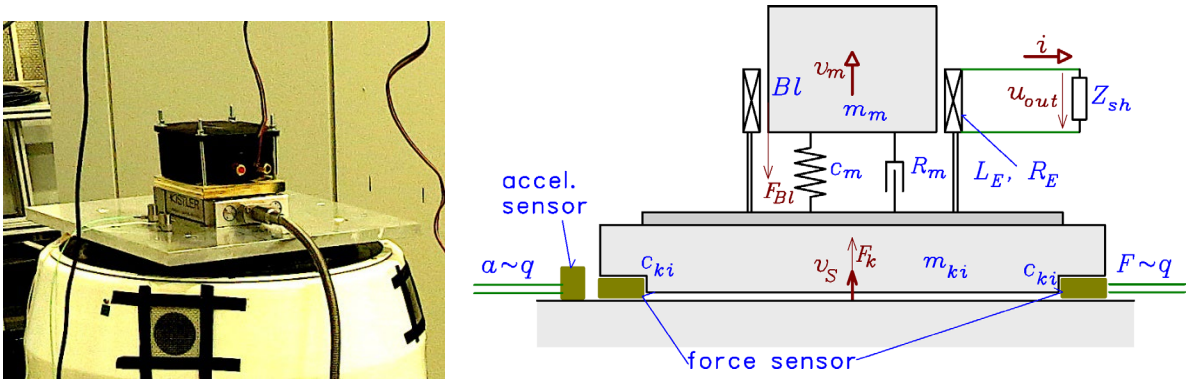

Fig. 2. Test setup (left), measurement schematic layout (right)

4. Measurement Results

The example of model frequency dependencies of dynamic force $\hat{F}_k$ and output voltage $\hat{u}_{sh}$ amplitudes, calculated using Eqs. (1)-(3) for different shunt impedance values, and their comparison with measurement is shown in Fig. 3 and 4 in the frequency range to 100 Hz.

The diagrams were calculated from model or measured data using FFT and converted to phasors. The phase of all quantities was expressed relative to the phase of acceleration $\hat{a}_S$.

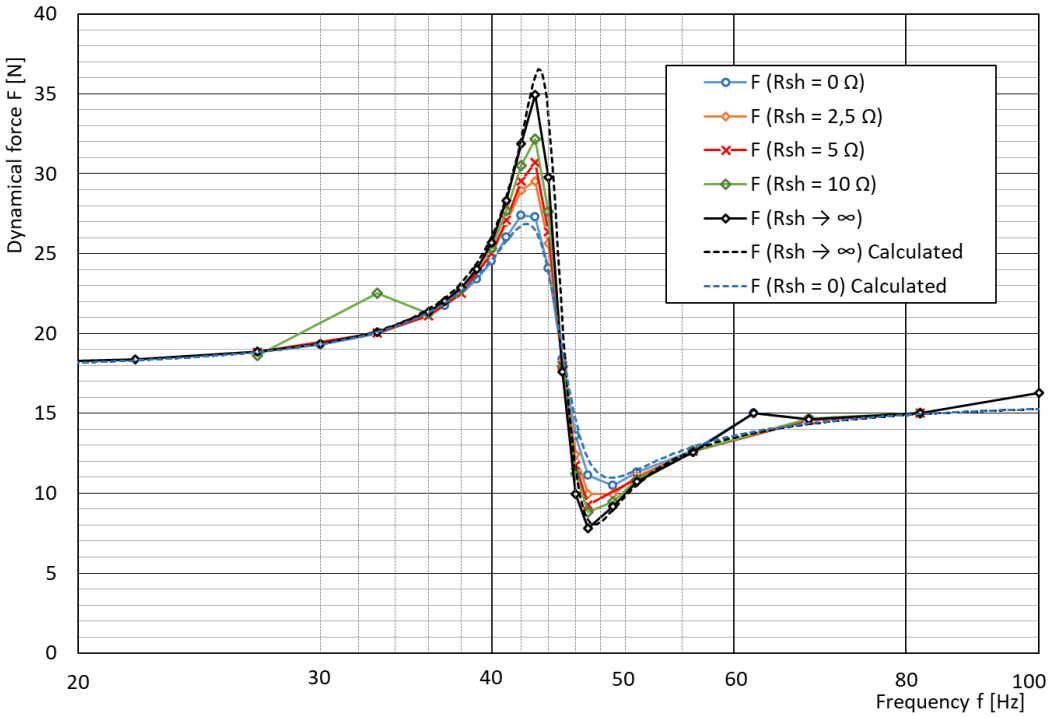

Fig. 3. Influence of shunt impedance on dynamic force amplitude, model and measurement

ISBN 978-80-69159-00-6

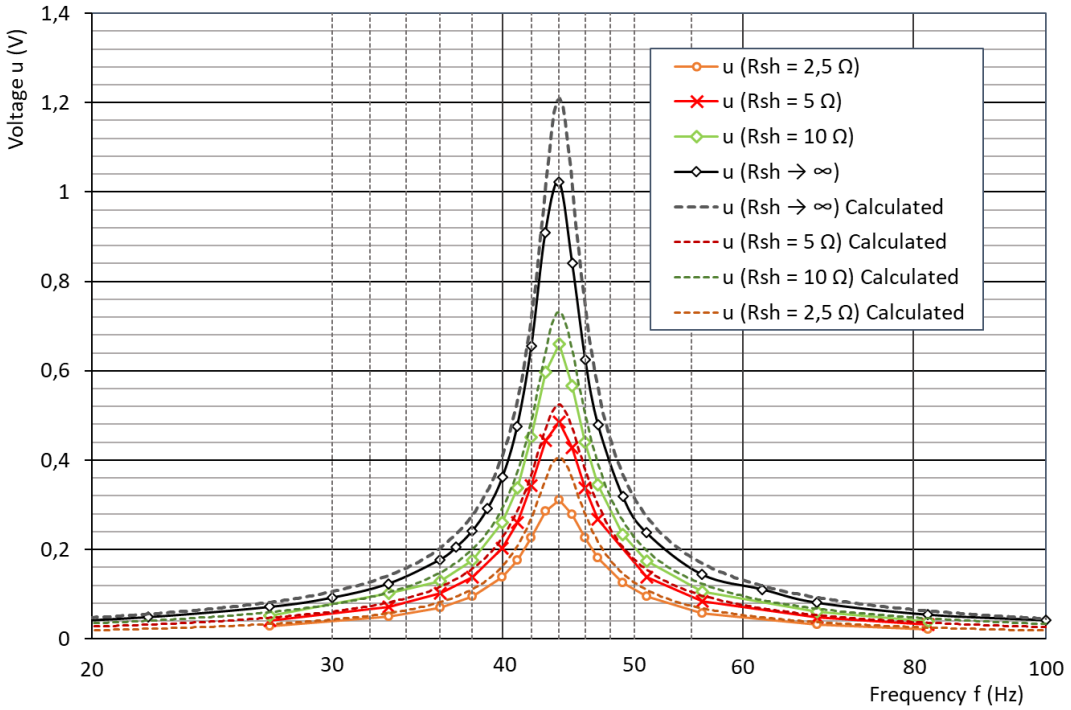

Fig. 4. Influence of shunt impedance on output voltage, model and measurement

5. Conclusions

The equivalent model of an electrodynamic exciter externally excited by an electrodynamic shaker was used for frequency dependence evaluation of dynamic force, exciter magnet velocity, output voltage and output current. The results show good agreement of calculated values with measured data. It was further verified that the physical model based on the mechanical-electrical analogy is suitable for the estimation of exciter frequency characteristics. For high-quality exciters with linear performance, the calculated physical quantities are virtually identical to real values. It is possible to assume that the model presented in this paper can be implemented in the design of vibration systems utilizing electrodynamic exciters.

Acknowledgements

This work was supported by the Czech Ministry of Industry and Trade in the framework of the institutional support for long-term conceptual development of research organization - recipient VÚTS, a.s.

References

[1] Boulandet, R., Michau, M., Herzog, P., Micheau, P., Berry, A. (2016). A sensorless method for measuring the mobility of mechanical structure. *Journal of Sound and Vibration*, 378, 14-27.

[2] Martino, J., Harri, K. (2019). Two-port modeling and simulation of an electrodynamic shaker for virtual shaker testing applications. *Journal of Sound and Vibration*, 460, 114835.

[3] Olson, H. F. (1944). *Dynamical Analogies*. D. Van Nostrand.

[4] Pustka, M., Černík, M., Palsovics, N. (2025): Estimation of electrodynamic exciter parameters by means of circle-fit method. *Acta IMEKO*, 14(1), 1-6.

Measurement of Electrodynamic Exciter Parameters

Martin Černík, Norbert Palsovics, Martin Pustka

VÚTS, a.s., Measurement Department, Liberec, Czech Republic
Email: martin.cernik@vuts.cz

Abstract. *Electromechanical parameters of several commercial dynamic exciters were obtained by means of static measurements, impedance measurements, and dynamic measurements under electrical and mechanical excitation. The measurement procedure was determined using the electromechanical model and the electrical equivalent circuit of the exciter.*

Keywords: Electrodynamic Exciter, Thiele-Small Parameters, Equivalent Circuit

1. Introduction

Small electrodynamic exciters are currently a commonly used electronic component. They are mainly applied in multimedia or gaming systems as a source of mechanical vibration for sound tactile sensation. Another interesting area is the application in medical devices for therapeutic procedures. The electrodynamic exciter is, in principle, composed of a single-degree-of-freedom mechanical oscillator coupled to the electrical circuit by means of the electromagnetic field. The oscillating mass is an elastically mounted magnet positioned inside a solenoidal coil (a voice coil), which is connected to an external electric circuit. The exciter in operation generates the dynamic inertial force acting on its base, which is forced by an AC electric current in the coil. This energy conversion is reversible, and the exciter can operate reciprocally, i.e., the dynamic voltage at the terminals can be generated mechanically by forced magnet oscillation. The energy conversion reciprocity is also very convenient for the exciter application in active vibration suppression using a control circuit.

The circuit and mechanical parameters of the exciter are necessary for development and design purposes or for effective vibration control. However, the information given in the datasheets is commonly brief in comparison with published parameters of loudspeakers, which have the same operating principle. In general, the mechanical parameters or electrodynamic coupling are not available in the producer's data. This paper introduces the procedure of exciter parameters assessment.

2. Exciter Parameters

The performance of electrodynamic exciters can be specified by linear Thiele-Small parameters common for electrodynamic loudspeakers [1]. Since the exciters have no diaphragm, the set of electromechanical parameters consists of the moving system mass m_m, the mechanical compliance c_m, the equivalent mechanical resistance derived from the mechanical Q-factor R_m, the coil inductance L_E, the coil resistance R_E and the force factor Bl (effective product of magnetic flux density and active length of coil current wire). The electromechanical model of the exciter containing all Thiele-Small parameters is shown in Fig. 1.

The exciter is commonly represented by an electrical equivalent circuit (Fig. 2), which is based on the mechanical-electrical analogy [2]. Using circuit analysis, the system of dynamic equations for both the electrical and mechanical sides of the exciter can be derived. The electromechanical model and electrical equivalent circuit are important tools for determining the procedure for parameter measurement [3].

ISBN 978-80-69159-00-6

Because the electromechanical energy conversion is reversible, the parameters can be assessed either by mechanical or by electrical excitation of the exciter. We further assume linear behavior and neglect possible nonlinearities.

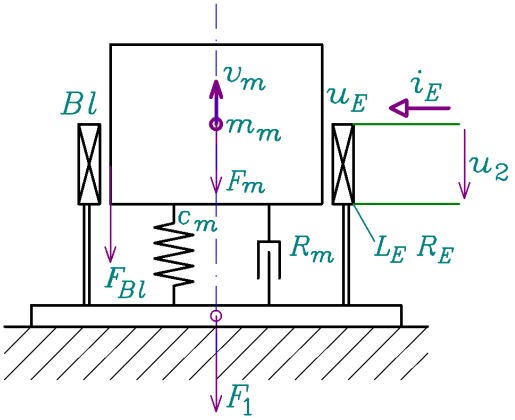

Fig. 1. Electromechanical model of the exciter with electrical and mechanical parameters and relevant physical quantities

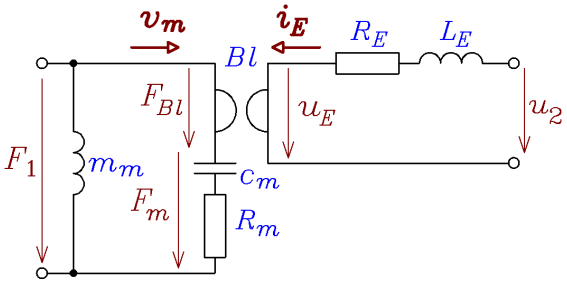

Fig. 2. Electrical equivalent circuit of the exciter with electrical and mechanical parameters and relevant physical quantities

3. Parameters Measurement and Evaluation

For linearity reasons, the measurements were performed at levels lower than maximal mechanical displacement or maximal electrical input power. All dynamic measurements were carried out with stepped harmonic excitation in the wide frequency range. The data acquisition was carried out using DEWE-2600 measurement analyzer.

Static measurement

The weight of the moving mass m_{mst} could directly be determined by weighing for exciters that can be non-destructively disassembled. Otherwise, the moving mass was estimated from the total weight. The static mechanical compliance was found by putting small weights m_l on the moving mass and measuring the induced displacement d_l by the laser sensor Micro-Epsilon ILD2220-10. The exciter had to be fixed on a horizontal solid base. The mechanical compliance was calculated using the formula $c_{mst} = d_l/(m_l \cdot g)$, where $g = 9.806$ ms^{-2}. The "static" resonance frequency can be calculated using c_{mst} and m_{mst} as $f_{rst} = 1/(2\pi\sqrt{c_{mst}\, m_{mst}})$ and later compared with the dynamically measured value.

The force factor Bl was found by measurement of the compensating current i_E, which balanced the constant position of the moving mass loaded by a small weight m_l, this dependence is given by the relation $Bl \cdot i_E = -m_l \cdot g$. The moving mass position was measured by the laser sensor, these measurements were possible only if the moving mass was well accessible for the sensor (i.e. not covered).

Electrical Impedance Measurement

The measurement of exciter frequency-impedance characteristics was carried out by means of HIOKI-3522-20 LCR HiTester at a low current level (tens of mA). The impedance analyzer does not supply sufficient power for synchronous measurement of mechanical parameters, the latter were measured subsequently at a higher excitation level.

The exciter electric parameters are presented by a serial LR circuit (see Fig. 2) with a complex impedance $Z = R + jX$. The mechanical resonance frequency f_{res} corresponds to the local maximum of the real part of impedance Z_{res}, while the imaginary part is zero. Because the

ISBN 978-80-69159-00-6

value of Z near f_{res} is affected by the mechanical resonance due to electromechanical coupling, the inductance L_E was obtained as reactance maximum above resonance divided by its angular frequency, i.e. $L_E = X_{max}/(2\pi f_{Xmax})$. The minimal value of the impedance real part in the measured frequency range was used as value of the serial resistance R_E.

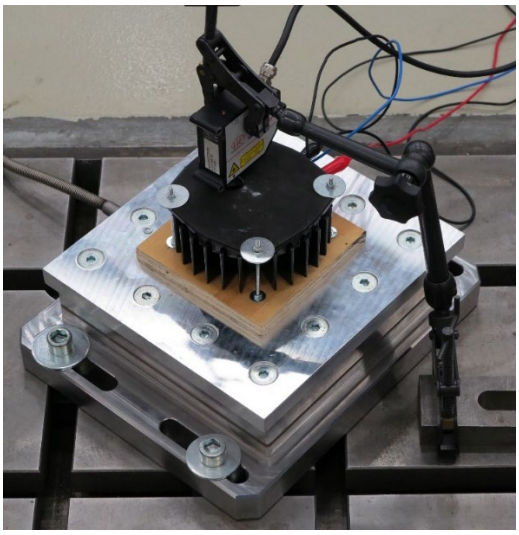

Fig. 3. Measurement under electrical excitation

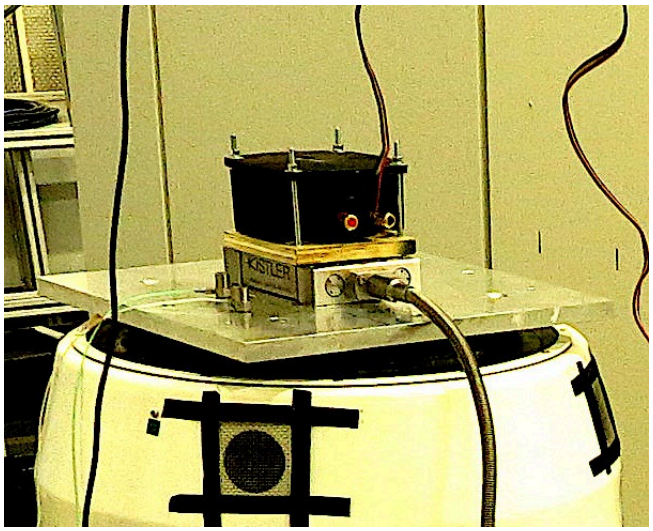

Fig. 4. Measurement under mechanical excitation

Measurement under Electrical Excitation

The mechanical parameters and the force factor were assessed by dynamic measurement under electrical excitation. The exciter was driven by a stepped sine signal generated by a signal generator and amplified by a D-class amplifier. The excitation voltage at the transducer terminals was approximately 2 V (rms).

The exciter base was fixed to the multicomponent dynamometer Kistler 9255B, which was mounted on a solid base (see Fig. 3). For each excitation frequency following quantities were recorded: the input voltage on the exciter terminals u_2, the input current i_E (measured across the shunt resistor using the four-wire method), the dynamic force F_1 (measured by the dynamometer) and the moving mass displacement d_m (measured using laser displacement sensor Micro-Epsilon ILD2220-10). The measured data were evaluated by means of FFT and converted to phasors.

The force factor Bl was calculated from the dynamic force at the frequency sufficiently higher than the resonance frequency ($f > 5f_{res}$) as $Bl = |\hat{F}_1/\hat{I}_E|$. The resonance frequency f_{res} corresponds to the frequency of force maximum. The weight of the moving mass was obtained from $m_m = |\hat{F}_1|/(\omega^2|\hat{d}_m|)$. Using the resonance frequency and moving mass values, the mechanical compliance was computed as $c_m = 1/(\omega_{res}^2 m_m)$, where $\omega_{res} = 2\pi f_{res}$. The difference between the values m_m, c_m, f_{res} and m_{mst}, c_{mst}, f_{rst} was commonly in percents.

The mechanical Q-factor was obtained from $\hat{F}_1/\hat{I}_E$ - characteristics as the peak-magnitude frequency f_{res} divided by 3dB-bandwidth using the relation $Q_m = f_{res}/\Delta f_{3dB}$. The mechanical resistance can be then calculated by means of formula $R_m = 2\pi f_{res} m_m/Q_m$.

Measurement under Mechanical Excitation

Alternatively, the mechanical parameters and the force factor can be assessed under mechanical excitation. The exciter base was fixed to the multicomponent dynamometer Kistler 9129AA,

ISBN 978-80-69159-00-6

which was connected to DataPhysics V400LT shaker table. The excitation acceleration at the table was approximately 4.91 m/s^2 (peak).

The same quantities were measured as in the case of electrical excitation, for the measurement of moving mass velocity $v_m = 1/j\omega d_m$ Polytec PDV-100 vibrometer was used. For exciters with linear properties, the resulting parameters should equal the values obtained under electrical excitation.

4. Results

The parameters of several types of electrodynamic exciters estimated by the abovementioned procedure are summarized in Table 1.

Table 1. Exciter electromechanical parameters

Parameter	AuraSound AST-2B-4	Dayton Audio BST-1	Visaton EX 80 S	Visaton EX 60 R	Visaton EX 30 S
R_E [Ω]	3.64	6.64	6.95	6.75	7.34
L_E [μH]	415	466	280	193	86.7
f_{res} [Hz]	43.6	26.0	42.0	58.2	302.5
Z_{res} [Ω]	5.23	7.21	16.0	13.0	8.9
Bl [Tm]	4.2	4.5	5.0	5.5	2.5
m_m [g]	370	366	109	105	34
c_m [m/N]	3.60×10^{-5}	1.15×10^{-4}	9.94×10^{-5}	6.0×10^{-5}	1.2×10^{-5}
Q_m [-]	14.2	14.3	16.6	11.7	7.2

5. Conclusions

The mechanical, electrical, and electromechanical parameters of several commercial electrodynamic exciters were obtained by means of static and dynamic measurements. The difference between the values measured under electrical and mechanical excitation was small in most cases, and the results confirmed the linearity and repeatability of most exciters. The results can be used in many technical applications where the electrodynamic exciter is utilized as a sensor or a transducer.

Acknowledgements

This work was supported by the Czech Ministry of Industry and Trade in the framework of the institutional support for long-term conceptual development of research organization - recipient VÚTS, a.s.

References

[1] Beranek, L. L., Mellow, T. J. (2012). *Acoustic: Sound Field and Transducers*. Academic Press.

[2] Olson, H. F. (1944). *Dynamical Analogies*. D. Van Nostrand.

[3] Boulandet, R. (2019). Sensorless measurement of the acoustic impedance of loudspeaker. In *Proceedings of the 23rd International Congress on Acoustics*. DEGA, 9-13.

A Partial Current Pulse Response as an Alternative to EIS Measurements for Accurate Internal Temperature Estimation of Lithium-Ion Battery Cells

M. Novák, M. Kemény, M. Mikolášek

Institute of Electronics and Photonics, Slovak University of Technology in Bratislava, Ilkovičova 3, 841 04 Bratislava, Slovakia
Email: matej.novak@stuba.sk

Abstract. *Electrochemical Impedance Spectroscopy (EIS) has become an essential tool for battery characterization. However, traditional EIS measurements suffer from limitations in real-world applications. This work proposes a novel approach to address these limitations by supplementing EIS measurements with partial current pulse measurements. The results revealed a strong correlation between impedance obtained from EIS and pulse excitations. Moreover, a possible utilization of such data for internal temperature estimation is discussed.*

Keywords: Li-ion Battery, Electrochemical Impedance Spectroscopy, Data analysis, Partial current pulses

1. Introduction

Electrochemical Impedance Spectroscopy (EIS) with its suitability for studying complex electrochemical systems, is one of the most dominant techniques for the characterization of lithium-ion batteries (LIBs) [1]. This technique provides indicators, which can be used to assess the State of Charge (SoC) and the State of Health (SoH) and the real part of impedance (Z_R) of the studied LIBs and is valuable due to its non-destructive nature [1].

As interpretation of impedance spectrum from EIS can be complex, non-linear behavior of LIBs poses challenges for EIS analysis and the use of advanced data processing methods to accurately capture the dynamic responses of the system in real-life applications is needed [3].

One of the promising approaches for the estimation of Z_R parameter is to substitute the EIS measurements with partial current pulse (PCP) measurements. This method focuses on the extraction of the Z_R parameter from the voltage responses on PCP and further analysis lead to the internal temperature estimation. This estimation is important as fast increase in internal temperature can lead to irreversible phenomena such as thermal runaway [2].

This approach aims to bridge the gap between the traditional EIS measurements conducted in ideal laboratory conditions and between the dynamic nature of real-world conditions of LIBs operation. PCP measurements offer a faster approach to the LIB's electrochemical processes characterization by applying partial pulses during LIB charging and discharging.

2. Subject and Methods

To evaluate the proposed approach, we employed NMC811 Li-ion cells from Molicel (INR-21700-P45B LIB). These cells were subjected to a comprehensive experimental regimen using a battery cycler (Neware BTS4000 series 5V6A) and a potentiostat-galvanostat (Gamry Interface 5000P). To simulate real-world conditions, the measurements were conducted within a climate chamber, spanning a temperature range from 20 °C to 50 °C with 10 °C step. Two parallel experimental approaches were adopted: Galvanostatic EIS and PCP measurement.

ISBN 978-80-69159-00-6

Measurements procedures

Galvanostatic EIS measurement procedure was performed at various SOC, incrementing by 10% steps. A constant current of 0.8 A (both charge and discharge) was used to transition between SoC levels. Prior to each EIS measurement, a 30-minute relaxation period was applied to ensure steady-state conditions. After each EIS measurement, the open-circuit voltage (OCV) was recorded. Fig. 1a shows Nyquists plots from various SoC levels.

PCP measurement procedure consists of multiple partial charging/discharging current pulses, while the voltage response is recorded. The LIB cells were subjected to 5 A current pulses to induce significant changes in SoC (Fig. 1b). For each 5% change in SoC, the current was reduced to 4.5 A for 60 seconds to allow for voltage stabilization.

By combining these experimental approaches, the correlation between EIS measurements and PCP responses is sought to explore the feasibility of using pulse-based techniques for accurate internal temperature estimation of LIBs.

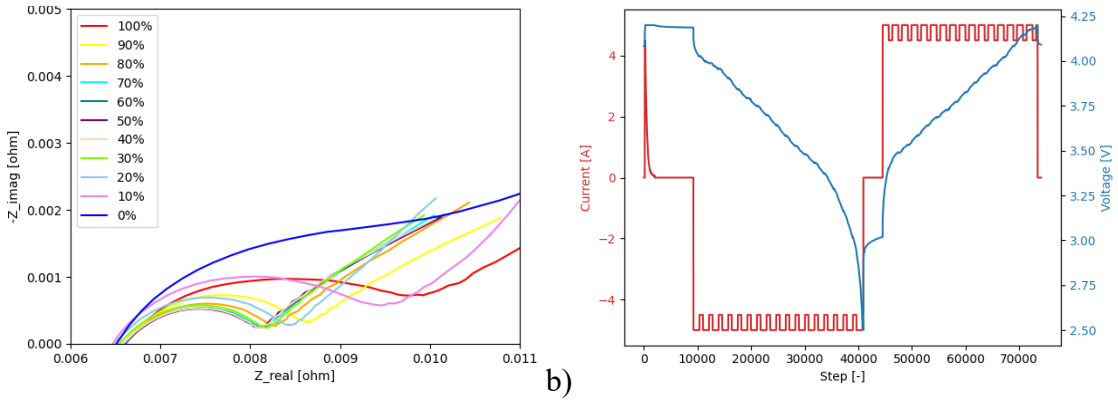

a) b)

Fig. 1. Experiment procedures and it's outcome, where a) represents Nyquist plots from galvanostatic EIS measurement procedure and b) represents PCP measurement procedure, where the whole charging and discharging cycle (with 5% SoC step) is indicated.

Longest usable pulse (LUP) estimation

When a PCP is applied, due to the slow diffusion reactions of LIBs, only certain period of the pulse is usable before the calculation of the Z_R parameter starts to be inaccurate. To investigate the influence of pulse magnitude and to find maximal usable pulse length, the experiment was repeated with different current levels ranging from 1 A to 5 A. The analysis shown in Fig. 2a aimed to identify the optimal pulse amplitude for maximizing measurement precision and minimizing cell stress. The plot of the LUP estimation is shown on Fig. 2b.

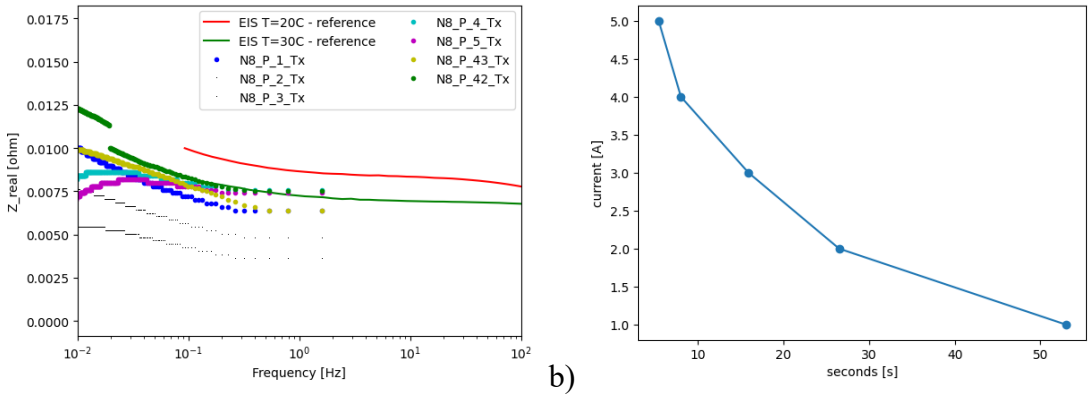

a) b)

Fig. 2. a) Example of the experiment procedure with multiple current levels for temperature level *Tx*=25 °C, where the most accurate one was chosen for further research and analysis, which lead to b) the plot of the LUP estimation.

ISBN 978-80-69159-00-6

3. Results

The values of Z_R calculated from the voltage response to PCP are displayed in Fig. 3. This parameter is calculated as a total voltage drop during the PCP cycle. Fig. 3a illustrates comparison between traditional EIS measurement and PCP measurement from the same LIB cell. In this scenario, Gamry potentiostat-galvanostat is used for PCP measurement, which create precise measurements of the voltage response, but the application to the real-life scenario is limited due to the next interface between LIB and final application. Fig. 3b shows traditional EIS measurement in comparison to PCP measurement on Neware battery cycler. This cycler acts like a final application device, so voltage response data shall be taken as data from real-world applications.

The results demonstrate a strong correlation between the impedance values derived from both pulse-based and traditional EIS methods, indicating the potential for PCP measurements to serve as a viable alternative or supplement to EIS in certain applications.

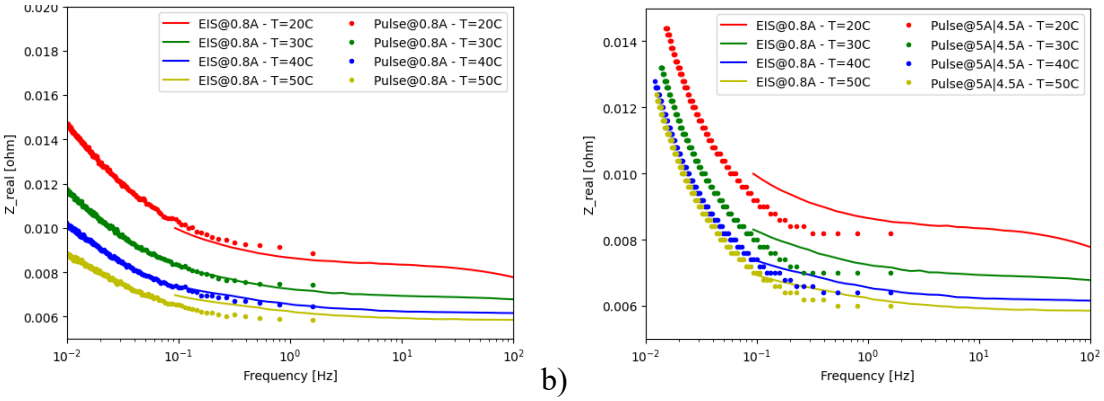

a) b)

Fig. 3. Values of Z_R, calculated from the voltage response to current pulses from a) Gamry potentiostat-galvanostat and b) Neware battery cycler. These values are compared with Z_R obtained from traditional EIS measurements. The results demonstrate a strong correlation between the impedance values derived from both pulse-based and EIS methods.

Furthermore, Fig. 4 highlights the inverse relationship between temperature and Z_R of the LIB. This established correlation aligns with existing understanding of LIB behavior. The observed consistency between the pulse-based and EIS-derived impedance values suggests that pulse measurements can effectively capture the underlying electrochemical processes and accurately reflect the LIB's internal state. However, it is crucial to acknowledge that this relationship might be influenced by factors such as the SoC, SoH and even specific battery chemistry. Future investigations will focus on the multi-variate dependencies of Z_R on these influences, aiming to develop more comprehensive models, such as machine learning models, which shall use to online internal temperature estimation in real-life applications.

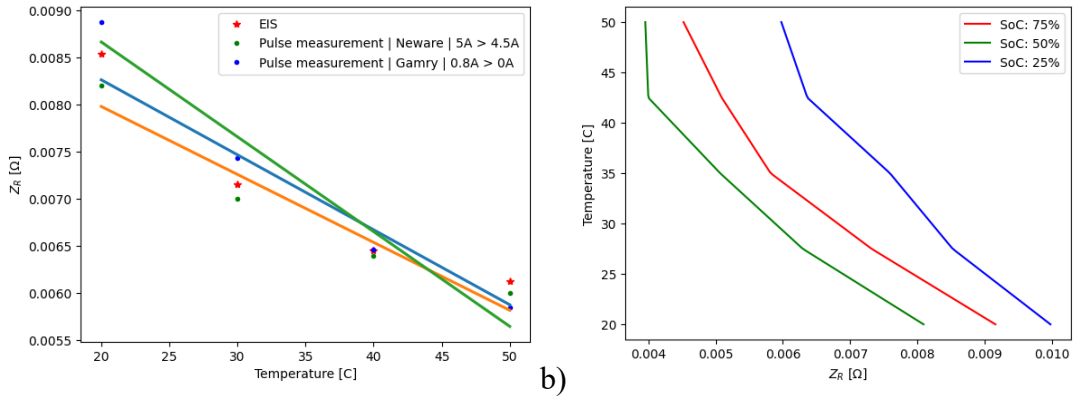

a) b)

Fig. 4. Z_R parameter value fits for given temperature levels and trendline approximation for the given temperature level a) for each experimental procedure scenario and b) for various SoC levels.

ISBN 978-80-69159-00-6

4. Discussion

The findings of this study support the feasibility of utilizing pulse measurements as a valuable tool for monitoring LIB internal temperature and condition in real-world scenarios. By supplementing traditional EIS measurements with pulse-based techniques, we can enhance the accuracy and reliability of battery management systems in real-life applications, ultimately contributing to the safer and more efficient operation of LIB-powered devices.

To further validate these promising results, subsequent experiments shall extend the pulse measurement methodology to a wider range of battery operating conditions, including temperature variations and high cycling rates. The plan is to conduct long-term cycling tests under dynamic load profiles, as the influence of ageing and degradation mechanisms on the PCP measurement shall be also investigated.

To fully leverage the potential of this approach, machine learning techniques shall be employed to process the pulse data and extract meaningful features related to temperature and battery condition. These machine-learning models will be trained on datasets collected and validated using independent test sets, enabling the development of adaptive and predictive BMSs that can ensure safety in real-time applications.

Acknowledgements

This work was funded by the EU NextGenerationEU through the Recovery and Resilience Plan for Slovakia under the project No. 09I04-03-V02-00028 (ENSAMAT), by the Ministry of Education, Science, Research, and Sport of Slovakia under the grant VEGA 1/0707/24, by the Slovak Research and Development Agency under grants APVV-20-0111 and APVV-22-0132 and university's internal grant ESG 23-03-15-A. This work was supported by an Industry Cooperation funded by Infineon Technologies Austria AG in the course of IPCEI Microelectronics.

References

[1] Meddings, N., Heinrich, M., Overney, F., Lee, J., Ruiz, V., Napolitano, E., Seitz, S., Hinds, G., Raccichini, R., Gaberšček, M., & Park, J. (2020). Application of electrochemical impedance spectroscopy to commercial Li-ion cells: A review. *Journal of Power Sources*, *480*, 228742.

[2] Lalinde, I., Berrueta, A., Soto, A., Arza, J., Sanchis, P., & Ursúa, A. (2023, June). Temperature Indicators and Overtemperature Detection in Lithium-Ion Batteries based on Electrochemical Impedance Spectroscopy. In *2023 IEEE 32nd International Symposium on Industrial Electronics (ISIE)* (pp. 1-6). IEEE.

[3] Rawat, S., Saini, D. K., Choudhury, S., & Yadav, M. (2024). Advanced Monitoring and Real-Time State of Temperature Prediction in Lithium-Ion Cells Under Abusive Discharge Conditions Using Data-Driven Modelling. *World Electric Vehicle Journal*, *15*(11), 509.

Enhancing Temperature Measurement Accuracy and Reliability in Nuclear Power Plants

[1]Orest Kochan, [1]Ivan Pytel, [2]Roman Borukh, [3]Jacek Majewski, [4,5]Roman Kobylianskyi, [3]Krzysztof Przystupa, [1]Mykola Beshley, [1]Iryna Petrovska

[1]Lviv Polytechnic National University, Ukraine;
[2]JSC Research and Production Association «Termoprylad», Lviv, Ukraine,
[3]Lublin University of Technology, Lublin, Poland,
[4]Institute of Thermoelectricity of the NAS and MES of Ukraine, Chernivtsi, Ukraine,
[5]Yuriy Fedkovych Chernivtsi National University, Chernivtsi, Ukraine
e-mail: orest.v.kochan@lpnu.ua

Abstract. *Thermocouples are used in nuclear power plants to measure temperature. Thermocouples are located in guide tubes. It is proposed to check the correctness of their installation in the guide tubes from their thermal transient response. The experimental studies show that the transient response of a correctly installed thermocouple is considerably lesser that that in case of improper installation. The time constant of the thermal transient response considerably depends on the thermocouple diameter. So the proposed method can be used to check the correctness of installation of thermocouples in guide tubes of the reactor of nuclear power plants.*

Keywords*: Nuclear Power Plant, Thermocouple, Time Constant, Thermal Transient, Loop Current Step Response Method.*

1. Introduction

The reactor of a nuclear power plant (NPP) generates thermal energy as a result of the nuclear fission reaction. This thermal energy heats the working body, which subsequently conveys the heat to a steam generator. It is essential to ensure efficient heat removal from the reactor core to prevent overheating. Temperatures are measured by thermocouples (TCs in fuel assemblies located across the core). The TC is placed in the cavity of the cylindrical part of the cassette head. The efficient and safe functioning of the reactor is largely determined by the reliability of monitoring over the fuel assemblies. The placement of TCs in the outlet of each fuel assembly is complicated. That is why, the question arises how to check the correctness of TC installation in the cassette head. The goal of this paper is to check the correctness of the TC installation in the guide tube using the value of time constant of thermal transient.

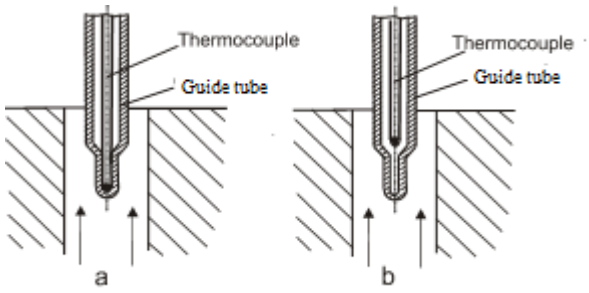

Fig. 1. Correct position of the TC's measuring junction in the guide tube (a); incorrect position of the TC in the guide tube (b).

ISBN 978-80-69159-00-6

A major problem is the complexity of installing TCs at the measurement positions. It is reasonable to install a TC in a special guide tube. The cross-section of the end of the guide tube and the TC is shown in Fig. 1.

When placing a new TC, it is pushed through this guide tube until it reaches the end, which is the correct destination of the TC. In this case, the TC is in close contact with the wall of the guide tube, which, in turn, is rinsed from the outside by the flow of coolant, whose temperature the TC measures. If the TC does not reach the end of the guide tube, there is no contact with the tube wall and therefore the TC does not measure the temperature of the coolant properly. One method for determining the contact between the hot junction of a TC and the guide tube is to measure the time constant (τ) of the TC by heating the sensing element and analyzing the response under operating conditions.

2. Methods for determining the dynamic characteristics of the TC

There are several methods to determine the dynamic characteristics of the TC:

1. Time series method. It is used to determine the dynamic characteristics of TCs. Time series spectrum allows examining frequencies of the process components. Using this method, it is possible to identify periodic components, oscillation amplitudes, and other dynamic characteristics of a signal. Another approach is the analysis of autocorrelation functions. This method allows identifying correlations between signal values at different instants. By analyzing the autocorrelation function, the nature of the signal's time changes and its periodicity can be determined.

2. Spectral analysis method [1]**.** This method is based on the decomposition of the signal into a spectrum, which allows analyzing frequency components of the signal. To apply the method to a TC, a time series of temperature measurements must first be obtained. This time series is then analyzed using spectral analysis techniques such as the Discrete Fourier Transform or Fast Fourier Transform. Once the spectrum a signal is obtained, its characteristics can be analyzed. The amplitude spectrum allows determining amplitudes of the signal's frequency components, and the phase spectrum allows determining the phase shift between different frequency components of the signal. Power spectral density allows determining the power distribution in a spectrum. This method can help identify dynamic characteristics of the TC, such as periodic oscillations, response time to temperature changes, and detection of any anomalies in the signal.

3. Induced temperature disturbance method. It is an effective way to determine the dynamic characteristics of the TC. It involves applying temperature changes in a controlled manner and measuring the response in the TC's thermopower [2]. The main idea is to introduce temperature disturbances that are induced in the system and to measure the corresponding changes in the output signal. Changes in the electrical signal can be analyzed to determine dynamic characteristics such as response time, stability, and sensitivity. This method can be used to evaluate the response of a TC to various temperature changes and to determine its dynamic properties. It allows to measure parameters such as TC response time to temperature changes and the degree of influence of external factors on the measurement.

4. Electrothermal analogy method. There is an analogy between thermal and electric systems [3]. The idea behind this method is to use the electric laws to solve problems in thermal systems. A temperature sensor is represented as an equivalent electrical circuit, where thermal parameters of the TC can be viewed analogously to electrical components like the resistor and the capacitor. Temperature corresponds to voltage, and the thermal flow corresponds to the electric current [4].

ISBN 978-80-69159-00-6

5. Loop Current Step Response (LCSR) Method. The method involves passing an electric current through the TC legs to heat the TC up to several degrees above the ambient temperature with Joule heat [5]. The heating current is then turned off, and the output of the TC is measured as it cools down. To avoid the influence of the Peltier effect alternating current is used.

3. Determining the TC installation contact in the measurement channel of a NPP

DSTU 2389-94 standardizes the parameters of test and measuring equipment for determining the dynamic characteristics of sensors, methods for experimentally determining the characteristics, methods for evaluating experimental results, and recommended formulas for describing the dynamic characteristics from models of thermal processes. According to this standard, the τ of the TC is defined as the time required to change the instantaneous value of a thermal transient process, which corresponds to a change in the output signal of the TC by 63.2% of its total change during a thermal transient process [3]. The implementation of such a method for determining the thermal transient response is simple and is recognized in international practice. The experiment for determining τ for the TC based on the heating of TC legs by the LCSR method under operating conditions is to determine the time required for the TC to reach a certain proportion (usually 63.2%) after a sudden temperature change that caused heating. For internal excitation, the output terminals of the TC are wired to a temperature stabilizer of the reference junction, and, through a signal switch, to a high-power AC voltage source to heat the TC legs. Parameters of the method are as follows: AC voltage up to 40V and the current up to 4 amps from a power supply. During the measurement of the thermopower, the AC voltage source is switched off and the TC output signal is switched to a measuring device that records the thermal transient response. A microcontroller computes the τ of the TC and the results are indicated on a display (Fig. 2). The sampling rate 10-100 Hz and total number of samples 200 - 1000. High noise immunity was ensured with the technique described in [6] The data were processed using the least squares method (LSM) to identify the τ of the TC.

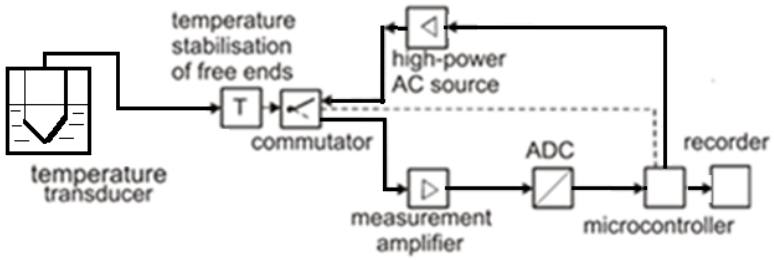

Fig. 2. Measurement system for determining the time constant of the thermocouple.

For this experiment, three TCs of type K (type TXA-1590) with the diameter of 3.5 mm and the length of 4.5 m with a simulator of the guide tube tip were used. The distance between the TC and the guide tube changed stepwise from 0 to 10 mm. The experiment was held in a non-stirred water bath. The results of the experiment are shown in Table 1.

Table 1 Time constant depending on the gap between the guide tube and the thermocouple.

Thermocouple number	Diameter of the bare TC wire, [mm]	The distance between the TC and the tip of the guide tube , [mm]/ Time constant, [s]			
		0	2	5	10
001ungrounded	0,5	5,6	8,4	9,0	18
002ungrounded	0,5	5,8	8,5	10	20
003grounded	0,3	3,2	4,8	5,1	7,6

ISBN 978-80-69159-00-6

The experimental results shows that inserting the tip into the TC (for ungrounded types) increases the time constant by the order of magnitude. Increasing the distance between the tip and the TC to 2 mm increases the τ further by approximately 50%, while the distance of 10 mm increases the τ by about 220% with respect to the τ with the tip. Similar results were obtained for grounded TCs. This indicates that the TCs respond more slowly to temperature changes when it is positioned farther from the guide tube tip. Table 2 shows the experimental data when measuring the time constant of TC of different diameters when steering water.

Table 2. Time constant of shielded TCs versus speed of water flow and diameter

Water flow speed, [m/s]	Percentage of the steady state [%]	Construction type	Thermocouple diameter, [mm] / Time constant, [s]		
			1,5	3,5	4,5
0,2	63,2	ungrounded	0,20	0,60	1,20
0,2	63,2	ungrounded	0,15	0,50	1,00
0,4	63,2	ungrounded	0,15	0,45	0,70
0,4	63,2	Grounded	0,10	0,34	0,45

From the Table 2, it is clear that for optimal use of the dynamic characteristics of TCs, it is important to take into account its diameter and speed of water. To validate the LCSR method, the time constant of the TC was measured directly under the same water flow conditions that were present during the LCSR test. The direct measurement (standard method) involved rapid immersion of the TC from one temperature to another. The data were processed using the LSM.

4. Conclusions

The LCSR method is relatively easy to implement, does not require sophisticated equipment, and allows for an accurate determination of the time constant of the TC. The magnitude of time constant allows determining if the TC is installed properly or no in the guide tube of the reactor of a NPP. The method allows the results to be quickly and relatively easily obtained compared to other methods.

References

[1] Puzdrowska, P. (2018). Method of Determining the Time Constant of Thermocouple Based on Measurement of the Quick – Changing Temperatures of Exhaust Gases in Marine Diesel Engines. Scientific Journal of Gdynia Maritime University. 108, 115–133

[2] Sharma, P., et al. (2014). Effect of thermocouple time constant on sensing of temperature fluctuations in a fast reactor subassembly. *Journal of Sensors and Sensor Systems*, *3*(1), 55-60.

[3] Sarnes, B., Schrüfer, E. (2007). Determination of the time behaviour of thermocouples for sensor speedup and medium supervision. *Proc. Estonian Acad. Sci. Eng*, *13*(4), 295-309.

[4] Gavrysh, V., et al. (2017). Mathematical model of thermal conductivity for piecewise homogeneous elements of electronic systems. In *14th International Conference The Experience of Designing and Application of CAD Systems in Microelectronics (CADSM)* (pp. 333-336).

[5] Jun, S., Kochan, O., & Kochan, R. (2016). Thermocouples with built-in self-testing. *International journal of thermophysics*, *37*(4), 37.

[6] Jun, S., & Kochan, O. (2015). Common mode noise rejection in measuring channels. *Instruments and Experimental Techniques*, *58*, 86-89.

ISBN 978-80-69159-00-6

Concept of Using Cloud to Improve Accuracy and Metrological Reliability of IoT Based Data Acquisition Systems

[1]Bogdan Maslyiak, [2]Mykola Beshley, [1]Nataliia Vozna, [1]Andriy Segin, [2]Roman Kochan, [3]Jacek Caban, [2]Halyna Beshley, [1]Valerii Yeromenko, [4,5]Roman Kobylianskyi

[1]West Ukrainian National University, Ternopil, Ukraine
[2]Lviv Polytechnic National University, Lviv, Ukraine
[3]Lublin University of Technology, Lublin, Poland
[4]Institute of Thermoelectricity of the NAS and MES of Ukraine, Chernivtsi, Ukraine;
[5]Yuriy Fedkovych Chernivtsi National University, Chernivtsi, Ukraine;
Email: roman.v.kochan@lpnu.ua

Abstract. *This paper presents a conceptual system for collecting and storing measurement data in Cloud to enhance the metrological characteristics of IoT sensors. The influence of operating conditions on signal drift and measurement accuracy is analyzed, and an adaptive method for determining the intercalibration period (ICP) is developed. A predictive algorithm for changes in metrological characteristics is proposed based on historical data, statistical methods, and machine learning techniques. The system utilizes cloud technologies for centralized data analysis and adaptive calibration interval adjustment, reducing sensor maintenance costs and improving measurement accuracy. It is demonstrated that predictive modeling enables the extension of the intercalibration period without compromising accuracy. The findings are particularly relevant for decentralized IoT systems where physical calibration is challenging or costly. The use of cloud platforms for data collection and analysis allows real-time detection of deviations and measurement error correction, contributing to improved efficiency and reliability of measurement systems.*

Keywords: Measurement Information, Metrological Characteristics, Intercalibration Interval, IoT Sensors, Cloud.

1. Introduction

In today's technological environment, where Internet of Things (IoT) systems are becoming widespread, sensors play a key role as a source of primary information. Data collected from sensors is used to make decisions in various industries: from agricultural production to medicine, from environmental monitoring to industrial critical infrastructure. However, as the lifetime of sensors increases and environmental conditions change, the problem of measurement accuracy decreases due to degradation, drift of metrological characteristics, and accumulation of errors. Traditionally, sensor calibration is performed periodically at fixed intervals, which does not take into account individual operating conditions. This approach is ineffective in distributed IoT systems, where the same type of sensors operate in different climatic, mechanical, or electromagnetic conditions. Accordingly, there is a need to develop an intelligent system that would adaptively determine the calibration time based on the analysis of the actual sensor behavior. The creation of such a system becomes especially relevant in conditions of a large number of sensors and limited access to them. In this paper, we propose a conceptual approach based on developing a distributed system that analyzes large amounts of sensor data, monitors their errors, records manual calibration events, and trains a neural network to predict future deviations. As a result, the system is able to recommend the calibration time for each device individually, taking into account its current state and conditions [1].

ISBN 978-80-69159-00-6

2. Materials and Methods

The primary metrological characteristics of measurement transducers (sensors) include the measurement range, measurement error (both primary and additional), reliability, and several other parameters. One of the most critical metrological characteristics is the intercalibration interval, as it defines the period during which a measurement transducer can maintain its specified measurement accuracy. This parameter depends on the stability of the device's metrological properties, its operating conditions, and the accuracy requirements in a specific application field. The more stable the sensor's characteristics, the longer the intercalibration interval can be. However, harsh operating conditions, such as elevated temperature, humidity, or mechanical stress, can gradually increase measurement error, thereby reducing the interval between calibrations. In industrial and scientific applications, the intercalibration interval is determined both based on manufacturer recommendations and following regulatory documents and standards. Modern Cloud technologies and predictive systems enable the forecasting of measurement error trends and the determination of the optimal intercalibration interval based on real-time sensor data analysis. The development of this comprehensive measurement data processing system involves selecting data for predicting measurement error trends and determining the intercalibration interval in a way that best corresponds to the operating conditions of the given sensor and IoT device [2] – Figure 1.

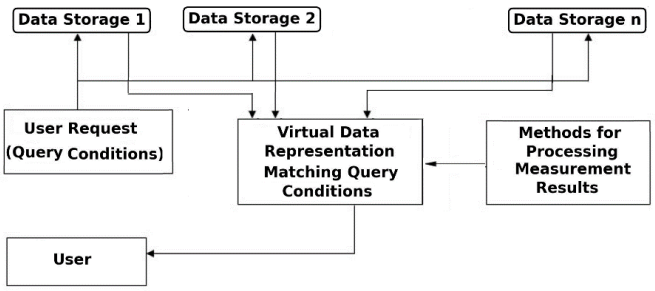

Fig. 1. Conceptual system of cloud-based measurement data processing to ensure accuracy and metrological reliability in distributed IoT systems.

According to the information processing scheme presented in Figure 1, upon a user request, sensor readings that match the operating conditions of the given IoT device are selected. This data selection is performed across all available storage sources. Based on the retrieved data, a virtual table is created, which, after processing, generates individual sensor drift values and evaluates measurement variations for the user. As the primary methods for data processing (block: "Methods for Processing Measurement Results"), statistical approaches are proposed, including:

- Linear regression – used to predict measurement error changes based on time dependence or other influencing factors;
- Polynomial regression – enables modeling of nonlinear error variation trends;
- Moving average methods (SMA, EMA) – help smooth measurement noise and assess overall trends;
- Error distribution analysis – allows determining the nature of error changes and identifying systematic biases.

The paper proposes an algorithm for a distributed intelligent system that combines data from a large number of sensors, monitors their errors, records manual calibration events, and uses a neural network to predict individual deviations over time (Figure 2). The following notations are used in Figure 2: Nm - number of measurements, V_L - limit value. As a result, the system

is able to dynamically determine the calibration time for each sensor individually, taking into account its current state, measurement history, and operating conditions.

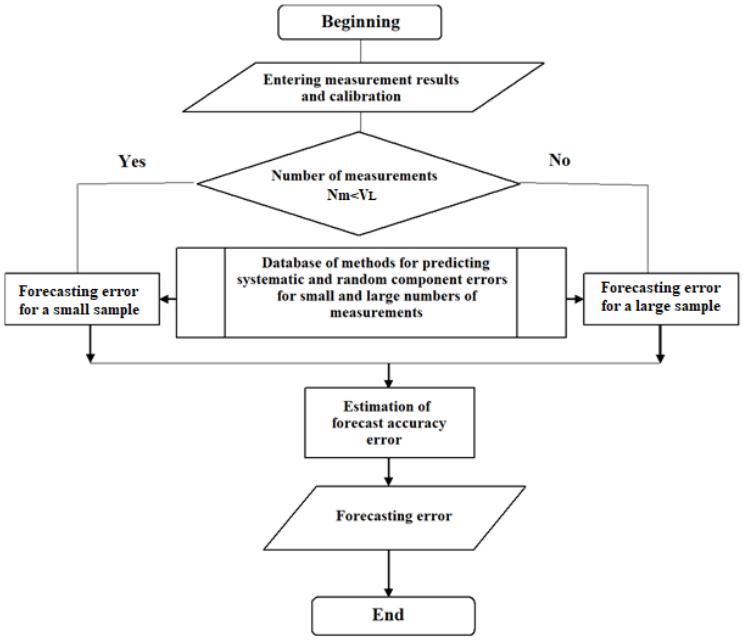

Fig. 2. Block diagram of the algorithm for error prediction assessment based on different measurement sample sizes and forecasting methods.

The determination of a sensor's intercalibration period (ICP) is based on analyzing the variation in its measurement error over time and predicting the moment when this error exceeds the acceptable threshold. This process relies on historical calibration data, sensor operating parameters, and established regulatory accuracy requirements. At the first stage, a mathematical model describing the sensor's error variation is developed. Various approaches are used for this purpose, including regression analysis, stochastic models, or machine learning techniques. The model is trained on previous calibration measurements and operational data, allowing it to account for factors such as temperature influence, load variations, and the sensor's natural drift.

Let us consider a set of identical sensors $S = \{S_1, S_2, \dots, S_n\}$, where each sensor S_i generates data $y_i(t)$ at time t, and is characterized by a set of environmental parameters $X_i(t) = [x_{i1}(t), x_{i2}(t), \dots, x_{im}(t)]$.

The measurement error is defined as:

$$\varepsilon_i(t) = y_i(t) - y_{\text{ref}}(t), \tag{1}$$

where $y_{\text{ref}}(t)$ is the reference or approximated value.

For analysis and forecasting, we use the dataset:

$$D_i = \{\big(X_i(t), \varepsilon_i(t), c_i(t)\big)\}_{t=1}^{T}, \tag{2}$$

where $c_i(t) = 1$ indicates a manual calibration event at time t.

The neural network model NN_θ implements the prediction function:

$$\hat{\varepsilon}_i(t+k) = \text{NN}_\theta\big(X_i(t), \varepsilon_i(t)\big), \tag{3}$$

which enables forecasting of future error deviation.
The moment when the predicted error exceeds a predefined threshold $\varepsilon_{\max}$ is considered optimal for calibration:

$$t_{\text{ICP}} = \min\{t: \hat{\varepsilon}_i(t) \geq \varepsilon_{\max}\}. \tag{4}$$

ISBN 978-80-69159-00-6

Once the prediction of measurement error is obtained, the intercalibration period (ICP) is defined as the shortest among several possible intervals. This value is determined by two factors:

1. The moment when the predicted sensor error exceeds the acceptable threshold.
2. Manufacturer guidelines and operational experience with similar sensors.

3. Results

The proposed methodology allows you to optimize the intervals between calibrations, increase accuracy, and reduce maintenance costs. Since prediction accuracy can vary over time, the ICP is adjusted dynamically. As new operational data becomes available, the predictive model is updated, and the ICP is recalculated to ensure continued reliability.

To address the challenges of distributed sensor environments, the following strategies are recommended:

- Cloud-Based Data Processing – Aggregates sensor data from across the network in a centralized environment for consistent analysis.
- Adaptive Algorithms for Error Prediction – Tailor forecasts to each device's conditions, enabling real-time adjustment to environmental and operational changes.
- Standard-Free Calibration Techniques – Extend ICP using internal reference comparisons, reducing reliance on centralized calibration procedures.

Distributed Databases – Support scalable storage and real-time processing of large volumes of sensor data across the network.

Based on the constructed model, future error variations are predicted. This enables the determination of when the sensor may lose accuracy and start exceeding permissible limits. A critical aspect is the calculation of the moment in time when the predicted error surpasses the established threshold. This moment defines the recommended ICP.

In decentralized Internet of Things (IoT) networks, enhancing error prediction, tracking measurement variations, and extending ICPs are essential for system reliability and maintenance efficiency.

These approaches enable autonomous, accurate, and scalable sensor maintenance across decentralized IoT ecosystems.

4. Conclusions

The proposed conceptual approach effectively addresses the limitations of decentralized IoT environments by combining predictive analytics with adaptive calibration strategies. It enhances the efficiency of network management, improves the accuracy of sensor measurements, and minimizes the need for frequent recalibration. By determining the optimal intercalibration period for each sensor based on real-time data and forecasted deviations, the approach ensures sustained measurement reliability while reducing maintenance efforts and associated costs.

References

[1] Guth, J. et al. (2018). A Detailed Analysis of IoT Platform Architectures: Concepts, Similarities, and Differences. In: *Di Martino, B., Li, KC., Yang, L., Esposito, A. (eds) Internet of Everything*. Internet of Things. Springer, Singapore.

[2] N. Vozna, B. Maslyak, I. Mamuzić Ontological approach to creating subject-oriented technologies in the fi eld of IoT. *Metallurgy and related tropics: Proceedings of 18th symposium „Materials and metallurgy"*. SHMD´2025, Croatia (published in: Metalurgija 64 (2025) 1-2). – P. 233-242.

Evaluation of Fat Suppression Effect on Evaluation of T_2^* Components in Achilles Tendons.

[1]P. Latta, [1]M. Kojan, [1]L. Vojtíšek, [2]Z. Starčuk Jr., [1,2]A. Malá, [3]V. Juras

[1]Central European Institute of Technology, Masaryk University, Brno, Czech Republic
[2]Inst. of Scientific Instruments, Czech Academy of Sciences, Brno, Czech Republic
[3]High Field MR Centre, Department of Biomedical Imaging and Image-Guided Therapy, Medical University of Vienna
Email: lattape@gmail.com

Abstract. *This study evaluates the impact of fat suppression on the bi-exponential T_2^* analysis of the Achilles tendon. Healthy volunteers underwent ultrashort echo time magnetic resonance imaging (UTE MRI) using both fat-suppressed and fat-unsuppressed acquisition methods. Our results showed statistically significant differences ($P < 0.001$) in the short- T_2^* and long- T_2^* component intensities between the two methods, with intensity variations ranging from 0.65 to 0.86. These differences likely result from fat suppression altering longitudinal magnetization, which predominantly affects the short- T_2^* component. These findings suggest that a tricomponent approach without fat suppression may offer a more accurate and unbiased assessment of the T_2^* composition of the Achilles tendon.*

Keywords: Achilles' Tendon, Ultrashort Echo Time (UTE), Fat Suppression

1. Introduction

In recent years, ultrashort echo time (UTE) imaging has emerged as a powerful technique for visualizing tissues with very short T_2^* relaxation times [1,2]. This method is particularly well-suited for musculoskeletal (MSK) imaging, as tissues such as cartilage, cortical bone, tendons, and ligaments exhibit very short transverse relaxation times.

A crucial aspect of MSK imaging is the use of fat suppression techniques to eliminate signal contamination from surrounding subcutaneous lipid structures, which might otherwise obscure the water signal from tissues of interest [3]. However, a common drawback of conventional fat suppression using chemical shift saturation is the accompanying partial attenuation of short- T_2^* signals, which can distort signal composition analysis [4].

To address this limitation, various strategies have been explored, including optimized composite fat suppression RF pulses [5], single-point Dixon fat suppression [6], and 3D-UTE with tri-component analysis [7].

The objective of this study is to investigate the impact of fat suppression on the quantification of short- and long-T_2^* components and to evaluate whether this effect can be mitigated using tri-component analysis. We hypothesize that tri-component analysis may provide a more precise and unbiased characterization of the T_2^* components of the Achilles tendon in vivo.

2. Subject and Methods

The experiments were conducted using a clinical whole-body 3T MRI system (Magnetom Prisma; Siemens Medical Solutions, Erlangen, Germany). A custom time-interleaved 2D-UTE pulse sequence with slice profile correction was used for this study [8]. A single sagittal and a single axial slice were acquired using the following parameters: FOV = 170 mm, TR = 60 ms,

ISBN 978-80-69159-00-6

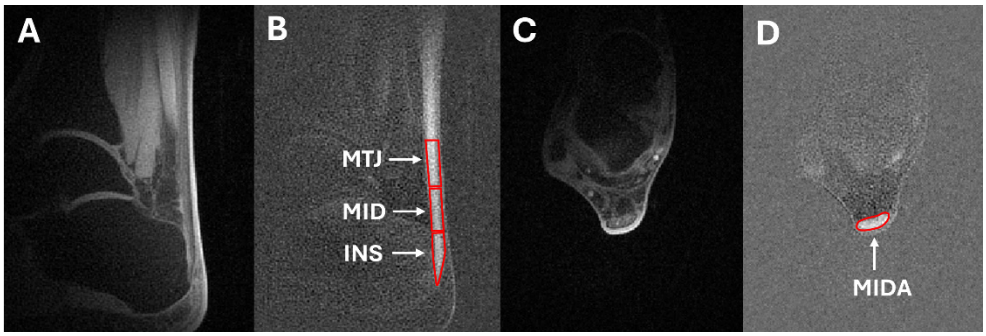

Fig. 1. Examples of 2D-UTE fat-suppressed images of the Achilles tendon in sagittal (A) and axial (C) views. Region-of-interest (ROI) placements - including the insertion part (INS), middle part (MID), muscle-tendon junction (MTJ), and middle part axial (MIDA) - are shown on the differential images (B) and (D). These differential images were obtained by subtracting images acquired at TE = 60 µs and TE = 800 µs.

flip angle (FA) = 25°, 64 echoes with echo times ranging from 60 µs to 35.2 ms, and a total scan time of 6:23 minutes. Each measurement was performed twice: once with the fat saturation module enabled and once without. Image reconstruction and data processing were performed offline using custom MATLAB (The MathWorks, Natick, MA, USA) routines.

Ten healthy volunteers (3 males, 7 females; mean age: 33.3 ± 6.9 years) with no history of Achilles tendon injury participated in the study. Institutional approval was obtained, and all participants provided written informed consent before the study.

The magnitude signal was calculated as the mean intensity within a region of interest (ROI) and was then fitted using the following two models:

Bicomponent model - this model was applied to fat-suppressed magnitude data and is described by the following equation:

$$|s(t_n)| = A_S e^{-\frac{t_n}{T_{2S}^*}} + A_L e^{-\frac{t_n}{T_{2L}^*}} + C \quad (1)$$

where A_S, A_L represents fractions of the short T_{2S}^* and long T_{2L}^* relaxation components, respectively, and the parameter C accounts for noise.

Tricomponent model - this model was applied to fat-unsuppressed data and is given by the following equation:

$$|s(t_n)| = \left(A_S e^{-\frac{t_n}{T_{2S}^*}} + A_L e^{-\frac{t_n}{T_{2L}^*}} + \left(A_F \sum_{p=1}^{P} \alpha_p \, e^{i2\pi f_p t_n} \right) e^{-\frac{t_n}{T_{2F}^*} + i2\pi \Delta f_{WF} t_n + \Delta P_{WF}} \right) + C \quad (2)$$

The fat signal is represented as a sum of relative amplitudes α_p, where $\sum_{p=1}^{P} \alpha_p = 1$, each associated with specific frequency shifts f_p. The parameter A_F represents the total fat fraction with a common T_{2F}^* relaxation rate. The fat model parameters were set up according to Ren's study [9]. The subcutaneous fat fraction typically originates outside the selected slice and, due to B_0 field inhomogeneity, may experience an additional frequency shift between water and fat, which is accounted for by the Δf_{WF} parameter [10]. The parameter ΔP_{WF} represents the accrued phase difference between the water and fat signals during HP VERSE RF excitation. Compared to the bicomponent model, this model introduces four additional parameters, resulting in a total of nine parameters.

Examples of manually drawn ROIs used for analysis are shown in Fig. 1. Signal fitting was performed using a nonlinear data-fitting algorithm (lsqnonlin in MATLAB).

ISBN 978-80-69159-00-6

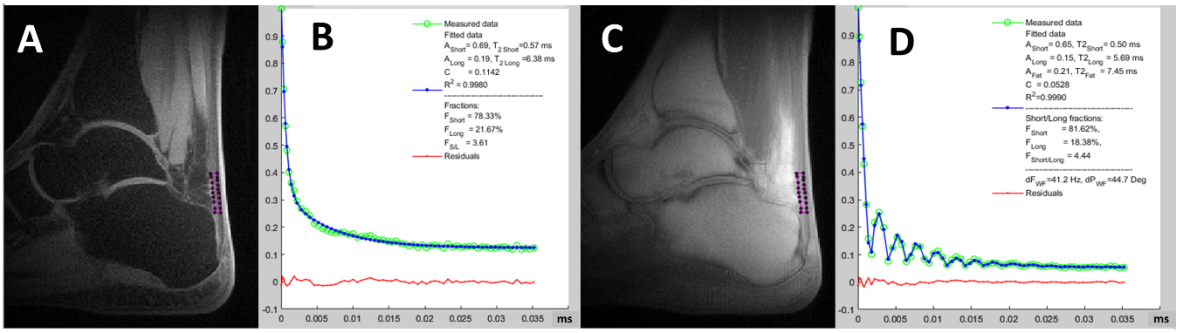

Fig. 2. Typical examples of T_2^* analyses for UTE images acquired with fat (A) and without fat suppression (C). The ROI was positioned over the middle part of the Achilles tendon, and multi-echo data fitted with a bicomponent (B) and tricomponent model (D).

3. Results

Figure 2 shows the results from bicomponent and tricomponent model fitting for an ROI selected in the mid part of the Achilles tendon. The relative abundance of short- and long-T_2^*components in the tendon can be expressed as the component fraction, defined as follows:

$$R_{SL} = \frac{A_S}{A_L} \tag{3}$$

Both types of analyses can be compared using the fraction ratio (FR), defined as:

$$FR = \frac{(R_{SL})_{2-comp}}{(R_{SL})_{3-comp}} \tag{4}$$

The results of the group analysis using both models are shown in Fig. 3. Figure 3(A) clearly demonstrates a considerably lower abundance of short-T_2^* components in fat-suppressed data, with FR values ranging from 0.65 to 0.86 across all examined ROIs. The results of the study are summarized in Table 1.

A Wilcoxon matched-pairs test was performed to compare the fat-suppressed and fat-unsuppressed experimental datasets, confirming significant differences between the groups ($p < 0.001$).

3. Discussion

The purpose of this study was to compare the performance of T_2^* analysis using two distinct approaches to address fat contamination of the measured water signal: (1) experimentally suppressing the fat signal during acquisition or (2) separating the fat signal during data analysis. We found that off-resonance fat oscillation can be reliably targeted using the tricomponent

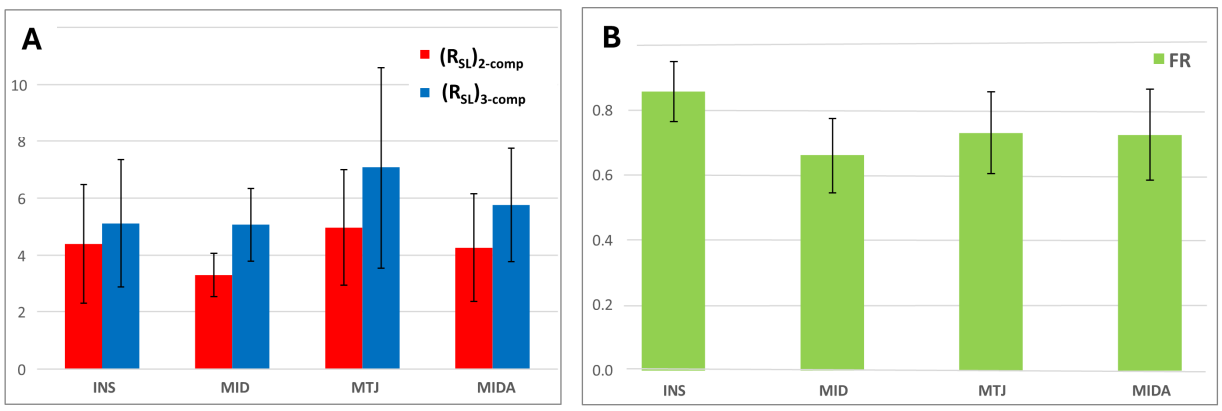

Fig. 3. Results of group analysis: Component fractions obtained from the bicomponent and tricomponent models are shown in (A), and the fraction ratio (FR) is plotted in (B).

ISBN 978-80-69159-00-6

Table 1. Summary of fraction ratios and short- and long-T_2^* components, presented as mean values ± standard deviations, obtained from both types of analyses (fat-suppressed and fat-unsuppressed datasets).

	Bicomponent Analyses				Tricomponent Analyses			
	INS	MID	MTJ	MIDA	INS	MID	MTJ	MIDA
SL	4.38±2.09	3.3±0.77	4.96±2.04	4.25±1.9	5.11±2.24	5.06±1.26	7.07±3.52	5.76±1.98
T_{2S}^*	0.58±0.11	0.54±0.13	0.55±0.26	0.54±0.09	0.62±0.16	0.51±0.11	0.58±0.24	0.59±0.08
T_{2L}^*	6.46±1.23	8.39±2.73	7.92±1.32	8.36±0.71	6.5±1.18	8.24±2.26	9.75±1.73	11.6±1.53

model, as previously suggested [7]. To improve the reliability and robustness of the tricomponent model, two additional parameters were introduced (see Eq. 2). Data analysis demonstrated that fat suppression tends to result in a lower FR, potentially underestimating the short-T_2^* fractions. However, a limitation of this study is that the experimental data were acquired from only a single slice.

4. Conclusions

The results of the study demonstrate that the experimental setup and methodology are suitable for in vivo examination. Additionally, the tri-component approach has the potential to provide more realistic information about the T_2^* composition of the Achilles tendon.

Acknowledgements

This work was funded by the Czech Science Foundation grant no. GF25-19984L. Also, this research was funded in whole or in part by the Austrian Science Fund (FWF) 10.55776/PIN5555423. We acknowledge the core facility MAFIL supported by MEYS CR (LM2023050 Czech-BioImaging), part of the Euro-BioImaging (www.eurobioimaging.eu) ALM and Multimodal Imaging Node (Brno, CZ).

References

[1] Juras V, Zbyn S, Pressl C, Valkovic L, Szomolanyi P, Frollo I, et al. Regional variations of T2* in healthy and pathologic achilles tendon in vivo at 7 Tesla: Preliminary results. Magnetic Resonance in Medicine 2012;68:1607–13. https://doi.org/10.1002/mrm.24136.

[2] Juras V, Apprich S, Szomolanyi P, Bieri O, Deligianni X, Trattnig S. Bi-exponential T2* analysis of healthy and diseased Achilles tendons: an in vivo preliminary magnetic resonance study and correlation with clinical score. Eur Radiol 2013;23:2814–22. https://doi.org/10.1007/s00330-013-2897-8.

[3] Del Grande F, Santini F, Herzka DA, Aro MR, Dean CW, Gold GE, et al. Fat-Suppression Techniques for 3-T MR Imaging of the Musculoskeletal System. RadioGraphics 2014;34:217–33. https://doi.org/10.1148/rg.341135130.

[4] Carl M, Nazaran A, Bydder GM, Du J. Effects of fat saturation on short T2 quantification. Magnetic Resonance Imaging 2017;43:6–9. https://doi.org/10.1016/j.mri.2017.06.007.

[5] Ma Y-J, Jerban S, Jang H, Chang EY, Du J. Fat suppression for ultrashort echo time imaging using a novel soft-hard composite radiofrequency pulse. Magnetic Resonance in Medicine 2019;82:2178–87. https://doi.org/10.1002/mrm.27885.

[6] Jang H, Carl M, Ma Y, Jerban S, Guo T, Zhao W, et al. Fat suppression for ultrashort echo time imaging using a single-point Dixon method. NMR in Biomedicine 2019;32:e4069. https://doi.org/10.1002/nbm.4069.

[7] Lu X, Jerban S, Wan L, Ma Y, Jang H, Le N, et al. Three-dimensional ultrashort echo time imaging with tricomponent analysis for human cortical bone. Magnetic Resonance in Medicine 2019;82:348–55. https://doi.org/10.1002/mrm.27718.

[8] Latta P, Starčuk Z, Kojan M, Gruwel MLH, Tomanek B, Trattnig S, et al. Simple compensation method for improved half-pulse excitation profile with rephasing gradient. Magnetic Resonance in Medicine 2020;84:1796–805. https://doi.org/10.1002/mrm.28233.

[9] Ren J, Dimitrov I, Sherry AD, Malloy CR. Composition of adipose tissue and marrow fat in humans by 1H NMR at 7 Tesla. J Lipid Res 2008;49:2055–62. https://doi.org/10.1194/jlr.D800010-JLR200.

[10] Dong Y, Koolstra K, Riedel M, van Osch MJP, Börnert P. Regularized joint water–fat separation with B0 map estimation in image space for 2D-navigated interleaved EPI based diffusion MRI. Magnetic Resonance in Medicine 2021;86:3034–51. https://doi.org/10.1002/mrm.28919.

Image Similarity Measures for Autocorrelation Maps Comparison

Anna Přibilová, Jana Švehlíková

Institute of Measurement Science, Slovak Academy of Sciences, Bratislava, Slovakia,
Email: anna.pribilova@savba.sk

Abstract. *Autocorrelation maps (ACMs) determined from body surface potential maps are compared with those determined from the standard 12-lead electrocardiogram. Five image similarity measures (mean square error, mean absolute error, cross-correlation coefficient, structural similarity index, multi-scale structural similarity index) are used to evaluate similarity between 148 ACM pairs. The relative range of the measures is low, and their relative mean position is close to the theoretical value of the highest similarity.*

Keywords: Body Surface Potential Maps, Standard 12-Lead Electrocardiogram, Autocorrelation Maps, Image Similarity Measures

1. Introduction

Body surface potential maps (BSPMs) have long been used either for direct analysis and interpretation or for the solution of an inverse problem leading to the reconstruction of the cardiac source. Recording of BSPMs is usually carried out using 64 to 300 electrodes placed throughout the torso surface [1] that allow for better evaluation of the measured signals when compared with the standard 12-lead electrocardiogram (ECG) using ten electrodes.

One approach to BSPM processing uses autocorrelation maps (ACMs) consisting of correlation coefficients for every pair of the BSPMs in a given time interval [2]. Recently, it has been shown that the ACMs of the QRS complex may represent a promising tool to optimize cardiac resynchronization therapy (CRT) device timing settings [3]. The current ACM and/or its selected parameters could be displayed during the setting of stimulation timing of different parts of the heart, or eventually after changing the position of stimulation electrodes. However, a great number of body surface electrodes would be rather cumbersome in such a clinical situation.

In this study, we compare ACMs from BSPMs of 128 leads and ACMs from ECGs of 12 leads using image similarity criteria to find out whether the standard ECG could be used instead of the output of a multi-channel measuring system to create the ACMs.

2. Subject and Methods

The ACM is a visualization of the autocorrelation matrix computed from the signal matrix with signals arranged in rows and time samples arranged in columns. For the BSPMs, the columns represent individual surface maps during the whole QRS complex; for the standard 12-lead ECG, the columns represent “snapshots” of 12 ECG signal samples at the same time instants as the surface maps. The BSPMs are measured together with limb leads, and then the signals of precordial leads are determined by interpolation among the nearest torso leads. In both cases (BSPM, 12-lead ECG), the autocorrelation matrix is a square matrix of the order given by the number of signal samples within the examined time interval. The measurements were done at our institute for 33 healthy subjects and at the National Institute of Cardiovascular Diseases [3] for 115 various modes of CRT in 25 heart failure patients, so 148 signal-averaged QRS complexes were analyzed. An example of the ACM from the BSPMs of a healthy volunteer with a QRS duration of 100 ms in three image representations is shown in Fig. 1.

ISBN 978-80-69159-00-6

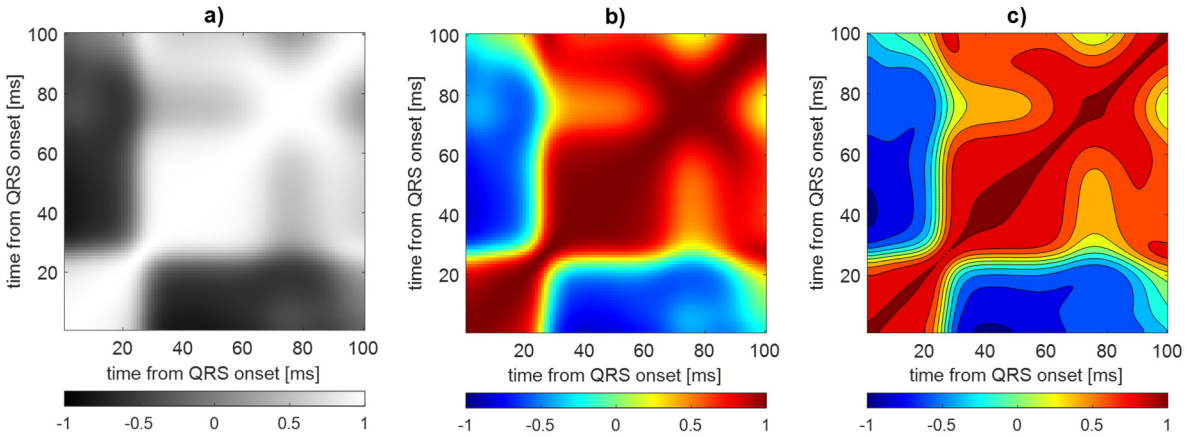

Fig. 1. ACM of a healthy volunteer H013 as: a) grayscale image with the highest positive value white and the lowest negative value black, b) color image with the highest positive value red and the lowest negative value blue, c) color contour plot with contour intervals of 0.2 and highlighted values greater than 0.995.

Various image similarity measures (ISMs) can be used for grayscale image comparison. We can use global similarity measures requiring spatial alignment of the two input images to compare ACMs from BSPMs of 128 leads and from ECGs of 12 leads. Mean square error *mse*, mean absolute error *mae*, and cross-correlation coefficient ρ are defined [4] as follows

$$mse = \sum_k \frac{(x_k - y_k)^2}{K}, \qquad mae = \sum_k \frac{|x_k - y_k|}{K}, \qquad \rho = \frac{\sum_k (x_k - \mu_x)(y_k - \mu_y)}{\sqrt{\sum_k (x_k - \mu_x)^2 \sum_k (y_k - \mu_y)^2}}, \tag{1}$$

where x_k and y_k are gray levels of the k-th pixel, μ_x, μ_y are mean gray levels of images **x** and **y**.

More elaborate image similarity criteria compare local patterns of pixel gray levels (intensities) that have been normalized for luminance and contrast as structural similarity index *ssim* [5]

$$ssim = \frac{(2\mu_x\mu_y + C_1)(2\sigma_{xy} + C_2)}{(\mu_x^2 + \mu_y^2 + C_1)(\sigma_x^2 + \sigma_y^2 + C_2)} \tag{2}$$

where, σ_x, σ_y, and σ_{xy} are the standard deviations and cross-covariance of the images **x** and **y**. Constants C_1 and C_2 depend on the dynamic range of the image.

Multi-scale structural similarity index *multissim* [6] incorporates image details at different resolutions and combines the measurement at different scales

$$multissim = |l_M(\mathbf{x},\mathbf{y})|^{\alpha_M} \prod_{j=1}^{M} |c_j(\mathbf{x},\mathbf{y})|^{\beta_j} \, |s_j(\mathbf{x},\mathbf{y})|^{\gamma_j}, \tag{3}$$

where $c_j(\mathbf{x},\mathbf{y})$ and $s_j(\mathbf{x},\mathbf{y})$ are the contrast comparison and the structure comparison at the j-th scale and $l_M(\mathbf{x},\mathbf{y})$ is the luminance comparison at scale M.

We evaluated ISMs with regard to their theoretical range $t_{max} - t_{min}$. For *mse* and *mae*, the theoretical minimum t_{min} corresponds to the greatest possible similarity (two identical ACMs) and its value is $t_{min} = 0$. For ρ, *ssim*, and *multissim*, the theoretical minimum corresponds to the greatest dissimilarity (one ACM with the values 1, another one with the values -1). Its value is $t_{min} = -1$ for ρ and *ssim*, and $t_{min} = 0$ for *multissim*. The real range of ISMs is bounded by the maximum r_{max} and the minimum r_{min} of all ACM pairs. The relative real range is calculated as $r_{range\ rel} = 100\ (r_{max} - r_{min}) / (t_{max} - t_{min})$ [%]. We calculate also the mean r_{mean} and the standard deviation r_{std} of all ACM pairs. Then the relative mean position is given by a relative distance between the r_{mean} and the border of the theoretical range corresponding to the maximum similarity. It means that for *mse* and *mae* the relative mean position can be calculated by the

relation $r_{mean\ rel} = 100\ (r_{mean} - t_{min}) / (t_{max} - t_{min})$ [%] or $r_{mean\ rel} = 100\ r_{mean} / t_{max}$ [%]. For ρ, *ssim*, and *multissim* the relative mean position is $r_{mean\ rel} = 100\ (t_{max} - r_{mean}) / (t_{max} - t_{min})$ [%].

3. Results

Evaluation of five ISMs for all 148 ACM pairs of 128 and 12 lead ECGs relatively to their theoretical range is shown in Table 1.

Table 1. ISMs, their ranges, and basic statistical values (t – theoretical, r – real) for 148 ACM pairs.

ISM	*mse*	*mae*	ρ	*ssim*	*multissim*
$[t_{min}, t_{max}]$	[0, 4]	[0, 2]	[–1, 1]	[–1, 1]	[0, 1]
$[r_{min}, r_{max}]$	[**.0004**, *.4779*]	[**.0106**, *.3709*]	[*.682*, **.999**]	[*.436*, **.993**]	[*.613*, **.987**]
$r_{range\ rel}$ [%]	11.938	18.015	15.820	27.859	37.457
$r_{mean} \pm r_{std}$	.0283 ± .0481	.0951 ± .0565	.955 ± .046	.831 ± .120	.894 ± .068
$r_{mean\ rel}$ [%]	0.708	4.757	2.253	8.453	10.572

4. Discussion

In Table 1, we can see that the trend for the relative range $r_{range\ rel}$ and the relative mean position $r_{mean\ rel}$ is the same: the lowest to the highest values are in the order of ISMs: *mse*, ρ, *mae*, *ssim*, *multissim*. The relative range of the *mse* reaches 12 % of the theoretically possible range and its relative mean position is only 0.7 % from the value of the best theoretically possible similarity. On the other hand, the relative range of 38 % and the relative mean position of 10.6 % for the *multissim* are still acceptable values. Figs 2 to 4 show the ACM pairs for those cases (out of all 148 cases) giving a) the best similarity corresponding to $[r_{min}, r_{max}]$ values in bold in Table 1, and b) the worst similarity corresponding to $[r_{min}, r_{max}]$ values in italic in Table 1.

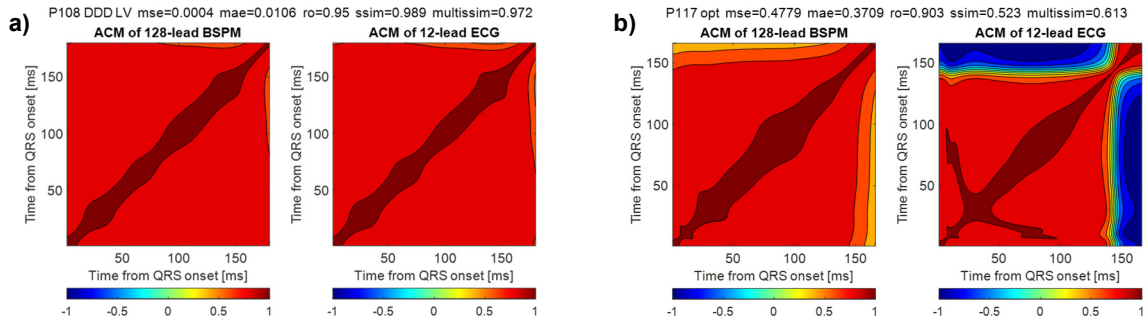

Fig. 2. ACM pairs with the best similarity by *mse*, *mae* (a) and the worst similarity by *mse*, *mae*, *multissim* (b).

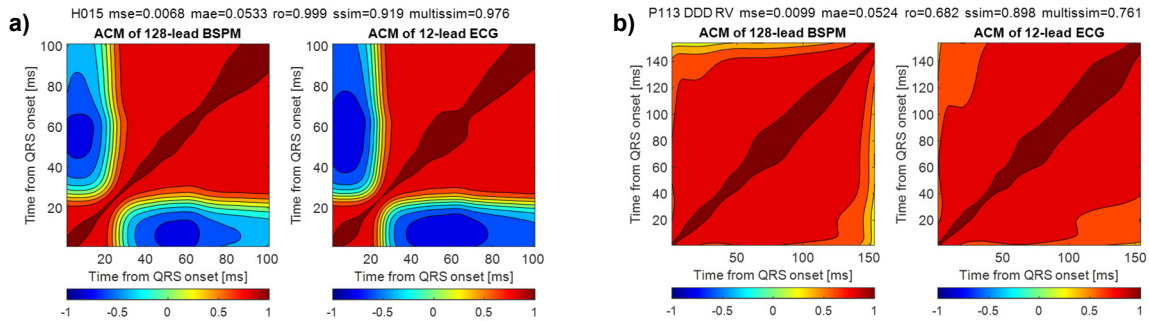

Fig. 3. ACM pairs with the best similarity by ρ (a) and the worst similarity by ρ (b).

ISBN 978-80-69159-00-6

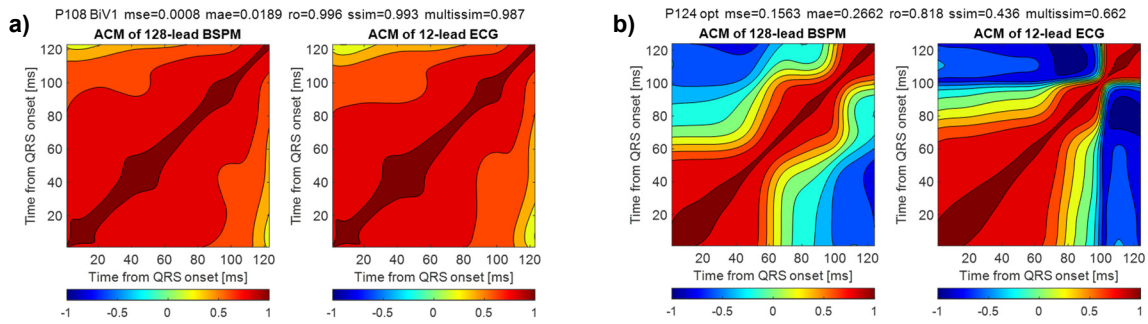

Fig. 4. ACM pairs with the best similarity by *ssim*, *multissim* (a) and the worst similarity by *ssim* (b).

5. Conclusions

The ISMs used for comparison of 128 and 12-lead ACMs examined in this paper are distributed near the value of the highest theoretical similarity. This fact might enable us to use only the standard ECG instead of the BSPMs in practice with CRT device implantation to achieve the same results. However, there exist discrete real values of ISMs corresponding to lower similarity (evidently visible for high *mse*, *mae*, and low *multissim*, *ssim* in Fig. 2b and Fig. 4b, less evident for low ρ in Figure 3b). Further investigation is necessary to determine whether these differences between 128-lead and 12-lead ACMs would affect the CRT optimization process if the ACMs were computed from the standard 12-lead ECGs instead of the 128-lead BSPMs. Therefore, in the near future, we plan to compare also the parameters extracted from the same ACMs as those analyzed in this paper.

Acknowledgements

This work was supported by the Slovak Research and Development Agency (APVV-19–0531) and the Slovak Scientific Grant Agency (VEGA 2/0106/25).

References

[1] Bergquist, J., Rupp, L., Zenger, B., Brundage, J., Busatto, A., MacLeod, R.S. (2021) Body surface potential mapping: Contemporary applications and future perspectives. *Hearts*, 2, 514–542.

[2] Corlan, A.D., Macleod, R.S., De Ambroggi, L. (2005) The effect of intrathoracic heart position on electrocardiogram autocorrelation maps, *Journal of Electrocardiology*, 38, 87-94.

[3] Přibilová, A., Švehlíková, J., Šašov, M., Zelinka, J., Ondrušová, B., Hatala, R., Tyšler, M. (2025). Autocorrelation maps for optimal setting in cardiac resynchronization therapy. *Computer Methods and Programs in Biomedicine*, 260, 108519.

[4] Mitchell, H.B. (2010). Image similarity measures. In Image Fusion: Theories, Techniques and Applications. Springer, 167-185.

[5] Wang, Z., Bovik, A.C., Sheikh, H.R., Simoncelli, E.P. (2004) Image quality assessment: From error visibility to structural similarity. *IEEE Transactions on Image Processing*, 13 (4), 600–612.

[6] Wang, Z., Simoncelli, E.P., Bovik, A.C. (2003) Multiscale structural similarity for image quality assessment. In *37th Asilomar Conference on Signals, Systems and Computers*, IEEE, 1398-1402.

Inferring a Gene Regulatory Network Involved in Drosophila Melanogaster's Muscle Development

Ivona Hrivová, Hana Krakovská, Anna Krakovská

Institute of Measurement Science, Slovak Academy of Sciences, Bratislava, Slovakia
Email: ivona.hrivova@savba.sk

Abstract. *The potential of Granger causality in identifying gene regulatory networks is investigated, with a specific focus on Drosophila melanogaster muscle development. Our study analyzes gene expression time series recorded across the insect's lifecycle, spanning embryonic, larval, pupal, and adult stages. The gene-gene regulatory interaction networks published so far show poor agreement, and our findings underscore the importance of longer gene expression time series for reliably identifying gene regulatory networks.*

Keywords: Gene Regulatory Network, Gene Expression, Drosophila Melanogaster, Granger Causality

1. Introduction

A notable application of Granger causality in genetic research is its use in gene expression datasets to infer causal regulatory interactions. Gene expression time series capture fluctuations in gene activity under various conditions, treatments, disease progressions, or stress levels. However, a major challenge is that while expression levels are usually measured for thousands of genes (variables), they are typically recorded at only a few points in time. This constraint presents a significant difficulty not only for deep learning approaches but also for conventional causal methods. For an overview of methods to infer gene regulatory networks (GRNs), see [1].

In the present study, our motivation is to explore the limitations of the classical Granger test when applied to short genetic time series. To address this challenge, we will examine gene expression data associated with muscle development in fruit flies (Drosophila melanogaster). Drosophila is among the species for which gene expression data have been collected over extended periods through RNA sequencing or microarrays, making it accessible for analysis [2].

As a simpler species than humans, Drosophila has fewer muscle types, each made up of just one fibre type. Its short lifespan and large, genetically homogeneous populations make it a valuable model organism. Many genes and regulatory pathways involved in muscle development are evolutionarily conserved across species, including mammals. Therefore, studying the fruit fly's gene regulatory networks (GRNs) provides insights with broader biological relevance.

In the following section, we describe the test data and the Granger causality inference method employed. We then present the results and compare the inferred gene regulatory network with prior findings obtained through probabilistic modelling [3], coupled differential equations for clustered expression profiles [4], and Kalman filter-based network topology tracking [5].

2. Subject and Methods

Data

We used gene expression data [2], freely accessible at the Gene Expression Omnibus database (https://www.ncbi.nlm.nih.gov/geo/query/acc.cgi?acc=GSE4347). The dataset consists of expression levels of 4028 Drosophila genes in wild-type flies examined during sequential periods through the four stages of the life cycle: embryonic, larval, pupal and the first 30 days of adulthood. We used time series consisting of 52 values, recorded simultaneously at uneven time

ISBN 978-80-69159-00-6

intervals. Because of the rapid developmental changes in embryos, overlapping 1-hour periods were sampled, while adults were measured at multiday intervals.

In earlier genetic and developmental biology research, certain gene sets have been linked to muscle development [2]. In this study, we analyzed 18 of those genes: CG1429 (mef2), CG17927 (mhc), CG18251 (msp-300), CG1915 (sls), CG2096 (flw), CG2328 (eve), CG2956 (twi), CG4376 (actn), CG4677 (lmd/gfl), CG4889 (wg), CG5596 (mlc1), CG5939 (prm), CG7107 (up), CG7438 (myo31DF), CG7445 (fln), CG7895 (tin), CG9155 (myo61F), CG9885 (dpp).

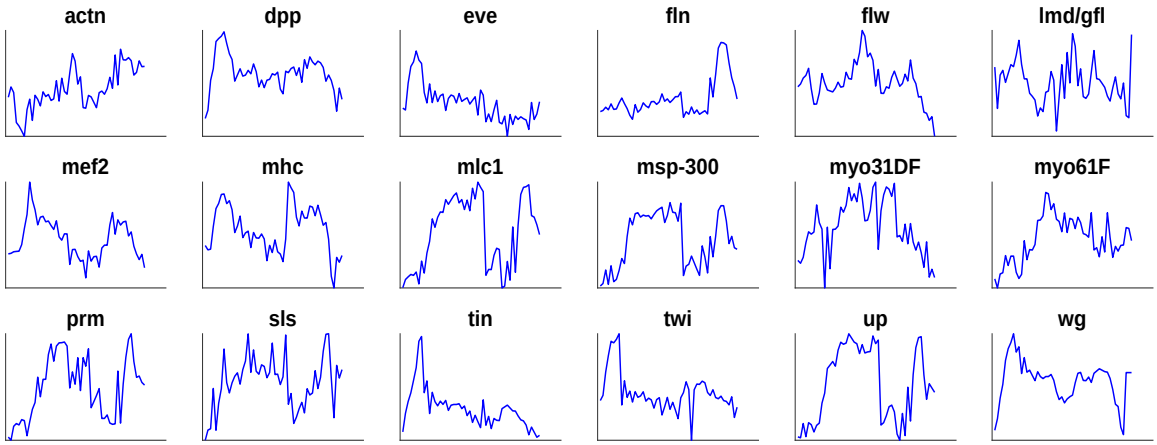

Fig. 1: Profiles of 18 gene expression time series analyzed in this work.

Granger causality test

Methods for detecting a causal link $X \rightarrow Y$ between two processes typically follow a similar principle: they assess whether past values of X contain information that helps predict the evolution of Y. The same holds for the Granger causality [6], where a variable X is said to Granger-cause a variable Y if the prediction error of Y, when using the past values of both Y and X as predictors, is significantly smaller than the prediction error obtained when using only past values of Y. The number of past values included in the model, known as the model order, is typically determined using the Akaike information criterion. The statistical significance of X's contribution to predicting Y is established via an F-test. Rejection of the null hypothesis means that the coefficients corresponding to the past values X are statistically significantly different from zero in the autoregressive model of Y (suggesting $X \rightarrow Y$). Here, the pairwise Granger causality test was performed using the MVGC MATLAB toolbox [7]. For multiple hypotheses testing, we used the Benjamini-Hochberg (FDR) correction and a significance level of 0.05.

3. Results and Discussion

Earlier experimental studies have identified transcriptional gene interaction networks that play a role in Drosophila muscle development [2]. However, directed (causal) network diagrams were not constructed until the works [3] and [4], where the authors used a set of 20 genes to propose their gene regulatory networks (GRNs).

In Fig. 2, we present the experimentally validated GRN, limited to the 18 genes considered here, alongside the data-driven reconstructions published earlier [3], [4], all formatted in a unified manner for easier comparison. The large discrepancies between the networks emphasize that GRN reconstruction remains an unresolved challenge. In the GRNs, we grouped multiple genes together within a surrounding contour to highlight that their activity is causally indistinguishable. This may result from having similar expression profiles due to being driven by an external factor or from mutually influencing each other within a regulatory loop.

ISBN 978-80-69159-00-6

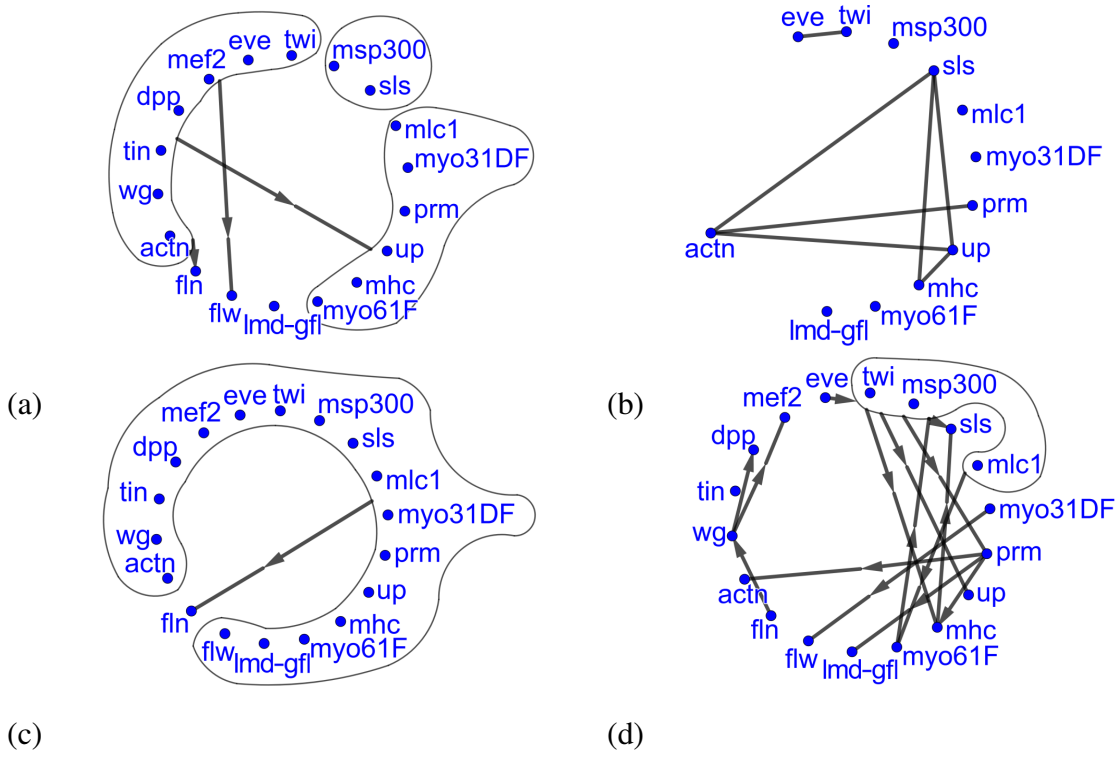

Fig. 2: Inconsistent gene networks proposed for the Drosophila muscle development. (a) links validated experimentaly [4]; (b) undirected 11-gene wing muscle network presented in [5] referring to Flybase [8]; (c) GRN proposed for the embryonic stage by Haye et al. [4]; (d) GRN proposed by Zhao et al. [3].

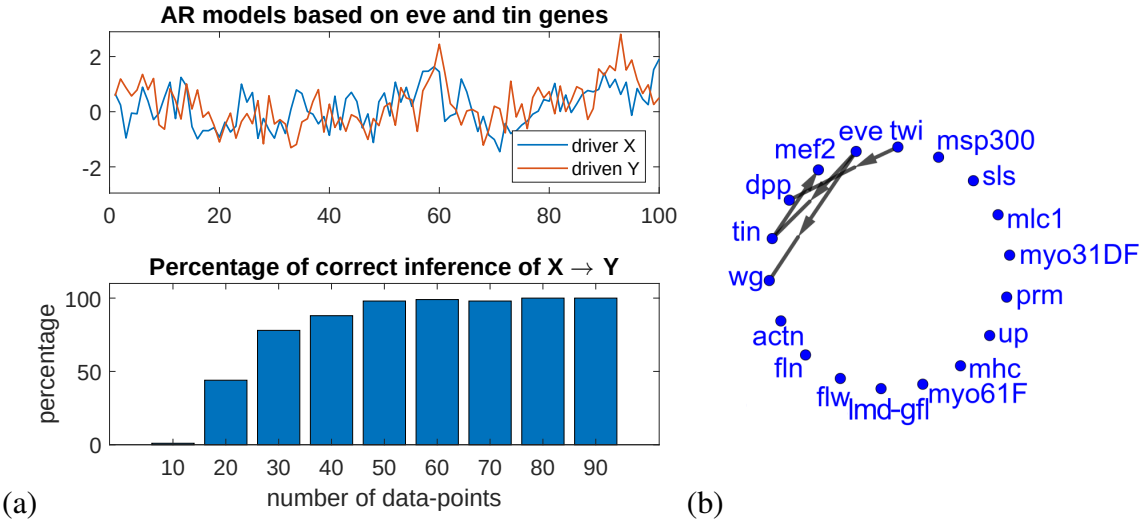

Fig. 3: (a) 100 points of the driving time series X (AR model based on gene eve) and driven Y (AR model based on gene tin), and percentage of correct $X \rightarrow Y$ inference as a function of the number of data. (b) Causal links between genes involved in Drosophila muscle development, detected in this study.

Fig. 3 (a) was generated to address concerns about whether as few as 52 points have any chance of providing correct and robust causal inference. Starting from the genes tin and eve, we simulated two unidirectionally coupled AR processes, each with 10000 points:

$$\begin{aligned} x_t &= 0.55x_{t-1} + 0.25x_{t-2} + \varepsilon_t^1, \\ y_t &= 0.44x_{t-1} + 0.02x_{t-2} + 0.28y_{t-1} + 0.27y_{t-2} + \varepsilon_t^2, \end{aligned} \tag{1}$$

ISBN 978-80-69159-00-6

where $\varepsilon_t^1 \sim \mathcal{N}(0, 0.46), \varepsilon_t^2 \sim \mathcal{N}(0, 0.38)$. We see that using a series with length of 50 points, we correctly identified the direction of causal connection in 98 out of 100 cases. This lends some credibility to the causal analysis of our short gene expression data, even though actual measurements may be noisier and less stationary than the AR simulations.

The four significant causal links detected by the Granger test, shown in Fig. 3(b), are:

$$\text{tin} \to \text{mef2} \qquad \text{eve} \to \text{tin} \qquad \text{eve} \to \text{wg} \qquad \text{twi} \to \text{dpp}$$

Their inference does not conflict with the experimentally validated connections in Fig. 2 (a), as the six genes involved belong to the same group of interrelated genes.

4. Conclusions

In this study, 18 genes involved in Drosophila muscle development have been used to propose the GRN. Although these genes interact with numerous others, external influences are not accounted for in the causal analysis. While this simplification is a common practice, it carries inherent risks, as mentioned above, that should be considered when interpreting the results.

We believe that causal analysis of time series, with its potential to infer gene regulatory networks, opens up an untapped opportunity for progress in genetic research. However, its success relies on the availability of long, reasonably clean time series, ideally spanning several hundred time points. We express scepticism toward efforts to develop a reliable methodology for reconstructing gene regulatory networks from measurements lacking sufficient length [1], given that causal inference inherently demands comprehensive temporal data. We place more hopes in collecting longer time series of gene expression data, which could prove essential for robust causal analysis and drive significant discoveries and advancements in the field.

Acknowledgements

The work was supported by the Slovak Grant Agency for Science (VEGA 2/0023/22), the Slovak Research and Development Agency (APVV-21-0216), and the COST Action CA21169 Information, Coding, and Biological Function: the Dynamics of Life (DYNALIFE), funded by the European Cooperation in Science and Technology (COST).

References

[1] Marku, M., Pancaldi, V. (2023). From time-series transcriptomics to gene regulatory networks: A review on inference methods, *PLoS Computational Biology*, 19 (8): e1011254.

[2] Arbeitman, M. N. et al. (2002). Gene expression during the life cycle of Drosophila melanogaster, *Science*, 297 (5590): 2270-2275.

[3] Zhao, W. et al. (2006). Inferring gene regulatory networks from time series data using the minimum description length principle, *Bioinformatics*, 22 (17): 2129-2135.

[4] Haye, A. et al. (2014). Modeling the Drosophila gene cluster regulation network for muscle development, *Plos One*, 9 (3): e90285.

[5] Ditzler, G. et al. (2019). Approximate kernel reconstruction for time-varying networks, *Biodata Mining*, 12: 1-14.

[6] Granger, C. W. (1969). Investigating causal relations by econometric models and cross-spectral methods, *Econometrica: Journal of the Econometric Society*, 37 (3): 424-438.

[7] Barnett, L., Seth, A. K. (2014). The MVGC multivariate Granger causality toolbox: a new approach to Granger-causal inference, *Journal of Neuroscience Methods*, 223: 50-68.

[8] Marygold, S. J. (2012). FlyBase: improvements to the bibliography, *Econometrica: Journal of the Econometric Society*, 41 (D1): D751-D757.

Optimization of Physical and Biological Parameters for Studying Microorganism Responses to Low-Frequency Magnetic Fields

[1]Hoang Vu Viet, [1]Michal Teplan, [2]Lubomír Kremnický, [3]Martin Bereta

[1]Institute of Measurement Science, Slovak Academy of Sciences, Bratislava, Slovakia,
[2]Institute of Chemistry, Slovak Academy of Sciences, Bratislava, Slovakia,
[3]Faculty of Health Sciences, Catholic University in Ruzomberok, Slovakia
Email: hoang.vuviet@savba.sk

Abstract. *This study introduces an experimental platform for systematically investigating the effects of low-frequency magnetic fields on biological systems. It addresses key challenges such as environmental variability and reproducibility by ensuring precise temperature control, high magnetic field homogeneity, and a modular design. Validated using Saccharomyces cerevisiae CCY 21-4-99, the platform demonstrated minimal growth variations, confirming its reproducibility. It supports diverse biological studies and can be adapted for different electromagnetic field sources, providing a controlled environment for studying cellular effects and advancing research on low-frequency magnetic field mechanisms and applications.*

Keywords: Low-Frequency Magnetic Fields, Biological Effects, Experimental Platform, Saccharomyces Cerevisiae, Reproducibility

1. Introduction

Low-frequency (LF) magnetic fields (MFs) (Hz–kHz) are prevalent in modern environments and may influence biological systems, though their effects remain uncertain. Studies suggest they can affect gene expression, protein synthesis, and cell signaling [1]. Epidemiological studies have linked LF MF exposure to childhood leukemia [2] and neurodegenerative diseases [3], but findings remain inconsistent. Variability in experimental setups and environmental factors contributes to these discrepancies [4], highlighting the need for more systematic research. On the other hand, potential applications include regenerative medicine [5] and cancer therapy [6]; however, safety concerns remain.

To improve reliability, we developed an experimental platform with precise environmental control and standardized evaluation methods. The introduced system addresses methodological limitations and enhances reproducibility in studying LF MF effects.

2. Methods

Microbial Strain & Culture Conditions

YPD liquid medium for yeast growth consisted of an aqueous solution containing 1% yeast extract, 2% peptone, and 2% glucose. Solid YPD agar medium contained an additional 1.5% agar. Trypan blue solution was used for viability assessment.

Saccharomyces cerevisiae CCY 21-4-99 was cultivated at 35 °C and stored at 7 °C. Before experiments, an inoculum was grown in liquid medium for 24 hours and then stored at 7 °C for up to 10 days. Viability (98.5-99.0%) was assessed using Trypan blue staining, and purity checks confirmed the absence of contamination. Biomass concentration was determined using a Bürker chamber or turbidity measurements (4.4×10^7 cells/ml ≙ 400 NTU).

To evaluate cell growth under experimental conditions, the inoculum was diluted in YPD medium and distributed into 10 flat-bottom vials, each containing 13 ml of culture to ensure

ISBN 978-80-69159-00-6

uniform cell distribution. Two sets of five vials were placed in separate cultivation chambers within Helmholtz coils and submerged in a water bath for temperature stability. Yeast cells were cultivated for 18 hours, either with or without MF exposure, depending on the experimental conditions.

3. Results

Experimental Platform Overview

The experimental setup consists of cultivation chambers, a temperature regulation system, an MF generation unit, an optical microscope with a digital camera, and a central control system. These components ensure optimal yeast growth conditions and reliable data acquisition.

Magnetic System

The MF system (Fig. 1a) features two independent channels, each supplying an MF to a cultivation chamber. A signal generator produces alternating currents, which are amplified and regulated to maintain system impedance. An oscilloscope monitors waveforms in real-time, while an ammeter measures electrical current. Helmholtz coils, optimized for 95% MF homogeneity, were modeled in MATLAB (Fig. 1b) and constructed with a 110 mm diameter and 50 turns of 2.2 mm copper wire. The system generates MF up to 5 mT within a 0-2 kHz range, ensuring stable exposure conditions.

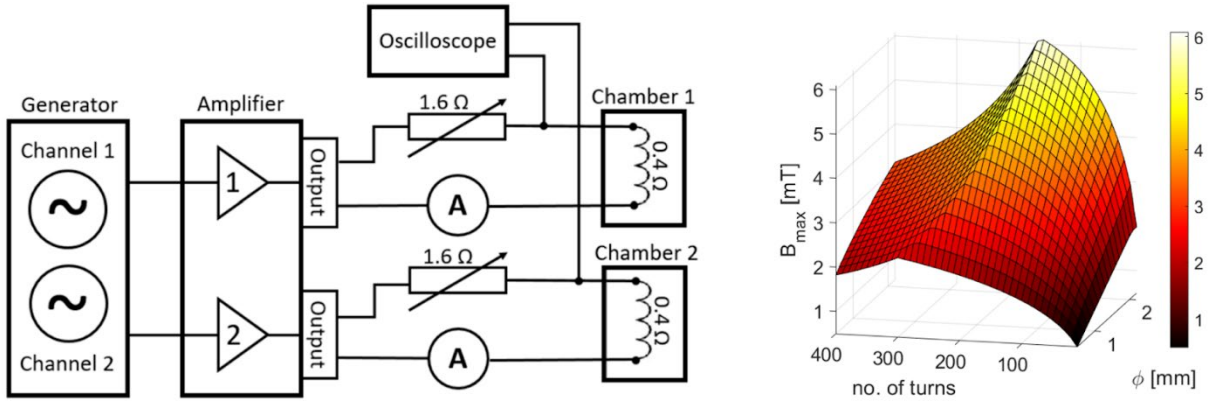

(a) (b)

Fig. 1. (a) Schematic diagram of the MF generation system, showing the signal generator, amplifier, rheostats, Helmholtz coils within two chambers, and an oscilloscope with ammeters. (b) Model of the maximum magnetic field flux as a function of the number of coil turns and wire diameter.

Temperature Regulation

Customized thermal boxes maintain stable conditions using heating foils and a PID regulator. A microcontroller with digital sensors (DS18B20) monitors the temperature every 10 seconds. Final sensor placement was optimized for accurate yeast sample monitoring. Tests confirmed that water bath temperatures remained stable at 35 °C despite heat from the coils (Fig. 2).

ISBN 978-80-69159-00-6

Fig. 2. Thermal image of the cultivation chamber, showing temperature sources in the form of coils and the foil heating system on the chamber walls.

Paired Experimental Design

A proof-of-concept paired experiment tested consistency under control (no MF) and test (50 Hz MF, 3.5 mT) conditions. Vials containing yeast cells in culture media (five per chamber) were used, with temperatures maintained at 35°C (±0.3°C variation). The depicted results (Fig. 3) show minimal growth differences between the chambers, with mean variations remaining below 1%. A one-sample t-test confirmed no significant variation from zero mean (p-values: 0.56, 0.78, 0.52), validating the chamber's consistency for MF studies.

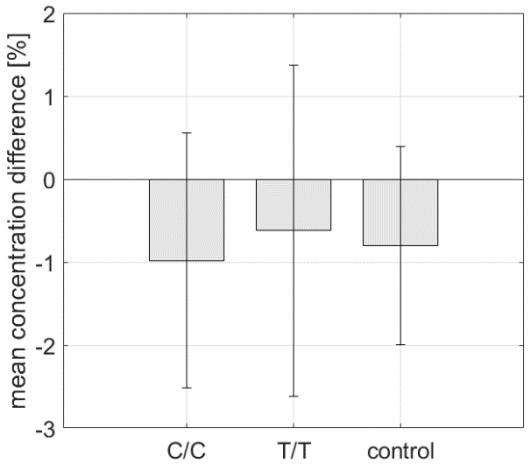

Fig. 3. Bar graphs showing the mean difference in cell concentration between cultures cultivated in two chambers. All error bars are equal to ±SD. C/C: Both chambers are in control mode without MF (N = 5). T/T: Both chambers are in test mode with MF (N = 5). Control: Merged data from the two previous sets (N = 10).

4. Discussion

The experimental platform ensures controlled and reproducible conditions for studying the effects of LF MF on biological systems. It features precise temperature regulation, with sensors in a water bath to maintain uniform conditions and minimize thermal gradients. Stability tests confirmed minimal temperature variations, supporting reliable paired experiments.

ISBN 978-80-69159-00-6

Saccharomyces cerevisiae CCY 21-4-99 was selected for its thermotolerance (optimal growth at 35 °C) and eukaryotic structure, making it a relevant model organism. Growth differences between chambers were statistically insignificant, validating the platform's precision.

The system supports multiple samples simultaneously and can be adapted for various microorganisms, biological systems, or different experimental setups, including alternative electromagnetic sources and environmental controls.

5. Conclusions

We have developed a versatile experimental platform that addresses key challenges in studying the effects of LF MF on biological systems. Future upgrades will integrate real-time monitoring of cell biomass and viability using electrical impedance spectroscopy. This high-precision system lays the foundation for advancing research on MF-induced biological effects and their biomedical applications.

Acknowledgments

The research was supported by the research grant 2/0160/25 from the VEGA Grant Agency.

References

[1] Tota, M. et al. (2024). Cellular and Molecular Effects of Magnetic Fields. *International Journal of Molecular Sciences*, 25(16), 8973.

[2] Brabant, Ch. et al. (2022). Exposure to magnetic fields and childhood leukemia: a systematic review and meta-analysis of case-control and cohort studies. *Environmental Health*, 38(2).

[3] Baaken, D. et al. (2021). Occupational Exposure to Extremely Low-Frequency Magnetic Fields and Risk of Amyotrophic Lateral Sclerosis: Results of a Feasibility Study for a Pooled Analysis of Original Data. *Bioelectromagnetics*, 42, 271-283.

[4] Buchachenko, A. (2016). Why magnetic and electromagnetic effects in biology are irreproducible and contradictory? Magnetic and electromagnetic effects in biology. *Bioelectromagnetics*, 37, 1–13.

[5] Caliogna, L. et al. (2021). Pulsed Electromagnetic Fields in Bone Healing: Molecular Pathways and Clinical Applications. *International Journal of Molecular Sciences*, 22, 7403.

[6] Sun, J. et al. (2023). Effects of extremely low frequency electromagnetic fields on the tumor cell inhibition and the possible mechanism. *Scientific Reports*, 13(1), 6989.

Automated Segmentation of Knee Articular Cartilages in 3D MRI Data of Human Patients: Using Deep Learning Approach

[1]Andrej Krafcik,[1,2]Iveta Pajanova, [1]Daniel Gogola, [1,3]Pavol Szomolanyi,

[1]Institute of Measurement Science, Slovak Academy of Sciences, Bratislava, Slovakia,
[2]Faculty of Electrical Engineering and Information Technology, Slovak University of Technology, Bratislava, Slovakia

[3]High-Field MR Center, Department of Biomedical Imaging and Image-Guided Therapy, Medical University of Vienna, Vienna, Austria

Email: andrej.krafcik@savba.sk

Abstract. *An effective convolutional neural network (CNN) with 3D U-Net architecture for automated segmentation of anatomical-morphological structures in high-resolution 3-dimensional double-echo steady state (3D-DESS) magnetic resonance imaging (MRI) data of human knee joint was proposed. The CNN was trained and validated on freely available manually segmented OAI-ZIB dataset of* 507 *subjects using high-performance computing (HPC) resources. Obtained CNN model for automated segmentation of bones and cartilages in knee-joint MRI data of subjects in testing subset of the dataset is in comparison with a currently available alternative Model-based segmentation algorithm from* 2.6 *to* 7.1% *more accurate (Dice similarity coefficient as a metric) with significantly shorter inference time per subject on currently available GPU accelerated personal computer.*

Keywords: Automated Knee-Joint Cartilage Segmentation, High-Resolution 3D-DESS MRI, U-Net3D Convolutional Neural Network, High Performance Computation

1. Introduction

Pathological conditions of musculo-skeletal systems or its degradation caused by injury or disease can be non-invasively investigated and monitored by magnetic resonance imaging (MRI) device using common 3D-double echo steady-state (3D-DESS) sequence. Such diagnostic tool can generate and capture data of morphological structures with high spatial resolution and high number of thin slices and also in different time points for long term monitoring of patients' condition before and after therapy. For the evaluation and interpretation of such volumetric images, it is necessary involvement of atested radiologist with high time costs. To automate and speed-up this process is therefore highly desired. One possible solution of this problem was presented in 2010 as the Model-based segmentation algorithm developed by Fripp et al. [1] currently also used in commercial software for automated segmentation of anatomical structures visualized in human knee-joint MRI data. The algorithm works very well on 3D-DESS MRI data of nonpathological knee-joint subjects, however, it does not perform well if there are present combinations of several pathological conditions. Therefore, more robust method, with respect to the degree of cartilage damage, has to be developed. The solution could be in deep learning methods using convolutional neural networks (CNNs) with currently well known U-Net 3D architecture [2] algorithms family. In this contribution we present our modification of CNN architecture more suitable to the analyzed problem. It shows our results of trained, validated and tested CNNs on freely available manually segmented high-resolution 3D-DESS MRI data of human knee-joint dataset of 507 subjects from osteo-arthritis initiative Zuse Institute Berlin (OAI-ZIB).

ISBN 978-80-69159-00-6

2. Subject and Methods

Architectures

For deep learning were used CNNs with full U-Net3D architecture derived from the works of Cicek et al. 2016 [2] and Krafcik et al. 2023 [3] by involvement of our few modifications. Our Full U-Net3D CNN with batch-normalization (BN) as directed acyclic graph (DAG) contains three decreasing resolution stage encoding blocks (each with two 3D convolution layers) via 3D max-pooling layers and doubling-up the number of filters, connected by skip connections (copy and concatenation) with three increasing resolution stage decoding blocks (each with two 3D convolutions) via 3D up-convolution with strides of two. Each layer of CNN is represented with the input and output tensor and operation in between (convolution, copy, concatenation, max-pooling, etc.). All convolution layers in analytic and synthetic paths was activated with the Rectified linear unit (ReLU). In the last layer of this DAG of CNN was used convolution layer with softmax activation. Data augmentation layer (augmenting the input data by random zoom and single plane rotation) at the beginning of graph, together with the drop-out (50%) layer as the penultimate layer at the end of the graph were also used. The architecture of the CNN has about 5.6×10^6 trainable variables.

Except of the described Full U-Net3D CNN BN we have also trained, validated and tested its modified version without BN layers and denoted it in further as the Full U-Net3D CNN.

Implementation

Our architectures of CNNs were created and realized in PYTHON 3.9 environment with open-source module for machine lerning TENSORFLOW 2.12.0 [4] without/with GPU acceleration. In this environment was training and validation of CNNs governed by sparse categorical cross-entropy (SCCE) loss function and with sparse categorical accuracy (SCA) metric using RMSprop optimizer [5] [6] for 300 epochs on the dataset of 507 subjects from osteoarthritis initiative Zuse Institute Berlin (OAI-ZIB) (URL: `https://pubdata.zib.de`, available online on Dec 1, 2022) divided into training, validation, and test subset in the ratio 304 : 102 : 101. Model of trained CNN for epochs with the best mean validation loss, validation accuracy, as well as of the last epoch were saved. For testing was used the model of the epoch with the best validation SCA.

Evaluation

Subjects from the testing subset were automatically processed in testing/inference mode of saved CNNs models with predicted segmentation masks (P, predicted values) and compared with manually segmented masks (T, true values). As the metric we used Dice similarity coefficient (DSC) score: $\mathrm{DSC}_i \equiv 2 \cdot |T_i \cap P_i| \,/\, (|T_i| + |P_i|) \cdot 100\%$, for $i \in \{\mathrm{FB}, \mathrm{FC}, \mathrm{TB}, \mathrm{TC}\}$, as segmentation classes, where FB, FC, TB, and TC are femur, femoral cartilage, tibia, and tibial cartilage, respectively. Next, for the testing group and morphological segmentation class was computed its mean value and standard deviation.

3. Results

Illustrative example of obtained results for our CNNs models compared with the manually segmented masks and the results for the Model-based segmentation algorithm [1], in the case of the worst DSC score for tibial cartilage segmented by the algorithm is shown in Fig. 1.

Comparison of segmentation methods for the whole testing subset — mean and standard deviations for each method and morphological structure class, together with the inference time per testing subject — is shown in Table 1.

ISBN 978-80-69159-00-6

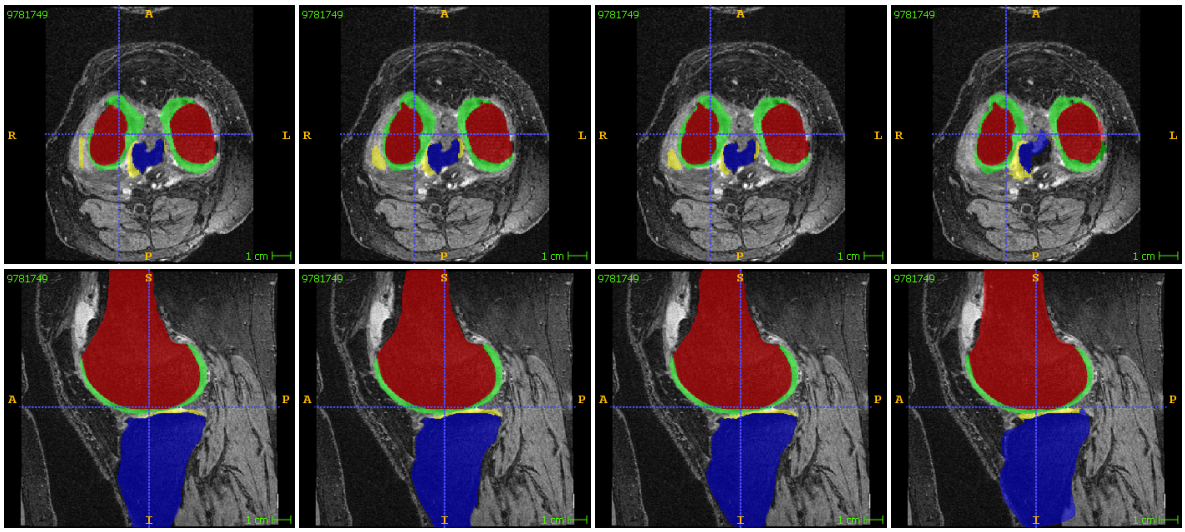

	FB	FC	TB	TC
DSC [%]	100	100	100	100

	FB	FC	TB	TC
DSC [%]	98.6	88.1	98.5	77.9

	FB	FC	TB	TC
DSC [%]	98.6	86.5	98.4	78.1

	FB	FC	TB	TC
DSC [%]	92.4	79.5	87.6	58.8

(a) Manual. (b) Full U-Net3D CNN BN. (c) Full U-Net3D CNN. (d) Model-based seg. alg. [1].

Fig. 1: (Color online.) Comparison of segmentation of human knee-joint (illustrative case; visualized using ITK-SNAP v.3.8.0 [7]): (a) manual segmentation as the true values, and predicted segmentation masks obtained with using of (b, c) our Full U-Net3D CNNs, and (d) available Model-based segmentation algorithm [1]. Morphological structures: (red) FB, femur; (green) FC, femoral cartilage; (blue) TB, tibia; and (yellow) TC, tibial cartilage. Shown subject from the test subset of OAI-ZIB dataset with the worst DSC for TC obtained with the Model-based segmentation algorithm.

4. Discussion

Obtained models of our CNNs, further used in testing/inference mode on testing subset of the OAI-ZIB dataset, were significantly more accurate than the alternatively used Model-based segmentation algorithm [1] (used Dice similarity coefficient score as the metric), as well as faster more about two orders of magnitude. Moreover, while the alternative Model-based segmentation algorithm fails in the cases of combination of several pathology conditions in human knee-joint, our approach will not.

The cost for this improvement was the relatively high computation time and hardware resources requirements for training of our CNNs. On the other hand, it has to be done only once for obtaining suitable robust with the respect to the cartilage damage, which can be further effectively used for inference on common GPU accelerated PC. Reduction of the computation time and hardware resources requirements can be reached by use of numerical mixed precision floating points data types approach for tensors' data store and and operations management on it, on which we currently work.

Acknowledgements

This work was supported by the Slovak Research and Development Agency (APVV-21-0299), and the Slovak Scientific Grant Agency (VEGA 2/0004/23). Funded by the EU NextGenerationEU through the Recovery and Resilience Plan for Slovakia under the project No. 09I03-03-V02-00016. (Part of the) Research results was obtained using the computational resources procured in the national project *National competence center for high performance computing (project code: 311070AKF2)* funded by European Regional Development Fund, EU Structural Funds Informatization of society, Operational Program Integrated Infrastructure.

Table 1: Dice similarity coefficient (DSC) score between manual (true values) and automated (predicted values) segmentation masks for each morphological structure class of our Full U-Net3D CNNs' architecture models compared with results of the available Model-based segmentation algorithm [1] (currently used also in commercial software). Our CNNs were trained and validated during 300 epochs. Next, were used models of epochs with the best mean SCA metric in test/inference mode. DSC scores were computed on testing subset with 101 subjects of OAI-ZIB dataset with high-resolution (size $384 \times 384 \times 160$ voxels). The best values are emphasized as bold font.

Method	Training & Validation				Testing					
	Precision	Device	RAM/VRAM [GB/GB]	TVT[a] $\left[\frac{\text{min}}{\text{epoch}}\right]$	DSC (mean ± std)[b] [%] for structure class				Device	IT[c] $\left[\frac{\text{s}}{\text{subject}}\right]$
					FB	FC	TB	TC		
Full U-Net3D CNN BN	float32	HPC CPU[e]	128/0	85	98.5 ± 0.5	88.3 ± 2.9	98.6 ± 0.4	84.8 ± 4.4	PC GPU[g]	**3.23**
Full U-Net3D CNN[d]	float32	HPC GPU[f]	64/40	**40**	$\mathbf{98.7 \pm 0.3}$	$\mathbf{88.5 \pm 3.1}$	$\mathbf{98.6 \pm 0.4}$	$\mathbf{85.0 \pm 4.1}$	PC GPU[g]	3.69
Model-based seg. alg. [1]					92.0 ± 2.3	81.4 ± 3.4	96.0 ± 1.2	78.3 ± 5.5	PC CPU[h]	338.00

[a] Training and validation time (TVT) per epoch on 304 training and 102 validation subjects in the overall high-resolution (size $384 \times 384 \times 160$ voxels) OAI-ZIB dataset performed on the particular device (on the HPC CPU/GPU device).

[b] Mean and standard deviations of DSC evaluated on 101 testing subjects with 3D-DESS MRI data in testing set of the OAI-ZIB dataset.

[c] Inference time (IT) per testing subject in the testing mode of the used method for testing set (101 subjects) of the OAI-ZIB dataset.

[d] The training with validation was prematurely stopped in the 250-th epoch due to expiration of the allocated time for use of computational resources on the HPC Devana device.

[e] Performed on one node of HPC Devana without GPU acceleration (2× Intel® Xeon® Gold 6338 CPU @ 2.00 GHz, 64 cores, 256 GB RAM), allocated 64 CPU cores and 128 GB RAM.

[f] Performed on one node of HPC Devana with GPU acceleration (2× Intel® Xeon® Gold 6338 CPU @ 2.00 GHz, 64 cores, 256 GB RAM, 4× NVIDIA A100 40 GB GPU), allocated 1 CPU core, 64 GB RAM, and 1 GPU.

[g] Performed on PC GPU device (Intel® Core™ i7-11700F @ 2.50 GHz, 8 cores CPU, 32 GB RAM, NVIDIA GeForce RTX 3090 24 GB GPU).

[h] Performed on PC CPU device (Intel® Xeon® W-2225 @ 4.10 GHz, 4 cores CPU, 16 GB RAM), GPU acceleration was not supported.

References

[1] Fripp, J., Crozier, S., Warfield, S. K., Ourselin, S. (2010). Automatic segmentation and quantitative analysis of the articular cartilages from magnetic resonance images of the knee. *IEEE Transactions on Medical Imaging* 29(1), 55–64.

[2] Cicek, O., Abdulkadir, A., Lienkamp, S. S., Brox, T., Ronneberger, O. (2016). 3D U-net: Learning dense volumetric segmentation from sparse annotation. *Lecture Notes in Computer Science (including subseries Lecture Notes in Artificial Intelligence and Lecture Notes in Bioinformatics)* 9901 LNCS, 424–432.

[3] Krafcik, A., Gogola, D., Szomolanyi, P., Trattnig, S. (2023). Automated knee articular cartilage segmentation using convolutional neural network (CNN): Preliminary results. In: *2023 14th International Conference on Measurement*. pp. 260–263.

[4] Abadi, M., Agarwal, A., Barham, P., Brevdo, E., Chen, Z., Citro, C., Corrado, G. S., Davis, A., Dean, J., Devin, M., Ghemawat, S., Goodfellow, I., Harp, A., Irving, G., Isard, M., Jia, Y., Jozefowicz, R., Kaiser, L., Kudlur, M., Levenberg, J., Mané, D., Monga, R., Moore, S., Murray, D., Olah, C., Schuster, M., Shlens, J., Steiner, B., Sutskever, I., Talwar, K., Tucker, P., Vanhoucke, V., Vasudevan, V., Viégas, F., Vinyals, O., Warden, P., Wattenberg, M., Wicke, M., Yu, Y., Zheng, X. (2015). TensorFlow: Large-scale machine learning on heterogeneous systems. `https://www.tensorflow.org/`. Software available from tensorflow.org.

[5] Chollet, F. (2021). *Deep Learning with Python*. Manning, second edition.

[6] Prince, S. J. D. (2023). *Understanding Deep Learning*. The MIT Press.

[7] Yushkevich, P. A., Piven, J., Hazlett, H. C., Smith, R. G., Ho, S., Gee, J. C., Gerig, G. (2006). User-guided 3D active contour segmentation of anatomical structures: Significantly improved efficiency and reliability. *Neuroimage* 31(3), 1116–1128.

ISBN 978-80-69159-00-6

Thermoelectric Cooling Devices for Ophthalmology

[1,2]Roman Kobylianskyi, [3]Krzysztof Przystupa, [1,2]Valentyn Lysko, [1]Lyudmyla Vikhor, [1,2]Andriy Prybyla, [1,2]Mykola Havryliuk, [1,4]Oleg Zadorozhnyy, [5,6]Orest Kochan, [4]Oleksandra Dorokhova, [4]Nataliya Pasyechnikova, [7]Arkadii Shulhai, [7]Mariana Levkiv

[1]Institute of Thermoelectricity of the NAS and MES of Ukraine, Chernivtsi, Ukraine,
[2]Yuriy Fedkovych Chernivtsi National University, Chernivtsi, Ukraine,
[3]Lublin University of Technology, Lublin, Poland,
[4]State Institution "The Filatov Institute of Eye Diseases and Tissue Therapy of the National Academy of Medical Sciences of Ukraine", Odesa, Ukraine,
[5]Lviv Polytechnic National University, Lviv, Ukraine,
[6]West Ukrainian National University, Ternopil, Ukraine,
[7]I. Horbachevsky Ternopil National Medical University, Ternopil, Ukraine
Email: orest.v.kochan@lpnu.ua

Abstract. *Local hypothermia of the eye can be beneficial for reducing the negative effects of ischemia and inflammation on ocular tissues. We designed and manufactured experimental samples of thermoelectric medical devices for controlled artificial cooling of the eye in three ways: by contact directly through the cornea of an open eye, by contact through the eyelids of a closed eye, by contactless cooling of the open eye. The device for contact ocular cooling includes a thermoelectric Peltier module, which can measure and maintain a specified temperature with an accuracy of ± 0.2 °C in real-time. The device for contactless ocular cooling can maintain a specified temperature with a resolution of ± 1 °C. Experimental studies of the devices showed their simplicity and reliability in operation.*

Keywords: Thermoelectric Medical Device, Ocular Surface Temperature, Ocular Bioheat Transfer, Artificial Local Hypothermia

1. Introduction

Artificial reduction of body temperature by the forced removal of heat from its surface (general hypothermia) or internal organs (local hypothermia) is successfully used in various fields of medicine in some critical conditions to increase the resistance of brain cells to ischemia/reperfusion [1]. Local hypothermia of the eye can be beneficial for reducing the negative effects of ischemia and inflammation on ocular tissues in various ophthalmological pathologies. The temperature of the ocular structures can be reduced by direct contact cooling of the corneal surface or by exposure to cold through closed eyelids. Bioheat transfer from the surface tissues of the human body, including the ocular tissues, to the environment is also known to be carried out mainly (about 60%) through radiation [2]. Therefore, the above-mentioned features of bioheat transfer of the human body create certain possibilities for heat dissipation from surface structures of the body in a contactless manner. The progress of biomedical engineering is highly prospective for developing special thermoelectric medical devices for managed artificial cooling of the eye, which is sure to enable more effective and controlled application of the beneficial effects of hypothermia.

The study aimed to develop a design and manufacture experimental samples of thermoelectric medical devices for contact and non-contact cooling of the eye based on a mathematical model of bioheat transfer of the eye under conditions of local hypothermia.

ISBN 978-80-69159-00-6

2. Bioheat transfer model of the eye under conditions of local hypothermia

It is quite a complex task to carry out thermal experiments, which is why thermal processes are usually modeled first [3], and then modeling results are tested in experiments [4]. The modeling of thermal processes can be either analytical [5] or numerical. The latter way is chosen in this paper. A mathematical bioheat transfer model of the eye under conditions of local hypothermia was developed, taking into account its anatomical structure, thermophysical features, blood circulation, and metabolic processes; the dynamics of intraocular temperatures under conditions of local artificial heat dissipation and the target ocular surface temperature (OST) were determined to achieve a potential therapeutic level of hypothermia using the developed thermoelectric medical devices. To develop a mathematical bioheat transfer model, the COMSOL Multiphysics® software package (COMSOL, Inc., USA) was used. The calculation of temperature distributions and heat flux density in the eye was carried out using the finite element method. Using object-oriented computer modeling, temperature and heat flux distributions in various structures of the eye were obtained (Figure 3).

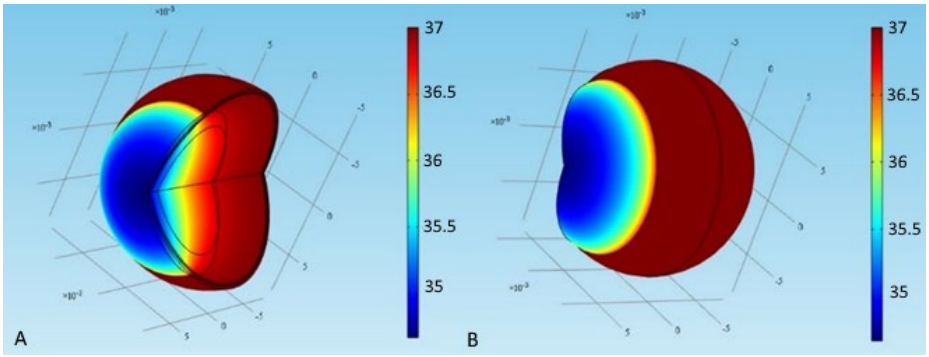

Fig. 1. Distribution of intraocular (A) and ocular surface (B) temperature at an ambient temperature of 22 °C.

The use of computer modeling enabled the establishment that the necessary decrease in the temperature of the vitreous body and, accordingly, the retina by 1-2 °C is achieved by cooling the corneal surface to a temperature of 20 °C. The results of mathematical modeling of ocular bioheat transfer under cooling conditions were considered to assess the efficiency of heat dissipation from the eye to the required therapeutic level of hypothermia in various ways using the developed thermoelectric medical devices. Modeling has demonstrated that cooling the eye directly through the cornea can reduce the temperature of the retina to a therapeutic level.

3. Thermoelectric devices for contact and non-contact ocular cooling

At the Institute of Thermoelectricity of the National Academy of Sciences and the Ministry of Education and Science of Ukraine, within the framework of a cooperation agreement with the State Institution “The Filatov Institute of Eye Diseases and Tissue Therapy of the National Academy of Medical Sciences of Ukraine”, thermoelectric medical devices for contact cooling of the eye (Figure 2) [6], and for contactless cooling of the eye (Figure 3) [7] were engineered.

Thermoelectric device for contact cooling of the eye consists of two main functional components: 1) a cooling liquid heat exchanger made of a highly thermally conductive material (copper); 2) a thermoelectric electronic cooling, control, and power unit based on a microprocessor temperature controller RE-202 (Thermoprylad, Ukraine). The thermoelectric cooling unit contains a thermoelectric Peltier module (TPM), liquid heat exchangers, and a circulation pump. The TPM is designed to cool or heat the liquid circulating in the external contour. The hot junction of this thermoelectric module is cooled by an internal liquid contour connected to the water supply network. The circulation pump ensures the circulation of the liquid coolant in the external contour. The technical characteristics of the thermoelectric device

ISBN 978-80-69159-00-6

are as follows: operating temperature range (+5 ÷ +40) °C; temperature maintenance accuracy ± 0.2 ºC; resolution of measured and set temperature ± 0.1 ºC; temperature measurement uncertainty of ± 0.2 ºC.

Fig. 2. Appearance of the device for contact cooling of the eye. Thermoelectric electronic cooling, control, and power unit with cooling liquid heat exchanger.

Thermoelectric device for contactless cooling of the eye consists of: a cooling device based on thermoelectric cooling modules (TCM) and an electronic control and power supply unit. The cooling device is based on thermoelectric Peltier modules and is designed to cool two metal surfaces located close to the eye surface. Due to the exchange of radiant energy between these surfaces, the ocular surface is cooled. The TCM hot junctions are cooled by an external liquid contour connected to the water supply network. Liquid heat exchangers (made of highly thermally conductive copper) with fittings for connecting to the water supply network are placed on the rear panel of the cooling device. The water consumption in cooling contours of the TCM hot junctions minor, 2-3 l/min is enough at a water temperature of up to 20 °C. The characteristics of the thermoelectric device are as follows: operating temperature range (-25 ÷ +10) °C; temperature maintenance accuracy ± 1.0 ºC; temperature measurement uncertainty, no more than ± 1.0 ºC.

Fig. 3. Appearance of the thermoelectric medical device for contactless cooling of the eyes. Electronic control and power supply unit with thermoelectric cooling module.

4. Discussion

A decrease in body temperature by only 1 °C can cause beneficial reactions in the human body. Mild hypothermia has a positive effect on the structural and functional state of nervous tissue under the conditions of ischemia [8]. Our study initially predicted the targeted OST needed to achieve a medically required retinal temperature reduction of 1–2 °C for therapeutic effects on retinal tissue. Computer modeling of ocular biothermal transfer showed that these conditions are reproducible without requiring extremely low temperatures for cooling. The possibility of controlled artificial cooling of the surface ocular structures in three different ways: by contact directly through the cornea of the open eye; by contact through the eyelids of the closed eye;

ISBN 978-80-69159-00-6

and also by cooling the open eye in a contactless way was confirmed. The most effective reduction in epibulbar temperature was predicted by direct contact heat transfer from the cornea of the open eye. Management of cooling parameters (temperature, exposure) potentially allows achieving the simulated target OST values to provide a therapeutic effect on retinal temperature without requiring extremely low temperatures for cooling. Other methods of cooling the eye in our study had a smaller effect on ocular temperature when using the same temperatures and duration of exposure, and these approaches do not appear to be effective enough to cool the retina, based on the modeling of ocular biothermal heat transfer. It was shown that the anterior segment of the eye can be cooled, avoiding direct contact of the cooling surface with the ocular surface (including a completely contactless one).

Devices for both contact and contactless ocular cooling were developed. Testing the developed devices has shown their simplicity and reliability in operation. The device for contact ocular cooling has several technical advantages. It includes a highly efficient thermoelectric Peltier module and the capability to measure and maintain a specified temperature with an accuracy of ± 0.2 °C in real time [6]. The technical advantages of the device for contactless ocular cooling include the safety of using the device due to the non-contact way of cooling the ocular surface and the ability to maintain the required temperature with the resolution of ± 1 °C [7].

5. Conclusions

For the first time, a design was developed, and experimental samples of thermoelectric medical devices were engineered, which allow controlled artificial cooling of the eye in three different ways: by contact directly through the cornea of an open eye; by contact through the eyelids of a closed eye; and also by cooling the open eye contactlessly. A mathematical model for ocular bioheat transfer was developed to predict the target OST required to achieve potential therapeutic levels of retinal hypothermia without excessive eye cooling. The patterns of distribution of intraocular temperature and heat flows under conditions of local artificial cooling were determined. Our study showed that cooling the eye directly through the cornea has the potential to reduce the temperature of not only the anterior segment structures of the eye but also the retina to therapeutic levels, in contrast to other proposed cooling methods.

References

[1] Jackson, T.C., Kochanek, P.M. (2019) A new vision for therapeutic hypothermia in the era of targeted temperature management: a speculative synthesis. *Therapeutic hypothermia and temperature management*, 9 (1), 13-47.

[2] Sullivan, G., Spencer, M. (2022) Heat and temperature. *BJA Educ*., 22 (9): 350-356.

[3] Jun, S., Kochan, O., Levkiv, M. (2017). Metrological software test for studying the method of thermocouple error determination during operation. *Proceedings of the 11th International Conference on Measurement (MEASUREMENT 2017)*, 171–174.

[4] Jun, S., et. al (2015). Theoretical and experimental research of error of method of thermocouple with controlled profile of temperature field. *Measurement Science Review*, 15(6), 304–312.

[5] Havrysh, V. I., Kosach, A. I. (2012). Boundary-value problem of heat conduction for a piecewise homogeneous layer with foreign inclusion. *Materials Science*, 47(6), 773–782.

[6] Anatychuk, L., et al. (2020) Thermoelectric device for contact cooling of the human eye. *Physics and Chemistry of Solid State*, 21 (1), 140-145.

[7] Anatychuk, L., et al. (2020) Thermoelectric device for non-contact cooling of the human eyes. *Journal of Thermoelectricity,* 4, 76-88.

[8] Nielsen, N., et al. (2013) Targeted temperature management at 33°C versus 36°C after cardiac arrest. *The New England journal of medicine*, 369 (23): 2197-2206.

ISBN 978-80-69159-00-6

Predictability as a Marker of Healthy and Pathological ECG

Anna Krakovská, Matej Salanci

Institute of Measurement Science, Slovak Academy of Sciences, Bratislava, Slovakia
Email: krakovska@savba.sk

Abstract. *This study examines the complexity of electrocardiographic (ECG) signals, focusing on their short-term predictability. Using predictability measures, 114 ECG recordings from both healthy individuals and cardiac patients are classified. Time series prediction is based on dynamical systems theory, with predictability assessed through the average magnitude and variability of prediction errors. The findings support the hypothesis that cardiovascular diseases may reduce the complexity of heart dynamics. The higher predictability of pathological ECGs compared to healthy ones, along with clustering results, suggests potential clinical applications, such as diagnosing extrasystoles or optimizing resynchronization therapy settings.*

Keywords: ECG, Predictability, Cluster Analysis, Time Series Prediction

1. Introduction

Recording the heart's electrical activity is crucial in cardiology. Heart dynamics are affected by factors like respiration and external stimuli, leading to complex behavior with cyclical patterns and variability in wave shapes and time intervals. State-space analysis shows that the heart's trajectory stays within a bounded region, often repeating similar patterns, much like some low-dimensional yet complex nonlinear systems [1].

Several studies suggest that the complexity of heart activity declines with aging and disease [2, 3], reflecting a weakened flexibility of the heart in adapting to sudden physiological stressors. In [4], reduced heart rate variability soon after a life-threatening injury was associated with an increased risk of mortality in trauma patients.

Complexity estimation approaches range from spectral analysis to entropy-based methods. This study evaluates ECG complexity through short-term predictability using two prediction methods within multidimensional state spaces. K-means clustering is then applied to differentiate signals based on prediction errors and their variability. Results suggest that pathological ECG signals have lower complexity, making them easier to predict than healthy ECG signals.

2. Subject and Methods

ECG recordings from 114 subjects were provided by the Institute of Measurement Science of the Slovak Academy of Sciences [5]. The dataset included 17 healthy males (H0), 30 patients with ventricular extrasystoles (P0), and 68 patients with heart failure (P1). P1 patients were diagnosed with either left or right bundle branch block and were undergoing cardiac resynchronization therapy (CRT) using pacemakers with various settings. Multiple ECG recordings were available for each P1 patient, corresponding to different pacemaker configurations.

ECG signals were recorded using 128 electrodes (64 on the front and 64 on the back of the torso, Fig. 1). When analyzing a single signal, we selected recordings from electrode 36, positioned near the heart. The recordings lasted 300-400 seconds and were sampled at 1 kHz. A bandpass FIR filter was applied during preprocessing using MatLab's built-in *filterDesigner* function, removing frequencies below 0.05 Hz (due to respiration) and above 45 Hz (caused by electrical network noise). The filtered signals were then normalized to have a mean of 0 and a standard deviation of 1. For further analysis, the signals were downsampled at various rates.

ISBN 978-80-69159-00-6

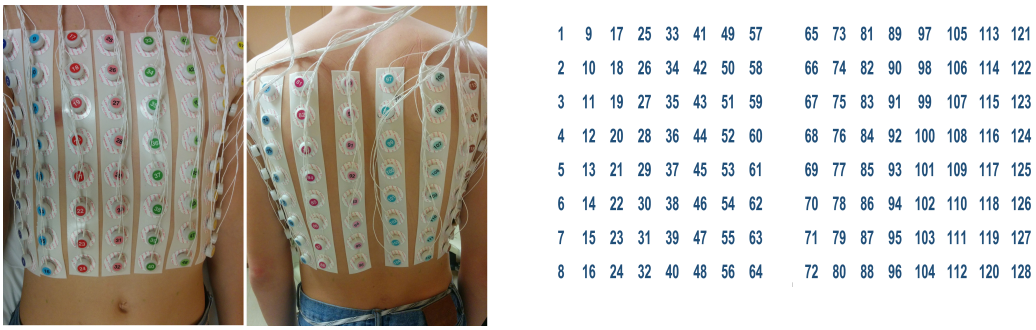

Fig. 1: Setup and electrode labeling for torso ECG recordings.

We applied *nonlinear prediction methods* designed for short-term forecasting of complex, potentially chaotic systems, where sensitivity to initial conditions limits long-term predictability [6]. If the observed process follows multidimensional dynamics, these can largely be studied from a single measured observable [7]. The famous Takens' theorem allows reconstructing multi-dimensional state portraits through time-delay embedding $[x(t), x(t-\tau), x(t-2\tau), \ldots, x(t-(d-1)\tau)]$, where $x(t)$ is the time series, τ is the time delay, and d denotes the embedding dimension. Under general conditions, the reconstruction is diffeomorphic to the original state-space portrait, preserving essential properties valuable for predicting the system's future evolution.

The prediction itself starts by identifying nearby points in the trajectory's history and extrapolating from past behavior. In the simplest case, if $X(t)$ is the last known point and $X(i)$ its closest past neighbor, the prediction is $\hat{X}(t+1) = X(i+1)$. Instead of this simple approach, which involves only the closest neighbor, we averaged past successors of multiple near neighbors, applying exponential weighting v_i based on their distances from $X(t)$.

The prediction (known as 0th order prediction) is then given by

$$\hat{X}(t+1) = \frac{\sum\limits_{i \in K} v_i X(i+1)}{\sum\limits_{i \in K} v_i}, \qquad \text{where} \quad v_i = e^{-\frac{\|X(t)-X(i)\|}{\min\limits_{j \in K} \|X(t)-X(j)\|}}.$$

We also used a 1st-order method based on the trends of past successors from nearby points:

$$\hat{X}(t+1) = \frac{\sum\limits_{i \in K} v_i (X(t) + X(i+1) - X(i))}{\sum\limits_{i \in K} v_i}.$$

To assess predictions, root mean squared error and mean absolute error (MAE) were used. With both yielding the same qualitative conclusions [8], here we report results based on MAE alone.

The usefulness of the predictability metrics was further evaluated by applying a machine learning method, specifically cluster analysis. We used *kmeans* function from MatLab, an iterative, data-partitioning algorithm that assigns data points to one of k clusters defined by centroids.

3. Results and Discussion

Here, we consider cardiac dynamics as a potentially nonlinear dynamical system and assess the predictability of its trajectories, reconstructed from a single ECG (36th electrode), using time-delay embedding with parameters d and τ carefully selected based on prediction errors.

Fig. 2: A 3-dimensional time-delay reconstruction ($\tau = 10$) of heart dynamics using 20000 points from a healthy ECG (36th electrode) followed by a plot based on ECGs from the 36th, 17th, and 34th electrodes.

ISBN 978-80-69159-00-6

Since we had multi-channel ECG measurements available, we also worked with reconstructions built from ECG signals from several different electrodes (see Fig. 2). Our selection strategy followed a greedy, stepwise optimization approach. We first predicted 5 seconds of ECG at the 36th electrode using the previous 50 seconds, then evaluated the remaining 127 electrodes to identify the best one for improving nonlinear prediction in a 2-dimensional state-space (see Fig. 3). The process of selecting additional electrodes was repeated until no significant improvement was seen. Although computationally efficient, the greedy algorithm may not always find the globally optimal set of electrodes. However, it performed well for our task, as it optimized performance based on the actual contribution to prediction accuracy, consistently selecting five electrodes regardless of signal density, prediction method, or error metric.

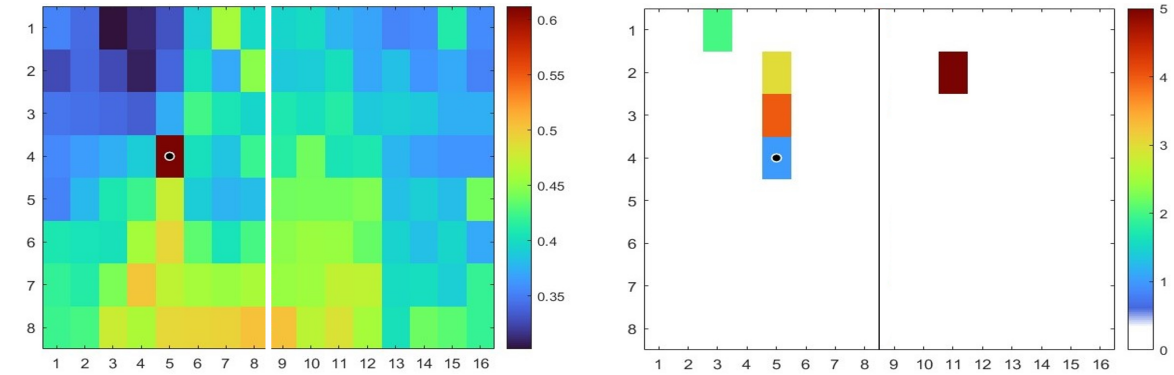

Fig. 3: Left: Color map reflecting the magnitude of average MAE errors (after adding the 2nd electrode) for 0th-order prediction of healthy recordings from electrode 36 (marked with a black dot), with 10 Hz sampling and using 10 nearest neighbours from 500 historical points to predict 50 points. The minimal error (dark blue cell at position [1, 3]) results from including the 17th electrode in the prediction process. Right: Placement of the final selection of electrodes used for prediction (36, 17, 34, 35, and 82), with the color intensity indicating the order in which the electrodes were selected.

After thoroughly examining the predictability of ECG signals with different sampling densities [8], we chose the following two measures for further analysis:

- predictability of a signal sampled at 100 Hz, predicted by the 1st-order method in a delay-time embedding reconstructed with dimension $d = 10$ and time lag $\tau = 1$
- predictability of a signal sampled at 10 Hz, predicted by the 0th-order method in a state space defined by 5 signals (measured at positions 36, 17, 34, 35, and 82)

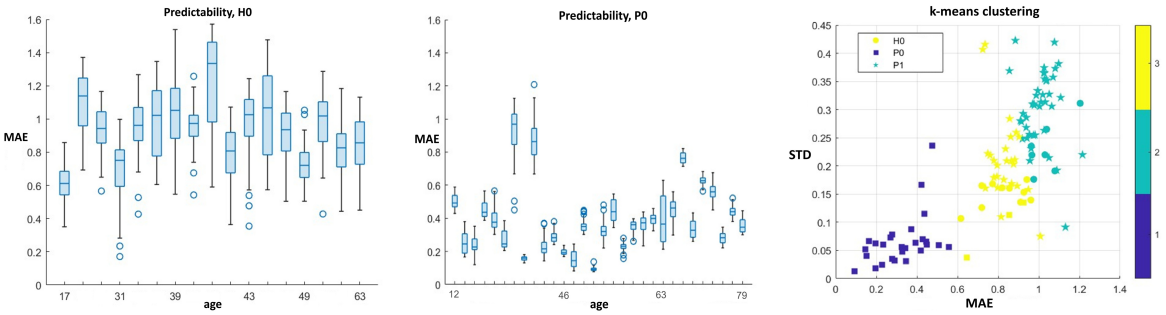

Fig. 4: Results of one-point predictions of ECG signals sampled at 10 Hz using five electrodes. Boxplots of MAE errors for H0 and P0 subjects, followed by k-means clustering of all subjects into three clusters.

From the prediction errors obtained using these procedures we calculated the mean and standard deviation (STD) for the ECG of each subject. We found that errors in pathological

ISBN 978-80-69159-00-6

P0 ECG were lower and had less variability compared to prediction errors in healthy ECG recordings. The prediction error boxplots alongside the clustering results are displayed in Fig. 4.

4. Conclusions

The findings support the growing evidence that cardiovascular diseases reduce heart activity complexity.

This study validated predictability metrics for ECG classification, focusing on k-means for its efficiency and importance as a benchmark of the clustering methods. However, future research should additionally examine whether alternative machine learning methods can improve classification performance.

Clustering results suggest ECG predictability could aid in clinical applications, such as diagnosing patients with extrasystoles (P0). Further analysis of longer recordings may reveal whether complexity measures can also help identify extrasystole precursors.

For P1 patients undergoing CRT, heart activity was slightly more predictable than in healthy subjects [8]. However, to reliably differentiate the H0 and P1 groups, it seems necessary to incorporate additional ECG metrics, such as heart rate and spectral characteristics. This could ultimately enhance the adjustment of cardiac resynchronization therapy settings, making selected metrics more consistent with those in healthy individuals.

It is also worth noting the result from Fig. 3, which highlights the selection of five electrodes that are particularly effective in predicting cardiac dynamics, showing that they capture essential information about the system under study. Thus, evaluating predictability could also contribute to the ongoing discussion on the optimal number and placement of measurement electrodes - an issue traditionally addressed via methods such as principal component analysis.

Acknowledgements

We sincerely thank Jana Švehlíková for providing the ECG data used in this study. The work was supported by the Slovak Grant Agency for Science (VEGA 2/0023/22) and by the Slovak Research and Development Agency (APVV-21-0216).

References

[1] West, B. J. (2012). *Fractal physiology and chaos in medicine.* Vol. 16. World Scientific.

[2] Kaplan, D. T., et al. (1991). Aging and the complexity of cardiovascular dynamics. *Biophysical Journal*, 59 (4), 945–949.

[3] Krakovská, A., et al. (2015). Does the Complexity of Sleep EEG Increase or Decrease with Age? In *Proceedings of the 10th International Conference on Measurement*. 77–80.

[4] Riordan Jr, W. P., et al. (2009). Early loss of heart rate complexity predicts mortality regardless of mechanism, anatomic location, or severity of injury in 2178 trauma patients. *Journal of Surgical Research*, 156 (2), 283–289.

[5] Švehlíková, J., et al. (2022). The importance of ECG offset correction for premature ventricular contraction origin localization from clinical data. *Measurement Science Review*, 22 (6), 246–252.

[6] Kantz, H., Schreiber, T. (2004). *Nonlinear time series analysis.* Vol. 7. Cambridge University Press.

[7] Takens, F. (1981). Detecting strange attractors in turbulence. In *Dynamical systems and turbulence*. Springer, Berlin, Heidelberg, 366–381.

[8] Salanci, M. (2024). Predpovedateľnosť zdravého a patologického EKG signálu (Predictabilty of Healthy and Pathological ECG Signals). Master's thesis. University of Žilina.

Theoretical Problems of Measurement II

ISBN 978-80-69159-00-6

The Uncertainty of the Indirect Thermographic Measurement of the Temperature of the Semiconductor Element

Krzysztof Dziarski[1], Arkadiusz Hulewicz[2], Przemysław Otomański[2]

[1]Institute of Electric Power Engineering, Poznan University of Technology,
Piotrowo Street 3A, 60-965 Poznan, Poland,
[2]Institute of Electrical Engineering and Electronics, Poznan University of Technology,
Piotrowo Street 3A, 60-965 Poznan, Poland
Email: krzysztof.dziarski@put.poznan.pl

***Abstract**: The indirect thermographic measurement of the temperature of a semiconductor element consists of two parts. The first part consists of performing a thermographic measurement of the temperature case. The second part consists of determining the relationship between the temperature case and the temperature of the semiconductor element. Such a measurement is the subject to the uncertainty. As a result of the carried out work, the uncertainty of the indirect thermographic measurement of the temperature of the semiconductor element was determined.*

Keywords: Uncertainty, Thermography, Semiconductor

1. Introduction

The temperature of the semiconductor element is an important piece of information. Its value determines the operating time of the semiconductor element and the values of its parameters. The shape of its characteristics and the way it works depend on the temperature of the semiconductor element. It consists of a case made of epoxy resin, inside which an encapsulated semiconductor chip called die has been placed. The die is placed on a base plate made of tinned copper. Leads are connected to the epoxy from the base plate and the die using bond wires. They are immersed in the epoxy resin. In the further part of the work, the temperature of the semiconductor element T_{die} should be understood as the temperature of the die.

The literature describes a method for performing an indirect thermographic measurement of the temperature of a semiconductor element. Such a measurement consists of two parts: performing a thermographic measurement of the temperature case T_c and determining the relationship between T_c and T_{die}. This measurement is burdened with the uncertainty.

The measurement uncertainty defines the range within which the actual value of the measured quantity is located. It defines how much the measured value may differ from the actual value. For this reason, information on the measurement uncertainty is important especially when the temperature of the semiconductor element is in the upper part of the range of permissible values. The uncertainty can be determined using the classical method in accordance with the document [1].

The uncertainty consists of type A uncertainty and type B uncertainty. The type A uncertainty can be determined based on the statistical analysis of the series of the observations. The type B uncertainty can be determined based on the experience of the person performing the measurement, the calibration certificates, the observations of the conditions prevailing during the measurement and available literature. In this work, the uncertainty of a single measurement is determined. For this reason, the determination of the type B uncertainty is limited.

The literature describes the determination of the type B uncertainty of thermographic temperature measurement. The authors are aware of few works on the determination of the

ISBN 978-80-69159-00-6

uncertainty of the indirect thermographic measurement of the temperature of a semiconductor element.

2. Subject and Methods

The C2M0280120D transistor was selected for the research. It is characterized by a drain current of I_d = 10 A and a Gate-Source Threshold Voltage $V_{gs\ th}$ = 2.8 V [2]. First, a reliable value of the transistor case temperature T_c was determined. For this purpose, it was necessary to construct a measurement circuit. Its key element was the Flir E50 thermographic camera, operating in the far infrared band (LWIR – Long Wavelength Infrared). This camera uses a matrix of microbolometer detectors (uncooled microbolometer) with a spatial resolution of 180 × 240 detectors. The IFOV (Instantaneous Field of View) parameter value is 1.82 mrad, which allows for the placement of nine fields of a single detector on the observed surface of the transistor case. In turn, the NEDT (Noise Equivalent Differential Temperature) value of 50 mK is sufficient for precise monitoring of temperature changes on the case.

The camera was mounted on a tripod at a distance of d =33 mm. The camera with the tripod was placed in a special chamber made of Plexiglas. The chamber had dimensions of 40 cm × 30 cm × 30 cm, and its interior was lined with polyurethane foam to eliminate reflections. The diagram of the described stand is shown in Fig. 1a.

The second stage of the developed method included determining the relationship between temperatures T_c and T_{die}. A three-dimensional model of the relay was created and the Finite Element Analysis (FEA) method was used. The SolidWorks software was used to perform the simulation. An example of the thermal simulation result for the created three-dimensional model is shown in Fig. 1b.

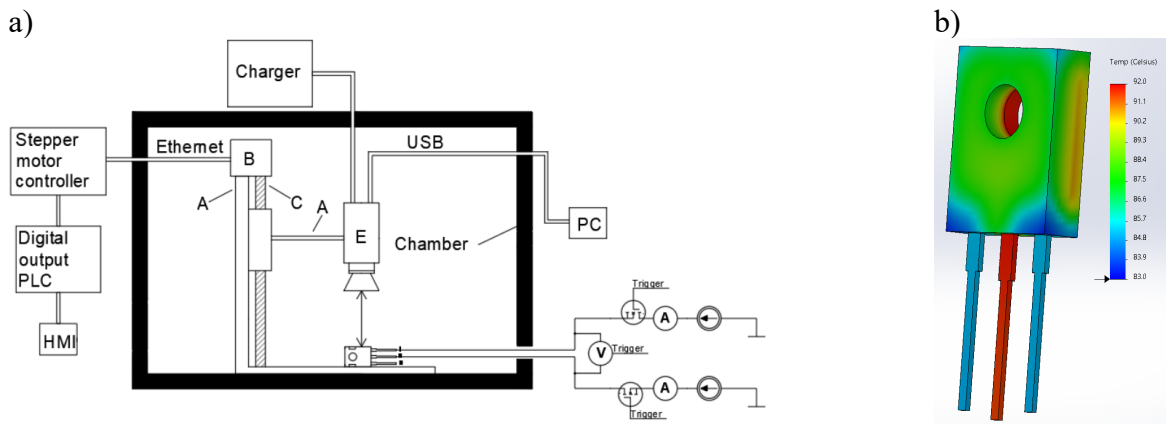

Fig. 1. a) the diagram of the measurement circuit. A – the tripod, B – the stepper motor, C – the screw, E – the thermographic camera, b) simulation result of the C2M0280120D transistor made in SolidWorks.

The materials that were assigned in the defined model and their thermal conductivity properties λ are shown in Table 1.

Table 1. Materials that are assigned in the defined model and their λ values

Internal Structure Component	Material	k [W/m·K]
Black part of the case	EME 590	0.25
Back part of the case	Copper	400
Semiconductor element	Silicon carbide	150
Lead, Internal connections	Copper	400
Grease	Melamine resin	0.20

ISBN 978-80-69159-00-6

The determination of the type B uncertainty requires the definition of the processing equation. It allows the calculation of the temperature T_{die} from the thermographic measurement T_c according to the Eq. (1).

$$\boldsymbol{T_c} = \sqrt{\frac{W_{\text{tot}} - A - B \cdot \sigma \cdot T_l^4}{\varepsilon \cdot \tau_a \cdot \sigma \cdot \tau_l}} + \boldsymbol{T_{us}} \tag{1}$$

where: $A = (1-\varepsilon) \cdot \tau_a \cdot \sigma \cdot T_{\text{refl}}^4 \cdot \tau_l$, $B = (1-\tau_a) \cdot \sigma \cdot T_a^4 \cdot \tau_l + (1-\tau_l)$, W_{tot} – the total radiation energy reaching the lens of the thermographic camera, T_a – the ambient temperature, τ_a – the air transmittance, T_l – the thermographic camera lens temperature, T_{refl}– the reflected temperature, ε – the emissivity, τ_l – the lens transmittance, T_{us} – the unsharpness temperature.

The temperature difference between the temperatures T_{die} and T_c is described by the Eq. 2.

$$\Delta_T = T_{\text{die}} - T_c \tag{2}$$

To determine the uncertainty, taking into account the range of variability of the quantity x_i from the Eq. 1, the Eq. 3 was used [3].

$$u^2(x_i) = \frac{1}{12}(a_+ + a_-)^2 \tag{3}$$

where: a_+- the upper range limit a_- – is the lower range limit.

The uncertainty $u_t(y)$ associated with the analyzed input quantity x_i was determined. Its value was equal to the standard uncertainty u(x_i) of this quantity multiplied by the sensitivity coefficient c. This coefficient describes the influence of the changes in the estimate of the input quantity on the estimate of the output quantity.

The standard uncertainty T_{die}, denoted $u(T_{\text{die}})$, was calculated as the square root of the sum of squares u_t(y) for all values on the right-hand side of the Eq. 1. The Eq. 4 was used to calculate it [3].

$$\text{u}^2(T_{\text{die}}) = \sum_{t=1}^{N} u_t^2(y) \tag{4}$$

The expanded uncertainty $U(T_{\text{die}})$ given by the Eq. 5 was the standard combined uncertainty $u(T_{\text{die}})$ multiplied by the coverage factor k. For k = 2, the probability that the measured value was within the specified range was 95% [3].

$$U(T_{die}) = 2 \cdot u(T_{die}) \tag{5}$$

3. Results

An example uncertainty budget for T_{die} = 90 °C is presented in Table 2

Table 2. The example uncertainty budget of an indirect thermographic measurement die for T_{die} = 90 °C.

Symbol X_i	Unit	Estimate of Quantity x_i	Standard Uncertainty u(x_i)	Distribution of Probability	Sensitivity Coefficient c_i	Contribution of Uncertainty u_i(y)
τ_a	-	0.9987	0.0010	normal	0.4488	0.0004
W_{tot}	W/m^2	0.1554	0.0066	rectangular	67.7701	0.4472
ε	-	0.97	0.0086	rectangular	−7.6450	−0.0657
T_{refl}	°C	30	2.8868	rectangular	0.0119	0.0344
τ_l	m	0.95	0.0289	rectangular	−10.3189	0.2982
T_a	°C	26.5	4.9000	rectangular	−0.0151	−0.0740
T_l	°C	26.5	4.9000	rectangular	−0.0151	−0.0740
T_{us}	°C	3.25	1.88	normal	1	1.63
T_{die}	°C	90				3.25

Analyzing the values given in Table 2, it can be seen that the largest share in the determined uncertainty given in the last column of the table is taken by W_{tot}, τ_l, and in particular τ_{us}. The

ISBN 978-80-69159-00-6

authors declare further work in this area aimed at reducing the values of these parameters, which will allow for reducing the final value of uncertainty.

Table 3 lists the Type B uncertainty values for different temperatures T_{die} ranging from 30 °C to 120 °C.

Table 3. The summary of Type B uncertainty values for different T_{die} values in the range from 30 °C to 120 °C.

No.	T_{die} [°C]	U(T_{die}) [°C]
1	30	1.62
2	60	2.44
3	90	3.25
4	105	4.21
5	120	5.17

As it can be seen, the value of the type B uncertainty strongly depends on the value of the temperature T_{die}. An increase in the temperature T_{die} from 30 °C to 120 °C causes a more than 3-fold increase in the type B uncertainty.

4. Discussion and Conclusions

The indirect thermographic measurement of the temperature of a semiconductor element is a subject to the uncertainty. As a result of the carried out work, the values of the type B uncertainty were determined, which take into account the number of the influencing quantities, which are presented in Table 2. The factor related to the blurriness of the T_{us} thermogram has a very significant influence on the value of the type B uncertainty. The issue of the influence of blur on the thermographic temperature measurement of an electronic component's case is not widely described in the literature. It is described in the document [4].

References

[1] JCGM, *JCGM 100:2008 - GUM: Guide to the Expression of Uncertainty in Measurement*, Bureau International des Poids et Mesures, 2008. [Online]. Available: https://www.bipm.org/documents/20126/2071204/JCGM_100_2008_E.pdf. [Accessed: Mar. 6, 2025].

[2] Silicon Carbide Power MOSFET C2M0280120D [Online]. Available: https://www.mouser.com/datasheet/2/90/c2m0280120d-1795432.pdf?srsltid=AfmBOoosrZksIKO0jueWqfI5d_BaM6RS3iqRoAre-2nbhIbBgFBAKSnW [Accessed: Mar. 6, 2025]

[3] European Cooperation for Accreditation (EA), *EA-INF/04 rev. 06: September 2020 - Guidance on the Use of Accreditation Symbols*, European Cooperation for Accreditation, 2020. [Online]. Available: https://european-accreditation.org/wp-content/uploads/2020/09/EA-INF_04-rev06-September-2020.pdf. [Accessed: Mar. 6, 2025].

[4] Thermographic measurements of semiconductor elements, PhD thesis, 2020. [Online]. Available: https://sin.put.poznan.pl/dissertations/details/d3168. [Accessed: Mar. 6, 2025].

ISBN 978-80-69159-00-6

Analysis of Fitting GNSS Data Provided by Stationary Receiver to Non-Gaussian distributions

Abu Bantu, Józef Wiora

Department of Measurements and Control Systems, Silesian University of Technology,
ul. Akademicka 16, 44-100 Gliwice, Poland,
Email: abu.feyo.bantu@polsl.pl

Abstract. *Understanding dataset characterisation is fundamental to achieving accurate statistical modelling, particularly in the context of Global Navigation Satellite System (GNSS) data analysis. GNSS data exhibit heavy-tailed and skewed distributions, prompting this study to evaluate non-Gaussian models (Cauchy, Student's t, lognormal, skew-normal) in modelling GNSS data collected from a stationary receiver. This study uses maximum likelihood estimation for parameter estimation with a confidence interval. It evaluates the model's performance using log-likelihood analysis, the Akaike Information Criterion, the Bayesian Information Criterion, and the Root Mean Squared Error. The comparative assessment of these models highlights that lognormal and skew-normal outperform in capturing extreme deviations and provide a better fit than the normal distribution. These findings underscore the importance of selecting appropriate statistical models to enhance uncertainty quantification in GNSS-based measurements.*

Keywords: Non-Gaussian, Maximum Likelihood Estimation, Goodness-of-Fit Test, GNSS, Confidence Interval

1. Introduction

Understanding dataset characterisation is crucial for accurate statistical modelling, especially for asymmetric and heavy-tailed data samples. The Global Navigation Satellite System (GNSS) latitude data was an example of such samples [1]. GNSS provides positioning data essential for navigation, mapping, and research [2]. Classical models assume Gaussian-distributed positioning errors, but empirical studies show heavy-tailed and skewed characteristics [3].

To improve error modelling, researchers have proposed combining probability density functions of individual error sources and applying nonclassical error theory for large datasets [4]. In urban environments, outliers from multipath effects and non-line-of-sight (NLOS) receptions further degrade GNSS accuracy. Raitoharju *et al.* [5] addressed this by introducing Kalman filtering with empirical noise models to handle non-Gaussian errors. The study of Alzaatreh *et al.* [6] introduces generalised Cauchy family, offering greater flexibility for heavy-tailed data than Gaussian models. Sun-Yong Choi *et al.* [7] evaluated multiple distributions for stock index returns using goodness-of-fit tests and information criteria.

Based on these findings, this study systematically evaluates the suitability of non-Gaussian distributions, including Cauchy, Student's t, lognormal, and skew-normal, for modelling GNSS latitude datasets. The parameter estimation with a confidence interval (CI) was done using maximum likelihood estimation (MLE) and evaluates model fitting through log-likelihood ($\mathscr{L}$), Akaike Information Criterion (AIC), Bayesian Information Criterion (BIC), and Root Mean Squared Error (RMSE).

2. Materials and Methods

To collect GNSS data, an Lc76g GPS module was deployed in a fixed outdoor location and connected to a Raspberry Pi for configuration, logging, and real-time monitoring. Over 72 hours,

ISBN 978-80-69159-00-6

the module recorded 1 303 376 NMEA sentences, from which 162 922 `$GPRMC` sentences were extracted for key positional and signal quality parameters. Python scripts filtered and structured the data for analysis. The latitude data distribution was characterised and filtered to multiple non-Gaussian models. Parameter estimation and uncertainty quantification were performed using MLE, with model performance evaluated via $\mathscr{L}$, AIC, BIC, and RMSE.

3. Synthetic data distributions

The Cauchy distribution is a continuous probability distribution characterised by its location parameter μ_0 and scale parameter σ [8].

$$f(x;\mu_0,\sigma) = \frac{1}{\pi\sigma\left[1+\left(\frac{x-\mu_0}{\sigma}\right)^2\right]} \tag{1}$$

Student's t distribution models the mean of a normal population when the sample size is small and the standard deviation is unknown [9]. Its general probability density function (PDF) is,

$$f(x;\nu,\mu_0,\sigma) = \frac{\Gamma\left(\frac{\nu+1}{2}\right)}{\sqrt{\nu\pi}\,\sigma\,\Gamma\left(\frac{\nu}{2}\right)}\left(1+\frac{(x-\mu_0)^2}{\nu\sigma^2}\right)^{-\frac{\nu+1}{2}} \tag{2}$$

where ν is degree of freedom, and Γ denotes the gamma function, a continuous generalisation of the factorial function for complex and real numbers, excluding negative integers.

A random variable X follows a **lognormal distribution** if its natural logarithm follows a normal distribution [10].

$$f(x \mid \mu_0,\sigma,\alpha) = \frac{1}{(x-\alpha)\sigma\sqrt{2\pi}}\exp\left(-\frac{(\ln(x-\alpha)-\mu_0)^2}{2\sigma^2}\right), \quad x>\alpha \tag{3}$$

where α is the shape, μ_0 is the mean, and σ^2 is the variance of $Y = \ln X$.

The **skew-normal distribution** extends the normal distribution with a shape parameter (α) to control skewness [7]. The PDF is:

$$f(x \mid \mu_0,\sigma,\alpha) = \frac{2}{\sigma}\phi\left(\frac{x-\mu_0}{\sigma}\right)\Phi\left(\alpha\frac{x-\mu_0}{\sigma}\right) \tag{4}$$

To evaluate and compare different distribution models, we apply multiple **goodness-of-fit** measures using empirical GNSS datasets. The study employs MLE to estimate distribution parameters and compute 95% CIs for each fitted model. Model performance is assessed using AIC and BIC, which penalise complexity (lower values indicate better fit), log-likelihood $\mathscr{L}$ (higher values suggest better), and RMSE (measuring average prediction error).

4. Results and Discussion

Fig. 1 shows empirical latitude data with PDFs of various distributions fitted. The histogram represents observed GNSS data, while the curves depict model fits. Lognormal and skew-normal distributions align best, capturing skewness and heavy tails, consistent with Table 1. In contrast, the Cauchy is overly broad, and Student's t overestimates tails. The table summarises estimated parameters, CIs, and compares goodness-of-fit metrics for GNSS error models. The location parameter ($\mu = 50.2885$) is consistent, while scale (σ) varies across distributions. Student's t, lognormal, and skew-normal include parameters (ν,α) to capture heavy tails and skewness.

ISBN 978-80-69159-00-6

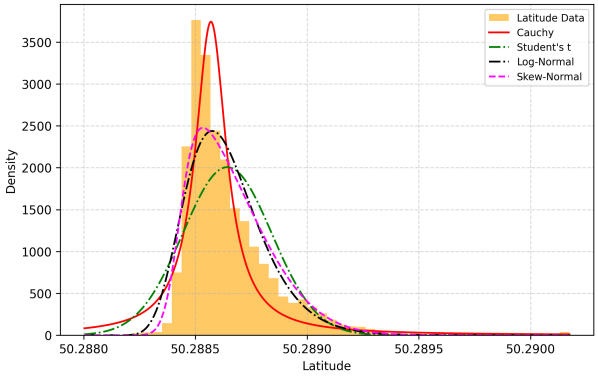

Fig. 1: Selected distributions fitting.

The lognormal and skew-normal show the tighter CI when compared to Cauchy and Student's t. The skew-normal's $\alpha = 5.22$ indicates moderate skew, and the lognormal $\alpha = 0.27$ reflects slight asymmetry, aligning with the data's non-Gaussian characteristics. The skew-normal and lognormal models achieved the highest log-likelihoods ($(1.19 \times 10^6$ and $1.18 \times 10^6)$) and lowest AIC/BIC, confirming superior fit. Their 95% CIs were 15-20% narrower than Cauchy/Student's t, improving uncertainty precision. In contrast, Cauchy had a high RMSE, and Student's t shows lower $\mathscr{L}$, reflecting poorer data alignment.

Table 1: Estimated parameters with confidence intervals and performance metrics for different models

Model	Parameters				CI	$\mathscr{L}$	AIC	BIC	RMSE
	μ	σ	ν	α					
	*	$\times 10^{-5}$	$\times 10^{3}$		*	$\times 10^{6}$	$\times 10^{6}$	$\times 10^{6}$	
Cauchy	857	9.0	–	–	[749,965]	1.17	-2.33	-2.33	$5.6 \cdot 10^{-2}$
Student's t	864	20	3.92	–	[875,903]	1.16	-2.31	-2.31	$2.8 \cdot 10^{-4}$
Lognormal	798	64	–	0.27	[836,905]	1.18	-2.37	-2.37	$2.7 \cdot 10^{-4}$
Skew-normal	843	29	–	5.22	[839,908]	1.19	-2.37	-2.37	$2.7 \cdot 10^{-4}$

*__Note__: Values presented in this column are the least significant digits of 50.28000.

The quantile-quantile (Q-Q) plots in Fig. 2 show that lognormal (c) and skew-normal (d) distributions best fit the GNSS data, closely matching theoretical quantiles. Cauchy (a) exhibits large tail deviations, and Student's t (b) displays curvature, indicating suboptimal fits.

5. Conclusions

This study evaluated probability distributions for modelling skewed and heavy-tailed GNSS error data. Using MLE, it estimated parameters and CI to assess reliability. Goodness-of-fit metrics confirmed that skew-normal and lognormal distributions best captured skewness and heavy tails, while Cauchy and Student's t struggled with peak-tail balance. Lognormal and skew-normal models demonstrated tighter CIs and better AIC/BIC scores. These findings underscore the need for flexible, asymmetric distributions for enhancing GNSS accuracy in challenging environments.

Acknowledgements

This research was funded by the Polish Ministry of Science and Higher Education, grant numbers 02/050/BKM-25/0042 (AF) and 02/050/BK-25/0047 (JW).

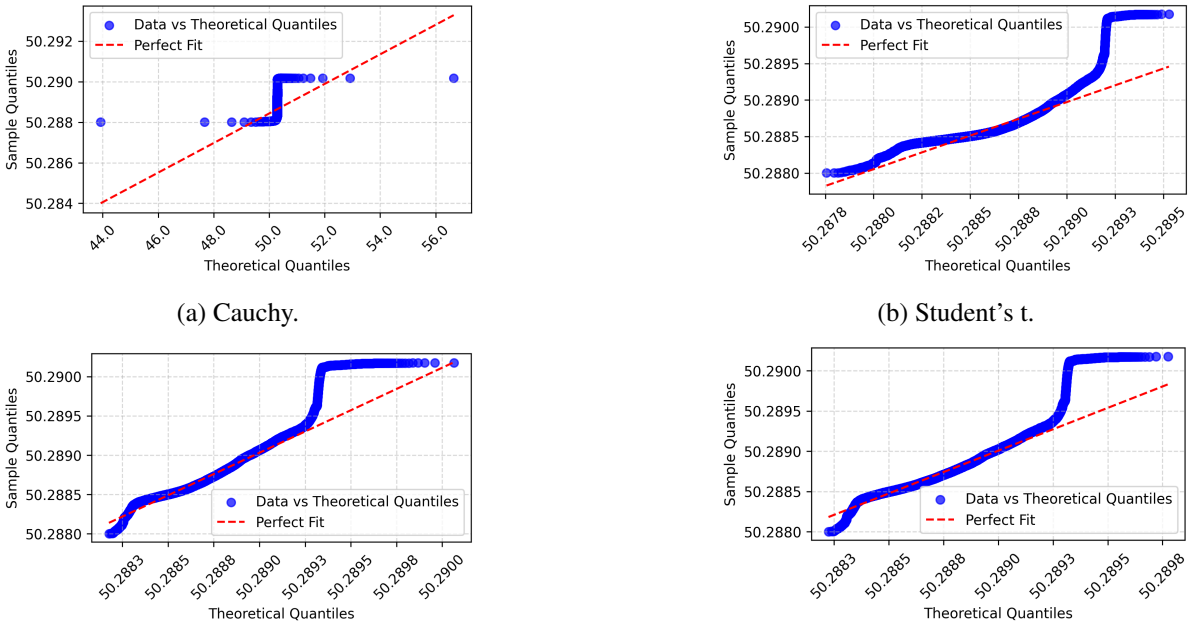

(a) Cauchy.

(b) Student's t.

(c) Lognormal.

(d) Skew-normal.

Fig. 2: Residual analysis of the selected distributions using Q-Q plot.

References

[1] Bantu, A., Wiora, J., Kozyra, A. (2024). Normality tests for transformed large measured data: A comprehensive analysis. In: *Proceedings of the XV Scientific Conference MASEP 2024*. Łódź, Poland, p. 123.

[2] Madry, S. (2023). *Global Navigation Satellite Systems and Their Applications*. Springer, 2 edition.

[3] Kanhere, A. V., Gupta, S., Shetty, A., Gao, G. (2022). Improving GNSS positioning using neural-network-based corrections. *NAVIGATION* 69(4).

[4] Dvulit, P., Savchuk, S., Sosonka, I. (2020). The processing of GNSS observation by non-classical error theory of measurements. *Geodynamics* 28, 19–28.

[5] Raitoharju, M., Nurminen, H., Cilden-Guler, D., Särkkä, S. (2021). Kalman filtering with empirical noise models. In: *2021 International Conference on Localization and GNSS (ICL-GNSS)*. pp. 1–7.

[6] Alzaatreh, A., Lee, C., Famoye, F., Nadarajah, S. (2016). The generalized Cauchy family of distributions with applications. *Journal of Statistical Distributions and Applications* 3(12).

[7] Sun-Yong Choi, J.-H. Y. (2020). Modeling stock index returns with parametric distributions. *Mathematical Problems in Engineering* 2020, 9763065.

[8] Jaber, A., Rashid, T., Rasheed, M., Mahmood, R. S., Maalej, O. (2024). Analysis of Cauchy distribution and its applications. *Journal of Positive Sciences* 4(4).

[9] Ahsanullah, M., Kibria, B. G., Shakil, M. (2014). *Normal and Student's t distributions and their applications*, Vol. 4. Springer.

[10] Aslam, M. (2024). Generating imprecise data from log-normal distribution. *Measurement: Interdisciplinary Research and Perspectives* pp. 1–9.

ISBN 978-80-69159-00-6

Less Dithering for Higher Accuracy in Stochastic Harmonic Instruments

Boris Antić, Marina Bulat

University of Novi Sad, Faculty of Technical Sciences, Novi Sad, Serbia
Email: antic@uns.ac.rs

Abstract. *This paper examines improvements in the design of stochastic harmonic instruments, which utilize dithering of input signals to enhance the precision of analog-to-digital conversion. Their original design employs a set of uncorrelated random dithering signals to ensure zero summing of their numerical integrals. Unfortunately, these random signals – some of which are embedded into the instrument's memory – are also the main source of the inherent measurement inaccuracy in practical implementations. To address this issue, we explore two potential modifications aimed at improving accuracy while preserving the benefits of high precision: (1) restricting dithering to low-resolution cases, and (2) eliminating dithering of the second signal. The proposed modifications are analyzed theoretically and validated through simulations across a representative space of measurement signals.*

Keywords: Stochastic Resonance, Measurement Accuracy, Harmonics, ADC

1. Introduction

Dithering of a signal prior to analog-to-digital conversion (ADC) is a variant of the stochastic resonance method originally proposed in scientific literature in 1956 [1]. Today, dithering is employed across a wide range of measurement and signal processing applications. Depending on the statistical properties of the measured signal, the core principle of this technique is to introduce noise with a specific probability distribution to randomize quantization error, thereby significantly reducing measurement uncertainty. Dither is routinely used to improve signal-to-noise ratio in voltage and current measurements [2], processing of audio and video data [3], as well as harmonic instruments in power quality measurements [4]. When applied to harmonic measurements, the dithering has to be performed multiple times, first on the input signal and then on each trigonometric basis representing a Fourier's expansion coefficient [4]. The architecture of one of the 2*n* identical blocks is illustrated in Fig. 1.

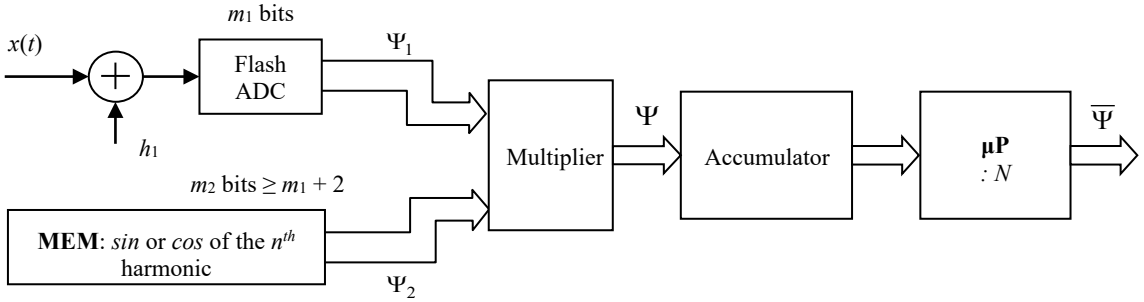

Fig. 1. Schematic block diagram of a single segment of the stochastic harmonic instrument for determining n^{th} spectral component.

In Fig. 1 signal $x(t)$ represents the measured periodic quantity with period T and an unknown discrete amplitude spectrum composed of harmonics at frequencies that are integer multiples of its fundamental frequency $f_0 = 1/T$. Resolutions of the ADC and the memory block are denoted with equivalent number of bits m_1 and m_2 respectfully. As demonstrated in [5], it is sufficient to consider m_2 to be at least 2 bits higher than m_1 to ensure measurement error is

ISBN 978-80-69159-00-6

independent of the ADC resolution and harmonic order and instead determined by the oversampling rate. The signal h_1 is a dithering signal added to the input signal to increase resolution of the analogue-to-digital conversion. The values stored in the memory block are also dithered, meaning they are precomputed using the known basis function $y(t)$ and a fictitious dithering signal h_2. Values Ψ_1 and Ψ_2 can be accurately described by equations (1) and (2).

$$\Psi_1 = Q\left[x(t) + h_1(t)\right] \tag{1}$$

$$\Psi_2 = Q\left[y_n(t) + h_2(t)\right], \tag{2}$$

where Q represents the quantization function and y_n takes the form of either $\sin(2\pi f_n t)$ or $\cos(2\pi f_n t)$. When the number of bits is sufficiently high, the effects of the quantization function become negligible. Consequently, the output of the block responsible for determining harmonic coefficient can be expressed by equation (3)

$$\begin{aligned}\overline{\Psi} &= \frac{1}{T}\int_{-T/2}^{T/2}\left[x(t)+h_1(t)\right]\left[y_n(t)+h_2(t)\right]dt = \\ &= \frac{1}{T}\int_{-T/2}^{T/2}x(t)y_n(t)dt + \underbrace{\frac{1}{T}\int_{-T/2}^{T/2}x(t)h_2(t)dt}_{I_1} + \underbrace{\frac{1}{T}\int_{-T/2}^{T/2}y_n(t)h_1(t)dt}_{I_2} + \underbrace{\frac{1}{T}\int_{-T/2}^{T/2}h_1(t)h_2(t)dt}_{I_3},\end{aligned} \tag{3}$$

I_1, I_2 and I_3 are equal to zero if the averages of h_1 and h_2 both zero and they are statistically independent. When a sufficiently large number of samples is used, the precision of the measurement can be reduced to an arbitrary small value, as demonstrated in [1], [2] and [4]. Considering current technological limitations, dithering signals h_1 and h_2 may not be fully integrated out of the equation (3), either due to various imperfections in electronic circuitry or due to the accumulation of the numerical error. In such case, a more general and accurate equation, given by (4), has to be used to describe the actual output $\hat{\overline{\Psi}}$.

$$\hat{\overline{\Psi}} = \frac{1}{N}\sum_{n=1}^{N} Q\left[x(n)+h_1(n)\right] Q\left[y_n(n)+h_2(n)\right] = \frac{1}{N}\sum_{n=1}^{N} Q\left[x(n)y_n(n)+\Delta\right] = \overline{\Psi} + \Delta\overline{\Psi} \tag{4}$$

Integrals I_1, I_2 and I_3 can assume nonzero values due to various factors, thereby introducing inaccuracy into the measurement process. This paper examines four possible improvements in instrument design aimed at mitigating the issue of measurement inaccuracy $\Delta\overline{\Psi}$ denoted in (4), while preserving the measurement precision.

The following hypotheses will be tested:

1) For a sufficiently high m_1, dithering no longer reduces measurement uncertainty and further only contributes to hardware and software complexity; and
2) Dithering of the basis function stored in the memory block can be omitted ($h_2 = 0$).

2. Subject and Methods

The complexity of the model necessitates simulations with a limited reliance on analytical calculations. The possible vast space of $x(t)$ functions will be limited to only three possible signals of interest: pure sinewave, maximally distorted signal in power grid according to the European Norm for power quality EN50160 [6] and the rectangular periodic function. Without any loss in generality, all signals are scaled to the hypothetical range of the ADC of ±5 V and the same period $T = 20$ ms. Selected signals are illustrated in Fig. 2.

ISBN 978-80-69159-00-6

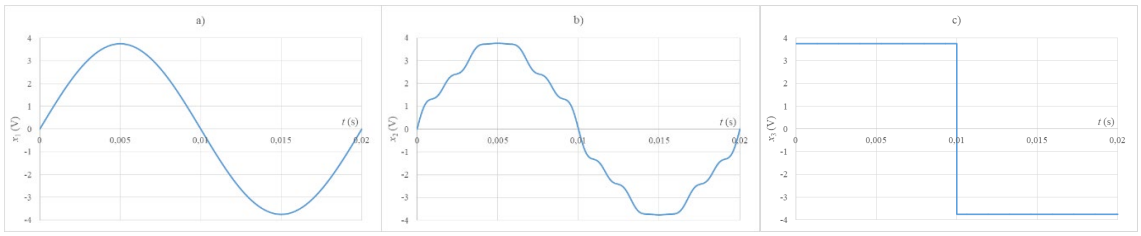

Fig. 2. Signals used in analysis for an ADC with $m_1 = 2$ bits, and range ±5 V: a) sine wave; b) maximally allowed distorted and scaled down signal according to the EN50160; c) rectangular periodic signal

Theoretical Considerations

For testing the hypothesis 1, the offset voltage of the comparators and the presence of substrate noise generated by switching activities in digital blocks were modelled as 7.84 mV Gaussian white noise added to the signal prior to quantization [7].

For hypothesis 2, theoretical analysis is already given with (3) and the follow up discussion on values of I_1 and I_3 in cases when h_2 is present and eliminated.

Simulations

In simulations, the following parameters were varied: m_1, m_2 (with the constraint that $m_2 \geq m_1 + 2$ bits), inclusion or exclusion of h_2. All simulations were conducted in Excel. For all hypotheses up to 10.000 samples per period were considered.

3. Results

Hypothesis 1

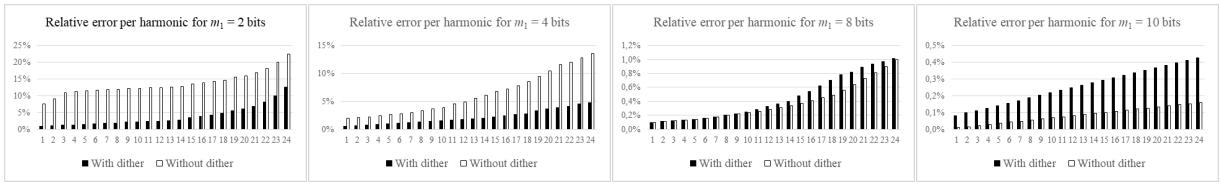

Fig. 3. Simulation results of the average relative measurement error for all three test signals in cases of 2-bit, 4-bit, 8-bit and 10-bit flash ADCs.

For hypothesis 1, some of the key results of simulations are summarized in Fig. 3. It is evident that for 8-bit flash ADCs, dithering provides results comparable to straightforward analogue-to-digital conversion. At even higher resolutions, the benefit of dithering is lost due to the accumulation of numerical error surpassing the noise threshold. This conclusion was used to narrow down the simulation space for other hypotheses to cases where $m_1 \leq 8$.

Hypothesis 2

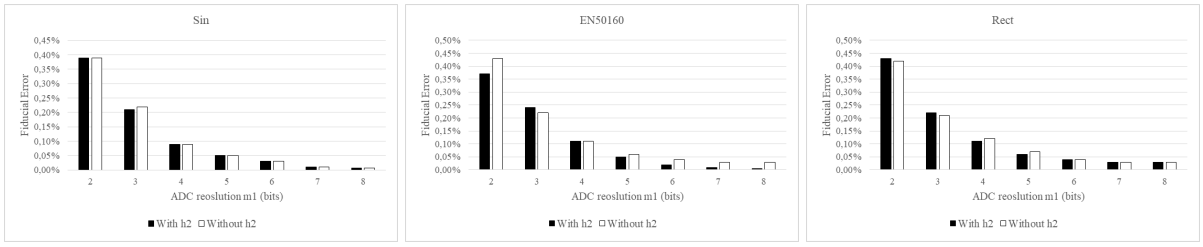

Fig. 4. Simulation results of the average fiducial error for the selected test signals as a function of the converter's resolution.

ISBN 978-80-69159-00-6

Simulation results revealed that the dithering signal h_2 provides little benefit to the measurement error, and that its contribution diminishes as the resolution of the used hardware increases. Fig. 4 illustrates values of the fiducial error - the error scaled with the range of the converter – for all three signals as function of ADC and memory resolutions varying from 2 to 8. The results suggest that the use of the dithering sequence h2 can be omitted without significantly impacting the instrument's performance.

4. Discussion and Conclusions

For the low resolution of the ADC, the nonlinearity of the quantization function Q ensures that approximation (3) is actually not a good model for the operation of the stochastic harmonic instrument. On the other hand (4) provides a much better model. In that model, a separation of dithering sequences from their adding signals $x(t)$ and $y_n(t)$ is not possible because Q is not interchangeable with the sum (integral). Therefore, dithering of the set of basis sin and cos functions can be performed, but it brings little or no benefit to the reduction of the measurement uncertainty. Omitting h_2, particularly when it has to be realized in an analogue version significantly saves the resources and simplifies the instrument design.

Through computer simulations conducted over a limited set of input ensembles, the hypotheses regarding potential improvements have been validated. The simulation results have validated hypotheses 1 and 2, which is further supported by theoretical explanations.

Without loss of generality, the conclusions drawn in this study are applicable to any stochastic resonance method, irrespective of the field of application, the type, or the shape of the input signal. This research thus demonstrates the potential for improving the design of future stochastic harmonic instruments by reducing dithering, while achieving higher measurement accuracy.

References

[1] von Neumann, J. (1956). Probabilistic logic and the synthesis of reliable organisms from unreliable components. *Automata Studies / Shannon, C., McCarthy, J. (eds.). Princeton : University Press*, pp. 43-98.

[2] Kamensky M, Kovac K. (2011). Correction of ADC Errors by Additive Iterative Method with Dithering. Measurement Science Review11(1): pp. 15-18. http://dx.doi.org/10.2478/v10048-011-0004-3

[3] Patil K.S. (2024) Digital Image and Video Processing: Algorithms and Applications. Journal of Electrical Systems 20(3s) pp. 1390-1396. http://dx.doi.org/10.52783/jes.1516.

[4] Antić B.M., Mitrović Z.L., Vujičić V.V. (2012) A Method for Harmonic Measurement of Real Power Grid Signals with Frequency Drift using Instruments with Internally Generated Reference Frequency. Measurement Science Review, Volume 12, No. 6. pp 277-285. http://dx.doi.org/10.2478/v10048-012-0038-1.

[5] Pjevalica V. Vujicic V. (2010) Further Generalization of the Low-Frequency True-RMS Instrument, IEEE Transactions on Instrumentation and Measurement 59(3) pp. 736 - 744. http://dx.doi.org/10.1109/TIM.2009.2030874

[6] CENELEC. (2025). EN 50160:2022/A1:2025 Voltage characteristics of electricity supplied by public electricity networks.

[7] Yadav A. Rai N. Verma A. Wairya S. (2021). Design of Flash ADC using low offset comparator for analog signal processing application. 021 8th International Conference on Signal Processing and Integrated Networks (SPIN), Noida, India, 2021, pp. 76-81, doi: 10.1109/SPIN52536.2021.9566050.

Large Scale Model for Radiation Pattern Measurement Methodology

Michal Dzuris, Jakub Krchnak, Michal Stibrany

Institute of Electrical Engineering, Faculty of Electrical Engineering and Information Technology, Slovak University of Technology, Ilkovicova 3, 812 19 Bratislava, Slovakia,
Email: michal.dzuris@stuba.sk

Abstract. *The article presents a digital twin simulation of a real antenna system (AS) inserted in complex terrain topology. The simulation of E-field distribution around the AS (450 meters in radius) illustrates the influence of reflective terrain - imported with a point cloud LiDAR scan. As shown in this paper, ignoring these effects could lead to severe measurement errors. Further study of this digital twin simulation will help to avoid introduced measurement error in the proposed quadcopter radiation pattern measurement of large AS.*

Keywords: Radiation Pattern Measurement, Antenna System, Digital Twin, Numerical Calculation

1. Introduction

Radiation pattern is one of the key parameters of any antenna. Radiation pattern measurement is complicated to perform and usually needs to be done in the controlled environment of an anechoic chamber. For relatively small antennas, there are standard procedures in place to ensure reproducible measurement results. In the case of large antenna system (AS) radiation pattern measurement, the standard measurement procedures are unclear and require a specially modified helicopter with a trained crew [1]. An alternative to the helicopter measurement can be a quadcopter measurement [2]. An example of a large AS can be seen in Fig. 1a. This AS is mounted on a tall monopipe structure, housing many more telecommunication antenna systems.

(a) (b)

Fig. 1: (**a**) Example of a large antenna system (in green rectangle) mounted on the monotube (**b**) quadcopter with the specialized measurement device „Pixla 1“.

A quadcopter with a specialized measurement device, as seen in Fig. 1b reduces the cost and time of the radiation pattern measurement. It is also possible for a quadcopter to fly closer to the AS, which in the case of the helicopter measurement is not possible due to its technical restrictions. This advantage in measurement flexibility for an affordable price leads to new ways of the antenna system diagnostics [3], which can again reduce the time and cost of the repairs in case of AS failure.

This paper illustrates the problem of reflective surfaces in the case of radiation pattern measurement in relatively close proximity to the measured AS. This analysis aims to supplement the methodology for quadcopter radiation pattern measurement of large AS.

ISBN 978-80-69159-00-6

2. Subject and Methods

The problem shown in this paper is focused on one specific antenna site. The digital twin of the antenna system corresponds with the geometry, orientation, and radiation pattern of the real antenna system. The presented results are for one site only, and it differs from other similar antenna system sites. However, every site is unique, similar terrain topology can suggest similar problems with the investigated surface reflections. The nearby vertical terrain gradient, but also the height of the installed AS and other structures, are subject of influence [4] [5]. With sufficient information about the AS (altitude, orientation, topology, etc.), the numerical calculation can be performed for any AS, although the complexity and detail of such calculation depends on the available computation power.

b) Digital twin of the antenna system and terrain

The antenna system is located ~ 40 meters above the ground on a steel tower, housing multiple antenna systems for various telecommunication purposes (shown in Fig. 2a). The terrain around the antenna mast has a complicated topology, including many different types of vegetation contributing as reflecting, diffracting, and absorptive surfaces. Simulation of a large-scale environment with full details would (due to hardware requirements) be impossible. To mitigate this problem, simplifications of the model in terms of terrain modeling, foliage removal, and AS equivalent substitution were made. Detail of the simulation model zoomed on the AS location and nearby terrain can be seen in Fig. 2b.

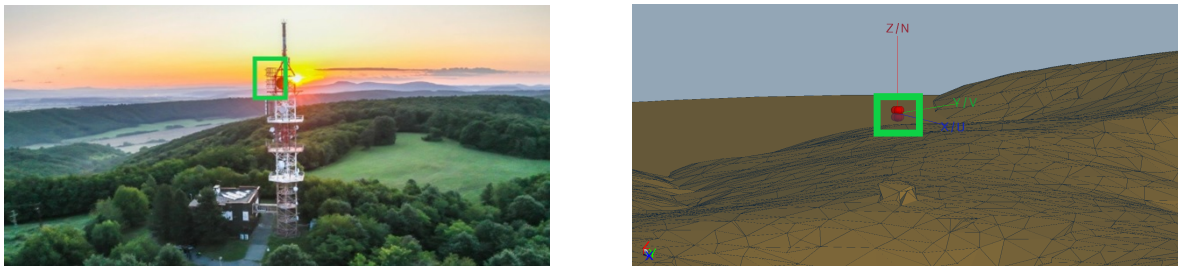

(a) (b)

Fig. 2: (**a**) View of the antenna system site to be modeled (AS is in green rectangle) (**b**) zoomed view of imported terrain nearby the AS (AS is in green rectangle).

The terrain (partially seen in Fig. 2b) was prepared by importing a simplified point cloud LiDAR scan. This method allows for high resolution and detailed terrain simulation. The terrain model used in this paper has a radius of 450 meters with its center located at the AS. The radii of the simulation model have been chosen based on the reasonable quadcopter measurement range.

The digital twin of the AS (1x AS = 6x antenna elements) seen in Fig. 3a was also prepared, and the radiation pattern for one antenna element was numerically computed. For simplification of the numerical model, the AS is further represented by the Hertzian dipole equivalent source (one for each antenna element), which has very similar radiation pattern characteristics but is much less demanding for computation power [6].

A hybrid solver based on physical optics in FEKO was used, as a model of this extent would be for a pure FEM or MoM solver again almost impossible to solve. A similar approach for IoT mesh in an urban environment was explored in [7], but the used solver would not be suitable for this application. With all these simplifications, it is now feasible to simulate electrical near-field distribution around the antenna system to better understand the nature of problematic surface reflections and its influence on the radiation pattern measurement.

ISBN 978-80-69159-00-6

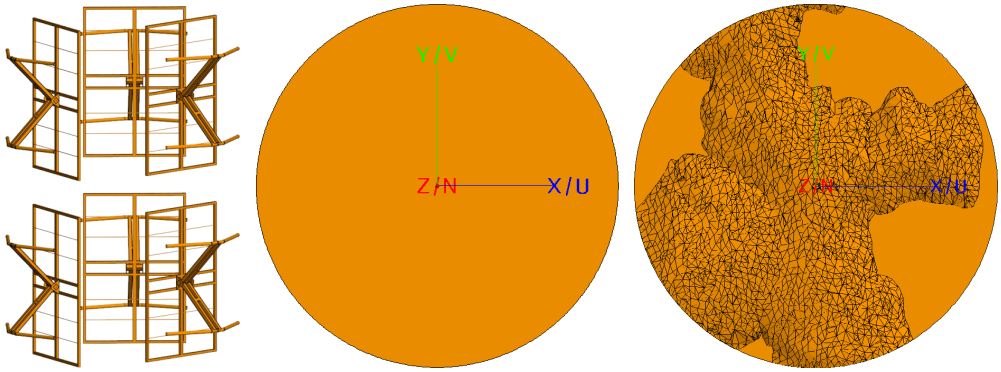

(a) (b) (c)

Fig. 3: (**a**) Digital twin of the antenna system (Illustrative) (**b**) Simple conductive surface below the antenna system with a radius of 450 meters (**c**) CAD model of the terrain of the nearby antenna system site (imported with point cloud LiDAR scan), also with a radius of 450 meters.

c) Simulation results

Even with the simplification, the simulation model has extensive boundaries and challenging complexity. The presented results are therefore in one plane only (at the height of the AS). Figures 4a to Fig. 4c shows the simulation results, visualizing the electric field distortion due to the various reflective surfaces. In Fig. 4a the electrical field distribution follows the exact radiation pattern characteristics and its intensity is droping as expected at the rate of $\frac{1}{r}$ (for far-field). With the conductive plane in Fig. 4b, the interference with the reflected EM wave forms local maxima and minima (as expected) based on the AS altitude above the ground and distance of the AS from the point of observation [8].

Fig. 4c clearly shows that the interference pattern is strongly influenced by the height difference of the terrain and creates interference "waves", "wrapping itself" around the hills. This can cause problems in radiation pattern measurement due to the nature of the measurement methodology itself. In the case of standard radiation pattern measurement, when the measurement probe has measurement points distributed in a circle, the measurement path could cross multiple of these interference "waves" and add measurement error in the orders up to 10 dB.

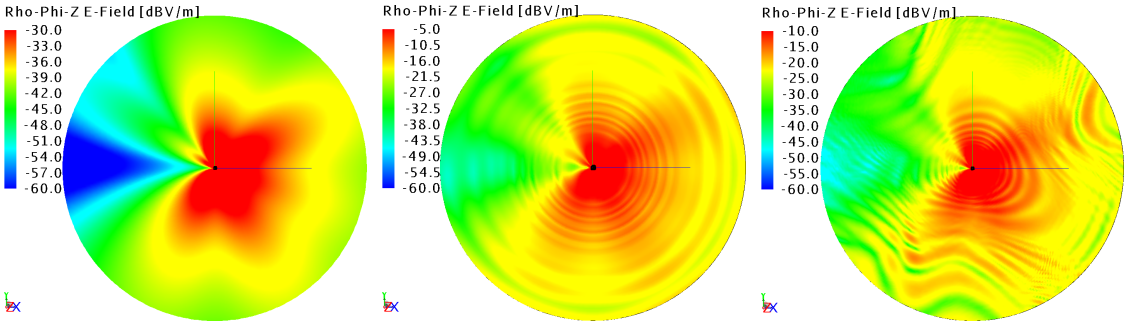

(a) (b) (c)

Fig. 4: E-field distribution in the horizontal plane around the AS with a radius of 450 meters at a constant height: (**a**) without a reflective surface (simulation of the AS in a vacuum) (**b**) with a simple planar conductive surface shown in Fig. 3b (**c**) with simplified real-world terrain (ideally conductive) shown in Fig. 3c

3. Conclusions

The radiation pattern measurement with the use of a quadcopter is a promising fast and cost-effective innovation, leading to new diagnostic methods for large AS. The methodology for the UAV based measurement is not fully formed yet, but preliminary measurement results

ISBN 978-80-69159-00-6

show a high degree of agreement between the expected radiation pattern (from the AS datasheet and from simulation data) and the measured data [6].

In special cases (such as the antenna system in this paper), where the AS is located at low altitude above the ground, or the terrain around the AS does not have the elevation advantage, the radiation pattern measurement can be severely influenced and distorted.

Results from the performed simulation analysis shows, that these special cases can be identified before the measurement itself and the methodology can be adapted even for these large antenna systems.

To confirm or detect such cases, it is possible to perform in-situ propagation flights, where the interference "waves" (as seen in 4c) should be noticeable. Comparing and confirming the simulation results with real measurement data is planned to be evaluated.

Acknowledgements

This work was supported by the project APVV 20-0042 "Microelectromechanical sensors with radio frequency data transmission", ENEFS 09I05-03-V02-00041 "Novel electrically enhanced wireless method for sensing of mechanical quantities" and project P324 “Pixla3_2024”.

References

[1] Witvliet B. (2006). Airborne evaluation / verification of antennapattern of broadcasting stations, *in 18th International Wroclawsymposium and exhibition on Electromagnetic compatibility in Wroclaw*. (1):433-438

[2] Dzuris, M., Hartansky, R., Krchnak. J. (2023). Measuring the Radiation Pattern of Large FM Antenna System, *in 14th International Conference on Measurement*. DOI: 10.23919/MEASUREMENT59122.2023.10164409

[3] Krchnak, J., Hartansky, R., Dzuris, M., Halgoš, J., Grilli, N., Stibrany M. (2023). Identification of Faulty Antenna in Large FM Antenna System Using Quadcopter Measurements, *in International Journal on Communications Antenna and Propagation (IRECAP)*. 13(5):238-248

[4] Balanis, C.A. (2015). *Antenna Theory: Analysis and Design, 4th ed*. John Wiley & Sons, Inc. ISBN 978-1-118-6422060-1

[5] Hartansky, R., Smieško, V., Marsalka, L. (2014). Numerical Analysis of Isotropy Electromagnetic Sensor Measurement Error, *in Measurement Science Review*. 13(6):311-314

[6] Krchnak, J., Dzuris, M., Hartansky, R., Halgoš, J., Kliuchka, A., Stibrany M. (2024). Investigation of the measurement distance for an UAV-performed radiation pattern measurement, *in Measurement: Sensors (In Press)*. DOI: 10.1016/j.measen.2024.101415

[7] Kliuchka, A., Hartansky, R., Halgos, J. (2023). Methods of computer modeling of electromagnetic field propagation in urban scenarios for Internet of Things, *in Journal of Electrical Engineering*. 74(5):422-433

[8] Balanis, C.A. (1989). *Advanced engineering electromagnetics*. John Wiley & Sons, Inc. ISBN 0-471-50316

Modeling and Simulations of Biological Signals

ISBN 978-80-69159-00-6

Influence of Limb Electrodes Placement on the Simulated ECG Signals

Elena Cocherová, Lukáš Zelieska, Milan Tyšler

Institute of Measurement Science, SAS, Bratislava, Slovakia
Email: elena.cocherova@savba.sk

Abstract. *The influence of the limb electrodes' placement on the simulated standard ECG signals during premature ventricular contractions (PVC) using a patient-specific torso model was studied in this article. Simulated electrical activation in the ventricular model was started at the position of the initial ectopic activation in the area near the His bundle. The propagation of electrical activation in the ventricular model was modeled using bidomain reaction-diffusion (RD) equations with the ionic transmembrane current density defined by the modified FitzHugh-Nagumo equations. The torso was modeled as a homogeneous passive volume conductor. The RD equations were numerically solved in the Comsol Multiphysics environment. Simulated body surface potentials (BSPs) and corresponding ECG signals were compared with those measured in a real PVC patient. The shape of simulated ECG signals during the PVC varied with the changed positions of the limb electrodes on the torso model, resulting in 11% average change of QRS complex amplitudes and 9% average change of correlation coefficients between simulated and measured QRS complexes in ECG leads I, II, and III.*

Keywords: Bidomain Reaction-Diffusion Model, Ventricles Model, ECG Lead Placement, Premature Ventricular Contraction

1. Introduction

Electrical activation of the heart is manifested on the torso in body surface potentials (BSPs). The changes of the ventricular activation can be observed in the measured electrocardiographic (ECG) signals during the QRS complexes. Positions of electrodes for standard 12-lead ECG comprise places at 3 limbs and 6 anterior chest places [1-2].

To model heart activity, the positions of limb electrodes are approximated by positions on the torso, near the right and left shoulder, and on the lower left part of the chest. Variations of limb leads placement on the torso may cause changes in the ECG signals [3].

In a healthy heart, the electrical activation of the ventricles starts from the atrioventricular node and propagates through the conduction system to the working ventricular myocardium [1]. In the case of premature ventricular contraction (PVC), the initial part of the conduction system is not involved, and the activation starts and propagates from some ectopic focus in the ventricles.

In this study, the positions of limb electrodes on the torso were varied, and the resulting changes in simulated ECG signals during PVC were evaluated.

2. Subject and Methods

We simulated ventricular activation and corresponding ECG signals and BSP distribution during the PVC and compared them to data measured in a real patient.

Measured data

The data were recorded from a 17-year-old sportsman with frequent PVCs (patient P001 from the Bratislava dataset). The information about the PVC origin received from the measurements in the electrophysiological lab was that the initial ectopic activation starts in the interventricular septum near the His bundle. ECG signals from limb leads and BSP maps from 128 electrodes

ISBN 978-80-69159-00-6

on the chest were recorded. The geometry of the heart ventricles and torso, as well as the real positions of 128 ECG electrodes on the torso surface (shown in Fig. 1 as small black points), were obtained from a CT scan.

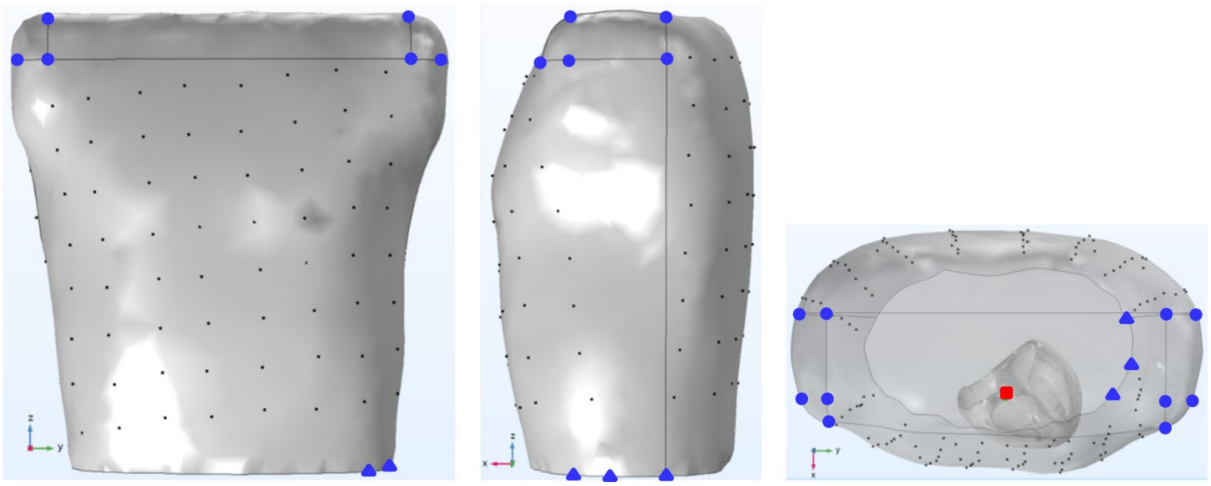

Fig. 1. The frontal (left), left sagittal (middle), and transverse transparent view (right) of the torso model with the positions of 128 measuring electrodes (black points). The tested positions for RA and LA limb electrodes are highlighted as blue circles, and positions for the LF limb electrode are highlighted as blue triangles. Position of PVC42 is shown as a red square in the ventricular model (right).

Model of the torso and heart ventricles

The model of heart ventricles and the patient torso (Fig. 1) were described in details in [4]. The propagation of electrical activation in the ventricular model was simulated using bidomain partial differential reaction-diffusion (RD) equations with the ionic transmembrane current density defined by the modified FitzHugh-Nagumo equations [4,5]. For homogeneous model of the ventricles, the used value of the tissue conductivity was $\sigma = 0.8$ S/m representing overall conductivity of the myocardial tissue and conductive system. Torso was treated as a passive volume conductor with conductivity set to $\sigma = 0.8$ S/m. As the site of the PVC origin, we used the position PVC42 found in our earlier article [4] situated in the septum near base and giving the best correspondence between measured and simulated ECG signals.

Positions of the limb electrodes

Generally, electrode positions for the standard 12-lead ECG measurements are defined as six places on the anterior chest and 3 places on limbs: right arm (RA), left arm (LA) and left foot (LF) [2]. For limb electrodes placement on the torso, we tested 5 positions for the RA and LA electrodes near the right and left shoulder and 3 positions of the LF electrode situated on the lower left part of the chest (shown in Fig. 1 as blue points). We used these positions to analyze the influence of limb electrodes placement on the simulated ECG signals.

3. Results

The measured and simulated ECG potentials (leads I, II, III) during QRS complex are shown in Fig. 2. The measured limb lead potentials V_{Im}, V_{IIm} and V_{IIIm} were computed from potentials V_{RAm}, V_{LAm} and V_{LFm} measured from standard limb electrode positions at ankle and wrists:

$$V_{Im} = V_{LAm} - V_{RAm}\,; \qquad V_{IIm} = V_{LFm} - V_{RAm}\,; \qquad V_{IIIm} = V_{LF}m - V_{LAm}\,. \tag{1-3}$$

Wilson central terminal (WCT) potential was computed according formula:

$$WCT_m = \ (V_{RAm} + V_{LAm} + V_{LFm})/3\,. \tag{4}$$

ISBN 978-80-69159-00-6

The simulated limb lead potentials V_{Is}, V_{IIs} and V_{IIIs} were computed from potentials V_{RAs}, V_{LAs} and V_{LFs} taken from limb electrodes placed on the torso (shown in Fig. 1). Simulated limb lead potentials were computed for all 75 combinations (5x5x3) of RA, LA and LF electrode positions.

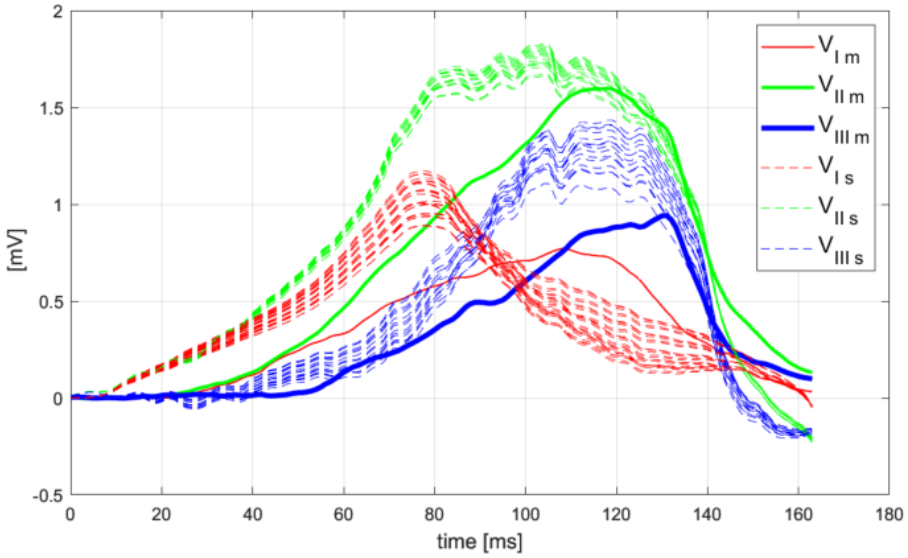

Fig. 2. The simulated (dashed lines) and measured (solid line) ECG potentials for limb leads I, II, III during QRS complex.

The beginning of the QRS complex was set at a time instant when RMS value from 128 BSPs crossed 1% threshold of the QRS peak value in both measured and simulated signals.

The end of the QRS complex was set at a time instant when RMS value from 128 measured BSPs has dropped below 10% of the QRS peak value. The higher threshold for the end of QRS signal was set because of partial fusion of QRS with the T wave in case of prolonged QRS in ectopic signals. The end of the QRS complex in simulated signals was defined in the same time instant as in the measured one.

The range and the mean values of R peak amplitudes (A_{Is}, A_{IIs} and A_{IIIs}) in simulated limb leads were evaluated in Table 1. The change of limb electrodes position caused the change of the R peak amplitudes up to about ±14% in leads I and III, and up to ±5% in lead II. The average value of R peak amplitude changes for leads I, II, III was up to ±11%.

Table 1. Range and mean values of selected parameters changes for all combinations of limb electrodes positions.

Parameter	Units	Range	Mean	Range/Mean [%]	Range/Mean [%]-100%
A_{Is}	mV	0.888 ÷ 1.171	1.038	86 ÷ 113	-14÷ 13
A_{IIs}	mV	1.664 ÷ 1.830	1.758	95 ÷ 104	-5 ÷ 4
A_{IIIs}	mV	1.107 ÷ 1.436	1.294	86 ÷ 111	-14 ÷ 11
C_{Is}	-	0.920 ÷1.000	0.981	94 ÷ 102	-6 ÷2
C_{IIs}	-	0.999 ÷ 1.000	1.000	99.95 ÷ 100.01	-0.05 ÷ 0.01
C_{IIIs}	-	0.979 ÷ 1.000	0.994	98.5 ÷ 100.6	-1.5 ÷ 0.6
C_{Ism}	-	0.493 ÷ 0.787	0.637	77 ÷ 124	-23 ÷ 24
C_{IIsm}	-	0.911 ÷ 0.921	0.917	99.4 ÷100.4	-0.6 ÷ 0.4
C_{IIIsm}	-	0.918 ÷ 0.959	0.940	98 ÷ 102	-2 ÷ 2

ISBN 978-80-69159-00-6

Correlation coefficients (C_{Is}, C_{IIs} and C_{IIIs}) between simulated limb lead potentials during the QRS complex computed for all combinations of limb electrodes positions on the torso were near to 1, since the signal shape changed very little. Relative changes were up to ±6% in lead I, up to ±0.05% in lead II and up to ±1.5% in lead III. The average value of these changes of correlation coefficients for leads I, II, III was up to ±3%.

Correlation coefficients (C_{Ism}, C_{IIsm} and C_{IIIsm}) between simulated and measured limb lead potentials during the QRS complex (Table 1) varied up to ±24% for lead I, up to ±0.6% for lead II, and up to ±2% for lead III. Average change for leads I, II, III was up to ±9%.

Relative change of correlation coefficients between WCT potentials simulated for all 75 combinations of limb electrodes positions was only up to ±0.02%. It means, that WCT was negligibly affected by variations of limb electrodes positions. Therefore, also BSPs and precordial leads potentials were only negligibly affected by these variations.

4. Conclusions

The influence of the limb electrodes positions variations on simulated ECG signals was more pronounced in changed R peak amplitudes of the QRS complex in limb leads I, II and III (average change up to ±11%) than in changes of the correlation coefficients between simulated signals (average change up to ±3%).

The correlation coefficients between simulated and measured limb leads potentials during the QRS complex were affected by the limb electrodes positions on the torso unequally for leads I, II and III. The highest effect was in limb lead I, where the R peak in simulated signal was shifted with respect to measured one and therefore the correlation coefficients C_{Ism} varied up to ±24%. The average change of correlation coefficients for leads I, II, III was up to ±9%.

Observed changes were caused by both positions changes of limb electrodes on the torso and model simplifications (e.g. isotropic heart muscle tissue and ventricular model without conduction system). In this model, the effects of changed placement of limb electrodes on the torso were not negligible but still smaller than effects of the model simplifications.

Acknowledgements

This work was supported by grant 2/0106/25 from the VEGA Grant Agency and by grant APVV-19-0531 from the APVV agency.

References

[1] Macfarlane, P. W., Van Oosterom, A., Pahlm, O., Kligfield, P., Janse, M., Camm, J. (2011). *Comprehensive electrocardiology*, Springer-Verlag.

[2] Moeinzadeh, H., Assad, J., Bifulco, P., et al. (2020). WCTECGdb: A 12-Lead Electrocardiography Dataset Recorded Simultaneously with Raw Exploring Electrodes' Potential Directly Referred to the Right Leg. *Sensors (Basel)*, 20 (11).

[3] Tung, R. T. (2021). Electrocardiographic limb leads placement and its clinical implication: Two cases of electrocardiographic illustrations. *Kans J Med*, 14 (3), 229-230.

[4] Cocherová, E., Zelieska, L., Tyšler, M. (2023). Simulation of premature ventricular contractions in patient specific bidomain ventricular model. *Clinician and Technology*, 53 (2), 46-51.

[5] Sovilj, S., Magjarevic, R., Lovell, N. H., Dokos, S. (2013). A simplified 3D model of whole heart electrical activity and 12-lead ECG generation. *Computational and Mathematical Methods in Medicine*, 2013.

In Silico Investigation of The Impact of the Ventricular Filling Heterogeneity on the Electrical Field Propagation Using a Patient-Specific Model

[1,2]Lukas Zelieska, [3]Beata Ondrusova, [1]Milan Tysler, [4,5]Jorge Sánchez

[1]Institute of Measurement Science, Slovak Academy of Sciences, Bratislava, Slovakia, FEI STU, STU in Bratislava, Bratislava, Slovakia
[3]Johannes Kepler University, Linz, Austria
[4]Centro de Investigación e Innovación en Bioingeniería, Universidad Politécnica de Valencia, Valencia, Spain
[5]Institute of Biomedical Engineering, KIT, Karlsruhe, Germany
Email: lukas.zelieska@savba.sk

Abstract. *This study investigates the influence of the ventricular blood pool (BP) on simulations of cardiac electrical activation using a patient-specific anatomical model and two computational approaches: the bidomain (BD) and pseudo-bidomain (P-BD) models. The simulations were performed for a 17-year-old patient with premature ventricular contractions (PVCs) originating near the His bundle. Both BD and P-BD models were tested with and without the inclusion of the BP. Local activation times (LAT) and body surface potentials (BSP) were analyzed to evaluate the effect of BP inclusion across different model configurations. The results showed that LAT was nearly identical across all four model configurations, with correlation coefficients above 0.99 and RMSE values below 1.39%. BSP, however, were more sensitive to both the choice of model and the inclusion of BP, particularly in signal amplitude, with maximum RMSE values reaching 8.194%. Despite these amplitude differences, the overall waveform morphology remained almost unchanged. These findings suggest that the BP has a negligible effect on LAT and signal morphology but can influence signal amplitude. Therefore, the computationally less demanding P-BD model without BP may be sufficient for simulating focal activation patterns. Further simulations involving more complex propagation patterns are needed to validate the general applicability of this approach.*

Keywords: Premature Ventricular Contractions (PVC), Bidomain Model, Pseudo-Bidomain Model, Cardiac Blood Pool (BP)

1. Introduction

Premature ventricular contractions (PVCs) are among the most common types of cardiac arrhythmias, often observed even in individuals without underlying structural heart disease [1]. Although typically benign, frequent PVCs can impair cardiac function or reduce quality of life, sometimes requiring clinical intervention. Treatment options include pharmacological therapy or catheter-based radiofrequency ablation (RFA). The success of RFA relies heavily on accurately understanding the propagation of ectopic activation and precisely localizing its source, as improper targeting can lead to suboptimal outcomes or recurrence.

To address these challenges, computational modeling of cardiac electrophysiology has become an important tool for supporting both research and clinical decision-making [2, 3]. In-silico simulations are increasingly used to study the propagation of ectopic activation and improve the localization of ectopic foci, both of which are essential for the effectiveness of RFA. Patient-specific models have shown promising results in reproducing ectopic activation patterns and supporting clinical decision-making. Despite significant advancements, certain aspects of torso modeling have received limited attention in computational studies. One example is the effect of heterogeneities such as the ventricular blood pool [4].

ISBN 978-80-69159-00-6

In this study, we developed a patient-specific anatomical model and used bidomain (BD) and pseudo-bidomain (P-BD) models to investigate the influence of the cardiac blood pool (BP) on the simulated cardiac electrical field. We focused on local activation times (LATs) and BSP, which reflect the heart's electrical activation propagation.

2. Subject and Methods

For our study, we used data from a 17-year-old athlete (patient P001) from the Bratislava dataset who frequently exhibited PVCs. The patient underwent RFA. The PVC origin was identified in the upper part of the septum near the His bundle, and its location was subsequently confirmed by the successful outcome of the ablation procedure.

Patient-Specific Anatomical Model of the Torso and Heart's Ventricles

We generated a patient-specific anatomical torso-heart model based on clinical CT data, incorporating anatomically realistic ventricles (Fig. 1A), the ventricular BP (Fig. 1B), and the torso (Fig. 1C). Images of the heart were manually segmented using the Tomocon software as explained in Švehlíková et al. [2].

Using the segmented surfaces, we generated computational volumetric tetrahedral meshes with an average edge length of 444 μm in the heart and 2076 μm in the torso. We used Cobiveco [4] to compute relative ventricular coordinates, which served to specify spatially varying electrophysiological parameters and tissue properties. We implemented myocardial fiber orientation within the ventricles using a Laplace–Dirichlet Rule-Based algorithm [5], with fiber angles rotated linearly from + 60° at the endocardium to − 60° at the epicardium.

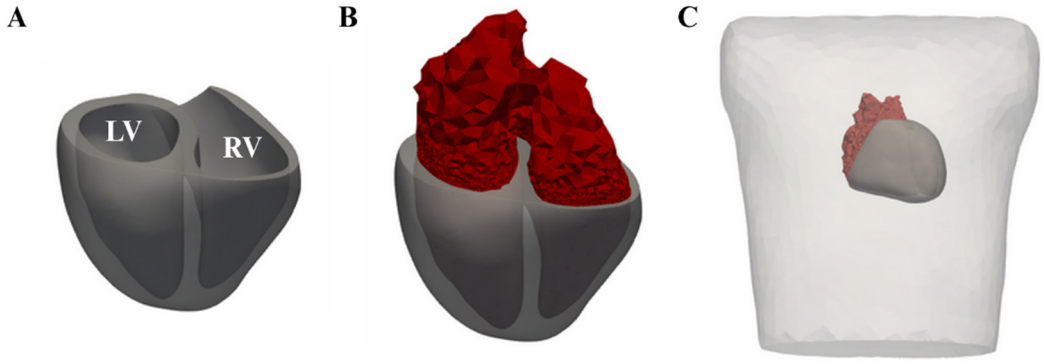

Fig. 1. A) Ventricular geometry without and B) with blood pool (BP) and C) torso-heart geometry.

Simulation of Ventricular Activation and Body Surface Potentials

We simulated ventricular electrophysiology using the bidomain (BD) and pseudo-bidomain (P-BD) models implemented in *openCARP* [6]. To describe the human ventricular myocyte electrophysiology, we used the model proposed by O'Hara et al. [7].

In our model implementation, we used a myocardial conduction velocity of 0.67 m/s. The tissue conductivity in the torso was defined as 0.4 S/m. The conductivity of the BP was set to 0.7 S/m. The initiation of electrical activation in our simulations was set at the anatomical location of the successful ablation site.

Analysis of Simulation Results

We computed the Pearson's correlation coefficient (CC) between the LAT, as well as between the BSP computed by the BD and P-BD models, with and without BP. Additionally, we calculated the relative root mean square error (RMSE) referred to the maximal amplitude of all values for both the LAT and the BSP. In computations, we considered LAT values in all heart

ISBN 978-80-69159-00-6

model points and a total of 128 signals were extracted from the BPS on the torso surface, corresponding to electrode positions used in a real patient measurement.

3. Results

Table 1 presents the CC and RMSE values for LAT and BSP, comparing the effects of BP, model type, and their combinations across four configurations. For LAT, the CC values are consistently high (≥ 0.99) across all simulations, indicating minimal variability in activation propagation and LAT patterns. The RMSE values remain low throughout all comparisons, with a maximum of 1.39% and values close to 0, showing that LAT maps are almost identical across the four models. In contrast, BSP show slightly more variability. All pairwise comparisons still exhibit high CC values (0.994 – 0.998), indicating similarity between BSP distributions. However, relative RMSE vary more noticeably, with the highest value of 8.194% observed between BD without BP and P-BD with BP, and the lowest value 0.686%, between P-BD without BP and P-BD with BP.

Table 1 CC and relative RMS differences between simulated LAT and BSP computed by BD and P-BD models with and without BP

Effect of	**Compared combinations of BD and P-BD models with and without BP**		**LAT**		**BSP**	
			CC	**RMSE [%]**	**CC**	**RMSE [%]**
Blood pool	(BD + BP)	vs (BD – BP)	1.000	0.102	**0.998**	1.281
	(P-BD + BP)	vs (P-BD – BP)	1.000	0.000	0.997	**0.686**
Model	(BD + BP)	vs (P-BD + BP)	0.999	1.390	0.997	7.386
	(BD – BP)	vs (P-BD – BP)	0.999	1.298	0.997	7.731
Combined	(BD + BP)	vs (P-BD – BP)	0.999	1.390	0.995	6.994
	(BD – BP)	vs (P-BD + BP)	0.999	1.298	**0.994**	**8.194**

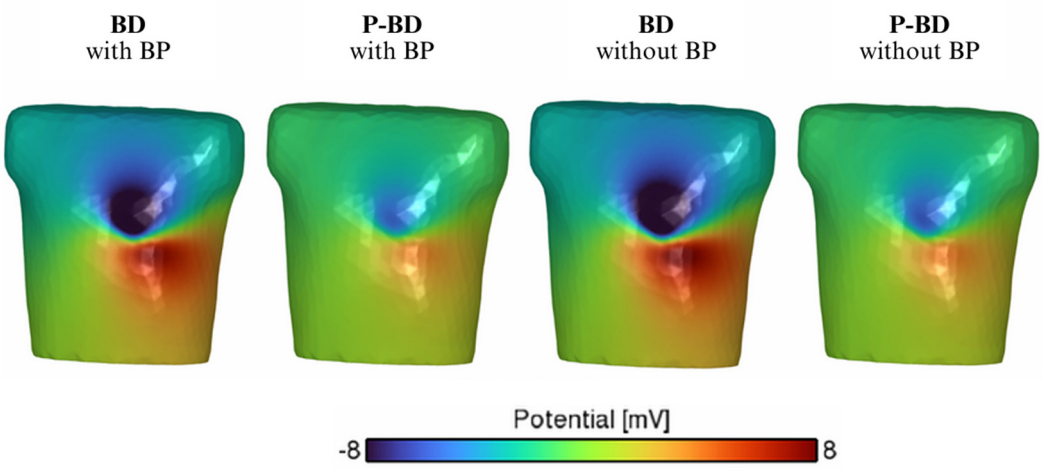

Fig. 2. BSP maps on the anterior chest at 90 ms computed by BD and P-BD models with and without BP.

Fig. 2 depicts an anterior view of the torso with the BSP map at 90 ms for the four model configurations. All maps exhibit a typical dipolar pattern, characterized by a region of negative potential in the upper half of the torso and a region of positive potential in the lower half of the torso.

ISBN 978-80-69159-00-6

4. Discussion and Conclusions

In this study, we compared four ventricular models using the BD and P-BD approaches, with and without inclusion of the BP. Our findings show that LAT remains consistent across all simulations, with correlation coefficients close to 1.0 and a maximum RMSE of only 1.39%. This suggests that the BP and model selection have no notable effect on LAT patterns and a negligible impact on their values. In contrast**,** BSP was sensitive to both the inclusion of the BP and even more to the model selection (BD vs. P-BD). The highest RMSE of 8.194% was observed between BD without BP and P-BD with BP, while the lowest (0.686%) occurred between the two P-BD models. These findings are in agreement with those of Zappone et al., who reported that excluding the BP leads to changes in amplitudes of the 12-lead ECG, with an RMSE of ~37% for the QRS complex, while the overall waveform morphology remained nearly unaffected [4]. Our results support the idea that not only the presence of the BP, but also the choice of the ventricular model itself, has a significant impact on signal amplitude.

A limitation of this study was that the propagation was initiated only from one site in the septum near the base of the right ventricle. While the findings provide valuable insight into the characteristics of LAT and BSP for such focal activity, further investigations are necessary to determine whether similar trends hold true for different propagation patterns in the ventricles. More complex propagation patterns need to be simulated to verify sufficient performance of the P-BD model and assess the impact of the BP on LAT and BSP.

Acknowledgements

This work was supported by grant APVV-19-0531 from the APVV agency and by grant 2/0106/25 of the VEGA Grant Agency. Part of the research results were obtained using the computational resources procured in the national project National Competence Center for High Performance Computing (project code: 311070AKF2) funded by the European Regional Development Fund, EU Structural Funds, Informatization of society, Operational Program Integrated Infrastructure.

References

[1] Kaya, Y., and Pehlivan, H. (2015). Classification of premature ventricular contraction in ECG. *International Journal of Advanced Computer Science and Applications*, 6(7), 34–40. https://doi.org/10.14569/IJACSA.2015.060706

[2] Švehlíková, J., Zelinka, J., Tyšler, M. (2024). Estimation of the PVC Origin from Simulations Using Cellular Automaton. In: *Computing in Cardiology*, 2024. https://doi.org/10.22489/CinC.2024.303

[3] Trayanova, N.A., Lyon, A., Shade, J., Heijman, J. (2024). Computational modeling of cardiac electrophysiology and arrhythmogenesis: toward clinical translation. In *Physiological Reviews*, 104(3), 1265-1333. https://doi.org/10.1152/physrev.00017.2023

[4] Zappon, E., Gsell, M.A.F., Gillette, K., Plank, G. (2025). Quantifying anatomically-based in-silico electrocardiogram variability for cardiac digital twins. *Computers in Biology and Medicine*, 189, 109930. https://doi.org/10.1016/j.compbiomed.2025.109930

[5] Schuler, S., Pilia, N., Potyagaylo, D., Loewe, A. (2021). Cobiveco: Consistent biventricular coordinates for precise and intuitive description of position in the heart—with Matlab implementation. Medical Image Analysis, 74, 102247. https://doi.org/10.1016/j.media.2021.102247

[6] Bayer, J.D., Blake, R.C., Plank, G., Trayanova, N.A. (2012). A novel rule-based algorithm for assigning myocardial fiber orientation to computational heart models. *Annals of Biomedical Engineering*, 40, pp. 2243-2254. https://doi.org/10.1007/s10439-012-0593-5

[7] Plank, G., Loewe, A., Neic, A. et al. (2021). The openCARP simulation environment for cardiac electrophysiology. Computer Methods and Programs in Biomedicine, 208, 106223. https://doi.org/10.1016/j.cmpb.2021.106223

[8] O'Hara, T., Virág, L., Varró, A., Rudy, Y. (2011). Simulation of the undiseased human cardiac ventricular action potential: model formulation and experimental validation. PLoS Computational Biology, 7(5), e1002061. https://doi.org/10.1371/journal.pcbi.1002061

Can Side Holes in Returning Cannula Improve VV-ECMO Effectiveness?

[1]Beata Ondrusova, [2]Argyrios Petras, [3]Johannes Szasz, [3]Jens Meier, [1]Luca Gerardo-Giorda

[1]Johannes Kepler University, Linz, Austria
[2]Johann Radon Institute for Computational and Applied Mathematics (RICAM), Linz, Austria
[3]Kepler University Klinikum, Linz, Austria
Email: beata.ondrusova@jku.at

Abstract. *Veno-venous extracorporeal membrane oxygenation (VV-ECMO) is a life-saving therapy used for patients with respiratory failure; however, its effectiveness may be compromised by high recirculation rates. Recirculation occurs when oxygenated blood from the returning cannula is drawn back into the ECMO circuit by the drainage cannula. In this study, we compared the recirculation rates between a returning cannula with 2 and 12 side holes for ECMO flow of* $4\,\mathrm{L/min}$ *using computational modeling of blood flow and oxygen diffusion. Simulations were computed using a patient-specific model of the right atrium, superior and inferior vena cava derived from the CT scan. For both cannulas, the recirculation rate was 12% and oxygen saturation was 86%, suggesting negligible influence of side holes on VV-ECMO efficacy. Further studies are needed to assess whether different designs could improve VV-ECMO performance. The pipeline used here can be used to evaluate and optimize such designs.*

Keywords: Veno-Venous Extracorporeal Membrane Oxygenation, Computational Fluid Dynamics, Navier-Stokes equations, Oxygen Diffusion

1. Introduction

Veno-venous extracorporeal membrane oxygenation (VV-ECMO) is used as a respiratory support system for patients with severe lung failure and was widely used during the COVID-19 pandemic. Oxygenation and carbon dioxide removal of blood is done externally, reducing lung workload and allowing the lungs to rest. The standard femoral-jugular configuration drains deoxygenated blood from the inferior vena cava (IVC) and returns oxygenated blood to the superior vena cava (SVC). A significant disadvantage of this configuration is that the drainage cannula is positioned in line with the returning cannula and thus the drainage cannula may unintentionally withdraw oxygenated blood from the return flow, reducing oxygen delivery efficiency. This phenomenon, known as recirculation, can be influenced by factors such as cannula configuration, positioning, size, shape, and ECMO flow [1]. Recirculation rates in VV-ECMO vary among patients, with a median of 14-16% and occasional outliers reaching up to 58% [2].

Computational modelling can provide valuable insights into the complex hemodynamics of the circuit, helping to optimize the settings to improve VV-ECMO efficiency. A computational study by Leoni et al. [3] demonstrated that ECMO blood flow has a greater impact on VV-ECMO efficacy than cannula positioning. Furthermore, modelling revealed a relationship between cardiac output and ECMO flow, with their ratio significantly influencing the recirculation rate as shown in Parker et al. [4]. Study by Wickramarachchi et al. [5] showed that the design of drainage cannulas affects flow dynamics. Such results also suggest that design modifications of the returning cannula could improve VV-ECMO performance.

In our study, we focus on returning cannulas and we examine the recirculation levels in two different models, which are loosely based on existing market designs and primarily differ in the number of side holes. The objective is to evaluate whether the presence of side holes helps reduce recirculation.

ISBN 978-80-69159-00-6

2. Subject and Methods

The geometric model, including the right atrium (RA), tricuspid valve (TV), SVC, and IVC, was reconstructed from a CT scan of a male patient from Kepler Klinikum, Linz, Austria. The distance between the returning and drainage cannula tips was set to 10 cm, reflecting common clinical practice. The drainage cannula was inspired by the Maquet BE-PVL 2155 cannula with a diameter of 21 Fr. The main difference between the returning cannulas is the number and arrangement of side holes, as shown in Fig. 1, panel A. Model A has two side holes, based on the Maquet BE-PAL 1923 cannula and model B has 12 side holes arranged in 3 rows of 4 inspired by the Bio-Medicus Flex cannula. While our designs were loosely inspired by existing commercially available models, we made specific modifications, such as adding more holes to model B, to better understand their impact on blood flow. Both returning cannulas have a diameter of 19 Fr.

Mathematical Model: Blood flow was modelled using the incompressible Navier-Stokes equations, while oxygen diffusion was governed by an advection-diffusion equation. Appropriate boundary conditions were applied to ensure physiological flow dynamics. A no-slip condition was imposed on all solid walls. A steady parabolic velocity profile with zero velocity in the initialization phase was assigned to the inlet of the returning and outlet of the drainage cannula. A time-dependent pressure boundary condition was set for the venae cavae inlets to prevent backflow. The TV was modelled as a dynamic boundary, switching between a closed state with zero velocity and an open state regulated by a time-dependent pressure drop based on the Wiggers diagram. Oxygen is assumed to be at full saturation at the inlet of the returning cannula and venous saturation in all the other inlets. No flux of oxygen is assumed through the walls. The detailed model is presented in Leoni et al. [3].

Simulation parameters: Simulation parameters were derived from the study [6], with the ECMO flow set to 4 L/min, heart rate to 76 bpm, and a targeted cardiac output of 6.5 L/min. Simulations with the finite element method were performed for both geometrical models using a custom-built FEniCSx code on the HPC cluster Radon1 at RICAM, Linz, running for 60 seconds and recording data for the final 30 seconds.

VV-ECMO Efficacy: Efficacy is measured in terms of saturation at the TV and recirculation. The latter denotes the average oxygen flux over time through the draining cannula outlet, normalized by the ECMO flow rate. More about the data and methods can be found in [3].

3. Results

The blood flow from the returning cannula is shown in different phases of the right ventricular (RV) diastole in Fig. 1, panel B, for both designs. One can observe the varying amount of blood coming through the cannula holes during individual phases. For better illustrations, please refer to the videos available via https://www.youtube.com/watch?v=v6HF9UFjT98&ab_channel=LinzLabforIn-SilicoMedicalInterventions. Panel C illustrates the pressure exerted on the walls, with an arrow indicating the highest pressure observed. Panel D shows the oxygen levels in the RA with corresponding saturation levels. Panels C and D are depicted for the phase when the TV is closed.

4. Discussion

The effectiveness of VV-ECMO is reduced in some patients due to high recirculation rates. In this study, we used computational modeling to analyze how side holes in the returning cannula affect recirculation and saturation.

ISBN 978-80-69159-00-6

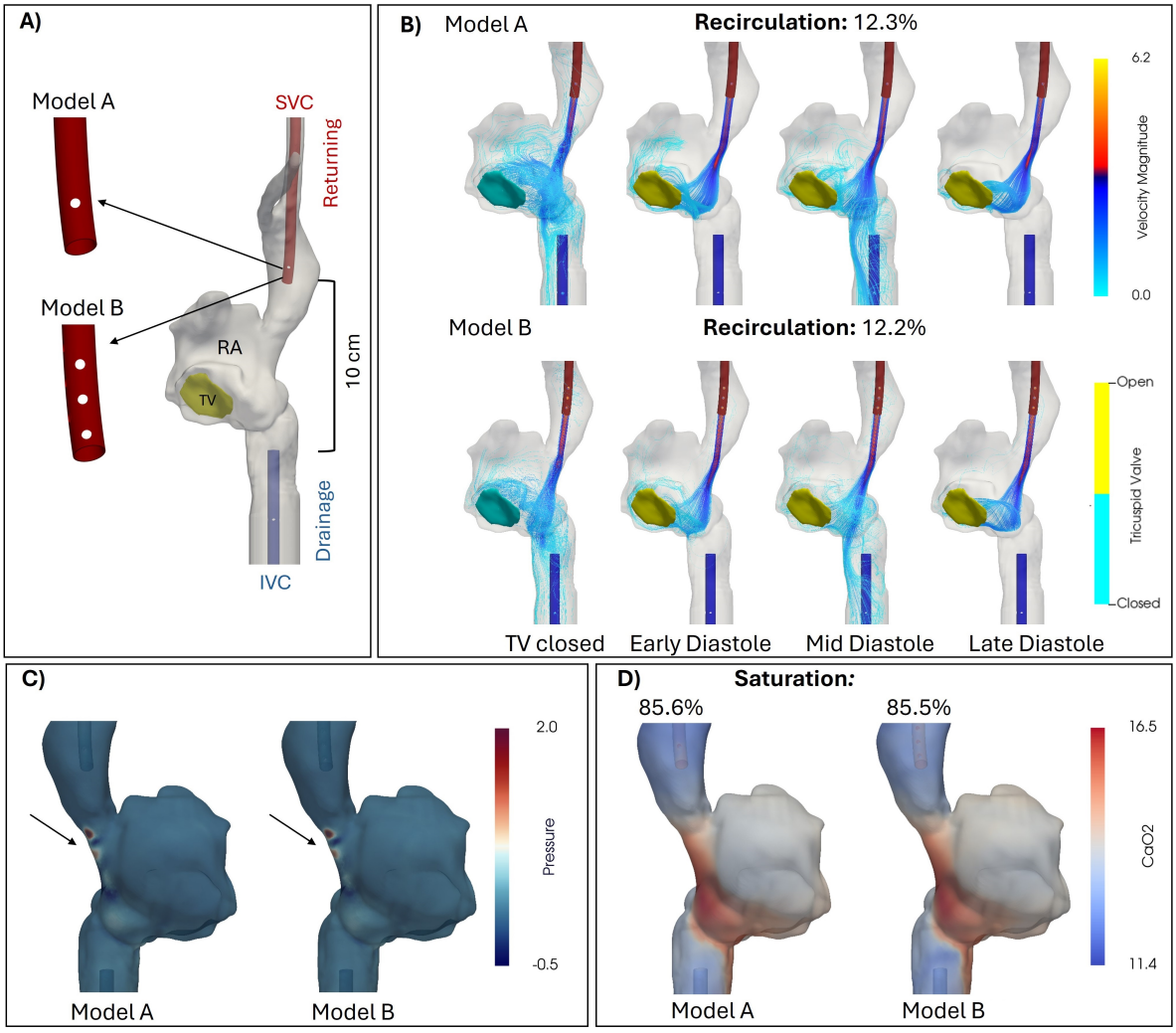

Fig. 1: A) Geometrical model derived from CT scan and both cannula designs. B) Blood flow from the returning cannula during different phases of ventricular diastole, with the TV color indicating whether it is open or closed. C) Pressure exerted on the walls. D) Oxygen content in the RA. Panels A and B show the anterior view, while Panels C and D display the posterior view when the TV is closed.

Our findings indicate that the presence of side holes does not improve VV-ECMO efficacy, as shown in Fig. 1, panel B, with recirculation of nearly 12% for both designs, thus in the range of values reported in [2]. Most of the returning blood is ejected from the distal tip rather than through the side holes, and the side holes are not effective in redirecting the blood flow. The amount of blood flowing through the TV and the side holes is influenced by cyclical pressure changes. Turbulence around the side holes is noticeable when the pressure difference between the RA and RV decreases, such as during late ventricular diastole or when the TV is closed. This turbulence should be further investigated, as it may contribute to clot formation or hemolysis.

Interestingly, a slight change in the orientation of blood flow is observed at the level of the cavoatrial junction, highlighting the importance of considering cannula positioning on a patient-specific basis. Additionaly, the highest pressure on the vessel walls was observed at this junction rather than at the side holes, as shown in panel C. However, the vein's compliance should help manage such localized ECMO flow pressure. The pressure on the walls may vary depending on the position of the returning cannula and the diameter of the SVC. In this study, the cannula was inserted along the vein centerline, which may not accurately reflect clinical practice. If the cannula tip would be closer to the SVC walls, higher pressure may be exerted on the SVC walls.

ISBN 978-80-69159-00-6

The saturation observed in the RA was approximately 86% and the presence of side holes did not contribute to an improvement in saturation, as seen in panel D. The highest oxygen levels are observed along the path of fully oxygenated flow from the returning cannula. Several factors could contribute to a lower saturation rate, including recirculation, cannula positioning, or the ratio of ECMO flow to cardiac output. In the latter case, the venous blood may dilute the oxygenated blood returning from the cannula, reducing the overall oxygen content. Increasing the flow rate, as observed in the study by Leoni et al. [3], may enhance the overall saturation levels. Nevertheless, studies have shown that a higher ECMO flow to cardiac output ratio leads to increased recirculation [4].

Our study has several limitations, such as using a single patient, one VV-ECMO setting, and fixed cannula positions. We also didn't account for vein compliance and simplified blood flow by assuming it to be Newtonian. Despite these limitations, the study demonstrates that patient-specific VV-ECMO modeling can offer valuable insights into blood flow dynamics and can be used to evaluate existing cannulas or computationally test new designs.

5. Conclusion

This study examined the effect of additional side holes in the returning cannula on recirculation rates in VV-ECMO. The results indicate that the presence of these holes does not lead to a reduction in recirculation nor increase in saturation. Future investigations should focus on alternative cannula designs to optimize blood flow dynamics and increase effectiveness.

Acknowledgements

This work was supported by LIT SeedPlusMED ECMOPT. A.P and L.GG acknowledge the partial support of the State of Upper Austria. The authors sincerely acknowledge Massimiliano Leoni for his previous contributions to the development of codes used in this study.

References

[1] Abrams, D., Bacchetta, M., Brodie, D. (2015). Recirculation in venovenous extracorporeal membrane oxygenation. *ASAIO journal*, 61(2), 115–121.

[2] Gehron, J., Bandorski, D., Mayer, K., Böning, A. (2023). The Impact of Recirculation on Extracorporeal Gas Exchange and Patient Oxygenation during Veno-Venous Extracorporeal Membrane Oxygenation-Results of an Observational Clinical Trial. *Journal of clinical medicine*, 12(2), 416.

[3] Leoni, M., Szasz, J., Meier, J., Gerardo-Giorda, L. (2022). Blood flow but not cannula positioning influences the efficacy of Veno-Venous ECMO therapy. *Scientific Reports*, 12, 20950.

[4] Parker, L. P., Svensson Marcial, A., Brismar, T. B., Broman, L. M., Prahl Wittberg, L. (2024). In silico parametric analysis of femoro-jugular venovenous ECMO and return cannula dynamics. *Medical engineering & physics*, 125, 104126.

[5] Wickramarachchi, A., Gregory, S. D., Burrell, A. J. C., Khamooshi, M. (2024). Flow characterization of Maquet and Bio-Medicus multi-stage drainage cannulae during venoarterial extracorporeal membrane oxygenation. *Computers in biology and medicine*, 171, 108135.

[6] Loosen, G., Conrad, A. M., Hagman, M., Essert, N., Thiel, M., Luecke, T., Krebs, J. (2021). Transpulmonary thermodilution in patients treated with veno-venous extracorporeal membrane oxygenation. *Annals of intensive care*, 11(1), 101.

Patient-Specific Simulation of PVC Activation Using Cellular Automaton

[1]Jana Svehlikova, [1,2]Miriam Zemanikova, [1]Jan Zelinka

[1]Institute of Measurement Science, Slovak Academy of Sciences, Bratislava, Slovakia
[2] Faculty of Electrical Engineering and Information Technology, University of Zilina
Email: jana.svehlikova@savba.sk

Abstract. *Premature ventricular contractions (PVCs) were simulated for ten patients' specific heart-torso models to estimate the position of the PVC origin.*
The simulations were calculated for several hundred starting points (SPs) defined in the ventricular volume. Standard 12-lead ECG and body surface potential map were calculated for each starting point. The simulated and measured signals were evaluated by Pearson's correlation coefficient (PCC). The distance between the starting point of the simulation with the best PCC and the true PVC origin was computed as a localization error (LE). The influence of the starting points' density and the number of compared signals on the LE was studied for homogeneous and inhomogeneous torso models.
The original number of starting points (103-306) was increased by 300-352. The mean LE for 12-lead ECG evaluated from the original and increased number of SP did not change significantly, and was 27.8±11.7 vs. 28.6±10.0 mm for homogeneous torso and 28.6±9.8 vs. 31.5±12.5 mm for inhomogeneous torso. Similar results were obtained for 128-lead ECG, where the mean LE for the original and increased number of SP was 23.7±9.3 vs. 24.8±11.0 mm for the homogeneous torso and 31.3±12.5 vs. 30.0±10.4 mm for the inhomogeneous torso. The increased number of starting points did not affect the LE. The comparison of 128 leads instead of 12 improved the mean LE by 4 mm for the homogeneous torso model.

Keywords: PVC Simulations, Patient-Specific Heart-Torso Model, Localization Error

1. Introduction

The preoperational estimation of the origin of premature ventricular contraction (PVC) can be very useful for the success and shortening of the medical intervention. Besides solving this aim by the inverse solution, which is ill-posed, there is also an attempt to find the PVC origin by computing the forward problem using the patient-specific model [1] [2]. Recently, we presented such an approach using the model of activation propagation based on the cellular automaton principle [3].

In this study, two limitations from the previous study are addressed: the density of the starting points of activation was increased, and also the number of compared measured and simulated signals was increased from 12 to 128.

2. Subject and Methods

Measured Data
Multiple leads body surface ECG mapping was performed on ten patients with PVC assigned for radiofrequency ablation procedure (RFA). Right after the measurement, the patient's torso was scanned by CT with the electrodes in their measuring positions. The measurements were conducted for 5 to 20 minutes, depending on the number of captured PVC beats. The resulting single PVC beat was computed by averaging the captured beats.

Heart and Torso Model
The heart and torso models were segmented from each patient's CT scan. The lung lobes and

heart cavities were also assumed to be the basis of the inhomogeneous torso model. The ventricular muscle was modeled by a cubic grid with a distance of 1 mm between the points. Each grid element represented a bulk of ventricular cells with a predefined action potential (AP) amplitude and duration. The AP propagation from cell to cell was simulated using the Huygens principle. The velocity of propagation was the same in the whole ventricular volume.

Simulations and Evaluation

In [3], the starting points mimicking the PVC origin were distributed in the whole ventricular volume. They were defined as a 10 mm grid inside the volume. In this study, we also added points on the endo-epicardial ventricular surface from the sparse triangulation using about 300 points. For each starting point position, the ventricular depolarization simulation was performed, and a multiple dipole equivalent heart generator was computed for each step of the simulation. Then, the potential on the torso model was calculated by the boundary element method.

The simulated ECG signals corresponding to the electrodes' position were derived, and the signal amplitude and the time scale were adjusted to the signals measured in the QRS complex time interval. Finally, Pearson's correlation coefficient (PCC) was computed between corresponding measured and simulated signals and averaged over all considered leads. The simulation with the best PCC was found, and the position of its starting point was compared with the position of the true PVC origin assigned by the physician during RFA. The distance between these points was defined as the simulation's localization error (LE).

Two approaches to improve the LE were investigated:

- the increased number of starting points for simulations
- the increased number of signals (standard 12 leads vs. 128 from mapping) used in the simulation evaluation

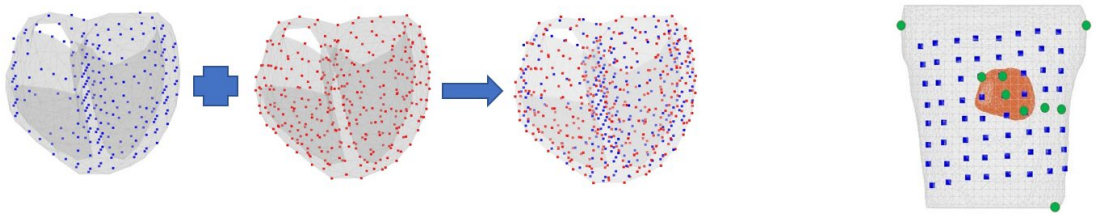

Fig. 1. Left: The example of the increased density of the SP used for PVC simulations. Right: The patient-specific heart-torso model. Green dots show the positions of the electrodes used for the standard 12-lead ECG computing, and blue dots are the positions of the 64 anterior out of all 128 electrodes used for body surface potential mapping.

3. Results

Table 1 summarizes the properties of the measured subjects and their signals: the number of captured PVC beats used to compute representative signals for each patient, and the number of starting points defined inside the ventricular volume and on its surface.

Table 1. Parameters of the patients and measured data

	P001	P002	P004	P008	P010	P020	P021	P023	P029	P036
sex	M	M	F	M	M	M	M	M	F	M
age	17	63	72	46	59	37	33	38	64	61
#PVC	62	9	210	267	203	34	110	305	366	616
#SP inside vol	230	250	211	245	306	260	252	289	103	175
#SP surf	352	328	312	326	326	319	320	303	299	300

ISBN 978-80-69159-00-6

The simulations of AP propagation were conducted for each patient and each SP in the ventricles. The corresponding ECG signals were computed assuming the torso was either a homogeneous or an inhomogeneous volume conductor. The lung lobes and heart cavities were assumed as piece-wise inhomogeneities, with the conductivity four times lower or three times higher than the mean conductivity of the torso, respectively.

The ECG signals were computed for 128 positions of the electrodes on the torso and three electrodes for limb leads assigned as R, L, and F.

The impact of the increased number of starting points on the localization of the starting point with the best correlation with the measured standard 12 signals or 128 signals, respectively, is depicted in Figure 1.

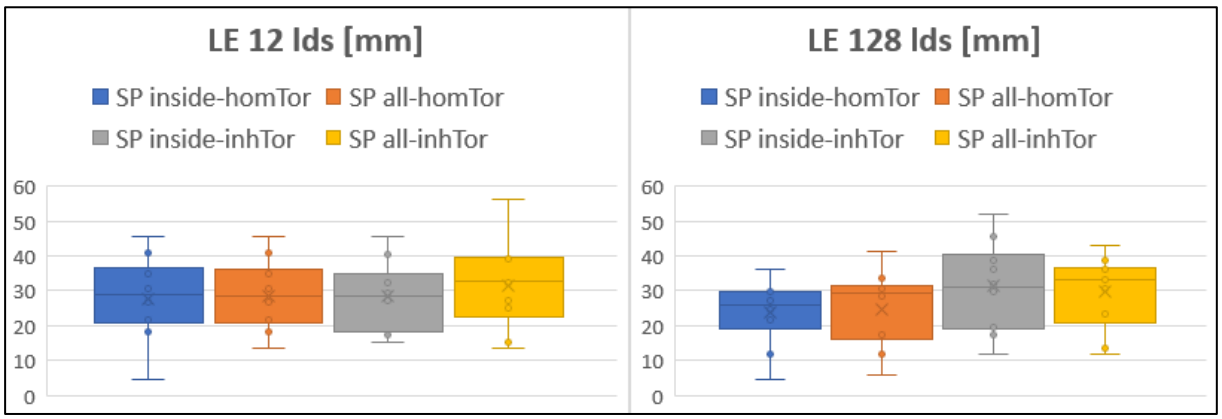

Fig. 2. LE of the PVC origin estimation for ten patients derived from forward simulations starting inside the ventricular volume (SP inside) and from all starting points (SP all), assuming homogeneous (homTor) and inhomogeneous (inhTor) torso models.

The dependence of the LE on the number of evaluated and correlated signals is illustrated in Figure 2. The best PCC values for all patients are summarized in Table 2.

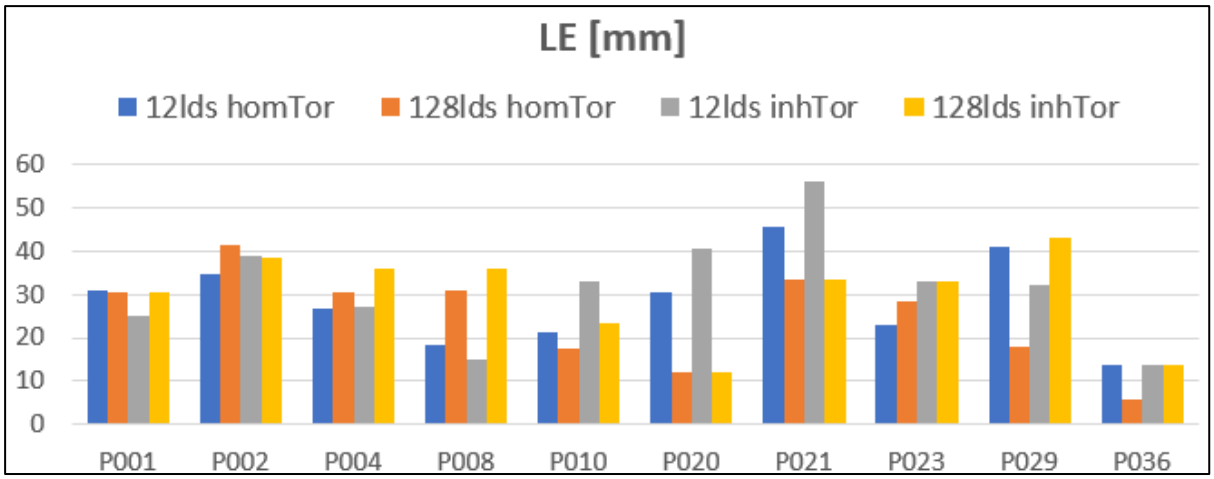

Fig. 3. LE for each patient, derived from forward simulations by the best correlation in 12 and 128 leads, assuming a homogeneous (homTor) and an inhomogeneous (inhTor) torso model.

4. Discussion and Conclusions

To find the most similar simulated ECG signals during a PVC, several hundred simulations were performed in ten patient-specific heart-torso models, assuming a homogeneous or inhomogeneous torso model. The similarity between the measured and simulated signals was

ISBN 978-80-69159-00-6

evaluated by PCC. The starting point leading to the best PCC was considered a probable position of the PVC origin, and its distance to the true origin was rated as a LE.

Table 2. Mean and median value of the best Pearson correlation coefficient from simulations for starting points in each patient's model.

PCC	SP inside 12lds		SP all 12lds		SP inside 128lds		SP all 128lds	
	homTor	inhTor	homTor	inhTor	homTor	inhTor	homTor	inhTor
mean	0.81±0.1	0.80±0.1	0.83±0.1	0.81±0.1	0.66±0.1	0.63±0.1	0.67±0.1	0.65±0.1
median	0.83	0.82	0.86	0.84	0.65	0.61	0.65	0.61

Figure 1 shows that defining approximately 300 additional SPs in each heart model did not improve the LE. It is visible from Table 2 that the PCC slightly increases, but the position of the new SPs is close to that of the previous ones.

Regarding the influence of the number of compared signals in Figure 2, the higher number of the evaluated signals improved the LE in five out of ten patients for the homogeneous torso model and three patients for the inhomogeneous torso model. On the other hand, it led to a deterioration of the LE in four patients and three patients for homogeneous and inhomogeneous models, respectively.

The heart model and similarity evaluation method have several limitations and simplifications that can be addressed in the future. In the heart model, different properties of the ventricular tissue can be implemented, such as fast conduction velocity in the endocardial layer of the ventricles and anisotropic activation propagation considering the fibers' direction in the ventricular muscle. Also, no local structural changes (ischemia) were considered. Regarding the simulated signals evaluation, in addition to the criterion of maximum PCC, other parameters can be assumed, such as the L1 norm of the difference between the signals or the range of PCC and L1 norm values in all considered signals, which should be minimized. The most suitable time interval for comparing the simulated and measured signals within the QRS complex can also be studied.

Despite the above-mentioned limitations, using the forward simulations in a patient-specific heart model, we obtained a similar LE as by an inverse solution [4].

Acknowledgments

This work was supported by the research grant 2/0106/25 from the VEGA Grant Agency. Slovakia.

References

[1] Pezzuto S., Prinzen F.W., Potse M., Maffessanti F., Regoli F., Caputo M.L., et al. (2021). Reconstruction of three-dimensional biventricular activation based on the 12-lead electrocardiogram via patient-specific modelling. *Europace*. (2021);23(4), 640–7.

[2] Sánchez J., Llorente I., Ros S., Atienza F., Climent A. M., Guillem Sánchez M. (2024). A Model Population-Based Approach to Enhance the Detection of Premature Ventricular Contraction of ECGI. In *Computing in Cardiology 2024*.

[3] Svehlikova J., Zelinka J., Tysler M. (2024). Estimation of the PVC Origin from Simulations Using Cellular Automaton. In *Computing in Cardiology 2024*.

[4] Dogrusoz Y.S., Rasoolzadeh N., Ondrusova B., Hlivak P., Zelinka J., Tysler M., et al. (2023). Comparison of dipole-based and potential-based ECGI methods for premature ventricular contraction beat localization with clinical data. *Frontiers in Physiology*. (2023);14.

Indirect Thermographic Measurement of the Contact Temperature of an Electromechanical Relay

[1]Krzysztof Dziarski, Łukasz Drużyński[1], Arkadiusz Hulewicz[2], Józef Piechocki[3]

[1]Institute of Electric Power Engineering, Poznan University of Technology, Piotrowo Street 3A, 60-965 Poznan, Poland,
[2]Institute of Electrical Engineering and Electronics, Poznan University of Technology, Piotrowo Street 3A, 60-965 Poznań, Poland
[3]Łukasiewicz Research Network – Poznan Institute of Technology, Ewarysta Estkowskiego 6 Street, 61-755 Poznań
Email: Krzysztof.dziarski@put.poznan.pl

Abstract. *The temperature of an electromechanical relay is related to the value of the contact resistance. The value of the contact resistance depends, among other things, on the degree of wear and oxidation of the contacts. Too high temperature of the relay contacts leads to their further degradation and an increase in the contact resistance. For this reason, monitoring this value is important. In this paper, monitoring of the contact temperature of an electromechanical relay using indirect thermographic temperature measurement is proposed.This approach consists of two parts: the first part is based on a thermographic measurement of the relay case, and the second part estimates the contact temperature based on the relationship between the case temperature (measured by a thermal camera) and the contact temperature. The Finite Element Method (FEM) was used in the second part. The results obtained using this method were validated through comparison with experimental measurements acquired by an alternative method.*

Keywords: Electromechanical Relay, Finite Element Method, Indirect Thermographic Measurement, Thermography,

1. Introduction

An electromechanical relay is a device that allows the control of an electric circuit (usually with a high amplitude signal) using a low amplitude control signal. It provides galvanic separation between these circuits. An electromechanical relay consists of a coil, contacts and a case. The simple design of the device and its low price mean that they are widely used in many industries and in railway control systems [1].

The literature describes two methods of conducting diagnostic tests of electromechanical relays: the electrical measurements (the direct tests) and measuring their indirect performance characteristics, in particular of the surface temperature (the indirect tests). The temperature of the contacts of an electromechanical relay is an important element - it affects its reliability, durability and correct operation.

According to the Joule–Lenz law [2], the relay contact temperature depends on the current flowing through the contact and the value of the contact resistance. In turn, the value of the contact resistance changes over time due to their wear and oxidation and depends on the contact material, the total contact surface, and the contact force. As a result, the contact temperature increases even more. The relay contact temperature can also increase due to the formation of the electric arcs [3], which cause the contact surface to heat up and gradually reduce its surface area.

Too high contact temperature can lead to the increased voltage drop on the relay contacts and the increased power losses generated in its current path. Additionally, it can cause improper

ISBN 978-80-69159-00-6

operation of the device. For this reason, monitoring the relay contact temperature is an important issue. Relay contacts are small and are located inside the case. For this reason, measuring their temperature is difficult.

Using the contact method to measure relay contacts is difficult. Due to their small size, applying a temperature sensor to the relay contact requires practice. The transition resistance between the relay contact and the temperature sensor is unknown. Additionally, using the contact method requires removing the case, which makes it impractical.

These problems can be avoided by using thermography. This non-contact method is based on detecting the infrared radiation emitted by the observed surface. The literature describes the use of thermography to examine relays, where histograms obtained during the experiments were compared [4]. However, the authors are not aware of any studies examining the relationship between relay contact temperature and the thermographic measurement of the relay case temperature. Nor are the authors aware of any research on indirect thermographic measurement of relay contact temperature. For this reason, it was decided to undertake a study addressing this issue.

2. Subject and Methods

The indirect thermographic measurement of relay contacts consists of two parts: thermographic measurement of the relay case temperature T_p and determination of the relationship between the contact temperature T_C and the measured T_p. The Relpol RM85-2011-35-1012 relay was selected for the research. It is characterized by a coil voltage V_c = 12 V and a contact current rating of 16 A [5].

To obtain a reliable thermographic measurement of T_p, a dedicated measuring system had to be constructed. Its main part was the Flir E50 thermographic camera operating in the LWIR (Long Wavelength Infrared) band. It is characterized by a matrix of uncooled microbolometer detectors with a spatial frequency equal to 180 x 240 detectors. The IFOV (Instantaneous Field of View) value is 1.82 mrad. This is enough to place nine fields of a single detector on the relay case. The NEDT (Noise Equivalent Differential Temperature) value is 50 mK [6]. This is enough to track the temperature change on the relay case. The camera was placed on a tripod, which was used to set the distance *d* between the camera lens and the observed surface of the relay. The whole thing was placed in a plexiglass chamber. The dimensions of the chamber were 40 cm × 30 cm × 30 cm. In order to eliminate reflections, the interior of the chamber was lined with polyurethane foam. The diagram of the described measurement system is shown in Fig. 1.

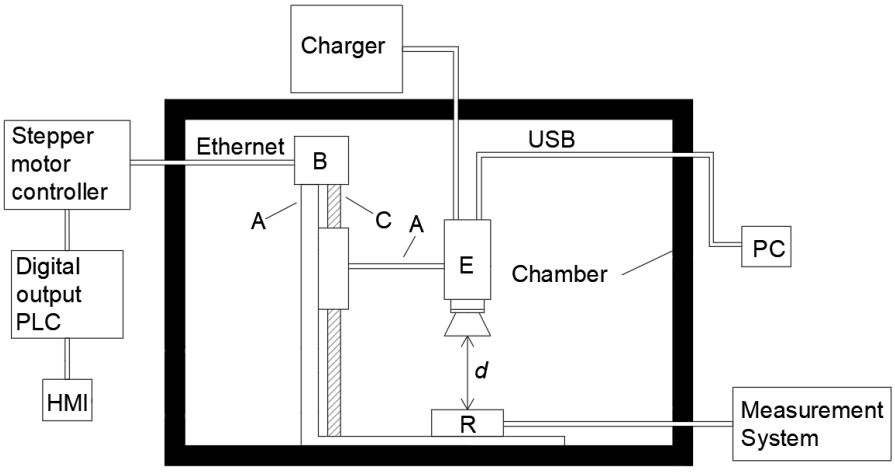

Fig. 1. The measurement system that enables thermographic measurement of the temperature of the relay case T_C. A – tripod, C – screw, E – thermographic camera, R – observed relay, d – distance between package and thermographic camera lens.

ISBN 978-80-69159-00-6

The change in the value of T_C was induced by varying the power dissipated in the main contact. The relay coil was powered from a 12 V DC source. The main contact was powered via an autotransformer, which allowed for precise voltage regulation and organic current control to the expected level. The diagram of the described station is shown in Fig. 2.

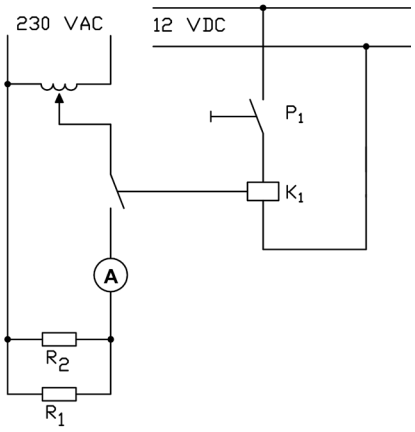

Fig. 2. Measuring system that enables relay control. K_1 – tested relay, R_1, R_2 – load, P_1 – button.

The second part of indirect thermographic measurement consisted in determining the relationship between T_C and T_p. For this purpose, a three-dimensional model of the relay had to be created and the FEM (Finite Element Method) method had to be used. The Solidworks software was used. The three-dimensional model created is shown in Fig. 3. The materials that were assigned in the defined model and their thermal conductivity properties λ are shown in Table 1.

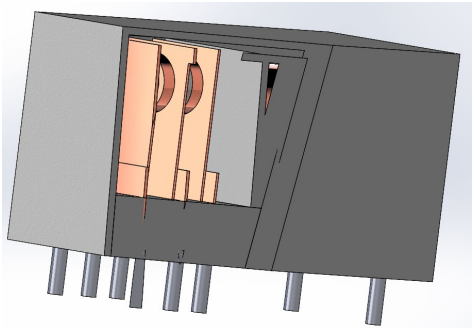

Fig. 3. Three-dimensional model of the tested relay.

Table 1. Values of the thermal conductivity coefficients λ and materials assigned to individual parts of the relay model.

Part of the relay	Matherial	λ [W/m·K]
Coil	Copper	385
Contact	Copper	385
Case	Plastics	0.22
Leads	Aluminum	204

In order to make the defined model (and the obtained results) credible, the results were compared with those obtained using another method. For this reason, the contact temperature was measured using a type K thermocouple (T_{Ct}). The case temperature (T_{pt}) was also measured using a thermocouple.

ISBN 978-80-69159-00-6

3. Results

As a result of the carried out work, the obtained results allowed determining the relationship between the temperature T_C and the temperature T_p. The values of the temperatures T_{Ct} and T_{pt} were also measured.

Table 2. The obtained values of the contact temperature T_C, temperature case T_p and the temperatures T_{Ct} and T_{pt} measured with the thermocouple.

Lp	T_C [°C]	T_{Ct} [°C]	T_p [°C]	T_{pt} [°C]
1	19.5	20	19.9	20
2	20.3	20	21.0	21
3	21.5	21	24.1	24
4	25.2	24	29.4	28
5	26.9	26	33.6	32
6	28.9	28	39.6	39
7	34.1	32	48.3	47
8	41.9	41	60.6	59
9	48.9	47	67.8	66

4. Discussion and Conclusions

In the conducted research work, an indirect thermographic measurement of the contact temperature of an electromechanical relay T_C was performed. The relationship between the T_C value and the temperature of the relay case T_p was determined. The T_C value was determined based on the FEM method. The results obtained using FEM were compared with the results obtained using the contact method (T_{pt},T_{Ct}). It was noted that the smallest difference between the values of T_C and T_{Ct} was 0.3 °C and T_p and T_{pt} was 1.8 °C. For this reason, the defined model can be considered reliable. The largest value between T_C and T_p was 18.9 °C.

References

[1] G. Wu, K. Dong, Z. Xu *et al.*, "Pantograph–catenary electrical contact system of high-speed railways: recent progress, challenges, and outlooks," *Rail. Eng. Sci.*, vol. 30, pp. 437–467, 2022, doi: 10.1007/s40534-022-00281-2.

[2] Y.-H. Li, F. Shen, and L.-L. Ke, "Multi-physics electrical contact analysis considering the electrical resistance and Joule heating," *Int. J. Solids Struct.*, vol. 256, p. 111975, 2022, doi: 10.1016/j.ijsolstr.2022.111975.

[3] S. N. Kharin, "Mathematical models of heat and mass transfer in electrical contacts," *2015 IEEE 61st Holm Conference on Electrical Contacts (Holm)*, San Diego, CA, USA, 2015, pp. 1-21, doi: 10.1109/HOLM.2015.7354949.

[4] A. V. Stoynova, "Infrared Thermography Inspection for Safer Rail Transport Automation," *2018 International Conference on Diagnostics in Electrical Engineering (Diagnostika)*, Pilsen, Czech Republic, 2018, pp. 1-4, doi: 10.1109/DIAGNOSTIKA.2018.8526118..

[5] Castor, Relpol S.A., "RM84, RM85, RM87 Relays – Datasheet," Mouser Electronics, Datasheet, 2023. [Online]. Available: https://www.mouser.pl/datasheet/2/16/RM84_RM85_RM87-612793.pdf. [Accessed: Mar. 1, 2025]

[6] Flir, " Technical Data FLIR E50" FLIR Systems, Datasheet, 2014. [Online]. Available: https://docs.rs-online.com/ca3e/0900766b81371810.pdf. [Accessed: Mar. 1, 2025].

ISBN 978-80-69159-00-6

Measurement of Physical Quantities III

ISBN 978-80-69159-00-6

The Water-Monopropylene Glycol Mixtures Flow Rate Measurement

[1,2]Jaroslav Foltýnek, [1,2]Jiří Tesař, [1]Jaroslav Synáč, [1]Miroslava Benková, [2]Jan Rybář, [2]Stanislav Ďuriš

[1]Czech Metrology Institute, Brno, Czech Republic
[2]Slovak University of Technology, Faculty of Mechanical Engineering, Bratislava, Slovakia
Email: jfoltynek@cmi.gov.cz

Abstract. *This paper presents measured errors of different measuring principles of flow meters, which are typically used in thermal energy measurement for cooling applications. The study involves single-jet, multi-jet, electromagnetic, and ultrasonic flow meters. Experimental measurements were performed at drinkable water and water-monopropylene glycol mixtures with varying concentrations, aiming to analyze the accuracy, repeatability, and reliability of the different flow meter types under variable fluid density and kinematic viscosity conditions. Reference measurements were performed by a mass flow meter, which allows precise determination of the mass flow rates. Based on the measured values and densities, the glycol mixtures and the volumetric flow rates were evaluated.*
The measured results reveal significant differences in the measurement errors of the various flow meter types, influenced by both the physical properties of the glycol mixture and the specifications of the measurement principle. The discussion focuses on recommendations of selecting an appropriate flow meter and the influence of parameterization of specific application and composition of the measured liquid. This study contributes to a deeper understanding of flow measurement challenges in cooling systems and highlights the importance of proper parameterization, setup, and calibration of the flow meter itself and of the entire cooling circuit

Keywords: Flow Meter, Cooling, Water-glycol Mixture, Flow Measurement, Monopropylene Glycol

1. Introduction

The aim of the experiment described in this paper was to analyze the effect of glycol concentration in water on the accuracy at flow measurement.

The content and approach of the experiment solving were generally based on the requirements for the current functionalities of the thermal energy meters (in follows TEM) for heating and cooling applications. These TEM are in accordance with Directive 2014/32/EU (MID), Annex MI-004 [1], the current version of the standard EN 1434-2022 [2], and the WELMEC Guide 13.1 document [3]. Specifically, this concerns the use of TEM for measuring thermal energy in cooling systems, where, in addition to water as a heat transfer fluid, the aforementioned (anti-freeze) mixtures of water and glycol are also used. The issue is related to implementation in the Czech (OOP) [4] and European metrological documentation [5, 6].

The flow sensor´s measuring principles used for thermal energy measurement were chosen for the practical experiments. This experiment was focused on the glycol-water concentration effect on the error measurement of a single-jet dry dial flow meter (water meter), multi-jet wet dial flow meter (water meter), ultrasonic flow meter (water meter), and electromagnetic flow meter.

ISBN 978-80-69159-00-6

2. Subject and Methods

2.1 Selection of used antifreeze liquid for experiment and weight concentration

After considering the ecological aspect, monopropylene glycol (hereafter referred to as glycol) was chosen for the experiment [7]. The glycol concentrations in water were chosen as follows: (0, 10, 30, 50) wt. %, which were corresponding to freezing points of (0, -3, -14, -34) °C.

2.2 Selection of used meters

Selected flow meters for experiment: Single-jet, dry dial flow meter (water meter) –Enbra, type: ETK-EAX; Multi-jet, wet dial flow meter (water meter) – manufacturer: Sensus, type: 420PC; Ultrasonic flow (water meter) – manufacturer: Apator Powogaz, type: UL2.5 Ultrimis; Electromagnetic flow meter – manufacturer: Krohne, type: Optiflux 5300.

The expected measurement errors should not exceed the maximum permissible errors according to the Article 9.2.2.3 of the standard EN 1434-1:2022 [2], for thermal energy measurement flow sensors. All used meters were adjusted for the measurement of water.

2.3 Selection of measuring method and reference meter

For measurement, the start-stop method was chosen with a direct reading of the mass totalizer of reference Coriolis mass flow meter [8]. Subsequently, the real density of the water-glycol mixture for the given glycol concentration at real measured temperature of the liquid during the measurement were determined. The density values were calibrated by CMI physical chemistry department on samples of water-glycol mixtures. The density calibrations were performed at the same temperature ranges, which were measured during the experiment. For direct comparison there were used the direct reading volume totalizer values of the individual flow meter and these values were compared with the calculated volume value from the flow measured by the reference mass flow meter (with density calculation and interpolation).

The reference meter selected for the experiment – reference mass flow meter is manufactured by Micro Motion, type: CMF050 (secondary standard) [9]. Testing flow rate points were chosen based on technical possibilities of the used testing facility, at nominal values: (500, 1000, 1500) L/h. The measurements were done by five repeating of every point for repeatability check, and reduction of measurement uncertainty (A-type) and B-type uncertainty was given by used testing facility (calibration certificates, rectangular distribution of partial uncertainties). Total uncertainty was expanded by coverage factor $k = 2$. The temperature of water and water-glycol mixtures were selected at the same temperature as the laboratory ambient temperature, approx. (20 – 23) °C.

2.4 Measuring Facility Selection

Due to the potential contamination of the testing facility by glycol and the time-consuming nature of the experiment, a simple test bench previously used at the CMI for long-term testing of water meters (Point 7.11 of the standard EN ISO 4064-2:2017 [10]) and flow meters at the selected flow rate and temperature was selected. The test bench works in a closed hydraulic circuit to eliminate the evaporation of liquid during measurement.

3. Results

The following chapters present the measured results for each of the used flow meter construction designs. The presented values provided the average values of five repetitions, followed by the determination of the overall expanded measurement uncertainty. Subsequently, a graphical comparison of the identified errors of measurements is made for drinking water, a mixture of water with 10 wt.% glycol, a mixture of water with 30 wt.% glycol, and a mixture of water with 50 wt.% glycol.

ISBN 978-80-69159-00-6

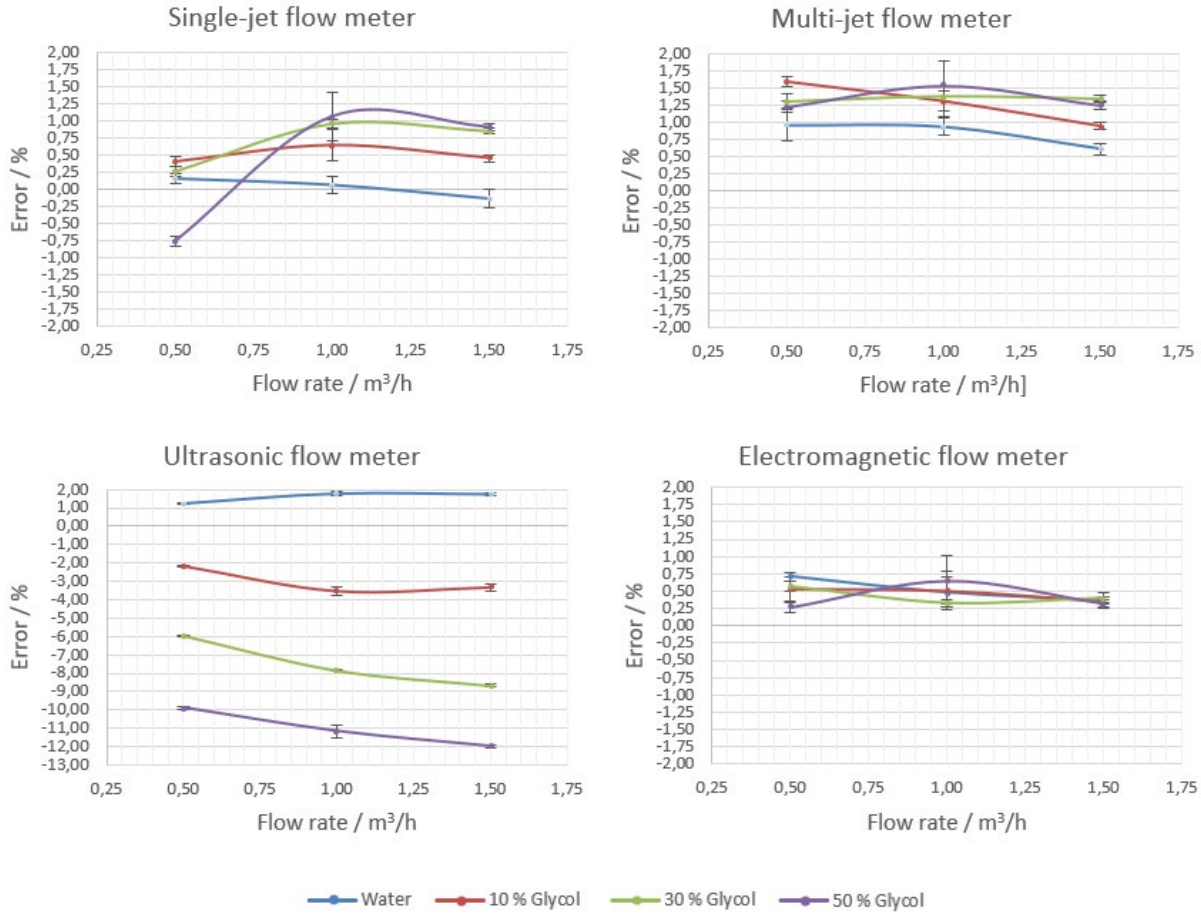

Note: The standard uncertainty of measurement has been determined in accordance with EA-4/02 M:2022 and JCGM 100:2008 document. The reported expanded uncertainty of measurement is stated as the standard uncertainty of measurement multiplied by the coverage factor k corresponding to a coverage probability of approximately 95 %, which for normal distribution corresponds to a coverage factor k = 2.

Fig. 1. Flow meters error curves graphical comparison

4. Conclusions

Relating measured results of sigle-jet, multi-jet and electromagnetic flow sensor (errors and uncertainties are in approx. range of 0.1 % up to 1.6 %) for selected flow rates and water-glycol concentrations, the anticipated compliance with the maximum permissible error (MPE) limits was confirmed, both according to the standard EN 1434-1:2022 for thermal energy meters and the standard EN ISO 4064-1:2017 for water meters. The limits are within the range of up to 5% (TEM, thermal energy meters) and up to 2% (water meters). The results indicate that with increasing concentration of glycol in the mixture, the single-jet and multi-jet flow meters show a shift in the measurement error towards positive values, meaning the meter indicates a higher flow and measured volume than the real value. From the measured results, it follows that the electromagnetic flow meter exhibits the least sensitivity to the influence of glycol concentration in the water. However, it is necessary to ensure a guaranteed sufficient electrical conductivity of the measured liquid. The electrical conductivity of glycol mixtures (0 – 50 wt.% of glycol) was acceptable for measurement by an electromagnetic flow sensor. If we compare the error curves of flow sensors (pictured above) for water with results for all water-glycol mixtures, a significant error limit is fulfilled (1 % declination).

The different situation appears by ultrasonic flow meter, mainly by concentration 30 wt. %, respectively 50 wt. % of glycols at water. Measuring errors are over the MPE limit (over 6 % and up to 12%). With increasing concentration of glycol in water the ultrasonic flow meter

ISBN 978-80-69159-00-6

measures the flowrate more less as real. This is a significant conclusion, because the ultrasonic flow meters make up the majority of meters used for measuring of the flowrate by TEM.

The ultrasonic flow meter was retested again on piston prover reference standard by water at water temperatures (10, 20, 30 and 50) °C and all results were below MPE limit for water meters (2 %). This measurement rejects the assumption of meter damage during the testing.

The measured errors were discussed with the manufacturer of the ultrasonic flow sensor. The meter is adjusted for physical correction properties for water only. The change in speed of sound and ultrasonic transducer reaction between water and a water-glycol mixture can cause these error shifts. This means that before measurement, the correct adjustment of settings for the measured liquid must be checked.

The measured results indicate that the glycol concentration in water have effect on the measurement error of the flow meters. As the glycol concentration increases, the thermal capacity of the liquid is changed also, which impacts the calculation of thermal energy. Therefore, for correct measurement the real parameters of the used liquid are necessary to input into SW of the flow meter´s electronic and into SW of TEM energy calculators too. For accurate measurements, it is also essential to ensure long-term stability of the glycol concentration in the heating (cooling) hydraulic circuit. This calls for subsequent metrological checks and comparison of the actual liquid parameters in the hydraulic circuit, with the real settings of the liquid parameters in the meter´s electronics during and after installation.

Acknowledgements

The authors would like to thank the Slovak University of Technology in Bratislava (Faculty of Mechanical Engineering), Czech Metrology Institute and, the grant agency KEGA project number 024STU-4/2023 (Building a laboratory of medical metrology) and the grant agency APVV project number APVV-21-0216 (Advanced mathematical and statistical methods for measurement and metrology) for their support.

References

[1] DIRECTIVE 2014/32/EU OF THE EUROPEAN PARLIAMENT AND OF THE COUNCIL of 26 February 2014, *Official Journal of the European Union L 96/149*.

[2] EUROPEAN STANDARD EN 1434-1,4:2022 Thermal energy meters, *European Committee for Standardization*, 2022 CEN.

[3] WELMEC 13.1 Guide, Measuring Instruments Directive 2014/32/EU Common Application for Utility meters (Water Meters and Thermal Energy Meters), 2020. (For more information see the https://www.welmec.org/).

[4] Measures of a general nature according Czech National metrological law No.: 505/2004coll.; 0111-OOP-C035-14 (water meters), 011-OOP-C047 (flow meters), 011-OOP-C049 (thermal energy calculators) and 011-OOP-C047 (combinate and complete meters). (For more information see the https://cmi.gov.cz/node/212).

[5] Baack S. Heat and cold meters with glycol-based heat transfer media, a look at stability and testability. *EMATEM conference, 2019, organised by PTB, Germany.*

[6] Baack S., Heat metering with glycol-water mixtures. *Dissertation,* 2019, Technische Universität Berlin, Germany.

[7] FICHEMA Monopropylene Glycol specification. (For more information see the https://fichema.cz/monopropylenglykol/1012-fichema-monopropylenglykol-pg-usp-995-3-kg-farmaceuticky-mpg-8592861512034.html).

[8] Ďaďo, Bejček, Platil. Měření průtoku a výšky hladiny. *BEN Praha 2005*, ISBN 80-7300-156-X.

[9] Micro Motion ELITE Coriolis Flow and Density Meters. Product Data Sheet PS-00374. December 2024 EMERSON. (For more information see the https://www.emerson.com/documents/automation/product-data-sheet-micro-motion-elite-coriolis-flow-density-meters-en-66748.pdf).

[10] EUROPEAN STANDARD EN ISO 4064-1,2:2017 Water meters for cold potable and hot wate, *European Committee for Standardization*, 2017 CEN.

Use of the LabVIEW Environment to Determine the Characteristics of Selected Industrial Temperature Sensors

[1]Przemysław Otomański, [2]Eligiusz Pawłowski, [3]Anna Szlachta

[1]Poznan University of Technology, Institute of Electrical Engineering and Electronics, Piotrowo street 3A, 60-965 Poznań, Poland,
[2] Lublin University of Technology, Faculty of Electrical Engineering and Computer Science, Nadbystrzycka street 38A, 20-618 Lublin, Poland,
[3]Rzeszow University of Technology, Department of Metrology and Measurement Systems, W. Pola street 2, Rzeszow, 35-959, Poland
Email: przemyslaw.otomanski@put.poznan.pl

Abstract. *This paper presents the construction of a test stand and a virtual measurement instrument developed in the LabVIEW environment, which allows the temperature characteristics of the sensor to be automatically determined as a function of the heating power for different values of the measurement current. The NI USB-6341 measurement module was used for the measurements. Example measurements were carried out on a representative group of resistive temperature sensors: four platinum metal, thin-film and wire sensors, in different cases, and two thermistor sensors: NTC and PTC.*

Keywords: Resistance Temperature Sensors, Virtual Instrument, LabVIEW

1. Introduction

Temperature is one of the basic parameters often measured in practice. Various sensors, transducers and devices are used to measure temperature. Some of the most commonly used sensors are resistive sensors: metal and semiconductor sensors (thermistors). Issues related to RTD resistance temperature sensors have been discussed in a number of normative documents. In practice, there are two types of resistive sensors, these are standard platinum resistance thermometers with high stability and accuracy (SPRT) and industrial platinum resistance thermometers (IPRT) [1]. In this paper, the authors have limited themselves to discussing the problem of temperature measurement using industrial sensors. An important issue for this group of sensors is the selection of an appropriate measurement current, depending on its design, mounting method and environmental conditions, which ensures that measurement errors are kept sufficiently low. For this purpose, it is necessary to determine the in-situ thermal resistance of the sensor.

2. The laboratory stand

2.1 Hardware part of the measurement system

In order to determine the value of the thermal resistance of the sensor, a measuring system must be constructed that allows the electrical resistance of the sensor to be measured for different current values. Such a system can be realised using two different measurement methods. The first method involves measuring the voltage drop across the resistance of the sensor under test using a suitable stable and regulated current source. The electrical resistance of the sensor R_{sens} is calculated based on Ohm's law. The second method, ratiometric, involves measuring two voltage drops: on the sensor resistance R_{sens} and on the reference resistor R_N

ISBN 978-80-69159-00-6

[2]. In this study, the ratiometric method is used. The resistance value R_{sens} is calculated from equation (1):

$$R_{sens} = \frac{U_{sens}}{U_N} R_N \tag{1}$$

where: U_{sens} – the voltage measured at the sensor, U_N – the voltage measured at the reference resistor, R_N – the nominal value of the reference resistor.

The value of the sensor's measurement current I_{sens} is calculated from the formula:

$$I_{sens} = \frac{U_N}{R_N} \tag{2}$$

The value of the power dissipated in the sensor P_{sens} under test is calculated from the formula:

$$P_{sens} = U_{sens} I_{sens} = \frac{U_{sens} U_N}{R_N} \tag{3}$$

A schematic of the measurement system for the in-situ determination of the thermal resistance of resistive temperature sensors is shown in Figure 1. A ratiometric system was used with a four-point connection between the sensor under test R_{sens} and the reference resistor R_N on the low potential side.

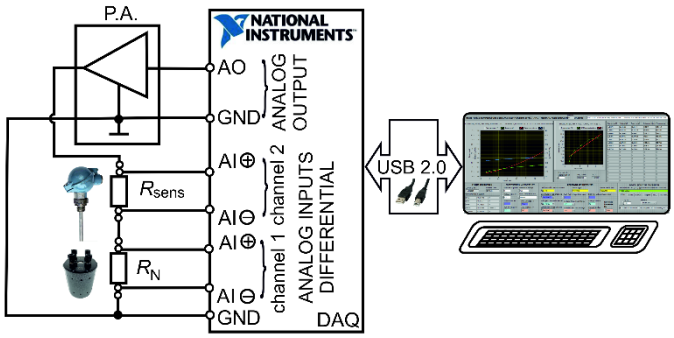

Fig. 1. A block diagram of the laboratory stand for the in situ determination of the thermal resistance of resistance temperature sensors.

The above system allows the automatic determination of the characteristics of the resistance temperature sensors under test. It consists of the following components: a PC with the National Instruments LabVIEW environment installed, a National Instrument measurement data acquisition module, a high-power DC amplifier and a set of sensors under test. The AO output voltage of the DAC is fed to the input of the power amplifier (PA). The output voltage from the PA supplies the resistance temperature measurement sensor R_{sens} and the reference resistor R_N. The R_{sens} sensor under test and the reference resistor R_N are connected in series between the amplifier output and the circuit's electrical ground. The differential analogue input of the analogue-to-digital converter in channel 2 was used to measure the U_{sens} voltage on the R_{sens} resistance sensor under test. Another differential analogue input of the analogue-to-digital converter in channel 1 was used to measure the U_N voltage on the reference resistor R_N. From this, the current flowing through the measurement system was determined.

ISBN 978-80-69159-00-6

2.2 LabVIEW application controling measurements

For the purposes of this work, a measurement control application prepared in the LabVIEW environment was developed. Figure 2 shows a block diagram of the algorithm performing the measurements and calculations, demonstrating the principle of the built application.

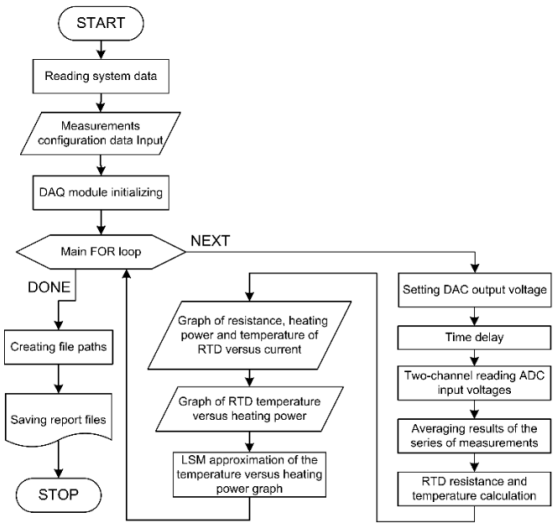

Fig. 2. Flowchart of the programme that performs the measurements on the VI instrument.

The most important part of the application is the main loop, where a series of individual measurements are taken. Once these are averaged, the desired values for resistance, temperature and sensor power are calculated. The number of averaged measurements n can be declared by the user in the initial part of the algorithm. However, before the algorithm starts taking measurements, the application checks the measurement modules available in the system. The user selects a module and declares its measurement configuration (range, input mode, number of averaged measurements n). Once the measurement module and the range of the ADC and DAC have been selected, the method of measurement should be configured. The number of measurement points m, the step of increment of the set voltage on the DAC, as well as the initial value of this voltage should be set. The last parameter to be set is the value of the main loop delay, between the assignment of a new value by the DAC and the taking of measurements by the ADC. The type of sensor under test and the value of the reference resistor R_N are also declared. The module is then initialised and the application proceeds to perform a series of measurements in the main loop. The measurement application controls the DAC, whose output voltage is amplified and supplies the circuit for the series connection of the reference resistor R_N and the temperature sensor R_{sens} under test. The two analogue inputs of the measurement module operating in differential mode are supplied with voltage values from the resistance sensor and the reference resistor. After measuring the U_{sens} and U_N voltages, the values of the other quantities are calculated in the developed application. Once the operation is complete, the application saves the results obtained in graphical and textual form. In the research presented here, each point on the graph is obtained by averaging $n = 100$ measurements. The number of n repetitions was selected experimentally based on an analysis of the measurement uncertainties. The developed application allows the use of various resistive sensors for temperature measurement.

3. Results of experimental studies

Figure 3 shows an example of the temperature dependence T_{sens} (green) of a Pt1000 sensor as a function of measurement current. In addition, the graph shows a plot of sensor resistance

ISBN 978-80-69159-00-6

R_{sens} (blue) and sensor heating power P_{th} (red). Each measurement was taken after a delay time of 50 s from the new set current value. The sensor has reached a thermal steady state. Figure 4 shows the temperature dependence of the sensor T_{sens} on the heating power P_{th}, for different delay times. The value of the thermal resistance R_{th} of the sensor is equal to the value of the directional coefficient of the straight line. For example, for a time of 50 s (red line) R_{th}=0.5461 °C/mW. Results for other sensors investigated will be presented during the conference.

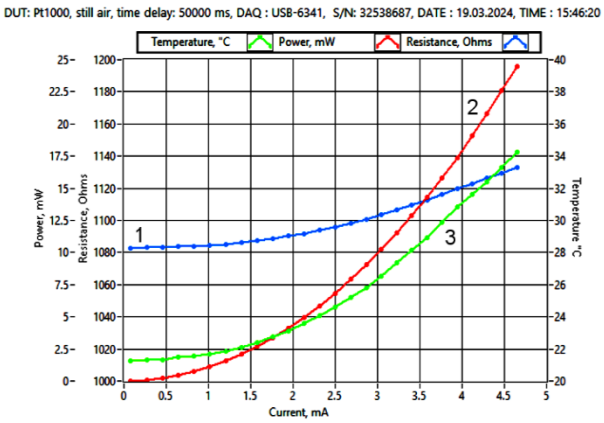

Fig. 3. Characteristic of the Pt1000 sensor obtained from measurements: 1 – resistance R_{sens} (blue), 2– heating power P_{th} (red), and 3 – sensor temperature T_{sens} (green), as a function of measurement current, delay time 50 s in still air.

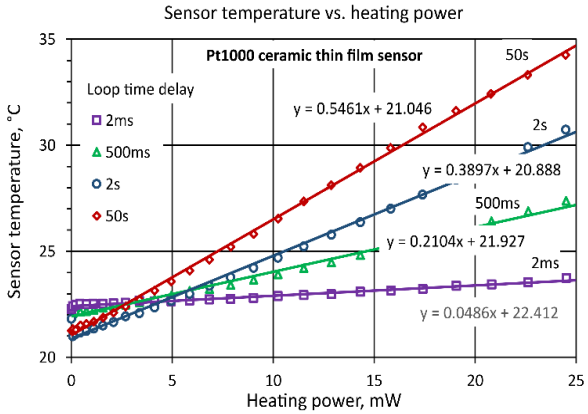

Fig. 4. Linear approximation of temperature dependence of sensor T_{sens} with respect to heating power P_{th}, delay time 2 ms, 500 ms, 2 s, 50 s, Pt1000 sensor in still air. The equation of the approximating straight line is shown.

4. Conclusion

This publication presents the developed measurement station together with a control application developed in the LabVIEW environment. The application allows automatic in-situ measurements of the thermal resistance of the sensor. Several IPRT sensors were investigated, which are often used in practice, but the self-heating effect of these sensors is sporadically reported in the literature [3]. According to the normative documents, calibration before testing is not required for this group of sensors. It is recommended to select the value of the measuring current in such a way that the effect of self-heating of the sensor does not exceed 25% of the tolerance value resulting from the declared tolerance of the sensor. At the same time, however, a higher measuring current provides greater accuracy in measuring the sensor resistance. Therefore, in order to correctly select the measuring current of the IPRT sensor, the thermal resistance of the sensor must be determined in-situ.

References

[1] International Standard IEC 60751:2022, Industrial platinum resistance thermometers and platinum temperature sensors, Edition 3.0, 2022-01.

[2] Otomański, P., Pawłowski, E., and Szlachta, A., (2023). Application of LabVIEW to Determine Characteristics of Two-Terminal Passive Components, In *14th International Conference on Measurement*, Slovakia, 305-308.

[3] Babita, et al., (2022). Evaluation of self-heating effect in platinum resistance thermometers. *Measurement* 203, 111994.

ISBN 978-80-69159-00-6

Realisation of New Primary Standard of Gas Flow

[1,2]Tomáš Valenta, [1,2]Jiří Tesař, [2]Jan Rybář, [2]Stanislav Ďuriš

[1]Czech Metrology Institute, Brno, Czech Republic
[2] Faculty of Mechanical Engineering, Slovak University of Technology, Bratislava, Slovakia
Email: tomas.valenta@cmi.gov.cz

Abstract. *This paper describes the process of developing a new national standard for gas flow in the Czech Republic. An important part is the result of a literature study on primary standards found in different laboratories of national metrology institutes around the world. The principles of operation, schematics and photographs of different types of primary standards and their usual range of flow rates and pressures are presented. In the following section the specification and detailed description of the selected type of primary standard is given. This primary standard is already under construction in the Czech Republic following the conclusions of literature study. In principle, it is a Bell Piston Prover with a planned flow range of 2 L/h to 2* m^3/h.

Keywords: primary standard, metrology, gas flow rate

1. Introduction

The gas flow measurement is one of the most important and widely used measurements of delivered media next to the measurement of liquid flow and electricity. Primary standards

Primary standards are the source of metrological traceability in the respective field of measurement and are often national standards. They are usually based on a physical principle. Below is a summary of the most commonly used primary standards in gas flow.

2. Materials and Methods

2.1 Equivalent Liquid Quantity Equipment (ELQE)

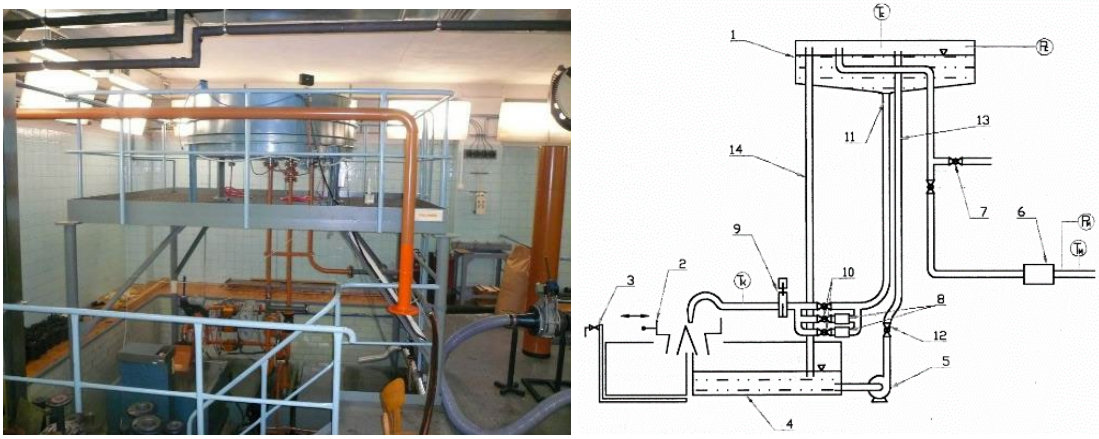

Fig. 1. Photograph and schematic drawing of Equivalent Liquide Quantity Equipment (ELQE) [1]

The basic design scheme of the ELQE, which serves as the national standard in the Czech Republic, is shown in Fig. 1 on the following page. The principle of determining the gas volume on this facility is based on the equality of the volume of liquid that is released from the tank and the volume of air that replaces the released liquid.

ISBN 978-80-69159-00-6

2.2 Bell Prover

A basic schematic drawing and a photo of the *Bell Prover*, that is a national standard in Czech Republic, is shown in Fig. 2 [1].

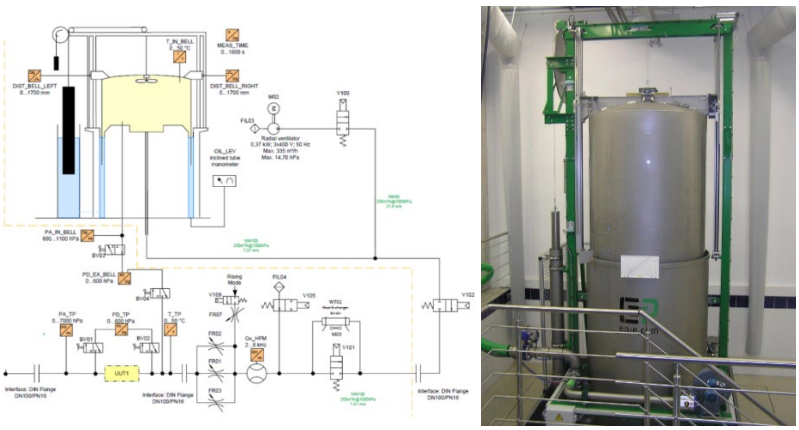

Fig. 2. Schematic drawing and photo of the Bell Prover [1]

For the new *Bell Provers*, the calculations are provided by the control software and are quite sophisticated, containing the calculation of the displaced volume according to the precise dimensional measurement of the bell in individual layers, including correction for the thermal expansion of the bell material, and calculating the air density at individual points of the test equipment.

2.3 Dynamic gravimetry flow standard (GFS)

The dynamic gravimetry flow standard (GFS) is a primary low-flow mass standard consisting of a dynamic gravimetric system [2]. The standard itself consists of a pressure vessel built on a precision electronic balance with an automated system for zeroing the balance, calibrating the balance and loading the cylinder (Fig. 3). These devices are typically used in the flow rate range (0.00006 - 0.3) m^3/h.

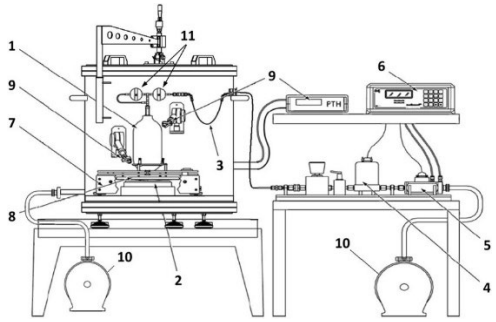

Fig. 3. Schematic diagram of a primary standard with low mass flow based on the dynamic gravimetric principle

2.4 Equipment based on PVTt method

The general principle of operation of a primary standard based on the measurement of pressure (*P*), volume (*V*), temperature (*T*) and time (*t*), referred to as "*PVTt*", is based on the determination of the change in density of the measured gas in a tank of known volume and a certain time interval.

ISBN 978-80-69159-00-6

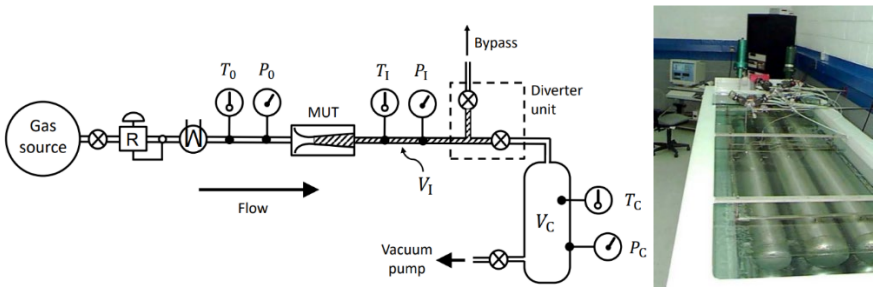

Fig. 4. Schematic diagram of PVTt device for injection mode and photo of PVTt equipment in NIST laboratory (USA) [4]

Due to the need to stabilize the tank temperature preferably at a constant value, the gas tank is often placed in a water tank (Fig. 4). The usual range of flow rates is from 0.2 m^3/h to 100 m^3/h.

2.5 Equipment based on piston method

It is a volumetric measuring principle, where a piston with a precisely defined effective area displaces the gas into the meter under test. The principle of measuring of a reference piston with "forced" motion is shown in Fig. 5.

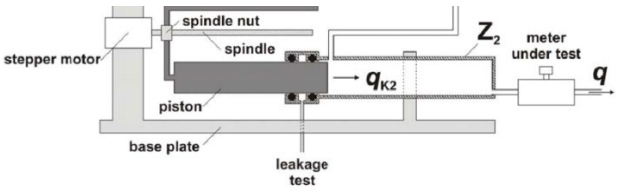

Fig. 5. Equipment based on piston method [5]

3. Building a new national standard BPP2 in CMI

The following paragraphs summarize the current state of the equipment in the gas flow laboratory in Czech Metrology Institute and specify the objective, what specifications the new primary standard should have.

3.1 Description of the initial state and selection

The existing national standard ELQE (*Equivalent Liquide Quantity Equipment*) was developed and built in principle already in 1980. Thus, it will be appropriate to build a new national standard ideally with a range of 0.002 m^3/h to 2 m^3/h.

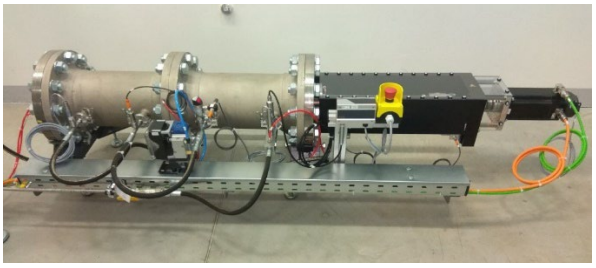

Fig. 6. Typical arrangement of a Bell-Piston Prover [6]

ISBN 978-80-69159-00-6

3.2 Specification of the new national standard BPP2

The basic element is a precisely dimensioned metal bell-piston, which is placed in a pressure resistant vessel and which displaces air into the meter under test during its horizontal movement. The piston is housed in a pressure vessel and is operated by a stepper motor and a ball screw spindle with a spindle nut. The flow range of the primary part of the *Bell-Piston Prover* (Fig. 6) should be from 0.002 m^3/h to 2 m^3/h with a measurement uncertainty $U(k=2) \leq 0.10$ % in the middle part of the measurement range. The principle was developed together with the *Physikalisch-Technische Bundesanstalt* (PTB), the national metrology institute in Germany.

4. Conclusions

The construction of a new primary standard based on the *Bell Piston Prover* principle will bring a significant improvement in the field of gas flow measurement. It will reduce the measurement uncertainty compared to the current situation and will place the Czech Metrology Institute among the laboratories with the lowest measurement uncertainty in the world that is approximately $U(k=2) \leq$ of 0.08 % It will also enable us to offer new services to many new customers.

Acknowledgements

The authors would like thank all the colleagues of the Slovak University of Technology in Bratislava (Faculty of Mechanical Engineering) and of Czech Metrology Institute, for providing consultations, study materials and for their support. We also thank the projects KEGA 024STU4/2023 (Building a laboratory of medical metrology), APVV-21-0195 (Research the possibility of digital transformation of continuous transport systems) and APVV-21-0216 (Advanced mathematical and statistical methods for measurement and metrology) for their support.

References

[1] Vančurová, K., Valenta, T. (14.11.2022). FINAL REPORT No. 0211-TR-Z0001-22 on the fulfilment of task No. UTR22B021101 Maintenance of National Standards [PRM No. II/1/22], Prague: Czech Metrology Institute, 222 p.

[2] Krajíček, Z., Pražák, D., Vičar, M., Tesař, J., Staněk, F. (2011). Ensuring the metrology of small gas flow - a new national standard for dynamic gravitometry - GFS. Metrology. Vol. 19, No. 1. p. 18-23

[3] Wright, J.D., Moldover, M.R., Johnson, A.N., Mizuno, A. (2003). Volumetric Gas Flow Standard with Uncertainty of 0.02 % to 0.05 %, ASME J. of Fluids Engineering, 125, p.1058-1066

[4] Wright, J., Johnson, A., Moldover, M. (2003). Design and Uncertainty Analysis for a PVTt Gas Flow Standard, Journal of Research (NIST JRES), National Institute of Standards and Technology, Gaithersburg, MD, USA

[5] Kramer, R., Mickan, B., Dopheide, D. (17.9-22.9. 2006). Double piston prover usable as flowrate comparator for various gases, XVIII IMEKO World Congress Metrology for a Sustainable Development September, Rio de Janeiro, Brazil

[6] Valenta, T., Actual photo of Bell Piston Prover located in the laboratory of Czech Metrology Institute, local inspectorate Pardubice, 10/2024

Relationship Between Errors of Thermoelectric Converters Due to Thermoelectric Inhomogeneity and Drift

[1,2]Orest Kochan, [2]Pavlo Hamula, [1]Su Jun, [3]Hongxing Bai, [1]Lingyu Yan, [3]Krzysztof Przystupa, [4,5]Roman Kobylianskyi
[1]Hubei university of Technology, Wuhan, China
[2]Lviv Polytechnic National University, Lviv, Ukraine,
[3]Lublin University of Technology, Lublin, Poland
[4]Hubei Galaxis Tongda Technology Co., Ltd, Wuhan, China
[5]Institute of Thermoelectricity of the NAS and MES of Ukraine, Chernivtsi, Ukraine;
[6]Yuriy Fedkovych Chernivtsi National University, Chernivtsi, Ukraine
orest.v.kochan@lpnu.ua

Abstract. *The interconnection between errors due to drift and due to inhomogeneity of thermocouples is considered in this paper. A mathematical model was developed to describe the process of developing a thermocouple electromotive force. A formula is derived to describe this interconnection, and modeling is carried out to prove the formula. It is shown that the sum of absolute values of errors due to drift and inhomogeneity is always equal.*

Keywords: *Thermocouple, Drift, Inhomogeneity.*

1. Introduction

The thermocouple (TC), is one of the most popular temperature sensors. The TC possesses several advantages, such as fast response time, wide temperature range, durability, low cost, reliability in harsh environments, robustness to vibrations, simple design, easy installation and maintenance, and high versatility. That is why it is used for measuring temperatures in industry, science, and commerce [1]. On the other hand, the TC has quite large errors; among the most significant errors are deviations of their conversion function (TC) from the nominal one, drift of conversion characteristics during long-term operation at high temperature, and acquired thermoelectric inhomogeneity (TIN) [2]. These errors are proper for all types of TCs. The most popular alloys for TCs were developed in the first half of the XX century. There were studies of new materials for TC to cope with these errors, but they are not widely used [3]. The TC operation is based on the Seebeck effect [1, 4], which can be given as

$$E = e \cdot \Delta t\,, \tag{1}$$

where E *(*measured in μV) is the thermo-electromotive force (henceforth emf) developed by the TC (or its section); e is the Seebeck coefficient of the TC leg's material, μV/°C; Δt is the temperature difference between the ends of the TC leg.

2. Results of the Studies and Discussion

There are four basic laws of thermoelectricity [4] for TCs: (i) The law of interior temperatures – the temperature distribution along the TC legs does not affect the developed by the TC emf. The developed emf is described by (1); (ii) The law of inserted metals – if two dissimilar metals form a circuit with two junctions at different temperatures, then inserting a third metal into the gap between one of the metals creates two new junctions. However, if the temperatures of these two new junctions are the same, then the developed emf of the circuit does not change; (iii) The law of

ISBN 978-80-69159-00-6

intermediate temperature – in a circuit made of two dissimilar homogeneous metals, whose ends have temperatures t_1 and t_2 ($t_1 \neq t_2$), a emf E_1 is developed. If the temperatures of these jumctions are t_2 and t_3, respectively, the developed emf is E_2. Then at the temperatures of these junctions of t_1 and t_3, respectively, the developed emf is $E_1 + E_2$; (iv) The law of summation of emf – if the Seebeck coefficients of two dissimilar metals with respect to a third metal are known, then the Seebeck coefficient of these two metals is equal to the algebraic sum of the mentioned Seebeck coefficients. The main source of error for the TC is TIN [2]. A long term operation at high temperatures leads to degradation of TC legs. For a section of TC that underwent degradation, (1) can be given as

$$E_i = (e + \Delta e_i)\Delta t_i, \tag{2}$$

where Δe_i is the change in the Seebeck coefficient of the TC section, Δt_i is the temperature drop across the section. Since the TC legs are exposed to different temperatures along their legs, each section has its own Δe_i (see Fig 1).

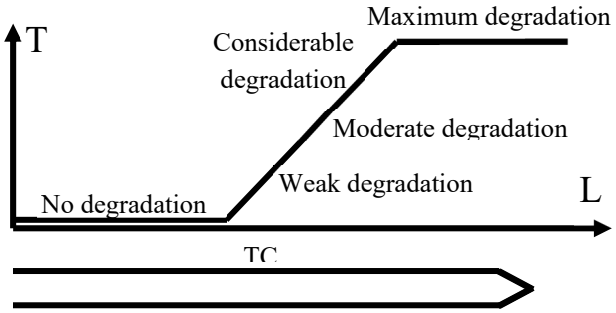

Fig. 1. Degradation patterns of TC sections with respect to operation temperature.

So, the total emf developed by the whole TC can be given as follows:

$$E = \sum_{i=1}^{n} (e + \Delta e_i)\Delta t_i \tag{3}$$

This can be rewritten when we consider total emf and infinitesimal length of sections as follows [2]:

$$E = \lim_{l \to 0} \sum_{i=1}^{n} (e + \Delta e_i)\Delta t_i = \int_0^L e(l)\frac{\partial l}{\partial t} dt \tag{4}$$

where l is the length of a section, $e(l)$ is the Seebeck coefficient as a function of coordinate, L is the total length of the TC. From (3) and (4) it is clear why the developed emf depends on the temperature distribution along TC legs – the contribution of each Δe_i changes with the change of temperature drop across a section. This contribution can be considerable. According to the sources mentioned in [2], it can be of the order of dozens of degrees when measuring temperatures about 800 °C or even more. That is why the four laws of thermoelectricity do not work well for inhomogeneous TCs. It is necessary to consider the properties of inhomogeneous TCs to show a considerable connection between errors due to drift and TIN that appear in such TCs. Thus, the goal of this paper is to theoretically derive the expression to describe the connection between these two errors. According to the definition, error due to drift is a gradual change of developed emf when the TC is under operation in a stable temperature field. It is determined as a difference between the emf

ISBN 978-80-69159-00-6

developed at a certain moment and that at the beginning of the operation. Error due to TIN appears when the temperature of the measuring and working junctions remains stable, but the temperature distribution along TC legs changes. In [5], it is shown that the maximum values of errors due to drift ΔE^{DR} and due to TIN ΔE_i^{TIN} for the TC used at high temperatures for a long time are equal. Such equality, for each combination of temperature T_{Ei} and operating time, τ_{Ei} corresponds to the limiting values of changes in the instantaneous temperature of a TC T_{Di}, i.e., for error due to drift, the change of the instantaneous temperature is zero $\Delta T_{Di} = 0$. For maximum error due to TIN, the change of the instantaneous temperature (the temperature at an instant of a certain measurement) must be maximum too, i.e. it is equal to the difference between the temperature of operation and the reference junctions temperature (for the sake of convenience, we assume it is 0 °C) $\Delta T_{Di} = T_{Ei}$. Then:

$$\Delta E_{MAX}^{DR}\left(T_{Ei},\ \tau_{Ei},\ \Delta T_{Di} = 0\right) = \Delta E_{MAX}^{NEOD}\left(T_{Ei},\ \tau_{Ei},\ \Delta T_{Di} = T_{Ei}\right). \tag{5}$$

Fig. 1 shows a TC, which, during stable operation, is located in the temperature field profile ABCD (to simplify the figure, the temperature fields are approximated by straight lines). The intensity of degradation processes depends on the temperature of stable operation [2], the maximum drift of the TC ΔE_{MAX}^{DR} will correspond to the section AB, i.e.

$$\Delta E_{AB}^{DR} = \Delta E_{MAX}^{DR}. \tag{6}$$

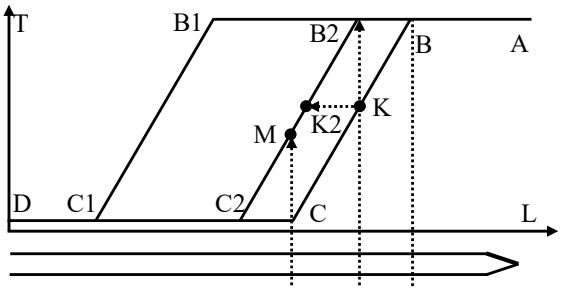

Fig. 2. Changes in the temperature field during operation of the TP

The maximum temperature change of an instantaneous temperature is $\Delta T_{Di} = T_{Ei}$. The section CD during long-term operation is at a temperature close to zero. Therefore, according to [2] its Seebeck coefficient does not change. The AB section changes its Seebeck coefficient maximally. But, according to law 2, this section does develop emf, for $T_A = T_B$. Therefore, only the BC section contributes, so only its Seebeck coefficient matters. Therefore, we can write:

$$\Delta E_{TC}^{DR} = \Delta E_{BC}^{DR} = \Delta E_{TC}^{MAX}, \tag{7}$$

where ΔE_{TC}^{DR} is TC error due to drift; ΔE_{BC}^{DR} is error due to drift of BC section only; ΔE_{TC}^{MAX} is the maximum error due to drift in operating conditions (temperature field ABCD). The emf E_{ABKCD} in temperature field ABKCD, according to the abovementioned third law of thermoelectricity can be written as follows:

$$E_{ABKCD} = E_{AB} + E_{BK} + E_{KC} + E_{CD}. \tag{8}$$

ISBN 978-80-69159-00-6

The of the emf in $E_{AB2K2MC2C1D}$ the temperature field A-B2-K2-M-C2-C1-D

$$E_{AB2K2MC2C1D} = E_{AB} + E_{BB2} + E_{B2K2} + E_{K2M} + E_{MC2} + E_{C2C1} + E_{C1D}. \quad (9)$$

There is an error due to TIN when the field of operation is ABKCD, and the measurement is carried out in the field A-B2-K2-M-C2-C1-D. From the text between formulae (2) and (5), it is clear that a change in the temperature field induces a change in the developed emf. According to [2] error due to inhomogeneity is equal to the difference between the emfs developed in the field operation and that in a certain field. We use the difference between the emf in a certain temperature field and that in the field of operation as a positive value of error due to inhomogeneity. This change can be found by subtracting (6) from (7). After some rearrangements, it can be written as

$$\Delta E^{NEOD}_{AB2K2CKC2C1D} = \Delta E_{CK} - \Delta E^{MAX}_{TC} = \Delta E_{CK} - \left(\Delta E_{BK} + \Delta E_{KC}\right) = -\Delta E_{BK} = -\Delta E^{DR}_{BK}, \quad (10)$$

Since point K was chosen arbitrarily, (9) can be generalized to [6]

$$\left|\Delta E^{NEOD}_{MAX}\right| = \left|\Delta E^{DR}_{MAX}\right| = \left|\Delta E^{NEOD}_{PROF-E}\right| + \left|\Delta E^{DR}_{PROF-E}\right|, \quad (11)$$

where the index PROF- E means that both errors belong to the same profile of the temperature field of operation. In other words, the sum of absolute values of errors due to drift and due to inhomogeneity remains constant in any temperature field, and this sum is equal to the absolute value of the maximum values of error due to drift and due to inhomogeneity. Modeling for different functional dependencies of Δe from the temperature of operation in different temperature fields confirms (11). One of the results is given in Fig. 3, where Δe was in the form of $\Delta e(t)=at+bt^2$ and the temperature fields were sigmoids with 0 °C for the reference junctions and 800 °C for the measuring junction.

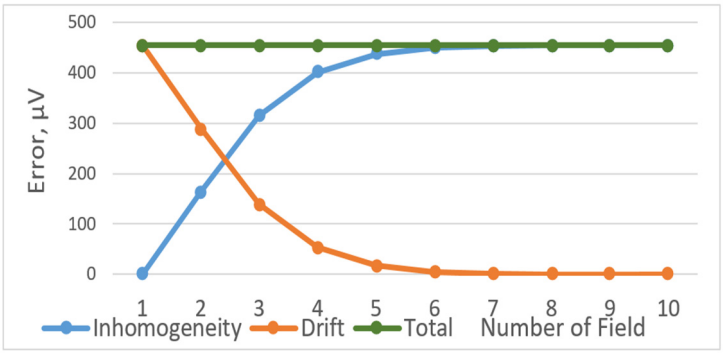

Fig. 3. Results of modeling

3. Conclusions.

In this paper, the process of the paper reveals a close relationship between errors due to drift and inhomogeneity of the TC, which can be expressed as a formula: the sum of absolute values of errors due to drift and due to inhomogeneity remains constant in any temperature field at any instant. This sum is equal to the absolute value of the maximum values of error due to drift and due to inhomogeneity. This relationship is confirmed during modeling.

References

[1] Webster, J. (1999). Measurement, instrumentation, and sensors handbook. CRCnetBase. https://shorturl.at/N3Cze

[2] Jun, S., Kochan, O. V., Jotsov, V. S. (2015). Methods of reducing the effect of the acquired thermoelectric inhomogeneity of thermocouples on temperature measurement error. Measurement Techniques, 58(3), 327–331.

[3] Pashkevych, V., et al. (2025). Research of sensitive elements of thermoelectric converters based on Hf1-xNbxNiSn. Measuring Equipment and Metrology, 86(1), 22-29.

[4] Park, R. M. (1993). *Manual on the use of thermocouples in temperature measurement*. ASTM International.

[5] Kochan, O. (2020) Methods and means for improving the accuracy of temperature measurement by thermoelectric transducers with inhomogeneous thermocouples. Dissertation of doctor of sciences. https://shorturl.at/z3rAI

[6] Kochan, O. (2024). Interconnection between errors due to drift and due to inhomogeneity of thermoelectric converters. Proceedings of the II International Conference “Information-measuring technologies”, Lviv, 13-14 November 2024, pp. 32-33 (in Ukrainian). https://shorturl.at/JPw7F

AUTHORS INDEX

ISBN 978-80-69159-00-6

ISBN 978-80-69159-00-6

ISBN 978-80-69159-00-6

Institute of Measurement Science
Slovak Academy of Sciences
Dúbravská cesta 9
841 04 Bratislava, Slovakia